frontiers
RESEARCH TOPICS

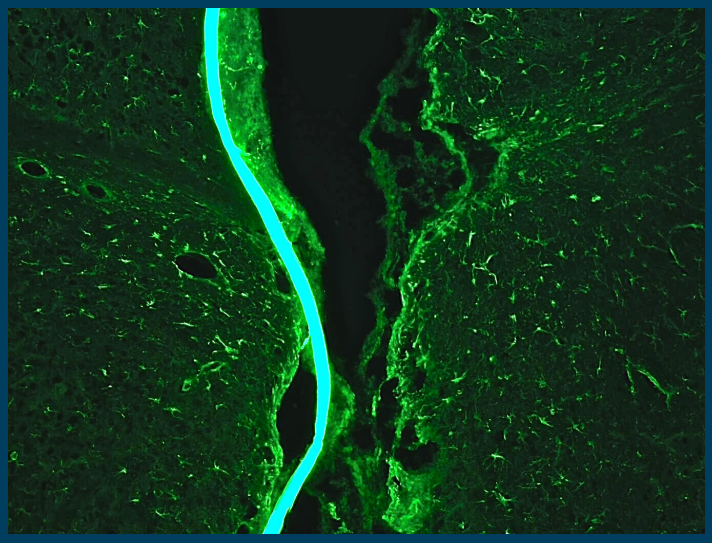

THE CHRONIC CHALLENGE - NEW VISTAS ON LONG-TERM MULTISITE CONTACTS TO THE CENTRAL NERVOUS SYSTEM

Topic Editors
Ulrich G. Hofmann and Jürgen Krüger

frontiers in
NEUROENGINEERING

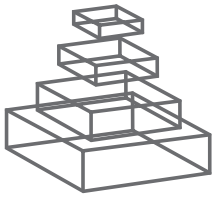

frontiers

ISSN 1664-8714
ISBN 978-2-88919-508-4
DOI 10.3389/978-2-88919-508-4

ABOUT FRONTIERS

Frontiers is more than just an open-access publisher of scholarly articles: it is a pioneering approach to the world of academia, radically improving the way scholarly research is managed. The grand vision of Frontiers is a world where all people have an equal opportunity to seek, share and generate knowledge. Frontiers provides immediate and permanent online open access to all its publications, but this alone is not enough to realize our grand goals.

FRONTIERS JOURNAL SERIES

The Frontiers Journal Series is a multi-tier and interdisciplinary set of open-access, online journals, promising a paradigm shift from the current review, selection and dissemination processes in academic publishing.
All Frontiers journals are driven by researchers for researchers; therefore, they constitute a service to the scholarly community. At the same time, the Frontiers Journal Series operates on a revolutionary invention, the tiered publishing system, initially addressing specific communities of scholars, and gradually climbing up to broader public understanding, thus serving the interests of the lay society, too.

DEDICATION TO QUALITY

Each Frontiers article is a landmark of the highest quality, thanks to genuinely collaborative interactions between authors and review editors, who include some of the world's best academicians. Research must be certified by peers before entering a stream of knowledge that may eventually reach the public - and shape society; therefore, Frontiers only applies the most rigorous and unbiased reviews.
Frontiers revolutionizes research publishing by freely delivering the most outstanding research, evaluated with no bias from both the academic and social point of view.
By applying the most advanced information technologies, Frontiers is catapulting scholarly publishing into a new generation.

WHAT ARE FRONTIERS RESEARCH TOPICS?

Frontiers Research Topics are very popular trademarks of the Frontiers Journals Series: they are collections of at least ten articles, all centered on a particular subject. With their unique mix of varied contributions from Original Research to Review Articles, Frontiers Research Topics unify the most influential researchers, the latest key findings and historical advances in a hot research area!
Find out more on how to host your own Frontiers Research Topic or contribute to one as an author by contacting the Frontiers Editorial Office: researchtopics@frontiersin.org

THE CHRONIC CHALLENGE - NEW VISTAS ON LONG-TERM MULTISITE CONTACTS TO THE CENTRAL NERVOUS SYSTEM

Topic Editors:
Ulrich G. Hofmann, Albert Ludwigs University of Freiburg and Cluster of Excellence "BrainLinks-BrainTools", Germany
Jürgen Krüger, AG Hirnforschung, Germany

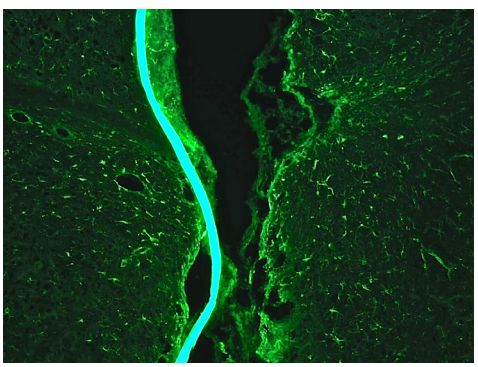

Sagittal slice of a rat brain with a flexible polyimide multisite probe in situ, implanted for 12 weeks. Immunostained glial fibrillary acidic protein (GFAP) labeled with Alexa Fluro 488. Picture by Nadja Martini and Yijing Xie, University of Freiburg, Freiburg.

Have you ever heard of a Hype-Cycle? It is a description that was put forward by an IT consultancy firm to describe certain phenomena that happen within the life cycle of new technology products. As Fenn and Raskino stated in their book (Fenn and Raskino 2008), a novel technology - a "Technology Trigger" - gives rise to a steep increase in interest, leading to the "Peak of Inflated Expectations". Following an accumulation of more detailed knowledge on the technology and its short-comings, the stake holders may need to traverse a "Trough of Disillusionment", which is followed by a shallower "Slope of Enlightenment", before finally reaching the "Plateau of Productivity".

In spite of the limitations and criticisms levied on this over-simplified description of a technology's life-cycle, it is nonetheless able to describe well the situation we are all experiencing within the brain-machine-interfacing community. Our technology trigger was the development of batch-processed multisite neuronal interfaces based on silicon during the 1980s and 1990s (Sangler and Wise 1990, Campbell, Jones et al. 1991, Wise and Najafi 1991, Rousche and Normann 1992, Nordhausen, Maynard et al. 1996). This gave rise to a seemingly exponential growth of knowledge within the neurosciences, leading to the expectation of thought-controlled devices and prostheses for handicapped people in the very near future (Chapin, Moxon et al. 1999, Wessberg, Stambaugh et al. 2000, Chapin and Moxon 2001, Serruya, Hatsopoulos et al. 2002). Unfortunately, whereas significant steps towards artificial robotic limbs could have been implemented during

the last decade (Johannes, Bigelow et al. 2011, Oung, Pohl et al. 2012, Belter, Segil et al. 2013), direct invasive intracortical interfacing was not quite able to keep up with these expectations. Insofar, we are currently facing the challenging, but tedious walk through the Trough of Disillusionment.

Undoubtedly, more than two decades of intense research on brain-machine-interfaces (BMI's) have produced a tremendous wealth of information towards the ultimate goal: a clinically useful cortical prosthesis. Unfortunately even today - after huge fiscal efforts - the goal seems almost to be as far away as it was when it was originally put forward. At the very least, we have to state that one of the main challenges towards a clinical useful BMI has not been sufficiently answered yet, regarding the long term – or even truly chronic – stability of the neural cortical interface, as well as the signals it has to provide over a significant fraction of a human's lifespan. Even the recently demonstrated advances in BMI's in both humans and non-human primates have to deal with a severe decay of spiking activity that occurs over weeks and months (Chestek, Gilja et al. 2011, Hochberg, Bacher et al. 2012, Collinger, Kryger et al. 2014, Nuyujukian, Kao et al. 2014, Stavisky, Kao et al. 2014, Wodlinger, Downey et al. 2014) and resolve to simplified features to keep a brain-derived communication channel open (Christie, Tat et al. 2014).

References:

Belter, J. T., J. L. Segil, A. M. Dollar and Richard F Weir (2013). "Mechanical design and performance specifications of anthropomorphic prosthetic hands: A review." J Rehab Res & Dev (JRRD) 50(5): 599-618.

Campbell, P. K., K. E. Jones, R. J. Huber, K. W. Horch and R. A. Normann (1991). "A Silicon Based Three Dimensional Neural Interface: Manufacturing Processes for an Intracortical Electrode Array." IEEE Trans. Biomed. Eng. 38: 758-768.

Chapin, J. K. and K. A. Moxon (2001). Neural prosthesis for restauration of sensory and motor function. Boca Raton, CRC Press.

Chapin, J. K., K. A. Moxon, R. S. Markowitz and M. A. L. Nicolelis (1999). "Real-time control of a robot arm using simultaneously recorded neurons in the motor cortex." Nature Neuroscience 2: 664-670.

Chestek, C. A., V. Gilja, P. Nuyujukian, J. D. Foster, J. M. Fan, M. T. Kaufman, M. M. Churchland, Z. Rivera-Alvidrez, J. P. Cunningham, S. I. Ryu and K. V. Shenoy (2011). "Long-term stability of neural prosthetic control signals from silicon cortical arrays in rhesus macaque motor cortex." J Neural Eng 8(4): 045005.

Christie, B. P., D. M. Tat, Z. T. Irwin, V. Gilja, P. Nuyujukian, J. D. Foster, S. I. Ryu, K. V. Shenoy, D. E. Thompson and C. A. Chestek (2014). "Comparison of spike sorting and thresholding of voltage waveforms for intracortical brain-machine interface performance." J Neural Eng 12(1): 016009.

Collinger, J. L., M. A. Kryger, R. Barbara, T. Betler, K. Bowsher, E. H. Brown, S. T. Clanton, A. D. Degenhart, S. T. Foldes, R. A. Gaunt, F. E. Gyulai, E. A. Harchick, D. Harrington, J. B. Helder, T. Hemmes, M. S. Johannes, K. D. Katyal, G. S. Ling, A. J. McMorland, K. Palko, M. P. Para, J. Scheuermann, A. B. Schwartz, E. R. Skidmore, F. Solzbacher, A. V. Srikameswaran, D. P. Swanson, S. Swetz, E. C. Tyler-Kabara, M. Velliste, W. Wang, D. J. Weber, B. Wodlinger and M. L. Boninger (2014). "Collaborative approach in the development of high-performance brain-computer interfaces for a neuroprosthetic arm: translation from animal models to human control." Clin Transl Sci 7(1): 52-59.

Fenn, J. and M. Raskino (2008). Mastering the Hype Cycle - How to Choose the Right Innovation at the Right Time. Boston, MA, Harvard Business Press.

Hochberg, L. R., D. Bacher, B. Jarosiewicz, N. Y. Masse, J. D. Simeral, J. Vogel, S. Haddadin, J. Liu, S. S. Cash, P. van der Smagt and J. P. Donoghue (2012). "Reach and grasp by people with tetraplegia using a neurally controlled robotic arm." Nature 485(7398): 372-375.

Johannes, M. S., J. D. Bigelow, J. M. Burck, S. D. Harshbarger, M. V. Kozlowski and h. V. Doren (2011). "An Overview of the Developmental Process for the Modular Prosthetic Limb." JOHNS HOPKINS APL TECHNICAL DIGEST 30(3): 207-216.

Nordhausen, C. T., E. M. Maynard and R. A. Normann (1996). "Single unit recording capabilities of a 100 microelectrode array." Brain Res. 726: 129-140.

Nuyujukian, P., J. C. Kao, J. M. Fan, S. D. Stavisky, S. I. Ryu and K. V. Shenoy (2014). "Performance sustaining intracortical neural prostheses." J Neural Eng 11(6): 066003.

Oung, S., B. M. Pohl and U. G. Hofmann (2012). Preliminary design of a tendon-based anthropomorphic robotic hand. Biomed Tech. O. Dössel. Jena, Walter de Gruyter. 57 (Suppl 1): 934-937.

Rousche, P. J. and R. A. Normann (1992). "A method for pneumatically inserting an array of penetrating electrodes into cortical tissue." Ann. Biomed. Eng. 20: 413-422.

Sangler, L. J. and K. D. Wise (1990). "A bulk silicon SOI process for active integrated sensors." SENSORS AND ACTUATORS A-PHYSICAL 24(2): 117-122.

Serruya, M., N. Hatsopoulos, L. Paninski, M. Fellows and J. Donoghue (2002). "Instant neural control of a movement signal." Nature 416: 141-142.

Stavisky, S. D., J. C. Kao, P. Nuyujukian, S. I. Ryu and K. V. Shenoy (2014). Hybrid Decoding of Both Spikes and Low-Frequency Local Field Potentials for Brain-Machine Interfaces. IEEE EMBS, Chicago, IEEE.

Wessberg, J., C. R. Stambaugh, J. D. Kralik, P. D. Beck, M. Laubach, J. K. Chapin, J. Kim, S. J. Biggs, M. A. Srinivasan and M. A. L. Nicolelis (2000). "Real-time prediction of hand trajectory by ensembles of cortical neurons in primates." Nature 408: 361 - 365.

Wise, K. D. and K. Najafi (1991). "Microfabrication techniques for integrated sensors and microsystems." Science 254: 1335 - 1342.

Wodlinger, B., J. E. Downey, E. C. Tyler-Kabara, A. B. Schwartz, M. L. Boninger and J. L. Collinger (2014). "Ten-dimensional anthropomorphic arm control in a human brain-machine interface: difficulties, solutions, and limitations." J Neural Eng 12(1): 016011.

Table of Contents

frontiers in Neuroengineering

EDITORIAL
published: 18 March 2015
doi: 10.3389/fneng.2015.00003

The chronic challenge—new vistas on long-term multisite contacts to the central nervous system

Ulrich G. Hofmann[1,2]* *and Jürgen Krüger*[3]

[1] Section for Neuroelectronic Systems, Clinic for Neurosurgery, Albert-Ludwigs-University Freiburg, Freiburg, Germany, [2] Cluster of Excellence "BrainLinks-BrainTools" EXC 1086, Freiburg, Germany, [3] AG Hirnforschung, Universität Freiburg, Freiburg, Germany

Keywords: multisite neuronal recording, gliosis, indwelling implants, compliance match hypothesis, flexible microprobes, hydrogel coating, polymeric microelectrodes

This Special Research Topic at hand is a collection of contributions from eminent research groups shedding light on several aspects of the still unresolved problem of a truly chronic cortical interface to enable long term brain-machine interfacing to human patients.

The hypothesis article of Fernandez et al. (2014) adds to the three generally agreed-on features for biocompatibility (bio-safety, bio-stability, and bio-functionality) with a fourth one that mirrors the demand for "bio-tolerability." Sommakia et al. (2014a) study aims to reduce the almost-immediate adsorption of non-cellular tissue components upon insertion by dip-coating polyethylene glycol (PEG) as a "stealth" cover. It points toward a beneficial alteration of adsorption on the probe, but cautions PEG's immediate use for long term implants in the brain. In fact, in a second contribution based on a mixed-brain culture (Sommakia et al., 2014b), they show evidence for a complex response of glia cells on micro-wires dip-coated with PEG and/or lipopolysaccharides (LPS), but not of neurons, which is somewhat contradictory to pure *in vivo* findings.

In the same context of passive probe coatings, De Faveri et al. (2014) moved toward a more "natural" method by coating glass-insulated micro-wires with fibrin hydrogel, as a biological cushion between brain and probe. Using immunofluorescence techniques, they were able to demonstrate a beneficial effect on longer term astrocytic responses and successful encapsulation of brain cells in fibrin as in Richter (2012).

Beyond the modulatory effects of passive surface coatings, two articles review organic coatings for micro-contacts in the nervous system. The contribution by Asplund et al. (2014) concisely reviews electrodes based on conductive polymers, not only for improving site-tissue coupling, but also for electrically eluting anti-inflammatory drugs using various stimulation patterns. They go to great depth on how to apply this elution process to a living being, since the active elution technique inherently requires compliance with demanding bio-compatibility issues.

The review of Aregueta-Robles et al. (2014) addresses the topic of organic and nanoscopic coatings with a wider perspective, and thus provides an excellent overview regarding a huge variety of the various reported approaches including the "living electrode" of Ochiai et al. (1980) and their adaptation by Richter et al. (2010, 2011).

Extending the time frame of all above mentioned studies, Prasad et al. (2014) investigate whether the brain's foreign body response is the sole cause for poor electrode yield using Pt/Ir micro wire arrays. They state that leading aspects include the suboptimal construction of the micro wires, as well as the severing of the blood brain barrier upon insertion. In order to achieve a deeper insight into the suboptimal micro array construction, another study of the same group (Sankar et al., 2014) analyses long-term impedance spectra using FEM simulation, and concludes that the initial increase in electrode-tissue impedance *in vivo* can be attributed

Edited and reviewed by:
Laura Ballerini, University of Trieste, Italy

***Correspondence:**
Ulrich G. Hofmann, ulrich.hofmann@coregen.uni-freiburg.de

***Received:** 18 February 2015*
***Accepted:** 27 February 2015*
***Published:** 18 March 2015*

Citation:
Hofmann UG and Krüger J (2015) The chronic challenge—new vistas on long-term multisite contacts to the central nervous system. Front. Neuroeng. 8:3. doi: 10.3389/fneng.2015.00003

to cell attachment and gliosis on the micro wires. Furthermore they show that the long-term decrease is probably caused by de-lamination and cracks in the wire's insulation layer.

Even though the contribution of Castagnola et al. (2014) discusses the use of nano materials for improving the signal quality from brain micro-recordings as well, its main theme is the interpretation of the so called "compliance match hypothesis" (Stieglitz and Meyer, 1999) by making cortical interfaces softer reducing the permanent mismatch between rigid micro probes and the brain's softness. Obviously, comparing elastic moduli of brain and probe materials reveals a discrepancy of several orders of magnitude, and so the positive evidence of De Faveri et al. (2014) may be based on a compliance adaptation between both due to the fibrin layer. However, Castagnola et al. (2014) as well as Richter et al. (2013), Sohal et al. (2014) and Xie et al. (2014) all use substrate materials for their multisite arrays, which are still far away from brain's bulk modulus. More importantly, they are flexible ("soft" when compared to brain tissue) due to their geometrical setup. We hypothesize that this flexibility might be the reason for Krüger's 7 year recording record in the non-human primate using ultra-thin metal wires (Krüger et al., 2010). Castagnola et al. (2014) approaches a similar goal by electro-depositing microscopic spheres at the working end of very thin wires—intended for subarachnoidal recordings. Sohal et al. (2014) in contrast, intracortically implants a geometrically "wavy" structure and shows evidence for good recordings from a limited number of animals for up to 2 years. The histological findings from their and Richter's thin multisite implants depict a reduced gliosis, and thus corroborates the need for a matching compliance and intracortical softness. Richter's probes are made from polyimide (Rubehn et al., 2010), and they explain in detail how to implant them with help of a simple removable support.

This removable support in turn provides additional value, as Xie et al. (2014) state. Their use of label-free, endoscopic, *in vivo* Optical Coherence Tomography by the very same fiber supporting implantation demonstrates the first optical online monitoring of deep indwelling processes. This method may provide new vistas on the traditional problem of foreign body response, and may therefore shorten the time we have to spend in the Trough of Disillusionment.

Whatever effort is required, and whichever ideas will finally prove optimal for reaching the Plateau of Productivity for brain-machine interfaces, we are thankful that the need for biotolerability and reliability of brain implants over a substantial period of time, has already sunk into the community. Eleryan et al.'s (2014) single neuronal signal tracking method demonstrates this spirit of pro-active optimism by providing a highly valuable algorithm for following the progress of an individual neuron's participation in information processing.

This Special Research Topic's collection won't be the final word with respect to chronic implants, but for now it sets a road-sign toward truly stable neuro-cortical interfaces that lie on the horizon.

Acknowledgments

We are indebted to Dr. Richard C. Pinnell for making our manuscript comprehensible.

References

Aregueta-Robles, U. A., Woolley, A. J., Poole-Warren, L. A., Lovell, N. H., and Green, R. A. (2014). Organic electrode coatings for next-generation neural interfaces. *Front. Neuroeng.* 7:15. doi: 10.3389/fneng.2014.00015

Asplund, M., Boehler, C., and Stieglitz, T. (2014). Anti-inflammatory polymer electrodes for glial scar treatment: bringing the conceptual idea to future results. *Front. Neuroeng.* 7:9. doi: 10.3389/fneng.2014.00009

Castagnola, E., Ansaldo, A., Maggiolini, E., Ius, T., Skrap, M., Ricci, D., et al. (2014). Smaller, softer, lower-impedance electrodes for human neuroprosthesis: a pragmatic approach. *Front. Neuroeng.* 7:8. doi: 10.3389/fneng.2014.00008

De Faveri, S., Maggiolini, E., Miele, E., De Angelis, F., Cesca, F., Benfenati, F., et al. (2014). Bio-inspired hybrid microelectrodes: a hybrid solution to improve long-term performance of chronic intracortical implants. *Front. Neuroeng.* 7:7. doi: 10.3389/fneng.2014.00007

Eleryan, A., Vaidya, M., Southerland, J., Badreldin, I. S., Balasubramanian, K., Fagg, A. H., et al. (2014). Tracking single units in chronic, large scale, neural recordings for brain machine interface applications. *Front. Neuroeng.* 7:23. doi: 10.3389/fneng.2014.00023

Fernandez, E., Greger, B., House, P. A., Aranda, I., Botella, C., Albisua, J., et al. (2014). Acute human brain responses to intracortical microelectrode arrays: challenges and future prospects. *Front. Neuroeng.* 7:24. doi: 10.3389/fneng.2014.00024

Krüger, J., Caruana, F., Dalla Volta, R., and Rizzolatti, G. (2010). Seven years of recording from monkey cortex with a chronically implanted multiple microelectrode. *Front. Neuroeng.* 3:6. doi: 10.3389/fneng.2010.00006

Ochiai, H., Shibata, H., Sawa, Y., and Katoh, T. (1980). "Living electrode" as a long-lived photoconverter for biophotolysis of water. *Proc. Natl. Acad. Sci. U.S.A.* 77, 2442–2444.

Prasad, A., Xue, Q.-S., Dieme, R., Sankar, V., Mayrand, R. C., Nishida, T., et al. (2014). Abiotic-biotic characterization of Pt/Ir microelectrode arrays in chronic implants. *Front. Neuroeng.* 7:2. doi: 10.3389/fneng.2014.0000

Richter, A. (2012). *Biologisierung Tiefenhirn-Stimulierender Implantate Durch Besiedelung Mit Adulten Glandulären Stammzellen*. Ph.D. thesis, University of Lübeck.

Richter, A., Danner, S., Kruse, C., and Hofmann, U. G. (2010). Applying controlled shear stress on cell covered microprobes. *Biomed. Tech.* 55(Supp. 1), 4. doi: 10.1515/BMT.2010.678

Richter, A., Kruse, C., Moser, A., Hofmann, U. G., and Danner, S. (2011). Cellular modulation of polymeric device surfaces: promise of adult stem cells for neuro-prosthetics. *Front. Neurosci.* 5:114. doi: 10.3389/fnins.2011.0011

Richter, A., Xie, Y., Schumacher, A., Löffler, S., Kirch, R. D., Al-Hasani, J., et al. (2013). A simple implantation method for flexible, multisite microelectrodes into rat brains. *Front. Neuroeng.* 6:6. doi: 10.3389/fneng.2013.00006

Rubehn, B., Lewis, C., Fries, P., and Stieglitz, T. A. (2010). "Flexible shaft electrodes for transdural implantation and chronic recording," in *Proceedings of the 15th Annual Conference of the IFESS*, (Vienna: IFMBE), 4.

Sankar, V., Patrick, E., Dieme, R., Sanchez, J. C., Prasad, A., and Nishida, T. (2014). Electrode impedance analysis of chronic tungsten microwire neural implants: understanding abiotic vs. biotic contributions. *Front. Neuroeng.* 7:13. doi: 10.3389/fneng.2014.00013

Sohal, H. S., Jackson, A., Jackson, R., Clowry, G. J., Vassilevski, K., O'Neill, A., et al. (2014). The sinusoidal probe: a new approach to improve electrode longevity. *Front. Neuroeng.* 7:10. doi: 10.3389/fneng.2014.00010

Sommakia, S., Gaire, J., Rickus, J. L., and Otto, K. J. (2014a). Resistive and reactive changes to the impedance of intracortical microelectrodes can be mitigated with polyethylene glycol under acute in vitro and in vivo settings. *Front. Neuroeng.* 7:33. doi: 10.3389/fneng.2014.00033

Sommakia, S., Rickus, J. L., and Otto, K. J. (2014b). Glial cells, but not neurons, exhibit a controllable response to a localized inflammatory microenvironment in vitro. *Front. Neuroeng.* 7:41. doi: 10.3389/fneng.2014.00041

Stieglitz, T., and Meyer, J. U. (1999). Implantable microsystems. Polyimide-based neuroprostheses for interfacing nerves. *Med. Device Technol.* 10, 28–30.

Xie, Y., Martini, N., Hassler, C., Kirch, R. D., Stieglitz, T., Seifert, A., et al. (2014). *In vivo* monitoring of glial scar proliferation on chronically implanted neural electrodes by fiber optical coherence tomography. *Front. Neuroeng.* 7:34. doi: 10.3389/fneng.2014.00034

Conflict of Interest Statement: The authors declare that the research was conducted in the absence of any commercial or financial relationships that could be construed as a potential conflict of interest.

frontiers in
NEUROENGINEERING

HYPOTHESIS AND THEORY ARTICLE
published: 21 July 2014
doi: 10.3389/fneng.2014.00024

Acute human brain responses to intracortical microelectrode arrays: challenges and future prospects

Eduardo Fernández[1,2]*, Bradley Greger[3], Paul A. House[4], Ignacio Aranda[5], Carlos Botella[6], Julio Albisua[7], Cristina Soto-Sánchez[1,2], Arantxa Alfaro[1,2] and Richard A. Normann[8]

[1] Bioengineering Institute, Miguel Hernández University of Elche, Elche, Spain
[2] CIBER-BBN, Zaragoza, Spain
[3] School of Biological and Health Systems Engineering, Arizona State University, Tempe, AZ, USA
[4] Department of Neurosurgery, University of Utah, Salt Lake City, UT, USA
[5] Department of Pathology, Hospital General Universitario, Alicante, Spain
[6] Department of Neurosurgery, Hospital La Fe, Valencia, Spain
[7] Department of Neurosurgery, Fundación Jimenez Díaz and Hospital Rey Juan Carlos, Madrid, Spain
[8] Department of Bioengineering, University of Utah, Salt Lake City, UT, USA

Edited by:
Ulrich G. Hofmann, University of Freiburg, Germany

Reviewed by:
Winnie Jensen, Aalborg University, Denmark
Tobias Holzhammer, ATLAS Neuroengineering, Belgium

***Correspondence:**
Eduardo Fernández, Bioengineering Institute, Miguel Hernández University of Elche, Avda. Universidad s/n, Elche 03202, Spain
e-mail: e.fernandez@umh.es

The emerging field of neuroprosthetics is focused on the development of new therapeutic interventions that will be able to restore some lost neural function by selective electrical stimulation or by harnessing activity recorded from populations of neurons. As more and more patients benefit from these approaches, the interest in neural interfaces has grown significantly and a new generation of penetrating microelectrode arrays are providing unprecedented access to the neurons of the central nervous system (CNS). These microelectrodes have active tip dimensions that are similar in size to neurons and because they penetrate the nervous system, they provide selective access to these cells (within a few microns). However, the very long-term viability of chronically implanted microelectrodes and the capability of recording the same spiking activity over long time periods still remain to be established and confirmed in human studies. Here we review the main responses to acute implantation of microelectrode arrays, and emphasize that it will become essential to control the neural tissue damage induced by these intracortical microelectrodes in order to achieve the high clinical potentials accompanying this technology.

Keywords: neural prosthesis, intracortical microelectrode, *in vivo* recording, biocompatibility, neurosurgery

INTRODUCTION

Since 1990, the field of neuroprosthetics has grown at an ever increasing rate. Although current research is also pursuing non-invasive techniques to acquire signals from the human brain, important scientific and clinical information has been gained from *in vivo* experiments with microelectrode arrays able to record or stimulate the nervous system with the aim of improving or replacing motor or sensory abilities that have been lost due to disease or injury. For example, auditory brainstem implants are being used to restore auditory function (Merkus et al., 2014); deep brain stimulators have been implanted successfully in patients for control of motor disorders, tremor, dystonia and chronic pain (Beitz, 2014; Nardone et al., 2014) and micro-array type devices have been implanted in artificial vision systems (Grill et al., 2009; Hatsopoulos and Donoghue, 2009; Normann et al., 2009; Fernandez and Hofmann, 2011). Moreover advances in prosthetic limbs and brain-machine interfaces are now providing hope of increased mobility and independence for amputees and paralyzed patients (Raspopovic et al., 2014) and intracortical micro-electrodes are being used to study epileptiform discharges in cases of intractable epilepsy (Weiss et al., 2013a,b). As more and more patients have benefited from this approach, the interest in neural interfaces has grown significantly and a new generation of penetrating microelectrode arrays are providing unprecedented access to the neurons of the central nervous system (CNS).

These studies have shown the utility of microelectrode recordings to resolve neural activity at the single neuron level and to interpret brain derived commands for fine-grained control of movements and translation of these signals into command signals that are able to control external devices (Hochberg et al., 2006; Andersen et al., 2010; Rao and Donoghue, 2014). However most penetrating microelectrode arrays currently have maximum *in vivo* lifetimes from several months to a few years (Suner et al., 2005; Prasad et al., 2012; Barrese et al., 2013). Therefore much work still needs to be done before these penetrating microelectrodes can be used for many clinical purposes. In this work we focused on the acute effects of implantation of penetrating microelectrode arrays in the human brain, emphasizing the relevance of surgical techniques and biocompatibility approaches to control the neural tissue damage induced by these intracortical probes in order

to achieve the therapeutic benefits envisioned by these neural interfaces.

CURRENT MULTIELECTRODE-ARRAY TECHNOLOGIES

Technology partially achieved during the development of cardiac pacemakers has been successfully used in many other applications of implanted neural prostheses. During these years great efforts have been made to develop penetrating multi-electrode arrays with dimensions similar to the cortical neurons they target for recording or stimulation and that are able to maintain a stable signal in the CNS. The two main dominant approaches are multiple insulated metal microwires (Nicolelis and Lebedev, 2009; Freire et al., 2011; Carmena, 2013) and penetrating microelectrode arrays fabricated with micro-electro-mechanical-system technologies. These devices use various substrate materials that can either be flexible and based on polymers (Rousche et al., 2001; Chen et al., 2009; Kozai and Kipke, 2009; Hassler et al., 2011) or rigid such as the Utah Electrode Array (UEA; Normann, 2007), the Michigan array (Seymour and Kipke, 2007) or the NeuroProbes arrays (Neves, 2007; Calixto et al., 2013). However today, only a few of these devices are commercially available and do not yet exist as commercial, wireless, implantable, many-channel devices that can provide reliable recording and stimulation for many years.

An ideal neural interface would consist of an array containing many microelectrodes, which can "listen" and "talk" to still-functioning parts of the brain enabling bi-directional communication with ensembles of neurons. Each microelectrode would either record the electrical activity of a small population of neurons surrounding it or, when electrical current is passed through the electrode, activate small population of neurons. This approach has been difficult to realize because of the acute and chronic inflammatory reactions that can induce significant changes at the brain-electrode interface. Thus all neural probes need a stable electronic/neural interface that enables selective recording and/or activation of specific groups of neurons without deterioration of the electrodes or surrounding neural tissue. Consequently three areas have to be considered: the "*biosafety*", the "*biofunctionality*" and the "*biostability*" of the devices. Biosafety means that the microelectrodes do not harm the brain tissue in any significant way, biofunctionality is related to the ability of the microelectrodes to perform their intended function, and biostability means that the whole microelectrode array must not be susceptible to attack of biological fluids, proteases, macrophages or any metabolic byproducts (Marin and Fernandez, 2010). In addition successful devices should manifest "biotolerability" or the ability of the multielectrode-array to reside in the CNS for long periods of time. All these considerations impose extreme demands on stability and function of neural implants and place unique constraints on the architecture, materials, and surgical techniques used in the application of intracortical microelectrodes.

SURGICAL PROCEDURES FOR IMPLANTATION OF INTRACORTICAL MICROELECTRODES ARRAYS

Microelectrode arrays aimed to simultaneously record or stimulate neuronal populations have been successfully used in many animal models including non-human primates (Normann, 2007). However the only intracortical microelectrode array that has been FDA approved for long-term human studies is the UEA (Nordhausen et al., 1996). This microelectrode array consists of 100 small diameter silicon microneedles, built on a square grid with 400 μm spacing, that were designed to be inserted into the cerebral cortex to a depth of 1.5 mm, the level of thalamic input to the cerebral cortex (**Figure 1A**).

The UEA has been used in BrainGate clinical trials (Hochberg et al., 2006; Homer et al., 2013; Perge et al., 2013) and in research with epilepsy patients (Normann et al., 2009; Truccolo et al., 2011; Weiss et al., 2013a,b), and we have performed a number of preliminary experiments designed to establish the safety of the implantation procedures (House et al., 2006). These experiments were performed in persons suffering from epilepsy or brain tumors that had to undergo a surgical resection of a brain region. Briefly after exposure of the implantation site using standard neurosurgical equipment and procedures, the pia arachnoid was cut to allow access to the surface of the cerebral cortex. Even though the individual electrodes of the UEA are very sharp (with radius curvatures typically on the order of a few microns) we found that trying to push 100 electrodes into cortical tissues only depressed the surface of the tissue and resulted in only partial insertion of the electrode array. A pneumatically actuated precision instrument that allows the complete and safe insertion of the array in under 200 ms was developed to circumvent this difficulty (Rousche and Normann, 1992). Interestingly we found that it was necessary to fine adjust the parameters of the pneumatic inserter depending of the age of the patients, and that it was easier to get a complete insertion in young than in aged patients using low insertion pressures (around 15–20 psi).

HUMAN ACUTE REACTIVE RESPONSES AROUND IMPLANTED MICROELECTRODES

Implantation of any neural probe is always a traumatic procedure that implies some local damage of neurons, vasculature and other cells (**Figures 1C,D**). Thus, when a neural probe is inserted into the brain, some neurons and glial cells are killed or injured during insertion, blood vessels are disrupted, and the blood-brain barrier is compromised (**Figures 2A,B**). As a result, with most of our microelectrode array insertions in human cortex, we typically observed interstitial microhemorrhages emanating from the electrode tracks that extended in one or more directions. These microhemorrhages were limited to within a few millimeters of the microelectrode tracks although these were more evident around the edges of the arrays. This damage seemed to result from a combination of the numerous blood vessels encountered in the path of the penetrating electrodes plus some mechanical damage of small capillaries, especially at the borders of the array. Furthermore although the insertion of the UEA did not result in clinically relevant hemorrhages, some times we found petechial hemorrhages located below the tips of the electrodes (**Figures 2C,D**).

These microhemorrhages usually stopped spontaneously or after gentle irrigation with normal saline and we do not have any case where we had to remove the array due to the bleeding.

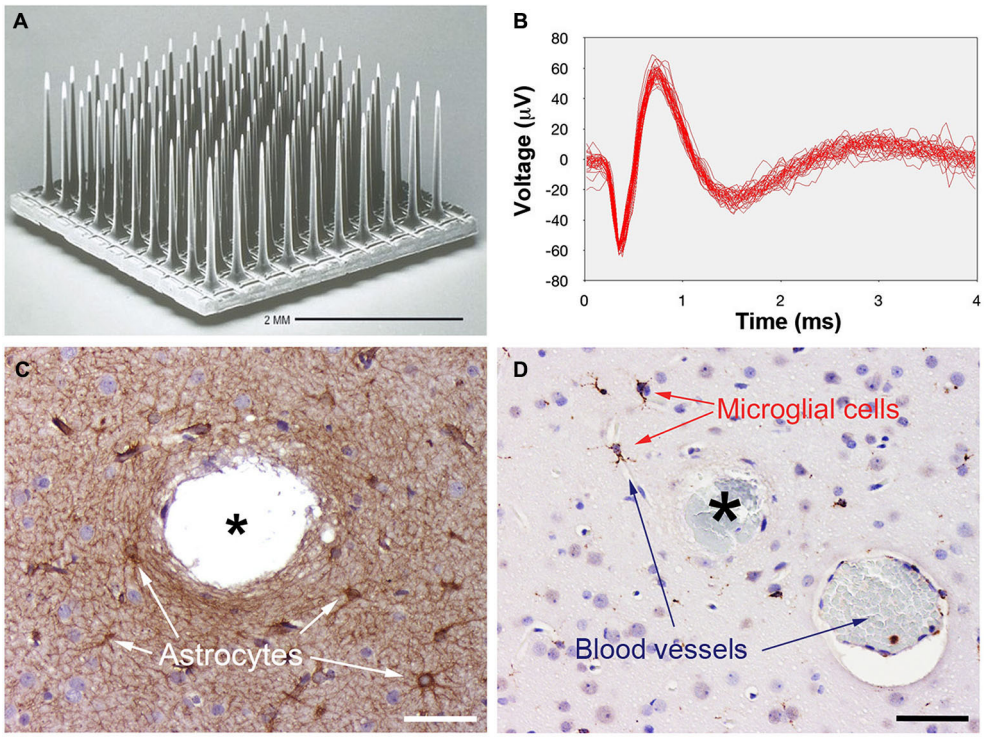

FIGURE 1 | Photographs showing the silicon-based Utah Electrode Array (UEA) and representative results of its implantation into human cortex. **(A)** Scanning electron micrograph of the UEA. **(B)** Single-unit responses recorded with the UEA from human temporal cortex (47 superimposed traces). **(C)** Astrocytes, labeled here with anti-glial fibrillary acidic protein antibody (GFAP) increase the thickness of their main processes, especially around electrode tracks (asterisk). **(D)** Resident microglial cells and blood-borne macrophages, labeled here with anti-CD45 antibody, become activated and migrate toward the electrodes. Note the electrode track filled with blood cells (asterisk) and a nearby blood vessel. Calibration bars = 50 μm.

However, due to this small bleeding various serum plasma proteins and blood cells stick on the surface of the electrodes and trigger complement system activation, platelet activation, clot formation and a large network of changes including the release of cytokines, invasion of blood-borne macrophages and edema. **Figure 2E** shows an example of the tip of an electrode after explantation. Many red blood cells are seen in close contact with electrode materials (see **Figure 2F**). Thus, microhemorrhaging is an important issue that should be taken into account to reduce the adverse nature of the reactions and maintain an ideal environment for the microelectrodes.

Array implantation also causes an early activation and migration of microglial cells towards the microelectrodes, which could reflect highly specific interactions mediated by selectins, integrins, cytokines and carbohydrate-binding receptors (Kaur et al., 2010; Linnartz et al., 2012). These microglial cells are very sensitive to pathological conditions, even if they respond only to variations in local extracellular ionic concentrations (Kreutzberg, 1996; Freire et al., 2011) and we have found that there is a rapid activation, in a matter of minutes, of these cells in human brain. **Figure 1D** shows an example in an experiment in which the UEA was kept in place for <10 min.

Usually these scavenger cells form a network of immune alert resident macrophages with a capacity for immune surveillance and control. Therefore the initial activation and migration of microglial cells are likely beneficial and include production of neurotrophic substances and cell adhesion molecules, which support injured neurons and appear necessary for restorative events to take place (Eddleston and Mucke, 1993). However, this largely beneficial initial phase can result in a more adverse long-term response that is dependent on the extent of the injury. Consequently more effort is needed to control these responses and ensure the function of the implant without eliciting either structural, cellular or metabolic changes that compromise the microelectrode array performance and/or that result in tissue degeneration around the implanted microelectrodes.

ELECTROPHYSIOLOGICAL RECORDINGS

As has been shown from experiments in rodents and non-human primates (Oliveira and Dimitrov, 2008), we found that the quality of the surgical implantation procedure plays a major role for tissue preservation and for the outcome of recordings. Our experimental results have demonstrated that high-quality microelectrode recordings from cerebral cortical neurons can be consistently obtained in both acute (intraoperative) and short term chronic (in an epilepsy monitoring unit) settings. An example of action potentials recorded with a UEA in the temporal cortex of a patient with medically intractable epilepsy is shown in **Figure 1B**. Single units are easily identifiable with a quality similar to that observed in rat, cat or non-human primate recordings. Furthermore,

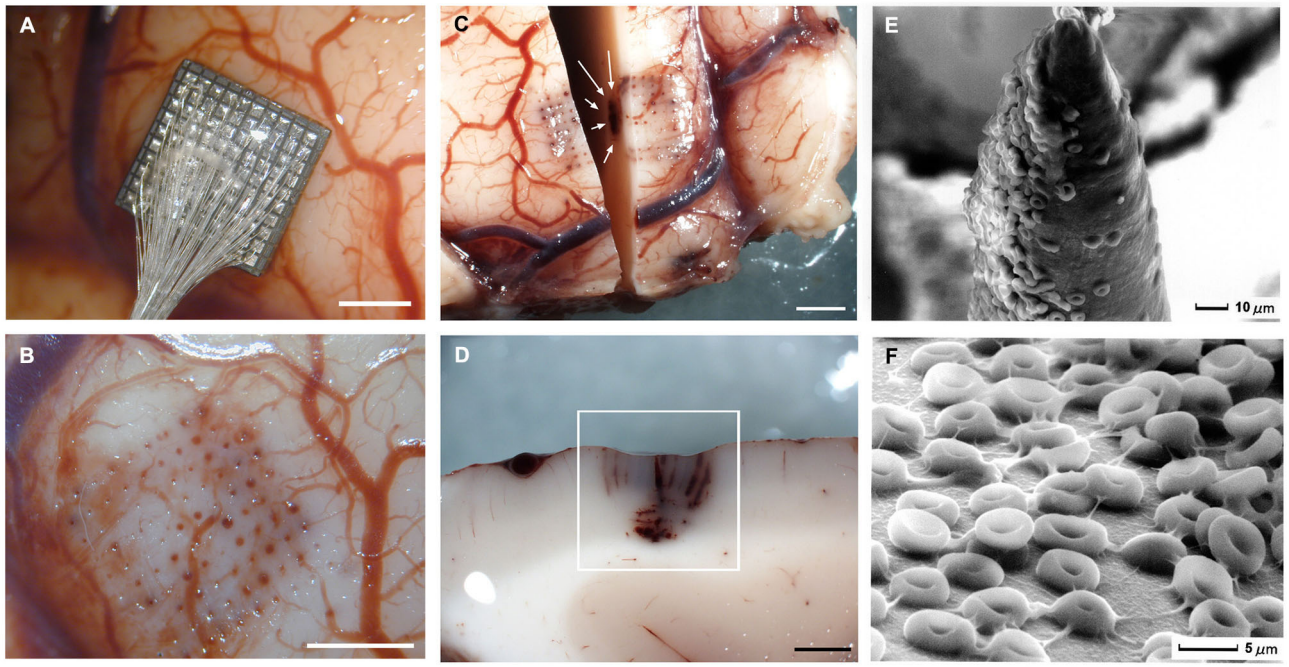

FIGURE 2 | Gross specimens of human temporal lobe implantations and scanning micrographs of the surface of the Utah Electrode Array after acute implantation in human brain. **(A)** Placement of an electrode array in temporal cortex. **(B)** Once the array has been removed there are some evident microhemorrhages. **(C)** Horizontal section showing blood in the outermost electrode tracks and petechial hemorrhages (white arrows) located below the tip of the electrodes. **(D)** Detail of the petechial hemorrhages. **(E)** Scanning electron micrograph of an electrode tip. Many red blood cells appear in close contact with electrode materials. **(F)** Detail of the red blood cells on the surface of the microelectrodes. Calibration bars A, B, C and D= 2 mm.

most of the presently available intracortical microelectrode arrays (including the UEA) allow recording of local field potentials that are very reliable and that can be used to detect changes in recording quality over time. Also, recording quality is affected by other surgical procedures: most drugs used for the induction and maintenance of general anesthesia decrease action potential firing rates and the information processing capacity in the neocortex (Hanrahan et al., 2013). In addition local fluctuation in K^+ and Ca^+ due to acute initial trauma can induce the silencing of neurons in the proximity of microelectrodes. Consequently recording sessions are usually initiated between 3–10 days after implantation.

The ability of intracortical microelectrodes arrays such as the UEA to record single units from human cortical neurons demonstrates that the implantation can be done without major complications, and emphasizes its potential role for studying encoding and processing of sensory and motor information by large neuronal ensembles. However significant variations in spike waveforms across time have been reported (Parker et al., 2011). These variations could reflect the initial acute response that can lead to chronic inflammatory reactions. Such reactions can negatively impact neurons and microelectrodes via induction of glial proliferation that produces a slow progressive decline in spike amplitude and in the number of viable channels. Furthermore recordings from individual neurons made with penetrating microelectrodes are often lost but then recover, possibly because of micro-motion of the device relative to the neural tissue (Parker et al., 2011). This problem can be mitigated with sophisticated action potential identification and daily recalibration.

CHALLENGES AND FUTURE WORK

Intracortical microelectrode arrays have several advantages over traditional macroelectrode brain electrophysiological techniques such as their ability to selectively access individual or small groups of cortical neurons and the possibility to deliver relevant spatio-temporal patterns of stimulation. This highlights their potential to restore some lost neural function through selective electrical stimulation or by recording activity from selected populations of neurons. Furthermore the procedures for the implantation of penetrating microelectrodes are straightforward and well within the reach of most well-trained neurosurgeons. Altogether these results suggest that intracortical microelectrodes could form the basis of new neuroprosthetic devices for treating many disorders of the nervous system. For example they are presently being used to obtain volitional command signals from primary motor cortex of people with high cervical spinal injuries or to provide a limited but useful sense of vision in profoundly blind. However the presence of acute inflammatory reactions that can lead to chronic inflammatory reactions affecting both the neural tissue and the surface of the microelectrodes must be better understood and new approaches pursued to mitigate these reactions. Controlling and reducing the neural tissue damage induced by these intracortical microelectrodes should aid in

keeping these devices biologically and electrically viable for many years.

Factors affecting brain tissue reactions to intracortical microelectrodes include the mechanical trauma during insertion, implantation method, biological acute responses and the physical properties of the microelectrodes. Because the brain is so richly vascularized, we have observed that there is inevitable bleeding associated with electrode array insertion and this suggests that bleeding is an important issue that should be taken into account to reduce the neural tissue damage induced by the microelectrodes. Moreover the reliability of recording the same spiking activity over long time periods still remains an unresolved problem that must be solved in longer term human studies before these penetrating microelectrodes can be used for some clinical purposes.

In this framework, important criteria for clinical success are tissue and microelectrode preservation and the maintenance of a stable signal in the CNS for the longest time possible. Remarkable progress has been reported in the use of these penetrating microelectrode arrays, but the electrode-tissue interface remains one of the major obstacles. Intracortical microelectrodes need a stable electronic/neural interface that facilitates selective recording and/or activation of specific groups of neurons without damage to the electrodes or surrounding neural tissues. Consequently it is essential to better understand the signals that lead to neuroglial activation in human brain and to create a targeted intervention strategy to prevent or at least to control this response.

Progress in this area relies on scientists being able to integrate and utilize methodologies from disparate disciplines, such as biomedical engineering, biomaterials, neuroscience, neurology, neurosurgery, information and communication technologies, molecular biology, etc. We are optimistic that with an emphasis on collaboration and a concerted push for additional clinical trials, these technologies will form the basis of devices and therapies that will substantially reduce the burden of lost neurological functions. However progress will be incremental and researchers must avoid creating false expectations that could damage the credibility of these new technologies.

ACKNOWLEDGMENT

This work has been supported in part by grants MAT2012-39290-C02-01 from the Spanish Government, by the National Organization of the Spanish Blind (ONCE).

REFERENCES

Andersen, R. A., Hwang, E. J., and Mulliken, G. H. (2010). Cognitive neural prosthetics. *Annu. Rev. Psychol.* 61, 169–190, C1–C3. doi: 10.1146/annurev.psych.093008.100503

Barrese, J. C., Rao, N., Paroo, K., Triebwasser, C., Vargas-Irwin, C., Franquemont, L., et al. (2013). Failure mode analysis of silicon-based intracortical microelectrode arrays in non-human primates. *J. Neural Eng.* 10, 1–23. doi: 10.1088/1741-2560/10/6/066014

Beitz, J. M. (2014). Parkinson's disease: a review. *Front. Biosci. (Schol. Ed.)* 6, 65–74. doi: 10.2741/s415

Calixto, R., Salamat, B., Rode, T., Hartmann, T., Volckaerts, B., Ruther, P., et al. (2013). Investigation of a new electrode array technology for a central auditory prosthesis. *PLoS One* 8:e82148. doi: 10.1371/journal.pone.0082148

Carmena, J. M. (2013). Advances in neuroprosthetic learning and control. *PLoS Biol.* 11:e1001561. doi: 10.1371/journal.pbio.1001561

Chen, Y. Y., Lai, H. Y., Lin, S. H., Cho, C. W., Chao, W. H., Liao, C. H., et al. (2009). Design and fabrication of a polyimide-based microelectrode array: application in neural recording and repeatable electrolytic lesion in rat brain. *J. Neurosci. Methods* 182, 6–16. doi: 10.1016/j.jneumeth.2009.05.010

Eddleston, M., and Mucke, L. (1993). Molecular profile of reactive astrocytes–implications for their role in neurologic disease. *Neuroscience* 54, 15–36. doi: 10.1016/0306-4522(93)90380-x

Fernandez, E., and Hofmann, K. (2011). "Visual prosthesis," in *Handbook of Medical Technology*, eds R. Kramme, K.-P. Hoffmann and R. S. Pozos (Würburg: Springer), 821–834.

Freire, M. A., Morya, E., Faber, J., Santos, J. R., Guimaraes, J. S., Lemos, N. A., et al. (2011). Comprehensive analysis of tissue preservation and recording quality from chronic multielectrode implants. *PLoS One* 6:e27554. doi: 10.1371/journal.pone.0027554

Grill, W. M., Norman, S. E., and Bellamkonda, R. V. (2009). Implanted neural interfaces: biochallenges and engineered solutions. *Annu. Rev. Biomed. Eng.* 11, 1–24. doi: 10.1146/annurev-bioeng-061008-124927

Hanrahan, S. J., Greger, B., Parker, R. A., Ogura, T., Obara, S., Egan, T. D., et al. (2013). The effects of propofol on local field potential spectra, action potential firing rate and their temporal relationship in humans and felines. *Front. Hum. Neurosci.* 7:136. doi: 10.3389/fnhum.2013.00136

Hassler, C., Guy, J., Nietzschmann, M., Staiger, J. F., and Stieglitz, T. (2011). Chronic intracortical implantation of saccharose-coated flexible shaft electrodes into the cortex of rats. *Conf. Proc. IEEE Eng. Med. Biol. Soc.* 2011, 644–647. doi: 10.1109/IEMBS.2011.6090143

Hatsopoulos, N. G., and Donoghue, J. P. (2009). The science of neural interface systems. *Annu. Rev. Neurosci.* 32, 249–266. doi: 10.1146/annurev.neuro.051508.135241

Hochberg, L. R., Serruya, M. D., Friehs, G. M., Mukand, J. A., Saleh, M., Caplan, A. H., et al. (2006). Neuronal ensemble control of prosthetic devices by a human with tetraplegia. *Nature* 442, 164–171. doi: 10.1038/nature04970

Homer, M. L., Nurmikko, A. V., Donoghue, J. P., and Hochberg, L. R. (2013). Sensors and decoding for intracortical brain computer interfaces. *Annu. Rev. Biomed. Eng.* 15, 383–405. doi: 10.1146/annurev-bioeng-071910-124640

House, P. A., Macdonald, J. D., Tresco, P. A., and Normann, R. A. (2006). Acute microelectrode array implantation into human neocortex: preliminary technique and histological considerations. *Neurosurg. Focus* 20, 1–4. doi: 10.3171/foc.2006.20.5.5

Kaur, G., Han, S. J., Yang, I., and Crane, C. (2010). Microglia and central nervous system immunity. *Neurosurg. Clin. N. Am.* 21, 43–51. doi: 10.1016/j.nec.2009.08.009

Kozai, T. D., and Kipke, D. R. (2009). Insertion shuttle with carboxyl terminated self-assembled monolayer coatings for implanting flexible polymer neural probes in the brain. *J. Neurosci. Methods* 184, 199–205. doi: 10.1016/j.jneumeth.2009.08.002

Kreutzberg, G. W. (1996). Microglia: a sensor for pathological events in the CNS. *Trends Neurosci.* 19, 312–318. doi: 10.1016/0166-2236(96)10049-7

Linnartz, B., Bodea, L. G., and Neumann, H. (2012). Microglial carbohydrate-binding receptors for neural repair. *Cell Tissue Res.* 349, 215–227. doi: 10.1007/s00441-012-1342-7

Marin, C., and Fernandez, E. (2010). Biocompatibility of intracortical microelectrodes: current status and future prospects. *Front. Neuroeng.* 3:8. doi: 10.3389/fneng.2010.00008

Merkus, P., Di Lella, F., Di Trapani, G., Pasanisi, E., Beltrame, M. A., Zanetti, D., et al. (2014). Indications and contraindications of auditory brainstem implants: systematic review and illustrative cases. *Eur. Arch. Otorhinolaryngol.* 271, 3–13. doi: 10.1007/s00405-013-2378-3

Nardone, R., Holler, Y., Leis, S., Holler, P., Thon, N., Thomschewski, A., et al. (2014). Invasive and non-invasive brain stimulation for treatment of neuropathic pain in patients with spinal cord injury: a review. *J. Spinal Cord. Med.* 37, 19–31. doi: 10.1179/2045772313y.0000000140

Neves, H. (2007). Advances in cerebral probing using modular multifunctional probe arrays. *Med. Device Technol.* 18, 38–39.

Nicolelis, M. A., and Lebedev, M. A. (2009). Principles of neural ensemble physiology underlying the operation of brain-machine interfaces. *Nat. Rev. Neurosci.* 10, 530–540. doi: 10.1038/nrn2653

Nordhausen, C. T., Maynard, E. M., and Normann, R. A. (1996). Single unit recording capabilities of a 100 microelectrode array. *Brain Res.* 726, 129–140. doi: 10.1016/s0006-8993(96)00321-6

Normann, R. A. (2007). Technology insight: future neuroprosthetic therapies for disorders of the nervous system. *Nat. Clin. Pract. Neurol.* 3, 444–452. doi: 10.1038/ncpneuro0556

Normann, R. A., Greger, B., House, P., Romero, S. F., Pelayo, F., and Fernandez, E. (2009). Toward the development of a cortically based visual neuroprosthesis. *J. Neural Eng.* 6:035001. doi: 10.1088/1741-2560/6/3/035001

Oliveira, L. M. O., and Dimitrov, D. (2008). "Surgical techniques for chronic implantation of microwire arrays in rodents and primates," in *Methods for Neural Ensemble Recordings*. 2nd Edn., ed M. A. L. Nicolelis (Boca Raton, FL: CRC Press), 21–46.

Parker, R. A., Davis, T. S., House, P. A., Normann, R. A., and Greger, B. (2011). The functional consequences of chronic, physiologically effective intracortical microstimulation. *Prog. Brain Res.* 194, 145–165. doi: 10.1016/b978-0-444-53815-4.00010-8

Perge, J. A., Homer, M. L., Malik, W. Q., Cash, S., Eskandar, E., Friehs, G., et al. (2013). Intra-day signal instabilities affect decoding performance in an intracortical neural interface system. *J. Neural Eng.* 10:036004. doi: 10.1088/1741-2560/10/3/036004

Prasad, A., Xue, Q. S., Sankar, V., Nishida, T., Shaw, G., Streit, W. J., et al. (2012). Comprehensive characterization and failure modes of tungsten microwire arrays in chronic neural implants. *J. Neural Eng.* 9:056015. doi: 10.1088/1741-2560/9/5/056015

Rao, N. G., and Donoghue, J. P. (2014). Cue to action processing in motor cortex populations. *J. Neurophysiol.* 111, 441–453. doi: 10.1152/jn.00274.2013

Raspopovic, S., Capogrosso, M., Petrini, F. M., Bonizzato, M., Rigosa, J., Di Pino, G., et al. (2014). Restoring natural sensory feedback in real-time bidirectional hand prostheses. *Sci. Transl. Med.* 6:222ra219. doi: 10.1126/scitranslmed.3006820

Rousche, P. J., and Normann, R. A. (1992). A method for pneumatically inserting an array of penetrating electrodes into cortical tissue. *Ann. Biomed. Eng.* 20, 413–422. doi: 10.1007/bf02368133

Rousche, P. J., Pellinen, D. S., Pivin, D. P. Jr., Williams, J. C., Vetter, R. J., and Kipke, D. R. (2001). Flexible polyimide-based intracortical electrode arrays with bioactive capability. *IEEE Trans. Biomed. Eng.* 48, 361–371. doi: 10.1109/10.914800

Seymour, J. P., and Kipke, D. R. (2007). Neural probe design for reduced tissue encapsulation in CNS. *Biomaterials* 28, 3594–3607. doi: 10.1016/j.biomaterials.2007.03.024

Suner, S., Fellows, M. R., Vargas-Irwin, C., Nakata, G. K., and Donoghue, J. P. (2005). Reliability of signals from a chronically implanted, silicon-based electrode array in non-human primate primary motor cortex. *IEEE Trans. Neural Syst. Rehabil. Eng.* 13, 524–541. doi: 10.1109/tnsre.2005.857687

Truccolo, W., Donoghue, J. A., Hochberg, L. R., Eskandar, E. N., Madsen, J. R., Anderson, W. S., et al. (2011). Single-neuron dynamics in human focal epilepsy. *Nat. Neurosci.* 14, 635–641. doi: 10.1038/nn.2782

Weiss, S. A., Banks, G. P., Mckhann, G. M. Jr., Goodman, R. R., Emerson, R. G., Trevelyan, A. J., et al. (2013a). Ictal high frequency oscillations distinguish two types of seizure territories in humans. *Brain* 136, 3796–3808. doi: 10.1093/brain/awt276

Weiss, S. A., Mckhann, G. Jr., Goodman, R., Emerson, R. G., Trevelyan, A., Bikson, M., et al. (2013b). Field effects and ictal synchronization: insights from in homine observations. *Front. Hum. Neurosci.* 7:828. doi: 10.3389/fnhum.2013.00828

Conflict of Interest Statement: The authors declare that the research was conducted in the absence of any commercial or financial relationships that could be construed as a potential conflict of interest.

Received: 29 March 2014; accepted: 19 June 2014; published online: 21 July 2014.
Citation: Fernández E, Greger B, House PA, Aranda I, Botella C, Albisua J, Soto-Sánchez C, Alfaro A and Normann RA (2014) Acute human brain responses to intracortical microelectrode arrays: challenges and future prospects. Front. Neuroeng. 7:24. doi: 10.3389/fneng.2014.00024
This article was submitted to the journal Frontiers in Neuroengineering.

frontiers in
NEUROENGINEERING

ORIGINAL RESEARCH ARTICLE
published: 04 August 2014
doi: 10.3389/fneng.2014.00033

Resistive and reactive changes to the impedance of intracortical microelectrodes can be mitigated with polyethylene glycol under acute *in vitro* and *in vivo* settings

Salah Sommakia[1,2], Janak Gaire[3], Jenna L. Rickus[1,2,4] and Kevin J. Otto[1,3]*

[1] Weldon School of Biomedical Engineering, Purdue University, West Lafayette, IN, USA
[2] Physiological Sensing Facility at the Bindley Bioscience Center and Birck Nanotechnology Center, Purdue University, West Lafayette, IN, USA
[3] Department of Biological Sciences, Purdue University, West Lafayette, IN, USA
[4] Department of Agricultural and Biological Engineering, Purdue University, West Lafayette, IN, USA

Edited by:
Ulrich G. Hofmann, Albert-Ludwigs-University Freiburg, Germany

Reviewed by:
Xuefeng F. Wei, The College of New Jersey, USA
Abhishek Prasad, University of Miami, USA

***Correspondence:**
Kevin J. Otto, Weldon School of Biomedical Engineering, Purdue University, 206 S. Martin Jischke Drive, West Lafayette, IN 47907, USA
e-mail: kotto@purdue.edu

The reactive response of brain tissue to implantable intracortical microelectrodes is thought to negatively affect their recordable signal quality and impedance, resulting in unreliable longitudinal performance. The relationship between the progression of the reactive tissue into a glial scar and the decline in device performance is unclear. We show that exposure to a model protein solution *in vitro* and acute implantation result in both resistive and capacitive changes to electrode impedance, rather than purely resistive changes. We also show that applying 4000 MW polyethylene glycol (PEG) prevents impedance increases *in vitro*, and reduces the percent change in impedance *in vivo* following implantation. Our results highlight the importance of considering the contributions of non-cellular components to the decline in neural microelectrode performance, and present a proof of concept for using a simple dip-coated PEG film to modulate changes in microelectrode impedance.

Keywords: intracortical microelectrodes, foreign-body reaction, impedance spectroscopy, polyethylene glycols, dip coating

INTRODUCTION

Failure of intracortical microelectrodes typically manifests as increased impedance and decreased signal to noise ratio, and is thought to be associated with the formation of a dense glial scar and loss of neuronal density. *In vivo* impedance monitoring is a common tool to assess the functionality of implanted intracortical microelectrodes, and has been used to infer the progression of the reactive tissue response to implanted intracortical microelectrodes (Williams et al., 1999, 2007; Vetter et al., 2004). Recent research shows that changes in electrical properties monitored by impedance spectroscopy do not always perfectly correlate with cellular responses (Prasad et al., 2012; Prasad and Sanchez, 2012), implicating additional biotic and abiotic factors. *In vitro* testing in 3D gel constructs reveal that different glial cells adhered to the surface of a microelectrode have different impedance profiles (Frampton et al., 2010). One factor that has not been well investigated is the adsorption of proteins and other biomolecules. While adsorbed proteins have been implicated in the biological response (Leung et al., 2008), their effects on the electrical impedance of intracortical microelectrodes have not been previously described with impedance spectroscopy. Prevalent electrical circuit models of the tissue electrode interface assume that adsorbed proteins result in purely resistive impedance changes (Johnson et al., 2005; Otto et al., 2006; Williams et al., 2007), but there is not sufficient empirical verification of this assumption. To the best of the authors' knowledge, there are no reports in the literature on the effects of adsorbed proteins or non-cellular components on the impedance of intracortical microelectrodes.

Another aspect to the problem of biomolecule adsorption is the question of preventing detrimental changes to the electrical characteristics of intracortical microelectrodes using simple and cost effective approaches. For implantable devices in other biological systems, protein-resistant or anti-fouling treatments are commonplace (Salacinski et al., 2001; Bluestein et al., 2010; Li and Henry, 2011). One of the most common materials used to enhance the biocompatibility of biomedical implants is polyethylene glycol (PEG). Due to its hydrophilic nature, PEG prevents the adsorption of proteins by reducing access to the more hydrophobic surface onto which proteins prefer to bind (Michel et al., 2005). Typically, PEG is chemically grafted onto a substrate and reliably reduces protein adsorption (Sharma et al., 2004a,b; Muthusubramaniam et al., 2011). In the context of intracortical microelectrodes, PEG has traditionally been used as a scaffold for thick drug eluting hydrogels (Winter et al., 2007; Rao et al., 2012), the size scale of which might exacerbate neuronal displacement. Thinner conformal microgel coatings which incorporate PEG as a cross linker have been investigated, but do not significantly improve the chronic tissue response (Gutowski et al., 2014).

Free-floating PEG injected intravenously has been reported to improve cellular and behavioral recovery following traumatic brain injury (Koob et al., 2005, 2008; Koob and Borgens, 2006). Because of the complexity of the reactive tissue response of the brain to implanted microelectrodes, and the fact that the cause of the majority of chronic microelectrode failures are unknown (Barrese et al., 2013), the long-term effects of a simply applied anti-fouling coating on the tissue response cannot be confidently predicted. In the short-term, however, it is possible that such a simply applied anti-fouling coating might improve the electrical properties of acutely implanted neural microelectrodes, which, in turn, might improve the accuracy of impedance monitoring as a predictive tool for the progression of the tissue response. The authors are not aware of any reports in the literature that examine the effects of a simple dip-coated PEG film on the electrical properties of neural microelectrodes under acute *in vitro* or *in vivo* settings.

The primary objective of this paper is to quantify the acute effects on microelectrode impedance of adsorbed proteins *in vitro*, and non-cellular molecular components *in vivo*. A secondary objective is to present a proof of concept on the use of an aqueous dip-coated PEG film in preventing impedance changes to neural microelectrodes during acute timescales. For this proof of concept experiment, a molecular weight of 4000 Da was chosen according to literature reports demonstrating optimal antifouling properties at this molecular weight (Su et al., 2009). We first present an analysis of changes in intracortical microelectrode impedance following immersion in a model protein solution mimicking *in vivo* brain protein concentration. Total impedance, resistance, and reactance are analyzed at different frequency values to quantify the contribution of adsorbed proteins to the impedance changes affecting electrode performance. We show that a dip-coated film of a relatively high molecular weight PEG prevents changes in impedance upon immersion in protein solution. We then demonstrate in an acute *in vivo* experiment that increases in microelectrode impedance after insertion into the cortex can be reduced by applying the same PEG treatment to the electrode shank and implantation site.

MATERIALS AND METHODS

IN VITRO STUDY WITH MODEL PROTEIN SOLUTION

Electrochemical measurements of 16-channel single shank Michigan electrode arrays (CNCT, Ann Arbor, MI) were made using an Autolab potentiostat PG-STAT12 with a built-in frequency response analyzer (EcoChemie, Utrecht, The Netherlands). For this study, a three-electrode cell configuration was used with the microelectrode site functioning as the working electrode, a large-area Pt wire functioning as the counter electrode, and an Accumet, gel-filled, KCl saturated calomel electrode (Thermo Fischer Scientific, Fair Lawn, NJ) functioning as the reference electrode. This three-electrode setup was chosen for this study because of its ability to isolate the electrode/solution interface impedance component.

For each electrode array, cyclic voltammetry (CV) was performed by sweeping the applied voltage from −0.6 to +0.8 V at a scanning rate of 1 V/s to determine sites with broken or poor connections, designated as those sites exhibiting a maximum current below 1 nA. These sites were discarded from the analysis, thus yielding a total of 30 functional sites on three different electrode arrays.

Electrochemical impedance spectroscopy (EIS), using the PGSTAT12, was used to measure the impedance of the electrode sites with the application of 15 sequentially applied sinusoidal waves at logarithmically spaced frequencies ranging from 46 Hz to 10 kHz, with an amplitude of 25 mVRMS. For each electrode, impedance spectroscopy was performed in PBS following each of three different treatments: (a) no treatment; (b) immersion in a 10% solution of bovine serum albumin (BSA) (Sigma-Aldrich, St. Louis, MO) in PBS, the concentration of which was chosen to mimic protein concentration in rat cerebral cortex (Banay-Schwartz et al., 1992); and (c) immersion in a 20% solution of 4000 MW PEG (Alfa-Aesar, Ward Hill, MA), air-drying for 1 min, then immersion in BSA. Immersion and subsequent removal from the described solutions was done at a controlled velocity using a micro-manipulator. An additional volume of 100 μl of PEG was further applied directly onto the microelectrode shank as it was immersed in BSA to mimic a topical application. Electrodes were rinsed with deionized water and anodically cleaned between the different treatments using 10-s long DC pulses, as described previously (Sommakia et al., 2009). Bode and Nyquist plots were generated for all treatment groups. Comparisons of the resistance, reactance and total impedance were done at 50 Hz, 100 Hz, 1 kHz, and 10 kHz.

ACUTE *IN VIVO* STUDY

The laboratory animal protocol for this work was approved through the Purdue Animal Care and Use Committee (West Lafayette, IN, USA), and conforms to the guidelines of the US National Institutes of Health. Three Sprague Dawley rats (Harlan Laboratories, Indianapolis, IN) were used for this study. Each rat was anesthetized with 2% isofluorane, then transferred to a stereotactic frame and maintained with 0.5–1% isofluorane delivered through a nose cone. The head was shaved and swabbed with alternating washes of betadine and alcohol, and an eye lubricating ointment applied. Lidocaine was injected subcutaneously at multiple positions in the head, and then a midline incision approximately 2 cm long was made along the cranium with a scalpel. The underlying pericranium was removed to expose the skull. A single burr hole was made with a dental drill towards the back of the head, slightly anterior to the ears, and a stainless steel bone screw attached to a segment of platinum wire was threaded into it to serve as a counter electrode. Bilateral craniotomies about 2.5 mm in diameter were made with a dental drill, approximately 2.5 mm anterior to Bregma and 2 mm lateral to the midline. For each craniotomy, a slit was made in the dura using surgical microscissors. One craniotomy serving as a control was wetted with 0.9% sterile saline before electrode insertion, while the other craniotomy was wetted with 20% w/v solution of 4000 MW PEG in MilliQ water prior to electrode insertion.

16-channel single-shank Michigan probes were also used for this study. Because of the difficulty of achieving a three-electrode setup in a surgical setting, a two-electrode setup was chosen instead. Prior to insertion into the cortex, baseline impedance was established *in vitro* by performing the same EIS procedure

described above, but in a two-electrode setup. The electrode was then manually inserted into the exposed cortex of the control craniotomy using a magnet-stabilized micromanipulator, and EIS was measured 5 min after insertion. The electrode was then removed, rinsed with MilliQ water, and cleaned by applying a DC bias of 1.5 V for 10 s in PBS, as described previously (Sommakia et al., 2009). After verifying the return of the 1 kHz impedance to baseline, the electrode was dip-coated at a controlled velocity using a micromanipulator in a 20% solution of 4000 MW PEG in MilliQ water for 1 min and allowed to dry for 2 min. The PEG-coated electrode was then inserted using the micromanipulator into the other craniotomy wetted with PEG, and EIS was performed again.

STATISTICAL ANALYSIS

Statistical analysis was performed using the SAS 9.3 statistical package (SAS Institute, Cary, NC). A general linear model (GLM) procedure was used to perform a one way ANOVA with block to remove variations between the different electrodes by treating electrodes as a statistical block. Tukey *post-hoc* tests were used to identify statistically significant differences between the groups at a significance level of $\alpha = 0.05$. Plots were generated using MATLAB (The MathWorks Inc., Natick, MA).

RESULTS

ANALYSIS OF IMPEDANCE CHANGES WITH MODEL PROTEIN SOLUTION AND PEG *IN VITRO*

An examination of Bode plots reveals that the gain for electrodes immersed into is higher than for uncoated controls for all frequencies, indicating an overall increase in impedance. Electrodes treated with PEG prior to BSA immersion show more congruence with the gain of uncoated electrodes (**Figure 1A**). The phase for non-PEG treated electrodes immersed in BSA exhibits lower angles at the lower end of the frequency spectrum, and the difference is most pronounced in the middle of the spectrum between 200–500 Hz (**Figure 1B**). In **Figure 2**, the Nyquist plot for non-PEG treated electrodes immersed in BSA reveal a shift up and the right compared to the controls, indicating both increased resistance and reactance, with the most pronounced divergence occurring toward the middle of the plot. In contrast, the plot for electrodes pretreated with PEG shows more congruence with uncoated controls in the middle of the plot and slight divergence at the lower end of the plot, corresponding to the higher frequencies. To better understand the details of these changes and their potential implication for mitigation attempts, we examined the percent changes in resistance, reactance, and total impedance at various points across the frequency spectrum.

Figure 3A shows percent changes in the real component of the impedance, i.e., resistance, relative to the control at four frequency values across the spectrum. Electrodes immersed in BSA without PEG pretreatment exhibited statistically significant increases in the resistance compared to the uncoated control at examined frequencies. The highest resistance increase relative to control was in the middle of the frequency spectrum, specifically at 1 kHz, with a 30.7% increase in resistance. At 50 Hz, the increase in resistance for the BSA coated electrodes without PEG pretreatment was 14.5%, at 100 Hz, the resistance increase was 23.9%, and 10 kHz, the resistance increase was 17%. The electrodes pretreated with PEG prior to BSA immersion, on the other hand, did not exhibit any significant differences in resistance compared to the uncoated controls at all examined frequencies.

Figure 3B shows percent changes in the imaginary component of the impedance, i.e., reactance, relative to the control at four frequency values. For electrodes not pretreated with PEG prior to immersion in BSA, no significant increase in reactance was observed at 50 Hz or 100 Hz, while increases of 12% and 15% were observed at 1 kHz and 10 kHz, respectively. In contrast, electrodes pretreated with PEG prior to immersion in BSA exhibited modest decreases in the reactance relative to control at all frequencies (−6.3% at 50 Hz, −6.3% at 100 Hz, −4.2 at 1 kHz, and −4.8% at 10 kHz). **Figure 3C** shows the percent changes in total impedance relative to the control at four frequency values. For electrodes not pretreated with PEG prior to BSA immersion, no significant difference in total impedance was observed at 50 Hz, but progressive increases in the impedance were observed at the higher frequencies (4.5% at 100 Hz, 13.5% at 1 kHz, 15.3% at 10 kHz). For electrodes pretreated with PEG prior to BSA immersion, modest decreases in total impedance were observed at the lower frequencies (−5.8% at 50 Hz, −5.6% at 100 Hz, −3.9 at 1 kHz), while no significant difference in the total impedance compared to the control was observed 10 kHz.

ANALYSIS OF IMPEDANCE CHANGES *IN VIVO* WITH AND WITHOUT PEG

Figure 4A shows the percent increase of the real component of the impedance, i.e., resistance, between the *in vitro* baseline and the *in vivo* measurement at four frequency values across the spectrum. In both cases of no treatment and PEG treatment, the resistance exhibited a significant increase when measured *in vivo* compared to the *in vitro* baseline. Insertion into the cortex without PEG treatment, however, resulted in a larger increase from the *in vitro* baseline at all frequencies compared to insertion with PEG treatment. The percent change in resistance was also frequency-dependent. For the no treatment condition, the percent increase from baseline was as follows: 71.8 ± 2.99% at 50 Hz, 89.8 ± 3.77% at 100 Hz, 209.5 ± 9.1% at 1 kHz, and 290.5 ± 13.7% at 10 kHz; while for the PEG treatment condition, the percent increase from baseline was: 44.6 ± 3% at 50 Hz, 58 ± 3.9% at 100 Hz, 149.5 ± 9.3% at 1 kHz, and 223.3 ± 14% at 10 kHz. The percent increase in resistance from baseline for the no treatment condition was significantly different from the percent increase in resistance from baseline for the PEG treatment at all frequencies.

Figure 4B shows the percent increase of the imaginary component of the impedance, i.e., reactance, between the *in vitro* baseline and the *in vivo* measurement at four frequency values across the spectrum. In both cases of PEG treatment or no treatment, the reactance increased significantly when measured *in vivo* compared to the *in vitro* baseline. Insertion into the cortex without PEG treatment, however, resulted in a larger increase in reactance from baseline compared to insertion with PEG treatment. The percent change in reactance was also frequency-dependent. For the no treatment condition, the percent increase from baseline was as follows: 45.4 ± 1.6% at 50 Hz, 48.1 ± 2%

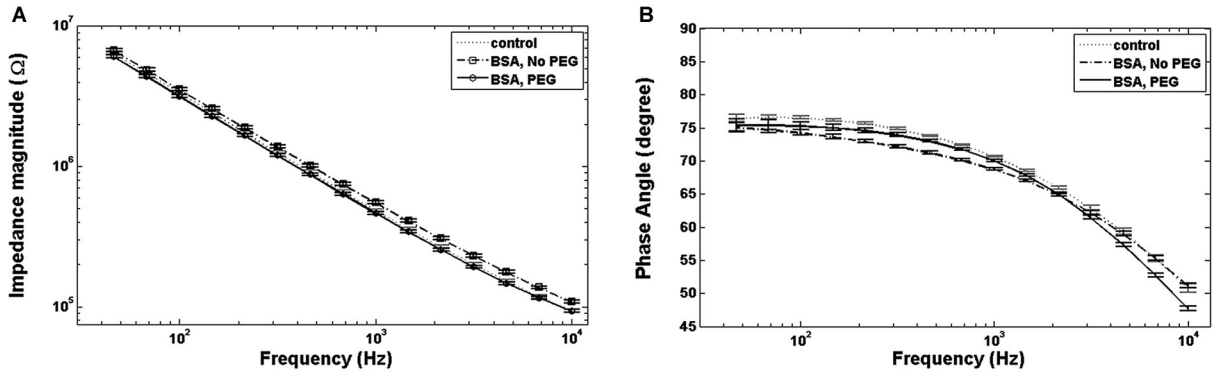

FIGURE 1 | Bode plots. (A) For electrodes immersed in BSA with no PEG coating, the total impedance magnitude plot is higher than the control, while electrodes coated with PEG prior to BSA immersion show an impedance magnitude plot indistinguishable from control. **(B)** Electrodes immersed in BSA with no PEG coating show lower phase angles at lower and intermediate frequencies compared to the control, while the phase angle for electrodes coated with PEG prior to immersion in BSA exhibit smaller phase angles at all frequencies.

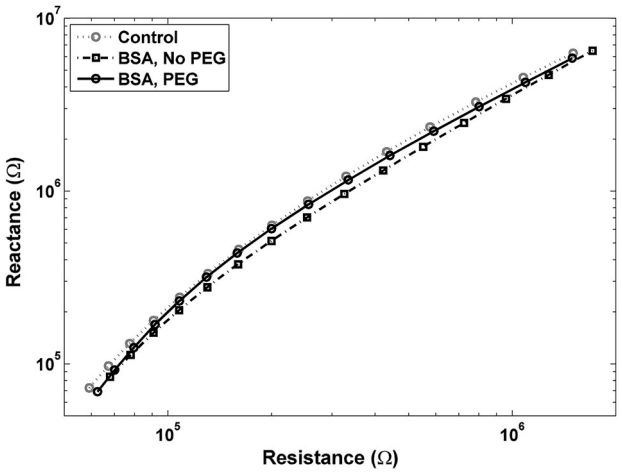

FIGURE 2 | Nyquist plot for electrodes pretreated with PEG prior to immersion in BSA is close to the control plot, with a slight shift to the left at lower frequencies, indicating a decrease in resistance. Nyquist plot for electrodes not pretreated with PEG before BSA shows a shift up and to the right, indicating increases in both resistance and reactance.

at 100 Hz, 66.4 ± 2.3% at 1 kHz, and 146.8 ± 6.2% at 10 kHz; while for the PEG treatment condition, the percent increase from baseline was: 30.8 ± 1.6% at 50 Hz, 31.4 ± 2% at 100 Hz, 41 ± 2.4% at 1 kHz, and 97.1 ± 6.4% at 10 kHz. The percent increase in reactance from baseline for the no treatment condition was significantly different from the percent increase in resistance from baseline for the PEG treatment at all frequencies. The amount of percent change in reactance is lower than the amount of percent change in resistance at each respective frequency. **Figure 4C** shows the percent increase in total impedance between the *in vitro* baseline and *in vivo* measurement at four frequency values across the spectrum. In both cases of PEG treatment or no treatment, the total impedance increased significantly when measured *in vivo* compared to the *in vitro* baseline. Insertion into the cortex without PEG treatment, however, resulted in a larger increase from baseline compared to insertion with PEG treatment. The percent change in total impedance was also frequency-dependent. For the no treatment condition, the percent increase in total impedance from baseline was as follows: 47.4 ± 1.7% at 50 Hz, 52.2 ± 2.1% at 100 Hz, 88.62 ± 2.9% at 1 kHz, and 214.5 ± 9.8% at 10 kHz; while for the PEG treatment condition, the percent increase in total impedance from baseline was: 33.6 ± 1.6% at 50 Hz, 33.5 ± 2.1% at 100 Hz, 57.1 ± 3% at 1 kHz, and 162 ± 10% at 10 kHz. The percent increase in total impedance from baseline for the no treatment condition was significantly different from the percent increase in total impedance from baseline for the PEG treatment at all frequencies.

DISCUSSION

RATIONALE

The prevalent narrative in the literature suggests that the *in vivo* reactive tissue response is an aggregate of amplified biological processes that begin with device insertion and accompanying trauma. The indwelling implant acts as a sink for various proinflammatory proteins, as well as a substrate for cell attachment (Leung et al., 2008). To the best of the authors' knowledge, the impedance changes resulting from protein adhesion onto neural microelectrodes have not been previously quantified, nor have the effects of anti-fouling treatments on impedance of neural microelectrodes. Most current efforts towards mitigating the reactive tissue response focus on targeting and quantifying the cellular component of the reactive tissue response. Recent findings, however, indicate that strong cellular responses to implanted microelectrodes do not necessarily correspond to similar changes in electrode impedance (Prasad and Sanchez, 2012). We posit that extracellular components of the reactive tissue response might be more instrumental in altering the electrical properties of implanted electrodes, and thus offer an attractive alternative for quantification and mitigation. The primary objective of this paper was to identify non-cellular components as potential modulators of impedance changes in neural microelectrodes, and to quantify the effects of a specific type of non-cellular component *in vitro*

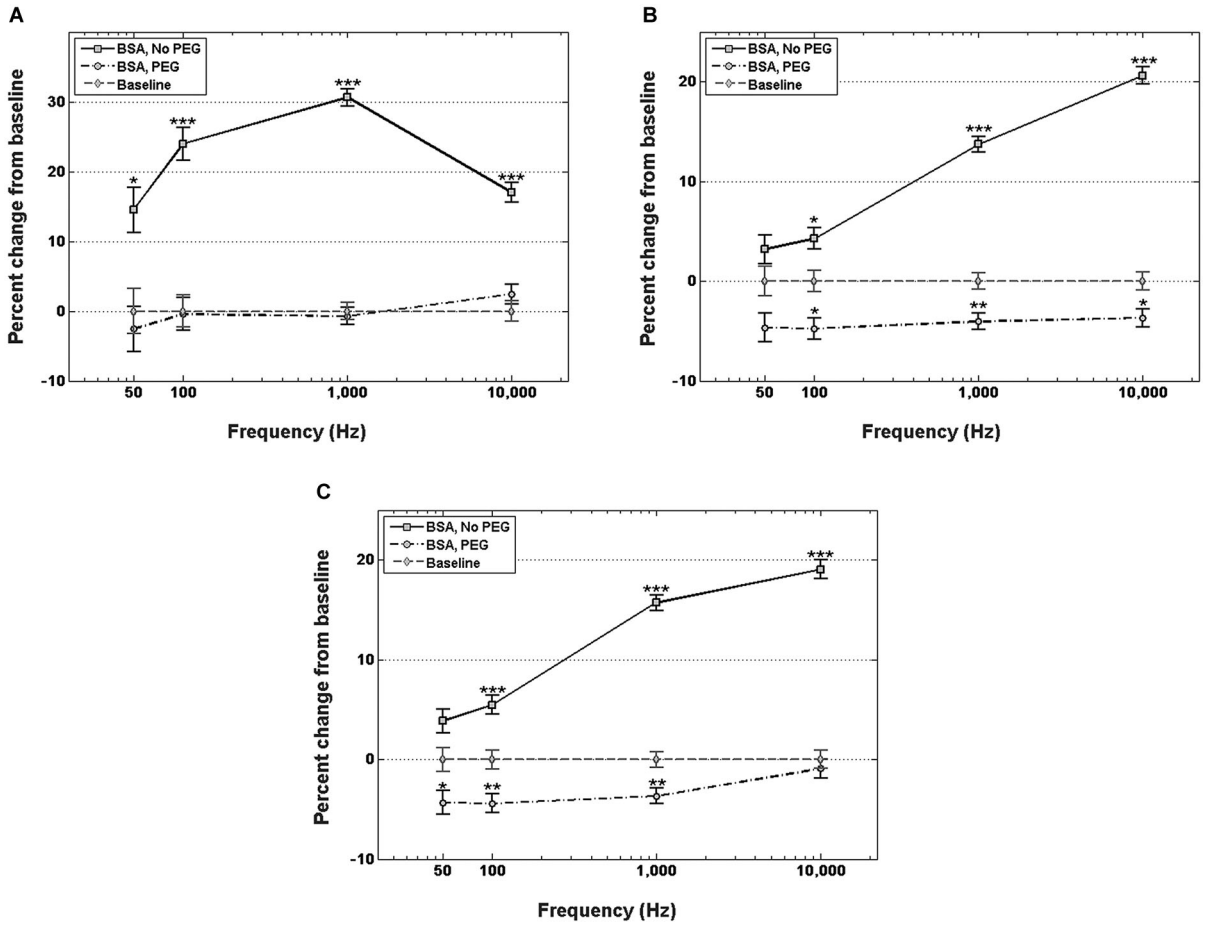

FIGURE 3 | Changes in electrode impedance following immersion in BSA, without and with PEG treatment. (A) Resistance of electrodes immersed in BSA with no PEG treatment exhibits significant increases compared to control at all observed frequencies, notably an increase in resistance of 30.7% compared to control at 1 kHz. Electrodes treated with PEG prior to immersion in BSA exhibit no significant changes in resistance compared to control. **(B)** Reactance of electrodes immersed in BSA with no PEG treatment exhibit significant increases at frequencies greater than 50 Hz, with the highest increase observed at 10 kHz. PEG treatment prior to immersion in BSA resulted in minor, but significant decreases at frequencies greater than 50 Hz. **(C)** Changes in total impedance closely match changes in reactance. Error bars represent the standard error of the means. Single asterisks (*) respresent $p < 0.05$, double asterisks (**) represent $p < 0.001$, triple asterisks (***) represent $p < 0.0001$.

(proteins). The secondary objective was to demonstrate a proof of concept at acute time scales for using PEG applied via a simple dip-coating process to prevent impedance changes caused by non-cellular components both *in vitro* and *in vivo*.

EXPLANATION OF RESULTS

For the *in vitro* study with the model protein solution, a three-electrode setup was chosen for its ability to isolate the electrode/solution interface impedance. Changes in impedance measured using this three-electrode setup indicate changes only at the electrode/solution interface (Bard and Faulkner, 2001). Because of the combination of low currents, short timescales, micro-scale working electrodes, and a large area counter, it was assumed that very minimal changes could have occurred at the recording surface. Using this measurement paradigm, our first finding was that significant increases in resistance at all examined frequencies occur immediately upon exposure to a model protein solution with a concentration mimicking *in vivo* concentrations. Furthermore, significant increases in the reactance are observed at higher frequencies, including the physiologically relevant 1 kHz. The aggregate impedance effect is that of a significant increase at frequencies higher than 50 Hz. These observed *in vitro* changes in impedance might not exactly match *in vivo* changes, given the difference in protein composition in the brain, and the presence of additional biomolecules with widely varying degrees of hydrophobicity, such as lipids and polysaccharides (O'Brien and Sampson, 1965; Pease, 1966; Margolis and Margolis, 1974; Norton et al., 1975). This finding of changes in both resistive and capacitive components following protein adsorption challenges current assumptions inherent in prevalent electrical circuit models of the device tissue interface. Such models typically assume that protein adsorption causes purely resistive changes in impedance (Johnson et al., 2005; Otto et al., 2006; Williams et al., 2007). We demonstrate that the exposure of microelectrodes to a protein solution

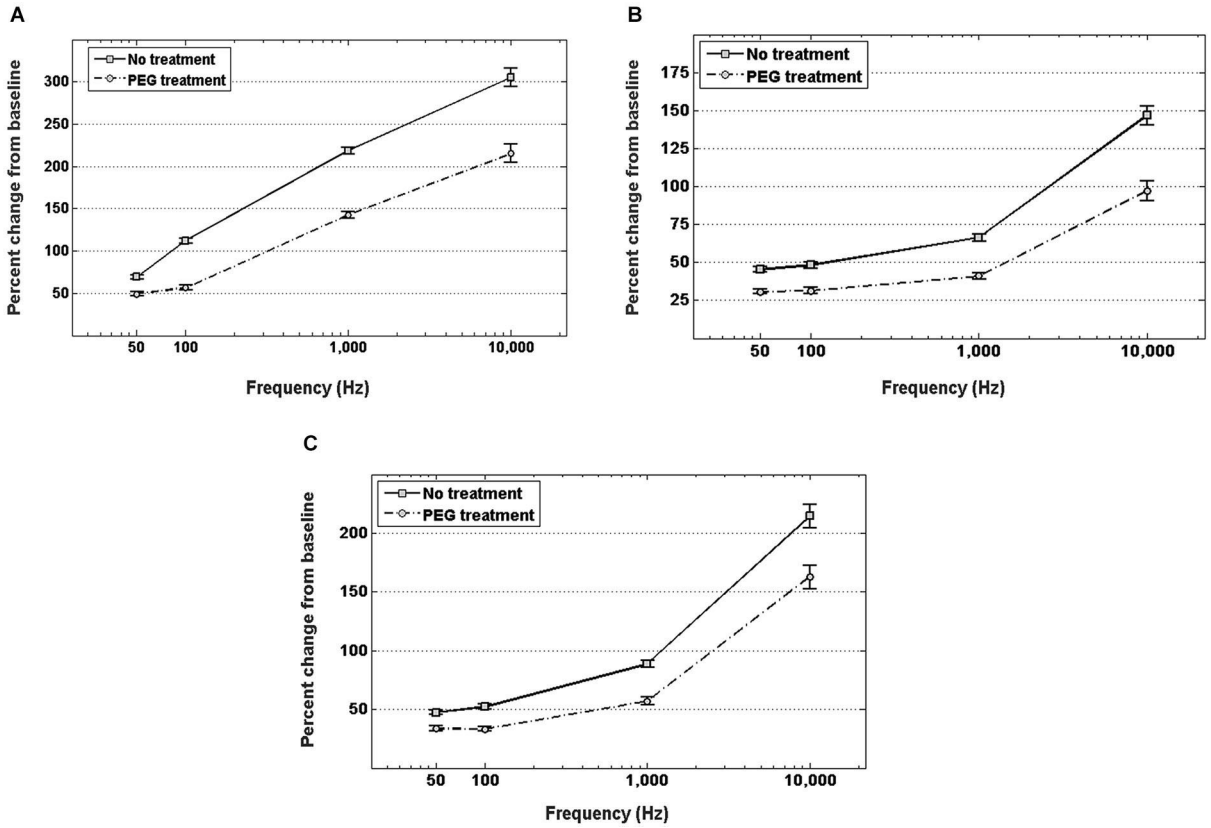

FIGURE 4 | ***In vivo*** **increase in resistance (A), reactance (B), and total impedance (C) from** ***in vitro*** **baseline, with and without PEG treatment**. For either treatment condition, a significant increase in impedance (both resistance and reactance) from the *in vitro* baseline is observed at all frequencies ($p < 0.05$). For electrodes with no treatment, the percent increase in impedance (both resistance and reactance) from baseline was significantly higher ($p < 0.05$) than the percent increase with PEG treatment at all frequencies.

results in both resistive and capacitive changes in impedance, rather than purely resistive changes. These findings suggest a need for the reexamination of assumptions upon which prevalent electrical circuit models for the tissue electrode interface are built. More accurate or representative equivalent circuit models might improve the utility of impedance monitoring to accurately deduce the progression of the reactive tissue response.

Our study further demonstrates that treating electrodes with a PEG film via dip coating prior to immersion in a protein solution negates these increases in impedance at physiologically relevant frequencies. That electrodes pretreated with PEG exhibit slight decreases in reactance supports our working hypothesis that the PEG film forms a hydrated layer close to the electrode surface that prevents proteins from accessing the surface of the electrode, while simultaneously avoiding detrimental effects on charge transfer at the electrode-electrolyte layer.

For the acute *in vivo* study, a two-electrode setup was used due to the difficulty of implementing a three-electrode setup within a surgical setting. The use of a two-electrode setup means that the impedance of the tissue/electrode interface and the impedance of the tissue are lumped into a single impedance source. The expected contribution of the tissue impedance component is confirmed by the considerable increase observed in both the resistance and capacitance following the insertion of the electrode into the rat brain. For this study, we wanted to examine the contribution of non-cellular components to the change in impedance, and therefore chose a short time scale during which no tissue remodeling occurs. Since cellular responses in the brain following electrode implantation are not observed until several hours post implantation (Kozai et al., 2012), our impedance measurement needed to be conducted within that time frame. We chose an arbitrary time point of 5 min post-insertion to minimize the exposure of the animals to unnecessary anesthesia, but it is possible for impedance changes to be time sensitive.

The application of an aqueous solution of a higher molecular weight PEG by dip-coating onto the microelectrode and directly into the craniotomy resulted in a reduction in the magnitude of the increase from the *in vitro* baseline impedance. Because the tissue impedance component is presumed not to change within this short time frame, we can assume that the difference in impedance with PEG treatment compared to the no treatment condition is due primarily to the modulation of the electrode/tissue interface impedance component. In the control craniotomy, we posit that a considerable portion of the immediate impedance increase comes from hydrophobic biomolecules that come into contact with the electrode surface and hinder charge transfer. The application

of free-floating high molecular weight PEG appears to confer some degree of protection from the effects of aforementioned biomolecules, and results in lower impedance. With this simple method of applying PEG via dip-coating, there are concerns about the uniformity of coatings between electrodes. While we did not directly quantify the morphology of our dip-coated PEG films, we did attempt to control the deposition process to minimize variability. Since the dip-coating velocity is a major contributing factor to the uniformity of dip-coated films (Scriven, 1988), we controlled our dip-coating velocity by using a micromanipulator. Because we did observe statistically significant changes in impedance in response to our dip coatings, we did not make further attempts to identify and reduce individual contributors to inter-electrode variations.

Much more research needs to be conducted into the use of PEG to understand its potential long-term effects on the functional longevity of implantable intracortical microelectrodes. While prior research in the field has found that conformal microgel PEG coatings that do prevent cellular adhesion *in vitro* do not result in significant improvement to the cellular composition of the chronic electrode tissue interface (Gutowski et al., 2014), the effects of such PEG-containing coatings on the electrical properties of functional electrodes have not been tested. It is possible that significant protective effects using grafted coatings have not been observed due to the use of lower molecular weights. For our proof of concept demonstration for PEG, we used a molecular weight of 4000 Da, which has been shown to be optimal for reducing biofouling in comparison with lower molecular weights (Su et al., 2009). With biopolymers, there are concerns about degradability which might limit the long-term potential for such coatings to modulate the reactive tissue response. PEG, however, is generally not considered easily degradable in physiological conditions, and degradable PEG hydrogels generally need to be engineered with special cleavage sites to facilitate biodegradability (Drury and Mooney, 2003). On the other hand, the effects of long-term presence of large polymeric molecules in the brain should be considered before employing such molecules as neurointegrative coatings.

These complex considerations surrounding such antifouling coatings present an attractive research area. While chemically immobilized coatings are a commonplace choice for neurointegrative coatings, there might be additional merits to weakly attached PEG films. For example, intravenous treatment with higher molecular weight PEG has been shown to improve cellular and behavioral recovery in traumatic brain injury (Koob et al., 2005, 2008; Koob and Borgens, 2006), due to its fusogen properties which allow it to induce membrane sealing of damaged cells and tissue (Shi, 2013). It is possible that these properties of higher molecular weight PEG can be similarly effective in disrupting deposition of proteins and other molecules at the electrode vicinity, in addition to mitigating chronic blood-brain barrier damage, a major factor in chronic device failure (Saxena et al., 2013). Before dip-coated PEG films can be prescribed as a long-term solution for preventing the reactive tissue response and increase the functional longevity of implantable neural microelectrodes, more extensive parametric studies need to be conducted. These studies should consider the molecular weight of the PEG used, in addition to the morphological characteristics of the applied films, such as roughness and thickness, and related properties such as degradation kinetics. The delivery method of PEG films is also an open question. It might be necessary to combine multiple delivery methods; for example, concurrently immobilizing PEG onto the electrode surface and applying free-floating PEG. One potential approach under investigation is the use of thin-film silica sol-gel coatings, which have the potential to incorporate released and immobilized molecules, and do not adversely affect electrical properties (Pierce et al., 2009). Such future experiments with PEG should combine impedance monitoring with histological analysis of the reactive tissue response on a chronic time scale. Our findings provide a first step by highlighting the potential contribution of non-cellular molecular components to impedance changes, and offer a proof of concept for dip-coated PEG films as a potential component within a holistic neurointegrative strategy.

ACKNOWLEDGMENTS

Funding for this research was provided by the Purdue Research Foundation, the Indiana Spinal Cord and Brain Injury Research Grant Program (Fund # 00015115), and the Defense Advanced Research Projects Agency (DARPA) Microsystems Technology Office (MTO), under the auspices of Dr. Jack W. Judy (jack.judy@darpa.mil) and Dr. Doug Weber (douglas.weber@darpa.mil) as part of the Reliable Neural Technology Program, through the Space and Naval Warfare Systems Command (SPAWAR) Systems Center (SSC) Pacific grant No. N66001-11-1-4013. Thanks to members of the Neuroprostheses Research Laboratory for feedback on the manuscript.

REFERENCES

Banay-Schwartz, M., Kenessey, A., DeGuzman, T., Lajtha, A., and Palkovits, M. (1992). Protein content of various regions of rat brain and adult and aging human brain. *Age (Omaha)* 15, 51–54. doi: 10.1007/bf02435024

Bard, A. J., and Faulkner, L. R. (2001). *Electrochemical Methods: Fundamentals and Applications.* 2nd Edn. Hoboken, NJ: Wiley Sons.

Barrese, J. C., Rao, N., Paroo, K., Triebwasser, C., Vargas-Irwin, C., Franquemont, L., et al. (2013). Failure mode analysis of silicon-based intracortical microelectrode arrays in non-human primates. *J. Neural Eng.* 10:066014. doi: 10.1088/1741-2560/10/6/066014

Bluestein, D., Chandran, K. B., and Manning, K. B. (2010). Towards non-thrombogenic performance of blood recirculating devices. *Ann. Biomed. Eng.* 38, 1236–1256. doi: 10.1007/s10439-010-9905-9

Drury, J. L., and Mooney, D. J. (2003). Hydrogels for tissue engineering: scaffold design variables and applications. *Biomaterials* 24, 4337–4351. doi: 10.1016/s0142-9612(03)00340-5

Frampton, J. P., Hynd, M. R., Shuler, M. L., and Shain, W. (2010). Effects of glial cells on electrode impedance recorded from neural prosthetic devices *in vitro*. *Ann. Biomed. Eng.* 38, 1031–1047. doi: 10.1007/s10439-010-9911-y

Gutowski, S. M., Templeman, K. L., South, A. B., Gaulding, J. C., Shoemaker, J. T., LaPlaca, M. C., et al. (2014). Host response to microgel coatings on neural electrodes implanted in the brain. *J. Biomed. Mater. Res. A* 102, 1486–1499. doi: 10.1002/jbm.a.34799

Johnson, M. D., Otto, K. J., and Kipke, D. R. (2005). Repeated voltage biasing improves unit recordings by reducing resistive tissue impedances. *IEEE Trans. Neural Syst. Rehabil. Eng.* 13, 160–165. doi: 10.1109/tnsre.2005.847373

Koob, A. O., and Borgens, R. B. (2006). Polyethylene glycol treatment after traumatic brain injury reduces beta-amyloid precursor protein accumulation in degenerating axons. *J. Neurosci. Res.* 83, 1558–1563. doi: 10.1002/jnr.20837

Koob, A. O., Colby, J. M., and Borgens, R. B. (2008). Behavioral recovery from traumatic brain injury after membrane reconstruction using polyethylene glycol. *J. Biol. Eng.* 2:9. doi: 10.1186/1754-1611-2-9

Koob, A. O., Duerstock, B. S., Babbs, C. F., Sun, Y., and Borgens, R. B. (2005). Intravenous polyethylene glycol inhibits the loss of cerebral cells after brain injury. *J. Neurotrauma* 22, 1092–1111. doi: 10.1089/neu.2005.22.1092

Kozai, T. D. Y., Vazquez, A. L., Weaver, C. L., Kim, S.-G., and Cui, X. T. (2012). *In vivo* two-photon microscopy reveals immediate microglial reaction to implantation of microelectrode through extension of processes. *J. Neural Eng.* 9:066001. doi: 10.1088/1741-2560/9/6/066001

Leung, B. K., Biran, R., Underwood, C. J., and Tresco, P. A. (2008). Characterization of microglial attachment and cytokine release on biomaterials of differing surface chemistry. *Biomaterials* 29, 3289–3297. doi: 10.1016/j.biomaterials.2008.03.045

Li, S., and Henry, J. J. (2011). Nonthrombogenic approaches to cardiovascular bioengineering. *Annu. Rev. Biomed. Eng.* 13, 451–475. doi: 10.1146/annurev-bioeng-071910-124733

Margolis, R. U., and Margolis, R. K. (1974). Distribution and metabolism of mucopolysaccharides and glycoproteins in neuronal perikarya, astrocytes and oligodendroglia. *Biochemistry* 13, 2849–2852. doi: 10.1021/bi00711a011

Michel, R., Pasche, S., Textor, M., and Castner, D. G. (2005). Influence of PEG architecture on protein adsorption and conformation. *Langmuir* 21, 12327–12332. doi: 10.1021/la051726h

Muthusubramaniam, L., Lowe, R., Fissell, W. H., Li, L., Marchant, R. E., Desai, T. A., et al. (2011). Hemocompatibility of silicon-based substrates for biomedical implant applications. *Ann. Biomed. Eng.* 39, 1296–1305. doi: 10.1007/s10439-011-0256-y

Norton, W. T., Abe, T., Poduslo, S. E., and DeVries, G. H. (1975). The lipid composition of isolated brain cells and axons. *J. Neurosci. Res.* 1, 57–75. doi: 10.1002/jnr.490010106

O'Brien, J. S., and Sampson, E. L. (1965). Lipid composition of the normal human brain: gray matter, white matter and myelin. *J. Lipid Res.* 6, 537–544.

Otto, K. J., Johnson, M. D., and Kipke, D. R. (2006). Voltage pulses change neural interface properties and improve unit recordings with chronically implanted microelectrodes. *IEEE Trans. Biomed. Eng.* 53, 333–340. doi: 10.1109/tbme.2005.862530

Pease, D. C. (1966). Polysaccharides associated with the exterior surface of epithelial cells: kidney, intestine, brain. *J. Ultrastruct. Res.* 15, 555–588. doi: 10.1016/s0022-5320(66)80128-4

Pierce, A. L., Sommakia, S., Rickus, J. L., and Otto, K. J. (2009). Thin-film silica sol-gel coatings for neural microelectrodes. *J. Neurosci. Methods* 180, 106–110. doi: 10.1016/j.jneumeth.2009.02.008

Prasad, A., and Sanchez, J. C. (2012). Quantifying long-term microelectrode array functionality using chronic *in vivo* impedance testing. *J. Neural Eng.* 9:026028. doi: 10.1088/1741-2560/9/2/026028

Prasad, A., Xue, Q.-S., Sankar, V., Nishida, T., Shaw, G., Streit, W. J., et al. (2012). Comprehensive characterization and failure modes of tungsten microwire arrays in chronic neural implants. *J. Neural Eng.* 9:056015. doi: 10.1088/1741-2560/9/5/056015

Rao, L., Zhou, H., Li, T., Li, C., and Duan, Y. Y. (2012). Polyethylene glycol-containing polyurethane hydrogel coatings for improving the biocompatibility of neural electrodes. *Acta Biomater.* 8, 2233–2242. doi: 10.1016/j.actbio.2012.03.001

Salacinski, H. J., Goldner, S., Giudiceandrea, A., Hamilton, G., Seifalian, A. M., Edwards, A., et al. (2001). The mechanical behavior of vascular grafts: a review. *J. Biomater. Appl.* 15, 241–278. doi: 10.1106/na5t-j57a-jtdd-fd04

Saxena, T., Karumbaiah, L., Gaupp, E. A., Patkar, R., Patil, K., Betancur, M., et al. (2013). The impact of chronic blood–brain barrier breach on intracortical electrode function. *Biomaterials* 34, 4703–4713. doi: 10.1016/j.biomaterials.2013.03.007

Scriven, L. E. (1988). Physics and applications of dip coating and spin coating. *MRS Proc.* 121, 717–729. doi: 10.1557/proc-121-717

Sharma, S., Johnson, R. W., and Desai, T. A. (2004a). Evaluation of the stability of nonfouling ultrathin poly(ethylene glycol) films for silicon-based microdevices. *Langmuir* 20, 348–356. doi: 10.1021/la034753l

Sharma, S., Johnson, R. W., and Desai, T. A. (2004b). XPS and AFM analysis of antifouling PEG interfaces for microfabricated silicon biosensors. *Biosens. Bioelectron.* 20, 227–239. doi: 10.1016/j.bios.2004.01.034

Shi, R. (2013). Polyethylene glycol repairs membrane damage and enhances functional recovery: a tissue engineering approach to spinal cord injury. *Neurosci. Bull.* 29, 460–466. doi: 10.1007/s12264-013-1364-5

Sommakia, S., Rickus, J. L., and Otto, K. J. (2009). Effects of adsorbed proteins, an antifouling agent and long-duration DC voltage pulses on the impedance of silicon-based neural microelectrodes. *Conf. Proc. IEEE Eng. Med. Biol. Soc.* 2009, 7139–7142. doi: 10.1109/IEMBS.2009.5332456

Su, Y.-L., Cheng, W., Li, C., and Jiang, Z. (2009). Preparation of antifouling ultrafiltration membranes with poly (ethylene glycol)-*graft*-polyacrylonitrile copolymers. *J. Memb. Sci.* 329, 246–252. doi: 10.1016/j.memsci.2009.01.002

Vetter, R. J., Williams, J. C., Hetke, J. F., Nunamaker, E. A., and Kipke, D. R. (2004). Chronic neural recording using silicon-substrate microelectrode arrays implanted in cerebral cortex. *IEEE Trans. Biomed. Eng.* 51, 896–904. doi: 10.1109/tbme.2004.826680

Williams, J. C., Hippensteel, J. A., Dilgen, J., Shain, W., and Kipke, D. R. (2007). Complex impedance spectroscopy for monitoring tissue responses to inserted neural implants. *J. Neural Eng.* 4, 410–423. doi: 10.1088/1741-2560/4/4/007

Williams, J. C., Rennaker, R. L., and Kipke, D. R. (1999). Long-term neural recording characteristics of wire microelectrode arrays implanted in cerebral cortex. *Brain Res. Brain Res. Protoc.* 4, 303–313. doi: 10.1016/s1385-299x(99)00034-3

Winter, J. O., Cogan, S. F., and Rizzo, J. F. (2007). Neurotrophin-eluting hydrogel coatings for neural stimulating electrodes. *J. Biomed. Mater. Res. B Appl. Biomater.* 81, 551–563. doi: 10.1002/jbm.b.30696

Conflict of Interest Statement: The authors declare that the research was conducted in the absence of any commercial or financial relationships that could be construed as a potential conflict of interest.

Received: 30 April 2014; accepted: 11 July 2014; published online: 04 August 2014.
*Citation: Sommakia S, Gaire J, Rickus JL and Otto KJ (2014) Resistive and reactive changes to the impedance of intracortical microelectrodes can be mitigated with polyethylene glycol under acute in vitro and in vivo settings. Front. Neuroeng. **7**:33. doi: 10.3389/fneng.2014.00033*
This article was submitted to the journal Frontiers in Neuroengineering.

frontiers in
NEUROENGINEERING

ORIGINAL RESEARCH ARTICLE
published: 14 November 2014
doi: 10.3389/fneng.2014.00041

Glial cells, but not neurons, exhibit a controllable response to a localized inflammatory microenvironment *in vitro*

Salah Sommakia*[1,2], *Jenna L. Rickus*[1,2,3] *and Kevin J. Otto*[1,4,5]

[1] *Weldon School of Biomedical Engineering, Purdue University, West Lafayette, IN, USA*
[2] *Physiological Sensing Facility at the Bindley Bioscience Center and Birck Nanotechnology Center, Purdue University, West Lafayette, IN, USA*
[3] *Department of Agricultural and Biological Engineering, Purdue University, West Lafayette, IN, USA*
[4] *Department of Biological Sciences, Purdue University, West Lafayette, IN, USA*
[5] *J. Crayton Pruitt Family Department of Biomedical Engineering, University of Florida, Gainesville, FL, USA*

Edited by:
Ulrich G. Hofmann, Albert-Ludwigs-University Freiburg, Germany

Reviewed by:
Hugues Berry, INRIA, France
Ian D. Dryg, University of Washington, USA

****Correspondence:***
Kevin J. Otto, J. Crayton Pruitt Family Department of Biomedical Engineering, University of Florida, 1064 Center Drive, NEB 363, Gainesville, FL 32611, USA
e-mail: kevin.otto@bme.ufl.edu

The ability to design long-lasting intracortical implants hinges on understanding the factors leading to the loss of neuronal density and the formation of the glial scar. In this study, we modify a common *in vitro* mixed cortical culture model using lipopolysaccharide (LPS) to examine the responses of microglia, astrocytes, and neurons to microwire segments. We also use dip-coated polyethylene glycol (PEG), which we have previously shown can modulate impedance changes to neural microelectrodes, to control the cellular responses. We find that microglia, as expected, exhibit an elevated response to LPS-coated microwire for distances of up to 150 μm, and that this elevated response can be mitigated by co-depositing PEG with LPS. Astrocytes exhibit a more complex, distance-dependent response, whereas neurons do not appear to be affected by the type or magnitude of glial response within this *in vitro* model. The discrepancy between our *in vitro* responses and typically observed *in vivo* responses suggest the importance of using a systems approach to understand the responses of the various brain cell types in a chronic *in vivo* setting, as well as the necessity of studying the roles of cell types not native to the brain. Our results further indicate that the loss of neuronal density observed *in vivo* is not a necessary consequence of elevated glial activation.

Keywords: intracortical microelectrodes, foreign body response, primary cortical cultures

INTRODUCTION

Implantable intracortical microelectrodes hold great potential as neural prostheses for the treatment of a wide range of traumatic and degenerative injuries to the central nervous system, but suffer from unreliability in chronic settings. This decline in chronic device performance correlates with a reactive response of brain tissue (Vetter et al., 2004). Designing therapeutic approaches to counter this decline in device performance is complicated by the lack of detailed mechanistic understanding of the progression of the reactive tissue. Dural and vascular damage appear to be major factors contributing to the reactive tissue response (Karumbaiah et al., 2013; Saxena et al., 2013). Using novel device capture techniques (Woolley et al., 2011, 2013a,b), this reactive tissue response has been shown to be non-uniform and depth dependent, with stronger scarring closer to the surface of the brain (Woolley et al., 2013c). Transdural implants elicit a much greater response than implants dwelling completely within the brain (Markwardt et al., 2013). These findings collectively suggest that the introduction of non-native cellular and molecular components into the brain amplifies inflammatory pathway activation, and that this activation is strongest at the site of injury to respective structures. Recently, potential therapeutic targets such as reactive oxygen species and toll-like receptor 4 (TL4) have been identified (Potter et al., 2013; Ravikumar et al., 2014), but the complexity underlying *in vivo* conditions can obscure investigations of biological mechanisms.

These obstacles can be somewhat overcome by studying simpler models, such as *in vitro* cell cultures. The most widely used model, first described by Polikov et al. (2006, 2009), presents microscale foreign bodies to primary mixed neural cultures., and has been applied to test biocompatibility of various materials as neural interfaces (Achyuta et al., 2010; Tien et al., 2013). This model requires the modification of the culture media to achieve a globally elevated activation state. We posit that a more localized inflammatory microenvironment may better represent the non-uniform reactive tissue response, and propose a modification to the model whereby the foreign objects are dip-coated in lipopolysaccharide (LPS) to simulate a localized inflammatory microenvironment. LPS is a known upregulator of microglial activation through TL4 binding (Lehnardt et al., 2003; Tzeng et al., 2005), and as such is an attractive option for modifying the Polikov model to test cellular responses to localized targeting of TL4 receptors. In contrast to the previous model, the creation of a localized inflammatory microenvironment also enables the analysis of neuronal responses.

Previous research in the neurotrauma field has also found that, due its surfactant properties, soluble polyethylene glycol (PEG) can induce membrane sealing of damaged cells and reduce edema

(Borgens et al., 2002). This effect significantly improves recovery from both spinal cord and traumatic brain injuries by inducing cellular and behavioral recovery (Koob et al., 2005, 2008; Koob and Borgens, 2006). Additionally, we have recently showed that a dip-coated PEG film can modulate impedance changes caused by non-cellular components both *in vitro* and *in vivo* (Sommakia et al., 2014). In this regard, a non-grafted dip-coated PEG film is a technically and economically attractive option to achieve both antifouling and membrane sealing. Our hypothesis is that a dip-coated layer of high molecular weight PEG will exhibit sufficient short term stability to modulate cellular responses to microelectrodes *in vitro*. Given the importance of the early stages of the injury response in shaping the later chronic stages, this approach might prove highly beneficial *in vivo*.

In this work we test our PEG hypothesis using the local inflammation-modified Polikov model. We show that, as expected, coating segments of microwire with LPS results in an increase in microglial activation at distances up to 150 μm, and, importantly, co-depositing LPS with a PEG solution prevents observed increases in microglial activation. We also observe a slight increase in astrocyte activation in response to LPS-coated microwire, but not at the same magnitude or spatial distribution as microglia. Interestingly, neuronal responses in this *in vitro* paradigm do not appear to be influenced by corresponding glial responses.

MATERIALS AND METHODS

CELL CULTURE AND MICROWIRE PLACEMENT

The experimental procedures complied with the Guide for the Care and Use of Laboratory Animals and were approved by The Purdue Animal Care and Use Committee (PACUC). Forebrains from E17 embryonic rat pups were received suspended in 5 ml of Solution 1 (NaCl 7.24 g/L; KCl 0.4 g/L; NaH2PO4 0.14 g/L; Glucose 2.61 g/L; HEPES 5.96 g/L; MgSO4 0.295 g/L; Bovine Serum Albumin 3 g/L) in a 50 ml centrifuge tube. Under sterile conditions, the tissue was gently triturated with an added 18 μl of trypsin solution (Sigma-Aldrich, St. Louis, MO) (7.5 mg/ml in 0.9% saline) and incubated for 20 min in a 37°C water bath. Following the incubation step, 100 μl of trypsin inhibitor/DNAase solution (Sigma-Aldrich, St. Louis, MO) (2.5 mg/ml trypsin inhibitor, 400 μg/ml DNAase in 0.9% saline) was added and tissue was again gently triturated. The tissue was then centrifuged at 1,000 rpm for 5 min at room temperature and supernatant was poured off. Cells were re-suspended in 16 ml of Hibernate-E (Brainbits, Springfield, IL) and triturated once again. Cells were filtered through a 70 μm cell strainer (Fisher Scientific) and centrifuged at 1,400 rpm for 5 min at room temperature. Supernatant was poured off and cells were re-suspended in a culture medium consisting of Dulbecco's modified Eagle's Medium (DMEM) with 10% Fetal Bovine Serum (FBS) and 10% horse serum (HS). The cells were then seeded in 96 well plates at a density of 500,000 cells/cm^2, and cultured for 7 days at 37°C and 5% CO_2, with the cell media being replaced every 48 h. At day 7 *in vitro*, lengths of 50 μm-diameter tungsten microwire (California Fine Wire Co., Grover Beach, CA) were autoclaved then cut into small segments of 5–7 mm in length using carbide scissors. The microwire segments were treated by dip coating with one of four treatments: LPS (50 ng/ml) only, PEG (20% aqueous solution, 4000 MW) only, a 1:1 mixture of LPS and PEG, or uncoated. A relatively low LPS concentration was chosen based on reported literature values (Das et al., 1995; Wang et al., 2005) in order to achieve localized activation of microglia, but prevent a generalized activation that might result from a higher concentration of LPS diffusing rapidly throughout the well. PEG concentration is based on our previous work demonstrating a proof of concept for using PEG to modulate impedance changes to neural microelectrodes (Sommakia et al., 2014). In each well, one segment of microwire was dropped into the medium and allowed to sink to the bottom of the well. The plates were then placed in the incubator for an additional 7 days.

CELL FIXING AND LABELING

At day 14 *in vitro*, the cultures were fixed with 4% paraformaldehyde for 10 min, rinsed 3× with HEPES Buffered Hank's saline (HBHS) (in g/L; 7.5 g NaCl, 0.3 g KCl, 0.06 g KH2PO4, 0.13 g Na2HPO4, 2 g Glucose, 2.4 g HEPES, 0.05 g MgCl2:6H2O, 0.05 g MgSO4:7H2O, 0.165 g CaCl2, 90 mg NaN3, at pH 7.4), then permeabilized with 0.2% Triton-X (Sigma-Aldrich, St. Louis, MO). The cultures were then blocked with 10% normal goat serum (Jackson Immunoresearch, West Grove, PA) for 1 h, after which primary antibodies to beta-3-tubulin (β-3-tub) (Covance, Princeton, NJ), which labels neurons; Glial Fibrillary Acidic Protein (GFAP) (Millipore, Billerica, MA), which labels astrocytes; and Ionized Calcium binding adaptor molecule 1 (Iba1) (Wako, Osaka, Japan), which labels microglia, were added, and the cultures incubated in a 4°C refrigerator overnight. The wells were then aspirated, rinsed in HBHS 3×, and the following secondary antibodies were added: Alexa Fluor 488 Goat anti-mouse, Alexa Fluor 555 Goat anti-chicken, and Alexa Fluor 635 Goat anti-rabbit (Invitrogen, Carlsbad, CA). After a 2 h incubation at room temperature, the secondary antibodies were rinsed 3× with HBHS, and a final volume of 100 μl of HBHS was left in the wells for imaging. Special care was taken to ensure the microwire segments remained attached to the bottom of the wells.

IMAGE ACQUISITION AND ANALYSIS

Fluorescent images (512 × 512 pixels) were obtained on a confocal microscope fitted with a long working distance 10× air objective using Fluoview software (Olympus, Center Valley, PA). The different channels were imaged sequentially, and noise reduction was achieved by applying a Kalman filter built into the acquisition software to 3 scans for each channel. Each plate was imaged using the same set of imaging parameters (laser power, aperture, acquisition time) to ensure uniformity. Source images were imported into ImageJ (ImageJ, U. S. National Institutes of Health, Bethesda, MD), visually inspected and rotated to place the microwire in a vertical orientation. When possible, two adjacent rectangular selections, 480 pixels high by 240 pixels wide (equivalent to 994 μm by 496 μm), were made with the long edge running on the center of the wire. If that was not possible due to excessive proximity to wall of the well, only a single rectangular selection was made facing the interior of the well. Each of these selections was considered a single sample for analysis purposes. From these selections, intensity profiles of average brightness of each vertical

line were generated, as shown in **Figure 1C**. Microwire segments were also imaged in three empty wells, and an average intensity profile was obtained and subtracted from the intensity profile generated from cell-containing wells. One response index (RI) per cell type was obtained for each region by summing the area underneath the intensity profile line between the distance points corresponding to the region boundaries and dividing by 10000.

Statistical analysis was performed using the SAS 9.3 statistical package (SAS Institute Inc., Cary, NC). A general linear model (GLM) procedure was used perform to a one way ANOVA with block, to remove the effects of variations between the plates by treating the plates as a statistical block. *Post hoc* Tukey tests were used to determine statistical significance between the treatment groups at a significance level of $\alpha = 0.05$. The error bars plotted

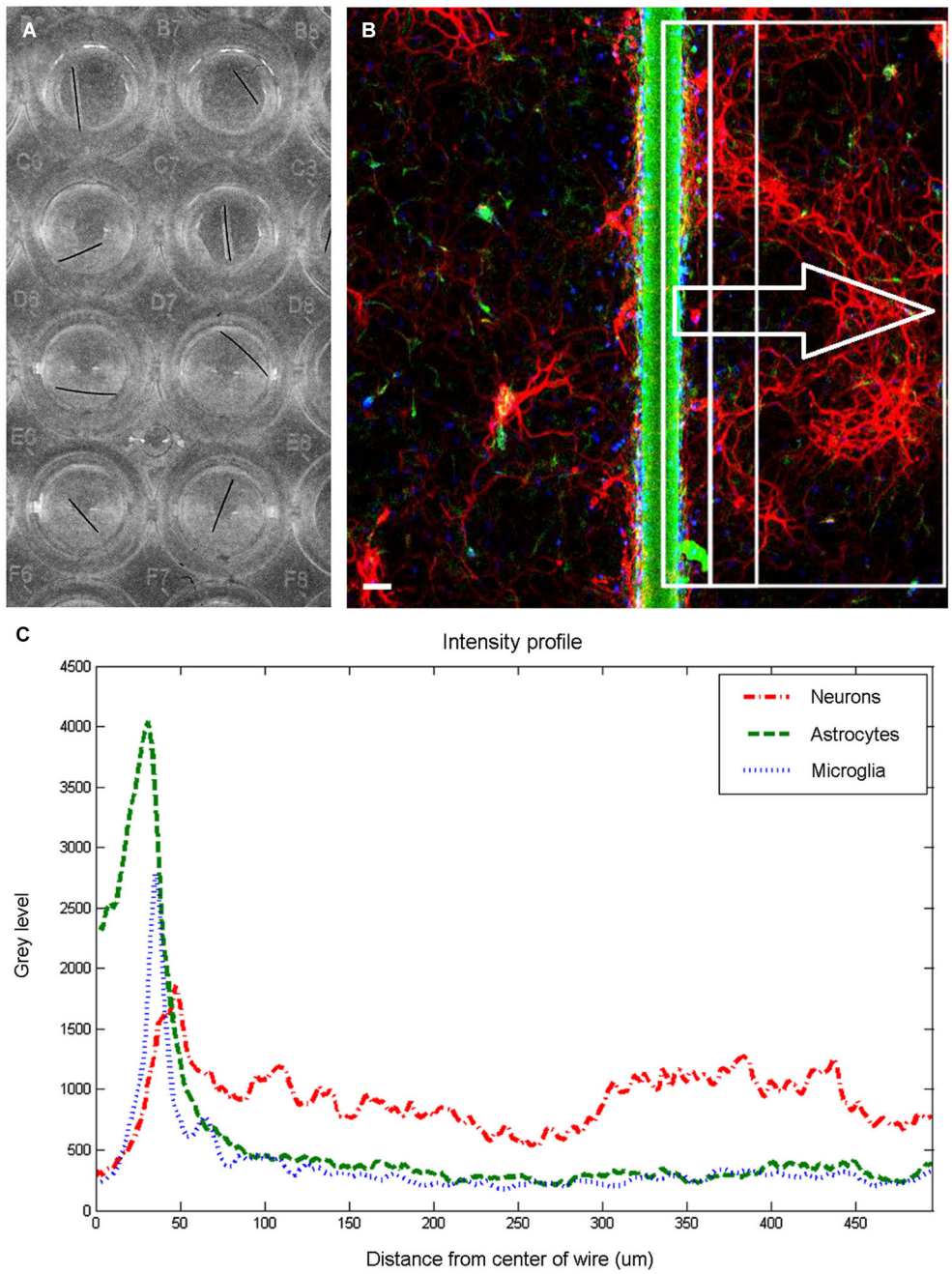

FIGURE 1 | Image quantification. Wells in 96 well plate **(A)** were imaged to produce a fluorescent image **(B)** and extract intensity profiles for each channel. The fluorescent image is pseudocolored to show neurons in red, astrocytes in green, and microglia in blue. Scale bar is 50 μm. For each examined region (examples shown within rectangles), three intensity profiles **(C)** are generated, and response indices calculated by summing the area under the graph corresponding to the chosen distances and dividing by 10000.

represent the standard error of the means. *P*-values less than 0.05 are denoted in the figures by a single asterisk, while *p*-values less than 0.001 are denoted by double asterisks. Plots were generated using MATLAB (The MathWorks Inc., Natick, MA).

RESULTS

Figure 1 shows an overview of the methodology employed to analyze the cellular responses to microwire segments. Microwire segments placed in the wells (**Figure 1A**) were imaged, resulting in sets of images such as the one shown in **Figure 1B**. Intensity profiles (**Figure 1C**) of areas of various widths were analyzed to obtain the results described below.

MICROGLIA

Figure 2 shows the different levels of aggregate microglial response in interface areas of different sizes. In the interface area containing only the microwire (i.e., 25 μm), the only significant difference in the microglial RI was between the PEG coated microwire and LPS coated microwire (RI = 1.37 vs. 2.2, $p = 0.007$). For the interface area containing the wire and extending over an adjacent 25 μm, significant pairwise differences were observed between the LPS coated wire (RI = 5.84) and the other wires (uncoated RI = 4.92, $p = 0.041$; PEG RI = 4.26, $p < 0.0001$; LPS + PEG RI = 4.82, $p = 0.022$). For a wider interface area containing the microwire and extending over the adjacent 50 μm, these pairwise differences get stronger between the LPS coated wire (RI = 8.27) and the other wires (uncoated RI = 6.58, $p = 0.0007$; PEG RI = 5.8, $p < 0.0001$; LPS + PEG RI = 6.4, $p = 0.0002$). Notably, the relative pattern of the microglia response indices for the different conditions is the same for all three regions. Only the overall magnitude of the responses increase as the anti-Iba1 fluorescence is summed over larger areas. This indicates that all three size regions up to the wire plus 50 microns are representative of interface. In all three cases LPS induced microglia activation rises to a level statistical significance. As more distance is included in the interface measurement, the ability of the PEG to relieve microglia activation by LPS rises to statistical significance.

Figure 3 shows the microglial responses at more distant regions. For the closest distant bin extending from 50 to 150 μm from edge of wire, the RI for LPS coated wire (RI = 5.62) was significantly higher than all the other treatments (uncoated RI = 4.21, $p = 0.0001$; PEG RI = 3.71, $p < 0.0001$; LPS + PEG RI = 3.91, $p < 0.0001$). For the next three distant 100 μm wide bins, the only significant difference observed was between LPS coated wire and PEG coated wire in all 3 bins. These calculated RI are as follows: for the bin extending from 150 to 250 μm from edge of wire: LPS RI = 4.5 vs. PEG 3.12, $p = 0.0001$; for the bin extending 250–350 μm from edge of wire: RI = 5.12 vs. 3.8, $p = 0.0003$; for the bin extending 350–450 μm from edge of wire): RI = 4.98 vs. 3.9, $p = 0.01$. Again the pattern of relative RI's is consistent at all distances in the distant regions and matches that of the interface region. In this case the size of each measurement area is the same across cases and is always 100 microns. Again LPS induces an increased RI in all regions reaching statistical significance when comparing LPS to the PEG coated wire and in the most near distant region (50–150 microns) when comparing LPS to an uncoated wire. The wire likely induces some basal level of microglial attachment or activation, which is reduced by PEG alone, therefore the effect of LPS is most pronounced when we compare the PEG wire. These results are consistent with a diffusion based model whereby the effect of LPS will decrease with increasing distance from the wire.

ASTROCYTES

Figure 4 shows the astrocyte RI at interface areas. For the interface area containing only the microwire, the astrocyte RI for LPS

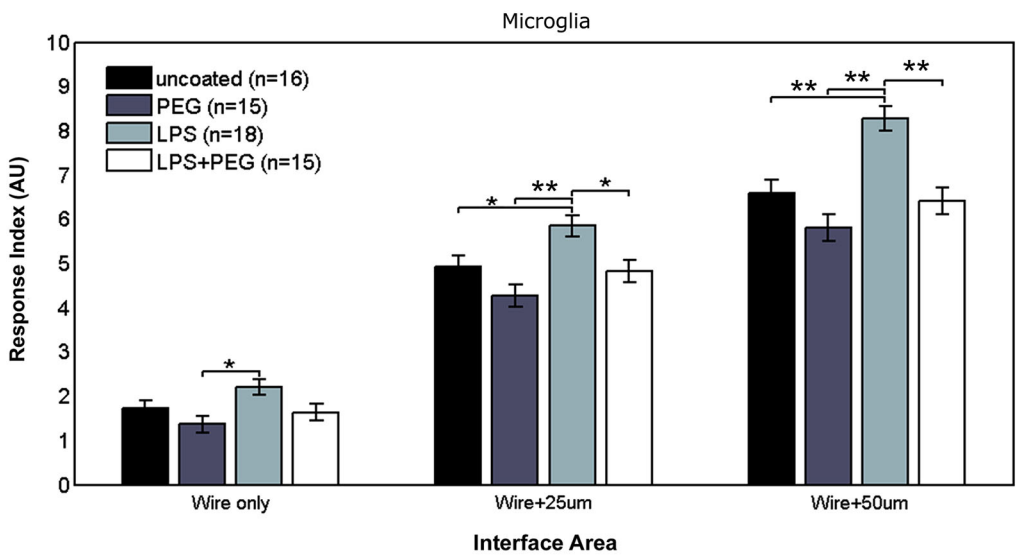

FIGURE 2 | LPS-coated microwire elicits higher microglial response in interface areas, and co-deposition of PEG with LPS reduces microglial response to control levels.

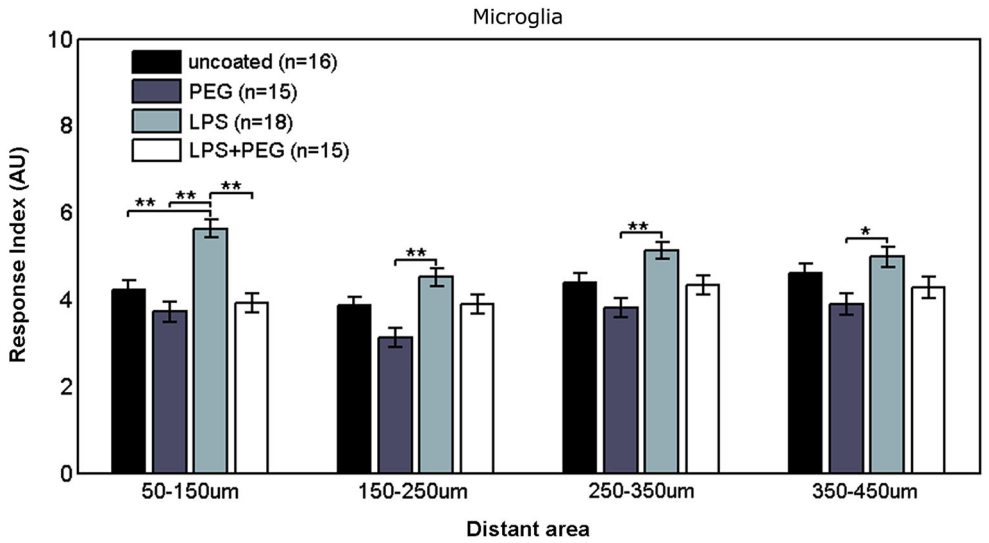

FIGURE 3 | Microglial response to LPS-coated microwire compared to all other treatments is elevated at distances up to 150 μm, after which a tiered response is observed.

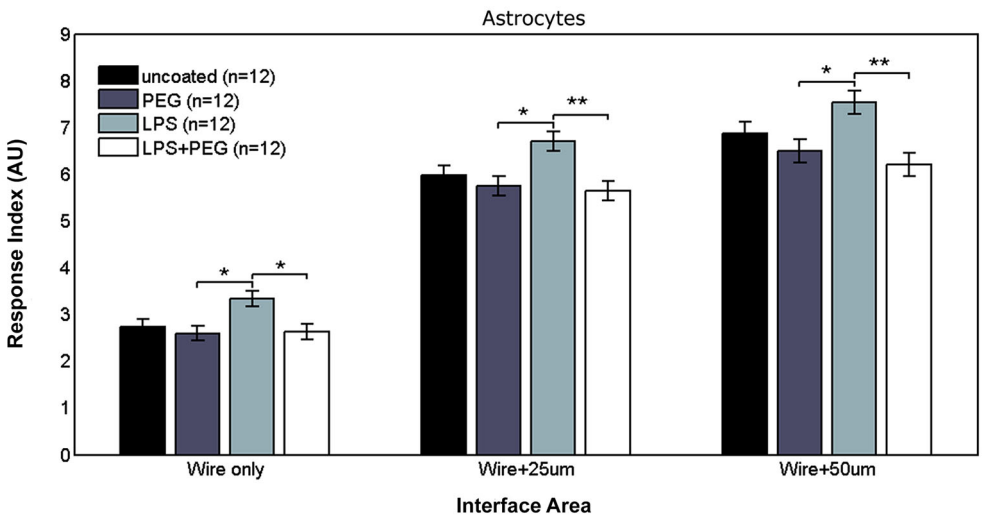

FIGURE 4 | Astrocytes in interface areas of varying width exhibit a tiered response to microwires coated with PEG, with or without LPS.

coated wire (RI = 3.33) was significantly higher than PEG coated and LPS + PEG coated wire (PEG RI = 2.59, $p = 0.015$; LPS + PEG RI = 2.63, $p = 0.02$). For the interface area containing the wire and extending an adjacent 25 μm, the same pairwise difference were observed, but with a stronger difference between the LPS coated wire (RI = 6.7) and the LPS + PEG coated wire (PEG RI = 5.75, $p = 0.012$; LPS + PEG RI = 5.64, $p = 0.0045$). For the interface area containing the microwire and extending an adjacent 50 μm, the same observation of the LPS astrocyte RI being higher than both PEG and LPS + PEG was noticed (LPS RI = 7.54, PEG RI = 6.49, $p = 0.02$; LPS + PEG RI = 6.19, $p = 0.002$). Overall the astrocytes show a similar pattern in the interface as the microglia, but to a lesser extent. Importantly, for all three interface sizes (at the wire, within 25 μm of the wire, and within 50 μm of the wire), the PEG coating is able to significantly reduce the LPS-induced astrocyte response.

Figure 5 shows the astrocyte RI at distant areas. No significant differences were observed between the different treatments for the closest distant bin extending from 50 to 150 μm from edge of microwire. For the middle two distant bins, a slightly significant difference was observed between LPS coated wire and LPS + PEG coated wire [bin 2 (150–250 μm from edge of wire): LPS RI = 2.31, LPS + PEG RI = 1.37, $p = 0.012$; bin 3 (250–350 μm from edge of wire): LPS RI = 2.73, LPS + PEG RI = 1.73, $p = 0.03$].

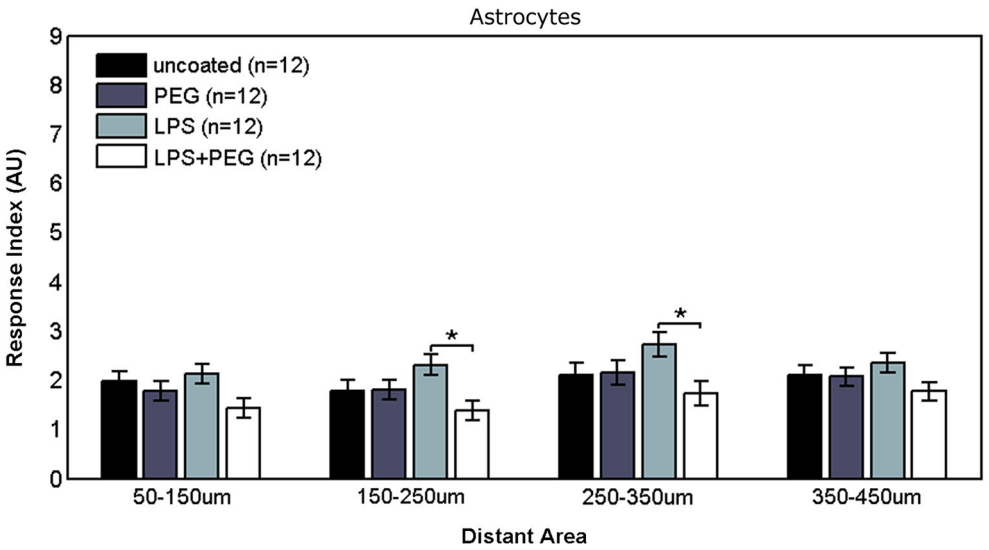

FIGURE 5 | Differences in astrocyte responses in distant areas appear between LPS and LPS + PEG coated microwires at the middle of the distance range analyzed.

NEURONS

Figures 6, **7** show the neuron RI in interface and distant regions respectively. No significant differences in the neuron response were found between any of the treatment conditions in either interface or distant region. In contrast to microglia and astrocytes, where the RI was higher in distant areas in comparison to the widest interface area examined, the neuron RI in distant areas was roughly equal to that in the widest interface area examined.

DISCUSSION

VALIDITY OF MODEL SYSTEM

To test the effects of a dip coated PEG film on the cellular responses to implanted electrodes, we modified a robust and frequently replicated *in vitro* mixed cortical culture model pioneered by Polikov et al. (2006, 2009, 2010; Achyuta et al., 2010; Tien et al., 2013). The anatomical and physiological complexity *in vivo* obscures mechanistic investigations into the reactive tissue response to implanted microelectrodes. Using an *in vitro* model allows us to simplify the biological system under study, and isolate particular components of interest. The challenge with *in vitro* models is to simulate physiological conditions in the absence of particular anatomical structures. In this particular model of primary cortical cell cultures, the cells exist in isolation from supporting vasculature, structural extra-cellular matrix components, and meninges. These aforementioned structures are heavily damaged during microelectrode insertion, which has been shown to strongly affect the chronic response of the brain to implanted microelectrodes (Karumbaiah et al., 2013; Markwardt et al., 2013; Saxena et al., 2013). The original model (Polikov et al., 2006) did not elicit a consistent glial scar, and it was necessary to alter the composition of the culture media to place all glial cells in the culture in an elevated reactive state, thereby ensuring a consistent glial scar (Polikov et al., 2009). By coating LPS directly onto microwire, we are able to create a localized inflammatory microenvironment that more closely mimics the reality of an indwelling cortical implant, rather than placing the glial cells in the culture in a globally activated state. This localized inflammatory microenvironment enables us to examine distance related effects on the cultured cells. For the LPS + PEG condition, concerns about cross contamination and the potential to disrupt the dip-coated PEG film led to the decision to co-deposit PEG and LPS via dip-coating from a single pot. While polymeric films containing PEG have the potential for prolonged drug release, they are typically crosslinked to form hydrogels (Peppas, 1997; Lin and Anseth, 2009) or composites (Ramakrishna et al., 2001). Dip-coated films of a pure hydrophilic polymer, such as PEG, are rarely used for prolonged drug release due to their burst release characteristics and potential for dissolution over timescales shorter than is therapeutically beneficial (Acharya and Park, 2006). PEG, in various conformations, has been shown to accelerate the release of small hydrophobic molecules similar to LPS (Ooya et al., 2003; Kang et al., 2007). For these aforementioned reasons, we were confident that our codeposition of PEG and LPS would not hinder the exposure of the cells to LPS.

To examine microglial response, we chose to quantify Iba1 fluorescence across relatively wide bins. The choice of Iba1 was due to its high specificity to the microglia/macrophage cell type. The function and level of Iba1 expression is directly related to the classic morphological changes associated with microglial activation (Ito et al., 1998). Iba1 crosslinks actin and is involved in the formation of membrane ruffles and rapid motility (Sasaki et al., 2001). Additionally, Iba1 levels correlate directly with morphological feature changes associated with microglial activation (Kozlowski and Weimer, 2012). While current morphological analysis methods have been found lacking (Beynon and Walker,

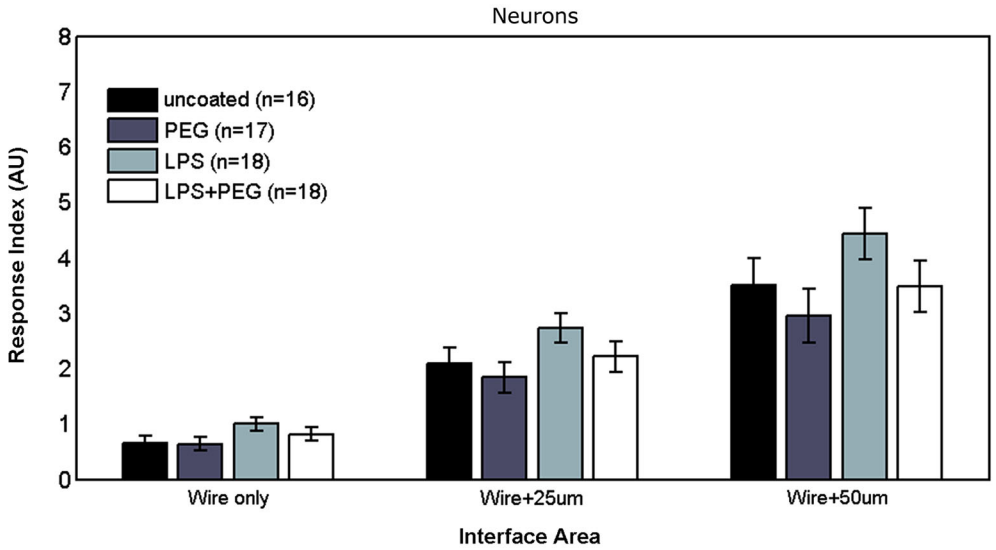

FIGURE 6 | No differences are observed in neuronal responses in interface areas of various widths.

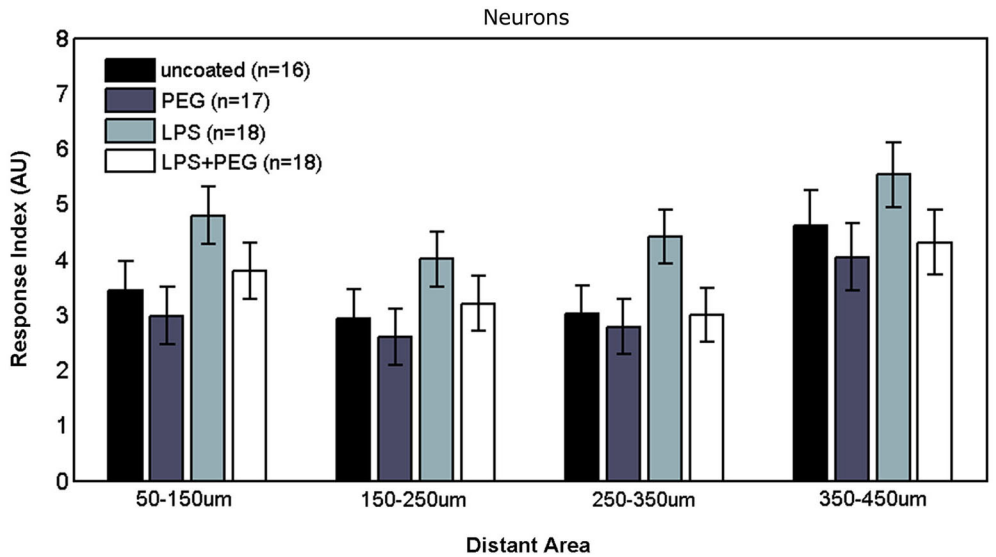

FIGURE 7 | No differences are observed in neuronal responses in distant areas.

2012), the method of quantification we employ is not without its shortcomings. Given our bin sizing, an increase in fluorescence in a bin could be attributed to either an increase in microglial cell numbers, or a higher level of Iba1 expression, or both. However, proliferation, migration, and morphological changes are all important components of microglial activation. Quantification of Iba1 fluorescence in a given area can therefore capture an aggregate of these aspects of microglial activation, but cannot distinguish between the individual components. We chose our method of quantification of Iba1fluorescence using bin sizes of up to 100 μm as an indicator of microglial response because we were most interested in quantifying gross activation across an extended distance from the foreign body. This resulted in a tradeoff against smaller bin sizes and higher magnification examination of individual microglia. Similar image analysis approaches quantifying fluorescence levels have been used *in vitro* (Polikov et al., 2009, 2010; Achyuta et al., 2010; Tien et al., 2013) and *in vivo* (Azemi et al., 2011; Potter et al., 2013, 2014) to analyze responses to microelectrodes and microscale foreign bodies., while presenting similar shortcomings in terms of elucidating separate aspects of microglial activation. Additional markers of microglial activation, such as secreted cytokines, are also a major factor of interest when

studying microglial responses. Commercially available biochemical assays are not sensitive enough to detect secreted cytokines in this particular *in vitro* injury model. Future studies should examine improved experimental and analysis methodologies to combine gross microglial responses with morphological changes and biochemical expression patterns.

ANALYSIS OF CELLULAR RESPONSES

Microglia

The microglial response in a narrow interface region comprising only the area under the microwire exhibits a three tiered response where a significant difference exists between the LPS only and the PEG only treatments, but not between the other conditions. This tiered response might be attributed to the difference between increased activation caused by the LPS and reduced cellular adhesion caused by PEG. The three data sets from the interfacial region included in **Figure 2** (wire only, wire + 25 μm, wire +50 μm) examine the RI of the microglia near the wire by summing the fluorescence over progressively increasing areas. We note that all three sets have the same relative trend when we compare each condition (bare wire, PEG only, LPS, LPS + PEG), only the magnitudes increase as the sets progress because the summation area increases. We observe a microglial monolayer forming at the surface of the wire, explaining the lack of a significant difference between the different treatments. The difference becomes significant only at the wire +50 μm because the magnitudes of the fluorescence become large enough to detect the differences given the variance of the assay. Even though this effect is not statistically significant when we analyze the wire only and wire +25 μm, the trend is consistent. The same is true for LPS vs. a bare wire, although this effect becomes significant at both wire +25 μm and wire +50 μm. We therefore think that the effect of LPS to locally activate microglia and mitigate that activation by a PEG coating is happening throughout the entire interfacial area. This increase in microglial response might be explained by elevated activation of microglia through amplification of inflammatory pathways precipitated by TL4 binding, leading to an increase in microglial response at distance. The observed elevation of Iba1 fluorescence persists in the next 100 μm wide distant region, again indicating an extended inflammatory response, potentially mediated by secreted cytokines produced by activated microglia but dissipates in further distant regions, reverting to a tiered response, where the only significant pairwise difference is between LPS and PEG. This tiered response can again be attributed to distinct pathway amplification between the two treatments; the difference appearing only between the increased upregulation of microglial activation due to LPS and the reduced microglial activation due to PEG.

Astrocytes

In interface regions of varying width, the astrocyte response also exhibits a three tiered response, where an elevated astrocyte response is observed with LPS, and a reduction occurs with both PEG conditions (with LPS and without). In the distant regions, the first and fourth 100 μm wide distant bin do not exhibit any differences between the different treatments, but we observe a difference between LPS and LPS + PEG in the middle two 100 μm wide bins, but surprisingly no difference between LPS and PEG in these distant areas. A potential explanation is that the astrocytes are exhibiting a dose dependent response to LPS. Under this explanation, the increased activation in the interface area for the LPS only treatment results in both astrocyte migration from distant regions and increased overall proliferation; delivering the LPS with PEG results in astrocyte migration without an accompanying equivalent increase in proliferation, resulting in a depletion of distant astrocytes; while PEG only results in even less astrocyte activation in interface areas, which in turn does not signal migration of distant astrocytes. Because we did not directly test for whether the LPS was acting through direct binding to receptors on astrocyte surfaces, we are merely discussing correlative effects. It is unclear whether the astrocyte response is due to direct action by LPS, or if it they are reacting to cytokines and chemokines secreted by microglia. While astrocytes are not typically thought to express TL4 receptors, there is some evidence to the contrary (Bowman et al., 2003). Additionally, while GFAP-positive astrocytes are observed in primary cultures, a considerable portion of them differentiate *in vitro* from astrocyte precursors (Abney et al., 1981). It is possible that due to these culture conditions that astrocyte response is altered from normally developing astrocytes *in vivo*.

Neurons

No significant differences were detected in neuron response to any of the treatments, in either interface or distant regions. While not statistically significant, a coupling between neuron and astrocyte response can be noticed, where slightly higher (but not significantly different) neuron growth was observed for the LPS treatment. Neuronal growth has been consistently shown to occur on a supporting substrate of astrocytes (Noble et al., 1984; Tomaselli et al., 1988). In contrast to the microglia and astrocytes, where the response in the widest interface bin was considerably higher than the first adjacent distant bin, the neuron RI in the first distant bin was comparable to the neuron RI in the wide interface bin, and we did not observe a decline in neuron density over distance. One explanation mirrors the concern expressed earlier about the maturity of the astrocytes, where immature astrocytes in culture provided a better substrate for neuron outgrowth compared to mature astrocytes (Smith et al., 1990). An alternative explanation is that elevated glial activation is not in and of itself neurotoxic or neurodegenerative within a foreign body reactive tissue response paradigm. If the latter explanation is correct, then the loss of neural density *in vivo* following implantation of a microelectrode might be better explained by displacement of neurons following insertion trauma and edema which fail to reoccupy depleted zones because of the glial scar formation, or that *in vivo* neurotoxicity occurs due to direct contact between neurons and extrabrain components.

CONCLUSIONS

We have shown that microglial response in a primary mixed cortical culture can be manipulated by dip-coated treatments. Microglial response can be increased by coating the surface of the foreign body with LPS, and this increase can be prevented by co-depositing LPS and PEG. We hypothesize that the film of high

molecular weight PEG, while allowing for LPS release, presents a hydrated physical barrier that disrupts cytokine, chemokine and adsorbed protein gradients that typically guide pathological responses. Astrocyte response also increased for LPS coated foreign bodies, but it is unclear whether this response is directly mediated by LPS or whether it is caused by other microglia-secreted factors. Neuron response was not negatively correlated with microglial response, suggesting mechanisms other than glial activation causing *in vivo* neuronal density loss. Our results highlight the importance of considering the *in vivo* chronic foreign body response as a complex phenomenon with multiple, interconnected yet parallel processes. Attempts to target an individual brain cell type to reduce the overall chronic response are unlikely to be successful. The differences between our findings and typical *in vivo* responses indicate the importance of components other than native brain cells in the progression of the reactive tissue response. Our findings additionally point to a viable alternative hypothesis regarding neuronal density depletion following microelectrode implantation in the brain.

ACKNOWLEDGMENTS

Funding for this research was provided by the Purdue Research Foundation, the Indiana Spinal Cord and Brain Injury Research Grant Program (Fund # 00015115), and the Defense Advanced Research Projects Agency (DARPA) Microsystems Technology Office (MTO), under the auspices of Dr. Jack W. Judy (jack.judy@darpa.mil) and Dr. Doug Weber (douglas.weber@darpa.mil) as part of the Reliable Neural Technology Program, through the Space and Naval Warfare Systems Command (SPAWAR) Systems Center (SSC) Pacific grant No. N66001-11-1-4013. Thanks to members of the Neuroprostheses Research Laboratory for feedback on the manuscript.

REFERENCES

Abney, E. R., Bartlett, P. P., and Raff, M. C. (1981). Astrocytes, ependymal cells and oligodendrocytes develop on schedule in dissociated cell cultures of embryonic rat brain. *Dev. Biol.* 83, 301–310. doi: 10.1016/0012-1606(81)90476-0

Acharya, G., and Park, K. (2006). Mechanisms of controlled drug release from drug-eluting stents. *Adv. Drug Deliv. Rev.* 58, 387–401. doi: 10.1016/j.addr.2006.01.016

Achyuta, A. K. H., Polikov, V. S., White, A. J., Lewis, H. G. P., and Murthy, S. K. (2010). Biocompatibility assessment of insulating silicone polymer coatings using an in vitro glial scar assay. *Macromol. Biosci.* 10, 872–880. doi: 10.1002/mabi.200900451

Azemi, E., Lagenaur, C. F., and Cui, X. T. (2011). The surface immobilization of the neural adhesion molecule L1 on neural probes and its effect on neuronal density and gliosis at the probe/tissue interface. *Biomaterials* 32, 681–692. doi: 10.1016/j.biomaterials.2010.09.033

Beynon, S. B., and Walker, F. R. (2012). Microglial activation in the injured and healthy brain: what are we really talking about? Practical and theoretical issues associated with the measurement of changes in microglial morphology. *Neuroscience* 225, 162–171. doi: 10.1016/j.neuroscience.2012.07.029

Borgens, R. B., Shi, R., and Bohnert, D. (2002). Behavioral recovery from spinal cord injury following delayed application of polyethylene glycol. *J. Exp. Biol.* 205, 1–12.

Bowman, C. C., Rasley, A., Tranguch, S. L., and Marriott, I. (2003). Cultured astrocytes express toll-like receptors for bacterial products. *Glia* 43, 281–291. doi: 10.1002/glia.10256

Das, K. P., McMillian, M. K., Bing, G., and Hong, J.-S. (1995). Modulatory effects of [Met^5]-enkephalin on interleukin-1β secretion from microglia in mixed brain cell cultures. *J. Neuroimmunol.* 62, 9–17. doi: 10.1016/0165-5728(95)00083-e

Ito, D., Imai, Y., Ohsawa, K., Nakajima, K., Fukuuchi, Y., and Kohsaka, S. (1998). Microglia-specific localisation of a novel calcium binding protein, Iba1. *Brain Res. Mol. Brain Res.* 57, 1–9. doi: 10.1016/s0169-328x(98)00040-0

Kang, E., Robinson, J., Park, K., and Cheng, J.-X. (2007). Paclitaxel distribution in poly (ethylene glycol)/poly (lactide-co-glycolic acid) blends and its release visualized by coherent anti-Stokes Raman scattering microscopy. *J. Control. Release* 122, 261–268. doi: 10.1016/j.jconrel.2007.05.007

Karumbaiah, L., Saxena, T., Carlson, D., Patil, K., Patkar, R., Gaupp, E. A., et al. (2013). Relationship between intracortical electrode design and chronic recording function. *Biomaterials* 34, 8061–8074. doi: 10.1016/j.biomaterials.2013.07.016

Koob, A. O., and Borgens, R. B. (2006). Polyethylene glycol treatment after traumatic brain injury reduces beta-amyloid precursor protein accumulation in degenerating axons. *J. Neurosci. Res.* 83, 1558–1563. doi: 10.1002/jnr.20837

Koob, A. O., Colby, J. M., and Borgens, R. B. (2008). Behavioral recovery from traumatic brain injury after membrane reconstruction using polyethylene glycol. *J. Biol. Eng.* 2:9. doi: 10.1186/1754-1611-2-9

Koob, A. O., Duerstock, B. S., Babbs, C. F., Sun, Y., and Borgens, R. B. (2005). Intravenous polyethylene glycol inhibits the loss of cerebral cells after brain injury. *J. Neurotrauma* 22, 1092–1111. doi: 10.1089/neu.2005.22.1092

Kozlowski, C., and Weimer, R. M. (2012). An automated method to quantify microglia morphology and application to monitor activation state longitudinally in vivo. *PLoS One* 7:e31814. doi: 10.1371/journal.pone.0031814

Lehnardt, S., Massillon, L., Follett, P., Jensen, F. E., Ratan, R., Rosenberg, P. A., et al. (2003). Activation of innate immunity in the CNS triggers neurodegeneration through a toll-like receptor 4-dependent pathway. *Proc. Natl. Acad. Sci. U S A* 100, 8514–8519. doi: 10.1073/pnas.1432609100

Lin, C.-C., and Anseth, K. S. (2009). PEG hydrogels for the controlled release of biomolecules in regenerative medicine. *Pharm. Res.* 26, 631–643. doi: 10.1007/s11095-008-9801-2

Markwardt, N. T., Stokol, J., and Rennaker, R. L. 2nd (2013). Sub-meninges implantation reduces immune response to neural implants. *J. Neurosci. Methods* 214, 119–125. doi: 10.1016/j.jneumeth.2013.01.020

Noble, M., Fok-Seang, J., and Cohen, J. (1984). Glia are a unique substrate for the in vitro growth of central nervous system neurons. *J. Neurosci.* 4, 1892–1903.

Ooya, T., Lee, J., and Park, K. (2003). Effects of ethylene glycol-based graft, star-shaped and dendritic polymers on solubilization and controlled release of paclitaxel. *J. Control. Release* 93, 121–127. doi: 10.1016/j.jconrel.2003.07.001

Peppas, N. A. (1997). Hydrogels and drug delivery. *Curr. Opin. Colloid Interface Sci.* 2, 531–537. doi: 10.1016/S1359-0294(97)80103-3

Polikov, V. S., Block, M. L., Fellous, J.-M. M., Hong, J.-S. S., and Reichert, W. M. (2006). In vitro model of glial scarring around neuroelectrodes chronically implanted in the CNS. *Biomaterials* 27, 5368–5376. doi: 10.1016/j.biomaterials.2006.06.018

Polikov, V. S., Hong, J.-S., and Reichert, W. M. (2010). Soluble factor effects on glial cell reactivity at the surface of gel-coated microwires. *J. Neurosci. Methods* 190, 180–187. doi: 10.1016/j.jneumeth.2010.05.002

Polikov, V. S., Su, E. C., Ball, M. A., Hong, J.-S., and Reichert, W. M. (2009). Control protocol for robust in vitro glial scar formation around microwires: essential roles of bFGF and serum in gliosis. *J. Neurosci. Methods* 181, 170–177. doi: 10.1016/j.jneumeth.2009.05.002

Potter, K. A., Buck, A. C., Self, W. K., Callanan, M. E., Sunil, S., and Capadona, J. R. (2013). The effect of resveratrol on neurodegeneration and blood brain barrier stability surrounding intracortical microelectrodes. *Biomaterials* 34, 7001–7015. doi: 10.1016/j.biomaterials.2013.05.035

Potter, K. A., Jorfi, M., Householder, K. T., Johan Foster, E., Weder, C., and Capadona, J. R. (2014). Curcumin-releasing mechanically-adaptive intracortical implants improve the proximal neuronal density and blood-brain barrier stability. *Acta Biomater.* 10, 2209–2222. doi: 10.1016/j.actbio.2014.01.018

Ramakrishna, S., Mayer, J., Wintermantel, E., and Leong, K. W. (2001). Biomedical applications of polymer-composite materials: a review. *Compos. Sci. Technol.* 61, 1189–1224. doi: 10.1016/s0266-3538(00)00241-4

Ravikumar, M., Hageman, D. J., Tomaszewski, W. H., Chandra, G. M., Skousen, J. L., Capadona, J. R., et al. (2014). The effect of residual endotoxin

contamination on the neuroinflammatory response to sterilized intracortical microelectrodes. *J. Mater. Chem. B Mater. Biol. Med.* 2, 2517–2529. doi: 10.1039/c3tb21453b

Sasaki, Y., Ohsawa, K., Kanazawa, H., Kohsaka, S., and Imai, Y. (2001). Iba1 is an actin-cross-linking protein in macrophages/microglia. *Biochem. Biophys. Res. Commun.* 286, 292–297. doi: 10.1006/bbrc.2001.5388

Saxena, T., Karumbaiah, L., Gaupp, E. A., Patkar, R., Patil, K., Betancur, M., et al. (2013). The impact of chronic blood—brain barrier breach on intracortical electrode function. *Biomaterials* 34, 4703–4713. doi: 10.1016/j.biomaterials.2013.03.007

Smith, G. M., Rutishauser, U., Silver, J., and Miller, R. H. (1990). Maturation of astrocytes in vitro alters the extent and molecular basis of neurite outgrowth. *Dev. Biol.* 138, 377–390. doi: 10.1016/0012-1606(90)90204-v

Sommakia, S., Gaire, J., Rickus, J. L., and Otto, K. J. (2014). Resistive and reactive changes to the impedance of intracortical microelectrodes can be mitigated with polyethylene glycol under acute in vitro and in vivo settings. *Front. Neuroeng.* 7:33. doi: 10.3389/fneng.2014.00033

Tien, L. W., Wu, F., Tang-Schomer, M. D., Yoon, E., Omenetto, F. G., and Kaplan, D. L. (2013). Silk as a multifunctional biomaterial substrate for reduced Glial scarring around brain-penetrating electrodes. *Adv. Funct. Mater.* 23, 3185–3193. doi: 10.1002/adfm.201203716

Tomaselli, K. J., Neugebauer, K. M., Bixby, J. L., Lilien, J., and Reichard, L. F. (1988). N-cadherin and integrins: two receptor systems that mediate neuronal process outgrowth on astrocyte surfaces. *Neuron* 1, 33–43. doi: 10.1016/0896-6273(88)90207-3

Tzeng, S. F., Huang, H. Y., Lee, T. I., and Jwo, J. K. (2005). Inhibition of lipopolysaccharide-induced microglial activation by preexposure to neurotrophin-3. *J. Neurosci. Res.* 81, 666–676. doi: 10.1002/jnr.20586

Vetter, R. J., Williams, J. C., Hetke, J. F., Nunamaker, E. A., and Kipke, D. R. (2004). Chronic neural recording using silicon-substrate microelectrode arrays implanted in cerebral cortex. *IEEE Trans. Biomed. Eng.* 51, 896–904. doi: 10.1109/tbme.2004.826680

Wang, A. L., Yu, A. C. H., Lau, L. T., Lee, C., Wu, L. M., Zhu, X., et al. (2005). Minocycline inhibits LPS-induced retinal microglia activation. *Neurochem. Int.* 47, 152–158. doi: 10.1016/j.neuint.2005.04.018

Woolley, A. J., Desai, H. A., Gaire, J., Ready, A. L., and Otto, K. J. (2013a). A systemic triple label strategy for fluorescent microscopy of inflammation in CNS and Non-CNS tissue. *Microsc. Microanal.* 19, 196–197. doi: 10.1017/S1431927611001607

Woolley, A. J., Desai, H. A., Gaire, J., Ready, A. L., and Otto, K. J. (2013b). Intact histological characterization of brain-implanted microdevices and surrounding tissue. *J. Vis. Exp.* 72, 50126. doi: 10.3791/50126

Woolley, A. J., Desai, H. A., and Otto, K. J. (2013c). Chronic intracortical microelectrode arrays induce non-uniform, depth-related tissue responses. *J. Neural Eng.* 10:026007. doi: 10.1088/1741-2560/10/2/026007

Woolley, A. J., Desai, H. A., Steckbeck, M. A., Patel, N. K., and Otto, K. J. (2011). In situ characterization of the brain-microdevice interface using device-capture histology. *J. Neurosci. Methods* 201, 67–77. doi: 10.1016/j.jneumeth.2011.07.012

Conflict of Interest Statement: The authors declare that the research was conducted in the absence of any commercial or financial relationships that could be construed as a potential conflict of interest.

Received: 01 May 2014; accepted: 28 October 2014; published online: 14 November 2014.

Citation: Sommakia S, Rickus JL and Otto KJ (2014) Glial cells, but not neurons, exhibit a controllable response to a localized inflammatory microenvironment in vitro. Front. Neuroeng. 7:41. doi: 10.3389/fneng.2014.00041

This article was submitted to the journal Frontiers in Neuroengineering.

frontiers in
NEUROENGINEERING

TECHNOLOGY REPORT ARTICLE
published: 10 April 2014
doi: 10.3389/fneng.2014.00007

Bio-inspired hybrid microelectrodes: a hybrid solution to improve long-term performance of chronic intracortical implants

Sara De Faveri[1,2] *, Emma Maggiolini[1], Ermanno Miele[3], Francesco De Angelis[3], Fabrizia Cesca[2], Fabio Benfenati[2,4†] and Luciano Fadiga[1,5†]

[1] *Department of Robotics, Brain and Cognitive Science, Istituto Italiano di Tecnologia, Genova, Italy*
[2] *Department of Neuroscience and Brain Technologies, Istituto Italiano di Tecnologia, Genova, Italy*
[3] *Department of Nanostructures, Istituto Italiano di Tecnologia, Genova, Italy*
[4] *Department of Experimental Medicine, University of Genova, Genova, Italy*
[5] *Section of Human Physiology, University of Ferrara, Ferrara, Italy*

Edited by:
Ulrich G. Hofmann, Albert-Ludwigs-University Freiburg, Germany

Reviewed by:
Christian K. E. Moll, University Clinic Hamburg-Eppendorf, Germany
Jürgen Krüger, University of Freibourg, Germany

****Correspondence:***
Sara De Faveri, Department of Robotics, Brain and Cognitive Science, Istituto Italiano di Tecnologia, via Morego 30, Genova 16163, Italy
e-mail: sara.defaveri@iit.it

† Fabio Benfenati and Luciano Fadiga have contributed equally to this work.

The use of implants that allow chronic electrical stimulation and recording in the brain of human patients is currently limited by a series of events that cause the deterioration over time of both the electrode surface and the surrounding tissue. The main reason of failure is the tissue inflammatory reaction that eventually causes neuronal loss and glial encapsulation, resulting in a progressive increase of the electrode-electrolyte impedance. Here, we describe a new method to create bio-inspired electrodes to mimic the mechanical properties and biological composition of the host tissue. This combination has a great potential to increase the implant lifetime by reducing tissue reaction and improving electrical coupling. Our method implies coating the electrode with reprogrammed neural or glial cells encapsulated within a hydrogel layer. We chose fibrin as a hydrogel and primary hippocampal neurons or astrocytes from rat brain as cellular layer. We demonstrate that fibrin coating is highly biocompatible, forms uniform coatings of controllable thickness, does not alter the electrochemical properties of the microelectrode and allows good quality recordings. Moreover, it reduces the amount of host reactive astrocytes – over time – compared to a bare wire and is fully reabsorbed by the surrounding tissue within 7 days after implantation, avoiding the common problem of hydrogels swelling. Both astrocytes and neurons could be successfully grown onto the electrode surface within the fibrin hydrogel without altering the electrochemical properties of the microelectrode. This bio-hybrid device has therefore a good potential to improve the electrical integration at the neuron-electrode interface and support the long-term success of neural prostheses.

Keywords: gliosis, intracortical microelectrodes, fibrin, bio-inspired, *in-vivo*, chronic implants

INTRODUCTION

Patients with various neurological disorders could benefit from the stereotaxic implant of chronic intracerebral microelectrodes to record endogenous activity and/or to electrically stimulate specific brain areas (Donoghue et al., 2007; Larson, 2008; Truccolo et al., 2008; Velliste et al., 2008; Benabid et al., 2009; Normann et al., 2009; Hemm and Wårdell, 2010). To be functional and safe, the implant should keep a stable electric interface with the tissue, enabling an efficient recording and/or activation of neurons over time. However, the long-term functionality of implanted electrodes has been very critical, because of the progressive deterioration of both the electrode surface and the surrounding neural tissue.

Electrode insertion is a traumatic event that induces acute injury to the brain tissue (Polikov et al., 2005; Grill et al., 2009; Marin and Fernández, 2010). The tissue is cut, stretched or compressed by the penetration of the electrode and neurons and glial cells within and around the electrode path are killed or severely injured during insertion. Since the first day of implantation, microglial cells -that are extremely sensitive to even small pathological changes- start to be activated to scavenge damaged neurons and cell debris. Moreover, activated microglia also releases pro-inflammatory cytokines that propagate the inflammatory reaction. The deepening of the electrode into the brain pushes aside the tissue and increases the local pressure of the surrounding tissue. Blood vessels and capillaries are disrupted and the blood–brain barrier is compromised (Bjornsson et al., 2006), leading to plasma extravasation and local edema, that further increase the intracranial pressure (Unterberg et al., 2004).

This initial acute tissue reaction triggers, and is followed by, a more adverse long-term response mainly operated by activated astrocytes that is dependent on the extension of the injury and ends up in the generation of a glial scar, neuronal loss and impairment of the regrowth of neuronal processes (Fawcett and Asher, 1999; Polikov et al., 2005; Grill et al., 2009; Marin and Fernández, 2010). The glial encapsulation surrounding the electrode becomes denser and organized over time pushing away neurons from the tip of the probe (the so-called "kill zone"). This leads to

a progressive increase of the electrode-electrolyte impedance and to a deterioration of the recordings. All these events reduce the long-term performance of the electrodes, making the long-term application of this type of technology to human subjects almost unfeasible.

The physical properties of the electrodes such as surface composition, size, shape and stiffness, the mechanical connection between the probe and the recording system, the functionalization of the electrode and the implantation method all have some impact on the intensity of the tissue reaction (Edell et al., 1992). Different approaches have been proposed to solve or reduce the inflammatory reaction. One is the reduction of the electrode size. Minimizing the device footprint is important to reduce the insertion trauma. A smaller device induces a much smaller increase in the local pressure and minimizes tissue displacement (Kozai et al., 2012). However, miniaturization of the electrode worsens its electrochemical characteristics in terms of contact impedance and signal-to-noise ratio (SNR). To circumvent this effect, various groups have used conductive polymers such as poly(3,4-ethylenedioxythiophene, PEDOT) or nanostructured materials (e.g., carbon nanotubes) to reduce the impedance of the recording site (Richardson-Burns et al., 2007; Kim et al., 2010b; Ansaldo et al., 2011; Baranauskas et al., 2011).

Other solutions employing untethered or flexible probes (Rousche et al., 2001; Takeuchi et al., 2005; Kim et al., 2010a; Castagnola et al., 2013; Zhang et al., 2013) have been adopted to decrease the formation of the glial scar. Indeed, when an electrode is tethered to the skull or the device has a different compliance with respect to the adjacent brain tissue, the brain, subject to normal movement induced by respiration and circulation, moves around the probe causing chronic trauma as well as instability of the recording (Kim et al., 2004b; Biran et al., 2007; Thelin et al., 2011).

Approaches aimed at reducing the mechanical mismatch at the interface between the stiff intracortical electrode and the soft brain tissue have been proposed. Intracortical wires were covered with soft materials (Kim et al., 2010b) or with polymeric nano-composite materials that switch from a stiff to a compliant state when inside the cerebral tissue (Harris et al., 2011). The soft coating, matching the host tissue softness, was shown to play an important role in limiting the severity of the inflammatory reaction over time in terms of the amount of reactive astrocytes, neuronal death, and density of active microglial cells around the probe (Harris et al., 2011). The use of hydrogel scaffolds has also been introduced to contrast the consequences due to the inflammatory and immune responses by astrocytes and oligodendrocytes involved in the assembly of the glial scar. Both biologically derived hydrogels (e.g., alginate, Frampton et al., 2011; hyaluronic acid, Hou et al., 2005) and synthetic hydrogels (e.g., polyethylene glycol Bjugstad et al., 2010) have provided promising results in terms of repair and regeneration after surgical implants (Nisbet et al., 2008; Green et al., 2010). Bioactive materials such as L1, growth factors, dextran or laminin, have also been used to functionalize the probe improving its tolerability (He et al., 2006; Klaver and Caplan, 2007; Azemi et al., 2011). Furthermore, cell-coated interfaces were proposed to increase the biocompatibility of the device and minimize the reaction of the host tissue (Purcell et al., 2009; Richter et al., 2011).

Although all the above-mentioned approaches may lead to potentially interesting results, the preservation of the performance of intracortical devices still remains an unresolved issue. To contribute to this challenge, we developed a strategy to improve the biocompatibility of the implant by coating microelectrodes with soft hydrogel and live cells to mimic both the mechanical properties and the biological composition of the host tissue. We used fibrin as hydrogel and either glial cells or neurons to immunologically hide the foreign object to the host tissue. By using such approach we obtained: (i) a strong adhesion of hydrogel and cells to the microelectrode without altering its electrochemical properties; (ii) a small and transient tissue reaction to the implant; and (iii) high quality of electrophysiological recordings.

MATERIALS AND METHODS

IMPLANTABLE WIRES

Quartz-coated metal microelectrodes

Single core quartz-insulated metal microelectrodes (Thomas Recording, Giessen, Germany) were prepared in-house by mechanically grinding 95% platinum, 5% tungsten microwires of 20 μm diameter coated with 30 μm of quartz (see **Figure 1A**). The measured impedance of these electrodes, measured in saline at 1 kHz, was typically between 500 and 700 kΩ (Ansaldo et al., 2011).

This probe was used as a seeding substrate and to evaluate the grip of the hydrogel to the electrode surface during intra-cortical insertion.

Black-lead sticks

Black-lead sticks were 350 μm in diameter and 3 mm long (see **Figure 1B**). The tip was mechanically ground. This probe was used to evaluate the time of hydrogel in-vivo reabsorption and the extent of tissue reaction to the implant without removing it from the brain, thanks to the possibility to cut the stick inserted in the brain with the microtome.

FIBRIN HYDROGEL COATING

Human fibrin (TISSEEL, Baxter, Deerfield, IL, USA) from pooled human plasma was used. It was composed by two sterile components, namely the sealer protein solution (aprotinin and fibrinogen) and thrombin solution (thrombin, $CaCl_2$ and factor XIII). To form a cross-linked fibrin gel, fibrinogen was dipped in the thrombin solution to generate fibrin monomers that were subsequently cross-linked by factor XIII (soluble transglutaminase). Wires were coated by alternate dippings in the two components of the fibrin sealant. The resulting electrode coating was uniform and its thickness was controllable by the number of dippings (Kim et al., 2010b). The radial thickness of the coating was evaluated by measuring the hemi-diameter of the covered probe in five points and subtracting the probe diameter. Thin films of fibrin were prepared by dropping 50 μl of the first component of the fibrin sealant and 50 μl of the second component over sterile glass slides. The drops broadened and they were left drying in air for 15 min in a laminar hood.

FIGURE 1 | Implantable wires used in this study. (A) Single-core quartz insulated metal microelectrode (Thomas Recording, Giessen, Germany). **(B)** Black-lead wire. Scale bar 100 μm.

EVALUATION OF THE ELECTROCHEMICAL PROPERTIES OF THE FIBRIN-COATED DEVICE

The electrochemical properties of the microelectrode were studied via electrochemical impedance spectroscopy (EIS) in a physiological aqueous solution (NaCl 0.9%). For the measurements, a sine wave (10 mV root mean square amplitude) was superimposed on the open circuit potential while varying the frequency from 1 Hz to 100 kHz. The electrochemical characterization was carried out using a potentiostat/galvanostat/ZRA (Reference 600, Gamry Instruments, Philadelphia, PA, USA) connected to a standard electrochemical cell used in a three-electrode configuration with a platinum counter-electrode (35 mm^2 area) and an Ag/AgCl reference electrode.

MODIFICATION OF THE MICROELECTRODE QUARTZ SURFACE

The roughness of the microelectrode quartz surface was manipulated by using an argon ion plasma etching. Sputter-coated and annealed nanometric gold islands acted as masks for quartz surface milling. The ions hit all the surface, etching both quartz and gold but where quartz was not covered, the generated holes were deeper than where it was covered by gold. The process stopped when all the gold coating was removed. Thanks to this etching, the peak-to-peak average distance was about 500 nm (Goyal et al., 2006).

EXPERIMENTAL ANIMALS

Adult Sprague-Dawley rats (from Charles River, Calco, Italy) and Long-Evans rats (born in house) were used. All experiments were carried out in accordance with the guidelines established by the European Communities Council (Directive 2010/63/EU of September 22nd, 2010), and were approved by the Italian Ministry of Health.

Neurons

Neurons were isolated from E18 rat embryos. Briefly, embryos were removed, placed in cold Hank's balanced salts solution (HBSS) and hippocampi were dissected under sterile conditions. Subsequently, the tissue was enzymatically digested with 0.125% Trypsin for 20 min at 37°C and disaggregated with a pipette. The cells were incubated with 1% Glutamax, penicillin-streptomycin, 2% B-27 supplemented Neurobasal medium in a humidified 5% CO_2 atmosphere at 37°C. Half of the medium was changed every week. All culture media and reagents were from Invitrogen (Milano, Italy).

Glial cells

Glial cells were isolated from the cerebral cortex of P0 rat pups. Cortices were dissected in cold HBSS, broken into small fragments by pipetting and enzymatically digested with 0.25% Trypsin – 1 mg/ml DNase for 15 min at 37°C. After centrifugation at 1200 rpm for 5 min at 8°C, the digestion medium was removed and the pellet was suspended in 10% horse serum, penicillin-streptomycin and 33 mM glucose-supplemented minimum essential medium. Cells were plated in culture flasks and half of the medium was changed every week.

SEEDING OF CELLS OVER THE MICROELECTRODES

Microelectrodes were fixed in a silicon cap by the end opposite to the tip and coated with 0.1% poly-D-lysine, which created a positively charged layer enhancing cell adhesion. Microelectrodes were dipped inside a vial containing the cells suspended in the medium (300000 cells/500 μl). Half of the medium was harvested from a high concentration cell culture, the so-called conditioned medium. The vials were kept in slow and continuous rotation in an incubator (2.31 rpm; relative centrifugal force $0.013 \times g$).

EVALUATION OF THE BIOCOMPATIBILITY OF THE FIBRIN FILM

Approximately 5000 astrocytes or neurons in 100 μl of medium were plated over a thin layer of fibrin. After the cells attached to the surface, the coverslip was covered by culture medium and the cell viability was analyzed at 1, 5, 7, and 11 days. Viability was evaluated by rating the surviving cells over the total number of cells. Samples were incubated for 3 min at room temperature in Ringer-Locke solution containing propidium iodide (PI; Sigma-Aldrich, Milano, Italy; 15 μg/ml), fluorescein diacetate (FDA; Sigma–Aldrich, Milano, Italy; 5 mg/ml) and Hoechst-33342 (Sigma-Aldrich, Milano, Italy; 3.3 μg/ml). After incubation, samples were washed once in Ringer-Locke solution and immediately imaged. At least 15 different fields of view were acquired for each sample. For each field, the ratio of PI-positive cells over the total number of nuclei, identified by Hoechst-33342, was calculated (Limongi et al., 2013).

ANIMAL SURGERY

Male Long Evans rats were anesthetized with a cocktail of Zoletil (Virbac, Carros cedex, France; 30 mg/kg) and Xylazine (Bayer, Leverkusen, Germany; 5 mg/kg) administered intraperitoneally. Their heads were then shaved and swabbed with ethanol. The anesthetized animal was placed in a stereotaxic apparatus (Myneurolab, St Louis, MO, USA). Lacrigel (Farmigea, Pisa, Italy) was distributed over the eyes to avoid dryness. An approximately 2 cm incision was made along the midline of the cranium. The underlying muscle and connective tissue were retracted to expose the skull. A craniotomy (5 mm × 3mm) was made in the parietal bone to expose the somatosensory cortex. Sterile saline was applied during pauses while drilling to help dissipate any local heating and to clean the surfaces. The exposed dura mater was wetted with saline, and carefully incised using surgical micro-scissors. Pia mater was incised too. Implantable wires were lowered perpendicularly through the cortical surface using a hydraulic microdrive (David Kopf Instruments, Tujunga, CA, USA) to 2800 μm from the surface of the brain (layer V). To minimize the variability associated with the surgery, all implants – both quartz-coated metal microelectrodes for acute experiments and black-lead sticks for chronic experiments – were performed by the same subject. During the surgery, the depth of anesthesia was monitored by testing for the absence of hindlimb withdrawal reflex and was maintained by additional doses of anesthetic (i.p. or i.m.), while the rat body temperature was kept at 36–38°C by positioning the animal onto a thermostatic heating pad.

ACUTE NEURAL RECORDING

Acute recordings in layer V of rat cortex were performed to characterize *in vivo* the electrical performance of the fibrin-coated microelectrodes. Recordings were acquired for 20 min using a custom-made, low-power recording system (Bonfanti et al., 2008; Borghi et al., 2008) composed of a compact headstage (amplification gain = 62 dB) and a control unit for data acquisition. Raw traces were band-pass filtered between 3 Hz (first-order Butterworth) and 8 kHz (fourth-order Butterworth). The amplified signals were multiplexed, digitally converted (10-bit, 40 k sample/s) and sent via USB to a PC for subsequent analysis. LabView-based (National Instruments, Austin, TX, USA) acquisition software was used for real-time data visualization and storage. All experimental sessions were conducted inside a Faraday cage to reduce the electromagnetic noise interference.

EVALUATION OF THE SIGNAL-TO-NOISE RATIO

To evaluate the SNR, each acquired trace was high-pass digitally filtered above 300 Hz. The signal was wavelet decomposed and thresholded to 3.5 standard deviations (SD) above and below the mean of the sample distribution to discriminate signal from noise. Waveforms were clustered using Run-Valley seeking sort method (Offline-Sorter; Plexon Inc., Dallas, TX, USA). Signal amplitude was defined as the peak-to-peak amplitude of the mean waveform for each cluster. Noise was defined as two times the calculated rms noise voltage. The SNR was calculated as follows:

$$SNR = \frac{S}{2Vrms_n} \quad (1)$$

where S is the signal amplitude and $\mathrm{Vrms_n}$ is the voltage root mean square of the noise. SNR values were sorted into categories (Ludwig et al., 2006, 2009; Abidian et al., 2009; Kim et al., 2010b). Clusters with a SNR greater than 4 were categorized as high-quality units, while clusters with a SNR between 3 and 4 were categorized as moderate units.

IMMUNOHISTOCHEMICAL AND IMMUNOCYTOCHEMICAL TECHNIQUES

Animals were anesthetized and transcardially perfused with cold fixative (2% paraformaldehyde, 1.25% glutaraldehyde, 2% sucrose in phosphate-buffered saline, PBS) 3, 7, and 30 days after the insertion. The brain was removed with the probe in place, fixed for an additional 24 h in the same fixative and then cryoprotected in 30% sucrose solution. Brain horizontal slices were cut (thickness, 50 μm) up to approximately 3 mm of cortical depth. Tissue sections were hydrated in PBS, blocked and permeabilized with 4% goat serum, 2% bovine serum albumin (BSA) and 0.5% Triton X-100 in PBS for 1 h with gentle rocking. Sections were then incubated overnight with primary antibodies against human fibrinogen (1:200; Dako, Milano, Italy) to visualize the presence of fibrin and glial fibrillary acidic protein (GFAP; 1:500; Sigma-Aldrich, Milano, Italy) to visualize reactive glia. The next day, sections were rinsed in PBS and incubated in secondary antibody (1:500; Invitrogen, Milano, Italy) for 3 h. All sections were mounted with ProLong™ Gold Antifade reagent with DAPI (Invitrogen, Milano, Italy) to stain nuclei.

Cultured cells were fixed in cold fixative (2% paraformaldehyde, PFA, 1.25% glutaraldehyde, 2% sucrose in PBS) for 20 min. Cell-coated substrates were rinsed in cold PBS, blocked and permeabilized with 10% goat serum, 2% BSA and 0.5% Triton X-100 in PBS for 1 h with gentle rocking agitation. Samples were later incubated for 90 min with the following primary antibodies in blocking solution: anti-GFAP (1:500; Sigma-Aldrich, Milano, Italy), anti-NeuN (1:500; Millipore, Milano, Italy) and anti-βIII tubulin (1:500; Sigma-Aldrich, Milano, Italy). The seeded microelectrodes were rinsed in PBS and then incubated for 3 h with Alexa-Fluor 633 goat anti-rabbit and Alexa Fluor 488 goat anti-mouse (1:500; Invitrogen, Milano, Italy). All samples were mounted with ProLong™ Gold Antifade reagent with DAPI (Invitrogen, Milano, Italy).

QUANTITATIVE IMMUNOFLUORESCENCE ANALYSES

Images were acquired using an Olympus BX51 fluorescence microscope (Melville, NY, USA) equipped with X-Cite 120 fluorescence illumination system (EXFO, Canada, USA) and with a color digital camera (MBF Bioscience, Williston, VT, USA). Images for the specific antibody were taken by keeping the same exposure time and gain. Fluorescence intensity profiles were obtained by using the custom written MATLAB program MINUTE (Microelectrode INterface Universal Tool for Evaluation; Potter et al., 2012). The mean intensity of fluorescence at discrete distances was compared by one-way repeated measures ANOVA followed by the Bonferroni's *post hoc* test when more than two groups were involved. Significance for all tests was determined at $P < 0.05$.

RESULTS

ELECTROCHEMICAL PROPERTIES AND QUALITY OF THE RECORDINGS OF FIBRIN-COATED MICROELECTRODES

We analyzed the effect of the fibrin layer on the electrical properties of the coated electrode. Coating thickness was progressively increased by dipping the electrode in both fibrinogen and thrombin from 2 to 7 times. **Figure 2A** shows that increasing the fibrin sheath did not significantly affect the electrochemical properties of the microelectrode at 1 kHz, that is the fundamental frequency of neuronal action potentials (Williams et al., 2007) both in terms of impedance modulus (**Figure 2A**) and impedance phase (**Figure 2B**). The lack of alteration of the electrical properties of the electrodes is likely due to the swelling of the hydrogel and to the associated absorption of water and ions from the saline solution that maintain an optimal conductivity (Kim et al., 2004a).

However, once the electrode is implanted in-vivo, the swelling of the fibrin hydrogel coating increases the distance between the tissue and the electrode. Under our conditions, the fibrin coating displayed a smaller swelling than other types of hydrogels, such as alginate (Kong et al., 2004; Kim et al., 2010b) and was controllable in thickness.

To obtain the desired thickness of coating, the following constraints had to be considered: (i) the hydrogel thickness should be less than 100 μm to avoid oxygen deprivation of cells seeded over the probe (Kim et al., 2004a); (ii) the thicker the hydrogel layer, the smaller the gap between the Young modulus of the device and that of the host tissue at the interface; (iii) the thicker the coating, the greater the damage of the host tissue; and, finally, (iv) the swollen hydrogel layer should be thinner than 140 μm to allow activity recordings with high SNR

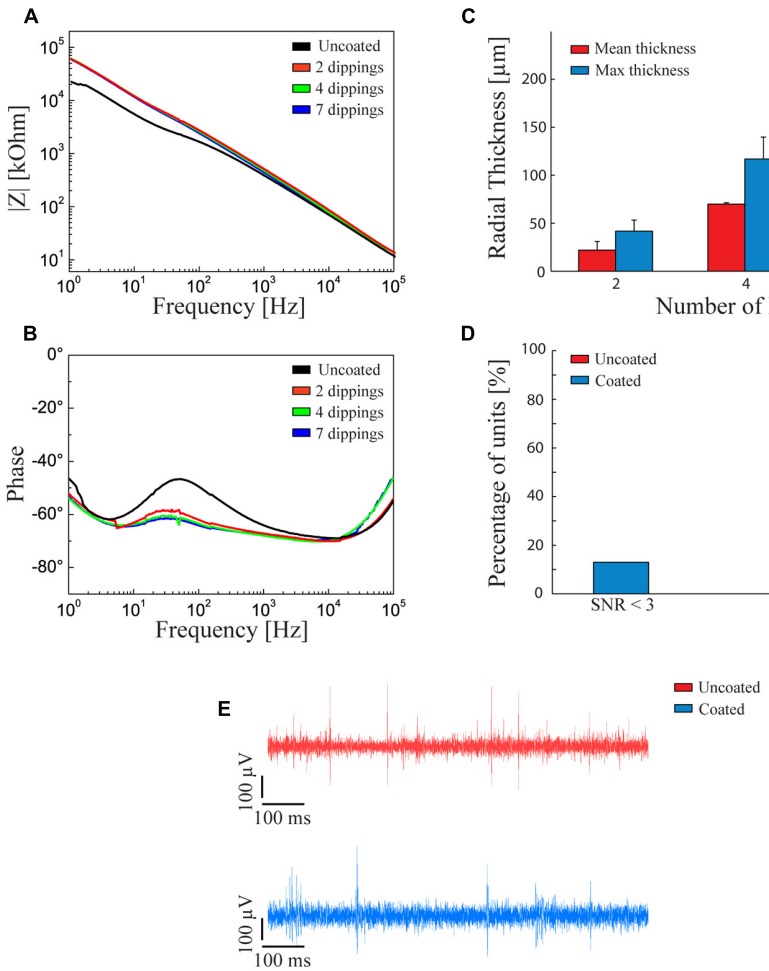

FIGURE 2 | Fibrin coated microelectrodes. (A,B) Electrochemical impedance spectroscopy. Impedance modulus **(A)** and phase **(B)** with respect to the frequency between 1 Hz and 100 kHz. The black line refers to the bare microelectrode. The red, green, and blue lines represent the behavior of fibrin-coated microelectrodes dipped two, four, and seven times into the two sealant components, respectively. **(C)** Thickness of the swollen fibrin coating deposited by two, four, and seven dippings into the two sealant components. Red and blue bars represent the mean and maximum (±SD) radial thickness of the coating, respectively. The procedure with four dippings allowed getting close to the optimal radial thickness of 100 μm, a critical value for the survival of underlying cells and the quality of neural recordings. **(D)** Signal-to-noise ratio in the recordings. Percentage of units with SNR < 3 (poor units), SNR > 3 (moderate or quality units) recorded with uncoated (red bars) and fibrin-coated (blue bars) microelectrodes. **(E)** Examples of recording traces with uncoated (red) and fibrin-coated (blue) microelectrodes. **(D,E)** The measurements were taken immediately after surgery.

(Henze et al., 2000). According to this evaluation, we decided to adopt a thickness of about 100 μm after swelling. **Figure 2C** shows the relationships between the number of dippings of the electrode in the two components of the fibrin sealant and the average and maximum thickness of the coating. Four dippings were found to be optimal to obtain the desired hydrogel thickness.

Recording capabilities of the coated versus non-coated electrodes were evaluated by calculating the SNR of neural waveforms recorded from rat cerebral cortex (see Methods). 85% of the waveforms recorded with fibrin-coated electrodes showed a SNR > 3. This performance is comparable (no statistically significant difference) to that of non-coated microelectrodes (**Figures 2D,E**).

BIOCOMPATIBILITY OF THE FIBRIN LAYER

A viability assay was used to assess the biocompatibility of the fibrin hydrogel deposited as a thin film for primary neurons and glial cells seeded onto the sample. Both astrocytes (**Figure 3A**) and primary neurons (**Figure 3B**) grew well onto the fibrin layer. The assay (**Figures 3C,D**) demonstrated that the viability of both types of cells over time in culture was comparable although, one day after seeding, the mortality of neurons was slightly higher than that of glial cells (86% of surviving glial cells versus 72% of surviving neurons; **Figure 3E**). Viability progressively increased up to 7 days in culture (98% of glial cells versus 95% of neurons; **Figure 3E**) and remained high up to 11 days in culture (95% of glial cells versus 94% of neurons; **Figure 3E**). The extent of viability was in

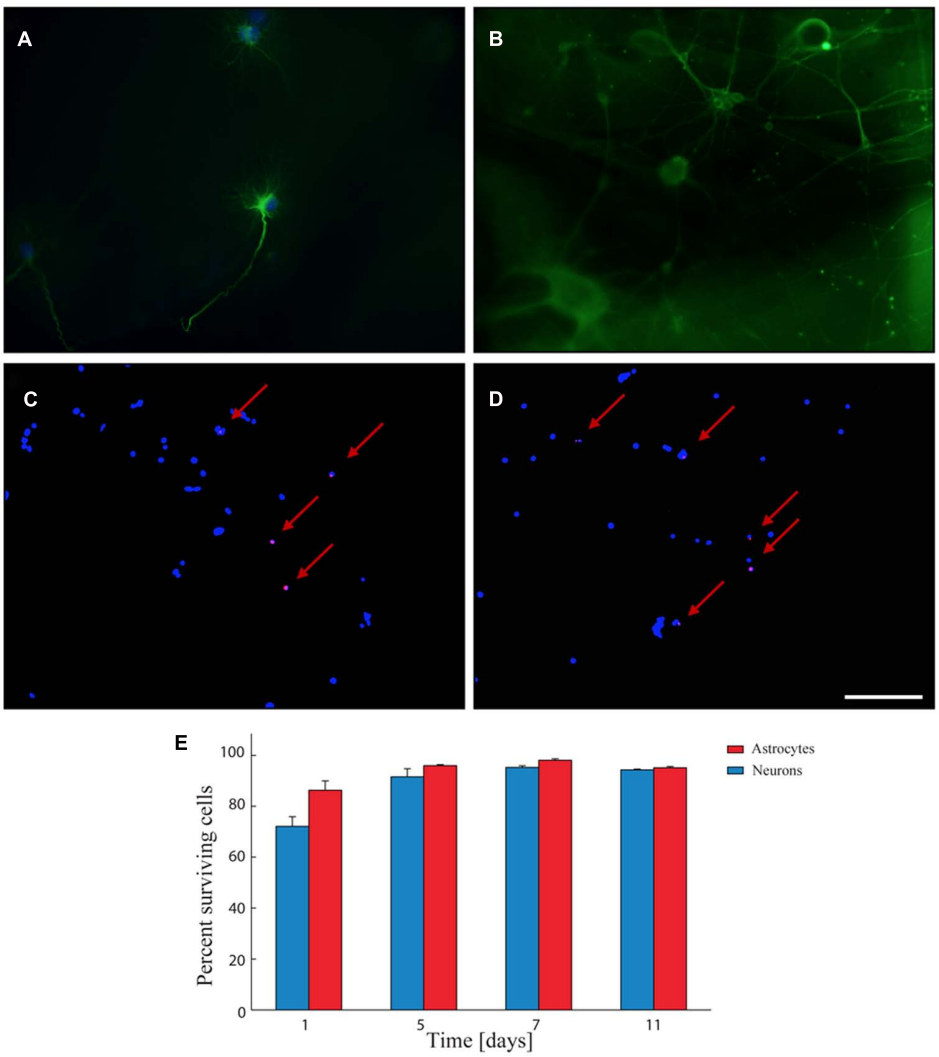

FIGURE 3 | Biocompatibility of the fibrin layer. (A,B) Representative immunofluorescence image of glial cells in fibrin layer **(A)** stained for GFAP (green) and DAPI (blue) and of primary neurons in fibrin layer stained for βIII-tubulin (green; **B**). **(C,D)** Representative images of glial cells **(C)** and primary neurons **(D)** grown in fibrin layer stained with Hoechst (blue-stained nuclei) and propidium iodide (red-stained nuclei). Red arrows indicate the PI-positive nuclei. Scale bar: 50 μm in **A**; 100 μm in **B–D**. **(E)** Quantitative analysis of the viability of primary neurons (blue bars) and astrocytes (red bars) cultured in the presence of fibrin at 1, 5, 7, and 11 days *in vitro*. The percentages of surviving cells (means ± SD) were calculated based on the ratio of total (Hoechst-positive) nuclei minus PI-positive nuclei divided by the total nuclei. Viability values increase and approach the 100% 7 days after seeding.

the same range of that obtained under standard conditions in the absence of the fibrin layer (Ghezzi et al., 2011).

MODIFICATION OF THE MICROELECTRODE SURFACE

The results of the preliminary experiments indicate that the fibrin coating seems to be ideal both in terms of modulation of the coat thickness and biocompatibility for primary cells. However, smoothness of the electrode quartz surface somehow prevented a tight anchorage of the hydrogel to the electrode surface. Thus, during implantation of the electrode into the brain tissue, the fibrin coating (**Figures 4A,B**) could not resist to the shear stress during insertion through the dura mater and detached from the electrode surface in 90% of the cases (**Figures 4C,D**). Also, after the removal of the dura mater, the hydrogel stayed attached to the microelectrode surface only in 40% of the penetrations. As these initial results were poorly reproducible and not sufficiently satisfactory, we etched the quartz surface of the microelectrode to increase its roughness and thereby the grip of the hydrogel to the surface (**Figures 5A,B**). After this treatment, microscopic inspections demonstrated that the fibrin layer was still firmly adherent to the quartz surface in the 100% of cases when the coated microelectrode was inserted and extracted from the somato-sensory cortex deprived of dura mater (**Figures 5C,D**).

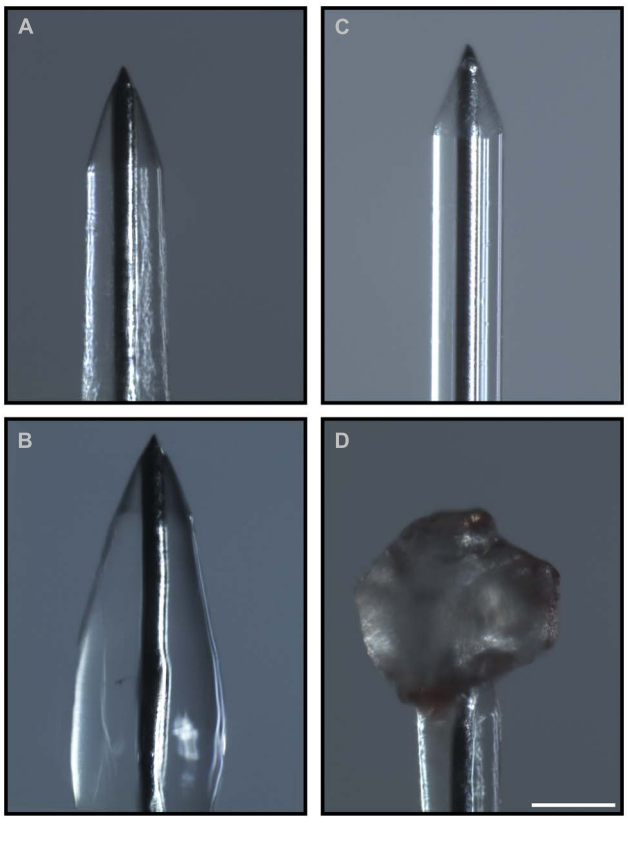

FIGURE 4 | Adhesion of the hydrogel to the microelectrode during the surgical procedure. Optical images of the coated microelectrodes before **(A,B)** and after **(C,D)** the insertion in the brain. Fibrin coating did not resist the shear stress during insertion through the dura mater and detached from the electrode surface in 90% of cases (60% of cases after removal of the dura mater). **(C,D)** Representative images of the adhesion of the hydrogel to the microelectrode before the treatment that increases the microelectrode roughness: during insertion the coating was entirely peeled **(C)** or partially piled up on the tip **(D)**. Scale bar 100 μm.

IN-VIVO REABSORPTION OF THE HYDROGEL AND TISSUE REACTION TO THE COATED ELECTRODE

To evaluate the time of reabsorption of the hydrogel in-vivo and the related tissue reaction, it was necessary to extract the implanted electrode before sectioning. However, during extraction of the implant from the perfused brain, part of the tissue could remain attached to the implant and be distorted or removed together with the probe, thus altering the evaluation of the electrode coating and of the surrounding tissue. To circumvent these problems, we implanted graphite sticks (black-lead rods) that, although thicker than quartz/tungsten microelectrodes, can be easily cut in the microtome, thus allowing to avoid their extraction from the brain before histochemical examination.

Fibrin reabsorption was determined by immunofluorescence after 3, 7, and 30 days from implant (**Figure 6A**). Quantitative analysis of fibrin immunoreactivity as a function of time and distance from the electrode edge (**Figure 6B**) revealed that the intensity of fluorescence steadily decreased in the days immediately after the insertion and that the coating was almost completely reabsorbed, in agreement with previous reports (de Vries et al., 2002). The intensity of the fibrin marker was significantly lower already 7 days after the insertion compared to the values obtained after 3 days, at any distance from the microelectrode edge, up to 90 μm ($P < 0.05$ after 7 days from the insertion; one-way repeated measures ANOVA followed by the Bonferroni's *post hoc* test), while no differences in the extent of fibrin reabsorption were present between 7 and 30 days up to 90 μm from the brain-microelectrode interface.

As astrocytes play a dominant role in the tissue reaction and in the formation of the glial scar, we investigated the glial reaction by monitoring the expression of GFAP around the implantation site. The implant of a bare electrode elicited a strong astrocytic reaction as determined 7 days after the insertion, that became denser and thinner over time, leading to a full encapsulation of the electrode (**Figure 7A**). In contrast, the implant of a fibrin-coated electrode elicited a weaker astrocyte reaction at 7 days, which further decreased to very low levels after 30 days (**Figure 7A**). Quantification of the immunostaining after 7 (**Figure 7B**) and 30 (**Figure 7C**) days as a function of the distance from the electrode-tissue interface revealed that GFAP expression was markedly more pronounced in response to the implant of a bare electrode than that of a fibrin-coated one at both 7 and 30 days post-implant at any distance from the brain-microelectrode interface ($P < 0.05$ after 7 or 30 days of implant; one-way repeated measures ANOVA). In the case of a bare electrode, the peak of GFAP immunoreactivity, localized at 50 μm from the wire-host tissue interface at 7 days became more intense and moved closer to the electrode edge at 30 days (distance: 30 μm). In contrast, in the case of fibrin-coated microelectrodes, the astrocyte reaction in the acute phase (7 days) was milder and evenly distributed around the implant, extending up to 250 μm, while it strongly decreased with time being barely detectable only for 90 μm from the electrode at 30 days.

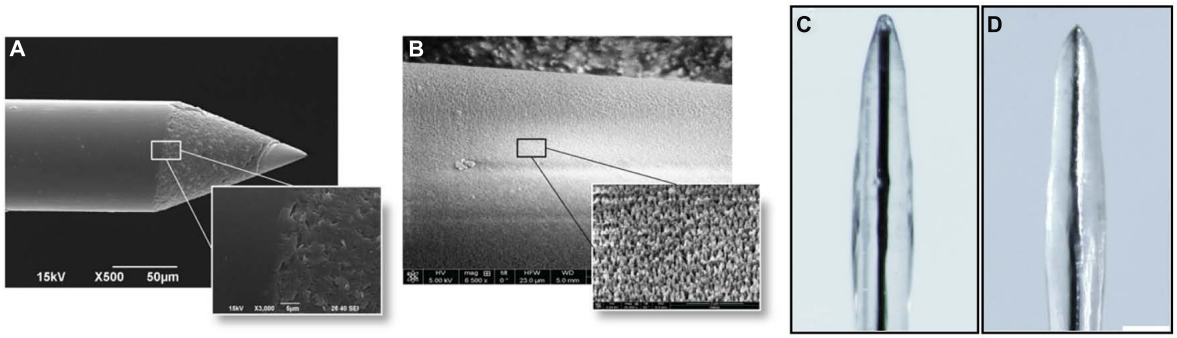

FIGURE 5 | Increase in roughness of the microelectrode surface. **(A)** Scanning electron micrographs of the microelectrodes before the etching treatment. **(B)** Scanning electron micrographs of the microelectrodes after the treatment. Scale bar 50 µm. The obtained peak-to-peak average distance was about 500 nm. **(C,D)** Microelectrodes with increased surface roughness are imaged before **(C)** and after **(D)** the insertion in the cerebral cortex. Coated nanostructured microelectrodes could be effectively inserted in the cerebral cortex deprived of dura mater without any noticeable damage or shift of the coating in the 100% of cases. Scale bar 100 µm.

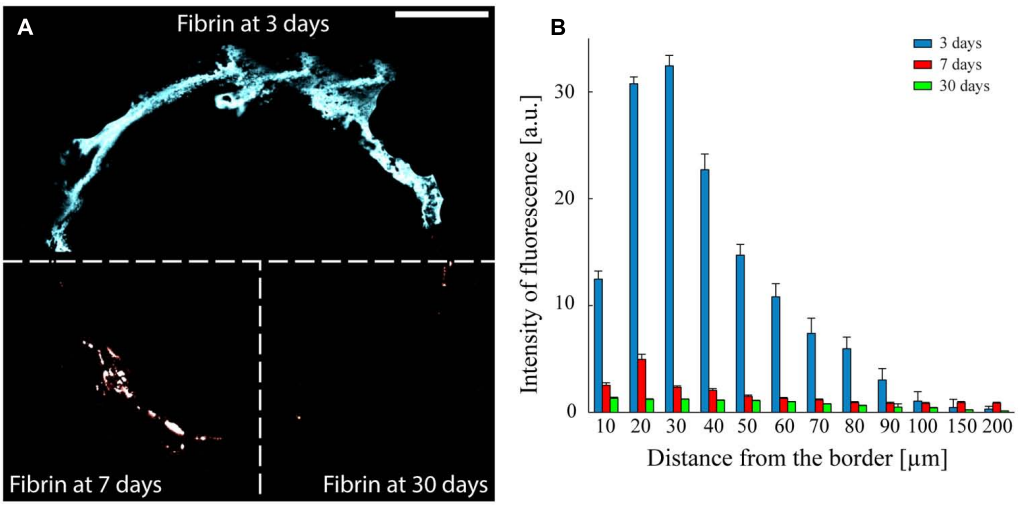

FIGURE 6 | Fibrin reabsorption after implantation. (A) Representative images to illustrate the presence of the fibrin over time. The three sectors of the panel represent the three analyzed implant times: 3, 7, and 30 days. Scale bar 100 µm. **(B)** Quantitative evaluation of fibrin immunoreactivity (a.u., arbitrary units; means ± SEM) as a function of distance from the tissue-implant interface after 3 (blue bars), 7 (red bars), and 30 (green bars) days from surgery. An almost complete dissolution of the fibrin hydrogel is already observed after 7 days *in vivo*. One-way repeated measures ANOVA followed by the Bonferroni *post hoc* test; $P < 0.05$ the intensity of fibrin immunoreactivity at 7 or 30 days *versus* 3 days in the distance range 10–90 µm from the implant-tissue interface ($n = 41$, 52, and 58 slices for 3, 7, and 30 days, respectively, from three implants/time point).

COATING MICROELECTRODES WITH CELLS AND FIBRIN HYDROGEL

We next attempted to seed and grow live cells on the electrode surface with the aim of making the artificial device well tolerated by the host tissue after the reabsorption of the fibrin layer. Both primary neurons and glial cells were seeded. The cells seeded with the method illustrated in this paper grew vigorously and formed a uniform compact monolayer on the curved surface of the electrode (**Figure 8A**). Specific staining of primary neurons with either NeuN or βIII-tubulin (**Figure 8B**) and of astrocytes with GFAP (**Figures 8C,D**) revealed that, using conditioned medium, both types of primary cells can grow on the device.

Cells adhered to the microelectrodes were partially stripped during device insertion into the brain (**Figures 9A–D**). Richter et al. (2011) quantified the effects due to the pulling force acting onto a cell layer and demonstrated the abrasion of the adhered cells and a protective role played by fibrin coating. We therefore decided to protect the cell layer by embedding the cells into a fibrin layer which could also increase the mechanical compliance of the inserted microelectrode (**Figures 10A–C**).

Although previous experiments demonstrated that hydrogel coating does not affect the electrochemical properties of the microelectrodes, we repeated these measures with the hybrid cell/hydrogel-coated electrodes, as the cell layer covering the device could alter the current passage. We demonstrated that the combined coating did not significantly affect either the impedance modulus or phase at 1 kHz with respect to uncoated or fibrin-coated electrodes (**Figures 11A,B**).

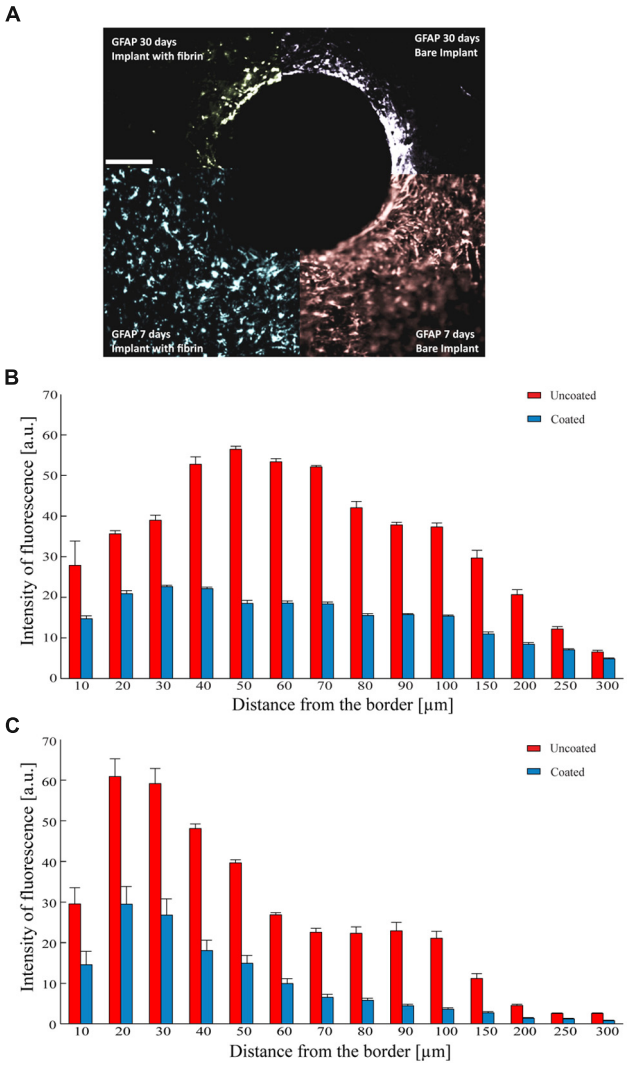

FIGURE 7 | Astrocyte reaction to the implant. (A) Representative images of GFAP immunoreactivity detected 7 (lower quadrants) and 30 days (upper quadrants) after the implant of uncoated (right quadrants) and fibrin-coated (left quadrants) black-lead wires. Scale bar 100 μm. **(B,C)** Analysis of GFAP-positive reactive astrocytes as a function of the distance from the tissue-implant interface. Mean (±SEM) intensity of GFAP immunoreactivity (a.u.) at 7 **(B)** and 30 **(C)** days from the implant. Red and blue bars refer to uncoated and fibrin-coated microelectrodes, respectively. One-way repeated measures ANOVA; $P < 0.05$ coated *versus* uncoated electrodes at all distances for both 7 and 30 days post-implant ($n = 54$ and 58 slices for 7 and 30 days, respectively from 3 implants/time point).

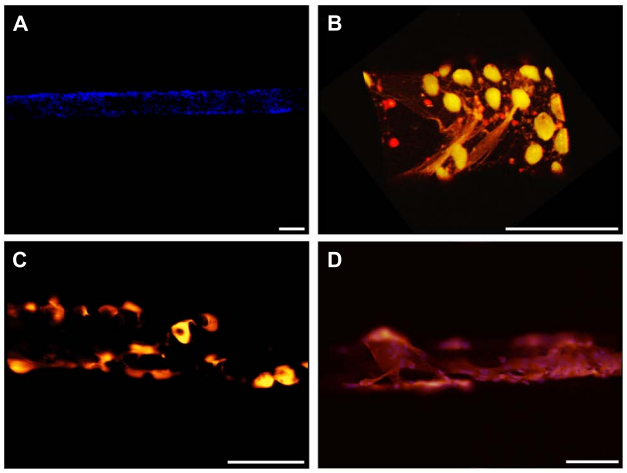

FIGURE 8 | Cell-coated microelectrodes. (A) Representative fluorescent image illustrating the layer of cells adhered to the microelectrode. DAPI staining (blue) reveals cell nuclei. **(B)** Three-dimensional reconstruction of a representative microelectrode coated with neurons. Cells were stained for NeuN (green) and βIII-tubulin (red). **(C,D)** Representative fluorescent images of astrocytes grown on the microelectrode. Cells were stained for GFAP (red) and DAPI (blue). Scale bars 100 μm.

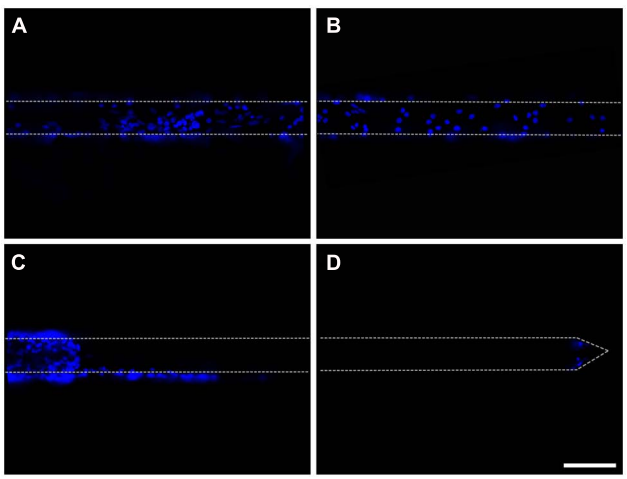

FIGURE 9 | Insertion of cell-coated microelectrodes. (A,B) Representative fluorescent images illustrating the layer of glial cells adhered to a microelectrode. DAPI staining (blue) reveals cell nuclei. The cell-coated microelectrode was inserted 2 mm in depth and the images were acquired from the non-inserted segment of the probe. **(C,D)** Representative fluorescent images of the same microelectrode, illustrating the effects of the insertion of the probe on the adhered glial cells (images acquired along the wire from the inserted segment of the wire). DAPI staining (blue) reveals cell nuclei. Scale bar 100 μm. Dot lines point out the microelectrode shape.

DISCUSSION

The aim of this study was to realize a bio-inspired hybrid device. We developed a strategy to improve the biocompatibility of microelectrodes mimicking the properties of the host tissue in order to increase the biocompatibility over time. To this aim, we modified the device surface to decrease the tissue reaction against the implant and thus increase the working life of the intra-cortical implant. The two main goals we achieved were: (i) to minimize the mechanical difference between the rigid microelectrode shaft and the soft and expanding-retracting brain tissue and (ii) to coat the electrode with a live and tissue-friendly autologous cell layer to improve the tissue tolerance to the foreign body. These aims were obtained by coating the microelectrode with a soft layer of fibrin hydrogel and by coupling it with a layer of living cells (either astrocytes or neurons). While both coatings did not alter the electrochemical properties of the electrode, the combination

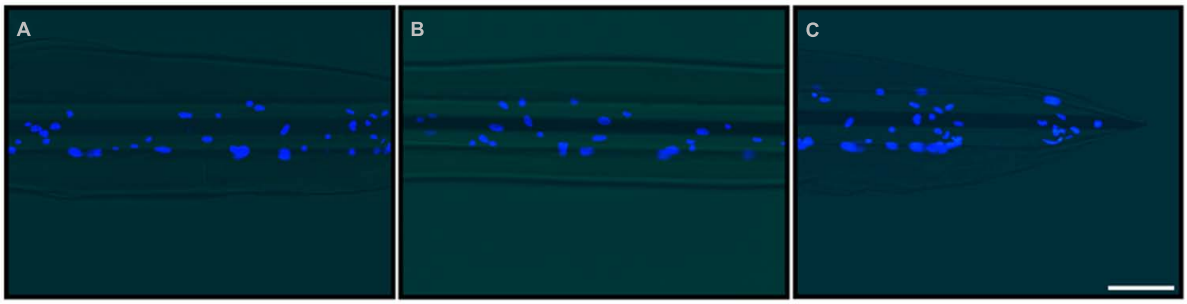

FIGURE 10 | Double-coating of microelectrodes with astrocytes and fibrin hydrogel. Representative images of the final prototype of the bio-inspired hybrid microelectrode: 3 mm far from the tip **(A)**, 1.5 mm far from the tip **(B)** and the tip **(C)**. Fluorescence images (DAPI staining of neuronal nuclei) were merged with the optical image of the microelectrode. The images revealed the microelectrode structure, the fibrin hydrogel sheath surrounding it and the layer of glial cells embedded within the hydrogel. Scale bar 100 μm.

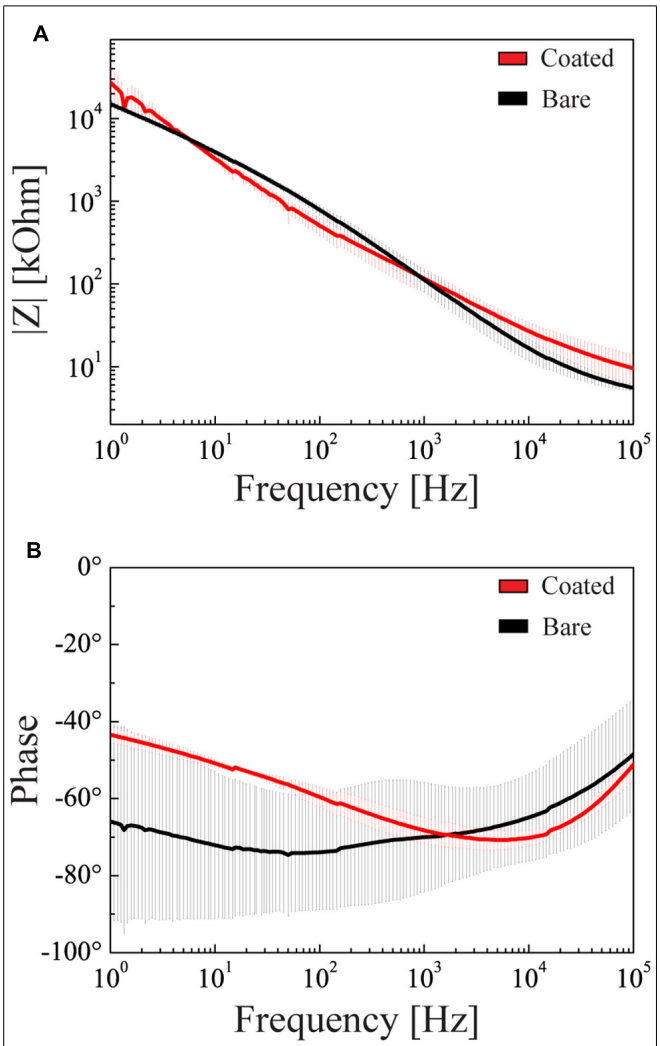

FIGURE 11 | Electrochemical properties of double-coated microelectrodes. Impedance modulus **(A)** and phase **(B)** as a function of the frequency in the 1 Hz–100 kHz range (mean ± SD). Black and red lines refer to the bare microelectrode and to the microelectrode coated with glial cells and hydrogel, respectively.

of the two seems particularly advantageous. In fact, the hydrogel minimizes the continuous trauma due to the different compliance of the electrode and the brain tissue and, at the same time, protects the cell layer from the stress due to the device insertion inside the brain. This can prevent the typical foreign body-dependent inflammation that ends up with a glial scar encapsulating and electrically insulating the device.

The thickness of the soft coating turned out to be a key point. In fact, while the compliance increases with the thickness of the hydrogel, the coating should not be too thick to allow for oxygen supply to the cells seeded on the probe and reliable extracellular recordings of spike activity over the background noise. Another important point is that hydrogels swell when immersed in a saline solution such as the extracellular fluid, and swelling *per se* can compress the surrounding tissue and increase the distance between the brain and the recording site. To comply with these requirements, we exploited fibrin as a hydrogel for the following reasons: (i) coating thickness can be precisely controlled by the number of dippings during the deposition procedure; (ii) it does not affect the electrochemical properties of the microelectrode; (iii) it allows a good quality of recordings (85% of the fibrin-coated electrodes recorded high-quality brain signals with SNR $>$ 3); and (iv) its swelling is moderate with respect to other types of hydrogel (i.e., alginate swelling is such that the recording from target neurons is prevented; Kim et al., 2010b).

Biocompatibility of the fibrin hydrogel was also an important issue. We demonstrated that fibrin coating markedly reduces the extent of astrocyte reaction at both 7 and 30 days after the implant, compared to the bare wire. The astrocyte activation following the implantation of coated wires is more diffuse and less intense, yielding to a significant lesser extent of glial scar and device encapsulation.

Another advantage of the fibrin hydrogel besides its biocompatibility is the progressive, almost complete enzymatic degradation by the host tissue over time. While the hydrogel thickness is an important issue to prevent acute reactions, the progressive degradation does not pose limitations for chronic recordings. While the soft fibrin layer is reabsorbed, cells seeded onto the electrode surface might have integrated with the host tissue both by exchange of extracellular messengers (such as growth factors or

neurotransmitters) and by growth of processes and establishment of new connections. Thus, after the disappearance of the fibrin hydrogel, the electrode could already be interfaced and well tolerated by the host tissue.

Another important point was to verify the integrity of the coating upon insertion of the device into the tissue. The shear stress of insertion not only had critical consequences on the unprotected cell coating of the electrode, but was also effective, in a large percentage of cases, in stripping the fibrin hydrogel from the smooth surface of the electrode. We set-up a treatment to increase the roughness of the quartz electrode surface, achieving a better grip for both the cell layer and the fibrin sheath.

Our study has demonstrated the possibility to produce tissue-friendly microelectrodes well-tolerated and functional over time. This is fundamental to realize electrodes for chronic recordings. Additionally, the use of materials that can be withdrawn directly from the individual patient before the implant is a fundamental approach to reduce the immunoreaction to the minimum. Our solution, using fibrin and cells fulfills both these requirements. The fibrin precursor, fibrinogen, can be easily extracted from the patient's blood. Neurons and glial cells can be reprogrammed from patient's fibroblasts either from iPS cell clones or, more safely, by direct reprogramming. The latter procedure has been successfully obtained for dopaminergic neurons (Broccoli et al., 2011; Caiazzo et al., 2011).

CONCLUSIONS

The properties of the tissue-electrode interface, including electrical and mechanical integration, are crucial in determining long-term reliability and functionality of neural implants. The major problems of chronic neural prostheses are the immune and inflammatory tissue responses that occur after device implantation. This causes a significant increase of the electric impedance because of the growth of a dense fibrous sheath. Additionally, target neurons are pushed away by the scar so that the electrode becomes isolated from the surrounding tissue.

In this work, we developed a new method to control the biological response to electrode implantation and promote a more efficient integration of implanted microelectrodes. We developed a bio-inspired hybrid probe obtained with the seeding of a compact sheath of cells encapsulated in a thin re-absorbable fibrin layer and demonstrated that such a device is biocompatible, does not alter the electrochemical properties of the electrode, allows recordings of good quality and markedly reduces the tissue inflammatory reaction. This device has therefore a good potential to improve the electrical integration at the neuron-electrode interface and support the long-term success of neural prostheses.

ACKNOWLEDGMENTS

The study was supported by research grants from the Italian Ministry of University and Research (PRIN to Fabio Benfenati and Luciano Fadiga) and from the EU grants FP7-NMP-2013-EU-China "NEUROSCAFFOLDS"(Grant Agreement No: NMP3-SL-2013-604263; to Fabio Benfenati).

REFERENCES

Abidian, M. R., Ludwig, K. A., Marzullo, T. C., Martin, D. C., and Kipke, D. R. (2009). Interfacing conducting polymer nanotubes with the central nervous system: chronic neural recording using poly(3,4-ethylenedioxythiophene) nanotubes. *Adv. Mater.* 21, 3764–3770. doi: 10.1002/adma.200900887

Ansaldo, A., Castagnola, E., Maggiolini, E., Fadiga, L., and Ricci, D. (2011). Superior electrochemical performance of carbon nanotubes directly grown on sharp microelectrodes. *ACS Nano* 5, 2206–2214. doi: 10.1021/nn103445d

Azemi, E., Lagenaur, C. F., and Cui, X. T. (2011). The surface immobilization of the neural adhesion molecule L1 on neural probes and its effect on neuronal density and gliosis at the probe/tissue interface. *Biomaterials* 32, 681–692. doi: 10.1016/j.biomaterials.2010.09.033

Baranauskas, G., Maggiolini, E., Castagnola, E., Ansaldo, A., Mazzoni, A., Angotzi, G. N., et al. (2011). Carbon nanotube composite coating of neural microelectrodes preferentially improves the multiunit signal-to-noise ratio. *J. Neural Eng.* 8:066013. doi: 10.1088/1741-2560/8/6/066013

Benabid, A. L., Chabardes, S., Mitrofanis, J., and Pollak, P. (2009). Deep brain stimulation of the subthalamic nucleus for the treatment of Parkinson's disease. *Lancet Neurol.* 8, 67–81. doi: 10.1016/S1474-4422(08)70291-6

Biran, R., Martin, D. C., and Tresco, P. A. (2007). The brain tissue response to implanted silicon microelectrode arrays is increased when the device is tethered to the skull. *J. Biomed. Mater. Res. A* 82, 169–178. doi: 10.1002/jbm.a

Bjornsson, C. S., Oh, S. J., Al-Kofahi, Y. A., Lim, Y. J., Smith, K. L., Turner, J. N., et al. (2006). Effects of insertion conditions on tissue strain and vascular damage during neuroprosthetic device insertion. *J. Neural Eng.* 3:196–207. doi: 10.1088/1741-2560/3/3/002

Bjugstad, K. B., Lampe, K., Kern, D. S., and Mahoney, M. (2010). Biocompatibility of poly(ethylene glycol)-based hydrogels in the brain: an analysis of the glial response across space and time. *J. Biomed. Mat. Res. A* 95, 79–91. doi: 10.1002/jbm.a.32809

Bonfanti, A., Borghi, T., Gusmeroli, R., Zambra, G., Spinelli, A. S., Oliynyk, A., et al. (2008). "A Low-power integrated circuit for analog spike detection and sorting in neural prosthesis systems," in *Proceedings of the Biomedical Circuits and Systems Conference, 2008* (Baltimore: IEEE), 257–260. doi: 10.1109/BIOCAS.2008.4696923

Borghi, T., Bonfanti, A., Gusmeroli, R., Zambra, G., and Spinelli, A. S. (2008). A power-efficient analog integrated circuit for amplification and detection of neural signals. *Conf. Proc. IEEE Eng. Med. Biol. Soc.* 2008, 4911–4915. doi: 10.1109/IEMBS.2008.4650315

Broccoli, V., Caiazzo, M., and Dell'Anno, M. T. (2011). Setting a highway for converting skin into neurons. *J. Mol. Cell Biol.* 3, 322–323. doi: 10.1093/jmcb/mjr029

Caiazzo, M., Dell'Anno, M. T., Dvoretskova, E., Lazarevic, D., Taverna, S., Leo, D., et al. (2011). Direct generation of functional dopaminergic neurons from mouse and human fibroblasts. *Nature* 476, 224–227. doi: 10.1038/nature10284

Castagnola, E., Maiolo, L., Maggiolini, E., Minotti, A., Marrani, M., Maita, F., et al. (2013). "Ultra-flexible and brain-conformable micro-electrocorticography device with low impedance PEDOT-carbon nanotube coated microelectrodes," in *Proceedings of the Sixth Annual International IEEE EMBS Conference on Neural Engineering*, San Diego, CA, 6–8.

de Vries, J., Menovsky, T., van Gulik, S., and Wesseling, P. (2002). Histological effects of fibrin glue on nervous tissue: a safety study in rats. *Surg. Neurol.* 57, 415–422. doi: 10.1016/S0090-3019(02)00736-X

Donoghue, J. P., Nurmikko, A., Black, M., and Hochberg, L. R. (2007). Assistive technology and robotic control using motor cortex ensemble-based neural interface systems in humans with tetraplegia. *J. Physiol.* 579(Pt 3), 603–611. doi: 10.1113/jphysiol.2006.127209

Edell, D. J., Toi, V. V., McNeil, V. M., and Clark, L. D. (1992). Factors influencing the biocompatibility of insertable silicon microshafts in cerebral cortex. *IEEE Trans. Biomed. Eng.* 39, 635–643. doi: 10.1109/10.141202

Fawcett, J. W., and Asher, R. A. (1999). The glial scar and central nervous system repair. *Brain Res. Bull.* 49, 377–391. doi: 10.1016/S0361-9230(99)00072-6

Frampton, J. P., Hynd, M. R., Shuler, M. L., and Shain, W. (2011). Fabrication and optimization of alginate hydrogel constructs for use in 3D neural cell culture. *Biomed. Mater.* 6:015002. doi: 10.1088/1748-6041/6/1/015002

Ghezzi, D., Antognazza, M. R., Dal Maschio, M., Lanzarini, E., Benfenati, F., and Lanzani, G. (2011). A hybrid bioorganic interface for neuronal photoactivation. *Nat. Commun.* 2, 166. doi: 10.1038/ncomms1164

Goyal, A., Hood, V., and Tadigadapa, S. (2006). "High speed anisotropic etching of quartz using SF6/C4F8/Ar/O2 based chemistry in inductively coupled plasma

reactive ion etching system," in *Proceedings of SPIE, the International Society for Optical Engineering*, eds D. M. Tanner and R. Ramesham (San Jose, CA: Society of Photo-Optical Instrumentation Engineers), 61110. doi: 10.1117/12.657730

Green, R. A., Baek, S., Poole-Warren, L. A., and Martens, P. J. (2010). Conducting polymer-hydrogels for medical electrode applications. *Sci. Technol. Adv. Mater.* 11, 014107. doi: 10.1088/1468-6996/11/1/014107

Grill, W. M., Norman, S. E., and Bellamkonda, R. V. (2009). Implanted neural interfaces: biochallenges and engineered solutions. *Annu. Rev. Biomed. Eng.* 11, 1–24. doi: 10.1146/annurev-bioeng-061008-124927

Harris, J. P., Capadona, J. R., Miller, R. H., Healy, B. C., Shanmuganathan, K., Rowan, S. J., et al. (2011). Mechanically adaptive intracortical implants improve the proximity of neuronal cell bodies. *J. Neural Eng.* 8:066011. doi: 10.1088/1741-2560/8/6/066011

He, W., McConnell, G. C., and Bellamkonda, R. V. (2006). Nanoscale laminin coating modulates cortical scarring response around implanted silicon microelectrode arrays. *J. Neural Eng.* 3, 316–326. doi: 10.1088/1741-2560/3/4/009

Hemm, S., and Wårdell, K. (2010). Stereotactic implantation of deep brain stimulation electrodes: a review of technical systems, methods and emerging tools. *Med. Biol. Eng. Comput.* 48, 611–624. doi: 10.1007/s11517-010-0633-y

Henze, D. A., Borhegyi, Z., Csicsvari, J., Mamiya, A., Harris, K. D., and Buzsáki, G. (2000). Intracellular features predicted by extracellular recordings in the hippocampus *in vivo*. *J. Neurophysiol.* 84, 390–400.

Hou, S., Xu, Q., Tian, W., Cui, F., Cai, Q., Ma, J., et al. (2005). The repair of brain lesion by implantation of hyaluronic acid hydrogels modified with laminin. *J. Neurosci. Methods* 148, 60–70. doi: 10.1016/j.jneumeth.2005.04.016

Kim, D. H., Abidian, M., and Martin, D. C. (2004a). Conducting polymers grown in hydrogel scaffolds coated on neural prosthetic devices. *J. Biomed. Mater. Res. A* 71, 577–585. doi: 10.1002/jbm.a.30124

Kim, Y. T., Hitchcock, R. W., Bridge, M. J., and Tresco, P. A. (2004b). Chronic response of adult rat brain tissue to implants anchored to the skull. *Biomaterials* 25, 2229–2237. doi: 10.1016/j.biomaterials.2003.09.010

Kim, D. H., Viventi, J., Amsden, J. J., Xiao, J., Vigeland, L., Kim, Y. S., et al. (2010a). Dissolvable films of silk fibroin for ultrathin conformal bio-integrated electronics. *Nat. Mater.* 9, 511–517. doi: 10.1038/nmat2745

Kim, D. H., Wiler, J. A., Anderson, D. J., Kipke, D. R., and Martin, D. C. (2010b). Conducting polymers on hydrogel-coated neural electrode provide sensitive neural recordings in auditory cortex. *Acta Biomater.* 6, 57–62. doi: 10.1016/j.actbio.2009.07.034

Klaver, C. L., and Caplan, M. R. (2007). Bioactive surface for neural electrodes: decreasing astrocyte proliferation via transforming growth factor-beta1. *J. Biomed. Mat. Res. A* 81, 1011–1016. doi: 10.1002/jbm.a.31153

Kong, H. J., Kaigler, D., Kim, K., and Mooney, D. J. (2004). Controlling rigidity and degradation of alginate hydrogels via molecular weight distribution. *Biomacromolecules* 5, 1720–1727. doi: 10.1021/bm049879r

Kozai, T. D. Y., Langhals, N. B., Patel, P. R., Deng, X., Zhang, H., Smith, K. L., et al. (2012). Ultrasmall implantable composite microelectrodes with bioactive surfaces for chronic neural interfaces. *Nat. Mater.* 11, 1065–1073. doi: 10.1038/nmat3468

Larson, P. S. (2008). Deep brain stimulation for psychiatric disorders. *Neurotherapeutics* 5, 50–58. doi: 10.1016/j.nurt.2007.11.006

Limongi, T., Cesca, F., Gentile, F., Marotta, R., Ruffilli, R., Barberis, A., et al. (2013). Nanostructured superhydrophobic substrates trigger the development of 3D neuronal networks. *Small* 9:402–412. doi: 10.1002/smll.201201377

Ludwig, K. A., Miriani, R. M., Langhals, N. B., Joseph, M. D., Anderson, D. J., and Kipke, D. R. (2009). Using a common average reference to improve cortical neuron recordings from microelectrode arrays. *J. Neurophysiol.* 101, 1679–1689. doi: 10.1152/jn.90989.2008

Ludwig, K. A., Uram, J. D., Yang, J., Martin, D. C., and Kipke, D. R. (2006). Chronic neural recordings using silicon microelectrode arrays electrochemically deposited with a poly(3,4-ethylenedioxythiophene) (PEDOT) film. *J. Neural Eng.* 3:59–70. doi: 10.1088/1741-2560/3/1/007

Marin, C., and Fernández, E. (2010). Biocompatibility of intracortical microelectrodes: current status and future prospects. *Front. Neuroeng.* 3:1–6. doi: 10.3389/fneng.2010.00008

Nisbet, D. R., Crompton, K. E., Horne, M. K., Finkelstein, D. I., and Forsythe, J. S. (2008). Neural tissue engineering of the CNS using hydrogels. *J. Biomed. Mater. Res. B Appl. Biomater.* 87, 251–263. doi: 10.1002/jbm.b.31000

Normann, R. A., Greger, B., Greger, B. A., House, P., Romero, S. F., Pelayo, F., et al. (2009). Toward the development of a cortically based visual neuroprosthesis. *J. Neural Eng.* 6:035001. doi: 10.1088/1741-2560/6/3/035001

Polikov, V. S., Tresco, P. A., and Reichert, W. M. (2005). Response of brain tissue to chronically implanted neural electrodes. *J. Neurosci. Methods* 148, 1–18. doi: 10.1016/j.jneumeth.2005.08.015

Potter, K. A., Simon, J. S., Velagapudi, B., and Capadona, J. R. (2012). Reduction of autofluorescence at the microelectrode-cortical tissue interface improves antibody detection. *J. Neurosci. Methods* 203, 96–105. doi: 10.1016/j.jneumeth.2011.09.024

Purcell, E. K., Seymour, J. P., Yandamuri, S., and Kipke, D. R. (2009). *In vivo* evaluation of a neural stem cell-seeded prosthesis. *J. Neural Eng.* 6:026005. doi: 10.1088/1741-2560/6/2/026005

Richardson-Burns, S. M., Hendricks, J. L., and Martin, D. C. (2007). Electrochemical polymerization of conducting polymers in living neural tissue. *J. Neural Eng.* 4:L6–L13. doi: 10.1088/1741-2560/4/2/L02

Richter, A., Kruse, C., Moser, A., Hofmann, U. G., and Danner, S. (2011). Cellular modulation of polymeric device surfaces: promise of adult stem cells for neuro-prosthetics. *Front. Neurosci.* 5:1–10. doi: 10.3389/fnins.2011.00114

Rousche, P. J., Pellinen, D. S., Pivin, D. P., Williams, J. C., Vetter, R. J., and Kipke, D. R. (2001). Flexible polyimide-based intracortical electrode arrays with bioactive capability. *IEEE Trans. Biomed. Eng.* 48, 361–371. doi: 10.1109/10.914800

Takeuchi, S., Ziegler, D., Yoshida, Y., Mabuchi, K., and Suzuki, T. (2005). Parylene flexible neural probes integrated with microfluidic channels. *Lab Chip* 5, 519–523. doi: 10.1039/b417497f

Thelin, J., Jörntell, H., Psouni, E., Garwicz, M., Schouenborg, J., Danielsen, N., et al. (2011). Implant size and fixation mode strongly influence tissue reactions in the CNS. *PLoS ONE* 6:e16267. doi: 10.1371/journal.pone.0016267

Truccolo, W., Friehs, G. M., Donoghue, J. P., and Hochberg, L. R. (2008). Primary motor cortex tuning to intended movement kinematics in humans with tetraplegia. *J. Neurosci.* 28, 1163–1178. doi: 10.1523/JNEUROSCI.4415-07.2008

Unterberg, A. W., Stover, J., Kress, B., and Kiening, K. L. (2004). Edema and brain trauma. *Neuroscience* 129, 1021–1029. doi: 10.1016/j.neuroscience.2004.06.046

Velliste, M., Perel, S., Spalding, M. C., Whitford, A. S., and Schwartz, A. B. (2008). Cortical control of a prosthetic arm for self-feeding. *Nature* 453, 1098–1101. doi: 10.1038/nature06996

Williams, J. C., Hippensteel, J. A., Dilgen, J., Shain, W., and Kipke, D. R. (2007). Complex impedance spectroscopy for monitoring tissue responses to inserted neural implants. *J. Neural Eng.* 4:410–423. doi: 10.1088/1741-2560/4/4/007

Zhang, H., Patel, P. R., Xie, Z., Swanson, S. D., Wang, X., and Kotov, N. A. (2013). Tissue-compliant neural implants from microfabricated carbon nanotube multilayer composite. *ACS Nano* 7, 7619–7629. doi: 10.1021/nn402074y

Conflict of Interest Statement: The authors declare that the research was conducted in the absence of any commercial or financial relationships that could be construed as a potential conflict of interest.

Received: 31 January 2014; paper pending published: 06 March 2014; accepted: 24 March 2014; published online: 10 April 2014.

*Citation: De Faveri S, Maggiolini E, Miele E, De Angelis F, Cesca F, Benfenati F and Fadiga L (2014) Bio-inspired hybrid microelectrodes: a hybrid solution to improve long-term performance of chronic intracortical implants. Front. Neuroeng. **7**:7. doi: 10.3389/fneng.2014.00007*

This article was submitted to the journal Frontiers in Neuroengineering.

frontiers in
NEUROENGINEERING

REVIEW ARTICLE
published: 13 May 2014
doi: 10.3389/fneng.2014.00009

Anti-inflammatory polymer electrodes for glial scar treatment: bringing the conceptual idea to future results

***Maria Asplund*[1,2,3]*, *Christian Boehler*[1,2,3] *and Thomas Stieglitz*[1,3]**

[1] *Biomedical Microtechnology, IMTEK, Albert-Ludwigs Universität, Freiburg, Germany*
[2] *Freiburg Institute for Advanced Studies FRIAS, Albert-Ludwigs Universität, Freiburg, Germany*
[3] *BrainLinks-BrainTools Cluster of Excellence, Albert-Ludwigs Universität, Freiburg, Germany*

Edited by:
Ulrich G. Hofmann, Albert-Ludwigs-University Freiburg, Germany

Reviewed by:
Pascal Darbon, Université de Strasbourg, France
Fabrice O. Morin, Fatronik-Tecnalia Foundation, Spain

***Correspondence:**
Maria Asplund, Biomedical Microtechnology, IMTEK, Albert-Ludwigs Universität, Georges-Köhler Allee 102, Freiburg 79108, Germany
e-mail: maria.asplund@imtek.de

Conducting polymer films offer a convenient route for the functionalization of implantable microelectrodes without compromising their performance as excellent recording units. A micron thick coating, deposited on the surface of a regular metallic electrode, can elute anti-inflammatory drugs for the treatment of glial scarring as well as growth factors for the support of surrounding neurons. Electro-activation of the polymer drives the release of the substance and should ideally provide a reliable method for controlling quantity and timing of release. Driving signals in the form of a constant potential (CP), a slow redox sweep or a fast pulse are all represented in literature. Few studies present such release *in vivo* from actual recording and stimulating microelectronic devices. It is essential to bridge the gap between studies based on release *in vitro,* and the intended application, which would mean release into living and highly delicate tissue. In the biological setting, signals are limited both by available electronics and by the biological safety. Driving signals must not be harmful to tissue and also not activate the tissue in an uncontrolled manner. This review aims at shedding more light on how to select appropriate driving parameters for the polymer electrodes for the *in vivo* setting. It brings together information regarding activation thresholds for neurons, as well as injury thresholds, and puts this into context with what is known about efficient driving of release from conducting polymer films.

Keywords: conducting polymer, dexamethasone, drug delivery, glial scarring, neural interfaces

INTRODUCTION

Recent advances in the field of conducting polymers point out their potential as drug delivery coatings from the surfaces of microelectrodes. This is of interest considering it comprises an opportunity to target cells in the close vicinity of an implant with high spatial and temporal control of release. Glial scarring is a physiological process that deteriorates electrode function by forming a substantial barrier for signal transduction. Persistent inflammation, following the scarring process, is believed to be the reason why neurons are lost at the site of the implant further complicating high resolution in recording and stimulation (Turner et al., 1999; Szarowski et al., 2003; Biran et al., 2005). Systemic treatment using anti-inflammatory drugs such as Dexamethasone (Dex) has been suggested as a possible strategy for facilitating close integration of the implant with neural tissue (Spataro et al., 2005). Conducting polymer electrodes designed to elute drugs upon electro-activation are an alternative to systemic treatment of glial scarring (Abidian et al., 2006; Wadhwa et al., 2006; Evans et al., 2009; Richardson et al., 2009; Luo and Cui, 2009a,b; Stevenson et al., 2010; Yue et al., 2013). Polymers in question are mainly Polypyrrole (PPy), poly(3,4-ethylene dioxythiophene) (PEDOT) but more recently also polyterthiophene (PTTh) has been suggested as a candidate (Stevenson et al., 2010). This functionality is until now almost exclusively studied *in vitro*. Here we discuss this intriguing possibility, its requirements in terms of electronic control of the implant, and the restrictions set by electrochemical safety limits, to form the basis for continued investigations *in vivo*.

Electro-activation is essential for triggering release but cannot be allowed to cause detrimental effects on the cellular microenvironment. The conducting polymer electrode is not analogous to a metallic electrode and direct currents can, and must, to some extent be tolerated to drive drugs out of the electrode. On the other hand, one must not overlook the possibility that by-products form in body fluids as a result of electro-activation, or that the neuronal circuitry is unintentionally activated, which means that potentials must be kept within strict boundaries. The solution that comes close at hand is to ensure that signals are maintained below the activation threshold. Then the question boils down to if this type of signal can be used to drive ionic drugs out of the electrode? The majority of studies focus on release by cyclic voltammetry (CV), a signal sufficiently slow to give room for diffusion limited processes to contribute, in contrast to fast stimulation pulses, generally designed to employ primarily capacitive effects.

Studies show that release can be precisely managed by the appropriate electrochemical driving signal. However, the means to keep exact control of charge and voltage are limited in an implant where three-electrode electrochemical systems are rarely implemented. Furthermore, the circuitry designed for stimulation *in vivo* cannot necessarily accommodate the same type of measurements and control as the electrochemical potentiostat.

Therefore, electronics and implantable reference electrodes that meet this requirement need to be developed. If glial scarring is really to be treated by the suggested method it cannot come at the cost of connecting lab animals to fully functional external potentiostats but the solution must come as a miniaturized implant.

Finally we intend to outline the possibilities in terms of quantities of drugs that can be delivered and, to some extent, the variety of drugs that could come in question. Most studies focus on delivery of the anti-inflammatory drug Dex but results point out that other drugs with similar size and charge could also be potential candidates.

In summary, we present the possibilities of conducting polymer based release for glial scar treatment. Benefits of the method will be put in perspective with design challenges that have to be met from the electronics side. This information is essential for enabling more studies to proceed to the implant stage, shedding light on how to make the best out of this novel and exciting concept.

ELECTRODEPOSITION OF CONDUCTING POLYMERS

Conducting polymers can be deposited on top of microelectrodes using an aqueous electrodeposition process. The reaction is driven in a supporting electrolyte in which the monomer (M) is dissolved or dispersed together with appropriate counter ions (CI). The monomers oxidized at the surface of the working electrode build up an insoluble layer of conducting polymer on its surface. To maintain charge neutrality, the negatively charged CI are at the same time electrostatically entrapped in the formed material according to the following reaction:

$$M + CI^- \xrightarrow{oxidize} (M)^+ CI^- \quad (1)$$

The nature of the counter ion is decisive for the ionic exchange properties of the formed polymer (Bobacka et al., 2000; Jager et al., 2000). The CI can be small or large, inorganic or organic molecules, or a combination of several different negatively charged molecules can be included in the supporting electrolyte to form a more complex material. If a biologically relevant molecule is used as counter ion, the formed polymer can be biofunctionalized since the molecule is efficiently entrapped in the porous polymer matrix yet still available for reactions on the surface of the polymer material (Asplund et al., 2008). In addition it can be released from the polymer upon altering the polymer redox state.

There are some restrictions in the choice of biological ions that can come in question for the counter ion incorporation technique. The one step approach described above would work exclusively for negatively charged biomolecules. For the delivery functionality to be efficient, a further constraint is that the molecule must be sufficiently small to be able to diffuse through the polymer matrix. It is difficult to give a precise estimate on what could be considered as sufficiently small, since the porosity is not an absolute property but can be influenced by the electrodeposition process. To give some figure of merit, successful release has been shown for molecules up to the range of 0.5 kDa. Although some authors report release of substantially larger substances such as protein fragments, it is clear that this is more challenging and might primarily rely on actuation of the polymer material rather than electrostatic binding and release (Thompson et al., 2006; Evans et al., 2009; Richardson et al., 2009). This topic is discussed in detail in section Release Systems and Mechanisms.

As an alternative to the direct incorporation in Equation 1, an ion exchange approach can be used to drive ions into the already formed polymer film for subsequent release upon reversing the potential (Xiao et al., 2007). Furthermore, a carrier phase can be introduced into the material by allowing the polymer to form within a network of beads or fibers already containing the substance to be delivered (Abidian et al., 2006; Luo et al., 2011). A non-charged substance in the larger size range, which is made available in the supporting electrolyte, can be adsorbed to the surface in parallel with the deposition process and thereby also be mechanically entrapped although not electrostatically bound (Asplund et al., 2008). All these methods could in principle lead to a material with controlled delivery functionality similar to what is accomplished with the direct incorporation technique. The release dynamics can however be expected to differ. The focus of this review is primarily on controlled release based on direct incorporation according to Equation 1, although some results based on materials using other methods are also included.

Dex DELIVERY—QUANTITIES AND EFFICIENCY

The theoretically possible inclusion of Dex in a polymer film, based on the counter ion incorporation technique, can be estimated by Equation 2 (Skotheim and Reynolds, 2006):

$$m_{dopant} = \frac{Q_{dep}}{F} \cdot \frac{\gamma M_{dopant}}{2+\gamma} \quad (2)$$

F stands for Faraday's constant and equals 96485 C/mol and Q_{dep} stands for deposition charge. With Dex as dopant, the commonly accepted assumption that the doping level $\gamma = 0.3$, and the molecular weight of Dex, $M_{Dex} = 392$ g/mol, Dex inclusion per charge consumed in the electrodeposition process would be approximately 700 μg/C. The deposition charge density that would be considered reasonable varies, depending on the stability of the polymer system, but 300 mC/cm^2 would clearly be within the realistic range. This would mean a total included Dex mass $m_{Dex} = 210$ μg/cm^2 according to Equation 2. Most likely higher deposition charges could be used (Li and Huang, 2007).

A handful of papers point out the Dex levels that would be required for efficient treatment of glial scarring. Based on the assumption that the volume of interest could be defined as a sphere of radius 500 μm enclosing the electrode (Wadhwa et al., 2006), and that an efficient concentration would be expected to lie within the range 0.2–1 μM (Golde et al., 2003; Shain et al., 2003; Zhong et al., 2005), further assuming a microelectrode radius of ∼15 μm, the electrode would need to be able to deliver a concentration of 6–30 μg/cm^2 from its surface.

Considering various papers report delivery of Dex in the range 3–126 μg/cm^2 in total, several single efficient doses would be possible with the presented technology (Wadhwa et al., 2006; Moulton et al., 2008; Stevenson et al., 2010; Sirivisoot et al.,

2011; Xiao et al., 2012). In light of these values one might argue that optimizing control is even more important than maximizing output per pulse or sweep.

RELEASE SYSTEMS AND MECHANISMS

The drug delivery from a conducting polymer is a result of the interplay between electrostatic interaction with the surrounding electrolyte, mechanical actuation of the film as a response to the different swelling states upon redox, and conformational changes in the polymer structure. To which extent each of the mechanisms contributes varies depending on the film morphology, the triggering signal and the use of any additional CI and must therefore be evaluated separately for each case. Three types of triggering signals are considered here namely redox sweeping, constant potential (CP) and pulsing (**Figure 1**). Redox sweeping is mainly referred to as the electrochemical measurement term CV.

The most simple release system would be a one-layer deposition where an anionic drug is included as a counter ion directly in the deposition process. Assuming that the drug is thereby homogenously distributed within the polymer film, and electrostatic interaction is the only responsible mechanism, the quantity of drug that is released should be proportional to the applied charge. This simplified view would imply that it is only the absolute charge transfer over the interface that matters for the quantity of drug delivered, regardless of if the charge is delivered as a pulse or a sweep. However, this is a crude simplification for a vastly more complex process (Kontturi et al., 1998; Majumdar et al., 2008). In fact, experimental data shows that the dynamics of the release signal greatly matters for the outcome.

In **Table 1** a short compilation of release trigger signals and experienced results from different conducting polymer based release systems can be seen. Signals vary from steady potentials over slow CV sweeps to faster pulsed signals. From the experimental data reported in these studies it is evident that release is not solely ruled by charge transfer. Multiple ions contribute to charge transfer making the direct correlation of interfacial charge transfer to delivery of a specific species less trivial (Pyo et al., 1994; Jager et al., 2000; Pernaut and Reynolds, 2000; Li and Huang, 2007).

Some early work on PPy:ATP membranes gives important insight into the different mechanisms responsible for CP based drug delivery (Pyo et al., 1994; Pernaut and Reynolds, 2000). Based on parametric studies on inclusion and release of Adenosin Triphosphate (ATP), it was found that small, highly mobile cations are initially driven into the film and first after several minutes the release of ATP becomes the dominant process. Furthermore, even though the dissociation of the ionic drug from the polypyrrole chain may be fast, the actual release from the film is driven by diffusion and is therefore a slow process (Pernaut and Reynolds, 2000; Wadhwa et al., 2006; Li and Huang, 2007; Leprince et al., 2010). Fast signals would according to these findings mainly result in exchange of small anions/cations at the superficial layer of the polymer, for which the diffusion coefficients are low.

The majority of studies report that CV is vastly more efficient for driving release than CPs (Pyo et al., 1994; Pernaut and Reynolds, 2000; Wadhwa et al., 2006; Li and Huang, 2007). This underlines the complexity of the events involved in the release process far beyond what can be accounted for by the simplified electrostatic equation. The structural changes in the polymer upon redox are expected to play a major part. Most likely all the stored drug is not immediately accessible for release. Diffusion of ions within the film, and rearrangement of the polymer chains over time, exposes new deposits of drug that were not immediately accessible for the first release attempt.

Electro-actuation contributes to such conformational changes but in addition is expected to serve as a purely mechanical release mechanism for any substance entrapped within the film (Abidian et al., 2006; Thompson et al., 2006; Li and Huang, 2007). The polymer film can both shrink and swell upon reduction depending on the size of the counter ion (Jager et al., 2000). For CI in the intermediate size range such as Dex and ATP it is not straight forward to predict which mechanism would dominate. Nevertheless, repeated redox cycling will swell and shrink the film interchangeably. Actively reversing the potential at a slow rate, such as in CV, contributes to more efficient release for the anodic cycle both through inner rearrangement and through mechanical contraction of the matrix.

In summary, the efficiency with which interfacial charge transfer can contribute to release of the intended drug depends on the dynamics of the trigger signal. Furthermore, depending on diffusivity and thickness of the individual polymer film, the

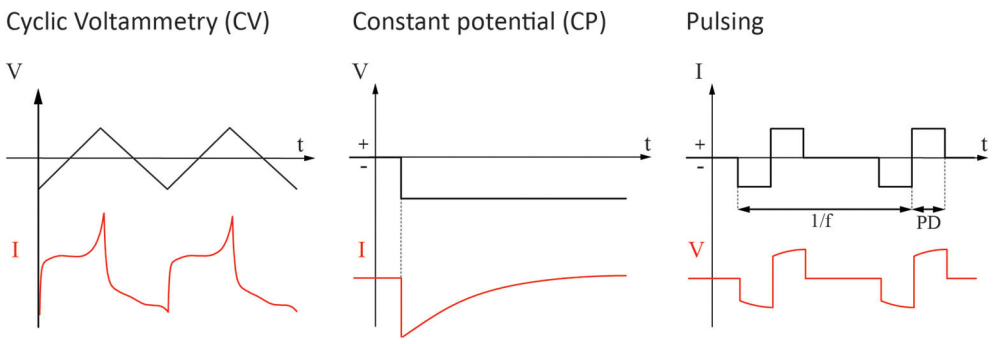

FIGURE 1 | The three different types of trigger signals for electrochemically controlled release that are discussed in the paper. The driving signal is outlined in black and the follower signal in red.

Table 1 | A compilation of experimental research concerning conducting polymer based drug delivery systems and the trigger signals used to control the release.

Study	Polymer:drug[a]	Delivery paradigm[b]	Detection scheme	Comment
Pyo et al., 1994	PPy:ATP	CV: −1 V to 0 V at 10 mV/s CP: −0.4 V; −0.5 V	Electrochemical Quartz Crystal Microbalance (EQCM)/UV	CV more efficient than CP, −0.5 V CP sufficient for release but not −0.4 V
Pernaut and Reynolds, 2000	PPy:ATP	CV CP, −0.4 V; 0.7 V; 0.8 V	UV	CV more efficient than CP. No release for −0.3 V and increase of release rate from −0.4 to −0.8 V
Abidian et al., 2006	PEDOT:Dex, nanofiber template technique	1 V with a scan rate of 0.1 V/s for 10 s Comment see ([c])	UV	–
Wadhwa et al., 2006	PPy:Dex	CV: −0.8 to 1.4 V at 100 mV/s	UV	CV more efficient than CP
Thompson et al., 2006	PPy:pTS:NT-3	Pulsed potential or current, −0.5 /+0.5 mA 5 Hz −20/+20 mA 5 Hz −0.6/+0.6 V 5 Hz CV: −0.8 to 1.0 V at 50 mV/s	Radiolabeling	–
Li and Huang, 2007	PPy:ATP	CV: 0 to −1.1 V at 10 mV/s Steps: −1.1 V, 60 s, 0 V, 60 s	Mass spectrometry	CV more efficient than a stepped potential
Evans et al., 2009	PPy:pTS:BDNF	Charged-balanced biphasic, 100 μs PD, 250 Hz, 60.2 mA, 25 μs open-circuit gap 3.78 ms short-circuit phase	Radio-labeling and ELISA	Comments see ([d])
Ge et al., 2009	PPy:ATP or PPy:SSA + PPy:Cl block layer	CP: −0.3 V; −0.5 V; −0.8 V; and −1.0 V	Fluorometer and bioluminescence	−0.3 V sufficient for ATP release. Higher potential −0.8/−1 V = faster release
Luo and Cui, 2009a	PPy:Dex nanosponge, direct incorporation + sponge	CP: −2.0 V; −0.5 V, 5 s + 5 s at 0 V	UV and fluorometer	−0.5 V gave linear and steady release
Richardson et al., 2009	PPy:pTS:NT3	Charge-balanced biphasic, PD 100 μs, 250 Hz, stimulation currents 350–825 mA	Radiolabeling	
Leprince et al., 2010	PPy:Dex	CV: −0.8 to 0.9 V at 100 mV/s	UV	Scan rate influences release rate
Stevenson et al., 2010	PTTh:Dex	CP: 0 V; 0.6 V pulsed potential 0 V to +0.6 V at 1 Hz	UV	0.6 V CP is used to suppress NOT activate release
Ru et al., 2011	PPy:ATP	CP: −0.8 V	UV	
Li et al., 2012	PPy:TCF	CP: −0.3 V; −0.4 V; and −0.5 V vs. SCE	Gas chromatography mass spectrometry	−0.4 V vs. SCE gave efficient release
Xiao et al., 2012	PEDOT:Dex and PEDOT:Dex CNTs	CV: −0.8 to 1.4V at 50 mV/s	UV	

Results were selected with regard to on if they presented a system based at least partially on direct incorporation of drug at electropolymerization.

[a] Direct incorporation at electropolymerization unless otherwise stated.

[b] Potentials given are vs. Ag:AgCl unless otherwise stated.

[c] Not reported as CV, direct quote from paper "1V with a scan range of 0.1 Vs^{-1} for 10 s."

[d] Should be noted that there was no dramatic difference between active and passive release.

Abbreviations: pTS, paratoluenesulphonate; NT-3, neurotrophin-3; BDNF, Brain Derived Neurotrophic Factor; SSA, sulfosalicylic acid; TCF, trichlorfon; CNTs, Carbon NanoTubes.

output of drug can be expected to vary. It is possible to alter the electrodeposition protocol to achieve higher diffusivity of the film, or even build layers with different properties to optimize the active vs. passive release behavior for matching a certain release protocol (Pernaut and Reynolds, 2000; Ge et al., 2009; Ru et al., 2011; Jiang et al., 2013). Moreover, the effect of the purely mechanical actuation can be further exploited by including pores in the film, for instance by a templated electrodeposition process (Abidian et al., 2006; Luo and Cui, 2009a; Luo et al., 2011). While in early work, the systems studied were single layers, advanced strategies to increase porosity of the films and boost their storage capacity are more frequently reported in recent times. In a system where entrapment is not solely based on electrostatic interaction, the mechanical actuation could be expected to be the dominant mechanism for release.

Despite the complexity of delivery mechanisms, one can make a few general assumptions on which type of signal that would be the most efficient for release from a polymer system regardless of its structure. It is clear that the theoretical arguments speak in favor for slow signals rather than fast pulsing, and especially for CV which would allow both mechanical actuation and electrostatics to contribute. There is a substantial risk that fast signals will not lead to efficient transfer of the intended ions. Furthermore, for a pulsed signal, the electrode will return to the open cell potential in between releases (mono-phasic pulsing) or even be actively reversed (bi-phasic pulsing). This means each delivery will be immediately followed by a signal actively driving the ionic flow in the opposite direction. This could in theory mean a reuptake of drug. However, the infiltration of small ions from solution to replace the larger ions delivered is more likely. One way to minimize the plausible reuptake of drug would be to allow the molecules additional time to diffuse away from the surface and be replaced by other ions at the reversed potential, speaking for the introduction of an interpulse delay time.

It should be noted that despite all these points speaking for active release with slow signals, release has been experimentally proven also for systems with fast pulsing (Evans et al., 2009; Richardson et al., 2009; Thompson et al., 2010). Thompson et al. do not specifically report pulse duration, only that they use biphasic stimulation delivered at a 5 Hz frequency. Granted that this means the full time was used for delivery of pulse trains this would however mean PDs in the range of 100 ms which is far from the PDs that would normally be used to trigger neural activity. The pulses reported by Evans et al. and also by Richardsson et al. come closer to real stimulation parameters with pulse widths of 100 μs delivered at 250 Hz (Evans et al., 2009; Richardson et al., 2009). It should be mentioned that there was no dramatic difference between active and passive release in the PPy/pTS/BDNF system but clearly an effect for the PPy:pTS:NT3 system. This would speak for a release controlled by conformational changes of the polymer rather than an electrostatic driving force. The authors in addition argue for that changes in hydrophobic properties of the polymer matrix would contribute to release in this case.

The CV ranges reported vary widely. The lowest vertex potential reported is at −1 V and the highest vertex potential at 1.4 V vs. Ag:AgCl. Commonly, only the anodic part of the sweep is used. It has also been pointed out that the scan rate further influences release efficiency of the single CV (Leprince et al., 2010). Sweep rates reported are in the range of 10–100 mV/s. For the constant potential driven systems, the potentials required to actively drive release are in the range of −0.3 to −0.5 V vs. Ag:AgCl. Clearly this will depend on the nature of the ionic drug, which conducting polymer that is used and the morphological properties of the individual polymer layer.

To some extent, a conducting polymer film that is physically degrading upon electrochemical stress can also act as a controlled delivery system. As the film falls apart, molecules that were immobilized in the structure are released at a rate that can be controlled by the level of stress. The weakest link is often the adhesion to the underlying substrate leading to complete or fragmental delamination, depending on the film cohesion. It might be difficult to judge whether a certain system performs delivery based on actuation, electrostatic interactions or simply by degradation, something that might be less favorable with an electrode intended for long term use, by only studying the release of the intended species. Ideally, one should therefore analyze if other molecules or particles are expelled from the film in parallel to the drug (Boehler and Asplund, in press). It should also be noted that conducting polymers degrade by over-oxidation meaning that the electronic structure is disrupted leading to a non-conducting material. PPy is more vulnerable to over-oxidation than PEDOT, and also the counter ion has an influence on the electronic stability (Yamato et al., 1995; Thaning et al., 2010). For this type of degradation the material itself remains at the electrode but progressive over-oxidation will influence the ion conducting properties and thereby the delivery mechanism over time.

RELEASE TRIGGER SIGNALS—FROM THE SIDE OF BIOLOGICAL SAFETY

In the previous section, the efficiency of the three release signals was discussed. However, other practical aspects such as the availability of devices capable of delivering these signals, as well as the safety for the biological environment, should naturally be taken into consideration. In the following section, the three trigger signals in **Figure 1** are therefore discussed with regard to the safety of neurons.

In general, the restrictions that would apply to a signal to be applied *in vivo* could be summarized as follows:

1. The signal transfer should take place through reversible processes which do not lead to the formation of electrochemical by-products in the tissue or corrosive reactions at the electrode.
2. The signal must not trigger undesired activity in the neural network.
3. The signal must not induce damage to neurons.

These conditions do not completely apply for the situation where the aim is to use the signal to drive controlled release. In this case, ideally the trigger signal should be designed to be practically invisible from the side of the neuron, yet still be efficient for pushing out drugs in a reasonable time frame and with good control of the delivered amount. While restriction 1 is of the utmost importance for metallic electrodes it is not directly transferrable to polymer

electrodes. The aim is to exchange the ionic drug in the polymer for other ions naturally available in tissue so irreversibility is to some extent here a necessity. However, the limitation of the electrode potential to prevent redox reactions in proteins and water as well as pH-shifts is a must.

It is also highly desirable that the signal used for drug release does not result in undefined excitation of surrounding neurons as in restriction 2. Normally, when evaluating how to stimulate neural tissue, the ambition is to assemble signals that are efficient in precise activation of a defined population of cells at current/pulse durations chosen to induce minimal electrochemical stress on the electrode. For the drug release approach, the signal needs to be optimized from close to the opposite perspective. The ambition would be to use a release signal that does not substantially influence surrounding cells but is efficient in pushing drugs out of the electrode.

Last, but not least, it is well-known that electrical stimulation of neurons can induce cellular injury even when the delivered stimulation is well within the boundaries given by the electrochemical safety (Shannon, 1992; Veraart et al., 2004). Normally such effects do not occur below the levels which can trigger neural activity which would ensure that a signal that confines to condition 2 is a conservative limit also for restriction 3. However, these injury thresholds are most of the time given with consideration to the pulsing parameters that would be considered normal for neural excitation. It is therefore advisable to take a closer look at the safety boundaries from this perspective when more unconventional pulsing parameters might be put into use.

PULSING

A standard pulse for recruitment of intracortical neurons would be a biphasic train of rectangular pulses of constant current delivered at a frequency in the range of 100–400 Hz, commonly around 200 Hz (see **Figure 1**). The minimum current strength needed to excite neuronal tissue (threshold current, I_{th}) depends on the pulse duration (PD) as in the strength-duration relationship depicted in **Figure 2**. PD should as a rule of thumb be chosen close to the chronaxy of the intended target tissue which in practice means durations in the range of 100–300 μs for myelinated nerve fibers. Longer pulse durations would not be energy efficient for activation of neurons and in addition would increase the probability for non-reversible corrosive processes at the electrode site (Tehovnik, 1996).

When stimulating at PDs close to the chronaxy, typical threshold currents for neural activation would be estimated to be around 10 μA, but recent studies show that actual activation thresholds can be expected to be even lower than 4 μA (reported for 200 μs PD and 250 Hz) (Tehovnik et al., 2006; Histed et al., 2009). Since the objective of the PEDOT electrode is drug delivery rather than activation, stimulation should be kept below threshold not to evoke neural activity unintentionally. In practice and according to the generally accepted current-duration relationship, this leaves two alternatives (Tehovnik, 1996). Either shortening the pulses to increase the threshold current, or use longer pulses and stay well-below the rheobase. For a pulse substantially longer than the chronaxy this means at least below 2 μA, preferably even lower. The longer the pulse, the more charge would be expected

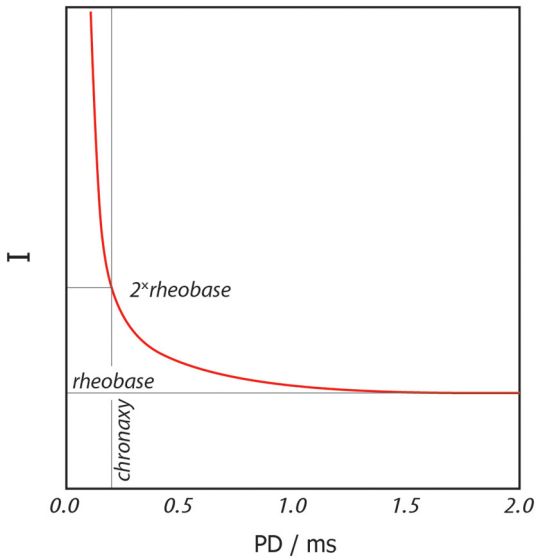

FIGURE 2 | Strength-duration relationship for excitable tissue. Red line shows the threshold current, I_{th}, at which neuronal tissue is excited for a rectangular stimulation pulse of duration PD.

to be required to activate neurons. This clearly rather speaks for maximizing charge and thereby possibilities for ionic delivery by driving longer pulses at lower currents.

If a small and highly local amount of activated neurons can be tolerated, currents can naturally be set higher. This is something that would have to be evaluated with respect to the exact placement of the particular electrode. With knowledge of the excitability constant, K, of the target tissue, efficient spread of stimulation can be estimated, over the radius r, for a given case according to $I = K*r^2$ (Tehovnik, 1996; Tehovnik et al., 2006). This would provide a reasonable estimate for the volume of cells affected by a pulse if exceeding the threshold in the given case.

Tissue damage can occur as a consequence of inappropriately chosen stimulation parameters, even though the given stimulation is within the electrochemical safety limits of the electrode material. It is broadly accepted that important factors to consider are charge per phase and charge density delivered from the electrode (McCreery et al., 1990; Shannon, 1992). The mechanisms behind such effects are not completely understood but it is believed that electroporation is a main contributor to this kind of tissue damage as well as mass action phenomena, for instance depletion of oxygen or glucose, or excessive release of glutamate, caused by local neural overactivity (Merrill et al., 2005). Since signals in the case discussed here should be chosen with the aim not to induce neural signaling, only electroporation would need to be considered.

Taking also restriction 3 into account, there is reason to ask if there is a risk for the occurrence of electroporation based on this type of pulsing? A detailed insight into how the threshold for electroporation can be expected to vary with other stimulation parameters is given by Butterwick et al. (2007). One conclusion of their work is that, for longer pulses (PDs in the range of ms), the threshold current density at which electroporation can be

expected to occur is lower than for shorter pulses. The threshold current density scales with PD approximately as 1/sqrt(PD). It is also clear from their results that with pulsing frequencies exceeding 50 Hz repetition frequency thresholds are significantly lower than for single shots. For electrodes smaller than 300 μm it is further concluded that total current would be the main limitation, and injury thresholds would not to the same extent be influenced by current density as is seen with the larger electrodes. Their results are based on measurements in chicken retinas but correlate well to measurements in earlier work concerning injury thresholds in cortical tissue (McCreery et al., 1990; Shannon, 1992; Veraart et al., 2004). It is therefore assumed that the safe limits reported would be a reasonable figure of merit for stimulation of any target tissue in the central as well as in the peripheral nervous system.

The lowest threshold where stimulation induced damage was detected in their experiments was determined to be 61 mA/cm^2 at a pulse duration of 6 ms for repetitive pulsing (>50 Hz). Translated to a microelectrode of 50 μm that would correspond to a charge per pulse of 7.2 nC. However, for pulses shorter than the ms, threshold currents are substantially higher. Deduced from the data presented by Butterwick, for the 600 μs, expected thresholds would rather be in the range of 0.2 A/cm^2. Due to the shorter pulse length this would in fact mean a lower charge per phase threshold, for the 50 μm electrode 2.3 nC/phase. This would speak for that electroporation could occur even with a minor elevation of the stimulation current.

The study also presents results regarding the influence of the size of the electrode and the values cited above relate to a large electrode, not a microelectrode. If taking their results concerning microelectrodes into account, here smaller than 300 μm in diameter, the threshold charge per phase that could safely be delivered did in fact not depend on electrode size. The smallest electrode used in their experiment was ∼100 μm in diameter and the threshold, when investigated on the retina cells using 600 μs single pulses, were found to be ∼70 nC per phase. This threshold should, according to their theory of size independence, also be valid for smaller electrodes. Even though these particular results describe thresholds for one single pulse, there is substantial margin to the 1.2 nC given by the 2 μA and 600 μs suggested as suitable sub-threshold stimulation (second paragraph, section Pulsing).

In summary, also from the perspective of restriction 3, it would be recommendable to work with PDs longer than the chronaxy. It further appears as if PDs are on the longer side, and threshold current is estimated to be below the rheobase, there is no substantial risk for disruption of cellular membrane integrity as a consequence of the pulsed trigger signal.

In order to establish boundaries for safety it is of interest to glance at the field of deep brain stimulation (DBS), where intracortical stimulation has been therapeutically used over more than a decade. The technology is FDA approved and one could thereby argue that these stimulation protocols have already been proven safe for use in patients. Kern and Kumar (2007) report common values for the Sub Thalamic Nucleus (STN) DBS to be in the range 130–185 Hz with typical pulse durations of 60 μs. However, the extremely short pulse durations used for DBS are most likely not efficient for drug expulsion. Release relies to large extent on slower processes as has already been discussed in the previous section.

CYCLIC VOLTAMMETRY

It has already been pointed out that slow redox sweeping of the electrode has been found efficient for delivery of ionic drugs. The stimulation effects of CV in brain tissue are not specifically addressed in the literature. Theoretically, if the current-duration curves are extrapolated into infinitely long pulses, which would be a reasonable approximation for the smooth transitions of a CV curve, the suggestion would be that as long as the current is still below the rheobase the neurons would not be excited.

If the neuronal activity is not directly influenced, the restrictions would rather be set by the possibly detrimental electrochemical reactions that could occur as a by-product of any excessive voltage. The two parameters to consider are the vertex potentials and the sweep rate. The non-conservative constraints for the vertex potentials would be given by the water window (−0.6 V to 0.8 V vs. Ag:AgCl) since the evolution of hydrogen (−0.6 V) and oxygen (0.8 V), respectively, would occur at the electrode upon exceeding this window. Over-oxidation of PEDOT would not be expected to occur at voltages lower than 1.1 V and is therefore not a limiting factor in this case. This is however not sufficient to support that no other electrochemical reactions of importance take place within this window. Furthermore, appropriate reference electrodes are often not available in the implanted situation meaning that possible variations in applied voltages must be taken into account. Materials do either not deliver a stable potential in chronic implantations or biofouling clogs pores in ion-selective membranes.

One example on actual parameters used in a similar biological setting can be found in recent work monitoring electrochemical characteristics of implanted electrodes. Kane et al. (2011) employs the full water window at a sweep rate of 50 mV/s for their *in vivo* CV investigations and do not report any adverse tissue response as a consequence. In the sensor literature, fast CV is often suggested for instance for *in vivo* monitoring of neurotransmitters. It should be noted that so far sweep rates used are in the range of 300 V/s and thus far beyond what has been proposed for drug release (Pihel et al., 1996). The biological response was not the primary target for the analysis in either study and was therefore not carefully observed. Scans used for analytical purposes in an experiment with a sedated animal, and limited to a few occasions, are not necessarily suitable for repeated use in proximity of a population of highly sensitive cells. In both studies animals were anaesthetized which might not be possible to perform on a bi-weekly to weekly basis needed to support efficient drug release.

BIAS POTENTIAL

A bias potential of approximately −0.5 V vs. Ag:AgCl could be used to drive drug release. Cells are not expected to respond adversely to a steady potential if kept within reasonable boundaries. For instance, a positive interpulse bias potential of 0.6 V has been suggested as a method for boosting performance of iridium oxide electrodes and has been applied to SIROF coatings *in vivo* (Cogan et al., 2006; Kane et al., 2011). The authors comment that the long-term consequences of the low net current needed to

maintain the bias potential has not yet been explored. However, for the drug release, the bias potential would only be applied at the specific occasions where drug release is requested which qualifies as a limited time frame and should be safe for use.

DISCUSSION

OTHER RELEASE STRATEGIES AND DRUGS

Apart from Dex, also various other anti-inflammatory drugs like α-MSH, IL-1-RA, or heparin have been proposed in literature for treatment of inflammatory reactions. These molecules target different receptor pathways in the inflammation cascade and can thus be interesting alternatives or complements to the Dex (Bridges and Garcia, 2008; Go et al., 2012). All of the listed molecules are typically delivered from passively eluting systems due to their chemical properties and overall size, which makes them incompatible with the ion-exchange principle provided by conducting polymers. In contrast, Dex is in the appropriate size range (392 Da) and features an anionic charge characteristic, which makes is eligible for both passive and actively controlled release systems. Furthermore, Dex is known to be the most potent glucocorticoid drug for anti-inflammatory treatment due to its effect in multiple receptor pathways, which reveals this drug as first choice for the realization of an anti-inflammatory drug eluting system for treatment of the glial scar. For a more detailed description of relevant molecules and their impact on the adverse host response to implanted biomedical devices the excellent review by Bridges et al. is strongly recommended (Bridges and Garcia, 2008). It should be mentioned that it would be possible to use a deposition technique not relying on direct incorporation to combine the active delivery approach also with these substances (Abidian et al., 2006; Luo et al., 2011).

It is a valid question to ask how the actively controlled release of Dex from a microelectrode would compare to a delivery coating passively leaking Dex into tissue, or systemic treatment (Shain et al., 2003; Spataro et al., 2005; Zhong and Bellamkonda, 2007). The latter has the clear downside of requiring much higher total doses distributed to reach an efficient concentration at the point of interest and side-effects would thus be a main concern. In situ delivery, avoiding the counterproductive neuroendocrine feedbacks, is from this perspective clearly beneficial regardless of if the system is based on a passive or active release approach.

The active release system offers controllability but for a limited quantity whereas the passive system can cover the complete surface of a probe, thereby storing a much larger quantity, but hold few options to influence release dynamics. From the data available in literature it is difficult to judge whether such a system would be more successful in mitigating inflammation than the actively triggered release approach. The answer to this question could only be given if the necessary time course of the treatment was known. It is still an open question whether the anti-inflammatory treatment over the time course of a month, which would be the critical period in which the scar forms, influences the state of the surrounding tissue also in the long term (Szarowski et al., 2003; Biran et al., 2005; Potter et al., 2012). If it does, the lower quantity delivered by the microelectrodes might still be sufficient, meaning higher drug load is not a substantial benefit but could be traded for more precise release control. On the other hand, treatment might be needed for a much longer time period which would make the opportunity to load a higher quantity of drug much more attractive. A certain control of release dynamics in the passive release system could still be accomplished by carefully tailoring the degradability properties of the release matrix. In theory, nothing speaks against that such a system in the future could include certain responsiveness to biological factors, for instance react to chemical factors present for a higher degree of inflammation, by increasing the release rate.

It should be noted that such a delivery matrix, which can act as the golden standard for passive release, does not yet exist. Thus, the passive release system relies on substantial development in this direction in the same way as the polymer electrodes hold room for future optimization. Recent result show that also surface immobilized Dex might have an effect for improving probe integration which illustrates the need for further work to elucidate the underlying mechanisms involved in the tissue response to Dex (Grand et al., 2010). In summary, the passive delivery approach should be pursued in parallel with the active delivery systems, as an interesting alternative or even additional approach, since the use of the one delivery system in fact does not exclude the use of the other as a complement.

RELEASE TRIGGER SIGNALS—CONCLUDING REMARKS

Taking all the considerations regarding efficiency and safety into account they all speak in favor for slow release signals. CV seems to be the most suitable from the efficiency perspective and most likely a moderate use of voltammetric sweeping will not be harmful to tissue or lead to undeliberate excitation of the neuronal network. This however needs to be confirmed in experiments.

In practice, the equipment needed to perform well-controlled CV at the implant site might however not always be available. Proper CV measurements require a three-electrode electrochemical control system and the technologies for on-probe integration of stable reference electrodes on implants are not yet established (Tolosa et al., 2013).

Considering this practical aspect, it might therefore still be the most convenient to use a pulsed signal for release rather than a sweep. In this case it would be advisable to aim for low currents and PDs significantly longer than the chronaxy. Furthermore, to present as little stress as possible to the tissue, low pulsing frequencies should be used. Lowering the pulsing frequency and compensating by extending the overall stimulation time should have little effect on the release itself but would allow higher currents before stimulation induced damage to neurons can be expected to occur (Butterwick et al., 2007). Charge balance is not a necessity for this kind of drug release. On one hand it might contribute to increased actuation, on the other hand it might be counterproductive if the Dex ions are immediately retrieved by the reversed pulse. An interpulse delay could mitigate the second effect.

One possibility to, with a simple device, imitate the effect of a CV is to exchange the sweep with interchangeable voltage steps, set to the upper and lower vertex potential. Microsized devices capable of maintaining a fixed voltage vs. a reference, and suitable for implantation, have been described by others (Islam et al., 2010). In **Figure 3**, the current response of a PEDOT:Dex

electrode to a cyclic voltammogram can be seen as well as the current response to a rectangular pulse. It is clear that the current flow follows another scheme than in the carefully controlled slow CV. What this in practice would mean for the drug release should be further investigated experimentally.

Finally, not only efficiency of release but also controllability should be considered. For the application, it is desirable that a precise dose of Dex can be delivered at each attempt, which means the response to the trigger signal must be predictable. Taking the complexity of events involved in release into account, such one to one correlation is not trivial to accomplish. More likely, the response of the polymer will change over time and with each delivery attempt, something that must be carefully considered to ensure the trigger signal has the intended effect throughout the full experimental time frame. This needs to be further investigated before a specific polymer delivery system is put into use.

Since the drug delivery systems reviewed here are intended for local treatment targeting only the cells in the immediate vicinity of the electrode, it is highly desirable that the very same electrode used for delivery can still function as a neural interface. For recording this is not expected to be a problem since both PEDOT and PPy are known for their low impedance in this respect. Although the drug delivery electrodes in general are outperformed by the regular surfactant based conducting polymer materials in terms of impedance, it has repeatedly been shown that also drug containing conducting polymer electrodes still lower the impedance in comparison to a bare metallic surface (Wadhwa et al., 2006; Luo et al., 2011).

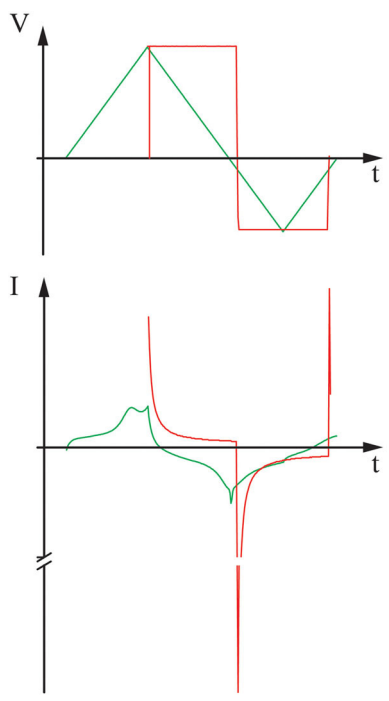

FIGURE 3 | A comparison between the current response to a swept voltage vs. a stepped voltage for a PEDOT:Dex delivery system. Measurement was performed in PBS and vs. an Ag:AgCl reference.

For stimulation the central question would be if stimulation can be performed without unintentionally triggering release? From the literature reviewed here it is not possible to make a conclusive statement on whether this would at all be possible. As discussed, some authors do indeed present release based on the type of fast pulsing that would be common to use for stimulation purposes (Evans et al., 2009; Richardson et al., 2009). However, it can be concluded that slow sweeps are vastly more effective for drug release (**Table 1**) and several authors report that they need to reach a certain voltage before actual release is triggered (e.g., Pyo et al., 1994; Pernaut and Reynolds, 2000). It is plausible that smart materials design can further exploit this effect making the release-free stimulation possible within certain boundaries.

REFERENCES

Abidian, M. R., Kim, D. H., and Martin, D. C. (2006). Conducting-polymer nanotubes for controlled drug release. *Adv. Mater.* 18, 405–409. doi: 10.1002/adma.200501726

Asplund, M., Von Holst, H., and Inganas, O. (2008). Composite biomolecule/PEDOT materials for neural electrodes. *Biointerphases* 3, 83–93. doi: 10.1116/1.2998407

Biran, R., Martin, D. C., and Tresco, P. A. (2005). Neuronal cell loss accompanies the brain tissue response to chronically implanted silicon microelectrode arrays. *Exp. Neurol.* 195, 115–126. doi: 10.1016/j.expneurol.2005.04.020

Bobacka, J., Lewenstam, A., and Ivaska, A. (2000). Electrochemical impedance spectroscopy of oxidized poly(3,4-ethylenedioxythiophene) film electrodes in aqueous solutions. *J. Electroanal. Chem.* 489, 17–27. doi: 10.1016/S0022-0728(00)00206-0

Boehler, C., and Asplund, M. (in press). A detailed insight into drug delivery from PEDOT based on analytical methods: effects and side-effects. *J. Biomed. Mater. Res. A.*

Bridges, A. W., and Garcia, A. J. (2008). Anti-inflammatory polymeric coatings for implantable biomaterials and devices. *J. Diabetes Sci. Technol.* 2, 984–994.

Butterwick, A., Vankov, A., Huie, P., Freyvert, Y., and Palanker, D. (2007). Tissue damage by pulsed electrical stimulation. *IEEE Trans. Biomed. Eng.* 54, 2261–2267. doi: 10.1109/TBME.2007.908310

Cogan, S. F., Troyk, P. R., Ehrlich, J., Plante, T. D., and Detlefsen, D. E. (2006). Potential-biased, asymmetric waveforms for charge-injection with activated iridium oxide (AIROF) neural stimulation electrodes. *IEEE Trans. Biomed. Eng.* 53, 327–332. doi: 10.1109/tbme.2005.862572

Evans, A. J., Thompson, B. C., Wallace, G. G., Millard, R., O'leary, S. J., Clark, G. M., et al. (2009). Promoting neurite outgrowth from spiral ganglion neuron explants using polypyrrole/BDNF-coated electrodes. *J. Biomed. Mater. Res. A* 91A, 241–250. doi: 10.1002/jbm.a.32228

Ge, D., Tian, X., Qi, R., Huang, S., Mu, J., Hong, S., et al. (2009). A polypyrrole-based microchip for controlled drug release. *Electrochim. Acta* 55, 271–275. doi: 10.1016/j.electacta.2009.08.049

Go, D. P., Palmer, J. A., Gras, S. L., and O'connor, A. J. (2012). Coating and release of an anti-inflammatory hormone from PLGA microspheres for tissue engineering. *J. Biomed. Mater. Res. A* 100A, 507–517. doi: 10.1002/jbm.a.33299

Golde, S., Coles, A., Lindquist, J. A., and Compston, A. (2003). Decreased iNOS synthesis mediates dexamethasone-induced protection of neurons from inflammatory injury *in vitro*. *Eur. J. Neurosci.* 18, 2527–2537. doi: 10.1046/j.1460-9568.2003.02917.x

Grand, L., Wittner, L., Herwik, S., Gothelid, E., Ruther, P., Oscarsson, S., et al. (2010). Short and long term biocompatibility of NeuroProbes silicon probes. *J. Neurosci. Methods* 189, 216–229. doi: 10.1016/j.jneumeth.2010.04.009

Histed, M. H., Bonin, V., and Reid, R. C. (2009). Direct activation of sparse, distributed populations of cortical neurons by electrical microstimulation. *Neuron* 63, 508–522. doi: 10.1016/j.neuron.2009.07.016

Islam, A. B., Haider, M. R., Atla, A., Islam, S. K., Croce, R., Vaddiraju, S., et al. (2010). "A potentiostat circuit for multiple implantable electrochemical

sensors," in *Electrical and Computer Engineering (ICECE), 2010 International Conference*, (Wuhan), 314–317.

Jager, E. W. H., Smela, E., and Inganas, O. (2000). Microfabricating conjugated polymer actuators. *Science* 290, 1540–1545. doi: 10.1126/science.290.5496.1540

Jiang, S., Sun, Y., Cui, X., Huang, X., He, Y., Ji, S., et al. (2013). Enhanced drug loading capacity of polypyrrole nanowire network for controlled drug release. *Synth. Met.* 163, 19–23. doi: 10.1016/j.synthmet.2012.12.010

Kane, S. R., Cogan, S. F., Ehrlich, J., Plante, T. D., and McCreery, D. B. (2011). Electrical performance of penetrating microelectrodes chronically implanted in cat cortex. *Conf. Proc. IEEE Eng. Med. Biol. Soc.* 2011, 5416–5419. doi: 10.1109/iembs.2011.6091339

Kern, D. S., and Kumar, R. (2007). Deep brain stimulation. *Neurologist* 13, 237–252. doi: 10.1097/NRL.0b013e3181492c48

Kontturi, K., Pentti, P., and Sundholm, G. (1998). Polypyrrole as a model membrane for drug delivery. *J. Electroanal. Chem.* 453, 231–238. doi: 10.1016/s0022-0728(98)00246-0

Leprince, L., Dogimont, A., Magnin, D., and Demoustier-Champagne, S. (2010). Dexamethasone electrically controlled release from polypyrrole-coated nanostructured electrodes. *J. Mater. Sci. Mater. Med.* 21, 925–930. doi: 10.1007/s10856-010-4008-6

Li, L. D., and Huang, C. B. (2007). Electrochemical/electrospray mass spectrometric studies of electrochemically stimulated ATP release from PP/ATP films. *J. Am. Soc. Mass Spectrom.* 18, 919–926. doi: 10.1016/j.jasms.2007.01.015

Li, Y., Ewen, R. J., Campbell, S. A., and Smith, J. R. (2012). Electrochemically controlled release of antischistosomiasis agents from polypyrrole. *J. Mater. Chem.* 22, 2687–2694. doi: 10.1039/c2jm15298c

Luo, X., and Cui, X. T. (2009a). Sponge-like nanostructured conducting polymers for electrically controlled drug release. *Electrochem. commun.* 11, 1956–1959. doi: 10.1016/j.elecom.2009.08.027

Luo, X., Matranga, C., Tan, S., Alba, N., and Cui, X. T. (2011). Carbon nanotube nanoreservior for controlled release of anti-inflammatory dexamethasone. *Biomaterials* 32, 6316–6323. doi: 10.1016/j.biomaterials.2011.05.020

Luo, X. L., and Cui, X. T. (2009b). Electrochemically controlled release based on nanoporous conducting polymers. *Electrochem. Commun.* 11, 402–404. doi: 10.1016/j.elecom.2008.11.052

Majumdar, S., Kargupta, K., and Ganguly, S. (2008). Mathematical modeling for the ionic inclusion process inside conducting polymer-based thin-films. *Polym. Eng. Sci.* 48, 2229–2237. doi: 10.1002/pen.21170

McCreery, D. B., Agnew, W. F., Yuen, T. G., and Bullara, L. (1990). Charge density and charge per phase as cofactors in neural injury induced by electrical stimulation. *IEEE Trans. Biomed. Eng.* 37, 996–1001. doi: 10.1109/10.102812

Merrill, D. R., Bikson, M., and Jefferys, J. G. (2005). Electrical stimulation of excitable tissue: design of efficacious and safe protocols. *J. Neurosci. Methods* 141, 171–198. doi: 10.1016/j.jneumeth.2004.10.020

Moulton, S. E., Imisides, M. D., Shepherd, R. L., and Wallace, G. G. (2008). Galvanic coupling conducting polymers to biodegradable Mg initiates autonomously powered drug release. *J. Mater. Chem.* 18, 3608–3613. doi: 10.1039/B805481a

Pernaut, J. M., and Reynolds, J. R. (2000). Use of conducting electroactive polymers for drug delivery and sensing of bioactive molecules. A redox chemistry approach. *J. Phys. Chem. B* 104, 4080–4090. doi: 10.1021/jp994274o

Pihel, K., Walker, Q. D., and Wightman, R. M. (1996). Overoxidized polypyrrole-coated carbon fiber microelectrodes for dopamine measurements with fast-scan cyclic voltammetry. *Anal. Chem.* 68, 2084–2089. doi: 10.1021/ac960153y

Potter, K. A., Buck, A. C., Self, W. K., and Capadona, J. R. (2012). Stab injury and device implantation within the brain results in inversely multiphasic neuroinflammatory and neurodegenerative responses. *J. Neural Eng.* 9:046020. doi: 10.1088/1741-2560/9/4/046020

Pyo, M., Maeder, G., Kennedy, R. T., and Reynolds, J. R. (1994). Controlled release of biological molecules from conducting polymer modified electrodes: The potential dependent release of adenosine 5'-triphosphate from poly(pyrrole adenosine 5'-triphosphate) films. *J. Electroanal. Chem.* 368, 329–332. doi: 10.1016/0022-0728(93)03071-V

Richardson, R. T., Wise, A. K., Thompson, B. C., Flynn, B. O., Atkinson, P. J., Fretwell, N. J., et al. (2009). Polypyrrole-coated electrodes for the delivery of charge and neurotrophins to cochlear neurons. *Biomaterials* 30, 2614–2624. doi: 10.1016/j.biomaterials.2009.01.015

Ru, X. N., Shi, W., Huang, X., Cui, X., Ren, B., and Ge, D. T. (2011). Synthesis of polypyrrole nanowire network with high adenosine triphosphate release efficiency. *Electrochim. Acta* 56, 9887–9892. doi: 10.1016/j.electacta.2011.08.063

Shain, W., Spataro, L., Dilgen, J., Haverstick, K., Retterer, S., Isaacson, M., et al. (2003). Controlling cellular reactive responses around neural prosthetic devices using peripheral and local intervention strategies. *IEEE Trans. Neural Syst. Rehabil. Eng.* 11, 186–188. doi: 10.1109/TNSRE.2003.814800

Shannon, R. V. (1992). A model of safe levels for electrical stimulation. *IEEE Trans. Biomed. Eng.* 39, 424–426. doi: 10.1109/10.126616

Sirivisoot, S., Pareta, R., and Webster, T. J. (2011). Electrically controlled drug release from nanostructured polypyrrole coated on titanium. *Nanotechnology* 22:085101. doi: 10.1088/0957-4484/22/8/085101

Skotheim, T. A., and Reynolds, J. R. (2006). *Conjugated Polymers: Theory, Synthesis, Properties and Characterization.* Boca Raton: CRC Press.

Spataro, L., Dilgen, J., Retterer, S., Spence, A. J., Isaacson, M., Turner, J. N., et al. (2005). Dexamethasone treatment reduces astroglia responses to inserted neuroprosthetic devices in rat neocortex. *Exp. Neurol.* 194, 289–300. doi: 10.1016/j.expneurol.2004.08.037

Stevenson, G., Moulton, S. E., Innis, P. C., and Wallace, G. G. (2010). Polyterthiophene as an electrostimulated controlled drug release material of therapeutic levels of dexamethasone. *Synth. Met.* 160, 1107–1114. doi: 10.1016/j.synthmet.2010.02.035

Szarowski, D. H., Andersen, M. D., Retterer, S., Spence, A. J., Isaacson, M., Craighead, H. G., et al. (2003). Brain responses to micro-machined silicon devices. *Brain Res.* 983, 23–35. doi: 10.1016/S0006-8993(03)03023-3

Tehovnik, E. J. (1996). Electrical stimulation of neural tissue to evoke behavioral responses. *J. Neurosci. Methods* 65, 1–17. doi: 10.1016/0165-0270(95)00131-X

Tehovnik, E. J., Tolias, A. S., Sultan, F., Slocum, W. M., and Logothetis, N. K. (2006). Direct and indirect activation of cortical neurons by electrical microstimulation. *J. Neurophysiol.* 96, 512–521. doi: 10.1152/jn.00126.2006

Thaning, E. M., Asplund, M. L., Nyberg, T. A., Inganas, O. W., and von Holst, H. (2010). Stability of poly(3,4-ethylene dioxythiophene) materials intended for implants. *J. Biomed. Mater. Res. B Appl. Biomater.* 93, 407–415. doi: 10.1002/jbm.b.31597

Thompson, B. C., Chen, J., Moulton, S. E., and Wallace, G. G. (2010). Nanostructured aligned CNT platforms enhance the controlled release of a neurotrophic protein from polypyrrole. *Nanoscale* 2, 499–501. doi: 10.1039/b9nr00259f

Thompson, B. C., Moulton, S. E., Ding, J., Richardson, R., Cameron, A., O'leary, S., et al. (2006). Optimising the incorporation and release of a neurotrophic factor using conducting polypyrrole. *J. Control. Release* 116, 285–294. doi: 10.1016/j.jconrel.2006.09.004

Tolosa, V. M., Wassum, K. M., Maidment, N. T., and Monbouquette, H. G. (2013). Electrochemically deposited iridium oxide reference electrode integrated with an electroenzymatic glutamate sensor on a multi-electrode arraymicroprobe. *Biosensors Bioelectron.* 42, 256–260. doi: dx.doi.org/10.1016/j.bios.2012.10.061

Turner, J. N., Shain, W., Szarowski, D. H., Andersen, M., Martins, S., Isaacson, M., et al. (1999). Cerebral astrocyte response to micromachined silicon implants. *Exp. Neurol.* 156, 33–49. doi: 10.1006/exnr.1998.6983

Veraart, C., Duret, F., Brelén, M., Oozeer, M., and Delbeke, J. (2004). Vision rehabilitation in the case of blindness. *Expert Rev. Med. Devices* 1, 139–153. doi: 10.1586/17434440.1.1.139

Wadhwa, R., Lagenaur, C. F., and Cui, X. T. (2006). Electrochemically controlled release of dexamethasone from conducting polymer polypyrrole coated electrode. *J. Control. Release* 110, 531–541. doi: 10.1016/j.jconrel.2005.10.027

Xiao, Y., Che, J., Li, C. M., Sun, C. Q., Chua, Y. T., Lee, V. S., et al. (2007). Preparation of nano-tentacle polypyrrole with pseudo-molecular template for ATP incorporation. *J. Biomed. Mater. Res. A* 80, 925–931. doi: 10.1002/jbm.a.31001

Xiao, Y., Ye, X., He, L., and Che, J. (2012). New carbon nanotube-conducting polymer composite electrodes for drug delivery applications. *Polym. Int.* 61, 190–196. doi: 10.1002/pi.3168

Yamato, H., Ohwa, M., and Wernet, W. (1995). Stability of polypyrrole and poly(3,4-ethylene dioxythiophene) for biosensor application. *J. Electroanal. Chem.* 397, 163–170. doi: 10.1016/0022-0728(95)04156-8

Yue, Z., Moulton, S. E., Cook, M., O'leary, S., and Wallace, G. G. (2013). Controlled delivery for neuro-bionic devices. *Adv. Drug Deliv. Rev.* 65, 559–569. doi: 10.1016/j.addr.2012.06.002

Zhong, Y. H., and Bellamkonda, R. V. (2007). Dexamethasone-coated neural probes elicit attenuated inflammatory response and neuronal loss compared to uncoated neural probes. *Brain Res.* 1148, 15–27. doi: 10.1016/j.brainres.2007.02.024

Zhong, Y., McConnell, G. C., Ross, J. D., Deweerth, S. P., and Bellamkonda, R. V. (2005). "A novel dexamethasone-releasing, anti-inflammatory coating for neural implants," in *Neural Engineering, 2005. Conference Proceedings. 2nd International IEEE EMBS Conference* (Arlington), 522–525.

Conflict of Interest Statement: The authors declare that the research was conducted in the absence of any commercial or financial relationships that could be construed as a potential conflict of interest.

Received: 30 January 2014; accepted: 02 April 2014; published online: 13 May 2014.
Citation: Asplund M, Boehler C and Stieglitz T (2014) Anti-inflammatory polymer electrodes for glial scar treatment: bringing the conceptual idea to future results. Front. Neuroeng. ***7****:9. doi: 10.3389/fneng.2014.00009*
This article was submitted to the journal Frontiers in Neuroengineering.

frontiers in
NEUROENGINEERING

REVIEW ARTICLE
published: 27 May 2014
doi: 10.3389/fneng.2014.00015

Organic electrode coatings for next-generation neural interfaces

Ulises A. Aregueta-Robles[1], Andrew J. Woolley[1,2], Laura A. Poole-Warren[1], Nigel H. Lovell[1] and Rylie A. Green[1]*

[1] *Graduate School of Biomedical Engineering, University of New South Wales, Sydney, NSW, Australia*
[2] *School of Medicine, University of Western Sydney, Sydney, NSW, Australia*

Edited by:
Ulrich G. Hofmann, Albert-Ludwigs-University Freiburg, Germany

Reviewed by:
Anja Kunze, University of California, Los Angeles, USA
Ulrich G. Hofmann, Albert-Ludwigs-University Freiburg, Germany

***Correspondence:**
Rylie A. Green, Graduate School of Biomedical Engineering, University of New South Wales, Sydney, NSW 2052, Australia
e-mail: r.green@unsw.edu.au

Traditional neuronal interfaces utilize metallic electrodes which in recent years have reached a plateau in terms of the ability to provide safe stimulation at high resolution or rather with high densities of microelectrodes with improved spatial selectivity. To achieve higher resolution it has become clear that reducing the size of electrodes is required to enable higher electrode counts from the implant device. The limitations of interfacing electrodes including low charge injection limits, mechanical mismatch and foreign body response can be addressed through the use of organic electrode coatings which typically provide a softer, more roughened surface to enable both improved charge transfer and lower mechanical mismatch with neural tissue. Coating electrodes with conductive polymers or carbon nanotubes offers a substantial increase in charge transfer area compared to conventional platinum electrodes. These organic conductors provide safe electrical stimulation of tissue while avoiding undesirable chemical reactions and cell damage. However, the mechanical properties of conductive polymers are not ideal, as they are quite brittle. Hydrogel polymers present a versatile coating option for electrodes as they can be chemically modified to provide a soft and conductive scaffold. However, the *in vivo* chronic inflammatory response of these conductive hydrogels remains unknown. A more recent approach proposes tissue engineering the electrode interface through the use of encapsulated neurons within hydrogel coatings. This approach may provide a method for activating tissue at the cellular scale, however, several technological challenges must be addressed to demonstrate feasibility of this innovative idea. The review focuses on the various organic coatings which have been investigated to improve neural interface electrodes.

Keywords: coatings, carbon nanotubes, conductive polymers, hydrogels, living electrodes, material properties

INTRODUCTION

Neurological injuries and disorders affect up to a billion people worldwide and this number is estimated to increase considerably as life expectancy continues to rise (World Health Organization, 2006). Neuroprosthetic intervention is an increasingly popular method for alleviating symptoms or returning function to patients suffering from these disorders. Despite the impressive results of some electrical therapies, such as auditory implants (McCreery, 2008; Shannon, 2012), deep brain stimulators (DBS; Andrade et al., 2006; Perlmutter and Mink, 2006; Lozano and Lipsman, 2013), functional electrical stimulation (FES) of the spinal cord (Collinger et al., 2013) and vision prostheses (Shepherd et al., 2013), considerable improvement in device technology is required to enable greater control of physiological outcomes (Normann, 2007). Current state-of-the-art neuroprostheses generate an electrical field in the target tissue using metallic electrodes to elicit or suppress neuronal action potentials (Perlmutter and Mink, 2006; Li and Mogul, 2007; Normann, 2007; Wilson and Dorman, 2008; Collinger et al., 2013; Shepherd et al., 2013). Many such devices also use the same metallic electrodes to record neural responses (Normann, 2007). Most metallic electrodes inject charge through the generation of electrons at the electrode surface, however in physiological systems charge is carried by electrolytes (ions). At the electrode–electrolyte interface, charge must be transferred from electrons to ions by either Faradic (electrochemical reactions) or capacitive (double-layer charging) mechanisms which are dependent on the material selected for the electrode (Merrill et al., 2005; Cogan, 2008). Typically platinum (Pt), gold and platinum-iridium (Pt-Ir) are used for fabricating biomedical electrodes (Brummer et al., 1983; Geddes and Roeder, 2003). Pt has historically been considered the preferred metal used for electrodes in neuroprostheses (Brummer et al., 1983; Cogan, 2008), with cochlear implants, DBS and retinal implants all using Pt for neural interfacing. This is due to the electrochemical stability and corrosion resistance of Pt (White and Gross, 1974) which has been demonstrated to have limited reactivity to biological environments compared to other metals (Merrill et al., 2005; Polikov et al., 2005). However, while technological advances have driven the miniaturization of electronics leading to smaller implant devices (Nakayama and Matsuda, 1995; Schuettler et al., 2005; Cheung, 2007; Wester et al., 2009), aspects of Pt electrical, mechanical, and biological performance remain as limiting factors which prevent the application of high-density microelectrode arrays for neural interfacing.

For every electrode there is an intrinsic charge injection limit, restricting the voltage that can be safely generated at the electrode's surface. Once this voltage is breached, purely capacitive charge transfer can no longer be maintained and irreversible faradaic reactions occur. Beyond this electrochemical limit, also known as the water window, irreversible electrolysis of water can result in tissue damage, electrode dissolution, pH changes and production of unwanted chemical species (McCreery et al., 1997; Zhong et al., 2001; Green et al., 2008a; Poole-Warren et al., 2010; Niina et al., 2011). Additionally, as an electrode is reduced in size the charge it must pass per unit area increases, directly increasing the voltage on the electrode and hence reducing the total charge which can be safely delivered. It has been shown that to stimulate light percepts by electrical stimulation of the retina in visually impaired patients, a charge density between 48 and 357 $\mu C/cm^2$ is required (Humayun et al., 2003; Mahadevappa et al., 2005), but the electrochemical injection limit of Pt has been reported as ranging from 20 to 150 $\mu C/cm^2$ (Rose and Robblee, 1990; Green et al., 2012c). This small range of overlap means that bare metal electrodes cannot be safely reduced in size and still maintain safe charge injection at a therapeutic level. With the increasing pressure to reduce the size of electrodes, driven by the need to make smaller but higher resolution implants, Pt electrical properties have become a challenging issue (Green et al., 2012c; Shepherd et al., 2013). New electrode geometries, materials, or coatings must be used to increase the charge transfer surface area such that the safety limits are preserved. Surface modifications, through electrode roughening or coating, have been reported to have great potential for increasing the charge injection capacity of microelectrodes, as detailed later in this review (Cogan et al., 2005; Schuettler et al., 2005; Abidian et al., 2010; Green et al., 2012b,c, 2013a).

Mechanically, Pt is significantly stiffer than the neural tissue with which it interfaces (Green et al., 2012b). The elastic modulus of Pt is about 164 GPa (Merker et al., 2001), but most neural tissue has a modulus of less than 100 kPa (Lacour et al., 2010). This mechanical disparity can exacerbate the chronic inflammatory response at the implant site, as the shear between a stiff electrode and the soft neural tissue continues to incite inflammation during tissue movement and device micromotion (Rousche et al., 2001; Leach et al., 2010). More flexible device designs move with the tissue, which can reduce damage at the neural interface (Richter et al., 2013), but require tethering which creates damage in adjacent tissue sites (Tyler and Durand, 2002). Electrode coatings, in particular polymeric films which utilize conductive polymers or hydrogels, have been shown to impart a softer electrode interface, around 1 MPa (Yang and Martin, 2006; Green et al., 2012b) and it is expected that these coatings can be used to dampen or mediate the mechanical difference between a metal electrode and the tissue with which it interfaces.

Chronic biological responses to metal electrodes have been reported to challenge the maintenance of an effective neural interface (Turner et al., 1999; Biran et al., 2005; Barrese et al., 2013). The implantation and chronic presence of a neural interfacing device in the central nervous system (CNS) induces a cascade of biological processes which can ultimately isolate the electrode and gradually decrease device performance. Reports and reviews on implantation trauma have detailed the cellular and molecular interactions involved in the acute inflammatory response which primarily includes immune cell activation and migration, and local ischemia (Fitch and Silver, 2008; Zhong and Bellamkonda, 2008; Whitney et al., 2009). The biological environment is further altered as the ongoing inflammatory response produces reactive astrocytosis in the damaged area (Banati et al., 1993; Fitch and Silver, 1997; Babcock et al., 2003). Over time, layers of activated microglia, invading macrophages, reactive astrocytes and migrating meningeal fibroblasts can encapsulate CNS implants (Turner et al., 1999; Cui et al., 2003). Extra layers of non-excitable cells will increase the neural interface impedance. For recording electrodes this reduces the possibility of recording and localizing single unit activity due to a diminished signal to noise ratio (SNR). As Pt is a relatively stable material which has limited interaction with the biological environment, immune cells are prevented from dissolving the electrodes. However, a persistent effort to disintegrate metal sites yields a constant environment of cytotoxic factors that may contribute to migration away from and cell death near the electrodes, including the target neurons (Weldon et al., 1998). Furthermore, Pt and other metallic electrodes are typically produced with smooth surfaces which do not encourage neural tissue integration, as a result immune cells can access the gap between the electrode and target cells. Several detailed studies have described the chronic biological response to implantable electrodes in animal models (Hascup et al., 2009; Ward et al., 2009; Leach et al., 2010; Woolley et al., 2011).

In the literature, the limitations associated with Pt electrode performance have been addressed through several varied approaches, which include passivation and surface texturing of electrodes to reduce impedance and enhance tissue integration (Cogan et al., 2005; Schuettler, 2007; Abidian et al., 2010; Green et al., 2012a,b). However, it is through the development of new coating technologies that improvement can be made more widely across the electrical, mechanical and biological properties of electrodes. In particular the use of carbon nanotubes (CNTs), CPs, hydrogels and conductive hydrogels (CHs), depicted in **Figure 1**, have shown that tailored approaches can be used to create multi-functional electrode arrays which not only improve the electrode material properties, but also provide biomolecules to aid in the establishment of a chronically stable neural interface. While substantial research has been conducted on CNTs, CPs, hydrogels and composite polymers, it is important to understand both the advantages and limitations of these materials and how they impact on the biological environment. Furthermore, as greater demands on electrode technologies drive the development of next-generation bionic devices, it is proposed that tissue engineered electrodes, such as that shown in **Figure 1** (bottom, right) may provide an avenue for directly interfacing with neural cells through synaptic communication. This review highlights the materials and emerging technologies that address some of the issues related to conventional smooth metallic electrodes including enhancing charge transfer, tissue integration and reducing mechanical mismatch. Furthermore it proposes an innovative approach to creating electrodes which use neural cells embedded within the electrode surface for a more natural approach to cell activation which may reduce scar tissue formation and aid in the establishment of a stable neural interface.

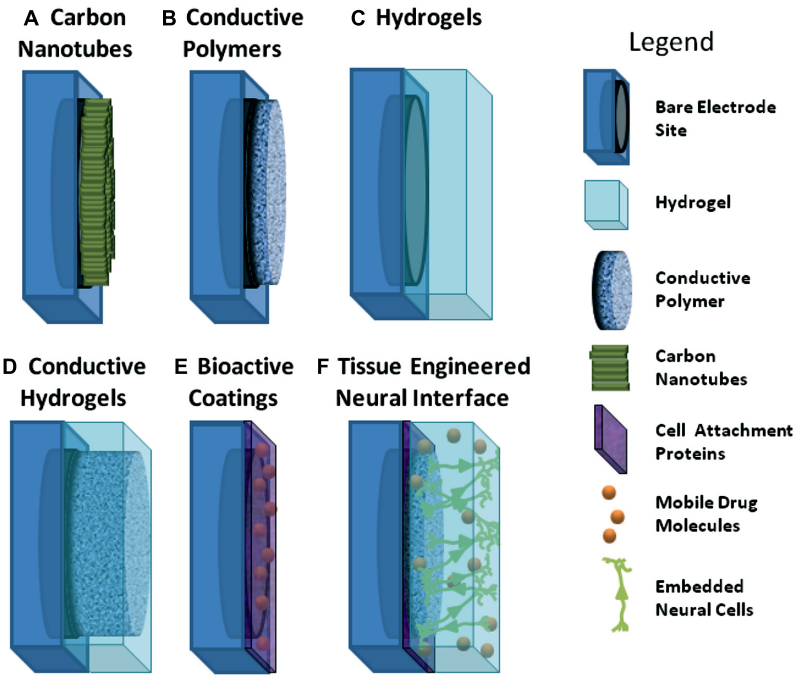

FIGURE 1 | Schematic of coating approaches used for addressing the limitations of metallic electrodes. (A) aligned carbon nanotubes on metallic electrodes; **(B)** conductive polymers electrodeposited on metallic electrodes; **(C)** hydrogels polymerised to coat electrode site and device; **(D)** interpenetrating network of conductive polymer grown through hydrogel coating to form conductive hydrogel over electrode sites; **(E)** electrode site coated with biologically active molecules; **(F)** schematic of ideal tissue engineered interface incorporating combined coating approaches of conductive polymers, hydrogels and attachment factors with neural cells.

COATINGS FOR NEURAL INTERFACES

A common objective of modifying an electrode surface is to impart roughening or rather an increased electrochemical surface area. Several roughened morphologies have been shown to enhance charge transfer to within safe stimulation limits (Rose and Robblee, 1990; Cogan et al., 2007; Green et al., 2013b) as well as providing a surface to improve neuronal attachment (Hallab et al., 2001; Fan et al., 2002). Roughening the surface can be achieved by altering the existing metallic surface or through coating with an alternate material. While direct modification of the metallic surface can impart roughness without significantly altering the electrode chemistry (Green et al., 2010c), the benefits are limited, in that the material stiffness and chemical compatibility with the biological system remains unchanged. Electrodes can be coated through a variety of methods including electrochemical deposition (Cui et al., 2003; Geddes and Roeder, 2003; Green et al., 2008a; Abidian et al., 2010; Hassler et al., 2011), physical vapor deposition (Geddes and Roeder, 2003; Gabay et al., 2007; Shoval et al., 2009; Chen et al., 2011) such as sputtering (Geddes and Roeder, 2003) or evaporation, spin-coating (Green et al., 2010c; Lacour et al., 2010) or dip-coating (Schuettler et al., 2005) from solutions which require curing (Fieberg and Reis, 2002; Chen et al., 2011; Rao et al., 2012) or cross-linking (Guimard et al., 2007). The method employed depends strongly on the type of material which is required for the coating. Electrochemical deposition is used to apply a material directly to an electrode site (Cui et al., 2001b; Bartlett et al., 2002; LaVan et al., 2003), but other methods coat the entire construct and often require post-processing to ensure the coating is applied only to the required areas of the electrode array (Kim et al., 2008; Abidian and Martin, 2009). Both organic coatings such as CNTs, CPs, and CHs, and inorganic coatings including Pt-Black, titanium nitride (TiN) and iridium oxide (IrOx) have been used to impart increased charge injection capacity to metallic electrodes (Cogan et al., 2005; Schuettler, 2007; Abidian et al., 2010; Green et al., 2012a,b). However, the organic coatings hold a significant benefit over the inorganic coatings as they can be easily modified to include functional molecules to influence the biological response. Organic polymers based on hydrogels present an alternate coating option. While hydrogels do not inherently impart a roughened surface area, they have been shown to provide mechanical and biological benefits to electrodes which, in turn improve the chronic electrical performance. Additionally, hydrogels have formed the basis of several composite coatings which utilize the combination of a conductive component embedded in a non-conductive polymer matrix.

CARBON NANOTUBES

Carbon nanotubes have remarkable mechanical and electrical properties that exhibit noted interaction with neural tissue. CNTs are cylinders formed from seamless sheets of graphene with a wall thickness of 1 atom. Single walled CNTs (SWCNTs) as the name suggests have only one sheet creating a single cylinder, but multi-walled CNTs (MWCNTs) have multiple concentric

cylinders of graphene. Some of the methods used to apply CNTs to electrodes are chemical vapor deposition (CVD) (Heim et al., 2012), immersion drying (Haghighi and Bozorgzadeh, 2011) and electrodeposition (Yang et al., 2010; Suzuki et al., 2013). CVD presents some drawbacks as it yields secondary toxic chemicals that require further purification (De Volder et al., 2013), also this technique requires higher temperatures process and this limits the possible materials that can be coated. CNT coatings produced by immersion are limited in durability, as the nanotubes are not bonded to surface. Electrodeposition is considered a simpler method to coat films with controllable thickness yielding a mechanically stable coating (Yang et al., 2010). It is worth noting that CNTs do not simply adhere to metallic substrates and as a result must be chemically modified or embedded within a polymer matrix to remain adhered to an electrode. As such all of the coatings described are composites of CNTs.

Perhaps one of the most important properties of CNTs is their ability to enhance electrical properties of metallic electrodes. The addition of CNTs to both insulating and conductive materials results in electrodes with higher charge storage capacity (CSC) and lower impedance (Green et al., 2008b; Xiao et al., 2012; David-Pur et al., 2013). By increasing the thickness of a coating containing CNTs the CSC has been reported to be as high as 70 mC/cm^2 (Luo et al., 2011b), although in this study the CNTs were embedded in a CP which likely contributed to the high CSC. It has also been shown that the presence of CNTs in a CP composite can stabilize the electrochemical properties of the coating (Green et al., 2008b). Similarly, several studies on electrodes coated with CNTs report a substantial increase in SNR for recording electrodes (Gabay et al., 2007; Yu et al., 2007; Keefer et al., 2008; Lin et al., 2009; Shoval et al., 2009; Hsu et al., 2010; Suzuki et al., 2013) which is thought to be predominantly due to the low impedance CNTs impart to electrodes (Keefer et al., 2008). In particular, (Shoval et al., 2009) presents an evident increase in SNR when recording neuronal activity from retina tissue. In this work CNT coatings increased the ability to record voltage spikes, increasing the SNR by up to three times in comparison with titanium nitride electrodes.

The low volume, high surface area of nanotubes means that they can dramatically increase the charge transfer area of an electrode. Their nanoscale features which enable them to penetrate cellular membranes, are also expected to enhance electrical performance by promoting a more intimate interaction with tissue. (Suzuki et al., 2013) detected action potentials and field postsynaptic potentials employing a multi-electrode array (MEA) coated with planar CNTs. In stimulation electrodes, a low impedance and decreased activation threshold have been achieved by several groups who have embedded CNTs in flexible polymer substrates including parylene-C, poly(dimethyl siloxane) (PDMS) and the CP polypyrrole (Nguyen-Vu et al., 2006; Wang et al., 2006; David-Pur et al., 2013). The safe charge injection limit of CNT containing coatings have been reported to be between 1.6 and 2.5 mC/cm^2 (Wang et al., 2006; Luo et al., 2011b). This is more than 10 times the charge injection reported for Pt.

Carbon nanotubes are very stiff materials with a Young modulus of 1.25TPa (Krishnan et al., 1998). This is a significant drawback when interfacing with neural tissue where mechanical mismatch between the device and cells is one of the main factors contributing to chronic inflammation. However, it is arguable that the nanoscale dimensions of these materials minimize the impact of shear stress at the cellular interface. In fact the ability for nanotubes to penetrate cells has been well detailed (Kagan et al., 2006; Tian et al., 2006; Gilmour et al., 2013). Additionally, nanotube morphology has promising properties for neural tissue engineering, with most coatings having a fibrillar surface, as shown in **Figure 2**. This morphology presents the cells with a nanometric roughness that is thought to create a more intimate cell-electrode interface (Keefer et al., 2008; Seidlits et al., 2008) suitable for cellular attachment.

Despite the promising electrical and physical properties of CNTs their biocompatibility is a subject of considerable discussion. Being small and biologically inert provides CNTs with the ability to infiltrate tissues without being identified by the immune system (Seidlits et al., 2008). While these nanoscale structures are less likely to be identified by reactive astrocytes and consequently may minimize scar tissue formation, (Kagan et al., 2006), it has been suggested this may represent a hazard as internalized CNTs can damage the intracellular bodies including the nuclei of cells. Additionally, it has been shown that high concentrations of CNTs induce cytotoxicity, either as un-functionalised SWCNTs or as composites with other polymers. Cell death in a dose dependent manner has been reported for lymphocytes (Bottini et al., 2006) and fibroblasts (Tian et al., 2006). Likewise, Webster et al. (2004) created CNT composites with polycarbonate urethane and their results showed that the toxicity of the composite increased whenever the proportion of the CNTs in the composite was 10% or more. It is clear that the biocompatibility of CNTs will remain a controversial subject, but coatings which can constrain the CNTs while utilizing their impressive electrical conductivity have significant potential in the future of neural interfaces.

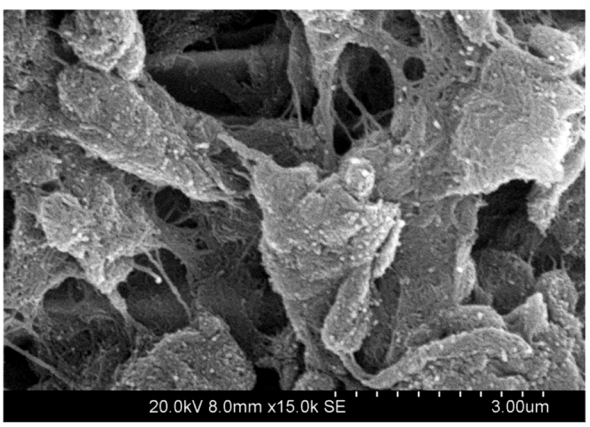

FIGURE 2 | Scanning electron microscope (SEM) image of multi-walled carbon nanotubes (MWNTs) coating a platinum disk electrode, demonstrate that CNTs produce fibrillar surface structures, imparting a high charge transfer area to the typically flat electrode. The platinum disk is not visible, as the entire substrate is covered with CNT bundles. Image produced at 15,000× magnification.

CONDUCTIVE POLYMERS

CPs are synthesized from chains of chemical compounds that present alternating double and single bonds in their structure (Guimard et al., 2007). This structure, known as a conjugated system, confers the conductive property to the polymer. When doped with an appropriately charged ion to stabilize the backbone, high conductivity can be obtained (Guimard et al., 2007). CPs can inject both electronic and ionic charge (Cogan, 2008) and have been used to both stimulate nerve tissue and record neuronal activity (Kim and Romero-Ortega, 2012). Among several conductive polymers, polypyrrole (PPy) (Cui et al., 2003; Kim et al., 2004; George et al., 2005; Stauffer and Cui, 2006; Green et al., 2008a) and poly(ethylene dioxythiophene) (PEDOT; Cui and Martin, 2003; Xiao et al., 2004; Yang et al., 2005; Ludwig et al., 2006, 2011; Green et al., 2008a), shown in **Figure 3** have been extensively used to coat neuroprosthetic electrode sites. Other CPs which have been investigated to a lesser extent include polyterthiophene (Stevenson et al., 2010), polyaniline (Huang et al., 2004; Bidez et al., 2006) and various modifications of PEDOT such as methoxy-PEDOT (PEDOT-MeOH), carboxylic acid modified PEDOT (PEDOT-COOH) and propylenedioxythiophene (Pro-DOT) (Martin and Feldman, 2012). PEDOT is considered one of the most promising CPs due its electrical and chemical stability in an oxygenated, hydrated environment (Cui and Martin, 2003; Guimard et al., 2007; Green et al., 2013b).

The fabrication method and the choice of CP components are critical to determining the resulting mechanical, chemical and electrical performance (Baek et al., 2013a). CPs can be fabricated by either chemical or electrochemical methods. While chemical synthesis enables the development of complex and highly ordered structures, the difficulties in applying these materials to metallic electrodes have largely hindered their investigation and application to neuroprosthetics. Additionally, chemically synthesized CPs require post-process doping to reach similar conductivities to electrochemically polymerized CPs. Electrodeposition is the most common method used to fabricate CP coatings on electrodes. This method enables direct formation of the polymer on the electrode site and by varying the time over which electrodeposition occurs, the thickness and roughness of the CP can be controlled (Fonner et al., 2008; Baek et al., 2013a). The dopant ion is included in the monomer electrolyte solution and is directly incorporated within the CP. Varying the dopant type and concentration also impacts on the CP electrical (Guimard et al., 2007) and morphological properties (Green et al., 2012a). While cations can be used to dope CPs, anions are almost exclusively used for electrodeposited CPs which are polymerized by oxidation producing a positively charge backbone, requiring a negatively charged dopant (Guimard et al., 2007). The most effective dopants for producing CPs with high charge transfer area and stable electrochemical properties are ions with sulfonate moieties, although phosphates and perchlorates have been successfully used to fabricate CP coatings with high charge transfer capacity. Common dopants which have been extensively investigated have included poly(styrene sulfonate) (PSS), para-toluene sulphonate (pTS), dexamethasone phosphate (Dex-P), and perchlorate (ClO_4).

CPs have been shown to improve on the electrical performance of Pt across various metrics important to electrode function, including the CSC (Cogan, 2008; Abidian et al., 2010; Green et al., 2013b), the electrochemical impedance (Kim et al., 2004, 2008; Abidian et al., 2010; Green et al., 2013b), and the charge injection limit (Kim et al., 2004, 2008; Green et al., 2012a,b). A summary of the various CPs and their electrical properties is shown in **Table 1**. In general CPs produced from PEDOT and doped with small sulfonate ions, namely pTS, have the highest charge storage capacity, lowest impedance and highest injection limit. Coating Pt electrodes with PEDOT/pTS can increase the CSC by one order of magnitude and the charge injection limit by up to two orders of magnitude (Cogan, 2008; Green et al., 2013b). Similarly, in the latter work the frequency dependant impedance is also reduced in the low frequency range, where it is proposed that capacitive double layers are the dominant mode of charge transfer (Green et al., 2013b). These improvements in electrical properties are primarily due to the increase in the charge transfer area of the electrode which occurs as a result of the intrinsic rough morphology of PEDOT. When large anions or polymers are used to dope PEDOT the surface is typically smoother which results in poorer electrical performance, such as that shown in **Table 1** for PEDOT/PSS. Small dopants enable more efficient polymerization than larger dopants, and structurally enable greater flexibility in the backbone during PEDOT formation. As a result these smaller

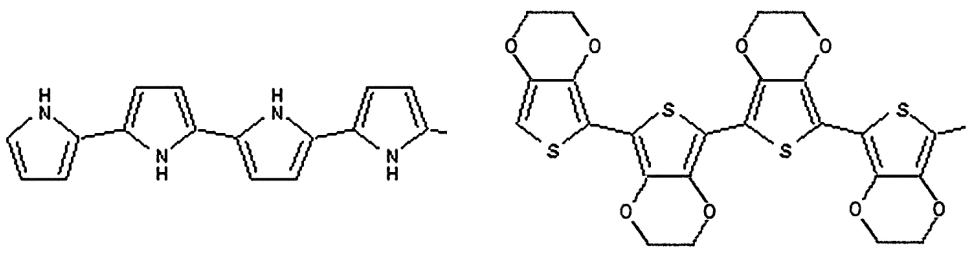

FIGURE 3 | Structure of PPy and PEDOT with alternating single and double bonds along the backbone which impart conductivity (Green et al., 2008a).

dopants create rougher, more nodular surfaces. The comparison of PEDOT/pTS and PEDOT/PSS surface morphology is shown in **Figure 4**. Since common analytical techniques such as stylus profilometry and indentation (including scanning AFM) can damage the CP surface, there are very few papers in the literature which quantify CP surface roughness. With the recent development of non-contact optical profilometry there is now an opportunity to provide measurements of roughness which can be related to the electrical performance of CPs. Using optical profilometry (Green et al., 2013b) have reported that PEDOT/pTS coatings can increase the surface area of a smooth electrode by a factor of 2, which closely correlated to the reduction in voltage drop across Pt electrodes coated with this CP (Green et al., 2013b). The electrical stability of CP electrode coatings is also related to the chemical constituents, with literature reporting minimal changes in PEDOT/pTS following more than 2 billion pulses (Boretius et al., 2011; Green et al., 2012a). However Yamato et al. (1995) reported loss of 95% of the electroactivity of PPy/PSS following 16 h of electrical polarization.

Mechanically CPs are largely claimed to reduce the stiffness of the electrode interface, however, few papers in the literature actually quantify the modulus of CPs. Several reports of dry CP films based on PEDOT demonstrate that the elastic modulus varies with dopant choice, but generally are in the range of 1–3 GPa (Yang and Martin, 2006; Baek et al., 2013a). More recent papers demonstrate that when hydrated the elastic modulus of CPs, in particular PEDOT/PSS can be as low as 40 MPa (Green et al., 2012b).This is substantially lower than the elastic modulus of Pt, but still more than two orders of magnitude higher than neural tissue. While CPs may have the capacity to dampen the mechanical mismatch at the neural interface, the mechanical stability is a greater concern. Several reports claim that delamination of these coatings can occur *in vivo* (Peixoto et al., 2009; Boretius et al., 2011) and moreover the surface, in particular of the highly rough PEDOT, is brittle and friable (Collier et al., 2000; Green et al., 2010b). While CPs have the benefit of being able to be functionalized to incorporate biological components, the addition of these large molecules further diminishes the mechanical stability of these coatings. Several approaches, including chemical tethering (Labaye et al., 2002) and mechanical interlocking (Green et al., 2012a) have been used to improve the adherence of CP coatings, but polymer cohesiveness requires improvement.

Various CPs have been shown *in vitro* to have cytocompatible properties, with several cell types including neuroblastomas (Bolin et al., 2009), spiral ganglion cells (Evans et al., 2009) and pheochromocytoma (PC12) neural model cells (Schmidt et al., 1997; Green et al., 2009). In spite of the promising results, little *in vivo* evidence has been presented to support the chronic stability and the benefit of applying CPs to neural interfacing electrodes. (Wilks et al., 2011) polymerized PEDOT *in vivo* within the rodent cerebral cortex, creating a direct CP interface with the neuronal tissue. In this work (Wilks et al., 2011) reported lowered impedance values, improved recording quality of local field potentials, and a tight cloud of PEDOT penetrating into the tissue surrounding the electrode. (Cui et al., 2003) were able to efficiently record neuronal activity for 2 weeks by implanting gold electrodes coated with PPy in guinea pigs cerebral cortex. After 2 weeks the polymer underwent structural changes and scar tissue encapsulation started to decrease electrode performance. Similarly, (Ludwig et al., 2006) demonstrated that CPs improve neural recordings using a PEDOT/PSS coated Michigan probe electrode array implanted in the rat motor cortex for 6 weeks. However impedance increased over time with a respective reduction in SNR correlating with a neural density decrease near the electrodes. It was suggested that neuronal loss was due to implant trauma. Recent evidence suggests that neurons not only may die following damage during the implantation process but can also migrate away from the electrode as the neuroglia isolates the device as a result of foreign body reactions (McConnell et al., 2009).

CPs address some of the limitations associated with reducing the size of Pt electrodes, providing electrical, mechanical and biological benefits. Despite the ability of CPs to enhance electrode performance, issues remain concerning mechanical stability and inflammatory reactions in the chronic implant environment. Approaches to improve the biological performance of CPs have included the development of composite CP-hydrogels and the use of biological inclusions intended to influence the cellular response.

Table 1 | Electrical properties of conductive polymers.

Conducting polymer	Charge storage capacity (CSC) (mC/cm^2)	Impedance @ 1000 kHz (Ω/cm^2)	Electrochemical charge injection limit (mC/cm^2)	Reference
PEDOT/pTS	245.59^S; 402.23^R	2.65×10^3	2.09 ± 0.2^S; 2.01 ± 0.4^R	Green et al. (2009, 2012a)
PEDOT/PSS	105.17^S; 243.48^R	2.03×10^3	1.36 ± 0.1^S; 1.52 ± 0.5^R	Green et al. (2012a), Baek et al. (2013a)
PEDOT/ClO_4	98.49^S; 389.88^R	2.03×10^3	2.39 ± 0.4^S; 2.09 ± 0.5^R	Baek et al. (2013a)
PPy/PSS	186.4	256.41×10^6	–	Cui et al. (2001a,b)
PTT/Dex-P	∼35	–	–	Stevenson et al. (2010)
PProDOT	5.8	–	–	Rosario-Canales et al. (2011)
Poly(EDOT-COOH)	–	∼10	–	Luo et al. (2012)
P(PRoDOT-OH)	–	∼10	–	Luo et al. (2012)

S, coated on smooth platinum. R, coated on roughened platinum.

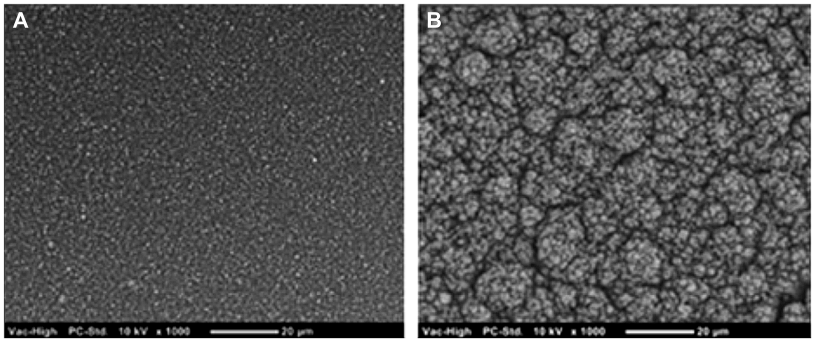

FIGURE 4 | Scanning electron microscope images show that (A) PEDOT doped with PSS produces a coating which is substantially smoother than that produced from (B) PEDOT doped with pTS.

HYDROGELS

The need to develop an electrode interfacing material with an elastic modulus similar to that of nerve tissue is a recurring concept (Kim et al., 2008). Hydrogels are polymer systems which have been extensively studied for tissue engineering (Lee and Mooney, 2001; Hoffman, 2002).The networks are held together by physical or chemical crosslinks and network design can incorporate a range of degradation profiles or may be non-degradable. Structure and mechanical properties of hydrogel networks can be controlled through selection of fabrication technique and chemical composition (Lacour et al., 2010). These crosslinked polymeric networks have high water contents making them an attractive platform for neural interfacing. Hydrogels are commonly fabricated from either natural materials such as collagen (Ma et al., 2004; Mao and Kisaalita, 2004; Suri and Schmidt, 2010), fibrin (Georges et al., 2006; Ahmed et al., 2008), and alginate (Novikova et al., 2006; Banerjee et al., 2009) or synthetic materials like polyvinyl alcohol (PVA) (Lu et al., 2009; Lim et al., 2012, 2013), polyethylene glycol (PEG; Drury and Mooney, 2003) and polyacrylamide (Georges et al., 2006). Synthetic polymers enable controlled hydrogel mechanical properties but lack cellular activity due to the absence of bioactive elements. On the other hand natural polymers support enhanced cellular interactions but form constructs that are less mechanically and dimensionally stable compared with synthetic hydrogels. Co-hydrogel or biosynthetic systems combine the benefits of natural and synthetic polymers and permit greater control over the polymer properties. While many hydrogel systems have been investigated for tissue engineering, only a few types have been applied to neuroprosthetic electrode arrays.

Although few hydrogels are considered conductive, most are poor insulators due to the open polymer mesh structure which swells in aqueous environments. Winter et al. applied poly(ethylene glycol)-poly(lactic acid) (PEGPLA) to multielectrode arrays and found that the electrochemical characteristics of the underlying IrOx coated electrode array were preserved (Winter et al., 2007) however, the thickness of the layer was not reported. Zhong and Bellamkonda coated electrode arrays with a nitrocellulose based hydrogel and found that impedance of the neural interface was reduced (Zhong and Bellamkonda, 2005). Hydrogel mesh structures provide minimal hindrance to the ions required for capacitive charge transfer. Furthermore, some hydrogels have a strongly charged backbone which encourages ion sequestering (Hoffman, 2002). These ions provide a ready source of charge for formation of a capacitive double layer at an underlying metallic electrode interface. However, it is also observed that when a hydrogel coating swells *in vivo*, it can push the target neural tissue further away from the electrode (Kim et al., 2010), necessitating higher charge delivery to activate the neurons.

By developing hydrogels with a mechanical modulus within the range of nerve tissue, less than 100 kPa (Lacour et al., 2010), it has been suggested that hydrogel coatings can reduce stress related to micromotion of stiff materials (Kim et al., 2010). The compression modulus of hydrogels is highly variable and strongly dependant on the type of polymer used for coating, a summary of hydrogel moduli is presented in **Table 2**. In a study by Baek, hydrophilic brushes fabricated from polyhydroxyethylmethacrylate (pHEMA) were applied to gold electrodes and found to reduce the modulus from 70 GPa to 143 MPa (Baek et al., 2013b). In a similar study by Green et al. (2012b), Pt was coated with the biosynthetic co-hydrogel polyvinyl alcohol-heparin (PVA-Hep) and the electrode modulus was reduced to near 100 kPa. Several studies on hydrogel chemistry and structure have shown that the mechanical properties of synthetic polymers can be controlled through varying the length of the polymer backbone, the number of crosslinks and the percentage polymer composition relative to the water content (LeRoux et al., 1999; Normand et al., 2000; Almany and Seliktar, 2005; Nilasaroya et al., 2008). However, a material that is as soft as the tissue presents difficulties during implantation (Kim et al., 2008; Richter et al., 2013). In an effort to address the latter issue, recent research has investigated novel hydrogel materials which have switchable properties when exposed to different environmental conditions. Capadona et al., developed a cellulose-whisker nanocomposite that softens when the temperature is increased from 25 to 37°C. It was shown that the initial stiffness of the arrays produced with this material were 4.2 GPa which was reduced to 1.6 MPa in 10 min following immersion in physiological fluid at 37°C (Capadona et al., 2008). It is conceivable that through choice of polymer and control of the hydrogel structural characteristics, the

Table 2 | Mechanical moduli of various hydrogels.

Hydrogel	Type (synthetic, natural, or biosynthetic)	Modulus range (kPa)	Reference
Polyvinyl alcohol (PVA)	Synthetic	2560–7360*	Baker et al. (2012)
Polyethylene glycol (PEG)	Synthetic		
Poly(2-hydroxyethyl methacrylate) (pHEMA)	Synthetic	440 ± 10	Jhaveri et al. (2008)
Poly(lactic-co-glycolic acid)	Synthetic	752 ± 54	Vaquette et al. (2010)
Collagen	Natural	0.5–12	Raub et al. (2010)
Agarose	Natural	1.5–2580**	Letherby and Young (1981), Normand et al. (2000), Aymard et al. (2001), Ahearne et al. (2005)
Alginate	Natural	1–8**	LeRoux et al. (1999)
PVA-heparin	Biosynthetic	60–68**	Nilasaroya et al. (2008)
PEG-Fibrinogen	Biosynthetic	0.01–2**	Almany and Seliktar (2005)

*Values change depending on confined compression **Values are proportional to the percent polymer composition.*

mechanical modulus of an electrode can be tailored for the neural interface.

Cell interactions with hydrogels, like the mechanical properties, depend on the polymer choice. Synthetic hydrogels generally have poor cell interactions which have made them useful as antifouling coatings for implants (Telford et al., 2010; Liu et al., 2012). This property may be of use in neural prosthetics where protein deposition, which increases the impedance of electrodes, can be prevented (Li et al., 2005; Green et al., 2010a). However, a significant benefit of synthetic hydrogel systems is that they can be modified to incorporate biological molecules. The ability to functionalize hydrogels has been extensively explored (Hoffman, 2002; Willerth and Sakiyama-Elbert, 2007) and they can be modified to include covalently bound bioactive molecules, to bind and release growth factors (Nilasaroya et al., 2008), or to degrade over time to allow controlled drug release (Anseth et al., 2002). (Zhong et al., 2001) demonstrated that natural hydrogels of collagen promoted cortical nerve cell attachment. Lim et al. have further shown that very small amounts of the collagen derivative gelatin, incorporated at 0.01–1 wt% within a synthetic PVA hydrogel can promote attachment of various cell types including neuronal cells (Lim et al., 2013). Further, Winter et al. used degradable PEGPLA to successfully deliver nerve growth factor (NGF) and promote the outgrowth of neuronal processes from PC12 cells (Winter et al., 2007). Several studies have examined release of drugs from hydrogel coatings (Zhong and Bellamkonda, 2005; Winter et al., 2007) and the issues related to drug delivery are discussed below in relation to bioactive coatings. Ultimately, further studies are required to develop a hydrogel which can soften device interfaces while limiting the gap between the electrode and tissue.

As hydrogels do not substantially improve the electrical properties of the underlying material, they can only go part of the way to addressing the limitations of metallic electrodes. However, there is a wealth of literature on the design, fabrication and characterisation of hydrogel systems for alternate biomedical applications (Lee and Mooney, 2001; Hoffman, 2002; Yu and Bellamkonda, 2003; Kurisawa et al., 2005; Lee et al., 2008; Nicodemus and Bryant, 2008; Winter et al., 2008; Zuidema et al., 2011; Abidian et al., 2012). It is expected that through consideration of this body of work a systematic assessment of various hydrogel chemistries and structures will allow selection of appropriate polymers for improving the mechanical softness and biological interaction of neural electrode arrays. It is proposed, however, that such a hydrogel will require additional modification to incorporate conductive components to ultimately improve charge transfer and facilitate the development of high density microelectrode arrays.

CONDUCTIVE HYDROGELS

Blending hydrogels with conductive components such as CNTs or CPs has provided an avenue for maintaining the desired electrical characteristics of a coated electrode while imparting reduced stiffness (Green et al., 2012b; Xiao et al., 2012). The hydrogel component also presents the opportunity to incorporate bioactive molecules at higher concentrations than in CNT or CP films alone. Since CNTs usually require a polymer matrix to constrain them within the electrode coating, composites based on CNTs have been discussed above. CP-hydrogel hybrids (known as conductive hydrogels) are a more recent development which address the limitations of homogenous CPs (Green et al., 2010a, 2012a). As the CP component is fabricated within the hydrogel matrix, the friable particulates are encapsulated, improving the mechanical stability of the coating. Few conductive hydrogel (CH) systems have been developed for neural interface purposes(Kim et al., 2004, 2010; Green et al., 2012a,b; Hassarati et al., 2014), but preliminary studies have demonstrated the potential of this coating technology.

The CSC, impedance and charge injection limit of CH coated electrodes are significantly better than bare metal electrodes, but are also often improved compared to homogenous CPs (Cheung, 2007; Green et al., 2012b; Hassarati et al., 2014). Kim et al. (2004) electrodeposited PPy through a 1% alginate hydrogel and found that the resulting construct had an impedance of 7 kΩ at 1 kHz (for

a 1257 μm^2 electrode) which was approximately 14 times lower than the PPy films alone. In a similar study Chikar et al. (2012) deposited PEDOT through an alginate hydrogel and found that the CSC increased exponentially relative to the amount of PEDOT deposited within the hydrogel. This increase in CSC relative to the amount of PEDOT was more pronounced than that reported for PEDOT as a homogenous film, indicating that the same amount of material when deposited in a hydrogel had a greater impact on the electrical properties. It is generally thought that the hydrophilic mesh provided by the hydrogel promotes a large three-dimensional surface of conductive material which is available for charge transfer. This increase in surface area compared to the relatively dense and hydrophobic surface of a homogenous CP is expected to be the source of the enhanced electrochemical properties. The increase charge transfer area also leads to significant improvements in charge injection limit. In a study by Hassarati et al. (2014) a CH fabricated from PEDOT/PVA-Hep was applied to cochlear implants and increased the charge injection limit of the Pt electrodes by up to 24 times. This coating was also shown to be stable over 1 billion stimulations at clinically relevant levels.

Several CH systems have been shown to reduce the stiffness of electrodes, and as expected the modulus of these hybrids typically lies between that of the component CP and hydrogel (Aouada et al., 2006; Baek et al., 2013b; Green et al., 2012b). Double network polymers of chemically synthesized PEDOT:PSS and polyacrylamide (PAAm) were found to have elastic moduli which ranged between 27 and 350 kPa. The increased stiffness was a function of both the percentage content of the stiffer PEDOT:PSS and the cross-link density of the PAAm (Aouada et al., 2006). When chemically synthesized CPs are used as a component of a CH the amount of CP can be carefully controlled, and has an impact on both the electrical conductivity and stiffness of the hybrid. However, when electrodeposited CPs are grown through hydrogels the elastic moduli of the resulting hybrid appears to be minimally variable (Green et al., 2012b). In a recent study, the stiffness of two different CHs was found to be close to 1 MPa, despite the CHs being fabricated from hydrogels with different chemistries and percentage of polymer content (Green et al., 2012b). The morphology of these CH variants was also dissimilar, as depicted in **Figure 5**, but both the electrical and mechanical properties were not significantly different. While there are several studies which report combining hydrogels with electrodeposited CPs for application to electrodes, few have quantified the modulus of these hybrids.

Conductive hydrogels have shown negligible *in vitro* cytotoxicity and good compatibility with several cell types (Green et al., 2010a; Mario Cheong et al., 2013). The biological properties of these composites reflect the properties of the component polymers, which have been shown to be compatible with a range of cell types. Specifically, CH materials have been used to support the attachment and growth of PC12 cells, the interleukin-3 dependent pro-B cell line (BaF3) and Schwann cells (Runge et al., 2010; Mario Cheong et al., 2013). *In vivo* PEDOT-alginate CHs (Kim et al., 2010) have been implanted in the auditory cortex area of the guinea pig. Despite the impedance of the hydrogel electrodes being much lower *in vitro*, the CH had similar impedance *in vivo* to that of uncoated electrodes. However, a significant improvement in SNR was found in the initial period following implantation. The impact of the material on the surrounding tissue was not examined histologically, but it was proposed that swelling of the construct increased the distance between the electrodes and target tissue (Kim et al., 2010). In a related field Abidian et al. (2012) developed PEDOT-agarose nerve conduits which were found to support nerve regeneration, although control autografts supported regeneration of significantly greater nerve fiber numbers. It was proposed that the PEDOT within the agarose inhibited cellular access to essential nutrients, limiting the development of functional nerve fascicles. It is also important to note that these studies did not utilize any active stimulation of tissue. It is clear that more information is required to successfully develop CHs and it is critical to assess the performance of these constructs *in vivo* under active implant conditions.

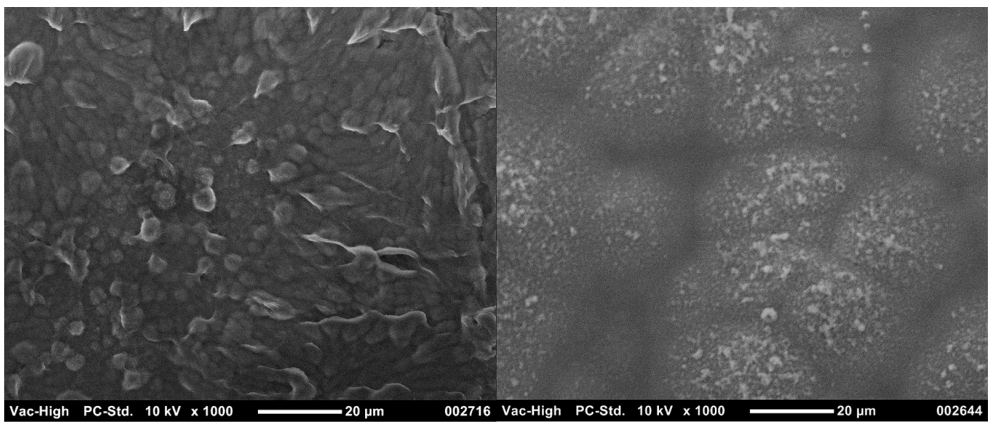

FIGURE 5 | Different morphologies of CHs can be produced through varying the hydrogel component. PEDOT grown through 30 wt% heparin has a more cobblestone appearance (left) compared to the nodular PEDOT grown through 20 wt% PVA-Hep (right).

In preliminary studies it has been shown that CHs have the properties which can address the limitations of both metallic and CP coated electrodes by reducing mechanical mismatch, while maintaining improved electrical properties. Initial *in vitro* studies demonstrate the benefit of these coatings, but there are no studies which systematically compare the different types of hydrogels and CPs used to fabricate these materials. Furthermore, the integration of the two polymer systems is poorly understood, which limits the ability to manipulate the CH structure and tailor the system to display specific characteristics for neural interfacing. Optimization of CHs will require studies which examine the long-term performance of coated electrodes in a stimulated biological environment.

BIOACTIVE COATINGS

All of the coating technologies discussed above can be modified to incorporate biological molecules. Cellular attachment molecules, anti-inflammatory agents and neurotrophins have been commonly investigated for improving the biological response of neural electrodes. Ideally, one of more of these molecules can be used to provide cues to bring neurons closer to electrodes and reduce the impact of the foreign body response. **Table 3** summarizes a range of biological molecules, which have been incorporated within or at electrode surfaces.

The provision of cell attachment molecules within coatings has been extensively explored. In studies which aim to restoring neuronal function, it has been proposed that extracellular matrix (ECM) molecules can provide structural and chemical cues to encourage regeneration at the neural interface (Chan and Mooney, 2008). ECM molecules such as collagen, laminin, and fibronectin among others, have been regarded as key elements in cellular attachment, cell growth, homeostasis, differentiation and cellular motility (Gumbiner, 1996; Banker and Goslin, 1998). Each molecule as well as related peptide sequences can provide mechanical, biological and chemical cues for neural tissue growth and development. Comprehensive reviews on the performance of specific proteins in the ECM have been previously published (Gumbiner, 1996; Banker and Goslin, 1998; Barros et al., 2011; Blau, 2013). **Table 3** lists some of the ECM molecules which have been included within synthetic polymers with an aim of imparting these cues at the device interface. The molecules are classified as proteins including laminin, fibronectin and collagen or related peptide sequences such as arginine–glycine-aspartic acid (RGD), polylysine and gelatin. Proteins and peptides can be incorporated within CNT, CP or CH coatings by simple adsorption, entrapment or covalent binding. It is known that adsorption does not produce a stable interface in the *in vivo* environment as competitive binding of the surrounding proteins can displace the adsorbed layer. Similarly, entrapped proteins can either diffuse through coatings, or if particularly large relative to the coating porosity, can be obstructed within the coating, such that they are not accessible to the cells. As a result cell attachment molecules are often covalently linked to either the coating surface or a component of the coating prior to fabrication. Such molecules have been bonded to CNTs or hydrogel macromer and alternatively used as a CP dopant ion (Cui et al., 2001b; Nguyen-Vu et al., 2007; Green et al., 2010b). Many studies have shown that these sequences encourage neural attachment, survival and differentiation *in vitro* (DeLong et al., 2005; Green et al., 2010b; Chikar et al., 2012). However, there is minimal evidence *in vivo* which supports the benefit of these components to the chronic neural interface. Cui et al. (2003) implanted PPy coated electrodes which were functionalized with laminin fragments in guinea pig cortex. It was shown that neuronal attachment was promoted on some of the electrodes but in spite of having good initial recordings, fibrotic tissues ultimately isolated the electrodes from the target tissue. While cell attachment proteins have clear benefit *in vitro*, there is a need to further explore their presentation and stability *in vivo*.

Anti-inflammatory molecules have been proposed for mitigating either the initial inflammatory reaction or the ongoing presence of fibrotic reactions at the neural interface. Unlike cell attachment proteins, anti-inflammatories must be delivered to the extracellular space to have an effect on the surrounding tissues. As a result these molecules are incorporated into coatings such that they can be delivered, either by passive diffusion or controlled delivery (Asplund et al., 2014). Dexamethasone is one of the most common drug molecules used to combat inflammation at the electrode interface, although hyaluronic acid (HA) and alpha-melanocyte-stimulating hormone (αMSH) have also been used. (Abidian et al., 2006) electrospun dexamethasone-loaded PLGA nanofibers, which were then encapsulated in PEDOT. In this highly conductive construct the dexamethasone could be delivered with a controlled dosage by electrical stimulation. However, due to the limited volume of the PEDOT coated nanofibres, the drug could only be delivered for 7 days at therapeutic levels. (Luo et al., 2011a) introduced dexamethasone to composite CNT-PPy coatings and also demonstrated release under electrical stimulation. The anti-inflammatory dose administered this way was enough to prevent microglia activation in a cell culture, but the ability to deliver therapeutic levels was restricted to a period of 24 h. In contrast (Zhong and Bellamkonda, 2005) entrapped α-MSH in nitrocellulose coatings which demonstrated slow, sustained release by diffusion over 21 days *in vitro*. The α-MSH was shown to retain bioactivity, and successfully inhibited microglial inflammatory responses. Nonetheless all of these approaches are limited as following depletion of the drug from the coating the desired low inflammation state was not maintained.

Inclusion of neurotrophins such as brain-derived neurotrophic factor (BDNF) (Richardson et al., 2007b) and nerve growth factor (NGF; Kim et al., 2007), within electrode coatings encourages the initial growth of neuronal processes towards implanted electrodes. This approach is designed to both initiate neural regeneration and also reduce the gap between the electrode and target tissue. However, several studies have shown that shrinkage of neurite growth occurs after the NGF supply is depleted (Fujita et al., 1989; Richardson et al., 2007a). While a substantial concentration of growth factor can be incorporated within hydrogels, there is only a very limited amount of any biological molecule which can be incorporated within CPs or CNTs (Richardson et al., 2007a). By removing the reliance on material loading and delivery rate (Gillespie et al., 2003) maintained spiral ganglion neurons for 28 days through BDNF administration via a mini-osmotic pump. It was expected that this method would provide a more controlled and

Table 3 | Summary of the combinations of coatings and biomolecules which have been investigated for improving the interaction of electrodes and neural cells.

Application	Coating	Biomolecule	Reference
Cell attachment	PEDOT	DCDPGYIGSR and DEDEDYFQRYLI	Green et al. (2010b)
	PEDOT	DCDPGYIGSR and DEDEDYFQRYLI	Green et al. (2009)
	PEDOT	Fibronectin fragments DCDPGYIGSR	Cui and Martin (2003)
	PPy	Fibronectin fragments Nonapeptide CDPGYIGSR	Cui et al. (2001b)
	CNT	Collagen type IV	Nguyen-Vu et al. (2006)
Anti-inflammatory	PPy	HA	Collier et al. (2000)
	PPy	Dexamethasone	Wadhwa et al. (2006)
	PEDOT electrodeposited on PLGA nanofibers	Dexamethasone	Abidian et al. (2006)
	Polyterthiophene	Dexamethasone phosphate	Stevenson et al. (2010)
	Alginate hydrogel loaded with Poly(lactic-co-glicolide)(PLGA) nanoparticles	Dexamethasone	Kim and Martin (2006)
	Nitrocellulose	αMSH	Zhong and Bellamkonda (2005, 2007)
	Silicon	αMSH	He et al. (2007)
	Multiwalled CNTs	Dexamethasone	Luo et al. (2011a)
Growth factors	Methylcellulose	PDGF-BB and IGF-1	Wells et al. (1997)
	Poly (ethylene-co-vinyl acetate) (EVA) (EVA rods)	NGF, NT-3, BDNF and GDNF,	Bloch et al. (2001), Barras et al. (2002), Fine et al. (2002)
	Agarose	NGF and Laminin	Yu and Bellamkonda (2003)
	Collagen	NT-3	Houweling et al. (1998)
	PEG and PEG-PLA	NT-3	Burdick et al. (2006), Piantino et al. (2006)
	Agarose	BNDF	Jain et al. (2006)
	Fibrin	Heparin binding delivery system (HBDS) and NT-3	Taylor and Sakiyama-Elbert (2006)
	PPy	Laminin fragments RNIAEIIKDI (p20)	Stauffer and Cui (2006)
	PEG-PLA	NGF,	Winter et al. (2007)
	pHEMA-lysine	NGF,	Jhaveri et al. (2008)
	Fibrin	NGF	Lee et al. (2003)
	Multiwalled CNT	NGF	Matsumoto et al. (2007)

HA, hyaluronic acid; αMSH, α-melanocyte stimulating hormone; NGF, nerve growth factor; PDGF-BB, platelet derived growth factor-BB; IGF-1, insulin-like growth factor-1; BDNF, brain derived neurotrophic factor; GDNF, glial cell-derived neurotrophic factor; NT-3 – neurotrophin 3; HBDS, heparin binding delivery system; PEG, poly(ethylene glycol); PEG-PLA, poly(ethylene glycol)-poly(lactic acid); and CNT, carbon nanotube.

longer treatment period than possible with coatings; however, an accelerated loss of neuronal survival occurred after cessation of the treatment. It is therefore expected that provision of neurotrophins at the neural interface will only be effective using a method which support chronic delivery. While current coating technologies do not meet this need, several tissue engineering constructs provide insight into approaches which may address this challenge.

While CNTs, CPs, and hydrogels can be functionalized with bioactive molecules to minimize inflammation and promote neuronal attachment, the main limitation is the ongoing administration of drugs at a therapeutic level. Additionally, at high concentrations it has been shown that these bulky molecules can severely impact on the coating physicochemical properties, in particular CP electrical and mechanical properties are diminished (Collier et al., 2000; Cui et al., 2001b; Green et al., 2009, 2010b). An advantage of CNTs is that their cylindrical morphology can been used as a reservoir for bioactive agents, however they require time intensive functionalization processes in order to be soluble and dispersed in common solvents and aqueous drug solutions (Georgakilas et al., 2002; Bianco et al., 2005).

Current coating technologies including CNTs, CPs, hydrogels, and CHs address several of the limitations of metallic electrodes used in neural interfacing. However, these materials by themselves do not provide a platform for chronic biochemical support which can prevent fibrotic tissue growth and encourage neural cell interactions. In the field of tissue engineering it has been shown that biochemical support (Bhatheja and Field, 2006; Allen and Barres, 2009). can be maintained through the provision of encapsulated cells (Johnson et al., 1989; Majumdar et al., 2011; Daud et al., 2012; Higashimori and Yang, 2012) which naturally produce a range of growth factors and extracellular matrix proteins (Bhatheja and Field, 2006; Allen and Barres, 2009).

A more complex, but highly functional interface will utilize coating technologies in combination with tissue engineered cellular constructs.

TISSUE ENGINEERING THE NEURAL INTERFACE

Ideally, materials used at the neural interface must both minimize the foreign body response as well as promote neuronal survival to maintain the target neurons in close proximity to the electrodes. A more recent idea which has evolved from the literature is the fabrication of electrodes which are intimately associated with neural tissue (Wilson and Dorman, 2008; Richter et al., 2011; Green et al., 2013a). This approach combines the principles of tissue engineering with neuroprosthetic electrode coatings and proposes the incorporation of neural cells within the device itself. Ultimately, polymer systems can be modified to not only improve the electrode properties, but also support the encapsulation and survival of neural cells.

The concept of integrating living cells with electrodes was first raised in 1980, when Ochiai et al. proposed using live blue-green algae embedded in an alginate gel to act as a solar to electric energy photoconverter (Ochiai et al., 1980). They coined the term, "living electrode." In a follow up study, (Ochiai et al., 1983) noted that although stability of these biological electrodes was good, the power conversion efficiency was very low at approximately 0.1%. The latter limitation in efficiency restricted further development of this concept. In 1999, non-nucleated cells were successfully embedded in the PPy electrodeposited onto metal electrodes (Campbell et al., 1999). Cell surface antigen integrity was maintained and because the biosensor application required only presentation of cell surface antigens, there was no requirement for long-term viability and cell function. More recently, Richardson-Burns et al. described electrodeposition of PEDOT on neuroblastoma-derived cell lines and primary mouse cortical cells grown on metal electrodes (Richardson-Burns et al., 2007). Cells survived initial short-term exposure to monomers, but apoptosis was observed at 72 h with up to a third of the cells dying by 120 h. Cytoskeletal disruption was noted soon after polymerization of PEDOT suggesting that focal adhesions may have been disrupted (Richardson-Burns et al., 2007). Despite subsequent research from the same group (Sarah et al., 2007; Ouyang et al., 2011), there has been little progress over the past 5 years on the concept of creating "living" electrodes that contain eukaryotic cells.

Pioneering studies by Richter et al. (2011) present polymeric devices seeded with stem cells. In this study, fibrin hydrogel was used to protect cells from shearing stress similar to that experienced upon neural electrode implantation. More recent reports have shown a proof of concept of the feasibility of building layered constructs of cell loaded hydrogels over CP coated Pt electrodes (Green et al., 2013a). This layered construct involves a hydrogel scaffold to hold neuronal cells while maintaining electrical characteristics of metallic electrodes coated with PEDOT. The concept behind this layered construct is that if neuroprogenitor cells can be supported and developed such that neurite processes are directed towards the target tissue, as depicted in **Figure 6**, then the electrode will be surrounded by a functional neural layer instead of fibrotic tissue. Several challenges arise in the fabrication of such a construct. Importantly, the hydrogel scaffold must be tailored to provide mechanical and biochemical properties that support the growth and differentiation of neural cells. Additionally, neurite outgrowth should be promoted in a vectorial fashion towards the target tissue. Finally, the encapsulated cells must form functional synaptic processes with the target neurons. These issues present great challenges, however, it is expected that recent

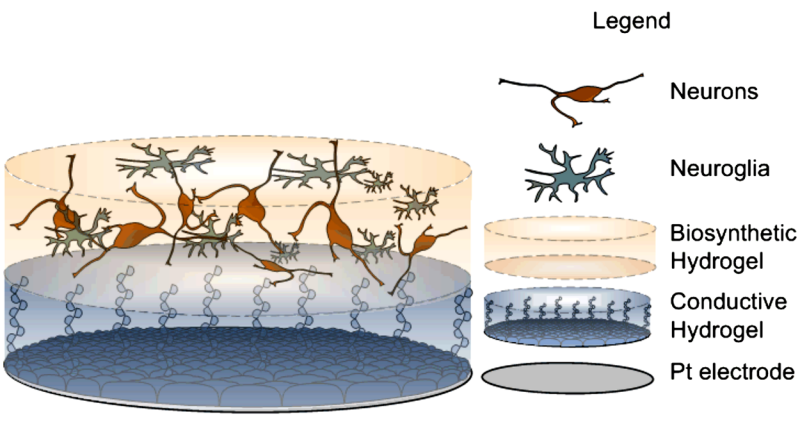

FIGURE 6 | Scheme of proposed construct, derived from Green et al. (2013a) bottom, Pt electrode site. Middle, conductive hydrogel coating and top, neural network encapsulated within degradable hydrogel.

research in tissue engineering will provide insights to guide development of such cellular constructs (Schmidt et al., 1997; Guimard et al., 2007; Sidhu et al., 2012). For example, it has been shown that cell survival and differentiation in three dimensional scaffolds is greatly improved by seeding cells with complementary accessory cells which would be normally present in the developing tissue (Sidhu et al., 2012). These cells generate a variety of biochemical cues producing ECM proteins and growth factors which support the attachment, survival, and differentiation of the functional cells within the scaffold. As such functional living electrodes are likely to require not only neural cells but also supporting neuroglia to achieve functional networks with target tissue.

Despite the substantial amount of research required to develop this technology, it has the potential to provide a pathway for maintaining neurons in close proximity with electrodes. Additionally, a fully realized tissue engineered electrode may prevent scar tissue encapsulation and provide a means of communicating with diseased or damaged cells using natural synaptic processes. Embedded neurons can provide single-cell electrodes which address individual target cells and this innovative method of communicating across the neural interface has the capacity to increase the spatial resolution of bionic devices.

CONCLUDING REMARKS

Carbon nanotubes, CPs, and hydrogels provide potential materials to enhance electrical performance of microelectrodes by increasing electrochemical area. However, to develop a long term neural interface it is critical to determine the interplay of the mechanical, electrical and biological properties. The true potential of these materials on neural interfaces is not completely understood as the many studies have been limited to characterization in the *in vitro* environment. An important component of future research is the assessment of organic coatings *in vivo* under chronic implant conditions. Systematic studies are required to assess the different coating technologies and provide direction on which material or combination of materials will provide the most beneficial characteristics for neural interfacing. Tissue engineered living electrodes may provide an alternate technology platform which will enable the development of a truly innovative way of communicating with the neural system through synaptic processes.

REFERENCES

Abidian, M. R., Corey, J. M., Kipke, D. R., and Martin, D. C. (2010). Conducting-polymer nanotubes improve electrical properties, mechanical adhesion, neural attachment, and neurite outgrowth of neural electrodes. *Small* 6, 421–429. doi: 10.1002/smll.200901868

Abidian, M. R., Daneshvar, E. D., Egeland, B. M., Kipke, D. R., Cederna, P. S., and Urbanchek, M. G. (2012b). Hybrid conducting polymer–hydrogel conduits for axonal growth and neural tissue engineering. *Adv. Healthc. Mater.* 1, 762–767. doi: 10.1002/adhm.201200182

Abidian, M. R., Kim, D. H., and Martin, D. C. (2006). Conducting-polymer nanotubes for controlled drug release. *Adv. Mater.* 18, 405–409. doi: 10.1002/adma.200501726

Abidian, M. R., and Martin, D. C. (2009). Multifunctional nanobiomaterials for neural interfaces. *Adv. Funct. Mater.* 19, 573–585. doi: 10.1002/adfm.200801473

Ahearne, M., Yang, Y., El Haj, A. J., Then, K. Y., and Liu, K. K. (2005). Characterizing the viscoelastic properties of thin hydrogel-based constructs for tissue engineering applications. *J. R. Soc. Interface* 2, 455–463. doi: 10.1098/rsif.2005.0065

Ahmed, T. A., Dare, E. V., and Hincke, M. (2008). Fibrin: a versatile scaffold for tissue engineering applications. *Tissue Eng. B Rev.* 14, 199–215. doi: 10.1089/ten.teb.2007.0435

Allen, N. J., and Barres, B. A. (2009). Neuroscience: glia – more than just brain glue. *Nature* 457, 675–677. doi: 10.1038/457675a

Almany, L., and Seliktar, D. (2005). Biosynthetic hydrogel scaffolds made from fibrinogen and polyethylene glycol for 3D cell cultures. *Biomaterials* 26, 2467–2477. doi: 10.1016/j.biomaterials.2004.06.047

Andrade, D. M., Zumsteg, D., Hamani, C., Hodaie, M., Sarkissian, S., Lozano, A. M., et al. (2006). Long-term follow-up of patients with thalamic deep brain stimulation for epilepsy. *Neurology* 66, 1571–1573. doi: 10.1212/01.wnl.0000206364.19772.39

Anseth, K. S., Metters, A. T., Bryant, S. J., Martens, P. J., Elisseeff, J. H., and Bowman, C. N. (2002). In situ forming degradable networks and their application in tissue engineering and drug delivery. *J. Control. Release* 78, 199–209. doi: 10.1016/S0168-3659(01)00500-4

Aouada, F. A., Guilherme, M. R., Campese, G. M., Girotto, E. M., Rubira, A. F., and Muniz, E. C. (2006). Electrochemical and mechanical properties of hydrogels based on conductive poly(3,4-ethylene dioxythiophene)/poly(styrenesulfonate) and PAAm. *Polym. Test.* 25, 158–165. doi: 10.1016/j.polymertesting.2005.11.005

Asplund, M., Boehler, C., and Stieglitz, T. (2014). Anti-inflammatory polymer electrodes for glial scar treatment. *Front. Neuroeng.* 7:9. doi: 10.3389/fneng.2014.00009

Aymard, P., Martin, D. R., Plucknett, K., Foster, T. J., Clark, A. H., and Norton, I. T. (2001). Influence of thermal history on the structural and mechanical properties of agarose gels. *Biopolymers* 59, 131–144. doi: 10.1002/1097-0282(200109)59:3<131::AID-BIP1013>3.0.CO;2-8

Babcock, A. A., Kuziel, W. A., Rivest, S., and Owens, T. (2003). Chemokine expression by glial cells directs leukocytes to sites of axonal injury in the CNS. *J. Neurosci.* 23, 7922–7930.

Baek, S., Green, R. A., and Poole-Warren, L. A. (2013a). Effects of dopants on the biomechanical properties of conducting polymer films on platinum electrodes. *J. Biomed. Mater. Res. A* doi: 10.1002/jbm.a.34945 [Epub ahead of print].

Baek, S., Green, R., Granville, A., Martens, P., and Poole-Warren, L. (2013b). Thin film hydrophilic electroactive polymer coatings for bioelectrodes. *J. Mat. Chem. B* 1, 3803–3810. doi: 10.1039/C3TB20152J

Baker, M. I., Walsh, S. P., Schwartz, Z., and Boyan, B. D. (2012). A review of polyvinyl alcohol and its uses in cartilage and orthopedic applications. *J. Biomed. Mater. Res. B Appl. Biomater.* 100, 1451–1457. doi: 10.1002/jbm.b.32694

Banati, R. B., Gehrmann, J., Schubert, P., and Kreutzberg, G. W. (1993). Cytotoxicity of microglia. *Glia* 7, 111–118. doi: 10.1002/glia.440070117

Banerjee, A., Arha, M., Choudhary, S., Ashton, R. S., Bhatia, S. R., Schaffer, D. V., et al. (2009). The influence of hydrogel modulus on the proliferation and differentiation of encapsulated neural stem cells. *Biomaterials* 30, 4695–4699. doi: 10.1016/j.biomaterials.2009.05.050

Banker, G., and Goslin, K. (1998). *Culturing Nerve Cells.* Cambridge, MA: MIT Press.

Barras, F. M., Pasche, P., Bouche, N., Aebischer, P., and Zurn, A. D. (2002). Glial cell line-derived neurotrophic factor released by synthetic guidance channels promotes facial nerve regeneration in the rat. *J. Neurosci. Res.* 70, 746–755. doi: 10.1002/jnr.10434

Barrese, J. C., Rao, N., Paroo, K., Triebwasser, C., Vargas-Irwin, C., Franquemont, L., et al. (2013). Failure mode analysis of silicon-based intracortical microelectrode arrays in non-human primates. *J. Neural Eng.* 10, 066014. doi: 10.1088/1741-2560/10/6/066014

Barros, C. S., Franco, S. J., and Müller, U. (2011). Extracellular matrix: functions in the nervous system. *Cold Spring Harb. Perspect. Biol.* 3, 1–24. doi: 10.1101/cshperspect.a005108

Bartlett, P., Baumberg, J., Birkin, P. R., Ghanem, M., and Netti, M. (2002). Highly ordered macroporous gold and platinum films formed by electrochemical deposition through templates assembled from submicron diameter monodisperse polystyrene spheres. *Chem. Mater.* 14, 2199–2208. doi: 10.1021/cm011272j

Bhatheja, K., and Field, J. (2006). Schwann cells: origins and role in axonal maintenance and regeneration. *Int. J. Biochem. Cell Biol.* 38, 1995–1999. doi: 10.1016/j.biocel.2006.05.007

Bianco, A., Kostarelos, K., Partidos, C. D., and Prato, M. (2005). Biomedical applications of functionalised carbon nanotubes. *Chem. Commun.* 571–577. doi: 10.1039/B410943K

Bidez, P. R., Li, S., Macdiarmid, A. G., Venancio, E. C., Wei, Y., and Lelkes, P. I. (2006). Polyaniline, an electroactive polymer, supports adhesion and proliferation of cardiac myoblasts. *J. Biomater. Sci. Polym. Ed.* 17, 199–212. doi: 10.1163/156856206774879180

Biran, R., Martin, D. C., and Tresco, P. A. (2005). Neuronal cell loss accompanies the brain tissue response to chronically implanted silicon microelectrode arrays. *Exp. Neurol.* 195, 115–126. doi: 10.1016/j.expneurol.2005.04.020

Blau, A. (2013). Cell adhesion promotion strategies for signal transduction enhancement in microelectrode array in vitro electrophysiology: an introductory overview and critical discussion. *Curr. Opin. Colloid Interface Sci.* 18, 481–492. doi: 10.1016/j.cocis.2013.07.005

Bloch, J., Fine, E. G., Bouche, N., Zurn, A. D., and Aebischer, P. (2001). Nerve Growth Factor- and Neurotrophin-3-releasing guidance channels promote regeneration of the transected rat dorsal root. *Exp. Neurol.* 172, 425–432. doi: 10.1006/exnr.2001.7778

Bolin, M. H., Svennersten, K., Wang, X., Chronakis, I. S., Richter-Dahlfors, A., Jager, E. W. H., et al. (2009). Nano-fiber scaffold electrodes based on PEDOT for cell stimulation. *Sens. Actuators B Chem.* 142, 451–456. doi: 10.1016/j.snb.2009.04.062

Boretius, T., Schuettler, M., and Stieglitz, T. (2011). On the stability of polyethylenedioxythiopene as coating material for active neural implants. *Artif. Organs* 35, 245–248. doi: 10.1111/j.1525-1594.2011.01210.x

Bottini, M., Bruckner, S., Nika, K., Bottini, N., Bellucci, S., Magrini, A., et al. (2006). Multi-walled carbon nanotubes induce T lymphocyte apoptosis. *Toxicol. Lett.* 160, 121–126. doi: 10.1016/j.toxlet.2005.06.020

Brummer, S. B., Robblee, L. S., and Hambrecht, F. T. (1983). Criteria for selecting electrodes for electrical stimulation: theoretical and practical considerations. *Ann. N. Y. Acad. Sci.* 405, 159–171. doi: 10.1111/j.1749-6632.1983.tb31628.x

Burdick, J. A., Ward, M., Liang, E., Young, M. J., and Langer, R. (2006). Stimulation of neurite outgrowth by neurotrophins delivered from degradable hydrogels. *Biomaterials* 27, 452–459. doi: 10.1016/j.biomaterials.2005.06.034

Campbell, T. E., Hodgson, A. J., and Wallace, G. G. (1999). Incorporation of erythrocytes into polypyrrole to form the basis of a biosensor to screen for rhesus (d) blood groups and rhesus (D) antibodies. *Electroanalysis* 11, 215–222. doi: 10.1002/(SICI)1521-4109(199904)11:4<215::AID-ELAN215>3.0.CO;2-#

Capadona, J. R., Shanmuganathan, K., Tyler, D. J., Rowan, S. J., and Weder, C. (2008). Stimuli-responsive polymer nanocomposites inspired by the sea cucumber dermis. *Science* 319, 1370-1374. doi: 10.1126/science.1153307

Chan, G., and Mooney, D. J. (2008). New materials for tissue engineering: towards greater control over the biological response. *Trends Biotechnol.* 26, 382–392. doi: 10.1016/j.tibtech.2008.03.011

Chen, Z., Ren, W., Gao, L., Liu, B., Pei, S., and Cheng, H.-M. (2011). Three-dimensional flexible and conductive interconnected graphene networks grown by chemical vapour deposition. *Nat. Mater.* 10, 424–428. doi: 10.1038/nmat3001

Cheung, K. C. (2007). Implantable microscale neural interfaces. *Biomed. Microdev.* 9, 923–938. doi: 10.1007/s10544-006-9045-z

Chikar, J. A., Hendricks, J. L., Richardson-Burns, S. M., Raphael, Y., Pfingst, B. E., and Martin, D. C. (2012). The use of a dual PEDOT and RGD-functionalized alginate hydrogel coating to provide sustained drug delivery and improved cochlear implant function. *Biomaterials* 33, 1982–1990. doi: 10.1016/j.biomaterials.2011.11.052

Cogan, S. F. (2008). Neural Stimulation and Recording Electrodes. *Annu. Rev. Biomed. Eng.* 10, 275–309. doi: 10.1146/annurev.bioeng.10.061807.160518

Cogan, S. F., Peramunage, D., Smirnov, A., Ehrlich, J., Mccreery, D. B., and Manoonkitiwongsa, P. S. (2007). *Polyethylenedioxythiophene (PEDOT) Coatings for Neural Stimulation and Recording Electrodes.* Norwood: EIC Laboratories, Inc.

Cogan, S. F., Troyk, P. R., Ehrlich, J., and Plante, T. D. (2005). In vitro comparison of the charge-injection limits of activated iridium oxide (AIROF) and platinum-iridium microelectrodes. *Biomed. Eng. IEEE Trans.* 52, 1612–1614. doi: 10.1109/TBME.2005.851503

Collier, J. H., Camp, J. P., Hudson, T. W., and Schmidt, C. E. (2000). Synthesis and characterization of polypyrrole–hyaluronic acid composite biomaterials for tissue engineering applications. *J. Biomed. Mater. Res.* 50, 574–584. doi: 10.1002/(SICI)1097-4636(20000615)50:4<574::AID-JBM13>3.0.CO;2-I

Collinger, J. L., Foldes, S., Bruns, T. M., Wodlinger, B., Gaunt, R., and Weber, D. J. (2013). Neuroprosthetic technology for individuals with spinal cord injury. *J. Spinal Cord Med.* 36, 258–272. doi: 10.1179/2045772313Y.0000000128

Cui, X., and Martin, D. C. (2003). Electrochemical deposition and characterization of poly(3,4-ethylenedioxythiophene) on neural microelectrode arrays. *Sens. Actuators B Chem.* 89, 92–102. doi: 10.1016/S0925-4005(02)00448-3

Cui, X., Wiler, J., Dzaman, M., Altschuler, R. A., and Martin, D. C. (2003). In vivo studies of polypyrrole/peptide coated neural probes. *Biomaterials* 24, 777–787. doi: 10.1016/S0142-9612(02)00415-5

Cui, X. T., Hetke, J. F., Wiler, J. A., Anderson, D. J., and Martin, D. C. (2001a). Electrochemical deposition and characterization of conducting polymer polypyrrole/PSS on multichannel neural probes. *Sens. Actuators A Phys.* 93, 8–18. doi: 10.1016/S0924-4247(01)00637-9

Cui, X. T., Lee, V. A., Raphael, Y., Wiler, J. A., Hetke, J. F., Anderson, D. J., et al. (2001b). Surface modification of neural recording electrodes with conducting polymer/biomolecule blends. *J. Biomed. Mater. Res.* 56, 261–272. doi: 10.1002/1097-4636(200108)56:2<261::AID-JBM1094>3.0.CO;2-I

Daud, M. F. B., Pawar, K. C., Claeyssens, F., Ryan, A. J., and Haycock, J. W. (2012). An aligned 3D neuronal-glial co-culture model for peripheral nerve studies. *Biomaterials* 33, 5901–5913. doi: 10.1016/j.biomaterials.2012.05.008

David-Pur, M., Bareket-Keren, L., Beit-Yaakov, G., Raz-Prag, D., and Hanein, Y. (2013). All-carbon-nanotube flexible multi-electrode array for neuronal recording and stimulation. *Biomed. Microdev.* 1–11. doi: 10.1007/s10544-013-9804-6

De Volder, M. F. L., Tawfick, S. H., Baughman, R. H., and Hart, A. J. (2013). Carbon nanotubes: present and future commercial applications. *Science* 339, 535–539. doi: 10.1126/science.1222453

DeLong, S. A., Gobin, A. S., and West, J. L. (2005). Covalent immobilization of RGDS on hydrogel surfaces to direct cell alignment and migration. *J. Control. Release* 109, 139–148. doi: 10.1016/j.jconrel.2005.09.020

Drury, J. L., and Mooney, D. J. (2003). Hydrogels for tissue engineering: scaffold design variables and applications. *Biomaterials* 24, 4337–4351. doi: 10.1016/S0142-9612(03)00340-5

Evans, A. J., Thompson, B. C., Wallace, G. G., Millard, R., O'Leary, S. J., Clark, G. M., et al. (2009). Promoting neurite outgrowth from spiral ganglion neuron explants using polypyrrole/BDNF-coated electrodes. *J. Biomed. Mater. Res. A* 91A, 241–250. doi: 10.1002/jbm.a.32228

Fan, Y. W., Cui, F. Z., Hou, S. P., Xu, Q. Y., Chen, L. N., and Lee, I. S. (2002). Culture of neural cells on silicon wafers with nano-scale surface topograph. *J. Neurosci. Methods* 120, 17–23. doi: 10.1016/S0165-0270(02)00181-4

Fieberg, A., and Reis, O. (2002). UV curable electrodeposition systems. *Prog. Org. Coat.* 45, 239–247. doi: 10.1016/S0300-9440(02)00065-6

Fine, E. G., Decosterd, I., Papaloïzos, M., Zurn, A. D., and Aebischer, P. (2002). GDNF and NGF released by synthetic guidance channels support sciatic nerve regeneration across a long gap. *Eur. J. Neurosci.* 15, 589–601. doi: 10.1046/j.1460-9568.2002.01892.x

Fitch, M. T., and Silver, J. (1997). Activated macrophages and the blood–brain barrier: inflammation after cns injury leads to increases in putative inhibitory molecules. *Exp. Neurol.* 148, 587–603. doi: 10.1006/exnr.1997.6701

Fitch, M. T., and Silver, J. (2008). CNS injury, glial scars, and inflammation: inhibitory extracellular matrices and regeneration failure. *Exp. Neurol.* 209, 294–301. doi: 10.1016/j.expneurol.2007.05.014

Fonner, J. M., Forciniti, L., Nguyen, H., Byrne, J. D., Kou, Y.-F., Syeda-Nawaz, J., et al. (2008). Biocompatibility implications of polypyrrole synthesis techniques. *Biomed. Mater.* 3:034124. doi: 10.1088/1748-6041/3/3/034124

Fujita, K., Lazarovici, P., and Guroff, G. (1989). Regulation of the differentiation of PC12 pheochromocytoma cells. *Environ. Health Perspect.* 80, 127–142. doi: 10.1289/ehp.8980127

Gabay, T., Ben-David, M., Kalifa, I., Sorkin, R., Abrams, Z. R., Ben-Jacob, E., et al. (2007). Electro-chemical and biological properties of carbon nanotube based multi-electrode arrays. *Nanotechnology* 18, 035201. doi: 10.1088/0957-4484/18/3/035201

Geddes, L. A., and Roeder, R. (2003). Criteria for the selection of materials for implanted electrodes. *Ann. Biomed. Eng.* 31, 879–890. doi: 10.1114/1.1581292

Georgakilas, V., Kordatos, K., Prato, M., Guldi, D. M., Holzinger, M., and Hirsch, A. (2002). Organic functionalization of carbon nanotubes. *J. Am. Chem. Soc.* 124, 760–761. doi: 10.1021/ja016954m

George, P. M., Lyckman, A. W., Lavan, D. A., Hegde, A., Leung, Y., Avasare, R., et al. (2005). Fabrication and biocompatibility of polypyrrole implants suitable for neural prosthetics. *Biomaterials* 26, 3511–3519. doi: 10.1016/j.biomaterials.2004.09.037

Georges, P. C., Miller, W. J., Meaney, D. F., Sawyer, E. S., and Janmey, P. A. (2006). Matrices with compliance comparable to that of brain tissue select neuronal over glial growth in mixed cortical cultures. *Biophys. J.* 90, 3012–3018. doi: 10.1529/biophysj.105.073114

Gillespie, L. N., Clark, G. M., Bartlett, P. F., and Marzella, P. L. (2003). BDNF-induced survival of auditory neurons in vivo: cessation of treatment leads to accelerated loss of survival effects. *J. Neurosci. Res.* 71, 785–790. doi: 10.1002/jnr.10542

Gilmour, A. D., Green, R. A., and Thomson, C. E. (2013). A low-maintenance, primary cell culture model for the assessment of carbon nanotube toxicity. *Toxicol. Environ. Chem.* 95, 1129–1144. doi: 10.1080/02772248.2013.844429

Green, R. A., Baek, S., Poole-Warren, L. A., and Martens, P. J. (2010a). Conducting polymer-hydrogels for medical electrode applications. *Sci. Technol. Adv. Mater.* 11, 014107. doi: 10.1088/1468-6996/11/1/014107

Green, R. A., Hassarati, R. T., Bouchinet, L., Lee, C. S., Cheong, G. L.M., Yu, J. F., et al. (2012a). Substrate dependent stability of conducting polymer coatings on medical electrodes. *Biomaterials* 33, 5875–5886. doi: 10.1016/j.biomaterials.2012.05.017

Green, R. A., Hassarati, R. T., Goding, J. A., Baek, S., Lovell, N. H., Martens, P. J., et al. (2012b). Conductive hydrogels: mechanically robust hybrids for use as biomaterials. *Macromol. Biosci.* 12, 494–501. doi: 10.1002/mabi.201100490

Green, R. A., Lim, K. S., Henderson, W. C., Hassarati, R. T., Martens, P. J., Lovell, N. H., et al. (2013a). "Living electrodes: tissue engineering the neural interface," in *Engineering in Medicine and Biology Society (EMBC), 2013 35th Annual International Conference of the IEEE)*, Osaka, 6957–6960.

Green, R. A., Lovell, N. H., and Poole-Warren, L. A. (2009). Cell attachment functionality of bioactive conducting polymers for neural interfaces. *Biomaterials* 30, 3637–3644. doi: 10.1016/j.biomaterials.2009.03.043

Green, R. A., Lovell, N. H., and Poole-Warren, L. A. (2010b). Impact of co-incorporating laminin peptide dopants and neurotrophic growth factors on conducting polymer properties. *Acta Biomater.* 6, 63–71. doi: 10.1016/j.actbio.2009.06.030

Green, R. A., Lovell, N. H., Wallace, G. G., and Poole-Warren, L. A. (2008a). Conducting polymers for neural interfaces: challenges in developing an effective long-term implant. *Biomaterials* 29, 3393–3399. doi: 10.1016/j.biomaterials.2008.04.047

Green, R. A., Matteucci, P. B., Hassarati, R. T., Giraud, B., Dodds, C. W., Chen, S., et al. (2013b). Performance of conducting polymer electrodes for stimulating neuroprosthetics. *J. Neural Eng.* 10, 016009. doi: 10.1088/1741-2560/10/1/016009

Green, R. A., Ordonez, J. S., Schuettler, M., Poole-Warren, L. A., Lovell, N. H., and Suaning, G. J. (2010c). Cytotoxicity of implantable microelectrode arrays produced by laser micromachining. *Biomaterials* 31, 886–893. doi: 10.1016/j.biomaterials.2009.09.099

Green, R. A., Toor, H., Dodds, C., and Lovell, N. H. (2012c). Variation in performance of platinum electrodes with size and surface roughness. *Sens. Mater.* 24, 15.

Green, R. A., Williams, C. M., Lovell, N. H., and Poole-Warren, L. A. (2008b). Novel neural interface for implant electrodes: improving electroactivity of polypyrrole through MWNT incorporation. *J. Mater. Sci. Mater. Med.* 19, 1625–1629. doi: 10.1007/s10856-008-3376-7

Guimard, N. K., Gomez, N., and Schmidt, C. E. (2007). Conducting polymers in biomedical engineering. *Prog. Polym. Sci.* 32, 876–921. doi: 10.1016/j.progpolymsci.2007.05.012

Gumbiner, B. M. (1996). Cell adhesion: the molecular basis of tissue architecture and morphogenesis. *Cell* 84, 345–357. doi: 10.1016/S0092-8674(00)81279-9

Haghighi, B., and Bozorgzadeh, S. (2011). Fabrication of a highly sensitive electrochemiluminescence lactate biosensor using ZnO nanoparticles decorated multiwalled carbon nanotubes. *Talanta* 85, 2189–2193. doi: 10.1016/j.talanta.2011.07.071

Hallab, N. J., Bundy, K. J., O'Connor, K., Moses, R. L., and Jacobs, J. J. (2001). Evaluation of metallic and polymeric biomaterial surface energy and surface roughness characteristics for directed cell adhesion. *Tissue Eng.* 7, 6. doi: 10.1089/107632700300003297

Hascup, E. R., Af Bjerkén, S., Hascup, K. N., Pomerleau, F., Huettl, P., Strömberg, I., et al. (2009). Histological studies of the effects of chronic implantation of ceramic-based microelectrode arrays and microdialysis probes in rat prefrontal cortex. *Brain Res.* 1291, 12–20. doi: 10.1016/j.brainres.2009.06.084

Hassarati, R., Dueck, W., Tasche, C., Carter, P., Poole-Warren, L., and Green, R. (2014). Improving Cochlear implant properties through conductive hydrogel coatings. *IEEE Trans. Neural Syst. Rehabil. Eng.* 22, 411–418. doi: 10.1109/TNSRE.2014.2304559

Hassler, C., Boretius, T., and Stieglitz, T. (2011). Polymers for neural implants. *J. Polym. Sci. B Polym. Phys.* 49, 18–33. doi: 10.1002/polb.22169

He, W., Mcconnell, G. C., Schneider, T. M., and Bellamkonda, R. V. (2007). A Novel Anti-inflammatory Surface for Neural Electrodes. *Adv. Mater.* 19, 3529–3533. doi: 10.1002/adma.200700943

Heim, M., Yvert, B., and Kuhn, A. (2012). Nanostructuration strategies to enhance microelectrode array (MEA) performance for neuronal recording and stimulation. *J. Physiol.* 106, 137–145. doi: 10.1016/j.jphysparis.2011.10.001

Higashimori, H., and Yang, Y. (2012). Imaging analysis of neuron to glia interaction in microfluidic culture platform (MCP)-based neuronal axon and glia co-culture system. *J. Vis. Exp.* 4448. doi: 10.3791/4448

Hoffman, A. S. (2002). Hydrogels for biomedical applications. *Adv. Drug Deliv. Rev.* 54, 3–12. doi: 10.1016/S0169-409X(01)00239-3

Houweling, D. A., Lankhorst, A. J., Gispen, W. H., Bär, P. R., and Joosten, E. A. J. (1998). Collagen containing neurotrophin-3 (NT-3) attracts regrowing injured corticospinal axons in the adult rat spinal cord and promotes partial functional recovery. *Exp. Neurol.* 153, 49–59. doi: 10.1006/exnr.1998.6867

Hsu, H.-L., Teng, I. J., Chen, Y.-C., Hsu, W.-L., Lee, Y.-T., Yen, S.-J., et al. (2010). Flexible UV-ozone-modified carbon nanotube electrodes for neuronal recording. *Adv. Mater.* 22, 2177–2181. doi: 10.1002/adma.200903413

Huang, J., Virji, S., Weiller, B. H., and Kaner, R. B. (2004). Nanostructured polyaniline sensors. *Chemistry* 10, 1314–1319. doi: 10.1002/chem.200305211

Humayun, M. S., Weiland, J. D., Fujii, G. Y., Greenberg, R., Williamson, R., Little, J., et al. (2003). Visual perception in a blind subject with a chronic microelectronic retinal prosthesis. *Vision Res.* 43, 2573–2581. doi: 10.1016/S0042-6989(03)00457-7

Jain, A., Kim, Y.-T., Mckeon, R. J., and Bellamkonda, R. V. (2006). In situ gelling hydrogels for conformal repair of spinal cord defects, and local delivery of BDNF after spinal cord injury. *Biomaterials* 27, 497–504. doi: 10.1016/j.biomaterials.2005.07.008

Jhaveri, S. J., Hynd, M. R., Dowell-Mesfin, N., Turner, J. N., Shain, W., and Ober, C. K. (2008). Release of nerve growth factor from HEMA hydrogel-coated substrates and its effect on the differentiation of neural cells. *Biomacromolecules* 10, 174–183. doi: 10.1021/bm801101e

Johnson, M. I., Higgins, D., and Ard, M. D. (1989). Astrocytes induce dendritic development in cultured sympathetic neurons. *Dev. Brain Res.* 47, 289–292. doi: 10.1016/0165-3806(89)90184-3

Kagan, V. E., Tyurina, Y. Y., Tyurin, V. A., Konduru, N. V., Potapovich, A. I., Osipov, A. N., et al. (2006). Direct and indirect effects of single walled carbon nanotubes on RAW 264.7 macrophages: role of iron. *Toxicol. Lett.* 165, 88–100. doi: 10.1016/j.toxlet.2006.02.001

Keefer, E. W., Botterman, B. R., Romero, M. I., Rossi, A. F., and Gross, G. W. (2008). Carbon nanotube coating improves neuronal recordings. *Nat. Nano* 3, 434–439. doi: 10.1038/nnano.2008.174

Kim, D. H., Abidian, M., and Martin, D. C. (2004). Conducting polymers grown in hydrogel scaffolds coated on neural prosthetic devices. *J. Biomed. Mater. Res. A* 71, 577–585. doi: 10.1002/jbm.a.30124

Kim, D.-H., and Martin, D. C. (2006). Sustained release of dexamethasone from hydrophilic matrices using PLGA nanoparticles for neural drug delivery. *Biomaterials* 27, 3031–3037. doi: 10.1016/j.biomaterials.2005.12.021

Kim, D.-H., Wiler, J. A., Anderson, D. J., Kipke, D. R., and Martin, D. C. (2010). Conducting polymers on hydrogel-coated neural electrode provide sensitive neural recordings in auditory cortex. *Acta Biomater.* 6, 57–62. doi: 10.1016/j.actbio.2009.07.034

Kim, D. H., Richardson-Burns, S., Povlich, L., Abidian, M. R., Spanninga, S., Hendricks, J. L., et al. (2008). "Soft, fuzzy, and bioactive conducting polymers for improving the chronic performance of neural prosthetic devices," in *Indwelling Neural Implants: Strategies for Contending with the In Vivo Environment*, ed. W. M. Reichert (Boca Raton, FL: CRC Press), 165–207.

Kim, D. H., Richardson-Burns, S. M., Hendricks, J. L., Sequera, C., and Martin, D. C. (2007). Effect of immobilized nerve growth factor on conductive polymers: electrical properties and cellular response. *Adv. Funct. Mater.* 17, 79–86. doi: 10.1002/adfm.200500594

Kim, Y.-T., and Romero-Ortega, M. I. (2012). Material considerations for peripheral nerve interfacing. *MRS Bull.* 37, 573–580. doi: 10.1557/mrs.2012.99

Krishnan, A., Dujardin, E., Ebbesen, T. W., Yianilos, P. N., and Treacy, M. M. J. (1998). Young's modulus of single-walled nanotubes. *Phys. Rev. B* 58, 14013–14019. doi: 10.1103/PhysRevB.58.14013

Kurisawa, M., Chung, J. E., Yang, Y. Y., Gao, S. J., and Uyama, H. (2005). Injectable biodegradable hydrogels composed of hyaluronic acid-tyramine conjugates for drug delivery and tissue engineering. *Chem. Commun.* 4312–4314. doi: 10.1039/B506989K

Labaye, D. E., Jérôme, C., Geskin, V. M., Louette, P., Lazzaroni, R., Martinot, L., et al. (2002). Full electrochemical synthesis of conducting polymer films chemically grafted to conducting surfaces. *Langmuir* 18, 5222–5230. doi: 10.1021/la011439n

Lacour, S. P., Benmerah, S., Tarte, E., Fitzgerald, J., Serra, J., Mcmahon, S., et al. (2010). Flexible and stretchable micro-electrodes for in vitro and in vivo neural interfaces. *Med. Biol. Eng. Comput.* 48, 945–954. doi: 10.1007/s11517-010-0644-8

LaVan, D. A., George, P. M., and Langer, R. (2003). Simple, three-dimensional microfabrication of electrodeposited structures. *Angew. Chem. Int. Ed. Engl.* 42, 1262–1265. doi: 10.1002/anie.200390323

Leach, J. B., Achyuta A. K. A., and Murthy, S. K. (2010). Bridging the Divide between Neuroprosthetic Design, Tissue Engineering and Neurobiology. *Front. Neuroeng.* 2:19. doi: 10.3389/neuro.16.018.2009

Lee, A. C., Yu, V. M., Lowe Iii, J. B., Brenner, M. J., Hunter, D. A., Mackinnon, S. E., et al. (2003). Controlled release of nerve growth factor enhances sciatic nerve regeneration. *Exp. Neurol.* 184, 295–303. doi: 10.1016/S0014-4886(03)00258-9

Lee, F., Chung, J. E., and Kurisawa, M. (2008). An injectable enzymatically crosslinked hyaluronic acid-tyramine hydrogel system with independent tuning of mechanical strength and gelation rate. *Soft Matter* 4, 880–887. doi: 10.1039/B719557E

Lee, K. Y., and Mooney, D. J. (2001). Hydrogels for tissue engineering. *Chem. Rev.* 101, 1869–1880. doi: 10.1021/cr000108x

LeRoux, M. A., Guilak, F., and Setton, L. A. (1999). Compressive and shear properties of alginate gel: effects of sodium ions and alginate concentration. *J. Biomed. Mater. Res.* 47, 46–53. doi: 10.1002/(SICI)1097-4636(199910)47:1<46::AID-JBM6>3.0.CO;2-N

Letherby, M. R., and Young, D. A. (1981). The gelation of agarose. *J. Chem. Soc.* 77, 1953–1966. doi: 10.1039/F19817701953

Li, Y.-T., Chang, C.-H., Chen, J.-J. J., Wang, C.-C., and Liang, C.-K. (2005). Dvelopment of implantable wireless biomicrosystem for measuring electrode-tissue impedance. *J. Med. Biol. Eng.* 25, 6.

Li, Y., and Mogul, D. J. (2007). Electrical control of epileptic seizures. *J. Clin. Neurophysiol.* 24, 197–204. doi: 10.1097/WNP.0b013e31803991c3

Lim, K. S., Alves, M. H., Poole-Warren, L. A., and Martens, P. J. (2013). Covalent incorporation of non-chemically modified gelatin into degradable PVA-tyramine hydrogels. *Biomaterials* 34, 7097–7105. doi: 10.1016/j.biomaterials.2013.06.005

Lim, K. S., Kundu, J., Reeves, A., Poole-Warren, L. A., Kundu, S. C., and Martens, P. J. (2012). The influence of silkworm species on cellular interactions with novel pva/silk sericin hydrogels. *Macromol. Biosci.* 12, 322–332. doi: 10.1002/mabi.201100292

Lin, C.-M., Lee, Y.-T., Yeh, S.-R., and Fang, W. (2009). Flexible carbon nanotubes electrode for neural recording. *Biosens. Bioelectron.* 24, 2791–2797. doi: 10.1016/j.bios.2009.02.005

Liu, S. Q., Yang, C., Huang, Y., Ding, X., Li, Y., Fan, W. M., et al. (2012). Antimicrobial and antifouling hydrogels formed in situ from polycarbonate and poly(ethylene glycol) via Michael addition. *Adv. Mater.* 24, 6484–6489. doi: 10.1002/adma.201202225

Lozano, A. M., and Lipsman, N. (2013). Probing and regulating dysfunctional circuits using deep brain stimulation. *Neuron* 77, 406–424. doi: 10.1016/j.neuron.2013.01.020

Lu, Y., Wang, D., Li, T., Zhao, X., Cao, Y., Yang, H., et al. (2009). Poly(vinyl alcohol)/poly(acrylic acid) hydrogel coatings for improving electrode–neural tissue interface. *Biomaterials* 30, 4143–4151. doi: 10.1016/j.biomaterials.2009.04.030

Ludwig, K. A., Langhals, N. B., Joseph, M. D., Richardson-Burns, S. M., Hendricks, J. L., and Kipke, D. R. (2011). Poly(3,4-ethylenedioxythiophene) (PEDOT) polymer coatings facilitate smaller neural recording electrodes. *J. Neural Eng.* 8, 014001. doi: 10.1088/17412560/8/1/014001

Ludwig, K. A., Uram, J. D., Yang, J., Martin, D. C., and Kipke, D. R. (2006). Chronic neural recordings using silicon microelectrode arrays electrochemically deposited with a poly(3,4-ethylenedioxythiophene) (PEDOT) film. *J. Neural Eng.* 3, 59–70. doi: 10.1088/1741-2560/3/1/007

Luo, S.-C., Sekine, J., Zhu, B., Zhao, H., Nakao, A., and Yu, H.-H. (2012). Polydioxythiophene nanodots, nonowires, nano-networks, and tubular structures: the effect of functional groups and temperature in template-free electropolymerization. *ACS Nano* 6, 3018–3026. doi: 10.1021/nn300737e

Luo, X., Matranga, C., Tan, S., Alba, N., and Cui, X. T. (2011a). Carbon nanotube nanoreservior for controlled release of anti-inflammatory dexamethasone. *Biomaterials* 32, 6316–6323. doi: 10.1016/j.biomaterials.2011.05.020

Luo, X., Weaver, C. L., Zhou, D. D., Greenberg, R., and Cui, X. T. (2011b). Highly stable carbon nanotube doped poly(3,4-ethylenedioxythiophene) for chronic neural stimulation. *Biomaterials* 32, 5551–5557. doi: 10.1016/j.biomaterials.2011.04.051

Ma, W., Fitzgerald, W., Liu, Q.-Y., O'Shaughnessy, T., Maric, D., Lin, H., et al. (2004). CNS stem and progenitor cell differentiation into functional neuronal circuits in three-dimensional collagen gels. *Exp. Neurol.* 190, 276–288. doi: 10.1016/j.expneurol.2003.10.016

Mahadevappa, M., Weiland, J. D., Yanai, D., Fine, I., Greenberg, R. J., and Humayun, M. S. (2005). Perceptual thresholds and electrode impedance in three retinal prosthesis subjects. *IEEE Trans. Neural Syst. Rehabil. Eng.* 13, 201–206. doi: 10.1109/TNSRE.2005.848687

Majumdar, D., Gao, Y., Li, D., and Webb, D. J. (2011). Co-culture of neurons and glia in a novel microfluidic platform. *J. Neurosci. Methods* 196, 38–44. doi: 10.1016/j.jneumeth.2010.12.024

Mao, C., and Kisaalita, W. S. (2004). Characterization of 3-D collagen hydrogels for functional cell-based biosensing. *Biosens. Bioelectron.* 19, 1075–1088. doi: 10.1016/j.bios.2003.10.008

Mario Cheong, G., Lim, K. S., Jakubowicz, A., Martens, P. J., Poole-Warren, L. A., and Green, R. A. (2013). Conductive hydrogels with tailored bioactivity for implantable electrode coatings. *Acta Biomater.* 10, 1216–1226. doi: 10.1016/j.actbio.2013.12.032

Martin, D. C., and Feldman, K. E. (2012). *Substituted 3,4-Propylenedioxythiophene Monomers and 3,4-Propylenedioxythiophene-Based Crosslinkers And Polymers Thereof.* Google Patents).

Matsumoto, K., Sato, C., Naka, Y., Kitazawa, A., Whitby, R. L.D., and Shimizu, N. (2007). Neurite outgrowths of neurons with neurotrophin-coated carbon nanotubes. *J. Biosci. Bioeng.* 103, 216–220. doi: 10.1263/jbb.103.216

McConnell, G. C., Rees, H. D., Levey, A. I., Gutekunst, C. A., Gross, R. E., and Bellamkonda, R. V. (2009). Implanted neural electrodes cause chronic, local inflammation that is correlated with local neurodegeneration. *J. Neural Eng.* 6, 056003. doi: 10.1088/1741-2560/6/5/056003

McCreery, D. B. (2008). Cochlear nucleus auditory prostheses. *Hear. Res.* 242, 64–73. doi: 10.1016/j.heares.2007.11.014

McCreery, D. B., Yuen, T. G. H., Agnew, W. F., and Bullara, L. A. (1997). A characterization of the effects on neuronal excitability due to prolonged microstimulation with chronically implanted microelectrodes. *IEEE Trans. Biomed. Eng.* 44, 931–939. doi: 10.1109/10.634645

Merker, J., Lupton, D., Töpfer, M., and Knake, H. (2001). High temperature mechanical properties of the platinum group metals. *Plat. Metals Rev.* 45, 74–82.

Merrill, D. R., Bikson, M., and Jefferys, J. G. R. (2005). Electrical stimulation of excitable tissue: design of efficacious and safe protocols. *J. Neurosci. Methods* 141, 171–198. doi: 10.1016/j.jneumeth.2004.10.020

Nakayama, Y., and Matsuda, T. (1995). Surface microarchitectural design in biomedical applications: preparation of microporous polymer surfaces by an excimer laser ablation technique. *J. Biomed. Mater. Res.* 29, 1295–1301. doi: 10.1002/jbm.820291017

Nguyen-Vu, T. D. B., Chen, H., Cassell, A. M., Andrews, R. J., Meyyappan, M., and Li, J. (2006). Vertically aligned carbon nanofiber arrays: an advance toward electrical–neural interfaces. *Small* 2, 89–94. doi: 10.1002/smll.200500175

Nguyen-Vu, T. D. B., Chen, H., Cassell, A. M., Andrews, R. J., Meyyappan, M., and Li, J. (2007). Vertically Aligned Carbon Nanofiber Architecture as a Multifunctional 3-D Neural Electrical Interface. *IEEE Trans. Biomed. Eng.* 54, 1121–1128. doi: 10.1109/TBME.2007.891169

Nicodemus, G. D., and Bryant, S. J. (2008). Cell encapsulation in biodegradable hydrogels for tissue engineering applications. *Tissue Eng. B Rev.* 14, 16 doi: 10.1089/ten.teb.2007.0332

Niina, O., Hirotaka, T., Yoshiuki, K., Toshiya, K., Risato, K., Tetsu, T., et al. (2011). Comparison of electrode materials for the use of retinal prosthesis. *Biomed. Mater. Eng.* 21, 83–97. doi: 10.3233/BME-2011-0658

Nilasaroya, A., Poole-Warren, L. A., Whitelock, J. M., and Jo Martens, P. (2008). Structural and functional characterisation of poly(vinyl alcohol) and heparin hydrogels. *Biomaterials* 29, 4658–4664. doi: 10.1016/j.biomaterials.2008.08.011

Normand, V., Lootens, D. L., Amici, E., Plucknett, K. P., and Aymard, P. (2000). New insight into agarose gel mechanical properties. *Biomacromolecules* 1, 730–738. doi: 10.1021/bm005583j

Normann, R. A. (2007). Technology insight: future neuroprosthetic therapies for disorders of the nervous system. *Nat. Clin. Pract. Neurol.* 3, 444–452. doi: 10.1038/ncpneuro0556

Novikova, L. N., Mosahebi, A., Wiberg, M., Terenghi, G., Kellerth, J.-O., and Novikov, L. N. (2006). Alginate hydrogel and matrigel as potential cell carriers for neurotransplantation. *J. Biomed. Mater. Res. A* 77A, 242–252. doi: 10.1002/jbm.a.30603

Ochiai, H., Shibata, H., Sawa, Y., and Katoh, T. (1980). "Living electrode" as a long-lived photoconverter for biophotolysis of water. *Proc. Natl. Acad. Sci. U.S.A.* 77, 2442–2444. doi: 10.1073/pnas.77.5.2442

Ochiai, H., Shibata, H., Sawa, Y., Shoga, M., and Ohta, S. (1983). Properties of semiconductor electrodes coated with living films of cyanobacteria. *Appl. Biochem. Biotechnol.* 8, 289–303. doi: 10.1007/BF02779496

Ouyang, L., Green, R., Feldman, K. E., and Martin, D. C. (2011). "Direct local polymerization of poly(3,4-ethylene dioxythiophene in rat cortex," in *Progress in Brain Research*, eds J. Schouenborg, M. Garwicz, and N. Danielsen (Oxford: Elsevier), 263–272.

Peixoto, N., Jackson, K., Samiyi, R., and Minnikanti, S. (2009). "Charge storage: stability measures in implantable electrodes," in *Engineering in Medicine and Biology Society, 2009. Annual International Conference of the IEEE*, Farifax.

Perlmutter, J. S., and Mink, J. W. (2006). DEEP BRAIN STIMULATION. *Annu. Rev. Neurosci.* 29, 229–257. doi: 10.1146/annurev.neuro.29.051605.112824

Piantino, J., Burdick, J. A., Goldberg, D., Langer, R., and Benowitz, L. I. (2006). An injectable, biodegradable hydrogel for trophic factor delivery enhances axonal rewiring and improves performance after spinal cord injury. *Exp. Neurol.* 201, 359–367. doi: 10.1016/j.expneurol.2006.04.020

Polikov, V. S., Tresco, P. A., and Reichert, W. M. (2005). Response of brain tissue to chronically implanted neural electrodes. *J. Neurosci. Methods* 148, 1–18. doi: 10.1016/j.jneumeth.2005.08.015

Poole-Warren, L., Lovell, N. H., Baek, S., and Green, R. (2010). Development of bioactive conducting polymers for neural interfaces. *Exp. Rev. Med. Dev.* 7, 35–49. doi: 10.1586/erd.09.58

Rao, L., Zhou, H., Li, T., Li, C., and Duan, Y. Y. (2012). Polyethylene glycol-containing polyurethane hydrogel coatings for improving the biocompatibility of neural electrodes. *Acta Biomater.* 8, 2233–2242. doi: 10.1016/j.actbio.2012.03.001

Raub, C. B., Putnam, A. J., Tromberg, B. J., and George, S. C. (2010). Predicting bulk mechanical properties of cellularized collagen gels using multiphoton microscopy. *Acta Biomater.* 6, 4657–4665. doi: 10.1016/j.actbio.2010.07.004

Richardson-Burns, S. M., Hendricks, J. L., Foster, B., Povlich, L. K., Kim, D.-H., and Martin, D. C. (2007). Polymerization of the conducting polymer poly(3,4-ethylenedioxythiophene) (PEDOT) around living neural cells. *Biomaterials* 28, 1539–1552. doi: 10.1016/j.biomaterials.2006.11.026

Richardson, R. T., Thompson, B., Moulton, S., Newbold, C., Lum, M. G., Cameron, A., et al. (2007a). The effect of polypyrrole with incorporated neurotrophin-3 on the promotion of neurite outgrowth from auditory neurons. *Biomaterials* 28, 513–523. doi: 10.1016/j.biomaterials.2006.09.008

Richardson, R. T., Thompson, B., Moulton, S., Newbold, C., Lum, M. G., Cameron, A., et al. (2007b). The effect of polypyrrole with incorporated neurotrophin-3 on the promotion of neurite outgrowth from auditory neurons. *Biomaterials* 28, 513–523. doi: 10.1016/j.biomaterials.2006.09.008

Richter, A., Kruse, C., Moser, A., Hofmann, U. G., and Danner, S. (2011). Cellular modulation of polymeric device surfaces: promise of adult stem cells for neuroprosthetics. *Front. Neurosci.* 5:114. doi: 10.3389/fnins.2011.00114

Richter, A., Xie, Y., Schumacher, A., Loffler, S., Kirch, R. D., Al-Hasani, J., et al. (2013). A simple implantation method for flexible, multisite microelectrodes into rat brains. *Front. Neuroeng.* 6:6. doi: 10.3389/fneng.2013.00006

Rosario-Canales, M. R., Deria, P., Therien, M. J., and Santiago-Avilés, J. J. (2011). Composite Electronic Materials Based on Poly(3,4-propylenedioxythiophene) and Highly Charged Poly(aryleneethynylene)-Wrapped Carbon Nanotubes for Supercapacitors. *ACS Appl. Mater. Interf.* 4, 102–109. doi: 10.1021/am201041p

Rose, T. L., and Robblee, L. S. (1990). *Electrical stimulation with Pt electrodes. VIII. Electrochemically safe charge injection limits with 0.*2 ms pulses (neuronal application). *IEEE Trans. Biomed. Eng.* 37, 1118–1120. doi: 10.1109/10.61038

Rousche, P. J., Pellinen, D. S., Pivin, D. P. Jr., Williams, J. C., Vetter, R. J., et al. (2001). Flexible polyimide-based intracortical electrode arrays with bioactive capability. *IEEE Trans. Biomed. Eng.* 48, 361–371. doi: 10.1109/10.914800

Runge, M. B., Dadsetan, M., Baltrusaitis, J., Ruesink, T., Lu, L., Windebank, A. J., et al. (2010). Development of electrically conductive oligo(polyethylene glycol) fumarate-polypyrrole hydrogels for nerve regeneration. *Biomacromolecules* 11, 2845–2853. doi: 10.1021/bm100526a

Sarah, M. R.-B., Jeffrey, L. H., and David, C. M. (2007). Electrochemical polymerization of conducting polymers in living neural tissue. *J. Neural Eng.* 4, L6. doi: 10.1088/1741-2560/4/2/L02

Schmidt, C. E., Shastri, V. R., Vacanti, J. P., and Langer, R. (1997). Stimulation of neurite outgrowth using an electrically conducting polymer. *Proc. Natl. Acad. Sci. U.S.A.* 94, 8948–8953. doi: 10.1073/pnas.94.17.8948

Schuettler, M. (2007). "Electrochemical properties of platinum electrodes in vitro: comparison of six different surface qualities," in *Proceedings of the 29th Annual International Conference of the IEEE EMBS*, Freiburg.

Schuettler, M., Stiess, S., King, B. V., and Suaning, G. J. (2005). Fabrication of implantable microelectrode arrays by laser cutting of silicone rubber and platinum foil. *J. Neural Eng.* 2, S121–128. doi: 10.1088/1741-2560/2/1/013

Seidlits, S. K., Lee, J. Y., and Schmidt, C. E. (2008). Nanostructured scaffolds for neural applications. *Nanomedicine* 3, 183–199. doi: 10.2217/17435889.3.2.183

Shannon, R. V. (2012). Advances in auditory prostheses. *Curr. Opin. Neurol.* 25, 6. doi: 10.1097/WCO.0b013e32834ef878

Shepherd, R. K., Shivdasani, M. N., Nayagam, D. A. X., Williams, C. E., and Blamey, P. J. (2013). Visual prostheses for the blind. *Trends Biotechnol.* 31, 562–571. doi: 10.1016/j.tibtech.2013.07.001

Shoval, A., Adams, C., David-Pur, M., Shein, M., Hanein, Y., and Sernagor, E. (2009). Carbon nanotube electrodes for effective interfacing with retinal tissue. *Front. Neuroeng.* 2:4. doi: 10.3389/neuro.16.004.2009

Sidhu, K., Kim, J., Chayosumrit, M., Dean, S., and Sachdev, P. (2012). Alginate Microcapsule as a 3D platform for propagation and differentiation of human embryonic stem cells (hesc) to different lineages. *J. Vis. Exp.* 61, e3608. doi: 10.3791/3608

Stauffer, W. R., and Cui, X. T. (2006). Polypyrrole doped with 2 peptide sequences from laminin. *Biomaterials* 27, 2405–2413. doi: 10.1016/j.biomaterials.2005.10.024

Stevenson, G., Moulton, S. E., Innis, P. C., and Wallace, G. G. (2010). Polyterthiophene as an electrostimulated controlled drug release material of therapeutic levels of dexamethasone. *Synth. Metals* 160, 1107–1114. doi: 10.1016/j.synthmet.2010.02.035

Suri, S., and Schmidt, C. E. (2010). Cell-laden hydrogel constructs of hyaluronic acid, collagen, and laminin for neural tissue engineering. *Tissue Eng.* 16, 1703–1716. doi: 10.1089/ten.tea.2009.0381

Suzuki, I., Fukuda, M., Shirakawa, K., Jiko, H., and Gotoh, M. (2013). Carbon nanotube multi-electrode array chips for noninvasive real-time measurement of dopamine, action potentials, and postsynaptic potentials. *Biosens. Bioelectron.* 49, 1–6. doi: 10.1016/j.bios.2013.05.023

Taylor, S. J., and Sakiyama-Elbert, S. E. (2006). Effect of controlled delivery of neurotrophin-3 from fibrin on spinal cord injury in a long term model. *J. Control. Release* 116, 204–210. doi: 10.1016/j.jconrel.2006.07.005

Telford, A. M., James, M., Meagher, L., and Neto, C. (2010). Thermally cross-linked PNVP films as antifouling coatings for biomedical applications. *ACS Appl. Mater. Interfaces* 2, 2399–2408. doi: 10.1021/am100406j

Tian, F., Cui, D., Schwarz, H., Estrada, G. G., and Kobayashi, H. (2006). Cytotoxicity of single-wall carbon nanotubes on human fibroblasts. *Toxicology Vitro* 20, 1202–1212. doi: 10.1016/j.tiv.2006.03.008

Turner, J. N., Shain, W., Szarowski, D. H., Andersen, M., Martins, S., Isaacson, M., et al. (1999). Cerebral astrocyte response to micromachined silicon implants. *Exp. Neurol.* 156, 33–49. doi: 10.1006/exnr.1998.6983

Tyler, D. J., and Durand, D. M. (2002). Functionally selective peripheral nerve stimulation with a flat interface nerve electrode. *IEEE Trans. Neural Syst. Rehabil. Eng.* 10, 294–303. doi: 10.1109/TNSRE.2002.806840

Vaquette, C., Slimani, S., Kahn, C. J. F., Tran, N., Rahouadj, R., and Wang, X. (2010). A poly(lactic-co-glycolic acid) knitted scaffold for tendon tissue engineering: an in vitro and in vivo study. *J. Biomater. Sci. Polym. Ed.* 21, 1737–1760. doi: 10.1163/092050609X12560455246676

Wadhwa, R., Lagenaur, C. F., and Cui, X. T. (2006). Electrochemically controlled release of dexamethasone from conducting polymer polypyrrole coated electrode. *J. Control. Release* 110, 531–541. doi: 10.1016/j.jconrel.2005.10.027

Wang, K., Fishman, H. A., Dai, H., and Harris, J. S. (2006). Neural stimulation with a carbon nanotube microelectrode array. *Nano Lett.* 6, 2043–2048. doi: 10.1021/nl061241t

Ward, M. P., Rajdev, P., Ellison, C., and Irazoqui, P. P. (2009). Toward a comparison of microelectrodes for acute and chronic recordings. *Brain Res.* 1282, 183–200. doi: 10.1016/j.brainres.2009.05.052

Webster, T. J., Waid, M. C., Mckenzie, J. L., Price, R. L., and Ejiofor, J. U. (2004). Nano-biotechnology: carbon nanofibres as improved neural and orthopaedic implants. *Nanotechnology* 15, 48–54. doi: 10.1088/0957-4484/15/1/009

Weldon, D. T., Rogers, S. D., Ghilardi, J. R., Finke, M. P., Cleary, J. P., O'Hare, E., et al. (1998). Fibrillar β-amyloid induces microglial phagocytosis, expression of inducible nitric oxide synthase, and loss of a select population of neurons in the rat cns in vivo. *J. Neurosci.* 18, 2161–2173.

Wells, M. R., Kraus, K., Batter, D. K., Blunt, D. G., Weremowitz, J., Lynch, S. E., et al. (1997). Gel matrix vehicles for growth factor application in nerve gap injuries repaired with tubes: a comparison of biomatrix, collagen, and methylcellulose. *Exp. Neurol.* 146, 395–402. doi: 10.1006/exnr.1997.6543

Wester, B. A., Lee, R. H., and Laplaca, M. C. (2009). Development and characterization of in vivo flexible electrodes compatible with large tissue displacements. *J. Neural Eng.* 6, 024002. doi: 10.1088/1741–2560/6/2/024002

White, R. L., and Gross, T. J. (1974). An evaluation of the resistance to electrolysis of metals for use in biostimulation microprobes. *IEEE Trans. Biomed. Eng.* 21, 487–490. doi: 10.1109/TBME.1974.324339

Whitney, N. P., Eidem, T. M., Peng, H., Huang, Y., and Zheng, J. C. (2009). Inflammation mediates varying effects in neurogenesis: relevance to the pathogenesis of brain injury and neurodegenerative disorders. *J. Neurochem.* 108, 1343–1359. doi: 10.1111/j.1471-4159.2009.05886.x

World Health Organization. (2006). "Public health principles and neurological disorders," in *Neurological Disorders: Public Health Challenges.* Geneva, Switzerland: WHO Press.

Wilks, S. J., Woolley, A. J., Ouyang, L., Martin, D. C., and Otto, K. J. (2011). In vivo polymerization of poly (3, 4-ethylenedioxythiophene)(PEDOT) in rodent cerebral cortex. *Conf. Proc. IEEE Eng. Med. Biol. Soc.* 2011, 5412–5415. doi: 10.1109/IEMBS.2011.6091338

Willerth, S. M., and Sakiyama-Elbert, S. E. (2007). Approaches to neural tissue engineering using scaffolds for drug delivery. *Adv. Drug Deliv. Rev.* 59, 325–338. doi: 10.1016/j.addr.2007.03.014

Wilson, B. S., and Dorman, M. F. (2008). Cochlear implants: a remarkable past and a brilliant future. *Hear. Res.* 242, 3–21. doi: 10.1016/j.heares.2008.06.005

Winter, J. O., Cogan, S. F., and Rizzo, J. F. (2007). Neurotrophin-eluting hydrogel coatings for neural stimulating electrodes. *J. Biomed. Mater. Res.* 81B, 551–563. doi: 10.1002/jbm.b.30696

Winter, J. O., Gokhale, M., Jensen, R. J., Cogan, S. F., and Rizzo Iii, J. F. (2008). Tissue engineering applied to the retinal prosthesis: neurotrophin-eluting polymeric hydrogel coatings. *Mater. Sci. Eng. C* 28, 448–453. doi: 10.1016/j.msec.2007.04.011

Woolley, A. J., Desai, H. A., Steckbeck, M. A., Patel, N. K., and Otto, K. J. (2011). In situ characterization of the brain–microdevice interface using device capture histology. *J. Neurosci. Methods* 201, 67–77. doi: 10.1016/j.jneumeth.2011.07.012

Xiao, Y., Cui, X., Hancock, J. M., Bouguettaya, M., Reynolds, J. R., and Martin, D. C. (2004). Electrochemical polymerization of poly(hydroxymethylated-3,4-ethylenedioxythiophene) (PEDOT-MeOH) on multichannel neural probes. *Sens. Actuators B Chem.* 99, 437–443. doi: 10.1016/j.snb.2003.12.067

Xiao, Y., He, L., and Che, J. (2012). An effective approach for the fabrication of reinforced composite hydrogel engineered with SWNTs, polypyrrole and PEGDA hydrogel. *J. Mater. Chem.* 22, 8076–8082. doi: 10.1039/C2JM30601H

Yamato, H., Ohwa, M., and Wernet, W. (1995). Stability of polypyrrole and poly(3,4-ethylenedioxythiophene) for biosensor application. *J. Electroanal. Chem.* 397, 163–170. doi: 10.1016/0022-0728(95)04156-8

Yang, J., Kim, D. H., Hendricks, J. L., Leach, M., Northey, R., and Martin, D. C. (2005). Ordered surfactant-templated poly(3,4-ethylenedioxythiophene) (PEDOT) conducting polymer on microfabricated neural probes. *Acta Biomater.* 1, 125–136. doi: 10.1016/j.actbio.2004.09.006

Yang, J., and Martin, D. C. (2006). Impedance spectroscopy and nanoindentation of conducting poly(3,4-ethylenedioxythiophene) coatings on microfabricated neural prosthetic devices. *J. Mater. Res.* 21, 1124–1132. doi: 10.1557/jmr.2006.0145

Yang, S., Xia, B., Zeng, X., Luo, S., Wei, W., and Liu, X. (2010). Fabrication of DNA functionalized carbon nanotubes/Cu2+ complex by one-step electrodeposition and its sensitive determination of nitrite. *Anal. Chim. Acta* 667, 57–62. doi: 10.1016/j.aca.2010.03.063

Yu, X., and Bellamkonda, R. V. (2003). Tissue-engineered scaffolds are effective alternatives to autografts for bridging peripheral nerve gaps. *Tissue Eng.* 9, 421–430. doi: 10.1089/107632703322066606

Yu, Z., Mcknight, T. E., Ericson, M. N., Melechko, A. V., Simpson, M. L., and Morrison, B. (2007). Vertically aligned carbon nanofiber arrays record electrophysiological signals from hippocampal slices. *Nano Lett.* 7, 2188–2195. doi: 10.1021/nl070291a

Zhong, Y., and Bellamkonda, R. V. (2005). Controlled release of anti-inflammatory agent α-MSH from neural implants. *J. Control. Release* 106, 309–318. doi: 10.1016/j.jconrel.2005.05.012

Zhong, Y., and Bellamkonda, R. V. (2007). Dexamethasone-coated neural probes elicit attenuated inflammatory response and neuronal loss compared to uncoated neural probes. *Brain Res.* 1148, 15–27. doi: 10.1016/j.brainres.2007.02.024

Zhong, Y., and Bellamkonda, R. V. (2008). Biomaterials for the central nervous system. *J. R. Soc. Interface* 5, 957–975. doi: 10.1098/rsif.2008.0071

Zhong, Y., Yu, X., Gilbert, R., and Bellamkonda, R. V. (2001). Stabilizing electrode–host interfaces: a tissue engineering approach. *J. Rehabil. Res. Dev.* 38, 627–632.

Zuidema, J. M., Pap, M. M., Jaroch, D. B., Morrison, F. A., and Gilbert, R. J. (2011). Fabrication and characterization of tunable polysaccharide hydrogel blends for neural repair. *Acta Biomater.* 7, 1634–1643. doi: 10.1016/j.actbio.2010.11.039

Conflict of Interest Statement: The authors declare that the research was conducted in the absence of any commercial or financial relationships that could be construed as a potential conflict of interest.

Received: 31 January 2014; accepted: 06 May 2014; published online: 27 May 2014.
Citation: Aregueta-Robles UA, Woolley AJ, Poole-Warren LA, Lovell NH and Green RA (2014) Organic electrode coatings for next-generation neural interfaces. Front. Neuroeng. 7:15. doi: 10.3389/fneng.2014.00015
This article was submitted to the journal Frontiers in Neuroengineering.

frontiers in
NEUROENGINEERING

ORIGINAL RESEARCH ARTICLE
published: 04 February 2014
doi: 10.3389/fneng.2014.00002

Abiotic-biotic characterization of Pt/Ir microelectrode arrays in chronic implants

Abhishek Prasad[1]*, Qing-Shan Xue[2], Robert Dieme[3], Viswanath Sankar[3], Roxanne C. Mayrand[4], Toshikazu Nishida[3], Wolfgang J. Streit[2] and Justin C. Sanchez[1,4,5]

[1] *Department of Biomedical Engineering, University of Miami, Coral Gables, FL, USA*
[2] *Department of Neuroscience, University of Florida, Gainesville, FL, USA*
[3] *Department of Electrical and Computer Engineering, University of Florida, Gainesville, FL, USA*
[4] *Department of Neuroscience, University of Miami, Coral Gables, FL, USA*
[5] *Miami Project to Cure Paralysis, University of Miami, Miami, FL, USA*

Edited by:
Ulrich G. Hofmann, Albert-Ludwigs-University Freiburg, Germany

Reviewed by:
Sofyan H. H. Hammad, Aalborg University, Denmark
Susanne Löffler, Karolinska Institute, Sweden

***Correspondence:**
Abhishek Prasad, Department of Biomedical Engineering, B91 University of Miami, 1251 Memorial Drive, McArthur Engineering Annex #219A, Coral Gables, FL 33146, USA
e-mail: a.prasad@miami.edu

Pt/Ir electrodes have been extensively used in neurophysiology research in recent years as they provide a more inert recording surface as compared to tungsten or stainless steel. While floating microelectrode arrays (FMA) consisting of Pt/Ir electrodes are an option for neuroprosthetic applications, long-term *in vivo* functional performance characterization of these FMAs is lacking. In this study, we have performed comprehensive abiotic-biotic characterization of Pt/Ir arrays in 12 rats with implant periods ranging from 1 week up to 6 months. Each of the FMAs consisted of 16-channel, 1.5 mm long, and 75 μm diameter microwires with tapered tips that were implanted into the somatosensory cortex. Abiotic characterization included (1) pre-implant and post-explant scanning electron microscopy (SEM) to study recording site changes, insulation delamination and cracking, and (2) chronic *in vivo* electrode impedance spectroscopy. Biotic characterization included study of microglial responses using a panel of antibodies, such as Iba1, ED1, and anti-ferritin, the latter being indicative of blood-brain barrier (BBB) disruption. Significant structural variation was observed pre-implantation among the arrays in the form of irregular insulation, cracks in insulation/recording surface, and insulation delamination. We observed delamination and cracking of insulation in almost all electrodes post-implantation. These changes altered the electrochemical surface area of the electrodes and resulted in declining impedance over the long-term due to formation of electrical leakage pathways. In general, the decline in impedance corresponded with poor electrode functional performance, which was quantified via electrode yield. Our abiotic results suggest that manufacturing variability and insulation material as an important factor contributing to electrode failure. Biotic results show that electrode performance was not correlated with microglial activation (neuroinflammation) as we were able to observe poor performance in the absence of neuroinflammation, as well as good performance in the presence of neuroinflammation. One biotic change that correlated well with poor electrode performance was intraparenchymal bleeding, which was evident macroscopically in some rats and presented microscopically by intense ferritin immunoreactivity in microglia/macrophages. Thus, we currently consider intraparenchymal bleeding, suboptimal electrode fabrication, and insulation delamination as the major factors contributing toward electrode failure.

Keywords: Pt/Ir microelectrodes, neural interface, blood brain barrier (BBB), neuroinflammation, abiotic, biotic, floating microelectrode arrays (FMA), impedance

INTRODUCTION

The development of clinically viable microelectrode arrays for humans has produced multiple engineering design and neurophysiological requirements that are believed to be necessary for facilitating high performance (Jackson and Zimmermann, 2012). These include the ability to target and access the activity in ensembles of neurons located in cortical and deep brain structures for treating a variety of neurological problems including paralysis (Ethier et al., 2012; Hochberg et al., 2012; Collinger et al., 2013), stroke (Iosa et al., 2012), movement disorders (Andrews, 2010; Rouse et al., 2011), epilepsy (Morrell, 2011; Truccolo et al., 2011), and neuropsychiatric disorders (Maling et al., 2012). Not only is short-term access of these neurons important but also the microelectrode arrays should be able to sense and stimulate targeted neurons reliably, which could be of the order of tens of years. From a materials science perspective, there are differences in the design considerations between sensing and stimulation but in general, it is desirable to have stable electrodes that do not corrode (Sanchez et al., 2006; Prasad et al., 2012), produce stable impedance (Ward et al., 2009; Prasad and Sanchez, 2012), and are

robust after repeated delivery of current through them (Johnson et al., 2005; Otto et al., 2005, 2006; Koivuniemi and Otto, 2011; Lempka et al., 2011). A variety of materials including tungsten, platinum, platinum-iridium, and iridium oxide coatings have been used to improve the reliability of recordings (Geddes and Roeder, 2003; Cogan, 2008; Ward et al., 2009). Closely coupled to the abiotic materials aspects are the biotic responses to chronically implanted microelectrode arrays. The biotic effects include the disruption of the blood-brain barrier (BBB) (Prasad et al., 2011; Karumbaiah et al., 2013; Saxena et al., 2013), tissue inflammatory response involving astroglial and microglial reactions occurring at/around the implanted site, and macrophage recruitment to the implanted site (Schmidt et al., 1976; Stensaas and Stensaas, 1978; Edell et al., 1992; Kam et al., 1999; Turner et al., 1999; Szarowski et al., 2003; Biran et al., 2005; Lee et al., 2005; Polikov et al., 2005; Biran et al., 2007; McConnell et al., 2009b; Winslow and Tresco, 2010; Thelin et al., 2011; Prasad et al., 2012). The abiotic effects include the changes occurring at the electrode recording sites such as corrosion and insulation delamination and cracking that alters the electrochemical properties of the electrode recording surface area (Geddes and Roeder, 2003; Patrick et al., 2011; Prasad and Sanchez, 2012; Prasad et al., 2012; Streit et al., 2012; Kane et al., 2013). Both these effects are dynamic in nature, occur concurrently, and cannot be isolated from one another. Therefore, high-performance arrays should produce minimal tissue reactivity including disruption of the blood-brain-barrier (Prasad et al., 2012), glial response (Frampton et al., 2010; Winslow and Tresco, 2010; Prasad et al., 2012), and neuronal damage (McConnell et al., 2009b). Finding the optimal balance of all of these design considerations is challenging and various electrode tip geometries (Andrei et al., 2012) and multiple array solutions have been proposed including microwire arrays, floating planar silicon arrays, floating 2-D silicon arrays, and floating microwire arrays (Drake et al., 1988; Rousche and Normann, 1998; Williams et al., 1999a,b; Rousche et al., 2001; Csicsvari et al., 2003; Kipke et al., 2003; Nicolelis et al., 2003; Vetter et al., 2004; Patrick et al., 2006; Jackson and Fetz, 2007; Musallam et al., 2007; Kozai et al., 2012a; Kim et al., 2013; Richter et al., 2013). Unique among these available solutions is the "floating" aspect of the array design. It is believed that floating arrays can mitigate many of the challenges of chronic implantation as they have been shown to cause reduced lesions due to electrode array micro-movements in the brain tissue (Biran et al., 2007). Systematic and quantitative study of each of these array types is necessary to prove their benefits and weaknesses in the context of electrode performance and failure.

In this work, floating microelectrode arrays (FMA) fabricated by Microprobes (Gaithersburg, MD) are studied. These electrodes are made of Pt/Ir which provide a more stable and inert electrode-recording site that is less prone to corrosion and surface changes compared to other metals such as tungsten and stainless steel (Geddes and Roeder, 2003; Cogan, 2008; Patrick et al., 2011; Prasad et al., 2012; Kane et al., 2013). In addition, they are laser cut with a conical tip to reduce the trauma during insertion. Unlike the Utah array, which is the only other commercial design that is similar, the FMA can be custom cut for both deep brain and cortical targets. The arrays are fabricated on a planar substrate and connected via a thin flexible cable, which allows the array to float with the brain. While FMAs have been used in a variety of cortical and spinal applications for basic neurophysiological and neuroprosthetic applications, they have not undergone comprehensive characterization to quantify their electrophysiological properties over long-durations (weeks to months) *in vivo*. We have recently developed an *in vivo* testbed (Prasad and Sanchez, 2012; Prasad et al., 2012; Streit et al., 2012) to quantify the failure mechanisms of microelectrodes and have shown that there are a variety of biotic and abiotic aspects that contribute to electrode performance. Since microelectrode array design is so diverse among the available options (Utah, FMA, microwires, Michigan), each design needs to be evaluated independently using a common set of relevant metrics. Toward developing a comprehensive characterization of FMA performance and failure, this study performs an *in vivo* long-term abiotic and biotic analysis with an aim to build a quality control system for microelectrodes. FMAs were implanted into the rat somatosensory cortex for implant duration ranging from 7 days up to 6 months. Abiotic analysis included (1) pre-implant and post-explant SEM imaging for qualitative comparison of the changes that occur at the electrode recording surface, and (2) chronic *in vivo* impedance spectroscopy for studying the changes in the electrode impedance chronically. Biotic analysis was assessed using microglial activation and degeneration and BBB disruption. Chronic electrode performance was quantified via array yield. The array yield, specified by the number of recording sites producing single neuron recordings, provides insight to the overall health of the array. High-performance electrode arrays produce single neuron recordings from a maximal number of recording sites. Likewise, failing electrode arrays produce low yields. It has been shown that impedance spectroscopy provides insight to the fundamental aspects of biotic and abiotic interactions that affect array performance (Grill and Mortimer, 1994; Merrill and Tresco, 2005; Ludwig et al., 2006, 2011; Williams et al., 2007; McConnell et al., 2009a; Karumbaiah et al., 2013). Combining standard electrophysiological measurements with abiotic and biotic analysis can produce comprehensive insight to electrode failure.

METHODS

All procedures were approved by the University of Miami Institutional Animal Care and Use Committee (IACUC). Twelve age-matched adult male Sprague–Dawley rats, all weighing between 300 and 350 grams (at implant time) were used in this study. Animals were divided into short-term implant group ($\leq$2 weeks) (Turner et al., 1999; Winslow and Tresco, 2010) and chronic groups ($\leq$6 months) (Williams et al., 1999b; Polikov et al., 2005; Winslow and Tresco, 2010). In this study, 3 animals were implanted for up to 7 days, 2 for 15 days, 1 for 3 weeks, 3 for up to 3 months, and 3 for 6 months, respectively. The 7-days and 15-days animals were classified in the short-term implant group whereas the remaining animals were classified in the chronic group. All animals were euthanized at the end of their prospective study period intentionally and the brain tissue was harvested for histological analysis. **Table 1** summarizes the pre-implant and post-explant SEM observations, functional performance, and histopathological summary for all 12 animals included in the study.

Table 1 | Summary of all animals used in this study.

Animal groups	Rat no.	Days post-implant	Scanning electron microscopy (SEM) imaging		Electrophysiology			Histopathology	
			Pre-implant	Post-explant	Impedance (MΩ) on day 1	Impedance (MΩ) at euthanasia	Average array array yield (%)	Activated microglia (Yes/No)	Degenerated microglia (Yes/No)
Short-term implants(≤15 days)	F11	15	Non-uniform insulation, cracks in insulation near recording tips	Bent tips, insulation delamination and cracks in insulation	0.45 ± 0.14	0.689 ± 0.17	39.3 ± 32.8	Y	Y
	F12	7	Crack in no. 1, some wires not straight, non-uniform insulation along wires	Cracks in insulation, insulation delamination, recessed insulation	0.37 ± 0.12	0.504 ± 0.29	65 ± 28.1	Y	Y
	F13	15	Electrode tip not straight for no. 13, cracks along wire shank, some wires not straight	Insulation delamination in some electrodes, cracks in insulation	0.41 ± 0.12	1.27 ± 0.43	78.1 ± 19.6	Y	Y
	F14	7	Electrode tip not straight for no. 16, cracks in insulation along shank	Broken tip, insulation delamination	0.51 ± 0.68	0.494 ± 0.23	33.3 ± 20	Y	Y
	F15	6	No. 2 crack on recording surface, cracks in insulation along shanks, no. 8 wire tip not straight	Electrode tip not straight, some deinsulation	0.4 ± 0.11	0.593 ± 0.22	81.2 ± 22.2	Y	Y
Chronic implants (≤6 months)	F9	71	Majorly flawed: cracks in insulation at recording tips for most electrodes, non-uniform insulation	Cracks in insulation, insulation delamination, recessed insulation	1.44 ± 0.59	0.947 ± 0.26	16.8 ± 22.4	Y	Y
	F10	21	Cracks on electrode shanks, cracks in insulation at recording tips	Cracks, delamination, insulation damage	0.47 ± 0.14	0.594 ± 0.19	4.8 ± 13.7	Y	Y
	F2	180	Non-uniform insulation on all wires, some wires not straight	Some bent tips, two electrodes have cracks in insulation	0.61 ± 0.65	1.96 ± 0.71	74.3 ± 13.9	Y	Y
	F4	180	Irregular insulation, some wires not straight, tip missing for no. 6, bent recording tip no. 9	Bent tips, insulation delamination	0.397 ± 0.134	1.43 ± 0.49	40.5 ± 22.5	N	N
	F6	180	Bent tips for nos. 3, 4, 5, 9, and 13, some wires not straight, cracks in insulation	Insulation delamination on some wires, bent tips	0.43 ± 0.2	0.7 ± 0.3	35.1 ± 19.6	N	N
	F7	90	Moderately flawed: bent tip no. 16, non-uniform insulation at recording tips, crack in insulation at tips	Insulation delamination in some electrodes, cracks, bent tips	0.59 ± 0.7	1.47 ± 0.81	12 ± 8.6	N	Y
	F8	91	Majorly flawed: crack in recording tip no. 5, cracks in insulation of 8 electrodes, some wires not straight	Insulation delamination	1.08 ± 0.24	2.14 ± 0.43	19.5 ± 21.4	Y	Y

Animals are divided into short-term implants (≤2 week) and long-term implants (≤6 months). The table provides summarizes general abiotic and biotic observations.

ELECTRODE

We characterized 16-channel FMA (MicroProbes, Inc, MD) for our implants in all animals (Musallam et al., 2007; Mollazadeh et al., 2011). The microelectrode array consisted of 16 microwires [Pt/Ir (70/30%) 75 μm diameter at the base which tapered to a fine tip] attached to a ceramic substrate (**Figure 1A**). Each of the microwires were 1.5 mm long and separated by 400 μm. The microwires were insulated with parylene-C, the thickness of which was 3 μm along the wire shaft and the microwires were laser cut at the tip, which produced a conical recording surface. The microwires were soldered to gold wires, which were bundled together and soldered to a 16-channel Omnetics connector that was fixed on the skull. The wire bundle was coated with medical grade silicone to provide insulation.

SCANNING ELECTRON MICROSCOPY (SEM) IMAGING

In order to evaluate the structural changes in chronically implanted microelectrode arrays, all arrays were imaged before implantation and after explantation using a variable pressure scanning electron microscope (Hitachi S-3000N VP-SEM). The environmental mode in the VP-SEM was chosen for imaging the arrays to enable direct placement of the samples into the SEM chamber without the use of carbon or conductive coating. This is very critical especially for pristine electrodes as they will be implanted into an animal after the SEM imaging procedure. Such a method was used so as to cause no damage to the arrays from the imaging process for both pre-implant as well as explanted arrays. When the pre-implant images were taken, electrode arrays were handled with care to prevent any damage to the microwires. The post-explant images were taken on the electrode arrays extracted from the implanted tissue. The post-explant arrays were carefully placed on a holder positioned on to the SEM stage. The following parameters were used to take the pre- and post-implant images: (1) environmental secondary electron detector (ESED) mode with an acceleration potential of 12 kV, (2) working distance range was set between 18 and 40 mm, and (3) magnification was varied according to need and the minimum magnification was set at 20X.

IMPEDANCE TESTING PROCEDURE

Electrode impedance spectroscopy was performed using NanoZ (TDT, Alachua, FL) using procedures described in detail elsewhere (Prasad and Sanchez, 2012). Briefly, NanoZ measures impedance by applying a small sinusoidal voltage of 4 mVpp at specific frequencies of 1 Hz, 2 Hz, 5 Hz, 10 Hz, 20 Hz, 50 Hz, 100 Hz, 200 Hz, 500 Hz, 1 kHz, and 2 kHz, respectively. The small amount of voltage applied by NanoZ causes a maximum test current of 1.4 nA RMS to flow through the measuring circuit. The impedance measurement protocol was approved by the electrode manufacturer. We combined repeated impedance measurements following the above protocol with scanning electron microscopy (SEM) imaging to verify that electrode recording surfaces were not altered due to the measurement process itself. Impedance spectroscopy *in vitro* was performed for electrode arrays with respect to a low impedance stainless steel reference wire prior to implantation in 0.9% phosphate buffered saline (PBS) for obtaining baseline values for each array. The two-electrode method has been deemed suitable for measuring microelectrode impedance owing to the large difference in impedance between the electrode being tested and the distant low impedance reference wire (Brett and Brett, 1993; Geddes, 1997; Williams et al., 2007). *In vivo* measurements were made with respect to the same stainless steel wire tied to the skull screw while the animals were lightly anesthetized during impedance measurements. *In vivo*, impedance was measured 3–4 times a week before electrophysiological recordings. In our testing, the NanoZ calculated the impedance values for each electrode by repeating the process 20 times and reported the average of those values to reduce errors due to measurement.

SURGICAL PROCEDURE

Electrodes were individually sterilized using ethylene oxide gas prior to implantation and sterile surgical techniques were followed for all implant surgeries. Animals were anesthetized with an induction of isoflurane (4%) and O_2 (2 L/min) and deep anesthesia level was maintained for the entire duration of the surgical procedure using isoflurane (1.5%) and 1 L/min O_2. Xylazine (5 mg/kg, subcutaneous) was used to maintain an even plane of anesthesia and as a muscle relaxant. Upon fixing the animal's head in a stereotaxic frame (Kopf Instruments, Tujunga, CA) to stabilize the skull, a midline incision was made on the skin from between the eyes up to the ears and the periosteum was scraped from on top of the skull. The skull surface was cleaned and the bregma and lambda landmarks were identified. Four stainless steel screws were manually drilled into the skull. Using stereotaxic coordinates, the craniotomy location (1 mm lateral and 1.8 mm caudal to the bregma) was marked which correspond to the somatosensory cortex. A 5 mm diameter circular craniotomy was drilled at the above marked location (**Figure 1B**) and the dura was then cut using microscissors to expose the cortical surface. The setup shown in **Figure 1C** was used to hold the electrode connector and position the electrode array using a vacuum pump wand. The electrode array was slowly (∼0.1 mm/min) lowered into the cortex using the micropositioner (Kopf Instruments, Tujunga, CA). Slow speed of insertion was used for these FMA as recommended by the manufacturer and similar to studies that have shown success in recording single neurons with a slow insertion speed for microwire arrays (Nicolelis, 1999). A small piece of gelfoam soaked in sterile saline was used to cover the craniotomy and dental acrylic (A-M Systems, Carlsborg, CA) was placed on and around the craniotomy. Extreme care was taken such that none of the acrylic entered the craniotomy. The ground and reference wires were tied to the skull screw and the entire area was filled with acrylic. Animals were placed under supervision in a recovery box kept on a heating pad post-surgery and housed individually upon recovery. Bupivacaine was used around the wound site after the surgery and Carprofen (5 mg/kg, subcutaneous) was used as the analgesic. No antibiotics or any other drugs were used in this study.

RECORDING PROCEDURE

Animals were recorded 3–4 times each week. Electrode impedance spectroscopy was performed prior to each recording session. The animal was connected to a preamplifier that was optically isolated from a real-time digital signal processor (RZ2, TDT, FL).

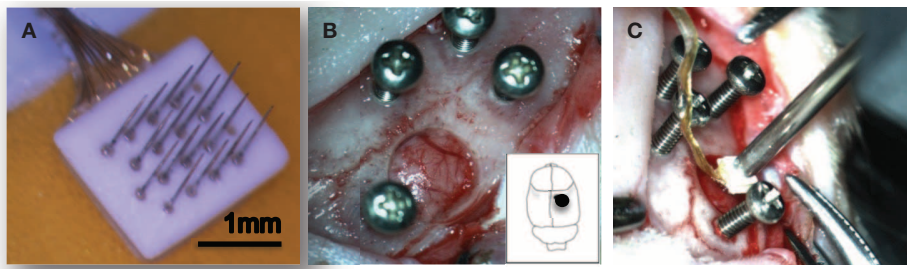

FIGURE 1 | Experimental setup. A 16-channel Pt/Ir floating microelectrode array (FMA) consisting of 1.5 mm long and 75 μm diameter with tapered microwires tips was used for all implants **(A)**. Surgical implantation procedure in the rat somatosensory cortex is shown **(B,C)**.

A custom made program (RPvDx, TDT, FL) was used to acquire neural signals sampled at 24414.06 Hz. Signals were band-pass filtered between 0.5 and 6 kHz and online spike sorting based on boxes and thresholding as determined by the experimenter was used to isolate neuronal waveforms. Offline spike sorting was then performed to verify isolated single units and remove other artifacts. Waveforms were classified as single units based upon the repeatability of waveform shape and peak-to-peak amplitude with respect to the background noise (Suner et al., 2005). Electrophysiological recordings were quantified via array yield, which was defined as the percentage of electrodes within an array that were able to isolate at least one neuron during a recording session. Array yield was used as a functional measure for electrode assessment. An electrode was said to isolate a neuron (single unit) when at least 100 reproducible biphasic waveforms could be collected during a session.

Signal-to-Noise ratio (SNR) was calculated using the formula: $SNR = \frac{V}{2*\sigma}$, where V is the peak-to-peak amplitude of the mean waveform and σ is the standard deviation of the noise. These methods have been described in detail elsewhere (Suner et al., 2005). **Figure 2A** provides a general measure of the signal quality where offline sorted waveforms from four isolated neurons is shown with SNR value calculated for each neuron. The neuron waveforms shown are for animal F6 and are from different electrodes and different sessions. All waveforms were collected and shown within a 1.2 ms time-window. Weekly signal-to-noise levels are shown for four animals (F6–9) during their respective implant durations in **Figure 2B**. In general, SNR values ranged between 3 and 6 and were comparable to those reported earlier by other studies (Suner et al., 2005; Ward et al., 2009). We found that SNR values were not dependent upon implant durations or daily changes in impedance values and also not correlated to the electrode performance.

IMMUNOHISTOCHEMICAL PROCEDURES

Immunohistochemical procedures have been described in detail elsewhere (Prasad et al., 2012). Briefly, microglial cells in brain sections were examined immunohistochemically using the rabbit polyclonal primary antibody Iba1 (Wako, 019–19741, diluted at 1:800). Phagocytic microglia were identified using ED1 antibody (mouse anti-rat monocytes/macrophages (CD68), Chemicon; MAB1435, diluted at 1:300). Immunolabeling for the iron storage protein was performed using antiferritin polyclonal antibody (rabbit anti-horse spleen ferritin, Sigma, F6136, diluted at 1:800). Ferritin, an iron storage protein that becomes expressed in some microglia in the human brain are often dystrophic rather than activated (Dijkstra et al., 1985). Ferritin staining of microglia seems to be induced under certain injury/disease conditions when the blood–brain barrier is disturbed and there is a need for iron sequestration. The ferritin antibody also binds to oligodendrocytes in the normal uninjured central nervous system (Lopes et al., 2008). Quantitative analysis of antigen expression was conducted on images using Image J program (NIH, Bethesda, MD). The total positive area of an antigen expression per unit section area (i.e., per microscopic field ×20; total area size 267320.12 μm^2) were scored in an image captured from each side of rat brain by using Image J program. The mean values and standard deviation of the counts were computed. An intact microglial cell was defined as a cell with a cell body area larger than 30 μm^2 and less than 300 μm^2 for Iba1 and ferritin labeling. The ED1 positive particle was defined as areas from 1 to 10 μm^2. The difference between the electrode implant side and the contralateral side was interpreted to reflect an approximation of microglial cell function.

RESULTS

SEM IMAGING OBSERVATIONS

A comparison of the pre-implant and post-explant SEM images of the electrode arrays was made to analyze qualitatively the changes at the electrode recording surface morphology for all animals. All electrodes prior to implantation were imaged to observe any pre-implant defects in the electrodes due to the manufacturing process. We observed several defects occurring as a result of manufacturing most commonly present in the recording surfaces and the interface between the recording surface and the insulation. The manufacturing defects most commonly present were cracks in the insulation material, non-uniform insulation, bent and broken recording tips, cracks on the recording tips, and non-uniform deinsulation (**Figure 3**). **Figure 3** shows examples of electrodes with pre-implant manufacturing imperfections for 4 of the longest term animals (3–6 months implant period). These images were taken prior to electrode implants. Note that not all the electrodes within an array had issues but approximately 25% or more electrodes tend to have one or the other issue as described above. Thus, there was a large variation between electrodes within an array with some electrodes with no issues whereas others with

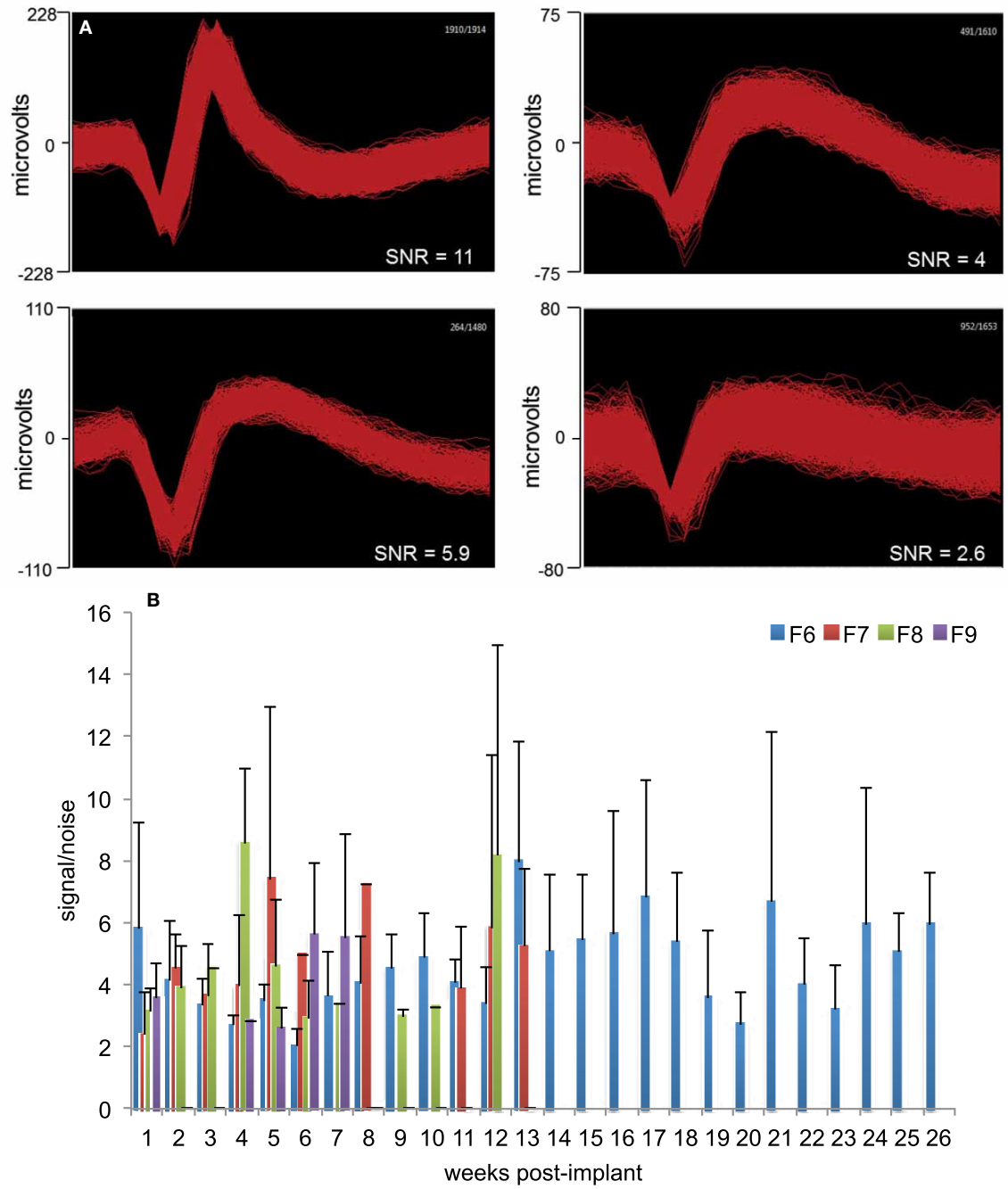

FIGURE 2 | Signal quality and SNR. (A) Representative offline sorted waveforms isolated from individual electrodes to depict signal quality. High (>5), medium (3–5), and low SNR (<3) waveforms are shown. In general, SNR values were in the range 3–6. Waveforms are shown within a 1.2 ms time-window. **(B)** Weekly signal-to-noise levels for animals F6, F7, F8, and F9 are shown. SNR values were comparable to those reported earlier by other studies. SNR values were not dependent upon implant durations or daily changes in impedance values.

pre-implant imperfections. Pre-implant and post-explant SEM images were taken for qualitative comparison of the changes that occur at the electrode recording surface and insulation material. **Figure 4A** shows such changes occurring after chronic implantation in animals where the electrodes underwent moderate to minimal changes at the recording surfaces. We observed that Pt/Ir undergoes little corrosion for implants up to 6 months. However, there was a great variability among individual electrodes even within the same array with regard to corrosion and/or insulation deterioration. While electrode corrosion did not appear to be a significant problem with Pt/Ir, we observed severe delamination and cracking of insulation material. Gross morphological

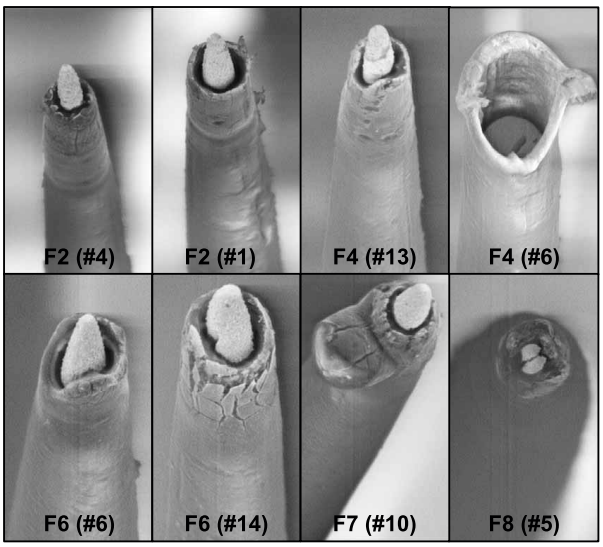

FIGURE 3 | Manufacturing variability. We observed large variation between electrodes within the same Pt/Ir array. Shown here are 8 wires from four arrays pre-implant with imperfections as a result of manufacturing process. One of the wires is missing the recording tip whereas others have cracks in the insulation/recording tip, and uneven insulation at the interface of the recording surface/insulation.

changes occurred at the recording surface in the form of bent tips, cracks appearing in the insulation material, and insulation delamination. **Figure 4B** show 12 representative electrodes from 7 long-term animals (3–6 months) where severe damage to the insulation material was observed. Insulation damage and delamination resulted in a decrease in electrode impedance during the chronic lifetime and affected functional performance (**Figure 5**). **Figure 5** shows such an example for 4 electrodes from 3 long-term animals (F4 and F6: 6 months; F9: 71 days) where electrode impedance declined during the latter part of the implant period. Interestingly, as the electrode was undergoing these morphological changes, the functional performance (electrode yield) became poor.

IMPEDANCE AND ELECTROPHYSIOLOGICAL OBSERVATIONS

To study general trends in impedance magnitude, 1 kHz impedance was chosen throughout this study as this is the fundamental frequency of an action potential and the value commonly used to report impedance in other studies (Ward et al., 2009). **Figure 6** shows the 1 kHz impedance trends and the array yield during the implant period for 4 long-term animals (F2, F4, F6: 6 months; F8: 3 months). The figure plots the average array yield (red bars) and average impedance (blue trace) from 16 electrodes on each of the recording days. Impedance values increased progressively to 2–3 times the post-implant values by the 1-week period. In general, impedance values continued to increase until the 3–4 week period with values in the range 1.5–2.5 MΩ after which they decreased. There was also greater variation in the daily impedance values as suggested by the large error bars. The impedance values generally decreased after the 15-day period with occasional fluctuations in the chronic period thereafter. These general impedance magnitude trends with large daily variations were consistent among all animals. Array yield generally was high post-implantation and declined in the days following surgery. In general, an inverse relationship between the daily impedance measurements and the array yield was observed for all our long-term animals.

HISTOPATHOLOGY OBSERVATIONS

Light microscopic examination of sections stained with microglial markers revealed a rather heterogeneous picture of histopathological changes (**Figure 7**), but some clear trends were apparent. In general microglial activation, as judged by cell hypertrophy and cell density on Iba1-stained preparations was strongest during early survival times and tended to decrease with increasing survival post-implantation, that is the intensity of neuroinflammation declined over time. Expression of ED1 antigen, indicative of ongoing phagocytic activity, was variable and showed no apparent correlation with post-implant survival times. The ED1 antigen was always present in microglia/macrophages. Expression of ferritin was not related to post-implantation survival times but instead was variable and likely related directly to the extent of vascular damage and hemorrhage (**Figure 8**). Dense encapsulation of electrodes was not observed in many of the animals and at most involved two cell layers surrounding electrode tracks (**Table 2**). The extent of encapsulation was not correlated with electrode performance, e.g., F8 (**Figure 7**; **Table 2**).

COMBINED ABIOTIC-BIOTIC ANALYSIS

One or more metrics can be used for predicting electrode failure through modeling approaches that would provide us with a reliable estimate of electrode failure. A combined analysis that included histopathological and morphological evaluation combined with functional assessment of these arrays was performed to support our hypothesis of the various abiotic and biotic failure modes that contributes to electrode failure (**Figure 9**). All histopathological markers (Iba1, ED1, and Ferritin) were normalized across all animals for comparison. We used the following measures to define functional performance: poor (<25% array yield), moderate (25–70% array yield), and good (>70% array yield). All the longest term animals (6-months implant: F2, F4, F6) had moderate to good performance with low histopathology marker levels. Among animals that had good performance, 4 out of 7 animals had very low levels of ferritin expression. The animals (F11, F12, F15) which had higher ferritin levels were very short-term implants. It is likely that ferritin along with other markers were upregulated due to surgical trauma. Even then, the ferritin levels in these animals were much lower than other animals (F7, F9, F10). Therefore, low levels of ferritin was correlated with better functional performance. Electrodes that were poorly manufactured to begin with underwent gross morphological changes overall and had poor functional performance (F7, F8, F9, F10). This supports our hypothesis that insulation delamination/cracking and manufacturing variability leads to reduced impedance over time and degradation in functional performance. There were animals (F11, F12, F15) that had good performance with high

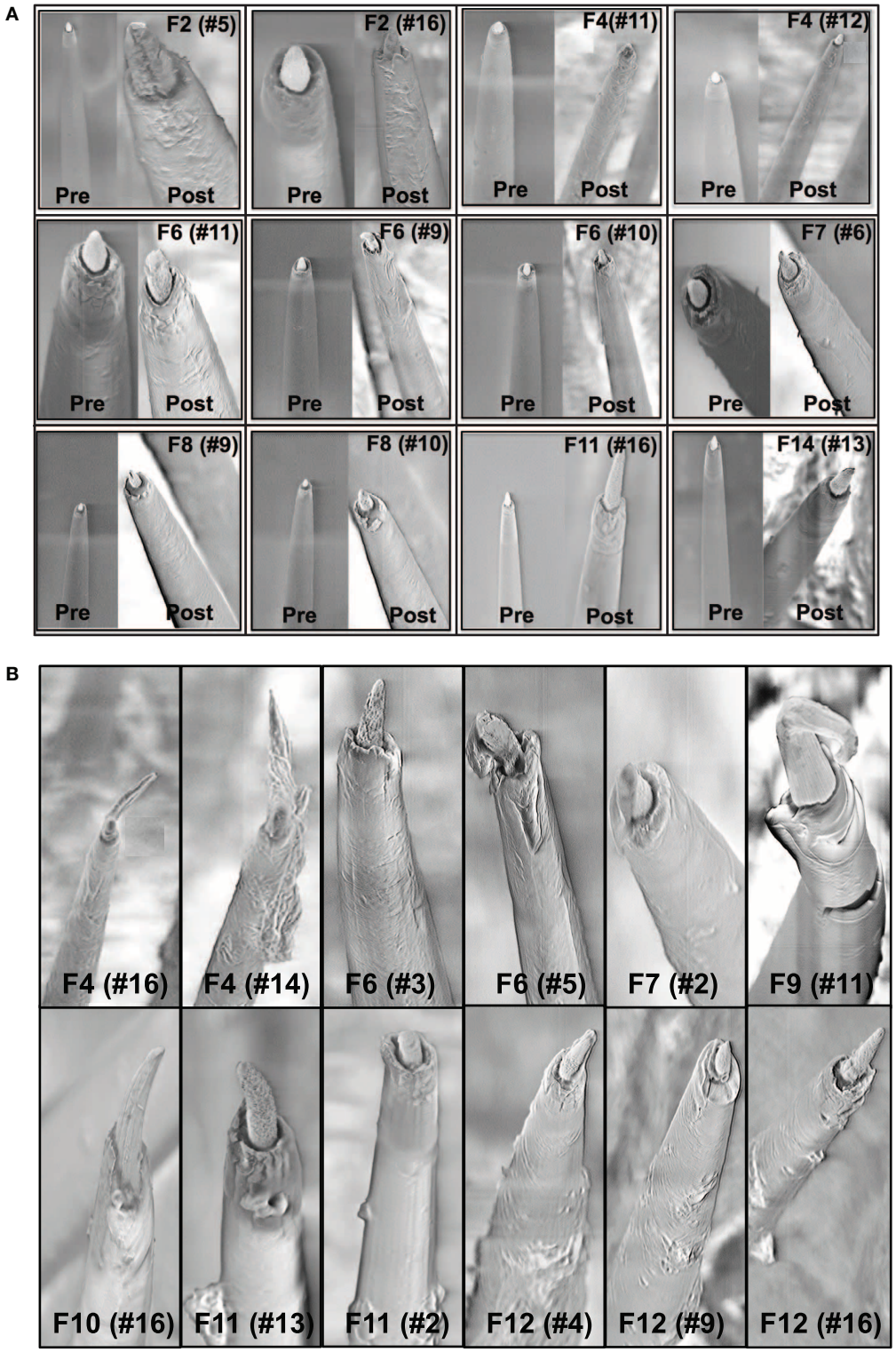

FIGURE 4 | (A) Pre-implant and post-explant SEM. Pre-implant and post-explant SEM images to show minimal to moderate changes at the recording site structure for the longest term animals. However, recording site changes occur as a result of corrosion of the recording surface for long-term implants. Shown here are three 6-month implants (F2, F4, F6), two 3-month animals (F7, F8), one 15-day animal (F11), and one 7-day animal (F14), respectively. A crack at the recording site can be observed to be developing in the electrode F2 (no. 5). **(B)** Insulation deterioration post-explant SEM. Post-explant SEM of individual microwire to indicate deterioration in electrode insulation for parylene-C coated Pt/Ir microwires. The deterioration occurs in the form of delamination and cracks. While the insulation deterioration varies among microwires even with the same array, we observed it to be present in all the wires across animals for all implant durations (7 days–6 months).

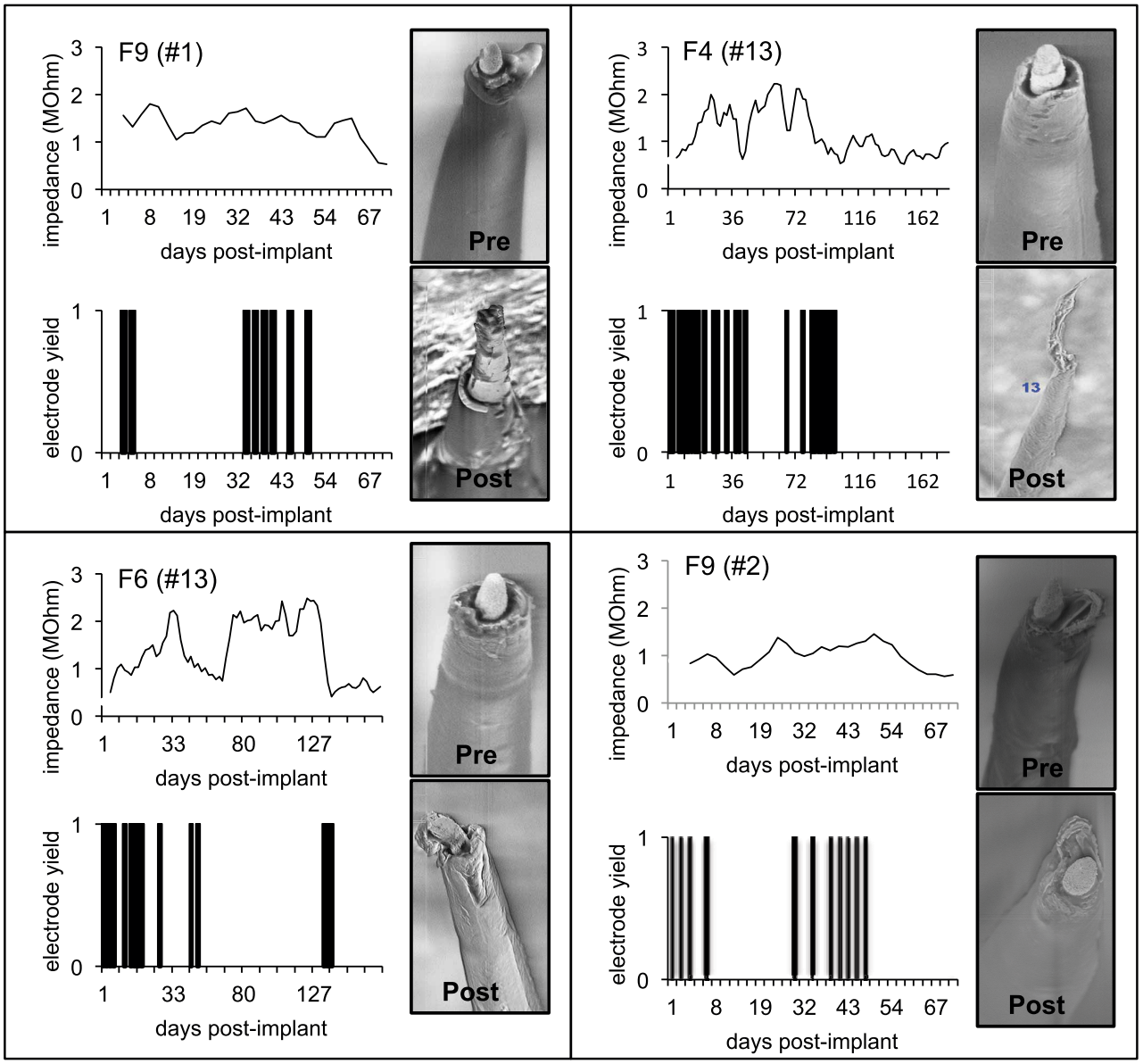

FIGURE 5 | Effect of insulation damage. Pre-implant and post-explant SEM images are shown for four Pt/Ir electrodes in three chronic animals that undergoes delamination during their respective implant durations. Insulation delamination results in a decline in 1 KHz electrode impedance combined with poor functional performance (low yield). Functional performance is characterized by electrode yield on each of the recording days. A zero yield suggests that the respective electrode was not able to record a single unit whereas a 1 suggests that the electrode was able to record a single unit.

histopathology markers which is consistent with our hypothesis that neuroinflammation was not correlated with electrode performance.

DISCUSSION

We presented in this study an *in vivo* abiotic and biotic characterization approach for Pt/Ir microelectrode arrays in chronic implants. The study combined SEM imaging, impedance spectroscopy, histopathology with electrode functional performance so that better understanding of long-term microelectrode performance can be achieved. Abiotic and biotic measurements were performed over 6-months of implant duration revealing changes that occurred at the electrode-tissue interface affecting functional performance of the microelectrodes. This study was predicated on the hypothesis that failure of this electrode type occurred as a result of both abiotic and biotic factors. Pre-implant SEM imaging showed significant variation between electrodes even within the same array indicating manufacturing imperfections. Post-explant SEM imaging indicated that Pt/Ir electrodes did not suffer from deterioration due to corrosion

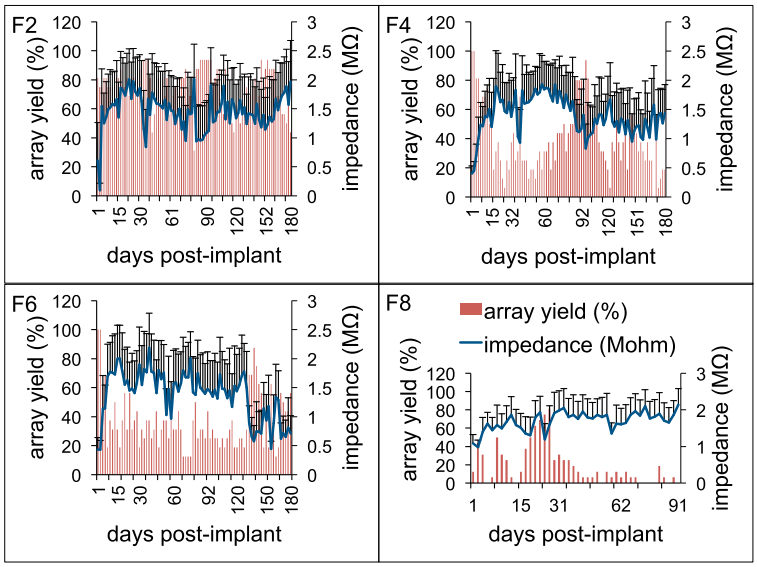

FIGURE 6 | Electrode impedance and electrophysiology trends. Daily array yield (red) and average 1 KHz impedance trends (blue) for four long-term animals (F2, F4, F6: 6-months; F8: 3-months) to show the large daily variations in electrode impedance that result in low array yield. Array yield was defined as the percentage of electrodes out of 16 electrodes in an array that was able to isolate at least a single neuron during a recording session. Error bars depict standard deviations among the impedance values recorded from 16 electrodes during a recording session.

like tungsten (Prasad et al., 2012), however electrodes exhibited deformation of the recording sites such as bent or cracked tips. In addition, deterioration of insulation material was observed among all electrodes in all animals in the form of insulation delamination and cracking. Generally, electrode impedance reduced chronically in electrodes that had insulation deterioration and poor functional performance. Histopathological evaluation suggested modest elevation of microglial markers for longest-term animals. In contrast, we show evidence in this study that the insulation deterioration, manufacturing, and corrosion were the likely abiotic factors contributing to the electrode failure. In addition to the chronic abiotic and biotic effects, we provide evidence that vascular disruption and concurrent intraparenchymal hemorrhaging during brain implantation is a major biotic factor that likely contributes to electrode failure.

The results of this study indicate a need for precision and consistency of manufacturing of microelectrode arrays, an improvement that will likely play a major role in the long-term performance (Prasad and Sanchez, 2012; Prasad et al., 2012; Streit et al., 2012; Barrese et al., 2013). Of particular interest is the recording site itself and interface between that site and the surrounding insulation. Pre-implant variations such as those depicted in **Figure 3** provide a weak or fault site on the microelectrodes that will lead to an accelerated deterioration of the recording surface of individual electrodes. We observed that electrodes with imperfections prior to implantation were more susceptible to morphological changes during the implant period (**Figure 5**). Manufacturing defects at the recording sites provided fault sites where accelerated deterioration happened resulting in a decreased electrode impedance and poor functional performance (**Figure 5**). Therefore, to mitigate the variability arising out of the manufacturing process, greater quality control measures should be employed pre-implant to ensure that implanted electrodes are all of good quality. The manufacturer of the FMAs manipulated the amount of deinsulation for each microwire during the laser cutting process to control the impedance. For this study, FMAs were custom-ordered with 100–150 KΩ as the impedance for each microwire. That value of impedance was chosen based upon our experience with tungsten microwires that had the best electrode yield for the impedance range 40–150 KΩ (Prasad and Sanchez, 2012). Pre-implant baseline impedance measurements for these Pt/Ir FMAs were in the range 100–400 KΩ at 1 kHz measured in PBS. While the intent of the deinsulation process was to control impedance, observations from the electrodes used in this study revealed that the process is not as precise as would be desired and there is inconsistency in the manufacturing process (**Figure 3**). Variance in the starting impedance and manufacturing is compounded by changes in impedance following surgery, which were approximately 2–3 times compared to that measured *in vitro*. The impedance increased progressively over the next 4-week period reaching up to 2–3 MΩ. We observed larger increase in impedance value for these microwires in the first 2–3 weeks as compared to tungsten microwires during the same time period (Williams et al., 2007; Ward et al., 2009; Prasad et al., 2012). While in general, impedance value for tungsten microwires was in the range 30–400 KΩ (Prasad and Sanchez, 2012), the impedance of Pt/Ir microwires were in the order of 1–3 MΩ for most electrodes during the course of chronic implant. This may be attributed to the sharp recording surfaces (smaller geometric surface area) of the Pt/Ir microwires compared to blunt cut recording tips (larger geometric surface area) of tungsten microwires. We and

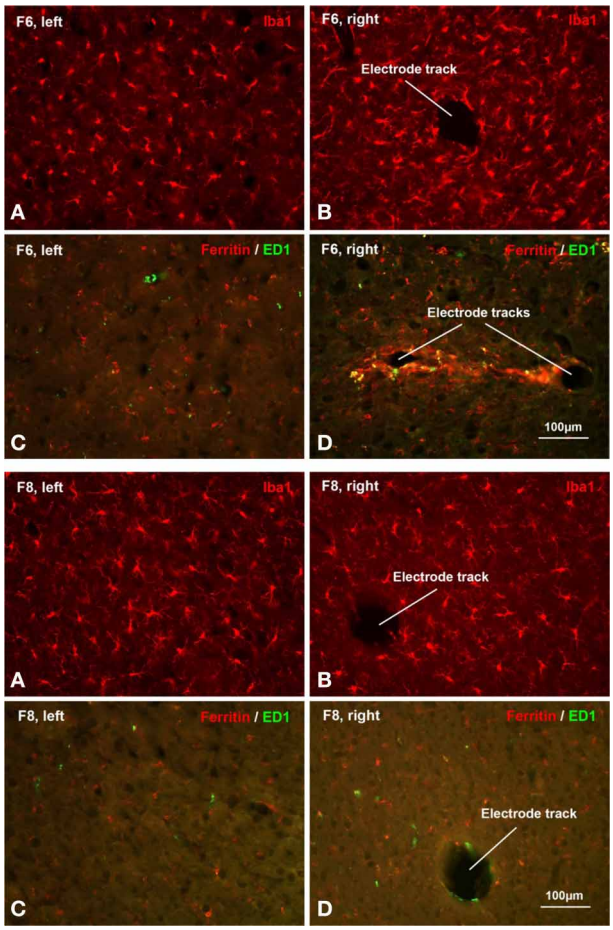

FIGURE 7 | Histopathology. Histopathological staining of microglial cells in two chronically implanted animals, F8 (91 days, top panel) and F6 (180 days, bottom panel). In F8, poor electrode array yield was correlated with minimal microglial activation. Comparing Iba1 labeling on the non-implanted contralateral side **(A)** with the implanted side **(B)** it is evident that microglia display a characteristic resting morphology as well as similar density on both sides. There was only modest upregulation of ED1 and ferritin expression in F8, as seen in **Table 2** and in panels **(C,D)**. In F6, a moderate-to-good array yield correlated with minimal microglial activation. Comparing panels **(A,B)** microglia appear slightly hypertrophic and somewhat increased in number. Ferritin expression was upregulated modestly and to a similar extent as in F8 (**Table 2**). Panel **(D)** shows an example of the maximal ferritin upregulation observed around electrode tracks in this animal.

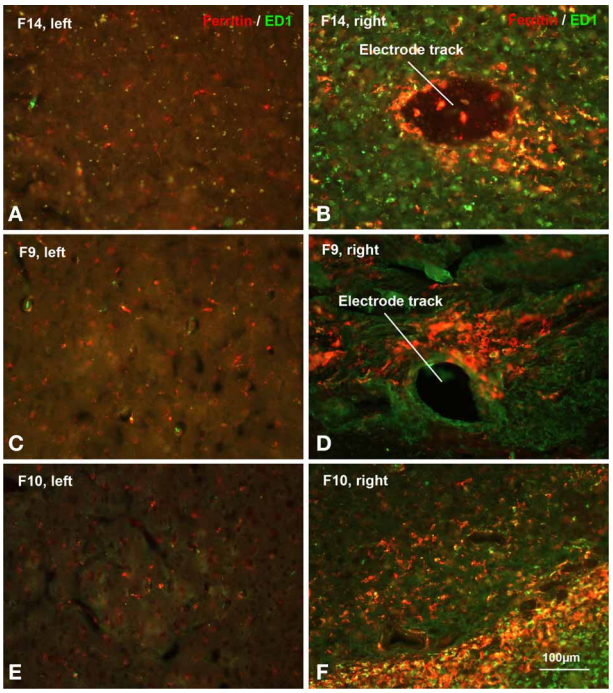

FIGURE 8 | Hemorrhage. Increased ferritin expression in animals with poor electrode performance. Shown are micrographs from three different rats all illustrating dramatic upregulation of ferritin (see also **Table 2**). **(A,B)** F14 is 7 dpi (days post-implantation) and shows a 20-fold increase; **(C,D)** F9 is 71 dpi and shows a 48-fold increase; **(E,F)** F10 is 21 dpi and shows a 91-fold increase in ferritin expression over the control (left) side. The animals also show strong upregulation of both Iba1 and ED1 markers (**Table 2**). These histopathological findings are indicative of significant tissue damage, hemorrhage, and BBB disruption.

others have reported for tungsten microwires large daily variation in impedance values within an array during the first 3–4 weeks after which the impedance reduced and there were smaller daily variations in the chronic period (Ward et al., 2009; Prasad and Sanchez, 2012; Prasad et al., 2012). In comparison, there was greater day-to-day variability in impedances for Pt/Ir microwires during the entire implant duration as suggested by large error bars (**Figure 6**). In addition to the abiotic factors affecting electrode impedance, the trends in impedance during the chronic lifetime of the electrodes also suggest the involvement of biotic factors. The cellular changes occurring in the local environment of the electrode tips is a likely contributor of the daily changes in the observed electrode impedance (Williams et al., 2007).

In addition to the electrode insulation interface, our results strongly suggest the bulk insulation itself is an important contributor leading to electrode failure. We have evaluated two of the most commonly used insulation materials in neural electrodes: Polyimide coated tungsten wires (Prasad et al., 2012) and Parylene-C coated Pt/Ir wires (in this study). Insulation delamination and cracking was evident among all wires across all animals for both insulation types (**Figure 4B**). However, there was a large variation in the extent of the insulation deterioration even between electrodes in the same array. We observed electrodes that had insulation damage pre-implant were more prone to undergo insulation deterioration during the chronic implant (**Figure 5**). Insulation damage results in leakage resistance and parasitic capacitance (Kane et al., 2013) and continuous decrease in impedance, which leads to an accelerated damage causing decrease in electrode functional performance (**Figure 5**). These results indicate that electrode delamination and cracking to be a significant failure mode and steps must be taken in order to evaluate better electrode insulation materials in future.

Material differences should also be considered while choosing electrode metals for recording purposes. In previous studies, we

Table 2 | Histopathology.

Animal groups	Rat No.	Days post-implant	Iba1		ED1		Ferritin	
			Left	Right	Left	Right	Left	Right
Short-term implants (≤15 days)	F11	15	2819	10,901	66	826	487	7104
	F12	7	2226	14,248	74	998	745	18,330
	F13	15	4219	14,747	78	687	288	2685
	F14	7	1731	15,941	131	881	248	4974
	F15	6	4761	17,966	19	999	367	5925
Chronic implants (≤6 months)	F9	71	850	16,137	16	253	64	3094
	F10	21	1555	15,149	59	1157	78	7106
	F2	180	3519	4133	594	280	911	2273
	F4	180	2402	3158	260	385	976	2481
	F6	180	1836	2647	125	125	950	2839
	F7	90	4058	4727	35	429	299	4893
	F8	91	1495	2225	24	74	493	1401

Total positive areas of each of the stains for all animals with Pt/Ir array implants. Right refers to the implanted tissue and left refers to the contralateral control tissue.

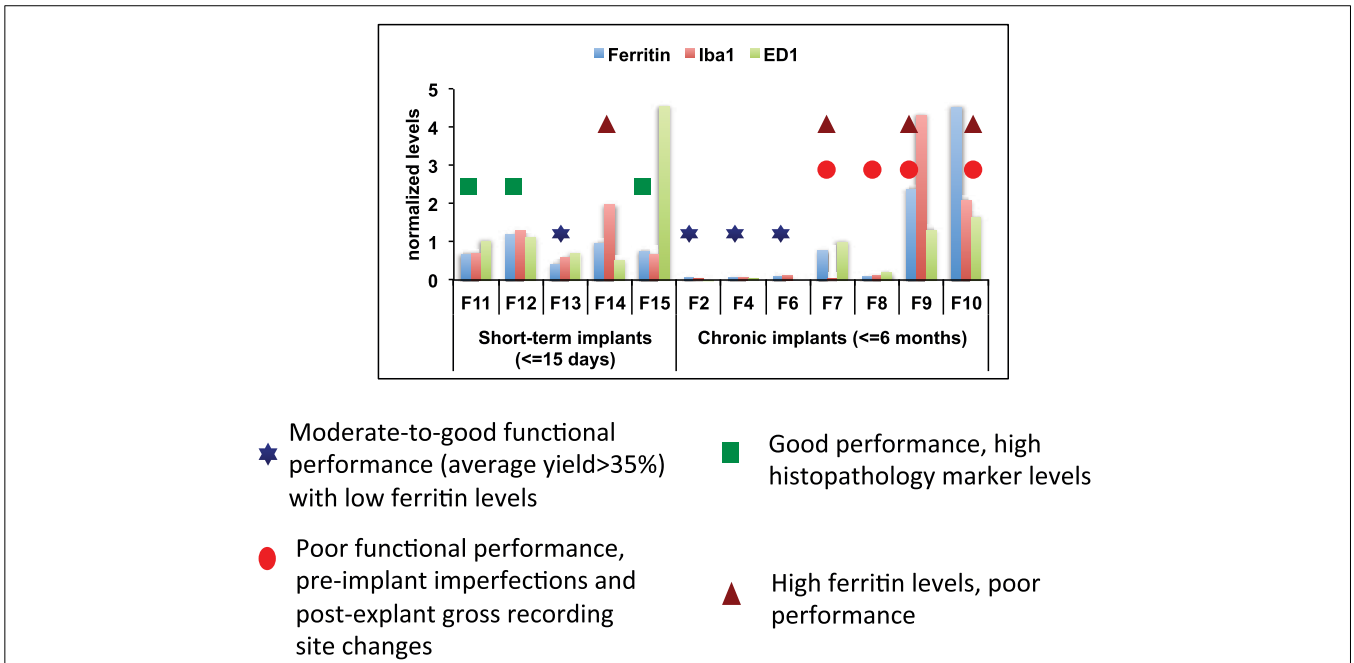

FIGURE 9 | Combined analysis. Combined abiotic-biotic analysis to include histological, morphological, and functional performance for all animals to indicate contributing failure modes.

have observed that tungsten undergoes rapid corrosion *in vitro* (Patrick et al., 2011) and *in vivo* for implants as early as 1-week following surgery (Prasad et al., 2012). We reported that deterioration of tungsten continued in the chronic phase in the form of recording sites becoming more recessed. Therefore, choice of recording material was one of the contributing abiotic failure modes for tungsten electrodes. However, we observed in this study that Pt/Ir provides better recording surfaces and corrosion was not as big of an issue as with tungsten. **Figure 4A** shows various Pt/Ir electrodes both pre-implant and post-explant for varying implant durations (7 days–6 months). We can observe that corrosion was not a significant problem. We did not observe recessed recording sites like tungsten in any of the electrodes and across animals. Even for electrodes, which underwent large morphological changes at the electrode recording sites (**Figure 4B**), electrodes were not as much affected by corrosion. Therefore, corrosion does not appear to be a significant contributing factor to electrode failure for Pt/Ir electrodes.

One of the experimental design factors that enabled deeper insight to electrode failure is that we coupled electrode array functional performance with impedance spectroscopy to study if there was a functional relationship between them. Electrode

array functional performance was quantified by array yield which was defined as the percentage of electrodes in an array that were able to isolate single units. Higher array yield are desirable for a neuroprosthetic application. In general for these floating arrays, 1 kHz impedance magnitude trends were similar for long-term animals where impedance increased progressively in the first 2–3 weeks and then decreased in the subsequent weeks with occasional increases and decreases in the chronic period (**Figure 6**). We observed that array yield generally declined during this initial 2–3 week period following implant attributed as a result of surgical trauma in other studies (Biran et al., 2005). Poor array yield (<25% yield) was observed when impedance was high (>1.5 MΩ) and yield increased when impedance was low during the late chronic period (>12 weeks) for long-term animals (**Figure 6**). The daily variations observed in average impedance magnitude corresponded with moderate (25–70% yield) to poor (<25% yield) functional yield from these Pt/Ir MEAs among all animals (**Table 1**).

There is a cascade of biological reactions that occur following an electrode implant surgery that in brief includes activation and recruitment of astrocytes, microglia, and macrophages at the implant site in order to isolate the implanted device and repair the damaged tissue (Polikov et al., 2005; Thelin et al., 2011; Kozai et al., 2012b). Several studies have pointed out the time course of such biological reactions occurring at the tissue-electrode interface that begin as early as right after insertion and continue as long as the implant is in the neural tissue (Szarowski et al., 2003; Freire et al., 2011; Prasad et al., 2012). Of course, the most obvious and inevitable biological consequence of intracerebral electrode insertion, or for that matter any type of traumatic brain injury, is a neuroinflammatory response. Neuroinflammation is mediated primarily by activated microglial cells which is why we have focused our attention on these cells in this and prior studies (Prasad et al., 2011, 2012; Streit et al., 2012). Our findings with regard to activated microglia were as expected in that electrode implantation elicited widespread microglial activation at the implantation site, which in most cases became somewhat attenuated over time. However, we also studied microglial degeneration, evident as cytoplasmic fragmentation, which we believe is a direct consequence of oxidative stress brought about by influx of free iron through intracerebral bleeding. In contrast to our prior study with tungsten microwires where microglial degeneration was observed only during early survival times, the current study shows that microglial degeneration can also occur during relatively late time points (**Figure 8**), especially in animals where there was significant intracerebral bleeding thus supporting our belief that microglial cytoplasmic fragmentation occurs as a direct consequence of iron-mediated oxidative stress.

In conclusion, the results of our study serve to further illuminate the problem of electrode failure by focusing attention on two major failure modes, one abiotic and the other one biotic. Future efforts geared toward prolonging the functional lifetime of electrodes should thus be focused on further improving electrode manufacturing practices and on innovative ways of minimizing intracerebral bleeding and associated oxidative stress.

ACKNOWLEDGMENTS

This work was sponsored by the Defense Advanced Research Projects Agency (DARPA) Microsystems Technology Office under the auspices of Dr. Jack Judy (jack.judy@darpa.mil) through the Space and Naval Warfare Systems Center, Pacific Grant No. N66001-11-1-4009.

REFERENCES

Andrei, A., Welkenhuysen, M., Nuttin, B., and Eberle, W. (2012). A response surface model predicting the *in vivo* insertion behavior of micromachined neural implants. *J. Neural Eng.* 9:016005. doi: 10.1088/1741-2560/9/1/016005

Andrews, R. J. (2010). Neuromodulation: advances in the next five years. *Ann. N.Y. Acad. Sci.* 1199, 204–211. doi: 10.1111/j.1749-6632.2009.05379.x

Barrese, J. C., Rao, N., Paroo, K., Triebwasser, C., Vargas-Irwin, C., Franquemont, L., et al. (2013). Failure mode analysis of silicon-based intracortical microelectrode arrays in non-human primates. *J. Neural Eng.* 10:066014. doi: 10.1088/1741-2560/10/6/066014

Biran, R., Martin, D. C., and Tresco, P. A. (2005). Neuronal cell loss accompanies the brain tissue response to chronically implanted silicon microelectrode arrays. *Exp. Neurol.* 195, 115–126. doi: 10.1016/j.expneurol.2005.04.020

Biran, R., Martin, D. C., and Tresco, P. A. (2007). The brain tissue response to implanted silicon microelectrode arrays is increased when the device is tethered to the skull. *J. Biomed. Mater. Res.* 82, 169–178. doi: 10.1002/jbm.a.31138

Brett, M. A. C., and Brett, A. M. O. (1993). *Electrochemistry: Principles, Methods and Applications.* New York, NY: Oxford Science.

Cogan, S. F. (2008). Neural stimulation and recording electrodes. *Annu. Rev. Biomed. Eng.* 10, 275–309. doi: 10.1146/annurev.bioeng.10.061807.160518

Collinger, J. L., Wodlinger, B., Downey, J. E., Wang, W., Tyler-Kabara, E. C., Weber, D. J., et al. (2013). High-performance neuroprosthetic control by an individual with tetraplegia. *Lancet* 381, 557–564. doi: 10.1016/S0140-6736(12)61816-9

Csicsvari, J., Henze, D. A., Jamieson, B., Harris, K. D., Sirota, A., Barthó, P., et al. (2003). Massively parallel recording of unit and local field potentials with silicon-based electrodes. *J. Neurophysiol.* 90, 1314–1323. doi: 10.1152/jn.00116.2003

Dijkstra, C. D., Dopp, E. A., Joling, P., and Kraal, G. (1985). The Heterogeneity of mononuclear phagocytes in lymphoid organs - distinct macrophage subpopulations in the rat recognized by monoclonal antibody-Ed1, antibody-Ed2 and antibody-Ed3. *Immunology* 54, 589–599.

Drake, K. L., Wise, K. D., Farraye, J., Anderson, D. J., and Bement, S. L. (1988). Performance of planar multisite microprobes in recording extracellular single-unit intracortical activity. *IEEE Trans. Biomed. Eng.* 35, 719–732. doi: 10.1109/10.7273

Edell, D. J., Vo Van, T., McNeil, V. M., and Clark, L. D. (1992). Factors influencing the biocompatibility of insertable silicon microshafts in cerebral cortex. *IEEE Trans. Biomed. Eng.* 39, 635–643. doi: 10.1109/10.141202

Ethier, C., Oby, E. R., Bauman, M. J., and Miller, L. E. (2012). Restoration of grasp following paralysis through brain-controlled stimulation of muscles. *Nature* 485, 368–371. doi: 10.1038/nature10987

Frampton, J. P., Hynd, M. R., Shuler, M. L., and Shain, W. (2010). Effects of glial cells on electrode impedance recorded from neuralprosthetic devices *in vitro*. *Ann. Biomed. Eng.* 38, 1031–1047. doi: 10.1007/s10439-010-9911-y

Freire, M. A., Morya, E., Faber, J., Santos, J. R., Guimaraes, J. S., Lemos, N. A., et al. (2011). Comprehensive analysis of tissue preservation and recording quality from chronic multielectrode implants. *PLoS ONE* 6:e27554. doi: 10.1371/journal.pone.0027554

Geddes, L. A. (1997). Historical evolution of circuit models for the electrode-electrolyte interface. *Ann. Biomed. Eng.* 25, 1–14. doi: 10.1007/BF02738534

Geddes, L. A., and Roeder, R. (2003). Criteria for the selection of materials for implanted electrodes. *Ann. Biomed. Eng.* 31, 879–890. doi: 10.1114/1.1581292

Grill, W. M., and Mortimer, J. T. (1994). Electrical properties of implant encapsulation tissue. *Ann. Biomed. Eng.* 22, 23–33. doi: 10.1007/BF02368219

Hochberg, L. R., Bacher, D., Jarosiewicz, B., Masse, N. Y., Simeral, J. D., Vogel, J., et al. (2012). Reach and grasp by people with tetraplegia using a neurally controlled robotic arm. *Nature* 485, 372–375. doi: 10.1038/nature11076

Iosa, M., Morone, G., Fusco, A., Bragoni, M., Coiro, P., Multari, M., et al. (2012). Seven capital devices for the future of stroke rehabilitation. *Stroke Res. Treat.* 2012:187965. doi: 10.1155/2012/187965

Jackson, A., and Fetz, E. E. (2007). Compact movable microwire array for long-term chronic unit recording in cerebral cortex of primates. *J. Neurophysiol.* 98, 3109–3118. doi: 10.1152/jn.00569.2007

Jackson, A., and Zimmermann, J. B. (2012). Neural interfaces for the brain and spinal cord-restoring motor function. *Nat. Rev. Neurol.* 8, 690–699. doi: 10.1038/nrneurol.2012.219

Johnson, M. D., Otto, K. J., and Kipke, D. R. (2005). Repeated voltage biasing improves unit recordings by reducing resistive tissue impedances. *IEEE Trans. Neural Syst. Rehabil. Eng.* 13, 160–165. doi: 10.1109/TNSRE.2005.847373

Kam, L., Shain, W., Turner, J. N., and Bizios, R. (1999). Correlation of astroglial cell function on micro-patterned surfaces with specific geometric parameters. *Biomaterials* 20, 2343–2350. doi: 10.1016/S0142-9612(99)00163-5

Kane, S. R., Cogan, S. F., Ehrlich, J., Plante, T. D., McCreery, D. B., and Troyk, P. R. (2013). Electrical performance of penetrating microelectrodes chronically implanted in cat cortex. *IEEE Trans. Biomed. Eng.* 60, 2153–2160. doi: 10.1109/TBME.2013.2248152

Karumbaiah, L., Saxena, T., Carlson, D., Patil, K., Patkar, R., Gaupp, E. A., et al. (2013). Relationship between intracortical electrode design and chronic recording function. *Biomaterials* 34, 8061–8074. doi: 10.1016/j.biomaterials.2013.07.016

Kim, B. J., Kuo, J. T., Hara, S. A., Lee, C. D., Yu, L., Gutierrez, C. A., et al. (2013). 3D Parylene sheath neural probe for chronic recordings. *J. Neural Eng.* 10:045002. doi: 10.1088/1741-2560/10/4/045002

Kipke, D. R., Vetter, R. J., Williams, J. C., and Hetke, J. F. (2003). Silicon-substrate intracortical microelectrode arrays for long-term recording of neuronal spike activity in cerebral cortex. *IEEE Trans. Neural Syst. Rehabil. Eng.* 11, 151–155. doi: 10.1109/TNSRE.2003.814443

Koivuniemi, A. S., and Otto, K. J. (2011). Asymmetric versus symmetric pulses for cortical microstimulation. *IEEE Trans. Neural Syst. Rehabil. Eng.* 19, 468–476. doi: 10.1109/TNSRE.2011.2166563

Kozai, T. D. Y., Langhals, N. B., Patel, P. R., Deng, X. P., Zhang, H. N., Smith, K. L., et al. (2012a). Ultrasmall implantable composite microelectrodes with bioactive surfaces for chronic neural interfaces. *Nat. Mater.* 11, 1065–1073. doi: 10.1038/nmat3468

Kozai, T. D., Vazquez, A. L., Weaver, C. L., Kim, S. G., and Cui, X. T. (2012b). *In vivo* two-photon microscopy reveals immediate microglial reaction to implantation of microelectrode through extension of processes. *J. Neural Eng.* 9:066001. doi: 10.1088/1741-2560/9/6/066001

Lee, H., Bellamkonda, R. V., Sun, W., and Levenston, M. E. (2005). Biomechanical analysis of silicon microelectrode-induced strain in the brain. *J. Neural Eng.* 2, 81–89. doi: 10.1088/1741-2560/2/4/003

Lempka, S. F., Johnson, M. D., Moffitt, M. A., Otto, K. J., Kipke, D. R., and McIntyre, C. C. (2011). Theoretical analysis of intracortical microelectrode recordings. *J. Neural Eng.* 8:045006. doi: 10.1088/1741-2560/8/4/045006

Lopes, K. O., Sparks, D. L., and Streit, W. J. (2008). Microglial dystrophy in the aged and Alzheimer's disease brain is associated with ferritin immunoreactivity. *Glia* 56, 1048–1060. doi: 10.1002/glia.20678

Ludwig, K. A., Langhals, N. B., Joseph, M. D., Richardson-Burns, S. M., Hendricks, J. L., and Kipke, D. R. (2011). Poly(3,4-ethylenedioxythiophene) (PEDOT) polymer coatings facilitate smaller neural recording electrodes. *J. Neural Eng.* 8:014001. doi: 10.1088/1741-2560/8/1/014001

Ludwig, K. A., Uram, J. D., Yang, J., Martin, D. C., and Kipke, D. R. (2006). Chronic neural recordings using silicon microelectrode arrays electrochemically deposited with a poly(3,4-ethylenedioxythiophene) (PEDOT) film. *J. Neural Eng.* 3, 59–70. doi: 10.1088/1741-2560/3/1/007

Maling, N., Hashemiyoon, R., Foote, K. D., Okun, M. S., and Sanchez, J. C. (2012). Increased thalamic gamma band activity correlates with symptom relief following deep brain stimulation in humans with tourette's syndrome. *PLoS ONE* 7:e44215. doi: 10.1371/journal.pone.0044215

McConnell, G. C., Butera, R. J., and Bellamkonda, R. V. (2009a). Bioimpedance modeling to monitor astrocytic response to chronically implanted electrodes. *J. Neural Eng.* 6:055005. doi: 10.1088/1741-2560/6/5/055005

McConnell, G. C., Rees, H. D., Levey, A. I., Gutekunst, C. A., Gross, R. E., and Bellamkonda, R. V. (2009b). Implanted neural electrodes cause chronic, local inflammation that is correlated with local neurodegeneration. *J. Neural Eng.* 6:056003. doi: 10.1088/1741-2560/6/5/056003

Merrill, D. R., and Tresco, P. A. (2005). Impedance characterization of microarray recording electrodes *in vitro*. *IEEE Trans. Biomed. Eng.* 52, 1960–1965. doi: 10.1109/TBME.2005.856245

Mollazadeh, M., Aggarwal, V., Davidson, A. G., Law, A. J., Thakor, N. V., and Schieber, M. H. (2011). Spatiotemporal Variation of Multiple Neurophysiological Signals in the Primary Motor Cortex during Dexterous Reach-to-Grasp Movements. *J. Neurosci.* 31, 15531–15543. doi: 10.1523/JNEUROSCI.2999-11.2011

Morrell, M. J. (2011). Responsive cortical stimulation for the treatment of medically intractable partial epilepsy. *Neurology* 77, 1295–1304. doi: 10.1212/WNL.0b013e3182302056

Musallam, S., Bak, M. J., Troyk, P. R., and Andersen, R. A. (2007). A floating metal microelectrode array for chronic implantation. *J. Neurosci. Methods* 160, 122–127. doi: 10.1016/j.jneumeth.2006.09.005

Nicolelis, M. A. L. (1999). *Methods for Neural Ensemble Recordings.* Boca Raton, FL: CRC Press.

Nicolelis, M. A. L., Dimitrov, D., Carmena, J. M., Crist, R., Lehew, G., Kralik, J. D., et al. (2003). Chronic, multisite, multielectrode recordings in macaque monkeys. *Proc. Natl. Acad. Sci. U.S.A.* 100, 11041–11046. doi: 10.1073/pnas.1934665100

Otto, K. J., Johnson, M. D., and Kipke, D. R. (2006). Voltage pulses change neural interface properties and improve unit recordings with chronically implanted microelectrodes. *IEEE Trans. Biomed. Eng.* 53, 333–340. doi: 10.1109/TBME.2005.862530

Otto, K. J., Rousche, P. J., and Kipke, D. R. (2005). Cortical microstimulation in auditory cortex of rat elicits best-frequency dependent behaviors. *J. Neural Eng.* 2, 42–51. doi: 10.1088/1741-2560/2/2/005

Patrick, E., Orazem, M. E., Sanchez, J. C., and Nishida, T. (2011). Corrosion of tungsten microelectrodes used in neural recording applications. *J. Neurosci. Methods* 198, 158–171. doi: 10.1016/j.jneumeth.2011.03.012

Patrick, E., Ordonez, M., Alba, N., Sanchez, J. C., and Nishida, T. (2006). Design and fabrication of a flexible substrate microelectrode array for brain machine interfaces. *Conf. Proc. IEEE Eng. Med. Biol. Soc.* 1, 2966–2969. doi: 10.1109/IEMBS.2006.260581

Polikov, V. S., Tresco, P. A., and Reichert, W. M. (2005). Response of brain tissue to chronically implanted neural electrodes. *J. Neurosci. Methods* 148, 1–18. doi: 10.1016/j.jneumeth.2005.08.015

Prasad, A., and Sanchez, J. C. (2012). Quantifying long-term microelectrode array functionality using chronic *in vivo* impedance testing. *J. Neural Eng.* 9:026028. doi: 10.1088/1741-2560/9/2/026028

Prasad, A., Sankar, V., Dyer, A. T., Knott, E., Xue, Q. S., Nishida, T., et al. (2011). Coupling biotic and abiotic metrics to create a testbed for predicting neural electrode performance. *Conf. Proc. IEEE Eng. Med. Biol. Soc.* 2011, 3020–3023. doi: 10.1109/IEMBS.2011.6090827

Prasad, A., Xue, Q. S., Sankar, V., Nishida, T., Shaw, G., Streit, W. J., et al. (2012). Comprehensive characterization and failure modes of tungsten microwire arrays in chronic neural implants. *J. Neural Eng.* 9:056015. doi: 10.1088/1741-2560/9/5/056015

Richter, A., Xie, Y., Schumacher, A., Loffler, S., Kirch, R. D., Al-Hasani, J., et al. (2013). A simple implantation method for flexible, multisite microelectrodes into rat brains. *Front. Neuroeng.* 6:6. doi: 10.3389/fneng.2013.00006

Rousche, P. J., and Normann, R. A. (1998). Chronic recording capability of the utah intracortical electrode array in cat sensory cortex. *J. Neurosci. Methods* 82, 1–15. doi: 10.1016/S0165-0270(98)00031-4

Rousche, P. J., Pellinen, D. S., Pivin, D. P. Jr., Williams, J. C., Vetter, R. J., and Kipke, D. R. (2001). Flexible polyimide-based intracortical electrode arrays with bioactive capability. *IEEE Trans. Biomed. Eng.* 48, 361–371. doi: 10.1109/10.914800

Rouse, A. G., Stanslaski, S. R., Cong, P., Jensen, R. M., Afshar, P., Ullestad, D., et al. (2011). A chronic generalized bi-directional brain-machine interface. *J. Neural Eng.* 8:036018. doi: 10.1088/1741-2560/8/3/036018

Sanchez, J. C., Alba, N., Nishida, T., Batich, C., and Carney, P. R. (2006). Structural modifications in chronic microwire electrodes for cortical neuroprosthetics: a case study. *IEEE Trans. Neural Syst. Rehabil. Eng.* 14, 217–221. doi: 10.1109/TNSRE.2006.875581

Saxena, T., Karumbaiah, L., Gaupp, E. A., Patkar, R., Patil, K., Betancur, M., et al. (2013). The impact of chronic blood-brain barrier breach on intracortical electrode function. *Biomaterials* 34, 4703–4713. doi: 10.1016/j.biomaterials.2013.03.007

Schmidt, E. M., Bak, M. J., and McIntosh, J. S. (1976). Long term chronic recording from cortical neurons. *Exp. Neurol.* 52, 496–506. doi: 10.1016/0014-4886(76)90220-X

Stensaas, S. S., and Stensaas, L. J. (1978). Histopathological evaluation of materials implanted in the cerebral cortex. *Acta Neuropathol.* 41, 145–155. doi: 10.1007/BF00689766

Streit, W., Xue, Q. S., Prasad, A., Sankar, V., Knott, E., Dyer, A., et al. (2012). Electrode failure: tissue, electrical, and material responses. *IEEE Pulse* 3, 30–33. doi: 10.1109/MPUL.2011.2175632

Suner, S., Fellows, M. R., Vargas-Irwin, C., Nakata, G. K., and Donoghue, J. P. (2005). Reliability of signals from a chronically implanted, silicon-based electrode array in non-human primate primary motor cortex. *IEEE Trans. Neural Syst. Rehabil. Eng.* 13, 524–541. doi: 10.1109/TNSRE.2005.857687

Szarowski, D. H., Andersen, M. D., Retterer, S., Spence, A. J., Isaacson, M., Craighead, H. G., et al. (2003). Brain responses to micro-machined silicon devices. *Brain Res.* 983, 23–35. doi: 10.1016/S0006-8993(03)03023-3

Thelin, J., Jorntell, H., Psouni, E., Garwicz, M., Schouenborg, J., Danielsen, N., et al. (2011). Implant size and fixation mode strongly influence tissue reactions in the CNS. *PLoS ONE* 6:e16267. doi: 10.1371/journal.pone.0016267

Truccolo, W., Donoghue, J. A., Hochberg, L. R., Eskandar, E. N., Madsen, J. R., Anderson, W. S., et al. (2011). Single-neuron dynamics in human focal epilepsy. *Nat. Neurosci.* 14, 635–641. doi: 10.1038/nn.2782

Turner, J. N., Shain, W., Szarowski, D. H., Andersen, M., Martins, S., Isaacson, M., et al. (1999). Cerebral astrocyte response to micromachined silicon implants. *Exp. Neurol.* 156, 33–49. doi: 10.1006/exnr.1998.6983

Vetter, R. J., Williams, J. C., Hetke, J. F., Nunamaker, E. A., and Kipke, D. R. (2004). Chronic neural recording using silicon-substrate microelectrode arrays implanted in cerebral cortex. *IEEE Trans. Neural Syst. Rehabil. Eng.* 51, 896–904. doi: 10.1109/TBME.2004.826680

Ward, M. P., Rajdev, P., Ellison, C., and Irazoqui, P. P. (2009). Toward a comparison of microelectrodes for acute and chronic recordings. *Brain Res.* 1282, 183–200. doi: 10.1016/j.brainres.2009.05.052

Williams, J. C., Hippensteel, J. A., Dilgen, J., Shain, W., and Kipke, D. R. (2007). Complex impedance spectroscopy for monitoring tissue responses to inserted neural implants. *J. Neural Eng.* 4, 410–423. doi: 10.1088/1741-2560/4/4/007

Williams, J. C., Rennaker, R. L., and Kipke, D. R. (1999a). Long-term neural recording characteristics of wire microelectrode arrays implanted in cerebral cortex. *Brain Res. Protoc.* 4, 303–313. doi: 10.1016/S1385-299X(99)00034-3

Williams, J. C., Rennaker, R. L., and Kipke, D. R. (1999b). Stability of chronic multichannel neural recordings: Implications for a long-term neural interface. *Neurocomputing* 26–27, 1069–1076. doi: 10.1016/S0925-2312(99)00106-X

Winslow, B. D., and Tresco, P. A. (2010). Quantitative analysis of the tissue response to chronically implanted microwire electrodes in rat cortex. *Biomaterials* 31, 1558–1567. doi: 10.1016/j.biomaterials.2009.11.049

Conflict of Interest Statement: The authors declare that the research was conducted in the absence of any commercial or financial relationships that could be construed as a potential conflict of interest.

Received: 09 December 2013; accepted: 14 January 2014; published online: 04 February 2014.

Citation: Prasad A, Xue Q-S, Dieme R, Sankar V, Mayrand RC, Nishida T, Streit WJ and Sanchez JC (2014) Abiotic-biotic characterization of Pt/Ir microelectrode arrays in chronic implants. Front. Neuroeng. ***7****:2. doi: 10.3389/fneng.2014.00002*

This article was submitted to the journal Frontiers in Neuroengineering.

frontiers in
NEUROENGINEERING

ORIGINAL RESEARCH ARTICLE
published: 08 May 2014
doi: 10.3389/fneng.2014.00013

Electrode impedance analysis of chronic tungsten microwire neural implants: understanding abiotic vs. biotic contributions

Viswanath Sankar[1], Erin Patrick[1], Robert Dieme[1], Justin C. Sanchez[2], Abhishek Prasad[2]* and Toshikazu Nishida[1]

[1] *Electrical and Computer Engineering Department, University of Florida, Gainesville, FL, USA*
[2] *Biomedical Engineering Department, University of Miami, Coral Gables, FL, USA*

Edited by:
Ulrich G. Hofmann, Albert-Ludwigs-University Freiburg, Germany

Reviewed by:
Thilo Bernhard Krueger, inomed Medizintechnik GmbH, Germany
David Krapohl, Mid Sweden University, Sweden

****Correspondence:***
Abhishek Prasad, Department of Biomedical Engineering, University of Miami, 1251 Memorial Drive, Rm#203, Coral Gables, FL 33146, USA
e-mail: a.prasad@miami.edu

Changes in biotic and abiotic factors can be reflected in the complex impedance spectrum of the microelectrodes chronically implanted into the neural tissue. The recording surface of the tungsten electrode *in vivo* undergoes abiotic changes due to recording site corrosion and insulation delamination as well as biotic changes due to tissue encapsulation as a result of the foreign body immune response. We reported earlier that large changes in electrode impedance measured at 1 kHz were correlated with poor electrode functional performance, quantified through electrophysiological recordings during the chronic lifetime of the electrode. There is a need to identity the factors that contribute to the chronic impedance variation. In this work, we use numerical simulation and regression to equivalent circuit models to evaluate both the abiotic and biotic contributions to the impedance response over chronic implant duration. COMSOL® simulation of abiotic electrode morphology changes provide a possible explanation for the decrease in the electrode impedance at long implant duration while biotic changes play an important role in the large increase in impedance observed initially.

Keywords: chronic neural implants, electrode impedance, corrosion, insulation delamination, finite element modeling

INTRODUCTION

Tungsten micro-wire electrode arrays continue to be used as chronic implants for single-unit neuronal recording (Williams et al., 1999a,b; Rennaker et al., 2005; Rizk et al., 2009; Freire et al., 2011). Implanted electrodes in general suffer recording performance degradation over time (Williams et al., 1999a; Ward et al., 2009). Understanding the reasons for poor recording performance over time is integral for the adaptive design of future electrode arrays. For tungsten micro-wire electrodes, structural modification of the recording site by corrosion and insulation delamination (Sanchez et al., 2006; Patrick et al., 2011; Prasad et al., 2012; Streit et al., 2012) as well as tissue encapsulation due to the foreign-body immune response (Szarowski et al., 2003; Biran et al., 2005, 2007; McConnell et al., 2009) are known to occur. Although it is known that both abiotic and biotic effects contribute to changes at the electrode recording site, it is still unclear to what extent each effect has on the chronic recording performance of the electrode.

Impedance is a metric commonly used to assess electrode performance. Chronic *in-vivo* studies (Prasad and Sanchez, 2012) have confirmed a functional correlation between the electrode impedance value at 1 kHz and the overall neuronal yield during the implanted duration. It was observed in that study that low array yields were associated with very low impedance values or very high impedance values, and the best array yield was observed for an impedance range of 40–150 kΩ at 1 kHz for the implanted 50 μm diameter blunt-cut tungsten micro-wires. The electrode impedance also varied over time increasing during the first few weeks of implantation followed by a drop in the impedance value in the latter phase of the implant duration. Though these observations suggest that the electrode impedance is affected by some short-term and long-term factors, the underlying driving mechanisms are not fully understood. Furthermore, the impedance variation for tungsten microwires itself varied across different implanted animals.

The working model is that network analysis of the complex impedance spectra of implanted electrode arrays may yield useful information about the changes occurring in the vicinity of the electrode recording sites in the neural tissue. This is supported by the results of Williams et al. who showed a distinction between severe and nominal inflammatory response to tungsten electrodes implanted in an animal model for 19 days by comparing the complex impedance spectra (Williams et al., 2007). Nyquist plots were used to show the progression of the inflammatory response over time. However, the effect of corrosion or insulation delamination was not considered in their paper.

In this paper, we analyze the complex impedance spectra of tungsten micro-wire electrodes that were previously implanted for 9-months into the rat somatosensory cortex. We show progress toward decoupling the abiotic (e.g., recording-surface structural modification) effects from the biotic (e.g., tissue encapsulation) effects with the analysis of the complex impedance spectra of the implanted electrodes. Graphical comparisons as well as

regression to an equivalent circuit model provide qualitative and quantitative results. Finite element analysis package COMSOL® Multiphysics® (Burlington, MA) is used to simulate abiotic effects of different electrode surface variations on the impedance. We used pre-implant and post-explant SEM imaging and surface roughness analysis to provide evidence of abiotic structural changes.

MATERIALS AND METHODS

ANALYSIS OF *IN-VIVO* ELECTRODE ARRAY DATA

Electrode array

Sixteen-channel micro-wire arrays [Tucker-Davis Technologies (TDT), Alachua FL] were used for this study. The microwires were 50 μm in diameter, 5 mm long, and blunt cut using a laser beam. The tungsten wires were plated with a thin film of gold of thickness ∼2–5 μm and insulated with a layer of polyimide of approximate thickness 10 μm. The wires were positioned in a 2 × 8 configuration with spacing of 250 μm between two adjacent microwires.

Implantation and recording

The electrode array was implanted in the somatosensory cortex of an adult male Sprague-Dawley rat. Aseptic surgical techniques were used for the implantation procedure. All procedures were approved by the Institutional Animal Care and Use Committee, University of Miami, FL. Electrophysiological recordings were made on the animal three to four times a week and each recording session lasted approximately 20 min. A custom testbed was developed that allowed the animal to move freely during the recording session. Impedance was measured before every recording session on all 16 microwires using a small current (maximum 1.4 nA) that did not affect the electrode properties. The surgical and recording procedures are described in detail in Prasad and Sanchez (2012). The structural changes were investigated by imaging the electrodes surfaces before and after the implant.

Characterization of structural changes

The structural changes in the implanted electrodes were studied by characterizing the microwire arrays through qualitative methods using scanning electron microscope (SEM) imaging and quantitative methods via laser scanning microscope surface roughness measurements. Tungsten microwires were imaged before and after explantation using SEMs (CarryScope SEM, JEOL, Inc., and FEI XL-40 field emission gun SEM). The imaging procedure is described in detail in Prasad et al. (2012).

The pre- and post-implant SEM images of the electrode provided only a qualitative idea of the variation in the surface morphology. In order to quantitatively assess the surface roughness and corrosion depth of the implanted electrodes, some of the arrays were analyzed for surface roughness using a laser scanning microscope (Keyence VK-9700 Color 3D Laser Scanning Microscope) at the Materials Evaluation and Testing Laboratory, South Dakota State University. The depth profile of the wires in the array was measured and the average height with respect to the reference line was calculated.

Impedance measurement and analysis of magnitude at 1 kHz

The NanoZ® impedance tester (TDT, FL) was used to measure the daily *in-vivo* impedance values. The NanoZ applies a constant voltage of 4 mVpp sinusoidal waveform which results in a maximum test current of 1.4 nA. Compared to an estimated corrosion current on the order of 100 nA at equilibrium from results in Patrick et al. (2011), the 1.4 nA current used for the impedance measurements will negligibly affect the normal corrosion processes. The impedance measurement process involved 40 cycles of measurement on each microwire and an average value was calculated to minimize measurement errors. The impedances were recorded at 1, 2, 5, 10, 20, 50, 100, 200, 500 Hz, 1 and 2 kHz. Prior to implantation, the impedance of each microelectrode was characterized in 0.9% phosphate buffered saline (PBS) that served as a baseline for the *in vivo* measurements. In the case of *in vitro* pre-implant testing, the reference was made to a stainless steel ground wire connected to the MEA assembly and dipped in the same saline solution, whereas for *in vivo* chronic testing, the reference was made to the same stainless steel ground wire connected to a stainless steel bone screw drilled into the skull.

From the measured *in vivo* impedance data, the percentage change in impedance was calculated for each individual wire and averaged for all wires for the implanted duration. The impedance value measured on the surgery day was considered as the reference value and the percentage change was calculated for this reference. Since the temporal variation of the *in vivo* impedance approximately follows a Gaussian profile, the calculated percentage change in impedance values were fitted with a Gaussian curve using the built-in curve fitting tool in OriginPro® (OriginLab Corporation, Northampton, MA) given by

$$y = y_0 + \frac{A}{w\sqrt{\pi/2}} e^{-2\frac{(x-x_c)^2}{w^2}} \quad (1)$$

where, w is the standard deviation, x is the individual calculated value, x_c is the average, and A and y_0 are constants. Percentage change higher than 600% were treated as outliers and were not included in the calculations.

GRAPHICAL ANALYSIS AND REGRESSION OF COMPLEX IMPEDANCE DATA

The real and imaginary parts of the complex impedance data as a function of frequency were plotted with logarithmic scales on both axes to capture both low as well as high frequency data. These complex-plane impedance plots, compared to Nyquist or Bode plots, can better identify physical processes (Orazem et al., 2006) and make trends in the temporal changes more apparent. Eight timestamps were chosen to adequately capture the temporal impedance trend, day 1 of implant and days 7, 15, 31, 60, 106, 149, and 205 post implant.

Regression of the complex impedance data was performed using the non-linear least squares regression function in Matlab. The real and imaginary parts of the impedance spectrum were fit to one of two equivalent circuits shown in **Figure 1**. The circuit in **Figure 1A**, commonly known as the "Randles circuit," models the electrochemical interface of a bare metal electrode in an electrolyte neglecting the diffusion related Warburg impedance

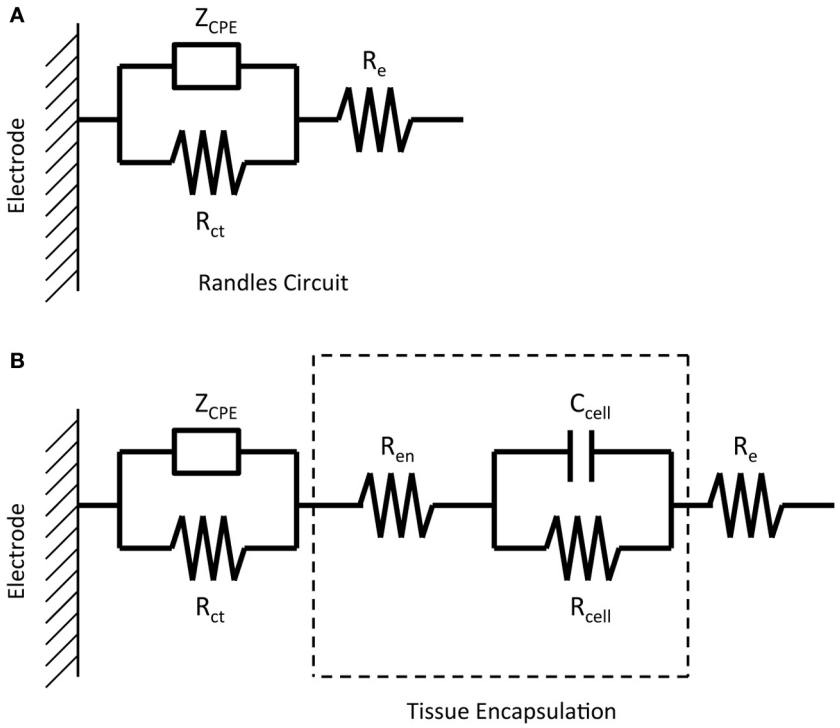

FIGURE 1 | Equivalent circuits representing the impedance of a micro-wire without the presence of tissue encapsulation due to the inflammatory response (A) and with the presence of tissue encapsulation (B).

(Brug et al., 1984; McAdams et al., 1995). R_{ct} is the charge transfer resistance, which models the resistive pathway due to electrochemical reactions (i.e., tungsten corrosion), and Z_{CPE} is the constant phase element impedance given by

$$Z_{CPE} = \frac{1}{(j\omega)^{\alpha} Q} \tag{2}$$

where ω is the frequency, α is a number from 0 to 1, and Q is the constant phase element (CPE) coefficient with units $s^{\alpha}/\Omega cm^2$. The CPE element is used to model the capacitive double layer at the electrode interface. The CPE, rather than an ideal capacitor, better accounts for non-idealities due to surface inhomogeneity (Brug et al., 1984) and is commonly used in electrode/electrolyte equivalent circuit models (McAdams et al., 1995; Johnson et al., 2005; Otto et al., 2006; Williams et al., 2007; Lempka et al., 2011). R_e models the resistance of the electrolyte seen by the electrode and is also referred to as the spreading resistance to a distant ground. **Figure 1B** adds a simplified circuit that models the tissue encapsulation layers through a series resistor R_{en} and parallel combination of a resistor R_{cell} and capacitor C_{cell}. (Johnson et al., 2005; Otto et al., 2006; Williams et al., 2007; Lempka et al., 2011). The tissue encapsulating the electrode due to the immune response consists of layers of extracellular matrix proteins (e.g., collagen, fibronectin, and laminin) and reactive glial cells and macrophages (Grill and Mortimer, 1994; Kim et al., 2004). R_{en} models encapsulation by extracellular matrix proteins, and C_{cell} and R_{cell} model the resistive and capacitive pathways through the cellular layer, respectively.

Figure 2 shows generic complex-plane impedance plots calculated using the two equivalent circuits in **Figure 1**. One distinguishing feature of the imaginary impedance as a function of frequency is the presence of only one peak for the Randles circuit and the presence of two peaks in the circuit that adds tissue encapsulation components to the Randles circuit. These peaks occur at the frequencies given by the reciprocal of the RC time-constants in the circuit. R_{ct} and Z_{CPE} determine the low-frequency peak and the high-frequency peak is determined by the adherent cellular components, C_{cell} and R_{cell}. Thus, the presence of a cellular biotic layer at the electrode surface may be inferred by examining the imaginary impedance data. The real impedance as a function of frequency provides information on the electrolyte and encapsulation resistance, R_e and R_{en}, at high frequencies where the impedance of CPE and C_{cell} are small compared to the parallel resistive components. The high-frequency asymptotic value converges to the electrolyte resistance R_e in the Randles circuit and the addition of R_e and R_{en}, for the circuit that includes encapsulation components. We use these graphical impedance analysis techniques to assess the factors causing temporal variation of impedance for our chronically implanted electrode array.

COMSOL® FINITE ELEMENT ANALYSIS (FEA)

Finite element analysis of the electrode-electrolyte interface was made in COMSOL® Multiphysics software package to investigate how the electrolyte resistance, R_e, changes over time due to

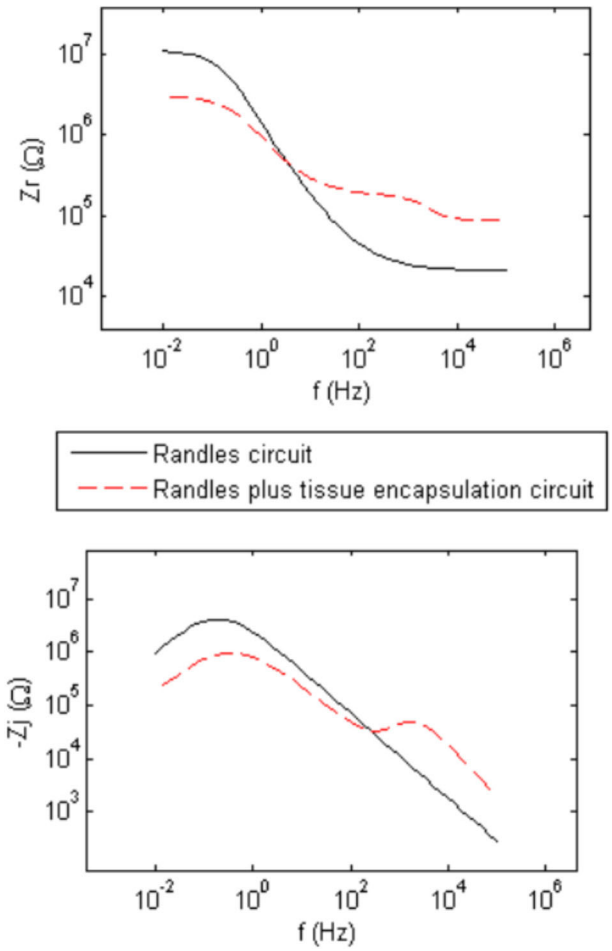

FIGURE 2 | Generic calculated real (Z_r) and imaginary (Z_i) parts of the complex impedance as a function of frequency representing the two equivalent circuits in Figure 1 having abiotic only and abiotic and biotic components which illustrate the presence of one peak for the Randles circuit and two peaks for the Randles combined with Tissue Encapsulation circuits for the imaginary impedance.

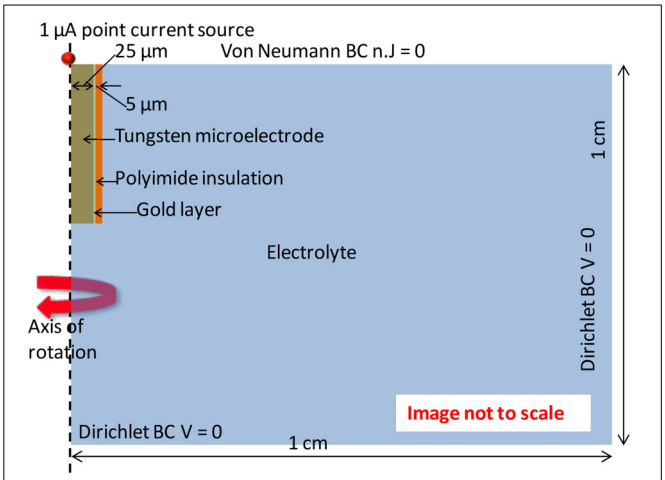

FIGURE 3 | Illustration of the electrode-electrolyte interface and the boundary conditions used in the COMSOL® finite element model.

Table 1 | Conductivity values used for the COMSOL® finite element model.

Material/layer	Conductivity (S/m)	References
Tungsten	18.94×10^6	Serway, 1998
Gold	40.98×10^6	Serway, 1998
Polyimide	1×10^{-16}	HD Microsystems, 2001
Cerebrospinal fluid	1.8	Baumann et al., 1997

simulated structural modifications. The tungsten electrode was modeled using a three-dimensional (3-D) geometry consisting of a 50 µm thick tungsten microwire surrounded by 1 µm thick gold layer and insulated with 5 µm thick polyimide insulation surrounded by a region of cerebrospinal fluid (CSF) electrolyte. The COMSOL® AC/DC module (or electric current physics) was selected to numerically solve the governing physics. The electrolyte boundaries were extended up to 1 × 1 cm to satisfy the semi-infinite boundary condition. A point current source of 1 µA was placed at the center of the top (cortex boundary) surface of the electrode. **Figure 3** shows an illustration of the COMSOL® finite element 3-D model of the electrode-electrolyte interface. The electrode was assumed to be a uniform conductor; hence the potential distribution across the electrode is constant. A Dirichlet boundary condition of $V = 0$ was assumed at the electrolyte boundaries since the boundaries are supposed to be semi-infinite, while a von Neumann boundary condition of $\vec{n} \cdot \vec{j} = 0$ was assumed at the cortex boundary, which ensured electrical insulation at the boundaries. The conductivities of the different materials used for the model are given in **Table 1**. Tetrahedral elements with size ranging from 1 to 400 µm were used for meshing the domains.

RESULTS

IN VIVO EXPERIMENTAL RESULTS

As described previously (Prasad et al., 2012), the electrode array under study was deemed a functionally optimal performing array having 50–70% of the wires functional during the extent of the implant (216 days). Also, the *in vivo* impedance magnitude measured at 1 kHz stayed within the 40–150 kΩ range determined optimal for functional electrophysiological recordings for this array type. The average temporal variation, averaged over 16 electrodes, is shown in **Figure 4**. The average change in impedance at 1 kHz follows a Gaussian profile. However since averaging can mask individual variation, it is also instructive to look at specific electrodes that highlight the variation between electrodes implanted at the same time in the same animal. Detailed data of the percent change in impedance magnitude at 1 kHz, complex-plane impedance plots over time, and neuronal yield data over time for one representative wire out of the array (wire 12) are shown in **Figure 5**. Data for all wires in the array are given in the supplemental materials.

Corrosion of the tungsten and delamination and cracking of the polyimide insulation are abiotic factors that contribute

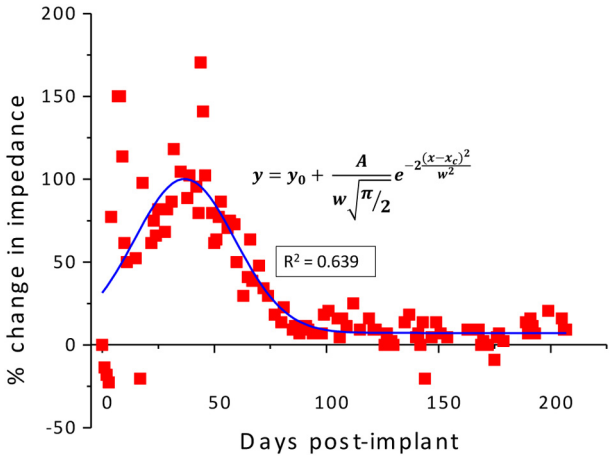

FIGURE 4 | Average percentage change in the *in-vivo* impedance averaged for all wires of electrode array R9 plotted against the implanted duration and fitted with a Gaussian curve.

to morphological changes at the electrode/tissue interface. SEM images of the recording site pre- and post-implant, and relief images of the surface showing a calculated corrosion depth for one wire out of the array (wire 12) are shown in **Figure 6**. Comparison between the pre-implant and the post-implant SEM images of the electrodes revealed similar amounts of tungsten corrosion in all the 16 wires. The tungsten core was recessed within the outer layers of gold and polymer insulation. The measured average corrosion depth for all of the wires was 38.8 μm with a standard deviation of 9.4 μm. Moreover, all wires had some variation of visible insulation damage including delamination and cracks. The majority of the damage was delamination at the electrode surface. In two electrodes out of the array, there were noticeable cracks in the insulation that reached, at maximum, 30 μm below the recording surface.

In all wires in the array, there were large variations in the impedance magnitude over time, with the largest variability occurring within the first few weeks. This large variability happens to occur when the abiotic and biotic factors are most in flux. For example, the rate of tungsten corrosion is larger within the first few weeks of implantation (Prasad et al., 2012), and the inflammatory response does not achieve its chronic stage until after 4–6 weeks (Turner et al., 1999). Thus it is unclear which factor, abiotic or biotic, contributes most to this trend.

We attempt to uncover the mechanisms for the temporal variations by examining the complex-plane impedance data for select days using the graphical analysis described in Graphical Analysis and Regression of Complex Impedance Data. **Figure 5** shows a trend in the complex impedance seen in all wires of the array. The imaginary impedance as a function of frequency (subfigure D) shows two peaks instead of one on every day except for the first day suggesting the presence of a second RC time-constant after day one. These observations suggest a definite biotic component to the impedance magnitude at 1 kHz after day one, since the peak due to a cellular component in the complex impedance vs. frequency is apparent. Our hypothesis that these temporal variations in the electrode impedance have a stronger biotic contribution in the days following implant surgery is supported by the large cellular changes that occur around the microelectrodes due to initial foreign body response. Also the peak occurring at higher frequencies (>400 Hz) is more pronounced primarily on days 7, 15, and 31 after implantation, which is usually the period during which the tissue encapsulation layer due to the inflammatory response is forming (Turner et al., 1999). The second peak is less pronounced in the later days and the impedance values at the higher frequencies decrease. The real part of the impedance as a function of frequency (subfigure C) shows a similar trend in all of the wires of the array in which the impedance value at higher frequencies (>50 Hz) increases to a maximum in the beginning (days 7–31) and then decreases and remains more constant over time. These results are also consistent with our previously reported results where we observed the tissue inflammatory response to be reducing for long-term animals such as the one examined here (Prasad et al., 2012). Further, an abiotic factor such as insulation deterioration is also one of the likely causes of the reduction of impedance in the chronic phase. Circuit elements R_e, and R_{en} are important factors in this trend and will shed more light on the influence of biotic and abiotic effects.

REGRESSION OF COMPLEX IMPEDANCE DATA

The goal of the regression is to quantify each circuit parameter such that the abiotic and biotic contributions to the impedance magnitude at 1 kHz may be identified. One electrode in the array, wire 12 (complex impedance shown in **Figures 5C,D**), was chosen as a representative sample for regression analysis. The impedance for day 1, since it only has one time constant, was fit to the Randles circuit and the remaining data sets were fit to the circuit that includes the encapsulation components. In the regression, one resistor encompassing R_e and R_{en} was used in the equivalent circuit that incorporated encapsulation components. **Figure 7** shows the regression results with fits to the limited data points.

Further analysis is needed to decouple the electrolyte resistance and the encapsulation resistance for all days after the first. The electrolyte impedance R_e is dependent on the surface morphology of the electrode. With corrosion and insulation deterioration occurring at the electrode surface, R_e will likely change over the implant time; however, the extent is not well understood. For example, what effect does a recessing electrode surface have on the electrolyte resistance? This question has not been addressed in the literature to the best of our knowledge. We rely on COMSOL numerical simulation to estimate the changes to R_e over time which is used to estimate a value for R_{en} (Discussion section).

COMSOL® FEA RESULTS

The response of structural changes to the electrolyte resistance is analyzed in COMSOL®. Our model for electrode surface morphology was developed based on our knowledge obtained from prior *in vitro* (Patrick et al., 2011) and *in vivo* (Prasad and Sanchez, 2012) impedance studies. It comprises morphological changes to the metal, tungsten, via corrosion and to the polymer insulation via crack formation and delamination.

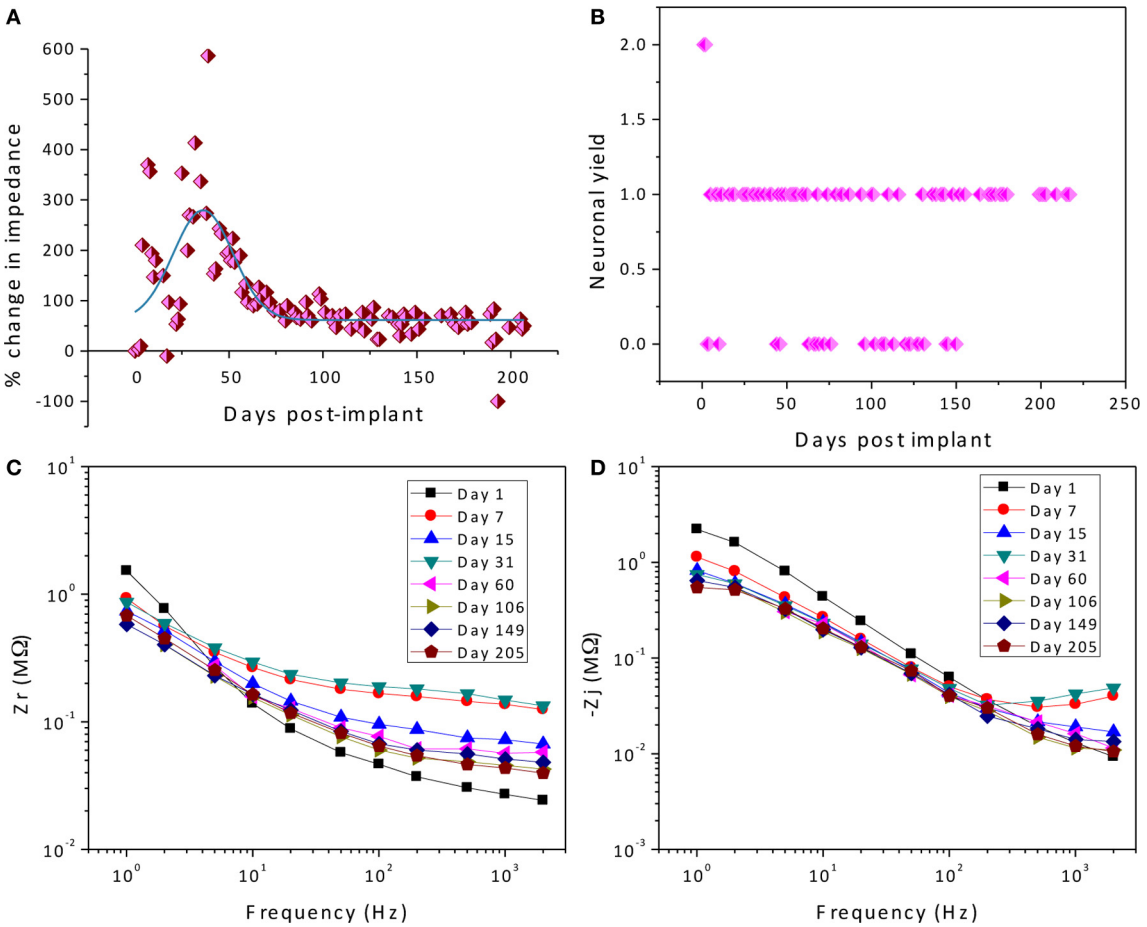

FIGURE 5 | Detailed data of the percent change in impedance magnitude at 1 kHz (A), neuronal yield data over time (B), complex-plane impedance plots over time (C,D) for wire 12.

The results from the *in vitro* and *in vivo* studies suggest that the electrode will undergo continuous corrosion during the implantation period. However, the corrosion rate may be highly dynamic. The rate of corrosion is influenced by the presence of chemical species such as hydrogen peroxide (H_2O_2) (Patrick et al., 2011), which is produced by reactive microglia that surround the implanted microwire. The *in-vitro* corrosion study showed that gold plated tungsten wires corrode at the rate of 10,000–20,000 μm/year in PBS in the presence of millimolar concentrations of H_2O_2, while the rate drops to 300–700 μm/year in the absence of H_2O_2 (Patrick et al., 2011).

In the *in vivo* setting, the immune response gives an indication for how corrosion may evolve. We have shown the corrosion to be present in all microwires but the rate of corrosion was found to be accelerated in the first few weeks following electrode implant compared to chronic periods (Prasad et al., 2012). Coincidentally, there are larger changes that occur in the vicinity of the electrode recording tips due to the inflammatory response in the early hours to weeks following implant. The inflammatory response activates the microglial cells, which produce superoxides and add unknown concentrations of H_2O_2 to the CSF (Burke and Lewis, 2000). During the first few weeks of implantation, we assume there is a higher concentration of H_2O_2, which leads to a higher rate of tungsten corrosion. When the inflammation response progresses to the gliosis phase, the number of surrounding glial cells decreases, and the glial sheath becomes more compact (Polikov et al., 2005). Hence, we assume the rate of corrosion decreases because there is a smaller amount of H_2O_2 being produced by the remaining glial cells, and the dense glial sheath may impede diffusion of reacting species, thereby making the corrosion rate mass-transfer limited. Thus far, our model for temporal tungsten morphology is that the exposed tungsten will uniformly corrode (as compared to pitting corrosion) as soon at it is implanted with a rate that will increase with time up to formation of the compact glial sheath and then decrease to a constant value. These assumptions were made after close observation of electrode recording sites for these arrays for varying implant durations (acute to up to 9 months).

The effect of two cases of electrode surface variations on the electrolyte impedance R_e were studied in detail. In both cases, corrosion is assumed to occur while in Case 1, the added variation due to insulation delamination/peeling is modeled and in Case 2, the added variation of insulation cracking is considered. **Figure 8** illustrates the model geometry for electrode surface

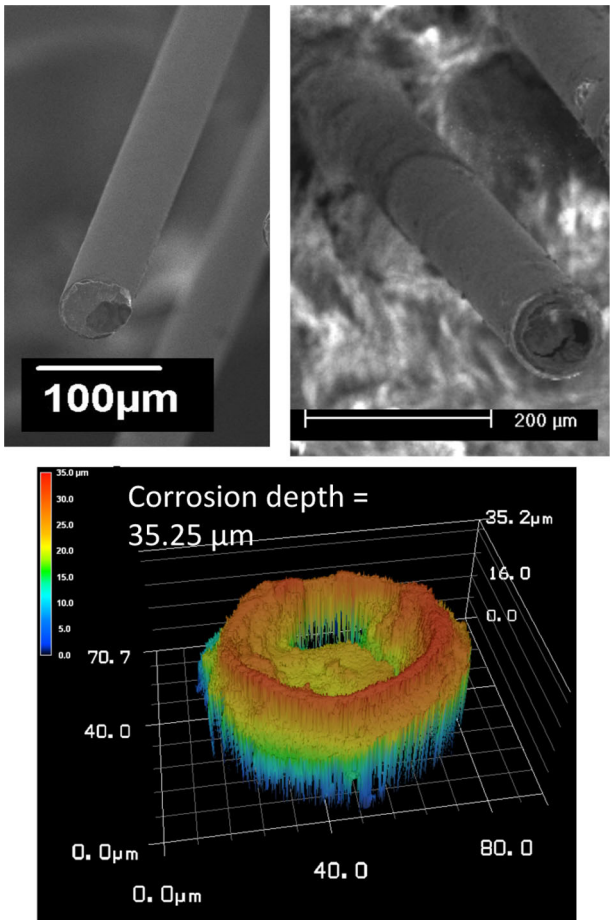

FIGURE 6 | SEM images of the recording site pre- and post-implant (top), and relief images of the surface showing a calculated corrosion depth (bottom) for wire 12.

modification over implant duration involving both corrosion and insulation delamination (Case 1) and both corrosion and insulation cracking (Case 2), respectively.

In Case 1, the insulation delamination was modeled as a gap between the electrode and the insulation (**Figure 8A**). Impedance was calculated at seven different instances with each instance representing a different surface. The first instance was a pristine wire with no corrosion or insulation delamination. Impedance calculated at this instance served as the baseline reference for the successive instances. The next two instances model the high corrosion phase of the electrode. No modification in insulation was included in these two instances. The final four instances model the simultaneous corrosion and insulation delamination phase. A rate of 15 µm per instance was assumed for modeling the high corrosion rate, while a rate of 0.5 µm per instance was assumed for the low corrosion rate. This ratio of 15:0.5 was chosen in accordance with the experimentally measured tungsten corrosion rate ratio of 10,000–20,000:300–700 in the presence and absence of hydrogen peroxide. A constant rate of 2 µm per instance was assumed for the increase in insulation gap width and length.

In Case 2, the insulation crack was modeled as a slit with a width that is proportional to the arc angle and a varying crack length (**Figure 8B**). Similar to Case 1, the impedance for Case 2 was calculated at seven different instances for the insulation-cracked case. As before, the first instance was a pristine wire serving as the baseline reference for the successive instances, and the next two instances model the high corrosion phase of the electrode, and the final four instances model the simultaneous corrosion and cracking in insulation phase. The same rate of 15 µm per instance was assumed for modeling the high corrosion rate, while a rate of 0.5 µm per instance was assumed for low corrosion rate. A constant rate of 2.5 µm per instance was assumed for the increase in insulation crack length and the width of the crack was set by fixing the arc angle at 15°, 30°, 60°, and 90° for each instance.

The COMSOL® simulated percentage changes in resistance for corrosion and (Case 1) insulation delamination and (Case 2) insulation cracking at different instances are given in **Figure 9**. Also the dimensions of the metal recession modeling corrosion and insulation delamination and cracks are also shown. It can be observed in **Figure 9** that the percent change in the electrode resistance increases steadily during the initial high corrosion-rate phase and decreases during the low corrosion and insulation damage phase, modeled either by insulation delamination or by insulation cracking, giving rise to a bell shape or Gaussian profile for both cases. The increase of resistance as a result of the tungsten recessing into its insulation is an interesting finding. However, it can be observed that the increase in resistance is only up to 14% and the decrease in resistance is up to −7% which is nearly one order of magnitude less than the observed *in-vivo* impedance changes.

DISCUSSION

ABIOTIC vs. BIOTIC CONTRIBUTIONS TO IMPEDANCE MAGNITUDE AT 1 kHz

Abiotic and biotic factors

Before estimating values for elements in the time-varying equivalent circuits, it is important to identify which factor, biotic or abiotic, will most affect the individual circuit elements. The biotic changes at the electrode/tissue interface are encapsulation by extracellular matrix proteins and glial cells brought on by the foreign-body immune response. The abiotic factors that lead to electrode surface morphology are corrosion and insulation deterioration.

The surface area of the recording electrode is constantly changing due to corrosion and insulation delamination. Hence, it is possible that the circuit elements that comprise the neural electrode equivalent circuit model will change over time due to the changing surface area. As seen from the COMSOL® results, the corrosion and subsequent recession of tungsten will cause an increase in the electrolyte resistance, R_e, while insulation delamination and cracking will decrease the resistance. Similarly, the Randles circuit parameters, charge transfer resistance (R_{ct}) and CPE coefficient Q, are also expected to vary with changes in the surface area. R_{ct} is inversely proportional to the surface area while Q (similar to a capacitance) is directly proportional to area.

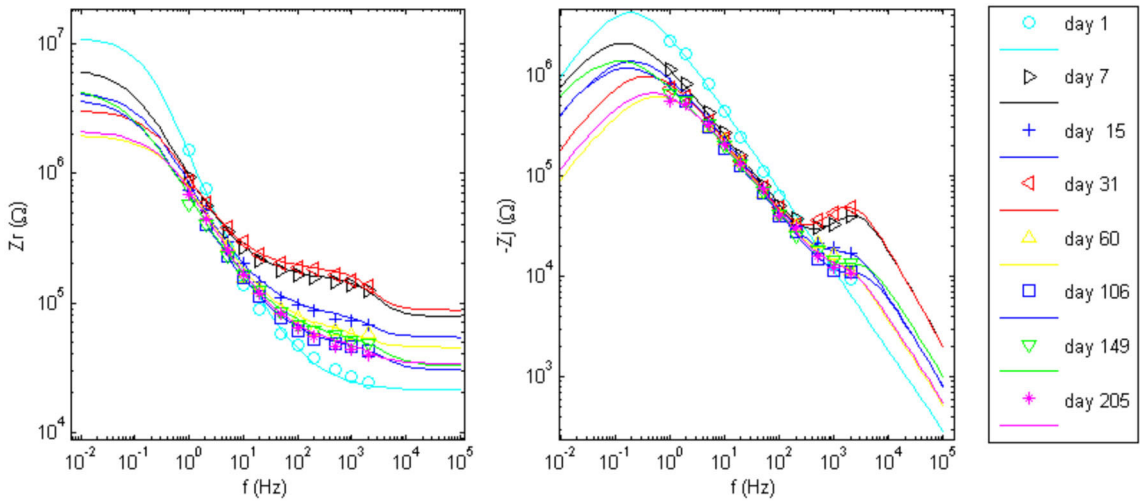

FIGURE 7 | Impedance data points and the regressed fit lines of complex impedance for wire 12 to the circuits shown in Figure 1. Day 1 was fit to the Randles circuit, only. The equivalent circuit with added tissue encapsulation components are used to fit the data for all other days post implant.

The key remaining question is whether the tissue encapsulation circuit will be affected, i.e., will abiotic changes affect biotic changes of the neural electrode? For a first order approximation, one would expect that the encapsulation components R_{cell} and C_{cell} will be unaffected by changes in surface area since they represent an independent cellular layer. However, it is possible that dynamic changes in abiotic factors such as the surface roughness and area compound the biotic changes due to re-engaging the immune response as fresh electrode surfaces are newly exposed over time. The biotic factors, encapsulation by extracellular matrix proteins and glial cells, will obviously control the circuit elements R_{en}, C_{cell}, and R_{cell}. However, R_{en} will be coupled with abiotic changes since it is also dependent on the surface morphology of the electrode. Moreover, the time-varying void left by the corroding tungsten and/or delaminating/cracking insulation might encourage ingrowth of extracellular matrix proteins and result in a larger encapsulation resistance than would be present for an ideal, non-corroded recording surface. Analysis of the regression suggests a multitude of factors contributing to the magnitude of the impedance change at 1 kHz for the array under study.

Analysis of regression

Using the results from the regression and the COMSOL® analysis, we can estimate the circuit elements in the equivalent circuits used to represent the electrode/tissue interface over the chronic implant time for wire 12. According to the COMSOL® results, R_e will initially increase a maximum of 14% from its day one value and decrease to only 7% below this value over time. These changes are small compared to the magnitude of the change of the combined regressed value for series resistance; thus for purposes of the regression analysis, R_e is assumed to be roughly constant and R_{en} is simply calculated to be the regressed value minus R_e for the Randles, day-one circuit. Nonetheless, the shape of the total impedance change (**Figure 4**) follows the shape of the electrolyte resistance change (**Figure 9**).

The real and imaginary parts of the complex impedance contribute to the overall magnitude of the impedance as described in Equation 3

$$Z_{mag} = \sqrt{Z_r^2 + Z_j^2}, \tag{3}$$

where Z_r and Z_j are the real and imaginary parts of the impedance, respectively. Thus it is useful to compare the real and imaginary parts of the different components in the equivalent circuits calculated at 1 kHz. The real and imaginary parts of the parallel combination of R_{ct} and Z_{CPE} are termed $Z_{r,j\text{-interface}}$ and given in **Table 2**. The estimated impedance for the parallel combination of R_{cell} and C_{cell} is termed $Z_{r,j\text{-cell}}$ and also given in **Table 2** along with estimated values for R_e and R_{en} from the regression analysis.

The contribution of the impedance at 1 kHz for components in the Randles circuit is $Z_{r\text{-interface}} + R_e$ and $Z_{j\text{-interface}}$ for the real and imaginary parts, respectively. The tissue encapsulation contribution is $Z_{r\text{-cell}} + R_{en}$ and $Z_{j\text{-cell}}$ for the real and imaginary parts, respectively. Since the real and imaginary parts have a non-linear relationship with the impedance magnitude, both are plotted separately and compared against the magnitude of the impedance in **Figure 10**. Here, key observations can be made. The real part of the impedance is much larger than the imaginary part at 1 kHz. Thus, the magnitude of the complex impedance is dominated by trends in the real part of the impedance as seen in **Figure 10A**.

There is no *a priori* assumed model for the time dependence of the tissue encapsulation process while the COMSOL® simulation of abiotic changes due to corrosion and insulation delamination/cracking indicate a Gaussian temporal dependence. There are several possible scenarios. Though regression analysis was

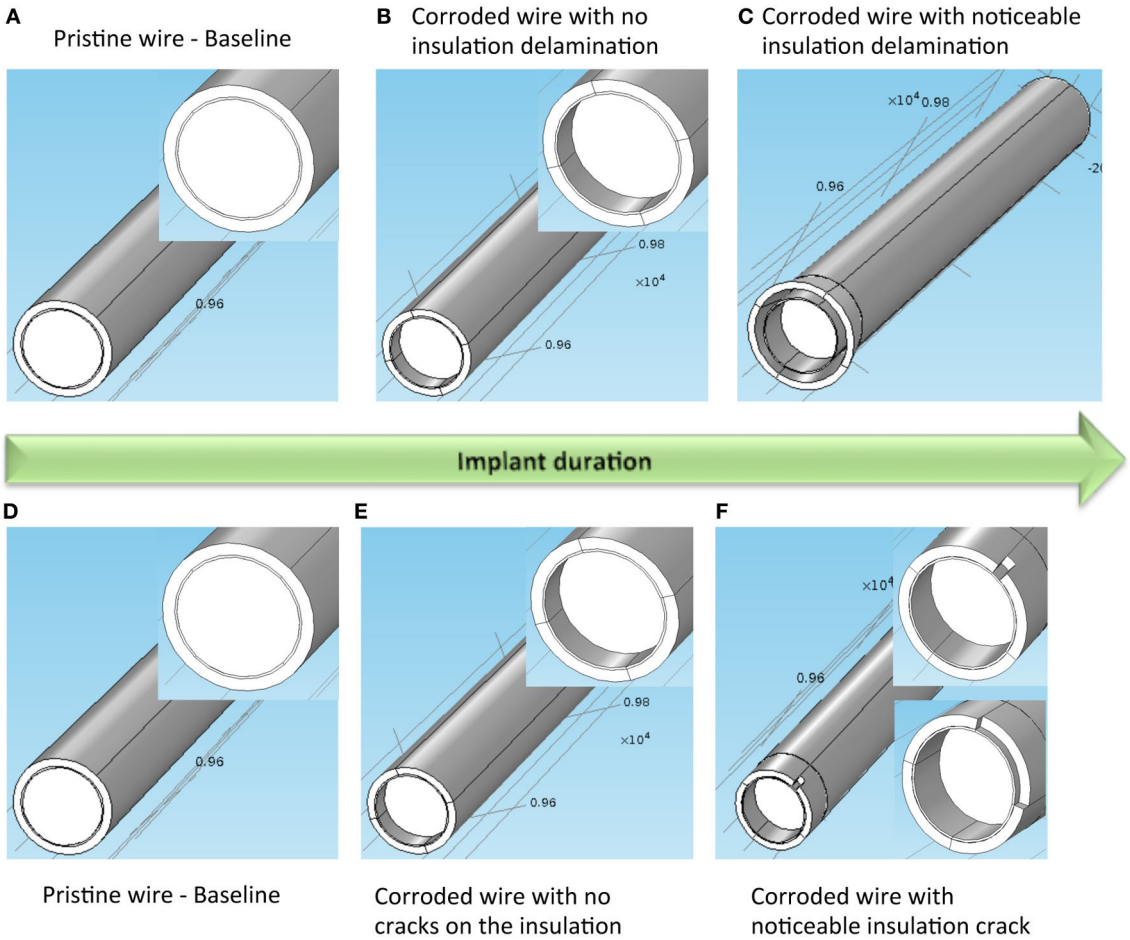

FIGURE 8 | Case 1 for modeled electrode surface modification over implant duration involving both corrosion and insulation delamination. **(A)** Pristine electrode with intact metal and insulation, **(B)** electrode with corroded metal and no insulation delamination, and **(C)** electrode with corroded metal and noticeable insulation delamination. Inset on the left and middle images shows a closer view of the gold layer around the tungsten. Case 2 for modeled electrode surface modification over implant duration involving both corrosion and insulation cracking. **(D)** Pristine electrode with intact metal and insulation, **(E)** electrode with corroded metal and no insulation crack, and **(F)** electrode with corroded metal and noticeable insulation crack. Inset on the left, middle and right images shows a closer view of the gold layer around the tungsten.

performed for only one electrode out of the array, because of the similarity of the trends in the complex impedance spectra for the remaining electrodes, the impedance changes are expected to be similar. We surmise that the rise in impedance magnitude, which resulted in an average increase of 100% is dominated by biotic tissue encapsulation factors; however, the coupling or acceleration of the biotic factors by the prolonged foreign body response due to corrosion is unknown. The subsequent fall in the impedance magnitude could be due to both biotic and abiotic factors. Since the tissue encapsulation layer is known to swell in the beginning and then decrease to a more compact layer in the chronic stage, a rise and fall in the impedance magnitude is possible. However, it should not decrease to a value that is lower than the initial value. In at least half of the electrodes in the array under study, the impedance magnitude decreased to a value that was 25–50% lower than the initial value. Therefore, abiotic effects that increased the surface area and perhaps greatly reduced the encapsulation R_{en} and electrolyte resistance R_e may be significant.

LIMITATIONS TO THE MODEL

The major source of error in our analysis is the assumption of the equivalent circuit for the *in vivo* electrode/tissue interface. Similar circuit elements were used previously to model the tissue encapsulation (Johnson et al., 2005; Otto et al., 2006; Williams et al., 2007; Lempka et al., 2011). The Randles circuit may not be a good model for an electrode undergoing corrosion where the microstructure contains numerous pores and other surface variations. Incorporation of porous electrode equivalent circuit models could provide a better fit to the experimental data. However, the dominance of the impedance due to tissue encapsulation at 1 kHz makes our estimation appropriate. The uncertainty in the regression was not calculated since a Monte Carlo approach would have been needed to calculate the error in the regressed

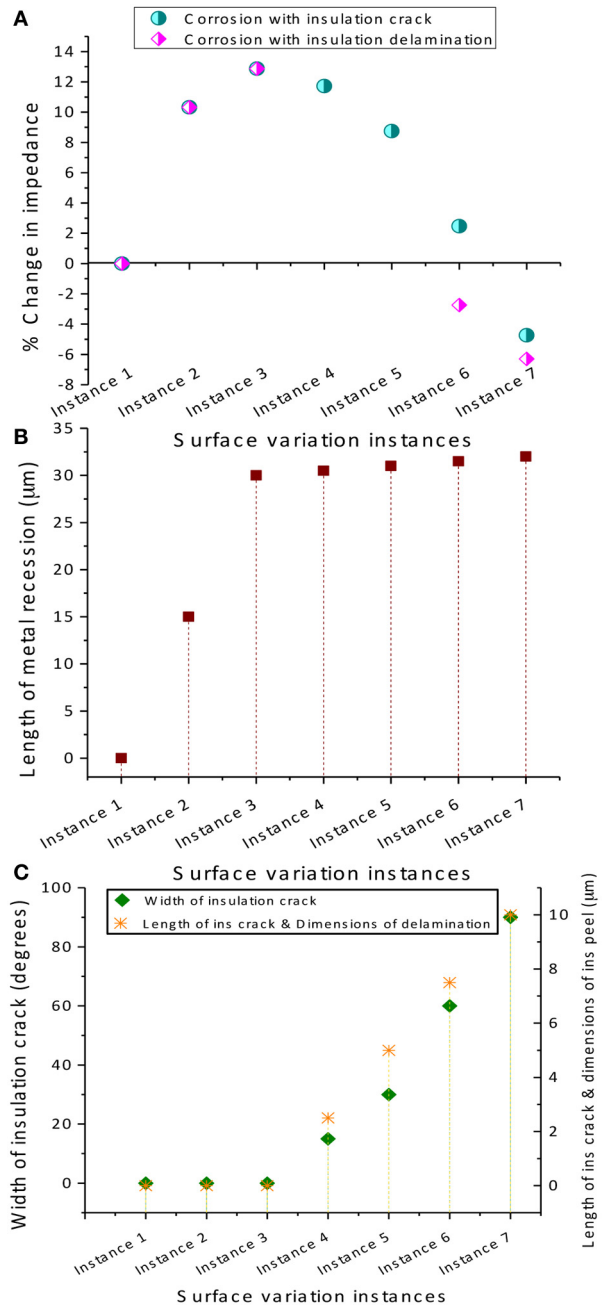

FIGURE 9 | COMSOL® 3D simulated results. (A) Percentage change in electrode impedance for corrosion and (Case 1) insulation delamination and (Case 2) insulation cracking at different instances, **(B)** variation in the metal recession length at different instances to model corrosion, and **(C)** variation of insulation crack width and length and delamination dimensions at different instances. Note that a converged solution could not be obtained for instances 4 and 5 for the insulation delamination case since the FEA solver could not generate a mesh for very small variations in geometry.

Table 2 | Real and imaginary parts of impedance of equivalent circuit parameters for wire 12.

	Impedance (kΩ) at 1 kHz					
Day	$Z_{r\text{-interface}}$	$Z_{j\text{-interface}}$	$Z_{r\text{-cell}}$	$Z_{j\text{-cell}}$	R_{en}	R_e
1	3.7	−11.4	0	0	0	21
7	4.2	−9.2	60.0	−24.8	57.4	21
15	3.2	−7.8	22.1	−9.8	32.6	21
31	3.8	−8.3	65.3	−30.1	77	21
60	4.2	−8.6	9.0	−5.8	24.0	21
106	4.4	−8.4	12.2	−3.4	9.0	21
149	5.1	−9.1	16.0	−4.7	11.4	21
205	4.4	−8.7	9.0	−4.7	12.7	21

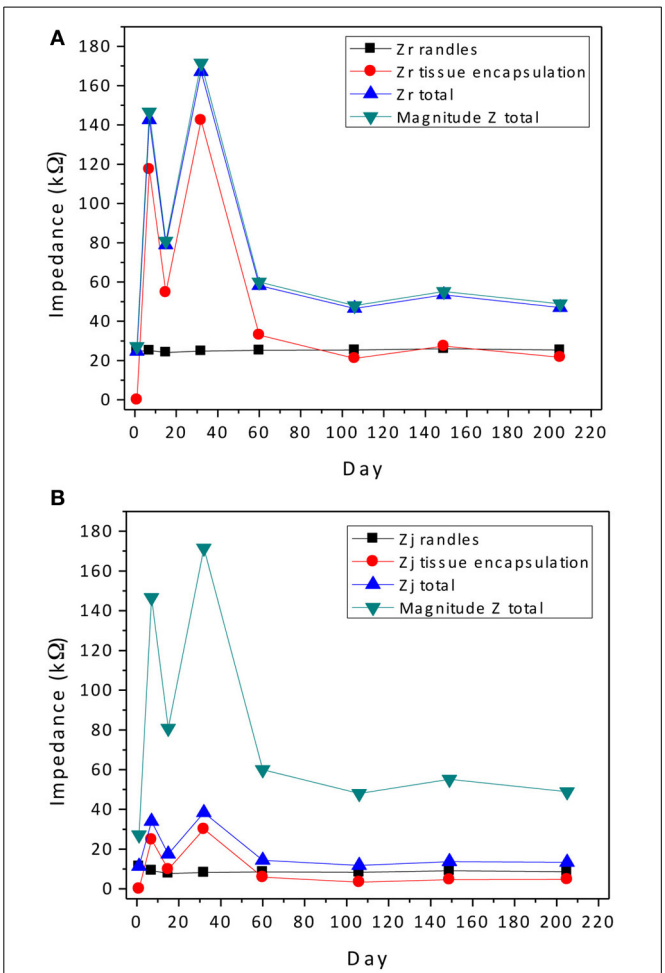

FIGURE 10 | Contribution of the abiotic and biotic components to the real (A) and imaginary (B) parts of the complex impedance compared to the magnitude of the total impedance. All impedance values were calculated at 1 kHz.

parameters. Finally, additional impedance data points at higher frequencies would improve the accuracy of the regression analysis. The maximum measurement frequency of 2 kHz was limited by the impedance tester used.

CONCLUSIONS

We examined the complex impedance trends of a 16 channel tungsten microwire array used in a chronic *in vivo* neural recording study. This array had good functional performance

throughout the implant duration and its impedance magnitude at 1 kHz showed temporal variability in the first few weeks that on average was Gaussian in shape. Time varying equivalent circuits that model the varying surface morphology and tissue response were shown to exhibit different structure in the complex impedance. To better understand the origin of the temporal change in the real part of the complex impedance, the abiotic electrolyte resistance was modeled in COMSOL® using a time varying geometry that simulated changes in the recession depth of the electrode surface due to corrosion and insulation changes due to delamination and cracking. A similar Gaussian shape in the electrolyte resistance was observed due to the competing effects of recessed electrode surface and increased exposure of the electrode shank area. The latter abiotic mechanism of insulation delamination can result in a lower impedance than the original reference impedance while the biotic mechanisms of tissue encapsulation cannot. Conversely, tissue encapsulation could be responsible for the larger magnitude increase in the electrode impedance initially. It can be concluded that both biotic and abiotic factors play key roles in the observed electrode impedance change in chronically implanted recording electrodes.

To generalize the results of this study, a Gaussian temporal variation of the impedance magnitude at 1 kHz with a rise and fall that changes to upward of 500% represents the effect of the biotic inflammatory response at the electrode/tissue interface and abiotic corrosion and insulation deterioration at the electrode surface that does not necessarily hinder functional performance during the implant duration of 9 months. These results suggest that an electrode array whose impedance magnitude at 1 kHz has very dissimilar temporal variations than the electrodes in this study may indicate that an abnormal abiotic malfunction such as a mechanical failure in the array or severe insulation delamination may have occurred.

ACKNOWLEDGMENTS

We thank the staff at the Major Analytical Instrumentation Center (MAIC) at the University of Florida for their help with the SEM imaging of the electrodes and the staff at the Materials Evaluation and Testing Laboratory (METLAB) at the South Dakota State University for their help with analyzing the surface roughness and measuring the corrosion depth of the electrodes. This work was sponsored by the Defense Advanced Research Projects Agency (DARPA) Microsystems Technology Office under the auspices of Dr. Jack Judy (jack.judy@darpa.mil) through the Space and Naval Warfare Systems Center, Pacific grant no N66001-11-1-4009.

REFERENCES

Baumann, S. B., Wozny, D. R., Kelly, S. K., and Meno, F. M. (1997). The electrical conductivity of human cerebrospinal fluid at body temperature. *IEEE Trans. Biomed. Eng.* 44, 220–223. doi: 10.1109/10.554770

Biran, R., Martin, D., and Tresco, P. (2005). Neuronal cell loss accompanies the brain tissue response to chronically implanted silicon microelectrode arrays. *Exp. Neurol.* 195, 115–126. doi: 10.1016/j.expneurol.2005.04.020

Biran, R., Martin, D., and Tresco, P. (2007). The brain tissue response to implanted silicon microelectrode arrays is increased when the device is tethered to the skull. *J. Biomed. Mater Res. A* 82, 169–178. doi: 10.1002/jbm.a.31138

Brug, G., den Eeden, A. V., Sluyters-Rehbach, M., and Sluyters, J. (1984). The analysis of electrode impedances complicated by the presence of a constant phase element. *Electroanal. Chem.* 176, 275–295. doi: 10.1016/S0022-0728(84)80324-1

Burke, B., and Lewis, C. E. (2000). *The Macrophage*. New York, NY: Oxford University Press.

Freire, M. A. M., Morya, E., Faber, J., Santos, J. R., Guimaraes, J. S., Lemos, N. A. M., et al. (2011). Comprehensive analysis of tissue preservation and recording quality from chronic multielectrode implants. *PLoS ONE* 6:e27554. doi: 10.1371/journal.pone.0027554

Grill, W. M., and Mortimer, J. T. (1994). Electrical properties of implant encapsulation tissue. *Ann. Biomed. Eng.* 22, 23–33. doi: 10.1007/BF02368219

HD Microsystems. (2001). *Product Information: Pyralin PI2525, PI2555, PI-2575 & PI2556 I2525, PI2555, PI-2575 & PI2556*. Available online at: www.hdmicrosystems.com

Johnson, M. D., Otto, K. J., and Kipke, D. R. (2005). Repeated voltage biasing improves unit recordings by reducing resistive tissue impedances. *IEEE Trans. Neural Syst. Rehabil. Eng.* 13, 160–165. doi: 10.1109/TNSRE.2005.847373

Kim, Y. T., Hitchcock, R. W., Bridge, M. J., and Tresco, P. A. (2004). Chronic response of adult rat brain tissue to implants anchored to the skull. *Biomaterials* 25, 2229–2237. doi: 10.1016/j.biomaterials.2003.09.010

Lempka, S. F., Johnson, M. D., Moffitt, M. A., Otto, K. J., Kipke, D. R., and Mcintyre, C. C. (2011). Theoretical analysis of intracortical microelectrode recordings. *J. Neural Eng.* 8:045006. doi: 10.1088/1741-2560/8/4/045006

McAdams, E. T., Lackermeier, A., McLaughlin, J. A., Macken, D., and Jossinet, J. (1995). The linear and non-linear electrical properties of the electrode-electrolyte interface. *Biosens. Bioelectron.* 10, 67–74. doi: 10.1016/0956-5663(95)96795-Z

McConnell, G. C., Rees, H. D., Levey, A. I., Gutekunst, C. A., Gross, R. E., and Bellamkonda, R. V. (2009). Implanted neural electrodes cause chronic, local inflammation that is correlated with local neurodegeneration. *J. Neural Eng.* 6, 056003. doi: 10.1088/1741-2560/6/5/056003

Orazem, M. E., Pébère, N., and Tribollet, B. (2006). Enhanced graphical representation of electrochemical impedance data. *J. Electrochem. Soc.* 153, B129–B136. doi: 10.1149/1.2168377

Otto, K. J., Johnson, M. D., and Kipke, D. R. (2006). Voltage pulses change neural interface properties and improve unit recordings with chronically implanted microelectrodes. *IEEE Trans. Biomed. Eng.* 53, 333–340. doi: 10.1109/TBME.2005.862530

Patrick, E., Orazem, M., Sanchez, J., and Nishida, T. (2011). Corrosion of tungsten microelectrodes used in neural recording applications. *J. Neurosci. Methods* 198, 158–171. doi: 10.1016/j.jneumeth.2011.03.012

Polikov, V., Tresco, P., and Reichert, W. (2005). Response of brain tissue to chronically implanted neural electrodes. *J. Neurosci. Methods* 148, 1–18. doi: 10.1016/j.jneumeth.2005.08.015

Prasad, A., and Sanchez, J. (2012). Quantifying long-term microelectrode array functionality using chronic *in vivo* impedance testing. *J. Neural Eng.* 9, 026028. doi: 10.1088/1741-2560/9/2/026028

Prasad, A., Xue, Q.-S., Sankar, V., Nishida, T., Shaw, G., Streit, W. J., et al. (2012). Comprehensive characterization and failure modes of tungsten microwire arrays in chronic neural implants. *J. Neural Eng.* 9, 056015. doi: 10.1088/1741-2560/9/5/056015

Rennaker, R. L., Ruyle, A. M., Street, S. E., and Sloan, A. M. (2005). An economical multi-channel cortical electrode array for extended periods of recording during behavior. *J. Neurosci. Methods* 142, 97–105. doi: 10.1016/j.jneumeth.2004.07.018

Rizk, M., Bossetti, C., Jochum, T., Callender, S., Nicolelis, M., Turner, D., et al. (2009). A fully implantable 96-channel neural data acquisition system. *J. Neural Eng.* 6, 26002. doi: 10.1088/1741-2560/6/2/026002

Sanchez, J. S., Alba, N., Nishida, T., Batich, C., and Carney, P. (2006). Structural modifications in chronic microwire electrodes for cortical neuroprosthetics: a case study. *IEEE Trans. Neural Syst. Rehabil. Eng.* 14, 217–221. doi: 10.1109/TNSRE.2006.875581

Serway, R. A. (1998). *Principles of Physics*. 2nd Edn. Fort Worth, Texas; London: Saunders College Pub.

Streit, W., Xue, Q., Prasad, A., Sankar, V., Knott, E., Dyer, A., et al. (2012). Electrode failure: tissue, electrical, and material responses. *IEEE Pulse* 3, 30–33. doi: 10.1109/MPUL.2011.2175632

Szarowski, D. H., Andersen, M. D., Retterer, S., Spence, A. J., Isaacson, M., Craighead, H. G., et al. (2003). Brain responses to micro-machined silicon devices. *Brain Res.* 983, 23–35. doi: 10.1016/S0006-8993(03)03023-3

Turner, J. N., Shain, W., Szarowski, D. H., Andersen, M., Martins, S., Isaacson, M., et al. (1999). Cerebral astrocyte response to micromachined silicon implants. *Exp. Neurol.* 156, 33–49. doi: 10.1006/exnr.1998.6983

Ward, M., Rajdev, P., Ellison, C., and Irazoqui, P. (2009). Toward a comparison of microelectrodes for acute and chronic recordings. *Brain Res.* 1282, 183–200. doi: 10.1016/j.brainres.2009.05.052

Williams, J. C., Rennaker, R. L., and Kipke, D. R. (1999b). Stability of chronic multichannel neural recordings: implications for a long-term neural interface. *Neurocomputing* 26–27, 1069–1076. doi: 10.1016/S0925-2312(99)00106-X

Williams, J., Hippensteel, J., Dilgen, J., Shain, W., and Kipke, D. (2007). Complex impedance spectroscopy for monitoring tissue responses to inserted neural implants. *J. Neural Eng.* 4, 410–423. doi: 10.1088/1741-2560/4/4/007

Williams, J., Rennaker, R., and Kipke, D. (1999a). Long-term neural recording characteristics of wire microelectrode arrays implanted in cerebral cortex. *Brain Res. Brain Res. Protoc.* 4, 303–313. doi: 10.1016/S1385-299X(99)00034-3

Conflict of Interest Statement: The authors declare that the research was conducted in the absence of any commercial or financial relationships that could be construed as a potential conflict of interest.

Received: 31 January 2014; accepted: 17 April 2014; published online: 08 May 2014.
Citation: Sankar V, Patrick E, Dieme R, Sanchez JC, Prasad A and Nishida T (2014) Electrode impedance analysis of chronic tungsten microwire neural implants: understanding abiotic vs. biotic contributions. Front. Neuroeng. ***7****:13. doi: 10.3389/fneng.2014.00013*
This article was submitted to the journal Frontiers in Neuroengineering.

frontiers in
NEUROENGINEERING

METHODS ARTICLE
published: 16 April 2014
doi: 10.3389/fneng.2014.00008

Smaller, softer, lower-impedance electrodes for human neuroprosthesis: a pragmatic approach

Elisa Castagnola[1], Alberto Ansaldo[1], Emma Maggiolini[1], Tamara Ius[2], Miran Skrap[2], Davide Ricci[1] and Luciano Fadiga[1,3]*

[1] *Robotics, Brain and Cognitive Sciences Department, Istituto Italiano di Tecnologia, Genoa, Italy*
[2] *Struttura Complessa di Neurochirurgia, Azienda Ospedaliero-Universitaria Santa Maria della Misericordia, Udine, Italy*
[3] *Section of Human Physiology, Department of Biomedical Sciences, University of Ferrara, Ferrara, Italy*

Edited by:
Ulrich G. Hofmann, Albert-Ludwigs-University Freiburg, Germany

Reviewed by:
Anirban Dutta, Case Western Reserve University, USA
Luciano Lopes Furlanetti, Albert-Ludwigs University of Freiburg, Germany

***Correspondence:**
Luciano Fadiga, Robotics, Brain and Cognitive Sciences Department, Istituto Italiano di Tecnologia, Via Morego 30, Genoa, 16163, Italy
e-mail: luciano.fadiga@iit.it

Finding the most appropriate technology for building electrodes to be used for long term implants in humans is a challenging issue. What are the most appropriate technologies? How could one achieve robustness, stability, compatibility, efficacy, and versatility, for both recording and stimulation? There are no easy answers to these questions as even the most fundamental and apparently obvious factors to be taken into account, such as the necessary mechanical, electrical and biological properties, and their interplay, are under debate. We present here our approach along three fundamental parallel pathways: we reduced electrode invasiveness and size without impairing signal-to-noise ratio, we increased electrode active surface area by depositing nanostructured materials, and we protected the brain from direct contact with the electrode without compromising performance. Altogether, these results converge toward high-resolution ECoG arrays that are soft and adaptable to cortical folds, and have been proven to provide high spatial and temporal resolution. This method provides a piece of work which, in our view, makes several steps ahead in bringing such novel devices into clinical settings, opening new avenues in diagnostics of brain diseases, and neuroprosthetic applications.

Keywords: micro-electrocorticography (ECoG), Intracortical microelectrodes, carbon nanotubes, conductive polymers, hydrogel, neural recording, neural stimulation, brain-conformability

INTRODUCTION

The larger part of our understanding of brain neurophysiology derives from electrical signals experimentally recorded using different types of intracortical penetrating microelectrodes, i.e., multiple-insulated metal microwires (Musallam et al., 2007; Nicolelis and Lebedev, 2009; Marin and Fernández, 2010) or micromachined penetrating microelectrode arrays (Suner et al., 2005; Wise, 2005; Marin and Fernández, 2010) and electrocorticography (ECoG) electrodes (Leuthardt et al., 2004; Kellis et al., 2009; Ritaccio et al., 2011). However, long-term stability is still an issue as regards the clinical application of neural implants, and two parallel avenues of research are currently being explored with a view to resolving this problem. One is the ongoing commitment to improving today's intracortical penetrating microelectrodes, which, despite their superior neural recordings in term of accuracy, bandwidth, and resolution (Leuthardt et al., 2006, 2009), tend to induce acute and chronic inflammatory reactions due to the trauma of mechanical insertion and the tissue response to such a foreign body. Indeed, the latter causes the formation of a glial scar, which distances neurons from the recording sites and thereby impairs signal recording (Schwartz, 2004; Marin and Fernández, 2010). Simultaneously, there is also great effort being expended in the attempt to improve the quality of cortical recording up to a level that could provide sufficient information to decode, for example, motor cortical signals, through the use of very high resolution micro-ECoG arrays (Leuthardt et al., 2004, 2006; Kellis et al., 2009, 2010; Chao et al., 2010).

Although advances have been made, both approaches would greatly benefit from a key improvement, namely reducing the impedance of recording sites. Lowering the impedance is fundamental to enhance the signal recording quality, reduce the background noise, and, consequently, increase the signal-to-noise ratio. At the same time a lower impedance with no dimensional increase enables the injection of relatively large capacitive currents whilst minimizing electrode degradation due to Faradaic effects. Increasing the active surface area of electrodes through the deposition of high-surface-area materials, i.e., nanostructured coatings, has been shown to induce a dramatic drop in impedance (Cui and Martin, 2003; Abidian and Martin, 2008; Green et al., 2008; Keefer et al., 2008; Ferguson et al., 2009; Castagnola et al., 2010; Ansaldo et al., 2011; Baranauskas et al., 2011). This increases their signal-to-noise ratio while enabling electrode miniaturization, which reduces their invasiveness and minimizes tissue damage during insertion. It is expected that very low-impedance and tiny recording sites would also dramatically improve micro-ECoG array technologies, enhancing their sensitivity and spatial selectivity, thereby increasing the information content of the recorded signal. As a consequence, their inter-electrode distance could be reduced, enhancing the spatial resolution (Castagnola et al., 2013a,b).

Another actively pursued key research target is the development of soft, flexible, and conformable electrode substrates, which would reduce implant-related tissue stress. Indeed, the reciprocal movements of brain and skull during behavioral and

metabolic processes can generate several negative effects when devices coupled to the bone are *in situ*. However, using a compliant material in penetrating micro-electrodes would help to minimize tissue damage arising from their micro-movements in brain tissue, thereby reducing long-term inflammation and glial scar formation (Rousche et al., 2001; Lee et al., 2004; Takeuchi et al., 2004). In the case of micro-ECoG arrays, the use of a conformable substrate would enable accommodation of both brain curvature and movement, keeping each electrode in the array in intimate contact with the cortical surface and improving the electrical coupling (Hollenberg et al., 2006; Leuthardt et al., 2009; Rubehn et al., 2009; Ritaccio et al., 2011; Khodagholy et al., 2011; Thongpang et al., 2011; Castagnola et al., 2013b). We set out to tackle all of these issues through the application of soft and high-surface-area material coatings to both intracortical and epicortical microelectrodes. We describe the use of a variety of such nanomaterial coatings, documenting their effects on impedance, charge transfer capability, signal-to-noise ratio, and signal recording quality of different types of miniaturized intracortical microelectrodes and very high-resolution micro-ECoG arrays. We also present a validated pragmatic approach to solving the biocompatibility issues and concerns raised by the use of nanomaterial-containing coatings, namely encapsulating nanocoated neural devices with a human fibrin hydrogel layer, which creates a mechanically stable barrier between the nanomaterials and the brain. Finally, we present our method of reducing the invasiveness and increasing the versatility of intracortical microelectrodes and micro-ECoG arrays, making them smaller, softer, and more flexible by exploiting a combination of nanocoatings and polymer-based circuits[1].

The results we present, in our opinion, provide a method which makes several steps ahead in bringing such novel devices into clinical settings, opening new avenues in diagnostics of brain diseases, and neuroprosthetic applications.

HIGH-SURFACE-AREA NANOCOATINGS

The impedance of electrodes is one of the main parameters influencing their suitability for both brain recording and stimulation. Assuming their metal surface is smooth and stable, the charge that can be exchanged with a saline solution, i.e., the current that can flow through it, is limited by the maximum voltage that can be applied without causing irreversible chemical reactions such as electrolysis. In the absence of Faradaic reactions, the metal interface will become charged, meaning that, practically speaking, the electrode must behave like a capacitor to prevent undesirable chemical reactions in the intracellular medium. One way to meet this requirement, which is particularly relevant for purely stimulating electrodes, is to introduce an active material that produces a controlled, reversible and rapid Faradaic reaction (pseudo-capacitive), for instance activated iridium oxide (Cogan et al., 2004; Gawad et al., 2009). A complementary approach, suitable for both stimulating and recording electrodes, would be to increase the electrode capacitance whilst containing its geometric size. This can be achieved, even when using electrochemically inert interfaces, by increasing the electrode surface area by augmenting its roughness/porosity. This, in turn, can be achieved by coating even commonly used metal electrodes with nanostructured high-surface-area (HSA) materials. Indeed, several HSA coatings made from a variety of nanostructured materials have been widely investigated as a means of enhancing the surface properties of traditional metal electrodes, decreasing their impedance, and increasing their charge transfer capability. These include platinum black (Robinson, 1968; Desai et al., 2010), various conductive polymers such as polypyrrole (PPy), polyaniline (PANI) and poly-[3,4 ethylenedioxythiophene] (PEDOT), (Cui et al., 2001; Cui and Martin, 2003; Yang et al., 2005; Ludwig et al., 2006; Kotov et al., 2009), and their carbon nanotube (CNT)-based nanocomposites (Keefer et al., 2008; Castagnola et al., 2009, 2013a,b; Ferguson et al., 2009; Jan et al., 2009; Lu et al., 2010; Ansaldo et al., 2011). As it would be preferable to record and stimulate using the same device, we set up a variety of CNT deposition methods, obtaining coatings to be tested in some of the most demanding electrode applications, i.e., intracortical and flexible epicortical neural recording and stimulation. By electrochemical deposition we were able to coat electrodes made from different metals with PEDOT-CNT, PPy-CNT, and Au-CNT nanostructured coatings. Using an *ad-hoc* process based on catalytic chemical vapor deposition (CVD), we synthetized CNTs directly on metal electrodes able to withstand high temperature (>600°C). It should be noted at this point that, although in the literature all CNT-containing composites (Keefer et al., 2008) are generally referred to as "CNT electrodes," only in few cases CNTs act as the ultimate electrochemical interface. In most instances, CNTs are mainly used to induce the surface nanostructuring, and, as they are encased in composites, the electrode-solution interface involves no graphitic carbon, but instead conductive polymers (CPs) or metals. In fact, similar results to these so-called "CNT electrodes" could be obtained by adding other additives, such as polyethylene glycol (PEG) or agar, to the deposition solutions, in place of CNTs, to promote HSA formation. However, CNTs are preferred because their high mechanical strength, good electrical properties, high specific area, and high aspect ratio confer composites with superior electrical conductivity and mechanical properties (Green et al., 2008; Gerwig et al., 2012). The main advantage in using electrochemical deposition for coating the electrode surface is that it can be carried out at room temperature, as opposed to *in situ* CNT synthesis, which requires high temperature. This means that it can be applied to a virtually unlimited variety of materials and devices. Conversely, when a direct interaction between CNTs and neural cells is allowed, it has been shown *in vitro* that the intimate contact achieved at this interface gives rise to an excellent electrical coupling (Mazzatenta et al., 2007; Shoval et al., 2009; Sorkin et al., 2009), hinting at a special affinity of exposed CNTs for neural tissue.

ELECTROPLATED HSA COATINGS

Deposition procedure

In the case of CP-CNT composites, polymer and CNT nanocomposites were co-electrodeposited from an aqueous suspension of 1 mg ml^{-1} multi-wall carboxylated CNTs (COOH-MWCNTs, NC 3151, <4% of -COOH functional groups,

[1]All animal experimental procedures were approved by the Italian Ministry of Health (Italian Law DL116/92) and were conducted in accordance with the guidelines established by the European Communities Council (Directive 2010/63/EU of September 22nd, 2010).

Nanocyl) containing 0.5 M of the corresponding monomer, 3,4-ethylenedioxythiophene (EDOT, Sigma-Aldrich) or pyrrole (Py, Sigma-Aldrich), and 0.4 wt% of poly(sodium 4-styrene sulfonate) (PSS, Sigma-Aldrich). COOH-MWCNTs were suspended in ultrapure water (Milli-Q, Millipore, USA) via horn sonication (6 s, 66% duty cycle pulses, 4 W ml^{-1}, for 30 min) while cooling in an ice bath. PSS and monomers were added to the suspension immediately afterwards, and the solution was kept deoxygenated by bubbling with nitrogen. The electrochemical deposition was carried out in an inert atmosphere in the potentiostatic mode. The polymerization potential was set to 0.55 V vs. Ag/AgCl reference electrode for PPy, and 0.8 V vs. Ag/AgCl reference electrode for PEDOT. For CP-agar coatings, the COOH-MWCNT suspension was replaced by 0.1 wt% agarose. PSS and monomer were added to the stirred solution before it jellified while cooling in an ice bath. Au-CNT nanocomposites were co-electrodeposited by applying monophasic voltage pulses (0.2–1.0 V, 240 s, duty cycle 50%), starting from a 10 mM potassium dicyanoaurate(I) (Sigma-Aldrich) aqueous solution containing 1.5 mg ml^{-1} of partially dispersed MWCNTs (NC 3100, Nanocyl) or 1.5 mg·ml^{-1} of partially dispersed SWCNTs (Cheaptubes). For Au-agar coating the CNTs were replaced by agarose (0.1 wt%).

Electroplated HSA coating benchmarking

We compared the electrochemical performance of different HSA coatings using identical planar 3.1 mm^2 gold and platinum electrodes as benchmarks. The electrochemical behavior of the microelectrodes was studied in a 0.9% sodium chloride (NaCl) aqueous solution, by both cyclic voltammetry (CV)—to quantify their capacitive charging—and electrochemical impedance spectroscopy (EIS)—to determine the electrical properties of the system over a large frequency range. During the CV tests, the working electrode potential was swept between 0.5 and −0.5 V or 0.6 and −1 V vs. Ag/AgCl, maintaining a scan rate of 100 mV/s. During the EIS measurements, a sine wave (10 mV RMS amplitude) was superimposed onto the open circuit potential while varying the frequency from 10^5 to 1 Hz.

All electrochemical depositions were carried out using a potentiostat/galvanostat (Parstat 2273, Princeton Applied Research), while a potentiostat/galvanostat/ZRA (Reference 600, Gamry Instruments, USA) was used for electrochemical characterization. The electrochemical cell was a three-electrode cell. A platinum wire was used as the counter electrode and an Ag/AgCl electrode was used as the reference electrode.

Figure 1A presents a comparison between the EIS spectra of identical planar platinum electrodes uncoated or coated with PPy-CNTs, PEDOT-CNTs, PEDOT-agar, Au-CNT, and Au-agar, respectively. In all cases the potentiostatic deposition of the CP composites was performed applying a charge density of 700 mC/cm^2. All nanocoatings tested resulted in a reduction in impedance across the entire frequency range (1–10^5 Hz). The impedance magnitude values at 100 Hz and 1 kHz are reported in **Table 1**, together with the corresponding total charge transfer capability (CTC_{tot}) values. The CTCs were calculated as the time-integral of an entire CV cycle between 0.5 and −0.5 V ($CTC_{tot}1$), or between 0.6 and −1V ($CTC_{tot}2$). Typical CVs measured for differently coated electrodes are reported in **Figure 1B** (0.5 to −0.5 V range) and **Figure 1C** (0.6 to −1.0 V range for PPy-CNT- and

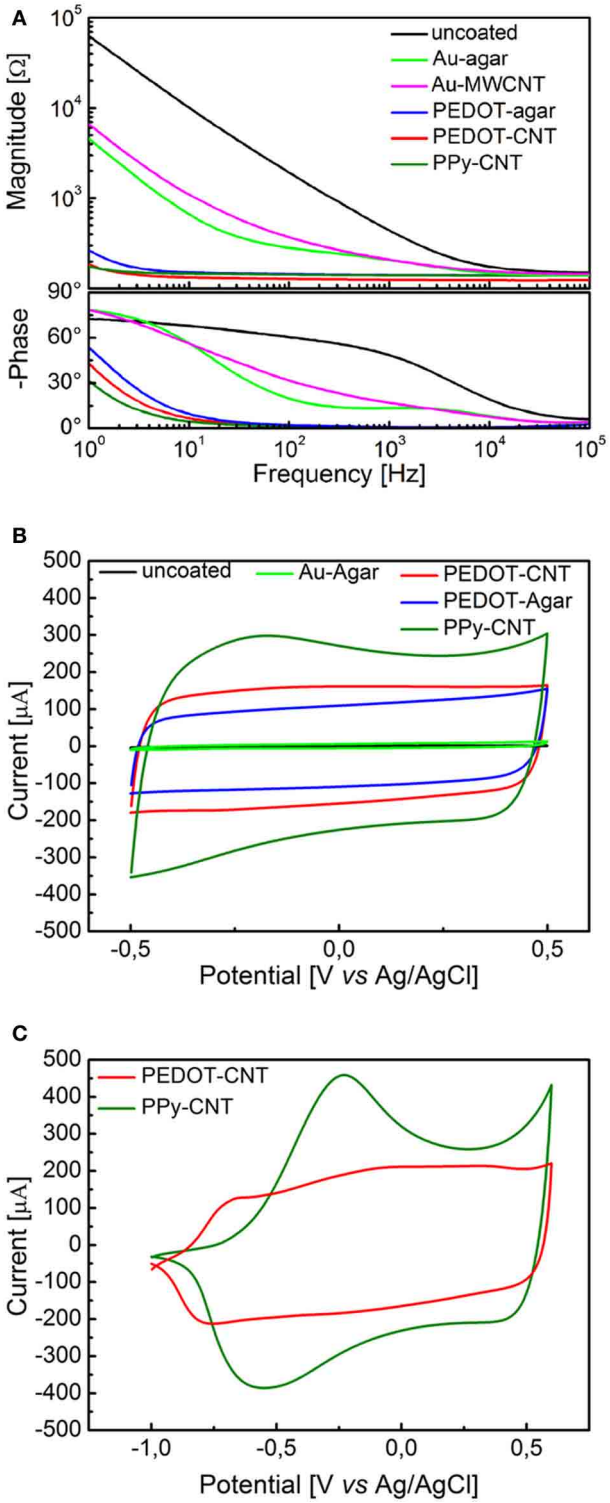

FIGURE 1 | (A) Impedance spectra of a 0.031 cm^2 Pt electrode, uncoated (black) and with electrodeposited Au-MWCNT (pink), Au-agar (green), PPy-CNT (dark green), PEDOT-agar (blue), or PEDOT-CNT (red). **(B)** Cyclic voltammograms between −0.5 and 0.5 V of a 0.031 cm^2 Pt electrode, uncoated (black), or with electrodeposited Au-agar (green), PPy-CNT (dark green), PEDOT-agar (blue), or PEDOT-CNT (red). **(C)**, Cyclic voltammograms between −1.0 and 0.6 V of a 0.031 cm^2 Pt electrode coated with PPy-CNT (dark green) and PEDOT-CNT (red).

Table 1 | Electrochemical characterization of HSA coatings.

	|Z|@ 100 Hz [Ω]	|Z|@ 1 kHz [Ω]	CTC_{tot} 1[mC cm-2]	CTC_{tot} 2[mC cm-2]
PEDOT-agar	142.6 ± 1.7	139.5 ± 1.6	149.7 ± 7.3	246.2 ± 4.9
PEDOT-CNT	127.6 ± 0.1	125.0 ± 0.2	92.3 ± 4.6	158.7 ± 8.2
PPy-CNT	138.7 ± 4.3	136.7 ± 4.1	67.7 ± 0.5	118.9 ± 4.8
Au-agar	291 ± 12	214.6 ± 8.3	3.1 ± 0.7	6.2 ± 0.5
Au-CNT	334 ± 50	192 ± 25	2.5 ± 0.3	4.6 ± 0.2
Uncoated	1915 ± 203	441 ± 7	0.5 ± 0.1	3.3 ± 0.2

PEDOT-CNT-coated electrodes). In both cases it can be observed that when the same charge density is applied during electrodeposition, the CTC_{tot} of the PPy-CNT coating is greater than that of the PEDOT-CNT coating, but that the peak potentials of the PEDOT composites are about 200 mV more negative than those of the PPy composite (**Figure 1C**), extending the PEDOT capacitive behavior over a wider potential window. Moreover, the PEDOT-CNT coating provided the lowest impedance at all frequencies above 2 Hz.

PROCEDURE FOR CHEMICAL VAPOR DEPOSITION OF CARBON NANOTUBES

In order to selectively synthetize CNTs on the metal tip of an electrode of arbitrary shape, we devised a nickel catalyst deposition method based on electrode electroplating, rather than relying on the more common physical deposition methods (such as dip-coating, spray-coating, evaporation, or sputtering). Nickel was electroplated from an aqueous solution containing 300 g l^{-1} nickel(II) sulfate hexaydrate ($NiSO_4 \cdot 6H_2O$, CAS 10101-97-0, *puriss*. p.a. Riedel-de Haën), 90 g l^{-1} nickel chloride hexaydrate ($NiCl_2$ 3 $6H_2O$, CAS 7791-20-0 *purum*, p.a.; >99.0% Fluka), and 45 mg l^{-1} boric acid (H_3BO_3, CAS 10043-35-3, *puriss*. p.a. Riedel-de Haën). Electrodeposition was performed in the potentiostatic mode at −0.9 V vs. an Ag/AgCl reference electrode. The depositions were carried out in an inert atmosphere at 45°C and pH 4. The amount of catalyst deposited onto the electrode was determined by controlling the charge passed during the deposition. The CVD process was performed in a quartz tube reactor, 120 cm long and 25 mm in diameter, passing through a Lenton PSC 12/--/600H split furnace. The catalyst was activated by flowing a forming gas (Ar 95 sccm, H_2, 5 sccm, ambient pressure) while heating the samples up to 650°C; the carbon feedstock was then introduced into the reaction chamber by bubbling the same gas mixture through a Drechsel washing bottle with glass filter disk, filled with absolute ethanol at room temperature. Reaction time was 15 min at 650°C.

APPLICATION OF NANOCOATINGS

INTRACORTICAL PLATFORM

Reduced impedance and increased charge transfer capability

In order to be able to compare all the previously described HSA coatings, including the CNTs directly synthetized on the electrode tip at high temperature, we selected as an intracortical electrode platform quartz glass insulated platinum/tungsten wires of 80 μm outer shank diameter and 20 μm metal core diameter (Thomas Recording, Giessen, Germany). We prepared and characterized identical electrodes coated with *in situ* synthetized CNTs (CVD-CNT) and with different electrochemically co-deposited composites, namely Au-CNT, Au-agar, PPy-CNT, PEDOT-CNT, and PEDOT-agar. The insulated wire was ground using a grinding machine (DIECKL-ST, Thomas Recording), thereby providing sharp tips with a typical geometric area of about 1000 μm^2 and an impedance magnitude ranging from 0.5 to 0.7 MΩ at 1 kHz. We used both of these single electrodes (**Figures 2A,B** reports optical and SEM images respectively) and 4-core quartz-platinum/tungsten microelectrodes (tetrodes) having similar electrical properties to perform direct comparisons of the coatings' performance in simultaneous neural recordings. The corresponding datasheet schematics from Thomas Recording are shown in **Figures 2C,D**. A SEM picture of the tetrode is shown in **Figure 2E**. Electrochemical characterizations of the typical uncoated (black), electroplated Au-CNT (green), PPy-CNT (red) and PEDOT-CNT (blue), and CNT-CVD coated (magenta) electrodes were performed using impedance spectroscopy (**Figure 3A**), and cyclic voltammetry between 0.6 and −1.0 V vs. Ag/AgCl (**Figure 3B**). The electrochemical performance reported here is related to "viable" electrodes, as defined in our previous work (Ansaldo et al., 2011), in which we emphasized that special attention must be paid when presenting "dramatic" changes in impedance and charge transfer capability in electrodes designed for intracortical neural recording and stimulation. Indeed, although electrode impedance could feasibly be lowered by many orders of magnitude by increasing the amount of material, thick coatings are usually mechanically unstable. Here we consider "viable" electrodes those capable of withstanding dura mater penetration, i.e., displaying no significant changes in appearance or electrochemical performance even after an acute intracortical recording session (Ansaldo et al., 2011). According to this definition, our viable CNT-CVD-coated electrodes typically had an impedance of 16.3 ± 4.8 kΩ at 1 kHz, with a 70.8 ± 1.1 mC·cm^2 CTC_{tot} (Castagnola et al., 2010; Ansaldo et al., 2011), a significant improvement with respect to the uncoated electrodes (typically 600 kΩ and 20 mC cm^{-2} CTC_{tot}). In the case of PPy-CNT and PEDOT-CNT coatings, viable electrodes were consistently produced by using charge densities of 0.6 C cm^{-2} during deposition. Impedance magnitude and CTC_{tot} were 5.7 ± 0.3 kΩ @1 kHz and 212.3 ± 23.9 mC cm^{-2}, respectively, for PPy-CNT-coated microelectrodes, and 4.5 ± 0.6 kΩ @1 kHz and 180.5 ± 40.2 mC cm^{-2} for PEDOT-CNT-coated microelectrodes. In the case of Au-CNT coatings, improvements were limited by the intrinsic behavior of gold, which produces nanorough lamellar surfaces rather that nanoporous ones. The best values obtained for viable electrodes were an impedance of 59.6 ± 11.2 kΩ@1 kHz and a

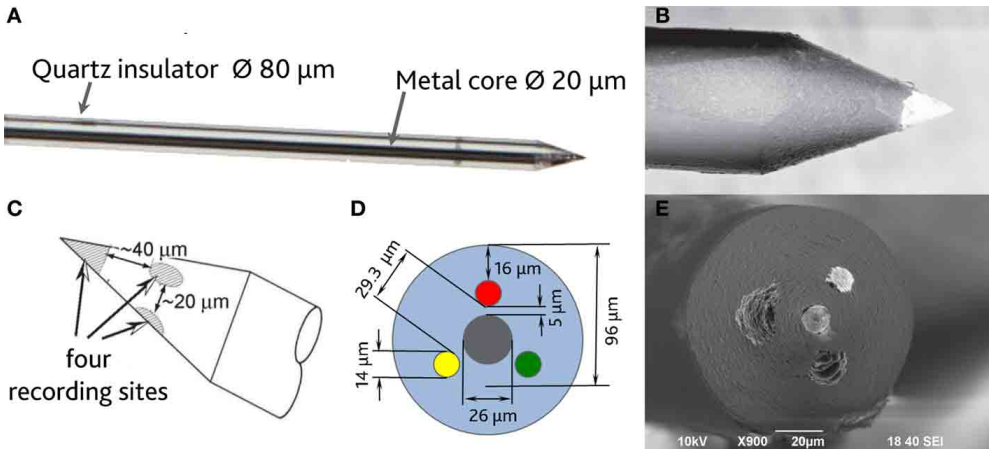

FIGURE 2 | (A) Optical image of a single sharp microelectrode. **(B)** Scanning electron micrograph of a single sharp microelectrode. **(C,D)** Schematic datasheet of a 4-core quartz-platinum/tungsten tetrode microelectrode (Thomas Recording, Giessen, Germany). **(E)** Tetrode scanning electron micrograph (s.e.m.).

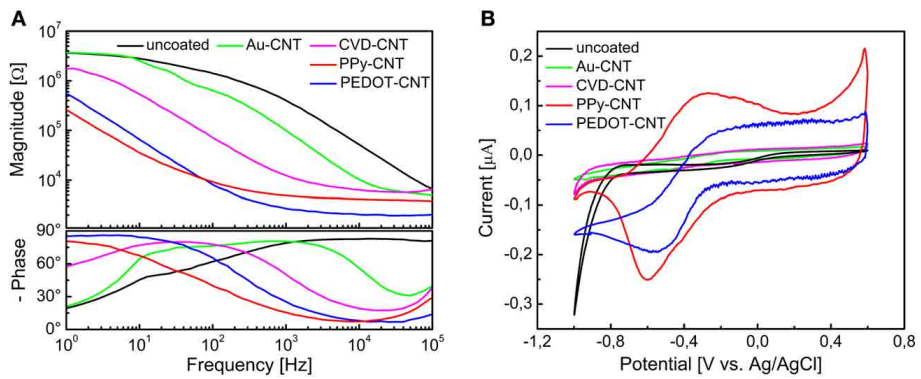

FIGURE 3 | (A) Impedance spectra of a single intracortical electrode, uncoated (black), or coated with Au-CNT (green) PPy-CNT (red), or PEDOT-CNT (blue), electrodeposited and CNT coated by direct growth with CVD. **(B)** Cyclic voltammograms of a single intracortical electrode, uncoated (black) or coated with Au-CNT (green), PPy-CNT (red) or PEDOT-CNT (blue), electrodeposited, and CNT coated by direct growth with CVD.

CTC_{tot} of 65.6 ± 13.6 mC cm^{-2} (Ansaldo et al., 2011). CTC_{tot} and $CTC_{tot}2$ were calculated as previously described. The reduction in impedance achieved depended on the coating, its nature and morphology, but all appeared to pave the way to a better signal-to-noise ratio in both single-neuron and multiunit recordings. The corresponding increase in CTC also makes these electrodes suitable for both recording and stimulation. The morphology of the different coatings can be appreciated by looking at the SEM pictures of grown CNT-CVD (**Figure 4A**), Au-CNT (**Figure 4B**), PPy-CNT (**Figure 4C**), and PEDOT-CNT (**Figure 4D**) electrodes. Nanorough lamellar coatings, similar to Au-CNT, can be also obtained by exploiting gold co-deposition in the presence of agarose gel (**Figures 5A,B**), or SWCNTs (**Figure 5C**).

To verify whether these coated microelectrodes are capable of stimulating the brain cortex, we estimated the charge injection limit for a set of typical electrodes, using cathodic-first charge-balanced biphasic symmetrical current pulses (Brummer et al., 1983; Cogan, 2008). The charge injection limit (Q_{inj}), defined as the maximum quantity of charge an electrode can inject before reaching the water electrolysis potential, was calculated as the time-integral of the current in the loading phase normalized by the geometric area of the uncoated microelectrode; water electrolysis potentials were determined experimentally via cyclic voltammetry. We used pulses having a total period of 2 ms and a cathodic duration of 500 µs (Ansaldo et al., 2011). To establish whether these electrodes could be used for long-term (chronic) neural stimulation and recording, we tested the stability of the different coatings under prolonged stimulation, and then compared the impedance of typical viable electrodes before and after applying a series of cathodic-first charge-balanced biphasic current pulses. The pulse duration was varied between 2 and 3 ms, the charge density between 0.4 and 1.6 mC cm^{-2}, and the cathodic pulse duration between 100 and 500 µs. The charge density applied was chosen according to the Q_{inj} for each material, namely 7 mC cm^{-2} for PPy-CNT microelectrodes, 4 mC cm^{-2} for CVD-CNT microelectrodes, and 0.8 mC cm^{-2} for Au-CNT microelectrodes. Even the relatively small Q_{inj} of Au-CNT electrodes is more than double that of the uncoated electrodes (0.2–0.4 mC cm^{-2}). As regards stability over time, CVD-CNT-coated electrodes were found to be stable, and could withstand a million 1.6 mC cm^{-2} pulses without

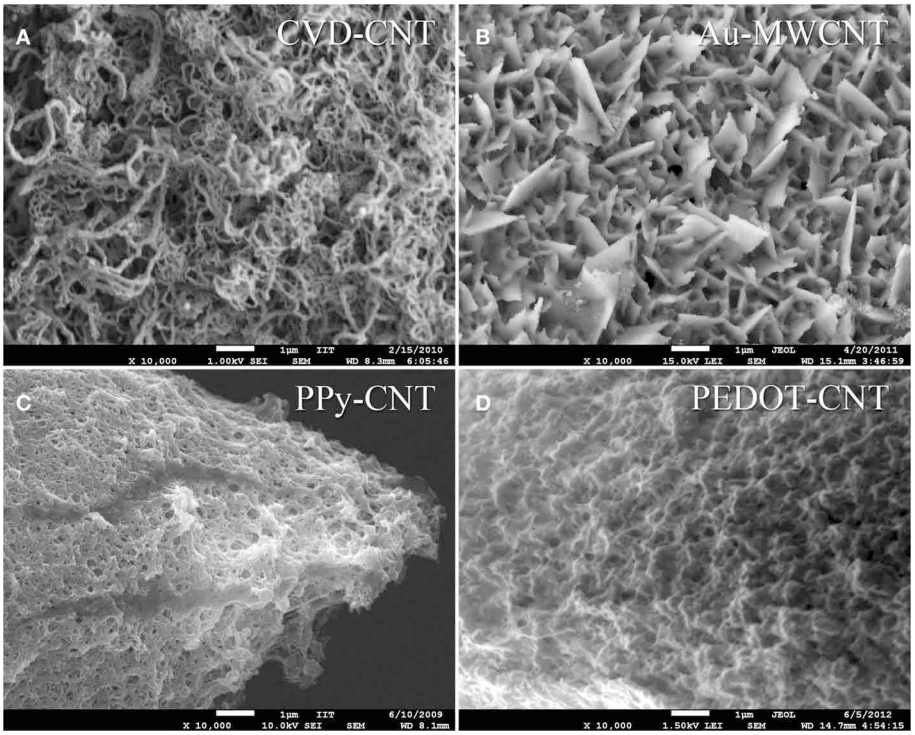

FIGURE 4 | Scanning electron micrograph of (A) as grown CNT-CVD coatings, (B) Au-MWCNT coating, (C) PPy-CNT coating, (D) PEDOT-CNT coating.

any degradation. PPy-CNT coatings rapidly degraded after a few thousand pulses at 1.6 mC cm^{-2}, while Au-CNT composite coatings were nearly as stable as CVD-CNTs, also being able to resist a million pulses, although their charge density had to be limited to 0.8 mC cm^{-2} in order to prevent Faradaic reactions (see Ansaldo et al., 2011). We can therefore conclude that CNTs selectively synthetized directly on the tip of neural microelectrodes by CVD are able to outperform the other so-called "CNT coatings" laid down by electrodeposition of CNT composites. Indeed, the CNT-CVD coating not only reduced microelectrode impedance, but was also able to withstand the repeated high-current pulses required for neural stimulation without degrading. This and its stability over time make it an excellent candidate for improving electrodes for use in chronic applications, especially when both neural recording and stimulation are required. Indeed, the only foreseeable limitation of CNT-CVD coatings resides in the high temperature (650°C) required for their deposition. Analysis of the PEDOT-CNT coating also yielded interesting results. In fact, it has already been reported in various studies that PEDOT may be a viable alternative to PPy for chronic, long-term implantations (Cui and Martin, 2003; Yang et al., 2005; Ludwig et al., 2006), as it is electrochemically more stable than PPy (Yamato et al., 1995). We measured a charge injection limit of 7 mC cm^{-2} on our PEDOT-CNT-coated microelectrodes. While this is identical to the charge on PPy-CNT-coated electrodes, PEDOT-CNT versions are able to withstand a million 1.6 mC cm^{-2}pulses without significant degradation, as demonstrated by the impedance spectra of a typical PEDOT-CNT coated electrode, reported in **Figure 6**. This suggests that PEDOT-CNT coatings are also excellent candidates for chronic applications, especially when both neural recording and stimulation have to be performed and a room-temperature deposition technique is required. Indeed, an initial validation of the suitability of these microelectrodes for *in vivo* use has already been obtained through acute intracortical recording sessions in rats (Ansaldo et al., 2011; Baranauskas et al., 2011).

CNT-composite coating improves multiunit signal-to-noise ratio of neural microelectrodes

Although it seems safe to assume that a low-impedance electrode has lower noise and is able to record larger signals, in fact the relationship between its resistivity and capacitance, and its ability to provide high-quality recordings are not straightforward. Indeed, the *in vivo* performance of an electrode is strongly influenced by many features of its surrounding environment (the brain), as well as the geometric area of the electrode (with respect to the size of the cells, i.e., the signal sources), and the presence of background biological activity, which remains too low to be properly detected, but contributes to the neural signal (the so-called biological noise) and therefore cannot be ignored. While the impedance reduction has a well-known impact on the Johnson-Nyquist noise (the thermal noise), any background signal that cannot be clearly isolated as neural activity will significantly contribute to total noise of a low-impedance electrode. Moreover, in the case of HSA-coated electrodes, the high specific capacitance, combined with the relatively high transversal resistivity of the coating, will significantly lower the speed of the signal on the electrode surface, meaning that the geometric size of the electrode can influence the frequency response at relatively low frequencies.

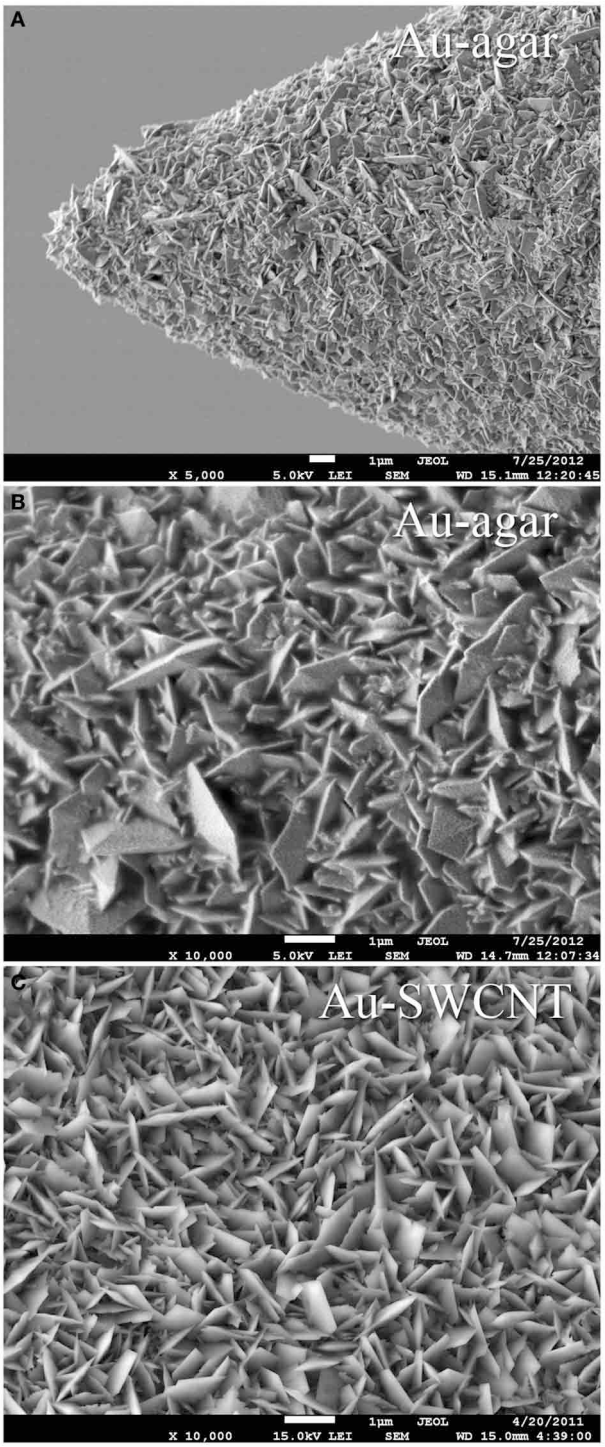

FIGURE 5 | Scanning electron micrograph of (A) a single tip Au-agar coated microelectrode, (B) Au-agar coating, (C) Au-SWCNT coating.

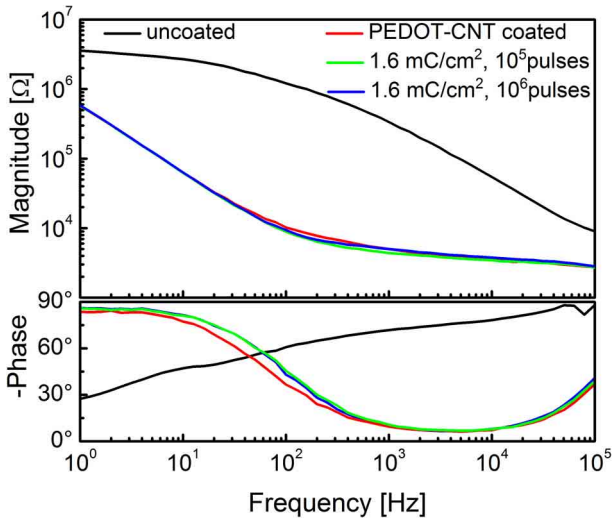

FIGURE 6 | Impedance spectra of a single intracortical electrode uncoated (black), and PEDOT-CNT-coated (red) and after stimulation experiments.

In order to investigate the effect of the very low impedance of CNT-based HSA coatings on signal acquisition, we devised a series of specific experiments using PPy-CNT coated electrodes to perform "acute" recording sessions on rats (Baranauskas et al., 2011). We studied in detail the impedance, the thermal, electronic and *in-vivo* noise, and the neural signals using ten single microelectrodes, PPy-CNT coated and uncoated, and two tetrodes, two of whose recording sites were coated with CNT-PPy while the other two remained untreated. This experiment enabled us to directly compare very closely positioned coated and uncoated electrodes during the same recording session.

As pointed out previously, during an *in vivo* recording session, neural signals are affected by several noise sources of both biological and non-biological origin. The non-biological sources include the electronic noise created by the amplifier, the thermal noise (Johnson-Nyquist), and the double-layer noise at the interface between the solution and microelectrode surface. The biological noise also includes additional thermal noise, created by the presence of brain tissue, and signals emitted by distant neurons. These neural signals are too small to be usefully distinguished, and therefore behave as noise for the majority of neural signal analyses (Harris et al., 2000; Quiroga et al., 2004; Ferguson et al., 2009). In the case of our electrodes, the non-biological noise contribution—including recording system noise, and filtering—was estimated by recording the noise signals from single microelectrodes immersed in a saline solution (NaCl 0.9%). In the case of PPy-CNT coated electrodes, we detected reduced noise over the entire useful frequency range (250–8000 Hz), and, in particular, in the range of frequencies corresponding to the multi-unit neural activity (MUA, ∼150–1500 Hz). In the 250–8000 Hz frequency band, the overall noise measured was reduced by ∼30%, from $5.9 \pm 0.2\,\mu$V rms to $4.2 \pm 0.3\,\mu$V rms. This difference was significant ($p < 0.015$; one-tailed t-test).

As discussed previously, the background noise is higher in the brain due to biological sources. Hence, in order to evaluate the biological noise contribution, we recorded from the deep layers of the primary somatosensory cortex (S1) in rats anaesthetized with Zoletil (30 mg/kg) and Xylazine (5 mg/kg). Indeed, under these

conditions S1 switches between periods of high neural activity ("bursts") and periods of much lower activity ("pauses"). These periods of high and low activity are synchronized across large brain areas (>1 mm), and during the "pauses" the noise contribution of distant neuronal activity is minimal (Erchova et al., 2002), but during "bursts" it is possible to evaluate the background noise caused by the maximal activity of such neurons. In order to eliminate the effect of the presence of these burst spikes, the noise amplitude was estimated using a median value (Quiroga et al., 2004). We demonstrated that during "pauses," when the neuronal activity was low, the observed noise reduction ranged between 30 and 40%, comparable to data reported in the literature (Gabay et al., 2007; Keefer et al., 2008) though smaller than that of the saline test (55%). In contrast, during "bursts" the increased sensitivity provided by the PPy-CNT coating resulted in a larger contribution from distant neuronal activity, and a slight uptrend was observed from $11.2 \pm 3.0\,\mu V$ rms (uncoated) to $13.8 \pm 4.0\,\mu V$ rms (CNT-PPy, $p < 0.2$).

Moving on to the analysis of recorded neural signals, we estimated the amplitude for single spikes, local field potentials (LFP) and MUAs (Baranauskas et al., 2011). Tests were carried out using platinum/tungsten tetrodes featuring two PPy-CNT-coated and two uncoated recording sites. Although the average spike amplitudes of the two types of electrodes were similar (0.45 ± 0.03 mV vs. 0.40 ± 0.03 mV), the maximal spike amplitude was greater with the coated versions (increased from 0.52 ± 0.03 mV to 0.75 ± 0.04 mV). Moreover, more neuronal units were detected using the PPy-CNT coated electrodes (22 with respect to 16 units), as these were able to detect signals arising from more distant neurons in which smaller spikes dominate. This ability to detect a certain number of weaker signals may explain why the increase in maximal recorded amplitude was not accompanied by a similar improvement in average, further suggesting that average spike amplitude cannot be assumed as a reliable indicator of recording ability.

The contribution of MUA to the overall spectral power density (SPD) was estimated by subtracting the SPD of the signal recorded during "bursts" from the one recorded during "pauses." A significant increase in the SPD of the signals recorded using the PPy-CNT-coated electrode in the frequency range 200–1000 Hz was observed. Notably, analysis of the low frequency part of the spectrum (∼1–250 Hz) recorded using PPy-CNT-coated microelectrodes revealed a marked reduction—of almost 3 orders of magnitude—in the 50 Hz interference (the frequency of the European electric power network), and total rejection of its higher harmonics. There are at least two reasons why this reduction in 50-Hz noise is particularly important from a neurophysiological standpoint. First, it reduces the risk of amplifier saturation during LFP recordings, and second the power line frequency of 50 Hz precisely matches the middle frequency of the so called "gamma range," which is thought to reflect a number of important brain functions (Gray et al., 1989; Fries et al., 2007). To sum up, we found that the most important improvements conferred by PPy-CNT coating of microelectrodes can be observed in the frequency range from 150 to 1500 Hz, which mainly corresponds to the multiunit signal and, partially, to the high-frequency end of LFPs. In this frequency range, the non-biological noise power is reduced by up to three-fold, while the neural signal power is increased by up to nine-fold. The combination of lower noise and stronger neural signal resulted in an approximately four-fold improvement in SNR in the middle of this frequency range. Our results also suggest that the coated microelectrodes offer considerable advantages for studying brain signals in the gamma frequency range, thanks to their greater electromagnetic noise rejection.

FLEXIBLE MICRO-ECoG ARRAYS

We developed a family of micro-electrocorticography (ECoG) arrays based on the commercially available flexible printed circuit (FPC) technology, tailoring the design according to the different neurophysiological experiments to be conducted. The choice of a well-established, reliable industrial process greatly reduced the time required to move from concept to prototype, and would likewise simplify production. We developed devices suitable for ECoG on both rats and primates (marmoset), as well as prototypes of devices suitable for the use on humans, having from 16 up to 128 recording sites with electrode diameters ranging from 75 up to 200 μm and an inter-electrode pitch from 300 up to 1.2 mm. Some examples are shown in **Figure 7**.

The FPCs consist of a double-sided copper circuit (9 μm thick) on a 25 μm polyimide film. After photo etching, the circuit is embedded in two polyimide coverlays (12.5 μm of polyimide plus 12.5 μm of pressure-sensitive acrylic adhesive) by cold lamination. The electrodes are then exposed by laser ablation, and passivated by a 1-μm thick layer of electroplated gold. The micro-ECoG devices were post-processed in our laboratory by electrochemical deposition of a nanostructured gold layer, which acts as an adhesion layer for PEDOT-CNT or PPy-CNT composites (Castagnola et al., 2013a,b). PEDOT-CNT or PPy-CNT nanocomposites were then co-deposited electrochemically onto the micro-ECoG recording sites to reduce their impedance and increase their charge transfer capabilities. SEM images showing the typical morphologies of these coatings when deposited on the micro-ECOG electrodes are shown in **Figure 8**.

Both the Au-CNT and Au-agar coatings present nanorough lamellar structures that reduce the electrode impedance by two-thirds with respect to the uncoated electrode (100 Hz, LFP central band), while the PEDOT-CNT and PPy-CNT composite coatings present a compact, sponge-like morphology, which provides a dramatic reduction in impedance of up to greater than 2 orders of magnitude over the whole frequency range of interest (1 Hz–1 kHz), and especially at 100 Hz. **Figure 9** reports the impedance spectra of 100 μm diameter ECoG array recording sites before and after Au-agar, PPy-CNT and PEDOT-CNT electrodeposition. The values shown were obtained by averaging the impedance spectra of 64 electrodes for each material studied. The impedance values (mean ± standard deviation) at 100 Hz were $774.5 \pm 198.0\,k\Omega$ for the uncoated electrodes, $138.9 \pm 24.9\,k\Omega$ for Au-CNTs, $5.0 \pm 0.1\,k\Omega$ for PPy-CNTs, and $4.5 \pm 0.2\,k\Omega$ for PEDOT-CNTs. It should be noted that our PEDOT-CNT-coated devices are fully compatible with sterilization in saturated water vapor at 122°C and 2 atm for 20 min, one of the most commonly used sterilization processes in hospitals, making them

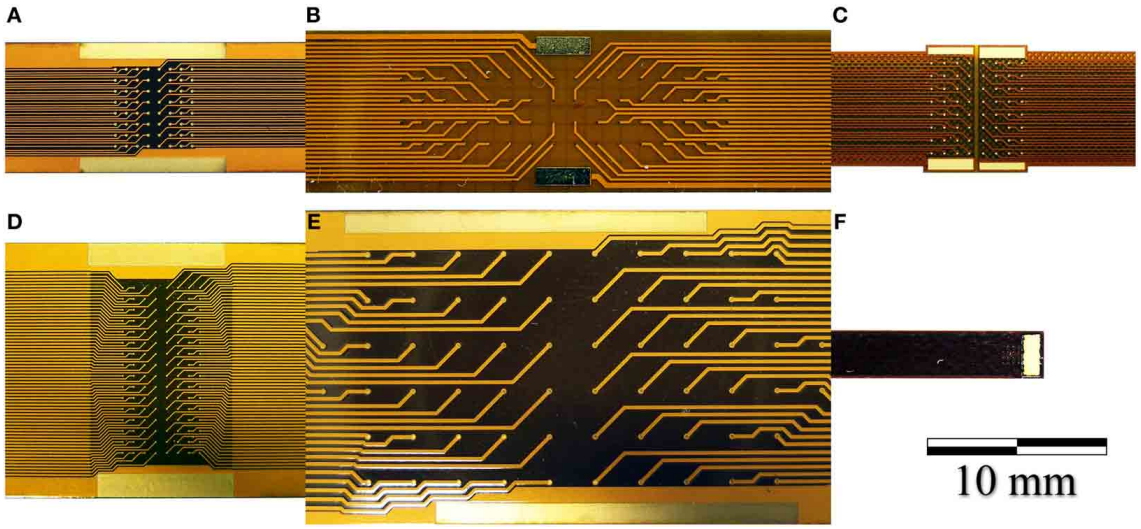

FIGURE 7 | Photographs of (A) a 64-electrode array with 4.2 × 4.2 mm total recording area and 140 μm diameter recording sites. (B) A 64-electrode array with 3.6 × 18.0 mm total recording area and 100 μm diameter recording sites; **(C)** A 64-electrode matrix with 5 × 5 mm total recording area, designed for the marmoset; **(D)** A 128-electrode array with 4.2 × 8.4 mm total recording area and 100 μm diameter recording sites; **(E)** A 64-electrode array with 12.5 × 27.5 mm total recording area and 200 μm diameter recording sites. **(F)** A 16-electrode array with 1.2 × 1.2 mm total recording area and 100 μm diameter recording sites.

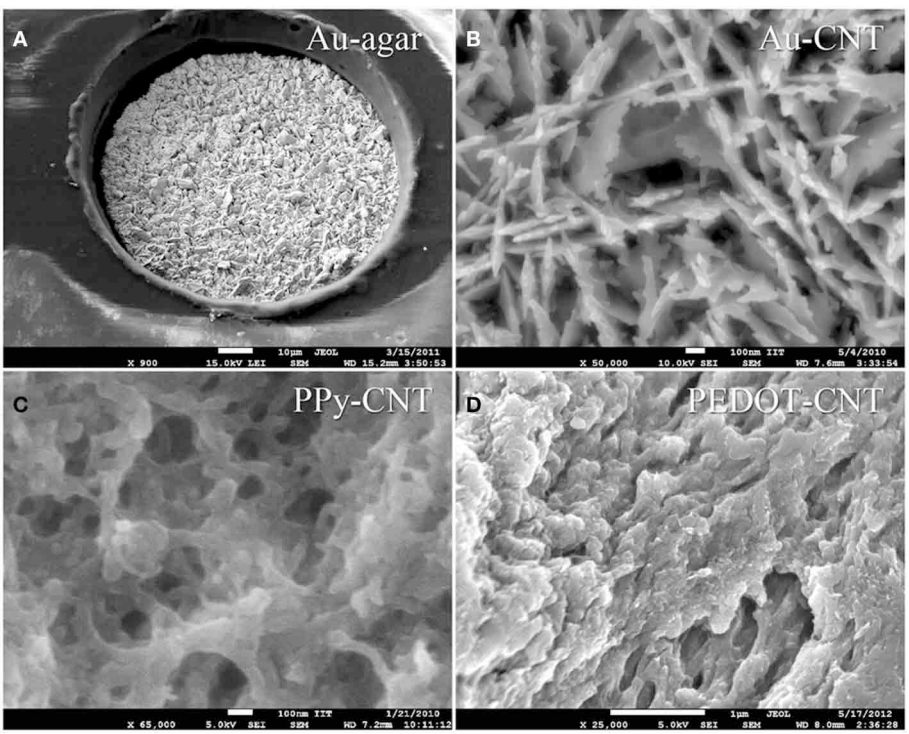

FIGURE 8 | s.e.m. images of: (A) a 100 μm Au-agar-coated recording site; (B) Au-CNT coating; **(C)** PPy-CNT coating; **(D)** PEDOT-CNT coating.

suitable candidates for clinical applications (see Castagnola et al., 2013a,b). In order to establish whether they are suitable for cortical stimulation, we investigated their ability to withstand a series of cathodic-first charge-balanced biphasic current pulses with a 2 ms pulse duration, 500 μs cathodic pulse duration, and 5.7 mC cm^{-2} charge density, measuring whether there was any change in the impedance spectra after each series. We chose to test PEDOT-CNT-coated micro-ECoG arrays alone, as we know from previous

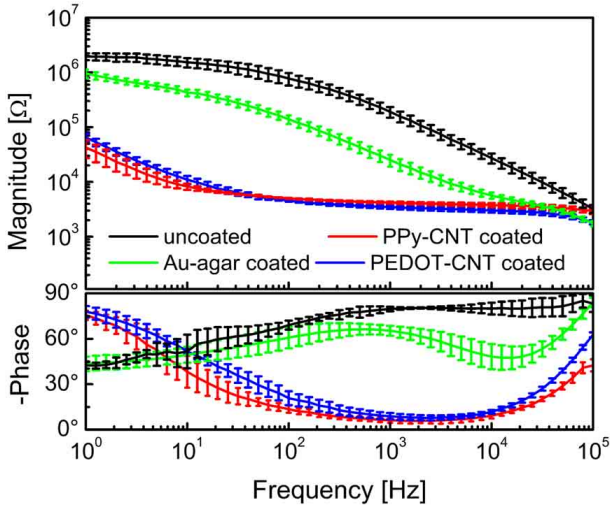

FIGURE 9 | Impedance spectra of 100-μm-diameter ECoG array recording sites (mean and standard deviation from 64 recording sites each) before (black) and after Au-agar (green), PPy-CNT (red) and PEDOT-CNT (blue) electrodeposition.

tests that PPy is not electrochemically stable under similar conditions. With our PEDOT-CNT arrays, impedance spectra did not change after four million pulses (data not shown), even when applying a ten times larger charge density, exhibiting the ability to handle the higher currents needed to stimulate neurons from the cortical surface. An example of somatosensory-evoked potentials (SEP) recorded using a 4 × 4 micro-ECoG array (inset) with a 1 × 1 mm total recording area, 100 μm diameter recording sites and 300 μm inter-electrode pitch coated with PEDOT-CNT is shown in **Figure 10**. The graphs show the response of each single electrode to the first 12-ms truncated Gaussian of a 9-Hz train of a rat multiwhisker deflections of 0.8 mm. The data are averaged from 20 repetitions of the stimulation pattern.

REDUCED INVASIVENESS AND INCREASED VERSATILITY THROUGH NANOCOATINGS AND POLYMER-BASED CIRCUITS: SMALLER AND SOFTER ELECTRODES

LOW-INVASIVE INTRACORTICAL MICROSPHERES

The insertion of any electrode into living brain tissue unavoidably results in a mechanical trauma that activates a cascade of events leading to a neural loss around the implant and its encapsulation in a high-impedance scar made of glial and immune cells, undermining the goal of maintaining long-term communication with neurons (Ward et al., 2009; Marin and Fernández, 2010). However, the physical properties of the whole device,—e.g., its size, shape and stiffness—can play a fundamental role in modulating the tissue reaction, and can be altered to reduce the insertion trauma and to aid accommodation of the large stiffness mismatch between the device and the nervous system tissue (Edell et al., 1992; Ward et al., 2009; Marin and Fernández, 2010). Aside from coating the electrodes with different biomolecules, anti-inflammatory compounds, hydrogels (Crompton et al., 2007; Zhong and Bellamkonda, 2007; Abidian and Martin, 2009), polymers (Ludwig et al., 2006; Leung et al., 2008; Grill et al., 2009) or carbon nanotubes (Lovat et al., 2005; Mazzatenta et al., 2007), another strategy is to modify the physical dimensions, and geometry of the neural probe (Stice et al., 2007; Ward et al., 2009).

Our approach was to minimize the physical size of the probe while maximizing the flexibility of the tether between the electrode and the connection to the external recording/stimulation system in order to be able to accommodate movements and motions of the brain with respect to the skull. As the smaller the size of the electrode, the greater the impedance, we endeavored to exploit the majority of the available surface of the probe, abandoning the standard shapes, which usually expose either flat or conical electrode surfaces. Instead we developed a process in which we created a conductive sphere (the electrode) that is much larger in diameter than the wire that connects it to the external recording chain. In fact, while the surface area of the electrode is crucial for recording and stimulation, even a very thin metallic wire used as connector will have a much lower impedance than that of the electrochemical interface. Another advantage of the spherical shape is that the electrode does not need a rigid stem, as it can be kept in position by the hydrostatic pressure of the brain.

To demonstrate this concept, we grew microspheres of fuzzy gold at the end of 12-μm polyimide-insulated Pt wires by electrochemical deposition, starting from a 10 mM potassium dicyanoaurate(I) agar gel (0.1 wt%), and applying monophasic voltage pulses (0.2–1.0 V, 240 s, duty cycle 50%). The temperature of the gel was kept at 45°C.

We characterized our microspheres both optically (**Figure 11A**) and electrochemically, measuring the size and impedance (**Figure 11B**) after 3, 6, 9, 12, and 13 h of electrodeposition. After the first 3 h, a huge reduction in impedance was observed, which can be linked to both the increased electrode size and the far greater surface area generated by the microstucturing. Over the following 10 h the impedance decreased by another order of magnitude, with a fairly linear trend in good accord with its increase in diameter. After 13 h we reached a diameter of 105 μm, and the corresponding impedance was less than 1 kΩ at 1 kHz. The impedance spectrum of a 105-μm diameter microsphere is shown in **Figure 11C**. An example of a signal trace recorded using a 100 μm diameter microsphere is shown in **Figure 11D**. The very thin Pt wire is extremely flexible and, once the microsphere is inserted, bends easily, reducing the mechanical stress on the surrounding tissue, while the sphere, as mentioned before, remains in place thanks to the hydrostatic pressure of the brain. The change in diameter of the microsphere can be better appreciated in **Figure 11E**.

ULTRA-FLEXIBLE AND BRAIN-CONFORMABLE micro-ECoG DEVICE WITH LOW-IMPEDANCE MICROELECTRODES

Although our flexible ECoG arrays were able to record brain activity in acute sessions, a long-term large-area implant comprising a high-resolution ECoG array would ideally require more flexible and brain-conformable devices that can accommodate brain curvature, compliantly covering neighboring gyri and crossing sulci while keeping the electrodes in intimate contact with the brain cortex. One way of attempting to meet this requirement is to reduce device thickness by developing appropriate technologies.

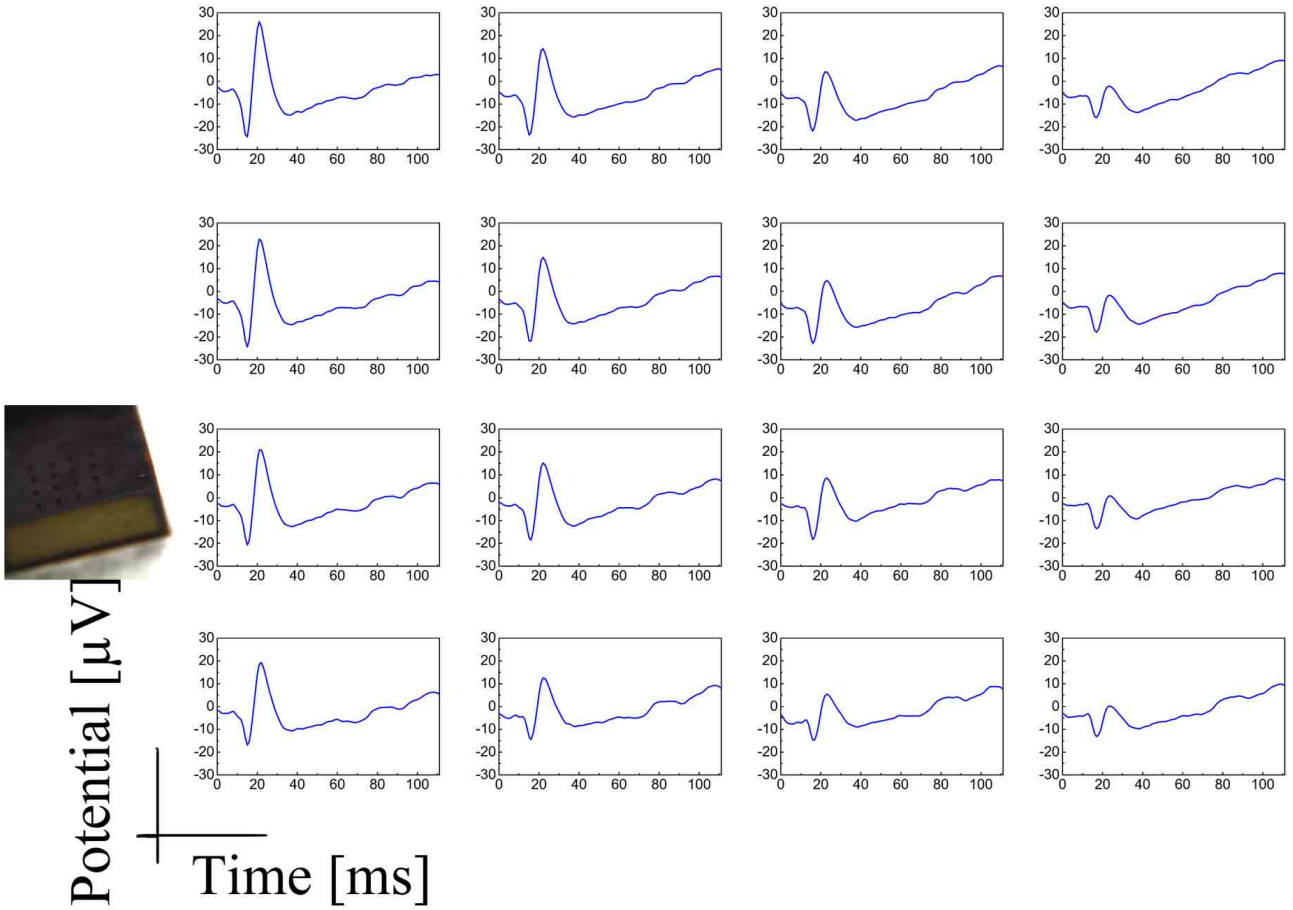

FIGURE 10 | SEP response of a 4 × 4 micro-ECoG array (inset) with a 1 × 1 mm total recording area, 100 μm diameter recording sites, and 300 μm inter-electrode pitch, coated with PEDOT-CNT to the first 12-ms truncated Gaussian of a 9-Hz train of rat multiwhisker deflections of 0.8° mm. The data are averaged on 20 repetitions of the stimulation pattern.

To this end we modified prototypes of gold-on-polyimide ultra-flexible micro-ECoG arrays. The fabrication procedure has been described elsewhere (Castagnola et al., 2013b), but relies on standard optical lithography. The ultra-flexible polyimide micro-ECoG arrays had a total thickness of approximately 8 μm. In spite of their thinness, these devices were mechanically quite robust, making their handling relatively unproblematic. We tested different layouts and electrode sizes (200 × 200 μm and 100 × 100 μm) suitable for different types of neurophysiological experiment. Some designs and details of the electrodes are reported in **Figure 12**.

We were able to selectively coat with PEDOT-CNT HSA composite both 100 × 100 μm and 200 × 200 μm electrodes, demonstrating that the absence of a well in the coverlay does not impair the possibility of obtaining spatially defined coatings, and we obtained reductions in impedance similar to those of our FCP ECoG arrays. Indeed, the impedance at 100 Hz was reduced from 1.6 ± 0.1 MΩ to 2.1 ± 0.7 kΩ with 100 × 100 μm electrodes and from 509.7 ± 177.5 to 0.63 ± 0.07 kΩ with 200 × 200 μm electrodes. The corresponding impedance spectra are shown in **Figure 13A**. Interestingly, the impedance decreased by up to four orders of magnitude in the 1–100 Hz frequency band (Castagnola et al., 2013b), where ECoG signals are typically recorded, with a significant downshift of the first frequency response pole. In order to validate the recording capability of our ultra-flexible micro-ECoGs, we tested our device *in vivo* by recording from the rat somatosensory cortex, using a stimulation protocol similar to the one described in section Flexible micro-ECoG arrays. An example of averaged SEP elicited using a 9-Hz train of truncated Gaussian 0.8-mm rat multiwhisker deflection (first 12 ms response) using PEDOT-coated 100 × 100 μm electrodes (average on 10 electrodes) is shown in **Figure 13B**, clearly demonstrating the ability of this device to record clear SEP responses.

BIOCOMPATIBILITY ISSUES AND FEAR OF NANOCOATINGS: A PRAGMATIC APPROACH AND PROOF OF CONCEPT

The toxicology of nanoparticles is hotly debated in scientific circles, and rather controversial results have been reported. However, experiments often document the *in vitro* or *in vivo* release of dispersed nanoparticles at very high concentrations, making it difficult to assess the real impact of nanomaterial-coated neural probes. Moreover, in the case of carbon nanotubes, a large

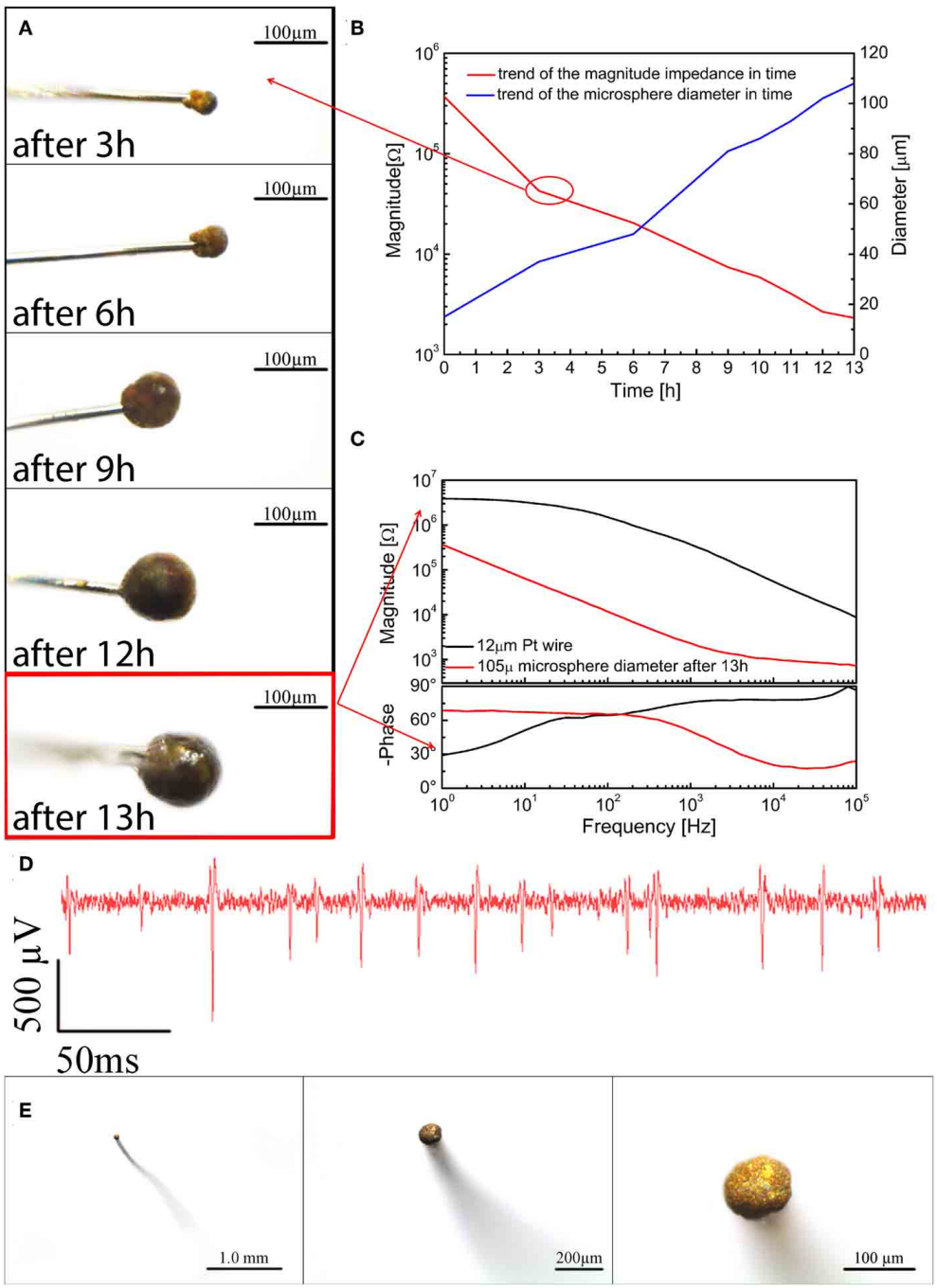

FIGURE 11 | (A) Optical images of the microspheres after 3, 6, 9, 12, and 13 h of electrodeposition; **(B)** impedance magnitude at 1 kHz and diameters of the microspheres after 3, 6, 9, 12, and 13 h of electrodeposition; **(C)** Impedance after 13 h of electrodeposition; **(D)** an example of spike activity recorded using a 100 µm microsphere; **(E)** from left to right different top view optical magnifications of a typical microsphere.

number of studies report effects that can easily be ascribed to the toxicity of the metal catalyst of unpurified CNTs.

One of the main sources of debate when dealing with nanoparticles, especially CNTs, lies in the fact that, as their properties are largely determined by their surface characteristics, any chemical functionalization will have a very strong influence on the way the particles are metabolized, and therefore any resulting tissue reaction. Some studies have demonstrated that specific types of CNTs can be biodegraded (Kagan et al., 2010; Bianco et al., 2011) even in the brain tissue, after internalization in the microglia (Nunes et al., 2012). The situation becomes even more complex if we consider that in many cases we are dealing with CNT composites, and

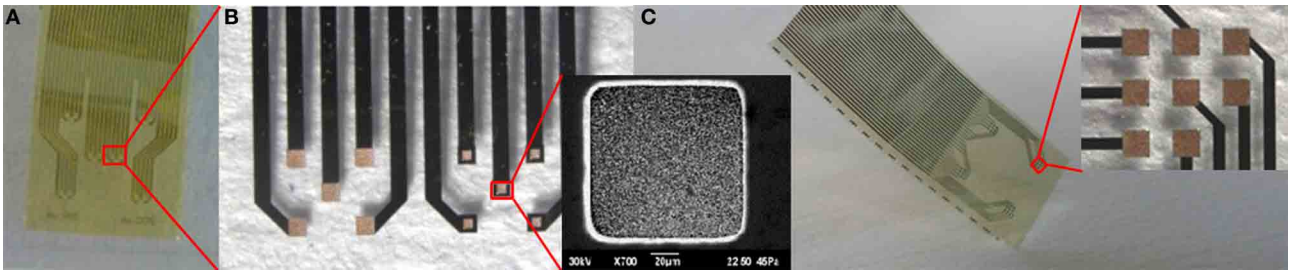

FIGURE 12 | (A) One possible ultraflexible micro-ECoG array layout. **(B)** Details of the two groups of five recording sites 200° × 200° μm and 100° × 100° μm in size, and a scanning electron micrograph of a 100 × 100 μm Au recording site (inset). **(C)** Other possible ultraflexible micro-ECoG array layouts and detail of a group of eight 200 × 200° μm recording sites (inset).

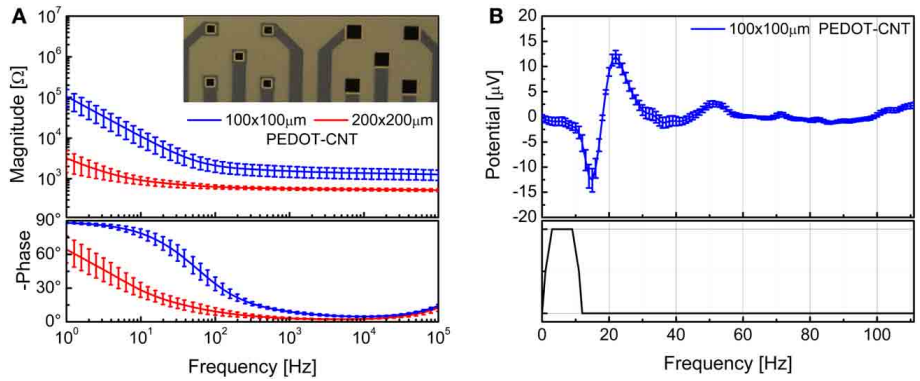

FIGURE 13 | (A) Impedance spectra of the 100 × 100 μm and 200 × 200 μm ultraflexible ECoG array recording sites (mean and standard deviation from 10 recording sites each) before and after PEDOT-CNT electrodeposition. **(B)** Averaged SEP elicited using a 9-Hz train of truncated Gaussian 0.8-mm rat multiwhisker deflection (first 12 ms response) using PEDOT-coated 100 × 100 μm electrodes (average on 10 electrodes).

not isolated particles. If the composite is stable, the surface interacting with the tissue can be considered as a macroscopic particle made of the matrix material, in which the CNTs are fully embedded and encapsulated. If one such composite (macro) particle is released, it may be degraded or not, depending on the material it is made of. If it were undegradable, it would, most probably, be encapsulated as a foreign body. If it were subject to particle degradation, the embedded CNTs would be released into the body in amounts that are vastly smaller than those used in current toxicological experimentation. This makes it very difficult to state whether or not there is a toxic effect at such low concentrations. In the case of nanocoated neural implants, addressing the toxicity of the HSA coating would itself take very long time, and it would be impossible to ascertain with absolute confidence that not one single tiny particle of nanocomposite detaches from the coating during the contact with the brain surface due to mechanical stress. For these reasons we proposed a completely different approach, namely to encapsulate the entire device with a coating that is transparent to ionic currents but, at the same time, protects the device from mechanical stress and prevents, in case of nanocoating failure, the release of particles into the brain tissue. To achieve this we used a hydrogel, specifically human fibrin, to encapsulate our HSA-coated neural micro-ECoG arrays, thereby creating a mechanically stable barrier that prevents direct exposure of the brain to nanomaterials, without, however, impairing their electrochemical and neural performance (Castagnola et al., 2013a,b).

We chose a commercially available two-component fibrin sealant that is approved for surgical purposes in both Europe and the United States (TISSEEL [fibrin sealant], Baxter, USA), and one that is commonly used in neurosurgical practice. We set out to develop a procedure compliant with the protocols approved by the competent medical surveillance agencies for the safe handling and use of fibrin in sterile operating theatres. We devised a process involving the sterilization of the HSA-coated micro-ECoG array before it is introduced to a sterile environment, the fibrin being applied to the device by the surgeon just before use (Castagnola et al., 2013a,b). To deposit the fibrin layer, the polyimide based FPC circuits were placed over an aluminium sample holder heated at 37°C. Meanwhile, the fibrin precursors, fibrinogen, and thrombin, were warmed up to the same temperature. The fibrinogen was spread over the electrodes with a spatula and, then, a large thrombin drop was placed over the whole fibrinogen-coated surface. After 5 min, a stable fibrin layer was formed and the micro–ECoG array was rinsed in ultrapure water to remove the residual thrombin solution.

A SEM image of a single recording/stimulation site after fibrin encapsulation is shown in **Figure 14A**, together with the

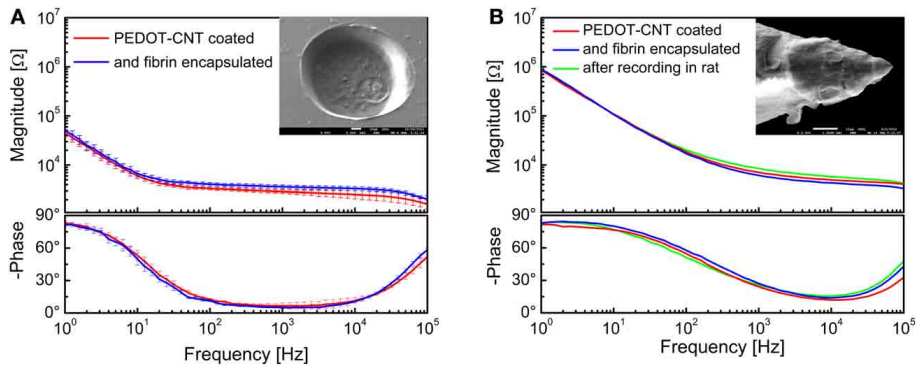

FIGURE 14 | Impedance spectra of (A) 140-μm-diameter ECoG array recording sites (mean and standard deviation from 64 recording sites each) coated with PEDOT-CNT composite, before and after fibrin encapsulation, and (B) intracortical PEDOT-CNT microelectrode before and after fibrin encapsulation and *in vivo* recording. s.e.m. images of a single recording/stimulation site encapsulated with fibrin are shown in the respective insets.

impedance spectra of a 140-μm diameter PEDOT-CNT-coated recording site ECoG array before and after fibrin encapsulation. We can observe that the fibrin encapsulation does not have any significant impact on the impedance spectra of PEDOT-CNT-coated microelectrodes (from 3.4 ± 0.2 kΩ to 3.9 ± 0.4 kΩ @ 100 Hz), confirming that the fibrin hydrogel acts as a good ionic conductor. These fibrin-encapsulated PEDOT-CNT-coated micro-ECoG arrays, being able to resist intense and prolonged current stimulation without the fibrin layer being affected by the current passage (Castagnola et al., 2013a,b) can therefore be considered suitable for cortical stimulation. Indeed, we used these devices *in vivo* to record SEPs from the rat somatosensory cortex, elicited through multiwhisker deflection using a protocol similar to the one reported above. We verified that after two 15-min-long epicortical recording sessions the fibrin coating was still in place, firmly adhering to the recording sites, and thereby effectively shielding the tissues from direct contact with the nanostructured coating. Furthermore, the microelectrode impedance did not change significantly, and the quality of the SEP recordings was not affected by the presence of the fibrin coating (Castagnola et al., 2013a,b).

After proving that the fibrin hydrogel is able to stay in place on the surface of micro-ECoG devices that are placed on the dura mater or cortex, we tested whether or not it can be used to encapsulate an intracortical electrode, and to withstand the mechanical stress generated by brain tissue penetration. To this end, we encapsulated our PEDOT-CNT-coated intracortical microelectrodes by a controlled two-stage dipping process, first into a vial containing fibrinogen, and then into a second vial containing thrombin. The impedance spectra of a PEDOT-CNT-coated electrode before and after fibrin encapsulation, and also after an *in vivo* intracortical recording session involving penetration of the rat brain tissue (including the dura mater), are shown in **Figure 14B**. A SEM picture of a microelectrode after fibrin encapsulation is shown in the inset. The fibrin encapsulation had no significant effect on the microelectrode impedance, which remained nearly identical, even after the intracortical recording. To check the persistence of the fibrin layer after the rat somatosensory cortex recording session, we stained it with methylene blue, which showed that the fibrin remained adherent to the HSA-coated tip. As previous experiments have shown us that fibrin tends to detach from uncoated, smooth electrodes, this experimental evidence suggests that there is an intimate adhesion between the fibrin layer and the rough HSA coating we applied to the tip (as previously hinted at by electrochemical measurements). In all probability, this adhesion is brought about by the hydrogel being trapped in the nanostructured microelectrode surface, preventing its slipping away.

As previously mentioned, we chose to test fibrin hydrogel due to its potentially ready transferral to human surgery applications. A particular advantage of fibrin hydrogel is that it can be autologous, i.e., obtained from the patient's own blood, thereby reducing to a minimum rejection risks, etc. However, while this approach appears feasible for acute use, unfortunately fibrin can be fully resorbed by the tissues within 2 weeks during *in vivo* implants (Schoeller et al., 2001; de Vries et al., 2002). Nevertheless, our results prove that it is possible to fully encapsulate recording and stimulation devices in hydrogel without impairing their performance, and suggests that it would be possible to extend the use of such a technique to chronic implants by replacing fibrin with an appropriate biocompatible non-resorbable hydrogel with similar physical properties. To this end, it may be advantageous to use synthetic hydrogels as they are better chemically defined, with respect to those composed of only natural materials, and it is possible to better control their polymerization, degradation, and biocompatibility (Aurand et al., 2012a,b). Among all, promising candidates are poly(2-hydroxyethyl methacrylate) (pHEMA) and polyurethane based hydrogels, that have a long-standing track record of successful biomedical applications and have been already tested in contact with the central and pheripheral nervous system (Woerly et al., 1998; Lukás et al., 2001; Dalton et al., 2002; Jhaveri et al., 2009; Rao et al., 2012). To be used for the encapsulation of nanocoated neural chronic implants, it is necessary to accurately fine-tune the hydrogel composition, the cross-linking molecules, and network mesh size, in order to achieve the desired properties in terms of

semi-permeability, mechanical stiffness, degree of swelling, and resistance to degradation.

PERSPECTIVES FOR LONG TERM IMPLANTS

Despite the great efforts and expectations, at present electrodes for brain stimulation and recording are still far from the reliability, affordability, and long term stability necessary for a widespread clinical use in human cortical prosthesis. However, over the last 5 years, by careful selection of readymade technologies, we have been able to modify electrodes to make them smaller, more sensitive, more flexible, less invasive, and more reliable.

With a particular focus on electrodes for human use, we have shown that it is also possible to improve their recording capabilities in terms of sensitivity, signal-to-noise ratio, and electromagnetic interference rejection, by using a variety of HSA coatings based on nanomaterials. We have developed and systematically studied and compared a variety of HSA coatings—CVD-CNT, PPy-CNT, PEDOT-CNT, Au-CNT, Au-agar, PEDOT-agar—proving that such technologies enhance performance in both epicortical and intracortical recording and stimulation. We have also made these coatings mechanically stable and able to withstand penetration through the dura and the brain of an animal model (rat).

Despite the advantages of rigid microprobes, (Campbell et al., 1991; Rousche and Normann, 1992; Richter et al., 2013) particularly in ensuring a precise positioning of the electrodes during insertion into specific brain areas (Schjetnan and Luczak, 2011), they cannot yet provide reliable and stable long-term recordings. Indeed, even state-of-the-art rigid microelectrodes cause severe mechanical trauma during their insertion, resulting in a thick glial scar formation and a consequent loss of tissue-electrode coupling as time goes by (Turner et al., 1999; Polikov et al., 2005; Leach et al., 2010; Richter et al., 2013). That being said, (Krüger et al., 2010) did manage to achieve stable recordings for several years from electrodes experimentally implanted in monkeys thanks to the minimal invasiveness of their device at the cortical recording site. Although this proved the importance of minimizing the mechanical damage to the cortical area under investigation, their electrodes were inserted using a device that enables brain penetration through the white matter from a different area, making the technique very invasive and unsuitable for clinical applications. Hence many other studies have focused on the replacement of rigid with flexible electrodes, which it is hoped will reduce insertion trauma, being more similar mechanically to the soft brain tissue and thereby minimizing the stiffness mismatch between device and nervous system tissue (Rousche et al., 2001; Rubehn and Stieglitz, 2010; Richter et al., 2013). We too aimed to reduce the invasiveness of insertion, by minimizing the physical size of the probe without compromising its electrical impedance, and keeping the tether between the electrode and the external recording/stimulation system as flexible as possible to enable accommodation of brain movement and motions within the skull. We achieved a reduction in probe size by electrochemically growing a HSA gold sphere on the tip of a very thin wire (12 μm in diameter), envisioning the sphere as the ideal shape to be kept in position by the hydrostatic pressure of the brain. This technique also provided us with a very flexible tether, which is not involved in the long term positioning of the device. In a parallel approach, we aimed to overcome the issue of foreign-body response in intracortical implants, developing high-resolution micro-ECoG arrays with enhanced recording capabilities thanks to our HSA coatings. We developed a variety of flexible micro-ECoG arrays of HSA-coated electrodes, whose better signal quality make it feasible to further reduce electrode size and increase spatial resolution. We further improved our technology using novel ultrathin electrodes, which enable intimate contact with the surface of the brain, thereby enhancing the electrical coupling. Finally, we proved that it is possible to reliably encapsulate both intracortical and epicortical devices with a biocompatible hydrogel, which provides a mechanical barrier between the nanocomposite HSA materials, and the human body, without any loss of device performance.

Altogether, these results converge in a method that we believe represents several steps forward in terms of bringing such novel devices into clinical settings, opening new avenues for neurodiagnostics, and neuroprosthetic applications.

ACKNOWLEDGMENTS

We would like to thank Luca Maiolo, Marco Marrani, Antonio Minotti, Francesco Maita, Alessandro Pecora, and Guglielmo Fortunato for providing the ultra-flexible micro-ECoG devices. We would like to thank Gian Nicola Angotzi, Marianna Semprini, and Alessandro Vato for support during the use of the recording/stimulation set-up.

REFERENCES

Abidian, M. R., and Martin, D. C. (2008). Experimental and theoretical characterization of implantable neural microelectrodes modified with conducting polymer. *Biomaterials* 29, 1273–1283. doi: 10.1016/j.biomaterials.2007.11.022

Abidian, M. R., and Martin, D. C. (2009). Multifunctional nanobiomaterials for neural interfaces. *Adv. Funct. Mater.* 19, 573–585. doi: 10.1002/adfm.200801473

Ansaldo, A., Castagnola, E., Maggiolini, E., Fadiga, L., and Ricci, D. (2011). Superior electrochemical performance of carbon nanotubes directly grown on sharp microelectrodes. *ACS Nano* 5, 2206–2214. doi: 10.1021/nn103445d

Aurand, E. R., Lampe, K. J., and Bjugstad, K. B. (2012a). Defining and designing polymers and hydrogels for neural tissue engineering. *Neurosci. Res.* 72, 199–213. doi: 10.1016/j.neures.2011.12.005

Aurand, E. R., Wagner, J., Lanning, C., and Bjugstad, K. B. (2012b). Building biocompatible hydrogels for tissue engineering of the brain and spinal cord. *J. Funct. Biomater.* 3, 839–863. doi:10.3390/jfb3040839

Baranauskas, G., Maggiolini, E., Castagnola, E., Ansaldo, A., Mazzoni, A., Angotzi, G. N., et al. (2011). Carbon nanotube composite coating of neural microelectrodes preferentially improves the multiunit signal-to-noise ratio. *J. Neural Eng.* 8:66013. doi: 10.1088/1741-2560/8/6/066013

Bianco, A., Kostarelos, K., and Prato, M. (2011). Making carbon nanotubes biocompatible and biodegradable. *Chem. Commun.* 47, 10182–10188. doi: 10.1039/c1cc13011k

Brummer, S. B., Robblee, L. S., Hambrecht, T., and Hambrecht, F. T. (1983). Criteria for selecting electrodes for electrical stimulation: theoretical and practical considerations. *Ann. N. Y. Acad. Sci.* 405, 159–171. doi: 10.1111/j.1749-6632.1983.tb31628.x

Campbell, P. K., Jones, K. E., Huber, R. J., Horch, K. W., and Normann, R. A. (1991). A silicon based three dimensional neural interface: manufacturing processes for an intracortical electrode array. *IEEE Trans. Biomed. Eng.* 38, 758–768. doi: 10.1109/10.83588

Castagnola, E., Ansaldo, A., Fadiga, L., and Ricci, D. (2010). Chemical vapour deposited carbon nanotube coated microelectrodes for intracortical neural recording. *Phys. Status Solidi (B)* 247, 2703–2707. doi: 10.1002/pssb.201000217

Castagnola, E., Ansaldo, A., Maggiolini, E., Angotzi, G. N., Skrap, M., Ricci, D., et al. (2013a). Biologically compatible neural interface to safely couple nanocoated electrodes to the surface of the brain, *ACS Nano* 5, 3887–3895. doi: 10.1021/nn305164c

Castagnola, E., Biso, M., and Ricci, D. (2009). Improvement of polypyrrole and carbon nanotube co-deposition techniques for high charge-transfer electrodes. *Phys. Status Solidi (B)* 246, 2469–2472. doi: 10.1002/pssb.200982283

Castagnola, E., Maiolo, L., Maggiolini, E., Minotti, A., Marrani, M., Maita, F., et al. (2013b). "Ultra-flexible and brain-conformable microelectrocorticography device with low impedance PEDOT-carbon nanotube coated microelectrodes," in *Proceeding of the 6th International IEEE/EMBS Conference on Neural Engineering* (San Diego, CA), 927–930. doi: 10.1109/NER.2013.6696087

Chao, Z. C., Nagasaka, Y., and Fujii, N. (2010). Long-term asynchronous decoding of arm motion using electrocorticographic signals in monkeys. *Front. Neuroeng.* 3:3. doi: 10.3389/fneng.2010.00003

Cogan, S. F. (2008). Neural stimulation and recording electrodes. *Annu. Rev. Biomed. Eng.* 10, 275–309. doi: 10.1146/annurev.bioeng.10.061807.160518

Cogan, S. F., Plante, T. D., and Ehrlich, J. (2004). Sputtered iridium oxide films (SIROFs) for low-impedance neural stimulation and recording electrodes. *Conf. Proc. IEEE Eng. Med. Biol. Soc.* 6, 4153–4156. doi: 10.1109/IEMBS.2004.1404158

Crompton, K. E., Goud, J. D., Bellamkonda, R. V., Gengenbach, T. R., Finkelstein, D. I., Horne, M. K., et al. (2007). Polylysine-functionalised thermoresponsive chitosan hydrogel for neural tissue engineering. *Biomaterials* 28, 441–449. doi: 10.1016/j.biomaterials.2006.08.044

Cui, X., Lee, V. A., Raphael, Y., Wiler, J. A., Hetke, J. F., Anderson, D. J., et al. (2001). Surface modification of neural recording electrodes with conducting polymer/biomolecule blends. *J. Biomed. Mater. Res.* 56, 261–272. doi: 10.1002/1097-4636(200108)56:2%3C261::AID-JBM1094%3E3.0.CO;2-I

Cui, X., and Martin, D. C. (2003). Electrochemical deposition and characterization of poly(3,4-ethylenedioxythiophene) on neural microelectrode arrays. *Sens. Actuators B Chem.* 89, 92–102. doi: 10.1016/S0925-4005(02)00448-3

Dalton, P. D., Flynn, L., and Shoichet, M. S. (2002). Manufacture of poly(2-hydroxyethyl methacrylate-co-methyl methacrylate) hydrogel tubes for use as nerve guidance channels. *Biomaterials* 23, 3843–3851. doi: 10.1089/neu.2009.0948

Desai, S. A., Rolston, J. D., Guo, L., and Potter, S. M. (2010). Improving impedance of implantable microwire multi-electrode arrays by ultrasonic electroplating of durable platinum black. *Front. Neuroeng.* 3:5. doi: 10.3389/fneng.2010.00005

de Vries, J., Menovsky, T., van Gulik, S., and Wesseling, P. (2002). Histological effects of fibrin glue on nervous tissue. *Surg. Neurol.* 57, 415–422. doi: 10.1016/S0090-3019(02)00736-X

Edell, D. J., Van Toi, V., McNeil, V. M., and Clark, L. D. (1992). Factors influencing the biocompatibility of insertable silicon microshafts in cerebral cortex. *IEEE Trans. Biomed. Eng.* 39, 635–643. doi: 10.1109/10.141202

Erchova, I. A., Lebedev, M. A., and Diamond, M. E. (2002). Somatosensory cortical neuronal population activity across states of anaesthesia. *Eur. J. Neurosci.* 15, 744–752. doi: 10.1046/j.0953-816x.2002.01898.x

Ferguson, J. E., Boldt, C., and Redish, A. D. (2009). Creating low-impedance tetrodes by electroplating with additives. *Sens. Actuators A Phys.* 156, 388–393. doi: 10.1016/j.sna.2009.10.001

Fries, P., Nikolic, D., and Singer, W. (2007). The gamma cycle. *Trends Neurosci.* 30, 309–316. doi: 10.1016/j.tins.2007.05.005

Gabay, T., Ben-David, M., Kalifa, I., Sorkin, R., Abrams, Z. R., Ben-Jacob, E., et al. (2007). Electro-chemical and biological properties of carbon nanotube based multi-electrode arrays. *Nanotechnology* 18:035201. doi: 10.1088/0957-4484/18/3/035201

Gawad, S., Giugliano, M., Heuschkel, M., Wessling, B., Markram, H., Schnakenberg, U., et al. (2009). Substrate arrays of iridium oxide microelectrodes for *in vitro* neuronal interfacing. *Front. Neuroeng.* 2:1. doi: 10.3389/neuro.16.001.2009

Gerwig, R., Fuchsberger, K., Schroeppel, B., Link, G. S., Heusel, G., Kraushaar, U., et al. (2012). PEDOT-CNT composite microelectrodes for recording and electrostimulation applications: fabrication, morphology, and electrical properties. *Front. Neuroeng.* 5:8. doi: 10.3389/fneng.2012.00008

Gray, C. M., Konig, P., Engel, A. K., and Singer,W. (1989). Oscillatory responses in cat visual cortex exhibit inter-columnar synchronization which reflects global stimulus properties. *Nature* 338, 334–337. doi: 10.1038/338334a0

Green, R. A., Williams, C. M., Lovell, N. H., and Poole-Warren, L. A. (2008). Novel neural interface for implant electrodes: improving electroactivity of polypyrrole through MWNT incorporation. *J. Mater. Sci. Mater. Med.* 19, 1625–1629. doi: 10.1007/s10856-008-3376-7

Grill, W. M., Norman, S. E., and Bellamkonda, R. V. (2009). Implanted neural interfaces: biochallenges and engineered solutions. *Annu. Rev. Biomed. Eng.* 11, 1–24. doi: 10.1146/annurev-bioeng-061008-124927

Harris, K. D., Henze, D. A, Csicsvari, J., Hirase, H., and Buzsáki, G. (2000). Accuracy of tetrode spike separation as determined by simultaneous intracellular and extracellular measurements. *J. Neurophysiol.* 84, 401–414.

Hollenberg, B. A., Richards, C. D., Richards, R., Bahr, D. F., and Rector, D. M. (2006). A MEMS fabricated flexible electrode array for recording surface field potentials. *J. Neurosci. Methods* 153, 147–153. doi: 10.1016/j.jneumeth.2005.10.016

Jan, E., Hendricks, J. L., Husaini, V., Richardson-Burns, S. M., Sereno, A., Martin, D. C., et al. (2009). Layered carbon nanotube-polyelectrolyte electrodes outperform traditional neural interface materials. *Nano Lett.* 9, 4012–4018. doi: 10.1021/nl902187z

Jhaveri, S. J., Hynd, M. R., Dowell-Mesfin, N., Turner, J. N., Shain, W., and Ober, C. K. (2009). Release of nerve growth factor from HEMA hydrogel-coated substrates and its effect on the differentiation of neural cells. *Biomacromolecules* 10, 174–183. doi: 10.1021/bm801101e

Kagan, V. E., Konduru, N. V., Feng, W., Allen, B. L., Conroy, J., Volkov, Y., et al. (2010). Carbon nanotubes degraded by neutrophil myeloperoxidase induce less pulmonary inflammation. *Nat. Nanotech.* 5, 354–359. doi: 10.1038/nnano.2010.44

Keefer, E. W., Botterman, B. R., Romero, M. I., Rossi, A. F., and Gross, G. W. (2008). Carbon nanotube coating improves neuronal recordings. *Nat. Nanotech.* 3, 434–439. doi: 10.1038/nnano.2008.174

Kellis, S., Miller, K., Thomson, K., Brown, R., House, P., and Greger, B. (2010). Decoding spoken words using local field potentials recorded from the cortical surface. *J. Neural Eng.* 7:56007. doi: 10.1088/1741-2560/7/5/056007

Kellis, S. S., House, P. A., Thomson, K. E., Brown, R., and Greger, B. (2009). Human neocortical electrical activity recorded on nonpenetrating microwire arrays: applicability for neuroprostheses. *Neurosurg. Focus* 27:E9. doi: 10.3171/2009.4.FOCUS0974

Khodagholy, D., Doublet, T., Gurfinkel, M., Quilichini, P., Ismailova, E., Leleux, P., et al. (2011). Highly conformable conducting polymer electrodes for *in vivo* recordings. *Adv. Mater.* 23, H268–H272. doi: 10.1002/adma.201102378

Kotov, N. A., Winter, J. O., Clements, I. P., Jan, E., Timko, B. P., Campidelli, S., et al. (2009). Nanomaterials for neural interfaces. *Adv. Mater.* 21, 3970–4004. doi: 10.1002/adma.200801984

Krüger, J., Caruana, F., Dalla Volta, R., and Rizzolatti, G. (2010). Seven years of recording from monkey cortex with a chronically implanted multiple microelectrode. *Front. Neuroeng.* 3:6. doi: 10.3389/fneng.2010.00006

Leach, J. B., Achyuta, A. K., and Murthy, S. K. (2010). Bridging the divide between neuroprosthetic design, tissue engineering and neurobiology. *Front. Neuroeng.* 2:18. doi: 10.3389/neuro.16.018.2009

Lee, K.-K., He, J., Singh, A., Massia, S., Ehteshami, G., Kim, B., et al. (2004). Polyimide-based intracortical neural implant with improved structural stiffness. *J. Micromech. Microeng.* 14, 32–37. doi: 10.1088/0960-1317/14/1/305

Leung, B. K., Biran, R., Underwood, C. J., and Tresco, P. A. (2008). Characterization of microglial attachment and cytokine release on biomaterials of differing surface chemistry. *Biomaterials* 29, 3289–3297. doi: 10.1016/j.biomaterials.2008.03.045

Leuthardt, E. C., Freudenberg, Z., Bundy, D., and Roland, J. (2009). Microscale recording from human motor cortex: implications for minimally invasive electrocorticographic brain-computer interfaces. *Neurosurg. Focus* 27:E10. doi: 10.3171/2009.4.FOCUS0980

Leuthardt, E. C., Schalk, G., Moran, D., and Ojemann, J. G. (2006). The emerging world of motor neuroprosthetics: a neurosurgical perspective. *Neurosurgery* 59, 1–14. doi: 10.1227/01.NEU.0000221506.06947.AC

Leuthardt, E. C., Schalk, G., Wolpaw, J. R., Ojemann, J. G., and Moran, D. W. (2004). A brain-computer interface using electrocorticographic signals in humans. *J. Neural Eng.* 1, 63–71. doi: 10.1088/1741-2560/1/2/001

Lovat, V., Pantarotto, D., Lagostena, L., Cacciari, B., Grandolfo, M., Righi, M., et al. (2005). Carbon nanotube substrates boost neuronal electrical signaling. *Nano Lett.* 5, 1107–1110. doi: 10.1021/nl050637m

Ludwig, K. A., Uram, J. D., Yang, J., Martin, D. C., and Kipke, D. R. (2006). Chronic neural recordings using silicon microelectrode arrays electrochemically

deposited with a poly(3,4-ethylenedioxythiophene) (PEDOT) film. *J. Neural Eng.* 3, 59–70. doi: 10.1088/1741-2560/3/1/007

Lukás, J., Smetana, K., Petrovický, P., Palecková, V., Vacik, J., Dvoránková, B., et al. (2001). Biological properties of copolymer of 2-hydroxyethyl methacrylate with sulfopropyl methacrylate. *J. Mater. Sci. Mater. Med.* 12, 639–646. doi: 10.1023/A:1011297828955

Lu, Y., Li, T., Zhao, X., Li, M., Cao, Y., Yang, H., et al. (2010). Electrodeposited polypyrrole/carbon nanotubes composite films electrodes for neural interfaces. *Biomaterials* 31, 5169–5181. doi: 10.1016/j.biomaterials.2010.03.022

Marin, C., and Fernández, E. (2010). Biocompatibility of intracortical microelectrodes: current status and future prospects. *Front. Neuroeng.* 3:8. doi: 10.3389/fneng.2010.00008

Mazzatenta, A., Giugliano, M., Campidelli, S., Gambazzi, L., Businaro, L., Markram, H., et al. (2007). Interfacing neurons with carbon nanotubes: electrical signal transfer and synaptic stimulation in cultured brain circuits. *J. Neurosci.* 27, 6931–6936. doi: 10.1523/JNEUROSCI.1051-07.2007

Musallam, S., Bak, M. J., Troyk, P. R., and Andersen, R. A. (2007). A floating metal microelectrode array for chronic implantation. *J. Neurosci. Meth.* 160, 122–127. doi: 10.1016/j.jneumeth.2006.09.005

Nicolelis, M. A. L., and Lebedev, M. A. (2009). Principles of neural ensemble physiology underlying the operation of brain-machine interfaces. *Nat. Rev. Neurosci.* 10, 530–540. doi: 10.1038/nrn2653

Nunes, A., Bussy, C., Gherardini, L., Meneghetti, M., Herrero, M. A., Bianco, A., et al. (2012). *In vivo* degradation of functionalized carbon nanotubes after stereotactic administration in the brain cortex. *Nanomedicine* 7, 1485–1494. doi: 10.2217/nnm.12.33

Polikov, V. S., Tresco, P. A., and Reichert, W. M. (2005). Response of brain tissue to chronically implanted neural electrodes. *J. Neurosci. Methods.* 148, 1–18. doi: 10.1016/j.jneumeth.2005.08.015

Quiroga, R. Q., Nadasdy, Z., and Ben-Shaul, Y. (2004). Unsupervised spike detection and sorting with wavelets and superparamagnetic clustering. *Neural Comput.* 16, 1661–1687. doi: 10.1162/089976604774201631

Rao, L., Zhou, H., Li, T., Li, C., and Duan, Y. Y. (2012). Polyethylene glycol-containing polyurethane hydrogel coatings for improving the biocompatibility of neural electrodes. *Acta Biomaterialia* 8, 2233–2242. doi: 10.1016/j.actbio.2012.03.001

Richter, A., Xie, Y., Schumacher, A., Löffler, S., Kirch, R. D., Al-Hasani, J., et al. (2013). A simple implantation method for flexible, multisite microelectrodes into rat brains. *Front. Neuroeng.* 6:6. doi: 10.3389/fneng.2013.00006

Ritaccio, A., Boatman-Reich, D., Brunner, P., Cervenka, M. C., Cole, A. J., Crone, N., et al. (2011). Proceedings of the second international workshop on advances in electrocorticography. *Epilepsy Behav.* 22, 641–650. doi: 10.1016/j.yebeh.2011.09.028

Robinson, D. A. (1968). The electrical properties of metal microelectrodes. *Proc. IEEE* 56, 1065–1071. doi: 10.1109/PROC.1968.6458

Rousche, P. J., and Normann, R. A. (1992). A method for pneumatically inserting an array of penetrating electrodes into cortical tissue. *Ann. Biomed. Eng.* 20, 413–422. doi: 10.1007/BF02368133

Rousche, P. J., Pellinen, D. S., Pivin, D. P., Williams, J. C., Vetter, R. J., and Kipke, D. R. (2001). Flexible polyimide-based intracortical electrode arrays with bioactive capability. *IEEE Trans. Biomed. Eng.* 48, 361–371. doi: 10.1109/10.914800

Rubehn, B., Bosman, C., Oostenveld, R., Fries, P., and Stieglitz, T. (2009). A MEMS-based flexible multichannel ECoG-electrode array. *J. Neural Eng.* 6:036003. doi: 10.1088/1741-2560/6/3/036003

Rubehn, B., and Stieglitz, T. (2010). *In vitro* evaluation of the long-term stability of polyimide as a material for neural implants. *Biomaterials* 31, 3449–3458. doi: 10.1016/j.biomaterials.2010.01.053

Schjetnan, A. G., and Luczak, A. (2011). Recording large-scale neuronal ensembles with silicon probes in the anesthetized rat. *J. Vis. Exp.* 56:e3282. doi: 10.3791/3282

Schoeller, T., Lille, S., Wechselberger, G., Otto, A., Mowlawi, A., and Piza-Katzer, H. (2001). Histomorphologic and volumetric analysis of implanted autologouspreadipocyte cultures suspended in fibrin glue: a potential new source for tissue augmentation. *Aesthetic Plast. Surg.* 25, 57–63. doi: 10.1007/s00266001096

Schwartz, A. B. (2004). Cortical neural prosthetics. *Annu. Rev. Neurosci.* 27, 487–507. doi: 10.1146/annurev.neuro.27.070203.144233

Shoval, A., Adams, C., David-Pur, M., Shein, M., Hanein, Y., and Sernagor, E. (2009). Carbon nanotube electrodes for effective interfacing with retinal tissue. *Front. Neuroeng.* 2:4. doi: 10.3389/neuro.16.004.2009

Sorkin, R., Greenbaum, A., David-Pur, M., Anava, S., Ayali, A., Ben-Jacob, E., et al. (2009). Process entanglement as a neuronal anchorage mechanism to rough surfaces. *Nanotechnology* 20:015101. doi: 10.1088/0957-4484/20/1/015101

Stice, P., Gilletti, A., Panitch, A., and Muthuswamy, J. (2007). Thin microelectrodes reduce GFAP expression in the implant site in rodent somatosensory cortex. *J. Neural Eng.* 4, 42–53. doi: 10.1088/1741-2560/4/2/005

Suner, S., Fellows, M. R., Vargas-Irwin, C., Nakata, G. K., and Donoghue, J. P. (2005). Reliability of signals from a chronically implanted, silicon-based electrode array in non-human primate primary motor cortex. *IEEE Trans. Neural Syst. Rehabil. Eng.* 13, 524–541. doi: 10.1109/TNSRE.2005.857687

Takeuchi, S., Suzuki, T., Mabuchi, K., and Fujita, H. (2004). 3D flexible multichannel neural probe array. *J. Micromech. Microeng.* 14, 104–107. doi: 10.1088/0960-1317/14/1/014

Thongpang, S., Richner, T. J., Brodnick, S. K., Schendel, A., Kim, J., Wilson, J. A., et al. (2011). A micro-electrocorticography platform and deployment strategies for chronic BCI applications. *Clin. EEG Neurosci.* 42, 259–265. doi: 10.1177/155005941104200412

Turner, J. N., Shain, W., Szarowski, D. H., Andersen, M., Martins, S., Isaacson, M., et al. (1999). Cerebral astrocyte response to micromachined silicon implants. *Exp. Neurol.* 156, 33–49. doi: 10.1006/exnr.1998.6983

Ward, M. P., Rajdev, P., Ellison, C., and Irazoqui, P. P. (2009).Toward a comparison of microelectrodes for acute and chronic recordings. *Brain Res.* 1282, 183–200. doi: 10.1016/j.brainres.2009.05.052

Wise, K. D. (2005). Silicon microsystems for neuroscience and neural prostheses. *IEEE Eng. Med. Biol. Mag.* 24, 22–29. doi: 10.1109/MEMB.2005.1511497

Woerly, S., Pinet, E., De Robertis, L., Bousmina, M., Laroche, G., Roitback, T. et al. (1998). Heterogeneous PHPMA hydrogels for tissue repair and axonal regeneration in the injured spinal cord. *J. Biomater. Sci. Polym. Ed.* 9, 681–711. doi: 10.1163/156856298X00091

Yamato, H., Ohwa, M., and Wernet, W. (1995). Stability of polypyrrole and poly (3, 4 _ ethylenedioxythiophene) for biosensor application. *J. Electroanal. Chem.* 397, 163–170. doi: 10.1016/0022-0728(95)04156-8

Yang, J., Kim, D. H., Hendricks, J. L., Leach, M., Northey, R., and Martin, D. C. (2005). Ordered surfactant-templated poly(3,4-ethylenedioxythiophene) (PEDOT) conducting polymer on microfabricated neural probes. *Acta Biomater.* 1, 125–136. doi: 10.1016/j.actbio.2004.09.006

Zhong, Y., and Bellamkonda, R. V. (2007). Dexamethasone-coated neural probes elicit attenuated inflammatory response and neuronal loss compared to uncoated neural probes. *Brain Res.* 1148, 15–27. doi: 10.1016/j.brainres.2007.02.024

Conflict of Interest Statement: The authors declare that the research was conducted in the absence of any commercial or financial relationships that could be construed as a potential conflict of interest.

Received: 20 February 2014; accepted: 29 March 2014; published online: 16 April 2014.
Citation: Castagnola E, Ansaldo A, Maggiolini E, Ius T, Skrap M, Ricci D and Fadiga L (2014) Smaller, softer, lower-impedance electrodes for human neuroprosthesis: a pragmatic approach. Front. Neuroeng. ***7****:8. doi: 10.3389/fneng.2014.00008*
This article was submitted to the journal Frontiers in Neuroengineering.

frontiers in
NEUROENGINEERING

METHODS ARTICLE
published: 24 July 2013
doi: 10.3389/fneng.2013.00006

A simple implantation method for flexible, multisite microelectrodes into rat brains

Anja Richter[1†], Yijing Xie[2,3†], Anett Schumacher[4], Susanne Löffler[1], Robert D. Kirch[3], Jaafar Al-Hasani[5], Daniel H. Rapoport[5], Charli Kruse[5], Andreas Moser[1], Volker Tronnier[1], Sandra Danner[5] and Ulrich G. Hofmann[3]*

[1] Neurochemistry Group, Department of Neurology, University of Luebeck, Luebeck, Germany
[2] Graduate School for Computing in Medicine and Life Sciences, University of Luebeck, Luebeck, Germany
[3] Neuroelectronic Systems, Department of General Neurosurgery, University Hospital Freiburg, Freiburg, Germany
[4] Department of Psychology, University of Toronto Scarborough, Toronto, ON, Canada
[5] Fraunhofer Institution for Marine Biotechnology, Fraunhofer Society, Lübeck, Germany

Edited by:
Jürgen Krüger, University of Freiburg, Switzerland

Reviewed by:
Anja Kunze, University of California, Los Angeles, USA
Victor Pikov, Huntington Medical Research Institutes, USA

***Correspondence:**
Ulrich G. Hofmann, Neuroelectronic Systems, Department of General Neurosurgery, University Hospital Freiburg, c/o Engesserstr. 4, 5th floor, 79108 Freiburg, Germany
e-mail: ulrich.hofmann@uniklinik-freiburg.de
† *These authors have contributed equally to this work.*

A long term functional and reliable coupling between neural tissue and implanted microelectrodes is the key issue in acquiring neural electrophysiological signals or therapeutically excite neural tissue. The currently often used rigid micro-electrodes are thought to cause a severe foreign body reaction resulting in a thick glial scar and consequently a poor tissue-electrode coupling in the chronic phase. We hypothesize, that this adverse effect might be remedied by probes compliant to the soft brain tissue, i.e., replacing rigid electrodes by flexible ones. Unfortunately, this flexibility comes at the price of a low stiffness, which makes targeted low trauma implantation very challenging. In this study, we demonstrate an adaptable and simple method to implant extremely flexible microprobes even to deep areas of rat's brain. Implantation of flexible probes is achieved by rod supported stereotactic insertion fostered by a hydrogel (2% agarose in PBS) cushion on the exposed skull. We were thus able to implant very flexible micro-probes in 70 rats as deep as the rodent's subthalamic nucleus. This work describes in detail the procedures and steps needed for minimal invasive, but reliable implantation of flexible probes.

Keywords: neuroelectrophysiology, brain, implantation, flexible device, rat, deep brain, microprobes

INTRODUCTION

Electrical stimulation of discrete brain areas is a clinically increasingly used symptomatic treatment for neurological movement and affective disorders (Schlapfer and Bewernick, 2009; Pizzolato and Mandat, 2012). To further improve this treatment, the necessity arises to optimize the brain-device-interface on the cellular scale (Martens et al., 2010). With respect to this goal, pre-clinically often used microprobes for brain stimulation and recording are tethered to the skull (Hiller et al., 2007) and by nature of their rigidity present strong mechanical provocation to the surrounding tissue (Szarowski et al., 2003; Biran et al., 2007; McConnell et al., 2009). Traditionally implantable electrodes are rigid, thus showing no probe deformation during insertion (Campbell et al., 1991; Rousche and Normann, 1992). Furthermore, clinical implantation equipment provides precise location control to access brain areas specifically (Schjetnan and Luczak, 2011). After implantation, however, electrophysiological connection is impaired e.g., due to chronic gliosis, mechanical trauma or long-term inflammation (Turner et al., 1999; Polikov et al., 2005; Leach et al., 2010).

Recently, flexible microprobes have been developed from different polymers to offset this tissue scar formation by better adapting the probe's mechanical properties to the target tissue (Takeuchi et al., 2005; Kozai and Kipke, 2009; Rubehn and Stieglitz, 2010; Lee et al., 2012; Kim et al., 2013). In contrast to rigid ones, flexible implants are supposed to follow intrinsic movements of the brain resulting from breathing, blood circulation, or body movements (Rousche et al., 2001; Mercanzini et al., 2009; Rubehn and Stieglitz, 2010; Andrei et al., 2012). To test the assumption, we needed to stereotactically implant flexible microprobes in brain structures (Williams, 2008; Hassler et al., 2011). However, thin (∼20 μm), film-like Polyimide microprobes are impossible to implant like the well-known rigid shank electrodes, since their inherent flexibility results in a buckling force leading to uncontrolled bending still outside the brain tissue. Instead we developed and present here a supported insertion method with the support removed after reaching the target requiring no change in Polyimide probe design. This method enables the insertion of Polyimide-based, ∼20 μm thick, 350 μm wide and 1.5 cm long electrodes down to the subthalamic nucleus (∼8.5 mm) of rat's brain using commercially available stereotactic equipment (David Kopf Instruments, Model 900).

MATERIALS AND METHODS

See the accompanying video for a visualized version of the protocol. A list of materials required for this procedure can be found in **Table 1**. We strongly recommend to practice this procedure with already euthanized animals from other experiments prior to *in vivo* application. A competent handling of all instruments is strongly recommended to achieve reproducible results.

Table 1 | Specific reagents and equipment required for this approach.

Name of the reagent	Company	Catalog number
Surgical disposable scalpel #21	Braun Aesculap AG	5518075
Surgical disposable scalpel #23	Braun Aesculap AG	5518016
Cotton swabs, walnut sized	Henry Schein Medical GmbH	9003187
5/0 Premilene-DS16 surgical sutures	Braun Aesculap AG	2090212
Leukofix fixing tape	Henry Schein Medical GmbH	220-544
Tungsten rod ø 140 μm	A-M Systems, Inc.	7166
Loctite 4061 rapid glue	Henkel Loctite GmbH	26085
0.9 mm drill bit	FineScienceTools, USA	19007-09
Rechargeable Cordless Micro Drill	Stoelting Co., USA	58610
Small Animal Stereotaxic Instrument	David Kopf Instruments, USA	Model 900
7.5% betaisodona solution	B. Braun Melsungen AG	3864154
Softasept (74.1% Ethanol and 10% 2-Propanol)	B. Braun Melsungen AG	3887138
Agarose, low gelling temperature (<65°C)	Sigma-Aldrich Co.	A9414

Anaesthetics and other medicine according to approved procedures.

PRESURGICAL PREPARATION PROCEDURE

Aseptic technique should be used for all survival surgical procedures. Disinfect the surgical work surface with commercial disinfectant and prepare sterile surgical packs of instruments, drapes, gauze, swabs, sutures, and scalpel blades. A surgical mask, hair bonnet and sterile gloves should be worn. A Germinator dry bead sterilizer is also used to re-sterilize surgical instruments between procedures if multiple rat surgeries will be done during one session. Preparation of the rats including disinfection, anesthesia and positioning in the stereotactic frame was performed according to standardized stereotactic procedures, which were reviewed and approved by committees of the University of Lübeck and the responsible Ministry for Agriculture, Environment and Rural Areas, Schleswig-Holstein, Germany.

Adult, male Wistar rats (250–300 g) were anesthetized using an i.p. injection of a Ketamine/Xylazine cocktail [100 mg/kg Ketamine (100 mg/ml), 8 mg/kg Xylazine (2%)]. This amount is generally sufficient for a typical 60 min surgery. If needed, rats can be redosed using a fraction of the original dose. Disinfectant (Softasept) was applied to the scalp starting from the center of the surgical region, spiraling outward and then rinsed with Ringer's solution. The surgical field was prepared by shaving the area using small animal shears. Protective ointment (Bepanthene® nose and eye cream) was applied to the eyes to prevent drying and to provide a physical barrier during surgery. Anesthetized and shaved rats were placed in a stereotactic frame with atraumatic ear bars (tooth bar = 0.0)[1].

As an insertion tool we clamped a tungsten rod (ø140–175 μm) to the head of a stereotactic arm. The length of the tungsten rod below the clamp head should be ∼2 cm to provide sufficient space for manipulations. The rod must be perfectly straight, as can be tested by rolling it on a flat ground.

SKIN INCISION AND PREPARATION OF SUBCUTANEOUS TISSUE TO EXPOSE SKULL

A midline incision of ∼1.5 cm length starting between the ears (bregma) and extending toward the nose was made with a scalpel. The subcutaneous tissue was prepared bluntly with two cotton swabs by vigorous but slow rubbing from the center to the periphery of the wound. This stretches the cutaneous and subcutaneous tissues and opens the operation area above the skull. It has to be performed until the necessary operation area is free of all tissues above the skull bone and bleeding has stopped. A well prepared skull is indicated by a typical squeaking sound when rubbing the swab on the bone.

WIDENING OF THE SURGICAL FIELD

A wide, flat operation area is essential for successful implantation. Wound rims were fixed using surgical suture loops (5/0 Premilene-DS16). Loop ends are fixed at the frame with a non-residue tape (Leukofix) while carefully pulling the wound boundaries apart and thus widening the surgical area. That way the desired anatomical orientation points become visible, in our case lambda and the interaural line. We strongly recommend folding the skin on the rostral end by a double stitch which lessens traumatization. If necessary such a loop can be used to fix the caudal end of the wound rim as well.

ADJUSTMENT OF THE STEREOTACTIC FRAME AND TARGETING

The wound area was washed with Ringer's solution and cleaned with walnut sized cotton swabs prior to targeting. The stereotactic arm is positioned such that the securely mounted insertion tool was moved to the anatomical reference point of choice (lambda in our case). The target coordinates were determined according to the medial:lateral and anterior:posterior axes found in a stereotactic atlas. The insertion arm of the stereotactic frame was positioned over the target point and the tungsten rod was carefully lowered until it touched the skull. The z-position was noted and the target depth was calculated[1].

TREPANNING THE SKULL

First, the target point was marked on the skull by careful circular nicking the bone with a 20 G needle below the tungsten rod. The produced cavity is used as starting point for drilling—otherwise the skull may be too slippery for precise drilling. When

[1]One of the reviewers recommends for improved animal welfare the following steps in addition to the demonstrated ones:

(a) Before securing ears in earbars, apply Antipyrine-Benzocaine otic solution to ears.

(b) For monitoring depth of anesthesia and overall animal health, it is helpful to insert rectal thermometer probe.

(c) Removal of subcutaneous tissue can be done more effectively by cutting the muscle with the scalpel and scraping periosteum with a Freer chisel while controlling the skull bleeding with bone wax.

(d) After drilling the skull and before puncturing the meninges, it is suggested to apply Sensorcaine (bupivacaine with epinephrine) to the cortex to produce local anesthesia and vasospasms (to reduce cortical bleeding).

not needed *in situ*, the stereotactic arm was moved out of harms way to carefully maintain insertion rod registration.

A handheld microdrill with a small drill bit (here 0.9 mm ø) was then used to make the burr hole. Drilling was done in short intervals (depending upon the power output of the drill) and drill progress was controlled visually in between. The complete penetration of the skull bone is clearly noticeable by a sudden loss in resistance to the drill bit. Carefully remove it from the drill site and flush all bone fragments with Ringer's solution. Lesser experienced surgeons may want to use a stop above the drill tip by slipping a cylinder, cut from a medical tubing, over the drill. For the price of a slightly diminished view, the drill won't penetrate deeper than the catch allows and thus minimizes uncontrolled brain penetration (Pohl et al., 2011).

PENETRATION OF THE MENINGES

A successful drilling procedure will leave meninges intact, shimmering opaque at the base of the burr hole. Removing them in a controlled way was done with a slightly nicked 23 G cannula tip. Twisting the cannula's now ridgy tip on the base of the hole and pulling it produces a noticeable rupture of the elastic dura mater. Severing the pia mater results in bleeding, which has to be flushed away until it stops. The repetition of this step along the boundary of the hole may be necessary until no more elastic resistance exists. If successfully performed, this step leaves no opaque meninges remaining in the burr hole. This part of the procedure may impair recordings from superficial layers of the cortex.

INTRODUCING AN AGAROSE BLOCK INTO THE OPERATION AREA

All of the steps up until this point are standard for any type of stereotactic intervention in a rat's brain. Next, we introduced a novel tool to facilitate implantation of flexible microprobes. A block of 2 mm height from 2% (w/v) agarose gel was placed over the burr hole on the skull with a sterile spatula. One edge of the block was lodged under the anterior wound fold with close contact to the anterior borders. The posterior part of the gel block extended over the caudal wound boundaries thus increasing the working area. This afforded a slight slope down to the anterior edge of the wound, which facilitated the subsequent microprobe insertion. The airspace between the agar block and the skull was filled by injecting Ringer's solution, which released trapped air bubbles from beneath the surface of the gel block. Ringer's solution was also used to maintain a moist and slippery working surface.

Using this agarose gel block improves the positioning of the flexible probes, keeps the exposed brain surface moist, and avoids scratching the probe's surface on skull bone. In addition, the 2% agarose gel block facilitates close wrapping of the probe around the insertion rod. To estimate the effects of using 2% agarose gel in probe insertion, we performed a dummy insertion experiment in a brain-tissue-like phantom (**Figures 1A,B**). **Figures 1C,D**. demonstrate the difference of implantation channel width without and with 2% agarose block in a brain phantom (Chen et al., 2004).

POSITIONING OF THE IMPLANT AND INSERTION START

The flexible microprobe was transferred with a pair of tweezers from its sterile storage onto the gel block, as precise and flat as possible, with the tip positioned 5–6 mm past the insertion site. The stereotactically mounted insertion rod was again positioned above the target point (**Figure 2A1**). As soon as the tungsten rod is inserted, it pushes the probe into the burr hole (**Figures 2A2–A4**). The flexible microprobe aligns itself along the rod, thus minimizing cross-section and trauma upon insertion into brain tissue (**Figures 2A5,A6**). To visualize and evaluate the insertion procedure, we showed here in **Figure 2B** a sequence of side-view images of probe insertion with a tungsten rod into a translucent brain-tissue-like phantom.

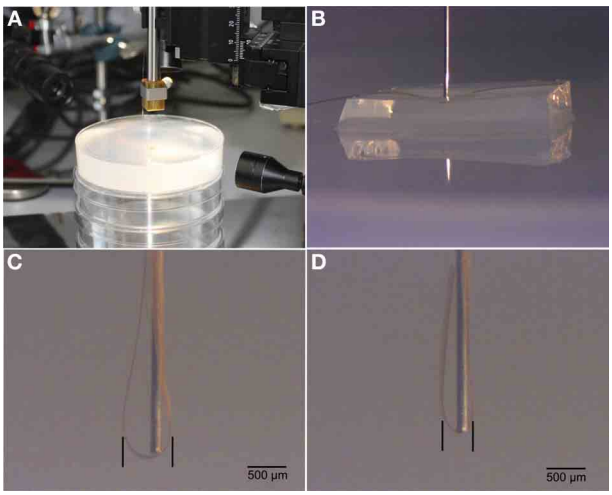

FIGURE 1 | Illustrations of test insertions of flexible probes into a brain phantom. (A). Experimental setup including 2% agarose gel. **(B)**. Micrograph of insertion rod on top of flex probe and agarose cushion. **(C)**. Insertion result in brain phantom without agarose cushion. **(D)**. Insertion result with agarose cushion. Note the difference of spread of flex probe around the implantation rod.

The transparent agarose block allowed for visual control of the relative alignment of the microprobe and the insertion rod. The diffraction at the gel/air boundary may give the appearance of missing the burr hole, which is a known optical illusion. Additional Ringer's solution applied to the gel block minimizes friction, which is essential for maintaining mobility of the microprobe during the insertion procedure. Additional bleedings upon insertion is usually a result of an incomplete disruption of the pia mater and thus must be avoided with proper preparation of the entry hole. Finally, the microprobe was partially inserted by advancing the insertion rod until a desired length of the microprobe remained outside of the skull.

REMOVAL OF THE AGAROSE BLOCK AND INSERTION FINISHING

The part of the agarose gel anterior to the insertion rod was cut parallel to the interaural line using a scalpel. The anterior gel block can now be removed by shoving it away from the insertion rod. The microprobe's connector pad, meanwhile, was very gently flipped toward the tungsten rod and thus moved out of harm's way. Subsequently, the posterior triangle of the gel is shoved out of the wound area. Manipulation of agarose gel was accomplished with a sharp scalpel tip, as it is too slippery for forceps, but easily pinned down by the blade. After the agarose block had been

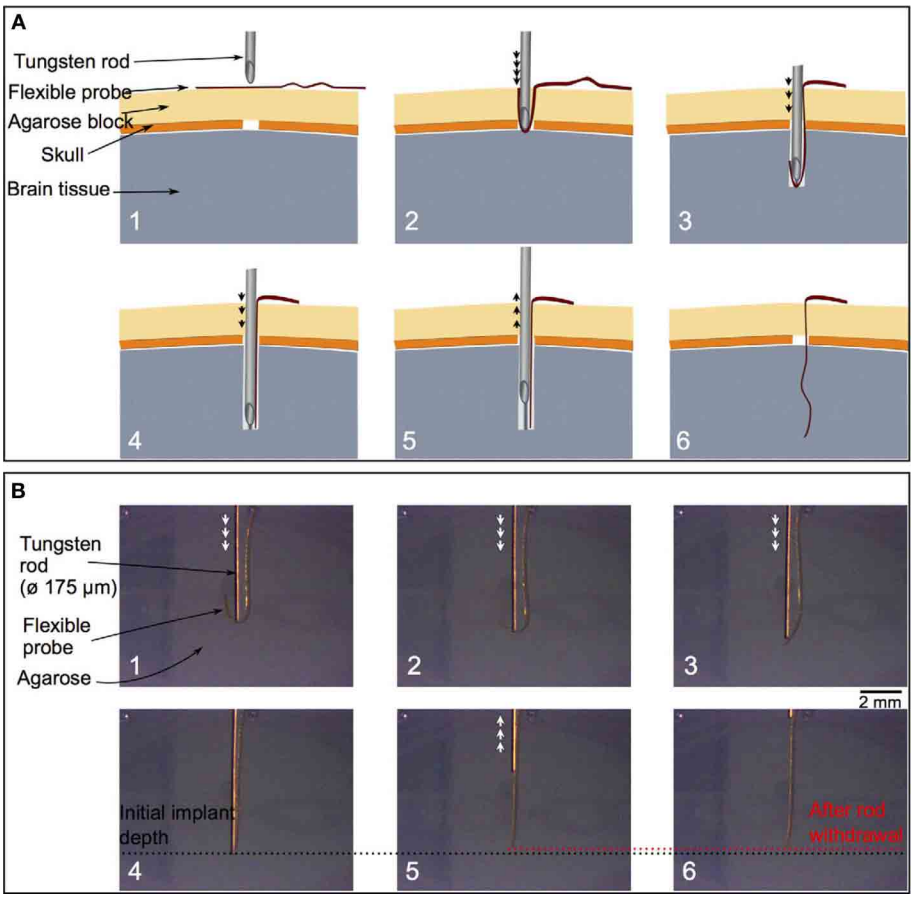

FIGURE 2 | A schematic cross-section of the insertion field (A). The arrows indicate the tungsten rod movement direction. Above the brain tissue (gray) the skull and meningeal layer (dark orange) display a burr hole (white space). The tailored agarose cushion (light orange) is used as an insertion matrix for the flexible probe (red) (A: 1). Advancing the insertion tungsten rod (upper grey structure) along the planned trajectory the probe wraps around the rod's tip and is thus arranged by the gel for optimal control (A: 2–4). After the flexible probe is completely straightened, the insertion rod is withdrawn slowly from the remaining probe (A: 5, 6). Image sequence of inserting a flexible probe with a tungsten rod (with flat tip, ø 175 µm) to a 0.5 % agarose gel **(B)**. The arrows indicate the tungsten rod movement direction. During the insertion, the flexible probe first folds and wraps around the rod (B: 1–3). Until it reaches the planned depth position (the black dotted line) and cis ompletely straightened, the insertion rod is withdrawn (B: 4, 6). The red dotted line in panels B5 and B6 indicates the depth position of the flexible probe tip after the rod is removed. It illustrates a misplacement of around 100 µm from the initial depth position.

removed completely, the microprobe insertion was finalized until the desired target depth was reached.

MOUNTING OF THE IMPLANT

Remaining Ringer's solution was removed and the skull thoroughly dried using cotton swabs. The microprobe was fixed to the skull using a small spot of medical super glue (Loctite) deposited at least 5 mm posterior to the burr hole. The connector pad was pushed down into the glue using a scalpel tip. Forceps are not recommended here, since the glue may rapidly fix their arms shut, which will destroy the entire implantation upon the ensuing struggle to free them. A scalpel, however, easily cuts itself free through gentle twisting.

The connector pad was covered with another drop of glue and upon solidifying, the tungsten rod was removed from the brain by smooth and continuous upward movements. The entire area is flushed clean with Ringer's solution, which polymerizes all leftover super glue. A pair of forceps were used to carefully scrape all inadvertently fixed connective tissue free.

The wound closure may be performed according to the experimental needs. In our histological study we sutured the skin over the implantation site, cleaned the suture with Ringer's solution and applied iodide disinfectant and local anesthetic. The animal was monitored and kept warm on a temperature controlled plate until it was fully awake.

RESULTS

The most significant result of this method is the successful implantation of very flexible, film-like microprobes into deep brain regions with minimal tissue disruption. Cross-sectional histology demonstrated that we reliably reached our target point deep in the brain of rats.

One week after surgery we observed in the implanted rats the inevitable lesion caused by the insertion needle next to the

implant (**Figure 3**). The tissue reaction was evident from a thin glial layer homogeneously surrounding the implantation lesion. A clear, but thin brain-probe-interface without cysts is indicative for a good connectivity to the target area adjacent to the implant. After four weeks a cyst-free tissue next to the implantation-site was visible (the central free space is the original position of the implant, moved upon slicing), indicating a good mechanical connectivity of the implant to the target area (**Figure 4**).

High precision and successful implantation was corroborated by recording electrophysiological signals from neuronal tissue adjacent to the target area (subthalamic nucleus) immediately following implantation (**Figure 5**) and four weeks post-surgery with flex probes of slightly different design. Detailed histological data will be published elsewhere. Seventy animals have undergone this procedure to date and all of them survived without incident until the planned euthanasia six months following surgery.

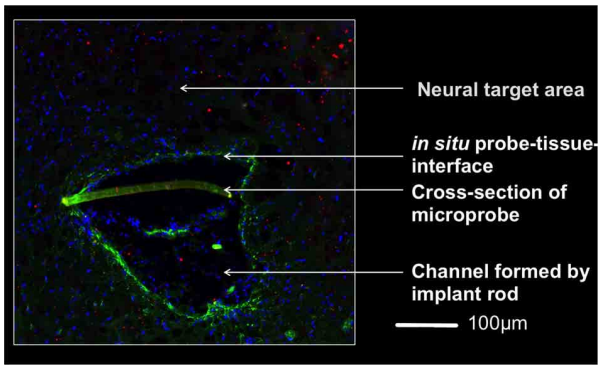

FIGURE 3 | Micrograph of the implantation area one week after implantation 4,5 mm below the brain surface. The rod supported insertion of the microprobe yields an implantation channel on one side of the slightly crescent-shaped probe (350 µm wide). Invading cells to this region are indicated by stained nuclei (DAPI, blue). A thin glial layer (glial fibrillary acidic protein, green) surrounds the lesion and reflects a mild tissue reaction. The lack of a pronounced extracellular matrix layer (chondroitinsulfate proteoglycan, red) supports this observation. The brain-probe-interface showed no cysts. Magnification 20x with an PlanApochromat-Objective at AxioObserver Z.1 (Carl Zeiss MicroImaging GmbH, Germany).

FIGURE 4 | Microprobe cross-section (crescent-shaped strip) in an horizontal slice of the subthalamic nucleus of an implanted rat 4 weeks after surgery. This micrograph combines fluorescence and bright-field illumination, where nuclei (blue) are stained with DAPI. Magnification 10x with an PlanApochromat-Objective using an AxioObserver Z.1 (Carl Zeiss MicroImaging GmbH, Germany).

DISCUSSION

Although the hypothesis on the beneficial effect of the probe's elasticity matching the brain's was mentioned more than a decade ago (Stieglitz and Meyer, 1999), all efforts to use flexible probes on a large scale were less efficient due to the difficulty to implant them in a reliable way in deeper brain regions (Rousche et al., 2001; Kozai and Kipke, 2009). We thus started with an established procedure for implantation of rigid electrodes and modified it to our needs. The animals implanted with our technique all survived the implantation without exception. No abnormalities of movements and/or behavior were developed post operatively. Histological examination confirmed the positioning of the implant in the target area with minimal tissue disruption. To ensure reproducibility and best possible use of limited time under anesthesia, we strongly recommend to exercise this procedure with agarose dummies or dead animals before starting on living ones. There are several finely tuned handling steps, which require sensitive use of instruments, microprobe and surgical technique. A well experienced experimenter will need less than one hour for the entire procedure, for which the initial dose of Ketamine/Xylazine-cocktail may not quite suffice. Deep anesthesia has to be maintained at all times by re-injecting fractions of the initial dose.

The extremely cautious use of the miniature power drill and the subsequent removal of the meninges is essential for exerting minimal tissue damage. An automatized drill system may reduce the risk of severe brain trauma (Pohl et al., 2012).

However, in our view the highest optimization potential remaining is the design of the insertion tool/microprobe connection. This study was based on temporarily fixating both by dynamic forces, a removable anchoring of the probe to the insertion tool might improve positioning even further as was

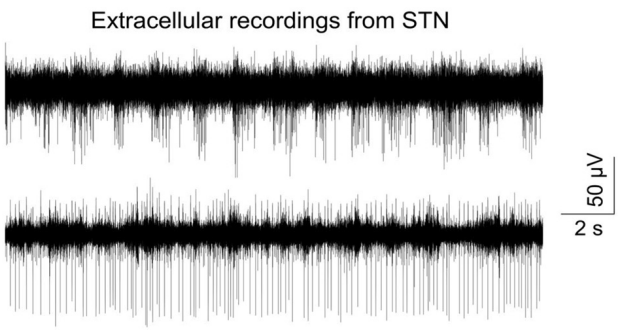

FIGURE 5 | Typical signal trace recorded from the subthalamic nucleus right after insertion of a flexible microprobe; bandpass filtered (400–4000 kHz) and sampled with 24414 kHz. Recording was done with an electrical connected flexible microprobe as described in Löffler et al. (2012).

frontiers in
NEUROENGINEERING

ORIGINAL RESEARCH ARTICLE
published: 29 April 2014
doi: 10.3389/fneng.2014.00010

The sinusoidal probe: a new approach to improve electrode longevity

Harbaljit S. Sohal[1,2], Andrew Jackson[1], Richard Jackson[2], Gavin J. Clowry[1], Konstantin Vassilevski[2], Anthony O'Neill[2] and Stuart N. Baker[1]*

[1] *Newcastle Movement Lab, Institute of Neuroscience, Newcastle University, Newcastle Upon Tyne, UK*
[2] *School of Electrical and Electronic Engineering, Newcastle University, Newcastle Upon Tyne, UK*

Edited by:
Ulrich G. Hofmann, Albert-Ludwigs-University Freiburg, Germany

Reviewed by:
Liang Guo, The Ohio State University, USA
Maria Asplund, Albert-Ludwigs Universität, Freiburg, Germany

***Correspondence:**
Stuart N. Baker, Newcastle Movement Lab, Institute of Neuroscience, Newcastle University, Framlington Place, Newcastle Upon Tyne NE2 4HH, UK
e-mail: stuart.baker@newcastle.ac.uk

Micromotion between the brain and implanted electrodes is a major contributor to the failure of invasive brain–machine interfaces. Movements of the electrode tip cause recording instabilities while spike amplitudes decline over the weeks/months post-implantation due to glial cell activation caused by sustained mechanical trauma. We have designed a sinusoidal probe in order to reduce movement of the recording tip relative to the surrounding neural tissue. The probe was microfabricated from flexible materials and incorporated a sinusoidal shaft to minimize tethering forces and a 3D spheroid tip to anchor the recording site within the brain. Compared to standard microwire electrodes, the signal-to-noise ratio and local field potential power of sinusoidal probe recordings from rabbits was more stable across recording periods up to 678 days. Histological quantification of microglia and astrocytes showed reduced neuronal tissue damage especially for the tip region between 6 and 24 months post-implantation. We suggest that the micromotion-reducing measures incorporated into our design, at least partially, decreased the magnitude of gliosis, resulting in enhanced longevity of recording.

Keywords: flexible, microelectrode, chronic, electrophysiology, gliosis, long term, electrode

INTRODUCTION

Brain–machine-interface (BMIs) decode motor information from cortical activity, providing control of computers, assistive devices or functional electrical stimulation to restore function after paralysis (Nicolelis, 2001; Taylor et al., 2002; Schwartz, 2004; Hochberg et al., 2006, 2012; Bartels et al., 2008; Zimmermann et al., 2011; Collinger et al., 2012). Invasive BMIs use intracortical microelectrodes to record from neurons in close proximity (∼100–150 μm) to the recording tip (Biran et al., 2005, 2007; Polikov et al., 2005; Perge et al., 2013). Unfortunately, sustained immune activation caused by the foreign body response with time leads to neuronal loss around microelectrodes (Polikov et al., 2005). Furthermore, immune mediators such as astrocytes and microglia ensheath electrode recording sites, isolating the electrode from surrounding brain tissue and releasing detrimental immune factors that compromise neuronal function (Biran et al., 2005; Polikov et al., 2005; Winslow et al., 2010; Winslow and Tresco, 2010; Collinger et al., 2012). These mechanisms cause instabilities in the recordings obtained from both microwire and silicon probes (Jackson and Fetz, 2007; Dickey et al., 2009) and can lead to device failure within weeks or months after chronic implantation (Polikov et al., 2005; Ward et al., 2009; Collinger et al., 2012).

An important contributor to the sustained tissue response is the modulus mismatch between the brain and implanted microelectrodes (Kozai and Kipke, 2009). Typical electrode materials include silicon (e.g., the "Utah" array, Rousche and Normann, 1998 and "Michigan" probe, Kipke et al., 2003) and metal microwires (Nicolelis et al., 2003; Jackson and Fetz, 2007) which have a higher Young's modulus (YM, ∼150 GPa) than brain tissue (5–30 KPa; Miller et al., 2000; Potter et al., 2012). This mismatch means microelectrodes anchored to the skull cannot accommodate movement of the brain within the cranial cavity (Biran et al., 2007; Thelin et al., 2011). Even if electrodes are designed to float with the brain, deformation of the tissue will change the position of deep neurons relative to an anchoring point at the brain surface (Biran et al., 2005; LaPlaca et al., 2005; Subbaroyan et al., 2005; Gilletti and Muthuswamy, 2006; Kozai and Kipke, 2009; Yoshida Kozai et al., 2012; Hwang and Andersen, 2013; Kim et al., 2013). Damage caused by electrode movement relative to surrounding tissue will be exacerbated by the sharp tip profiles typically used to aid insertion. The amount of damage around the tips can be estimated through cell loss over time for current electrode arrays. For the Utah array, 61% of cells that were recorded on the first recording session were lost after 2 weeks (Dickey et al., 2009). Similar neuronal loss has been shown for microwire electrodes (Nicolelis et al., 2003; Jackson and Fetz, 2007). Microelectrodes can record between 100 and 150 μm away from their recording sites (Polikov et al., 2005; Seymour et al., 2011). For a single electrode shank, this equates to a 6750 mm^3 (150 × 150 × 300 μm) volume around the electrode. For the human brain there are an estimated 6.66×10^4 neurons per mm^3 (Allen et al., 2005; Azevedo et al., 2009; Marblestone et al., 2013). Through extrapolation, if an estimated 61% of cells are lost for every two weeks of recording, then just a solitary cell will remain after ∼40 weeks post-implant around a single shank, assuming the electrode can record from every cell in that given brain volume and neurons are lost linearly over time.

Micromotion can be reduced using flexible materials (Polikov et al., 2005; Kozai and Kipke, 2009; Harris et al., 2011) or by decreasing the overall footprint of the microelectrode (Yoshida Kozai et al., 2012; Suyatin et al., 2013). Flexible arrays require specialized insertion techniques to penetrate the dura or pia. Proposed methods include temporary stiffening with biodegradable solutions (Chorover and DeLuca, 1972; Kohler et al., 2009; Witteveen et al., 2010; Hassler et al., 2011) or soluble polymers such as polyethylene glycol (PEG; Takeuchi et al., 2004) prior to insertion. Some flexible arrays have sharp anchoring structures to restrict further the movement of the recording site relative to the surrounding neuronal tissue (Kohler et al., 2009; Wu et al., 2011). Nevertheless, while flexible materials can bend to shorten the distance between the anchoring point and the tip, a straight electrode, no matter how flexible, cannot accommodate deformations of the brain that increase this distance.

All current chronic electrode designs, which have evolved from the straight shafts traditionally used for acute recording share this fundamental limitation. We propose a simple yet radical solution: a novel flexible electrode which is not straight and can therefore lengthen and shorten to accommodate brain deformations. Specifically, we designed an electrode shaft with a sinusoidal profile mechanically to decouple the recording site from the fixed end of the electrode. Moreover, we incorporated a spherical tip to anchor the recording sites relative to the surrounding tissue and minimize damage. The novel electrode was microfabricated and tested *in vivo* over a 6–24 month period in rabbits. The electrode was compared to conventional rigid microwires of the same recording tip diameter. Microwires were chosen as a comparison as they have been well characterized in many species in chronic studies (Nicolelis et al., 2003; Jackson and Fetz, 2007; Winslow et al., 2010) and have reduced gliosis responses compared to standard silicon probes (Winslow et al., 2010; Yoshida Kozai et al., 2012).

The electrophysiological recordings and post-mortem characterization of the tissue response compared to conventional microwires suggest that the novel design features incorporated in our sinusoidal electrode may improve the long-term stability of recordings for BMI applications.

MATERIALS AND METHODS

SINUSOIDAL PROBE: DESIGN AND MICROFABRICATION

The probe consisted of three W/Ti (80/20 wt %) recording sites encased in parylene-C. Tungsten is a good recording metal (Hubel, 1959). However, with a YM of 400 GPa, it is not flexible compared to other metals (Geddes and Roeder, 2003). Therefore, tungsten was sintered with titanium to increase flexibility, resulting in a YM of ∼200 GPa. Parylene-C was chosen as it is biocompatible, flexible, and a FDA-approved dielectric for biomedical applications (Seymour and Kipke, 2006; Kozai et al., 2010; Winslow et al., 2010; Yoshida Kozai et al., 2012).

The recording end of the electrode was a parylene disk of 100 μm diameter, with three protruding, exposed recording sites to aid single-unit isolation (Gray et al., 1995). Three metal tracks ran within an electrode shaft that was 20 μm deep, 35 μm wide and had a sinusoidal profile with cycles of 100 μm amplitude and 500 μm period. We report data from two design iterations, which differed in length and how connection to the electrode was made. The first generation electrode was 5.5 mm in length and had a bondpad (approximately 400 μm^2) at the end of the sinusoidal shaft, to which individual wires were attached. The second generation electrode was 3 mm in length (**Figure 1G**) and incorporated an integrated ribbon cable (3 cm long and 3 mm wide) leading to a standard connector (micro ps1/ps2 series, Omnetics Connector Corporation, USA).

Fabrication began with a three-inch silicon wafer (Compart, UK) onto which a 1 μm aluminum sacrificial layer was e-beam deposited (BOC-Edwards auto ebeam evaporator, UK) to increase adhesion between the first polymeric layer during the fabrication process and aid device release (**Figure 1A**). The first layer of parylene-C was deposited with a thickness up to 10 μm, through a chemical vapor deposition process (CVD; **Figure 1B**). Next, a 1 μm WTi layer (80/20 wt%) was magnetron sputter deposited (Kurt J. Lesker PVD 75 vacuum deposition, USA) with a power setting of 100 W (**Figure 1C**). After masking with AZ-5214e photoresist (HD microchemical, Germany), the metal layer was patterned with SF_6 reactive ion etch (RIE; Plasma-Therm 790, USA) using parameters of 200 W, 150 mTorr, and 10 sccm flow rate to define the overall electrode tracks, bondpad and recording site regions (**Figure 1C**). A slight over-etch was employed to surface roughen the first parylene-C layer to aid adhesion of the second layer, again deposited through CVD (**Figure 1D**). Subsequently both parylene-C layers were patterned using oxygen RIE (Plasma-Therm 790, USA) with parameters of 200 W, 50 mTorr, and 18 sccm flow rate to form the overall electrode shape and to re-open recording site/bond pad regions (**Figure 1E**). A 40 nm thick titanium mask was e-beamed deposited and patterned (Kurt J. Lesker PVD 75 vacuum deposition) for this process. Exposed WTi was unaffected by parylene-C oxygen RIE. Finally, the electrodes were released from the silicon substrate by etching the aluminum sacrificial layer using 3% tetramethylammonia hydroxide (TMAH) as found in AZ-326 MIF photoresist developer (HD MicroChemicals, Germany; **Figures 1E,H**). Post-release (**Figure 1F**), the recording end had three clearly isolated electrode recording sites (**Figure 1I**).

Connectors were attached to the bondpad region using conductive paint (RS Components, UK) and insulated with two-part epoxy (Araldite: Farnell, UK). A polyimide ball was added by dipping the recording end first in VM 652 adhesion promoter (HD Microchemicals, Germany) and then in PI-5878G (HD Microchemicals, Germany) forming a small sphere around the electrode tip. The added sphere had a diameter of less than 100 μm as confirmed through optical microscopy during fabrication and further confirmed through post-hoc histology via the implantation site size. The polyimide was soft-baked at 120°C for 30 min in a convection oven. To re-open the covered recording sites, the electrode tip was dipped into TMAH for a few seconds. Electrode tip exposure was confirmed by tip impedances (at 1 kHz in saline) comparable to pre-polyimide application.

To aid insertion in to the brain, we used carriers made from 0.229 mm diameter sharpened stainless steel electrodes (Microprobe INC., USA) emerging from 25 g hypodermic needles

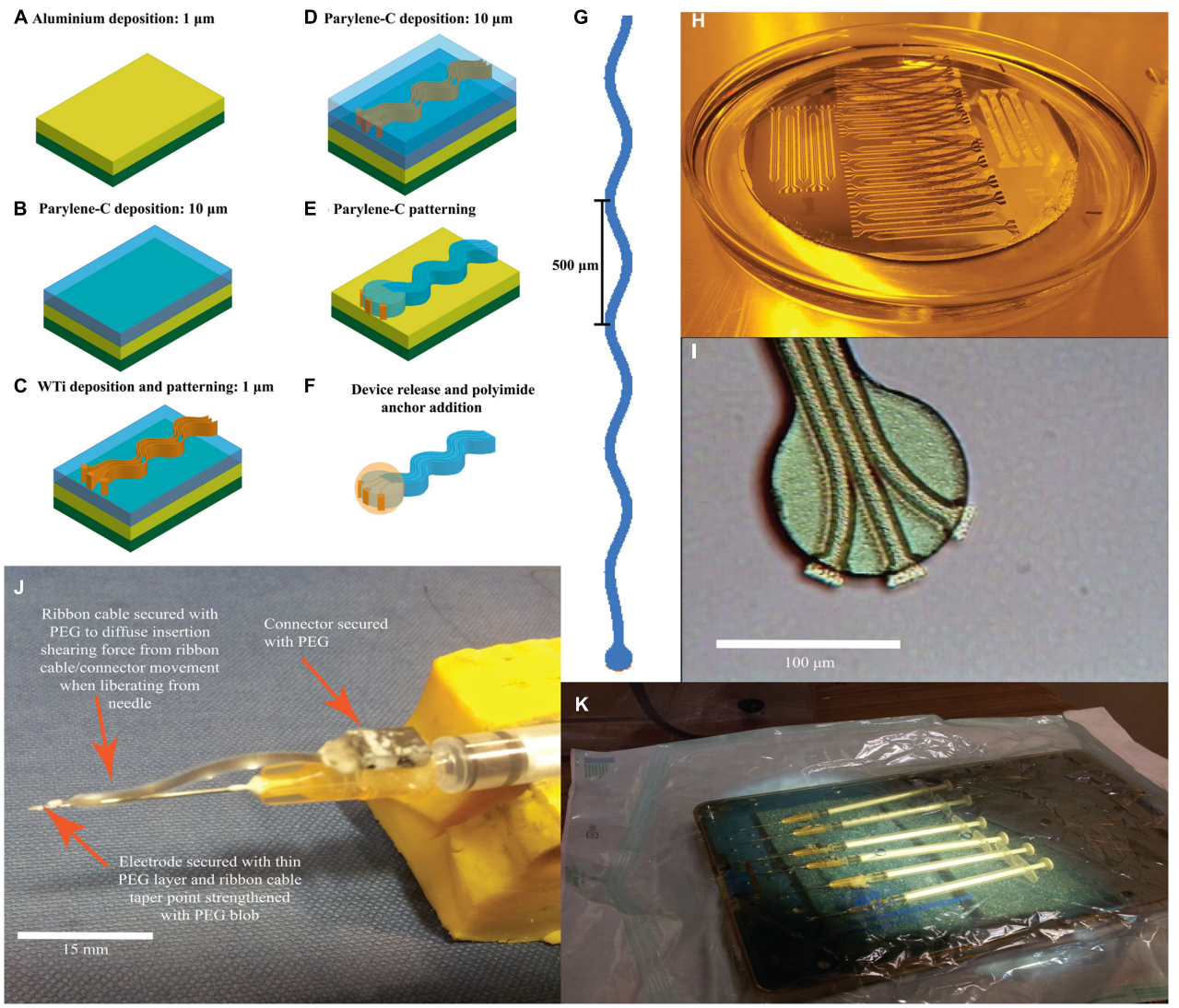

FIGURE 1 | Sinusoidal probe microfabrication and surgery preparation. **(A–F)** Sequential microfabrication steps for the sinusoidal probe concentrating on the recording end (illustrative and not to scale): **(A)** 1 μm aluminum ebeam deposition as a sacrificial layer on a silicon substrate. **(B)** Parylene-C deposition through a CVD process. **(C)** WTi sputter deposition and patterning to define electrode tracks, bondpad and recording site regions. **(D)** Second layer parylene-C deposition through CVD. **(E)** Patterning of both parylene-C layers using oxygen plasma. **(F)** Device release using a TMAH based photoresist developer and addition of 3D polyimide ball anchor. **(G)** Mask layout for the 3 mm version of the probe. Three metal tracks ran within an electrode shaft that was 20 μm deep, 35 μm wide and had a sinusoidal profile with cycles of 100 μm amplitude and 500 μm period. **(H)** Successful device release in TMAH. **(I)** Optical microscopy image of the recording end showing three separate and isolated electrode recording sites, pre-polyimide anchor addition. The protruding electrode recording sites may appear thicker due to the underlying first parylene-C layer, which is not removed during WTi etching. **(J)** Attached sinusoidal probe to improvised insertion carrier to allow for successful brain penetration and electrode insertion. **(K)** Electrodes under sterile conditions, placed in an autoclaved container and then into surgical bag primed for UV light sterilization.

(**Figure 1J**). Electrodes and carriers were cleaned with ethanol before being attached with PEG and sterilized with ultra-violet irradiation (**Figure 1K**).

ANIMALS AND SURGICAL PROCEDURES

All experiments were approved by the local ethics committee at Newcastle University and were performed under appropriate Home Office licenses in accordance with the UK Animals (Scientific Procedures) Act 1986. Electrodes were implanted into the sensorimotor representation of five New Zealand white rabbits (*Oryctolagus cuniculus*; Subjects R, J, N, L, Lo). After a midline skin incision and burr-hole craniotomies, electrodes were inserted stereotaxically at coordinates relative to bregma of 4 mm anterior to 4 mm posterior and 0.5 to 7 mm lateral (Gould, 1986; Swadlow, 1989, 1990, 1994; Swadlow and Hicks, 1996). Electrodes were inserted quickly (Bjornsson et al., 2006) using the stereotaxic manipulator. The PEG was dissolved with warm saline to release the electrode from the carrier, which was subsequently removed. Microwire electrodes (50 μm diameter Teflon-insulated tungsten) were inserted manually with surgical forceps. Connectors were

attached to the skull with skull screws and dental cement. A wire wrapped around one skull screw served as ground and reference for the recordings. In this study, 4–5 sinusoidal electrodes were inserted per animal for both the first generation (Rabbit N, L) and second generation (Rabbit- R, J, Lo). Between 2 and 4 microwire electrodes were also inserted for comparison in each animal.

ELECTROPHYSIOLOGY DATA ACQUISITION

Tri-weekly recording sessions began one week post-surgery. Animals were individually placed in a custom-made restraining box while neuronal activity was amplified (10× MPA8I headstage followed by 1000× PGA1632 amplifier; Multichannel systems, Germany) and recorded (Power 1401, Cambridge Electronic Design, UK). Spike channels were filtered between 0.3 and 8 kHz and sampled at 25 kHz while local field potentials (LFP) were filtered between 1 and 300 Hz and sampled at 1 kHz.

CHRONIC RECORDING PERFORMANCE EVALUATION

In this study, statistical comparisons combined data across all electrodes of the same type implanted in each animal.

We analyzed LFP, spike activity and high voltage spindle responses (HVS) from both sinusoidal and microwire electrodes. The HVS activity is characterized by highly synchronous spike and wave patterns, typically only seen when the animal remains motionless with eyes open (Buzsáki et al., 1988).

All analysis was performed within the Matlab environment (version 2009a, MathWorks, USA). LFP power spectra for each electrode were constructed using a fast-Fourier transform and the spectrum was divided into distinct bands. The mean power in each band was calculated for each session across the chronic recording period.

For HVS responses and spiking, principle component analysis spike sorting was performed with custom written software GetSpike. This enabled spikes to be sorted by initial thresholding and cluster cutting with times recorded. Accepted waveforms consisted of sections five sampling points before and 15 after the threshold crossing. The mean peak-to-peak amplitude, noise and signal-to-noise ratio (SNR) were evaluated daily across the chronic period. The SNR was calculated in accordance to Suner et al. (2005). For the signal, the peak-to-peak amplitude (A) of the mean waveform was calculated. For the noise, the mean waveform was subtracted from all waveforms, with the standard deviation calculated from the resulting values. Noise was then calculated as 2× the average standard deviation (ε). SNR was then calculated as A/ε. For statistical analysis to compare recorded responses, percentile-bootstrapping was used because of unequal sample sizes: each sinusoidal probe had three recording sites compared to one microwire recording site. Spike events from the full dataset were drawn randomly (with replacement) to create surrogate datasets with the same number of events as the real data, but distributed evenly between sinusoidal and microwire electrodes. This procedure was repeated 10000 times to estimate the expected difference in each measure under the null hypothesis of no difference between electrode types. The null hypothesis was rejected if the observed difference fell outside the 2.5–97.5% percentile range of the bootstrapped distribution.

HISTOLOGY ANALYSIS

Post-mortem histology was used to assess tissue response to implanted electrodes. After anesthesia was induced with hypnorm (0.3 ml/kg i.m.) and midazolam (2 mg/kg i.v.), animals were perfused transcardially with phosphate buffered saline (PBS) and then formal saline (10%). The relevant brain regions were removed and transferred to incrementally increasing sucrose solutions (10–30%) for cryoprotection before cutting into 50 μm sections perpendicular to the electrode tracks.

The tissue was stained for microglia, astrocytes, and neurofilament. Slices were incubated with 3% normal horse serum (Vector Labs, UK: S-2000) to prevent non-specific binding, and incubated overnight with relevant concentrations of the primary antibodies GFAP (1:500, Sigma-Aldrich, UK), isolectin-b4 [1:200, Vector Labs, UK: Biotinylated Griffonia (Bandeiraea) Simplicifolia Lectin 1] and where appropriate, SMI-32 (1:1000, Cambridge Biosciences, UK: R-500) diluted in PBS at 4°C. GFAP and Neurofilament slices underwent incubation with biotinylated antimouse for 2 h. All slices were then incubated with horseradish peroxide streptavidin (Vector Labs, UK: SA-5004) for 1 h.

Finally, the diaminobenzidine (DAB) reaction was performed (Sigma–Aldrich, UK). Slices were incubated with DAB and placed in PBS after the reaction. Slices were dehydrated in an ascending alcohol series (5 min of 70, 95, 100, and 100% ethanol) and 2, 10 min histoclear washes (Sigma-Aldrich, UK), before cover slips were mounted with histomount (Sigma-Aldrich, UK).

Images were taken at 10× magnification at a pre-saturation exposure time dependent on the staining using axiovision software (Carl Zeiss Microimaging, Germany) before normalization using custom Matlab software. Background levels were assessed from tissue at least 1 mm away from the electrode implantation site, and subtracted from electrode tract images to leave the glial response around electrodes which was inverted (using the "imcomplement" function on Matlab) and normalized by the background level. Images were imported into ImageJ64 software (NIH, USA) to determine the radial distribution of staining intensity around electrode tracks. This analysis was carried out on all sections stained for microglia, astrocytes and where appropriate neurofilament. To compare the overall differences between sinusoidal and microwire electrodes, the mean of at least 15 tracks were compared between each electrode type.

Graphs were plotted of mean intensity as a function of radial distance from each electrodes type. Paired *t*-tests were performed for distances between 50 and 500 μm away, with a significance level of $P < 0.05$, in accordance with previous literature (Biran et al., 2005; Winslow et al., 2010; Winslow and Tresco, 2010; Potter et al., 2012). In addition, we assessed the Bonferroni-corrected significance of the smallest *P* value for each depth.

RESULTS

ELECTRODE IMPEDANCE

All sinusoidal probes had pre-implantation impedances less than the 4–5 MΩ considered the limit for single unit recordings (Ludwig et al., 2006, 2011). The mean (±SEM) impedance at 1 kHz was 559 ± 88 kΩ ($n = 99$), compared with 200–400 kΩ for microwires.

ELECTROPHYSIOLOGY: LFP RECORDINGS

Figures 2A–C shows example LFP power spectra for sinusoidal and microwire electrodes (Rabbit-J, second generation probe). Two clear oscillatory bands can be seen: theta (4–8 Hz) and beta (13–30 Hz) which were separated by band-pass filtering (**Figures 2D,E**). In this animal, LFP recordings were obtained from one sinusoidal and two microwire electrodes over a 163 day period (**Figures 2A–C**). The LFP signal obtained from each of the three recording sites of the sinusoidal electrode were very similar ($R^2 = 0.98$, **Figures 2D,E**). Although the microwire electrode had higher LFP power values for both theta and beta frequency bands, the sinusoidal electrode recording was more stable over time (**Figures 2F,G**). Across the duration of the implant period, the standard deviation of the recorded power was 3.5, 7.8, and 9.9 μV^2 (theta frequency) and 5.5, 11.2, and 11.6 μV^2 (beta frequency) for the one sinusoidal and two microwire electrodes, respectively. Lower standard deviation values, measured across the recording sessions on different days, indicated that the LFP signal obtained for the sinusoidal probe appeared more stable across the chronic recording period in this animal than the comparator microwires. This result was also replicated for electrodes implanted in rabbit-R.

ELECTROPHYSIOLOGY: HIGH VOLTAGE SPINDLE RESPONSES

Figure 3A shows example HVS activity observed in rabbit-R ($n = 15$ sinusoidal and $n = 2$ microwire recording sites, second generation probe). This activity comprised high frequency

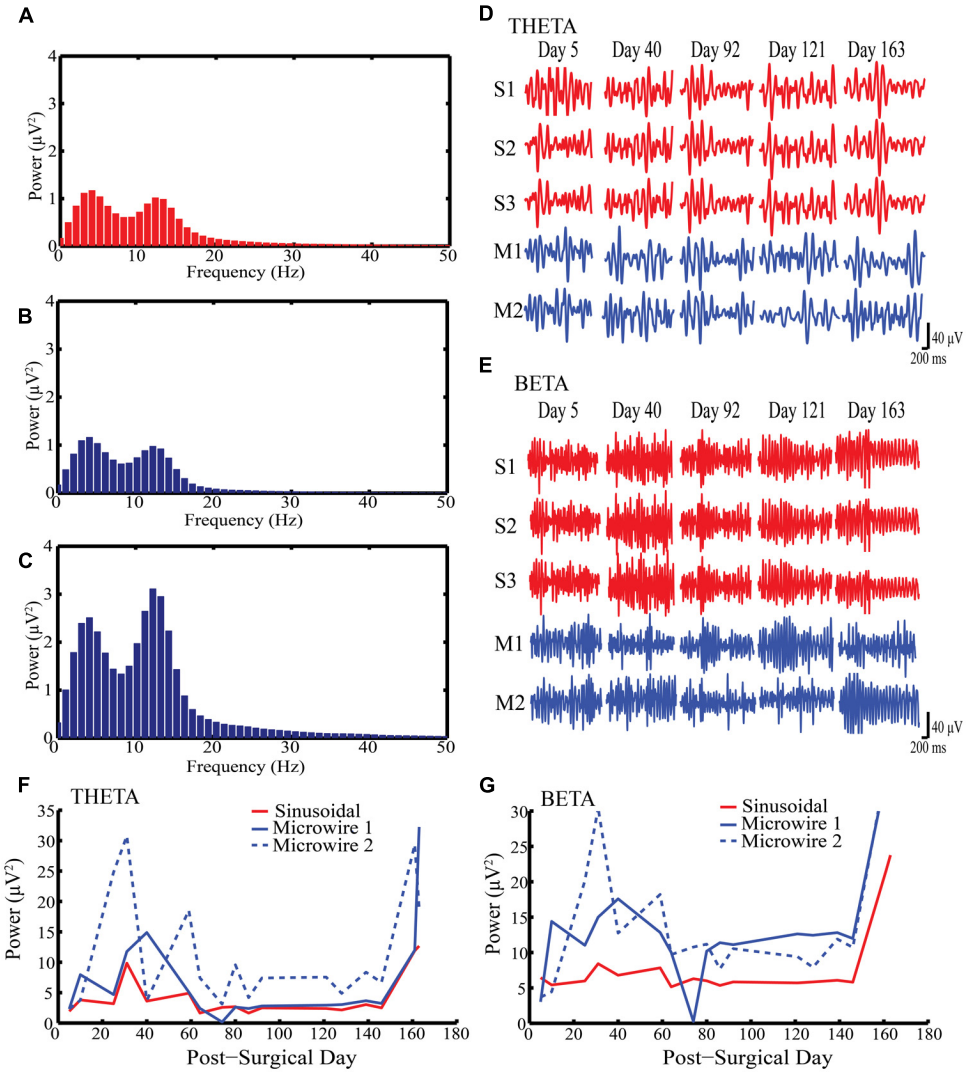

FIGURE 2 | Local field potential (LFP) recordings obtained from Rabbit-J over a 163 day indwelling period. (A–C) Example power spectra for one sinusoidal and two microwire electrodes respectively showing peaks at both theta and beta bands **(D)** Example of filtered recordings from selected days for theta band from all electrodes, S1–3 are the three individual electrode recording sites on the sinusoidal probe, M1–2 are two separate microwire electrodes. **(E)** Example of filtered recordings from selected days for beta band from all electrodes. **(F,G)** Daily recorded power over the indwelling period for both theta and beta activity, respectively. The same LFP signal was captured by all three electrode recording sites for the sinusoidal probe over the indwelling period. Note the stability in LFP power for the sinusoidal compared to the microwire electrode.

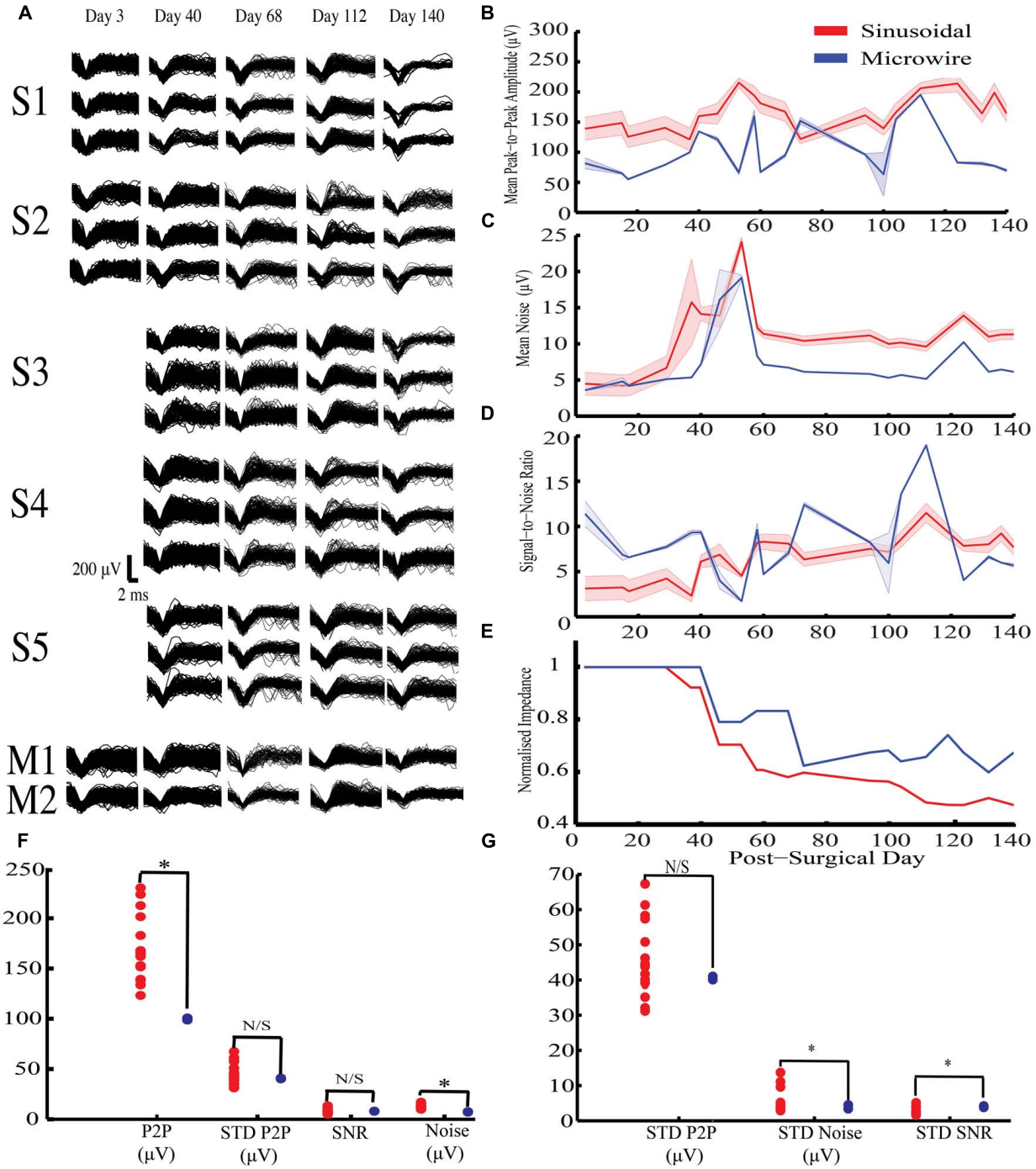

FIGURE 3 | Chronic high voltage spindle (HVS) responses from both sinusoidal and microwire electrode over a 140 day indwelling period from rabbit-R. (A) Selected overlain waveforms over the recording period, S1–5 are five different sinusoidal probes and M1–2 are two different microwire electrodes.**(B–E)** Overall sinusoidal (n = 15 recording sites) and microwire (n = 2 recording sites) chronic performance over a 140 day indwelling period (mean ± SEM): **(B)** Mean peak to peak amplitude recorded per recording session. **(C)** Average noise amplitude recorded per recording session. **(D)** Signal-to-noise ratio over the entire recording period. **(E)** Impedance normalized to the first recording session. There was an overall decrease in impedance for the sinusoidal (R^2 = 0.84) and microwire (R^2 = 0.78) electrode over the indwelling period. **(F)** Statistical comparison of daily obtained recording parameters using bootstrapping methods between the two electrode types. **(G)** Comparisons of standard deviation values obtained across the entire recording period to analyze overall recording parameter stability using bootstrapping methods between the two electrode types. P2P = peak-to-peak amplitude. STD = standard deviation. * indicates comparisons that fell outside the 2.5 to 97.5% percentile range of the bootstrapped distribution.

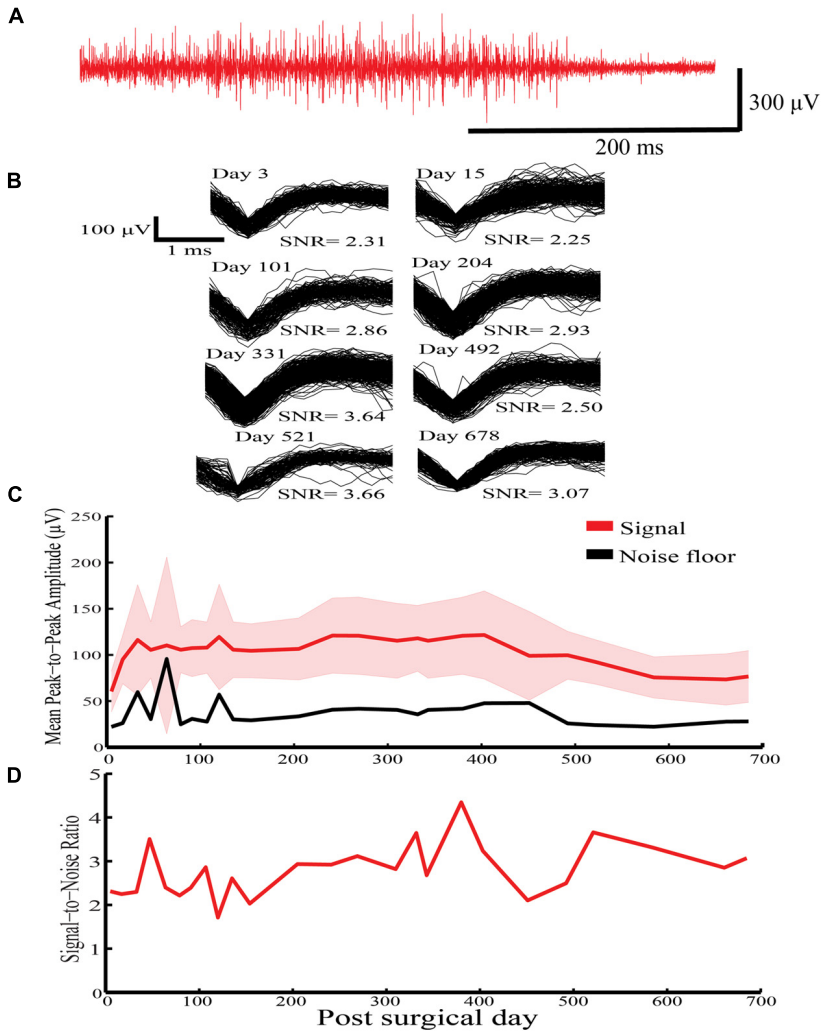

FIGURE 4 | High voltage spindle responses response recorded over a 678-indwelling period in Rabbit-N. (A) Example recording trace for the HVS activity. **(B)** Overlain waveforms for selected days for the HVS response. **(C)** Daily mean peak-to-peak amplitude (±SEM) with corresponding noise floor recorded across the recording period for HVS activity. **(D)** Daily signal-to-noise ratio (SNR) values recorded as a function of indwelling period for HVS activity.

spike-wave discharge, which was synchronous across all electrodes implanted on the same side of the brain, allowing accurate comparison of SNR across electrode types.

For this activity, the sinusoidal probes had higher mean peak-to-peak values compared to the microwire electrodes (**Figures 3B,F**) but also higher noise levels (**Figures 3C,F**). As a result there was no difference in the SNR between the two electrode types (**Figure 3D**). However, the SNR for the sinusoidal probe was more stable across the recording period, as revealed by a lower standard deviation across recording sessions (**Figure 3G**).

Overall impedance values were not significantly correlated with either mean peak-to-peak A ($R^2 = 0.037$) or noise ($R^2 = 0.015$) across all electrodes. However, impedance declined for both electrode types over the course of the implant period (**Figure 3E**). For the sinusoidal probe this resulted in improved SNR across the recording period ($R^2 = 0.76$), an effect not seen for microwire electrodes ($R^2 = 0.01$).

In summary, the sinusoidal electrode recorded higher mean peak-to-peak amplitude values with comparable stability to the microwire electrodes. Similar SNR values were obtained, however, the sinusoidal electrode had more stable SNR values across the recording period.

In Rabbit-N (first generation probe), HVS activity was recorded for a 678-day period on a solitary sinusoidal probe (**Figure 4A**). Similar waveforms were extracted over the 678-day indwelling period (**Figure 4B**). Further, stable mean peak-to-peak amplitude (**Figure 4C**) and SNR (**Figure 4D**) were recorded over the indwelling period. This initial result shows the potential for the sinusoidal electrode to record stable neuronal activity over chronic indwelling periods for >2 years.

ELECTROPHYSIOLOGY: SINGLE-UNIT RECORDING EXAMPLE

Figure 5 shows an example of a putative single unit obtained across all three electrode-recording sites of a sinusoidal electrode

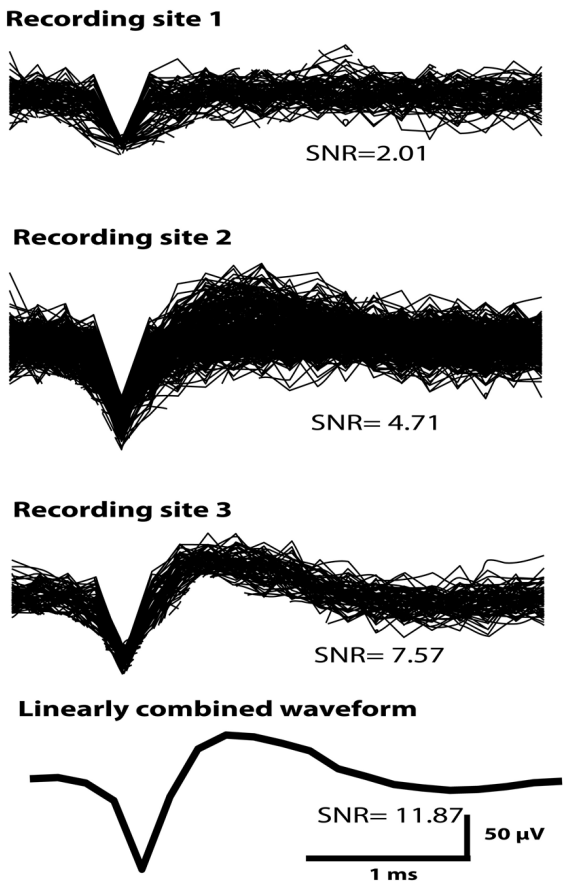

FIGURE 5 | A single unit recorded across all three sinusoidal recording sites in Rabbit-Lo. An algorithm was used that optimized the SNR by forming a linear combination of the three available channels; the SNR of the combined waveform was 11.87. The SNR values from the individual recording sites were lower than this value.

in Rabbit-Lo (second generation probe). The unit had different SNR and mean peak-to-peak amplitude on each contact, which allowed for effective unit isolation. Since the same action potential is observed on all three recordings, it is possible to improve SNR by linear combination. The three individual recording sites had SNR values of 2.01, 4.71, and 7.57. We used an algorithm, which chose the optimal linear combination to maximize the SNR; this achieved an SNR of 11.87. This example shows the utility of recording the same single unit across three electrode recording sites. An additional advantage of recording the same waveform on different electrodes is that differences in A may provide information additional to waveform shape that can be used for spike sorting (Gray et al., 1995; Harris et al., 2000).

THE GLIAL RESPONSE TO IMPLANTED ELECTRODES

The glial response to both electrode types was assessed over a 6–24 month chronic indwelling period by staining for astrocytes (**Figure 6**), microglia (**Figure 7**) and neurofilament (**Figure 8**). Overall there was a decrease in the astrocytic response at both 6 (**Figures 6A,D**) and 24 months (**Figures 6C,F**) close to the sinusoidal probe implantation site and where the classical astrocytic response is usually found (Polikov et al., 2005). No difference was found between the two electrode types at 12 months (**Figures 6B,E**). We found a decrease in overall microgliosis over a region of 0–500 μm at both 12 (**Figures 7A,C**) and 24 months (**Figures 7B,D**). Interestingly, for the same time points we also found an increase in neurofilament staining around the sinusoidal probe (**Figure 8**). Therefore it appears that the sinusoidal electrodes were better integrated into the neural tissue with decreased gliosis compared to microwires.

DISCUSSION

MICROFABRICATION

Microfabrication was successful with high functional yields generated from a single wafer. As dilute TMAH was used to release devices, a clean room wet bench was not needed for device release. This is an advantage over other polymeric probes requiring strong acids or bases (Kohler et al., 2009; Kozai and Kipke, 2009; Wu et al., 2011) for a similar release process. In some previous work, polymeric probes have been successfully peeled off the silicon wafer substrate without the inclusion of a sacrificial layer (e.g., Takeuchi et al., 2004). We found a similar approach to be problematic during initial testing as some probes remained attached, decreasing the yield of finished probe. Inclusion of the sacrificial aluminum layer in our process aided device adhesion during fabrication, but allowed reliable and straightforward release. This led to high functional yields.

Adhesion between two parylene-C layers can be problematic. Multiple groups bake parylene-C post device fabrication to promote this adhesion, however, this is time consuming and risks damaging devices as temperatures (200°C) above the parylene-C glass transition are used (Pang et al., 2005; Metzen and Stieglitz, 2012; Kim et al., 2013; Kuo et al., 2013). Here we show that a slight RIE over-etch when etching the WTi metal layer has the benefit of surface roughening the first parylene-C layer, improving parylene adhesion and preventing subsequent device delamination.

Other groups have attempted to increase neuronal recordings longevity by decreasing the footprint of the probe (Lind et al., 2010; Yoshida Kozai et al., 2012). Using the equation for the deflection of a rectangular cantilever beam, which takes into account the material dimensions and YM, a decrease in dimensions will lead to a decrease in overall stiffness values (Lempka et al., 2006; Yoshida Kozai et al., 2012). Decreasing the material's YM will have a similar effect. A limitation to decreasing probe dimensionality is the reduction in recording site area, which leads to higher obtained impedances (Ludwig et al., 2006). Electrodeposition of materials (e.g. PEDOT) onto the small recording site is required to achieve suitable impedance values for single-unit recording (Ludwig et al., 2011; Yoshida Kozai et al., 2012). However, these materials often have delamination issues >1 month post-implant (Yoshida Kozai et al., 2012).

The primary focus of this study was to compare the sinusoidal electrode to more conventional probes currently used for recording in non-human primates or humans. The improved performance over the rigid microwire electrode was largely due to reduced implant stiffness and reduced movement of the recording tip relative to the surrounding tissue. The contribution of the

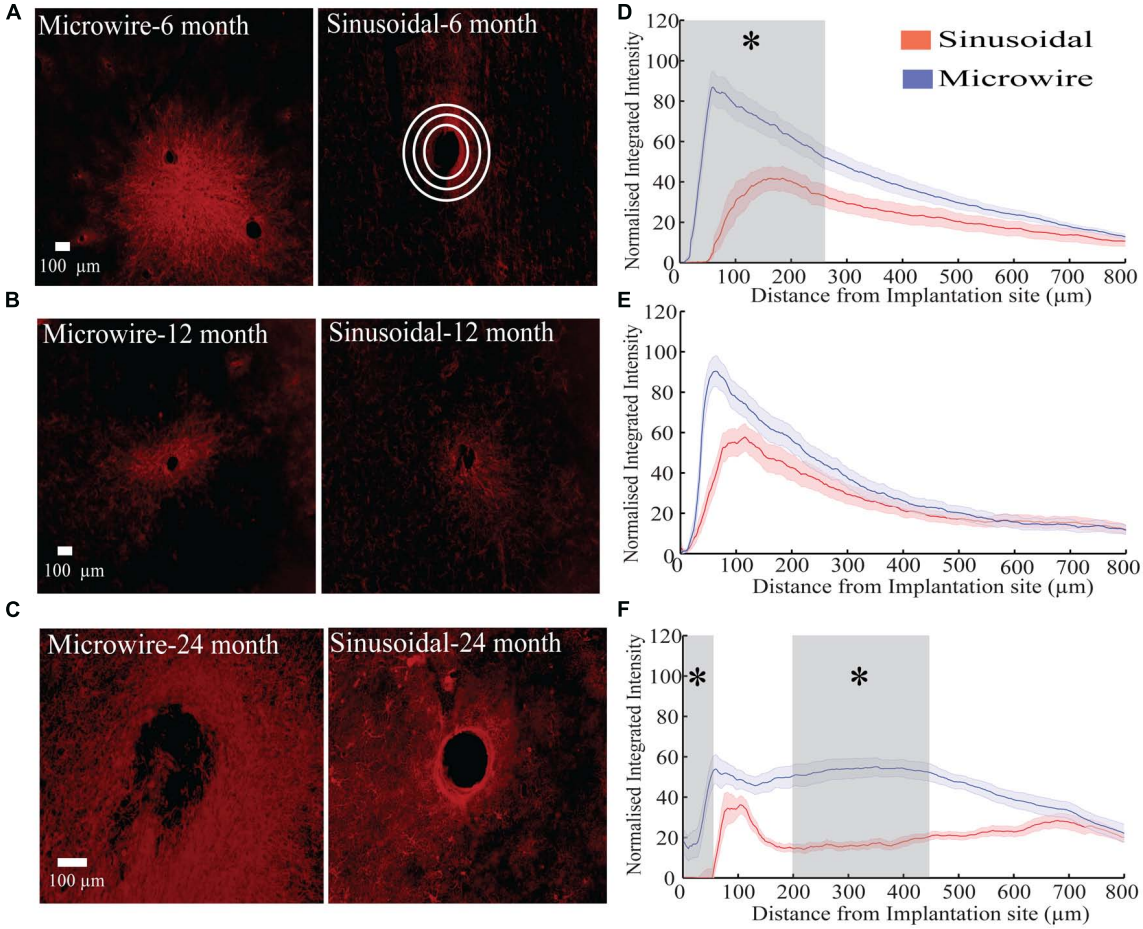

FIGURE 6 | The astrocytic response over a 6 (rabbit J, L), 12(rabbit P), and 24 (rabbit-N) month chronic indwelling period. (A) Representative images for the astrocytic response for both electrode types at the 6 month time point. Note the interaction between the two microwire recording sites. White concentric rings show an illustrative example of measurements taken for the radial distribution intensity as a function of distance from the electrode implantation site. **(B)** Representative images for the astrocytic response for both electrode types at the 12 month time point. **(C)** Representative images for the astrocytic response for both electrode types at the 24 month time point. **(D)** Overall normalized integrated intensity response (±SEM) for both electrode types for the 6 month time point ($n = 30$ electrode tracts). Significant differences (gray shading) were found at 50–250 μm away from the electrode implantation site ($P < 0.05$). **(E)** Overall normalized integrated intensity response (±SEM) for both electrode types for the 12 month time point ($n = 15$ electrode tracts). No significant differences were found. **(F)** Overall normalized integrated intensity response (±SEM) for both electrode types for the 24 month time point ($n = 15$ electrode tracts). Significant differences were found at 50 and 150–450 μm away from the electrode implantation site ($P < 0.05$).

sinusoidal shaft to the success of the design is difficult to quantify from this study, as a straight-shafted control was not used. This comparison can be addressed in future studies both with a modeling approach and through *in vivo* implantation of a straight-shaft version of the probe.

CHRONIC NEURONAL RECORDING

A striking result was the ability to record neuronal activity for >2 year period with stable recording parameters with the sinusoidal probe. Chronic recordings have also been obtained from other probes, such as the Utah array (>1–2 years; Rousche and Normann, 1998; Suner et al., 2005; Hochberg et al., 2006, 2012; Simeral et al., 2011; Collinger et al., 2012), Michigan probe (>6 weeks; Kipke et al., 2003; Vetter et al., 2004) and microwire probes (>1.5 years; Nicolelis et al., 2003; Jackson and Fetz, 2007). However, a distinct problem for all these probes is the lack of recording parameter stability. For microwires, Nicolelis et al. (2003) recorded activity from primate cortex. Based on the similarity of unsorted waveform clusters in principle component space, that study found 80% of the original units were still present after 2 days and 55% after 8 days (Nicolelis et al., 2003). Jackson and Fetz (2007) used the correlation coefficient between unsorted waveform averages and reported that 50% of original units were stable for a week, and 10% were stable through to 2 weeks. Dickey et al. (2009) used both average spike waveforms and interspike interval histograms to show that for a Utah array implanted in rhesus macaque monkeys 57, 43, and 39% of original units were stable for 7, 10, and 15 days respectively. In our hands, the sinusoidal probe provided more stable recordings judged from LFP and HVS activity than microwire electrodes.

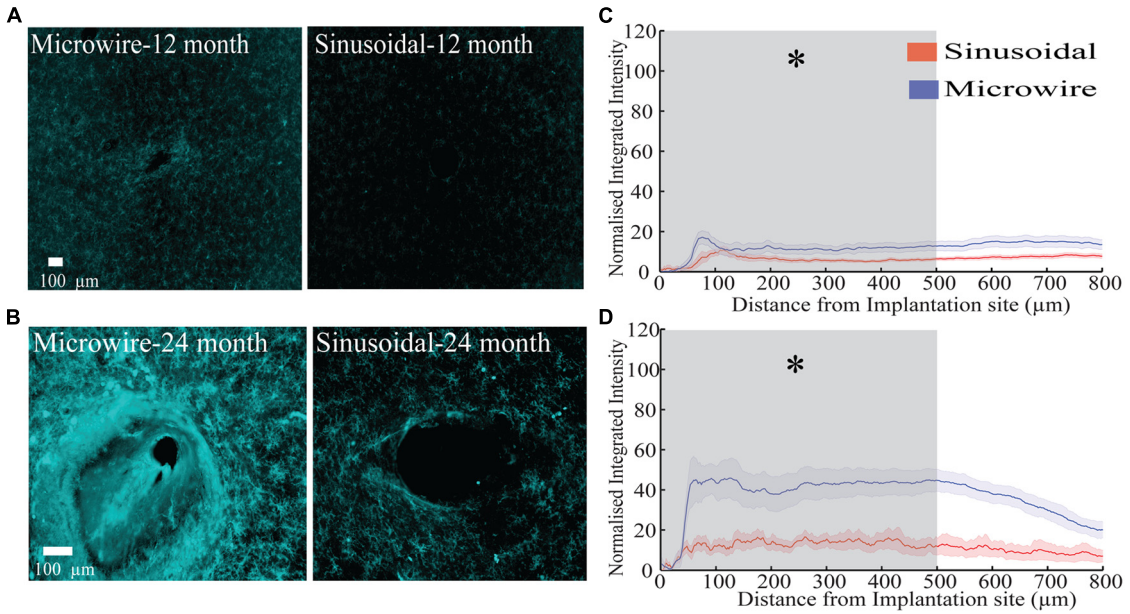

FIGURE 7 | The microglial response over a 12 (rabbit-P) and 24 (rabbit-N) month chronic indwelling period. (A) Representative images for the microglial response for both electrode types at the 6 month time point. **(B)** Representative images for the microglial response for both electrode types at the 12 month time point. **(C)** Overall normalized integrated intensity response (±SEM) for both electrode types for the 12 month time point (n = 15 electrode tracts per electrode comparison). Significant differences were found at 50–500 μm away from the electrode implantation site ($P < 0.05$). **(D)** Overall normalized integrated intensity response (±SEM) for both electrode types for the 24 month time point (n = 15 electrode tracts per electrode comparison). For the bottom profile representation, significant differences were found at 50–500 μm away from the electrode implantation site ($P < 0.05$).

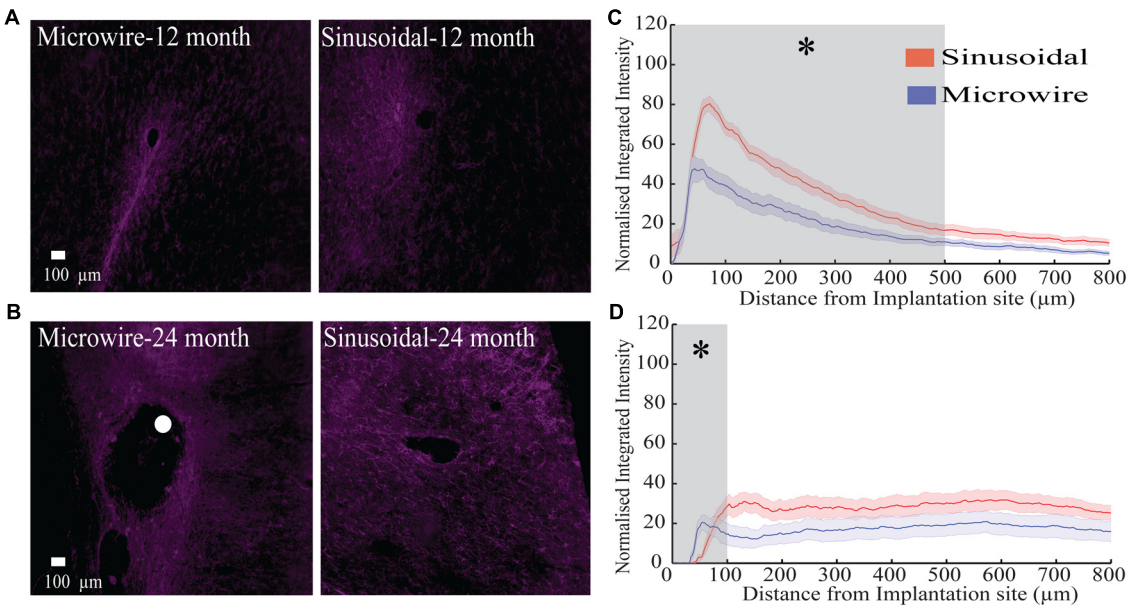

FIGURE 8 | The neurofilament response over a 12 (rabbit p) and 24 (rabbit-N) month chronic indwelling period. (A) Representative images for the neurofilament response for both electrode types at the 6 month time point. **(B)** Representative images for the neurofilament response for both electrode types at the 12 month time point. The white dot represents the microwire electrode implantation site. **(C)** Overall normalized integrated intensity response (±SEM) for both electrode types for the 12 month time point (n = 15 electrode tracts per electrode comparison). Significant differences were found at 50–500 μm away from the electrode implantation site ($P < 0.05$). **(D)** Overall normalized integrated intensity response (±SEM) for both electrode types for the 24 month time point (n = 15 electrode tracts per electrode comparison). Significant differences were found at 50 and 100 μm away from the electrode implantation site ($P < 0.05$).

However, further testing is needed to corroborate this recording stability.

To compare our electrode performance with other commercially available electrodes a commonly used SNR measure was used. For our electrode, peak SNR values for HVS were between 3 and 6. An appropriate comparison is the SNR measured from other electrode designs using multi-unit activity. Jackson and Fetz (2007) obtained values around 7 for their microwire electrode. Ward et al. (2009) obtained values between 6 and 7 for multiple electrode types including the Utah array, microwire, and Michigan probe electrodes over a 30 day recording period. For novel carbon fiber electrodes, SNR values of 3–8 were obtained over a 5 week indwelling period (Yoshida Kozai et al., 2012). Our electrode had comparable or slightly lower SNR values, although variability in recording stability was less than the microwire electrode.

Signal amplitudes of 60–400 μV (Ward et al., 2009), 120–250 μV (Suner et al., 2005), 60–100 μV (Vetter et al., 2004), and 60–200 μV (Yoshida Kozai et al., 2012) have been obtained for microwire, Utah array, Michigan probe and carbon fiber electrodes for chronic recording. We show recording amplitude of 100–230 μV for HVS responses, which is comparable to these electrode types.

Noise values are rarely reported in chronic electrode studies, however, from the Michigan probe, a value of 6–13 μV has been described (Vetter et al., 2004). We here report noise values of 7–13 μV during HVS responses. This is comparable to the Michigan probe electrode.

Overall, the SNR for a recorded unit can be increased by capturing that single unit across all three sinusoidal probe-recording sites. In addition, being able to record the same neuron on different sites on the probe may help sorting spikes in multi-unit recordings, as is commonly done with tetrode recording (Tseng et al., 2011).

Measurements of electrode impedance were not correlated with noise or signal values. For saline impedance testing, thermal noise is the main component of noise as there is no neuronal activity present. *In vivo*, SNR should follow impedance trends as thermal noise is directly related to the electrode impedance (Ludwig et al., 2006). As there was no correlation, it is possible that other sources of noise (e.g., biological or instrumentation noise) may have dominated the overall noise floor, as sources of noise summate in quadrature. Other groups have reported this phenomenon: SNR measurements are not related to 1 kHz *in vivo* impedance in both rodents and non-human primates for a variety of microelectrodes (Suner et al., 2005; Ward et al., 2009; Kim et al., 2013). Therefore, long-term impedance measurements may not be the best indicator for understanding chronic electrode performance.

Overall, our electrode had stable or initially declining impedances that stabilized over the indwelling period, similar to the microwire electrode. In contrast, silicon based probes have increasing impedances over both a 30 (Ward et al., 2009) and 81(Vetter et al., 2004) day indwelling period. For the Utah array there is a drop in impedance >1 year post-implant, which is related to electrode degradation (Suner et al., 2005). The drop in microwire impedance is related to the gradual insulation delamination surrounding the recording site, which increases the geometric surface area (GSA) available for recording (Patrick et al., 2011; Prasad et al., 2012).

For HVS responses, a few sinusoidal electrodes had drops in impedance after >20 days post-surgery, leading to improved recording characteristics. This may be related to the polyimide ball anchor. Gradual polyimide ball dissolution may have resulted in an increase in available GSA for recording. An alternative anchor which is more stable may need to be considered for future studies.

GLIAL RESPONSE

In this study, the sinusoidal probe was compared to microwire electrodes. Although the electrode was not compared to standard silicon probes, an emergent hierarchy is evident from the literature. In general silicon probes give a heightened immune response in relation to microwire style probes (Winslow et al., 2010; Yoshida Kozai et al., 2012). As we show decreased overall gliosis at multiple time points, it is reasonable to assume that we should also have a decreased response when comparing to standard silicon probes.

The sinusoidal probe had decreased overall gliosis measured by astrocytosis for the 6 month time point and by both astrocytosis and microgliosis for the 12 and 24 month time point. There was an increase in neurofilament staining around the sinusoidal probe at the 12 and 24 month time point. It appears that electrode designs incorporating micromotion-reducing measures can reduce gliosis and promote neuronal integration. Interestingly, we show an increase in neurofilament staining without the use of neurotropic factors, such as that used in the cone electrode (Kennedy, 1989; Kennedy et al., 1992; Bartels et al., 2008). The addition of a three dimension ball anchor seemed to attract neurites similar to the effect observed by Winslow and Tresco (2010) with cylindrical microwire electrodes over a 12-week indwelling period. The decreased microglial response is most likely the cause for the better neuronal integration seen with neurofilament staining for the sinusoidal probe. A heightened microglial response is associated with the loss of neurons in the immediate vicinity of the probe (∼100 μm away), designated the "kill zone" (Biran et al., 2007); this is also the maximum theorized distance over which an implanted neuronal probe can record neuronal activity (Polikov et al., 2005). Therefore, an advantage of the sinusoidal probe is a decreased microgliosis response over a chronic indwelling period that limits the "kill zone" region.

Intriguingly individual microwire electrode tracts can interact with one another, producing interacting tracks of glial scarring over chronic indwelling period of >6 months. This is not ideal, as interaction between two electrode tracts may induce biological noise and alter overall network effects for the specific recording cells of interest as astrocytes can interact with neurons (Giaume et al., 2010; Gourine et al., 2010; Sasaki et al., 2012).

There are reports that at long times post-implant, gliosis extends beyond a reported distance of 500 μm (Biran et al., 2005; Polikov et al., 2005). This raises the possibility that on-going gliosis could continue to spread far beyond the original implantation site, affecting considerable volumes of brain tissue. Such chronic spreading gliosis needs to be prevented to maintain stable recording parameters, especially in the presence of multiple implants.

FUTURE DIRECTIONS

Although the results of this initial study are promising, further testing is needed to corroborate the effectiveness of the sinusoidal probe as a chronic implant. Testing is needed in larger animals (e.g., non-human primates) where the problem of micromotion is far greater due to different patterns of animal behavior and skull sizes. We have verified that our insertion technique is suitable for non-human primates (data not shown), so this translational step beyond rodents and lagomorphs is a possibility.

CONCLUSION

To our knowledge this is the first study to show the usefulness of addressing micromotion-induced trauma with flexible electrodes more than 6 months after implant. We have shown that the sinusoidal probe appeared to be more stable in recording parameters over a 6–24 month chronic indwelling period in terms of LFP and HVS, especially in terms of LFP power and SNR. Further, we show that it is possible to register neuronal activity beyond 2-years post-implant with the sinusoidal probe. Gliosis was reduced at the recording tip of the sinusoidal compared to the rigid microwire electrodes at 6, 12, and 24-month time points, and there was better neuronal integration at 12 and 24 months. However, further studies are needed to corroborate these initial promising results. This initial study shows that the sinusoidal probe is a potential alternative to silicon, microwire and other polymeric probes for chronic neuronal recording.

ACKNOWLEDGMENTS

This work was supported by the Wellcome Trust, EPSRC, and MRC.

REFERENCES

Allen, J. S., Bruss, J., Brown, C. K., and Damasio, H. (2005). Normal neuroanatomical variation due to age: the major lobes and a parcellation of the temporal region. *Neurobiol. Aging* 26, 1245–1260. doi: 10.1016/j.neurobiolaging.2005.05.023

Azevedo, F. A. C., Carvalho, L. R. B., Grinberg, L. T., Farfel, J. M., Ferretti, R. E. L., Leite, R. E. P., et al. (2009). Equal numbers of neuronal and nonneuronal cells make the human brain an isometrically scaled-up primate brain. *J. Comp. Neurol.* 513, 532–541. doi: 10.1002/cne.21974

Bartels, J., Andreasen, D., Ehirim, P., Mao, H., Seibert, S., Wright, E. J., et al. (2008). Neurotrophic electrode: method of assembly and implantation into human motor speech cortex. *J. Neurosci. Methods* 174, 168–176. doi: 10.1016/j.jneumeth.2008.06.030

Biran, R., Martin, D. C., and Tresco, P. A. (2005). Neuronal cell loss accompanies the brain tissue response to chronically implanted silicon microelectrode arrays. *Exp. Neurol.* 195, 115–126. doi: 10.1016/j.expneurol.2005.04.020

Biran, R., Martin, D. C., and Tresco, P. A. (2007). The brain tissue response to implanted silicon microelectrode arrays is increased when the device is tethered to the skull. *J. Biomed. Mater. Res. A* 82, 169–178. doi: 10.1002/jbm.a.31138

Bjornsson, C. S., Oh, S. J., Al-Kofahi, Y. A., Lim, Y. J., Smith, K. L., Turner, J. N., et al. (2006). Effects of insertion conditions on tissue strain and vascular damage during neuroprosthetic device insertion. *J. Neural Eng.* 3, 196–207. doi: 10.1088/1741-2560/3/3/002

Buzsáki, G., Bickford, R. G., Ponomareff, G., Thal, L. J., Mandel, R., and Gage, F. H. (1988). Nucleus basalis and thalamic control of neocortical activity in the freely moving rat. *J. Neurosci.* 8, 4007–4026.

Chorover, S. L., and DeLuca, A. M. (1972). A sweet new multiple electrode for chronic single unit recording in moving animals. *Physiol. Behav.* 9, 671–674. doi: 10.1016/0031-9384(72)90030-3

Collinger, J. L., Wodlinger, B., Downey, J. E., Wang, W., Tyler-Kabara, E. C., Weber, D. J., et al. (2012). High-performance neuroprosthetic control by an individual with tetraplegia. *Lancet* 38, 557–564. doi: 10.1016/S0140-6736(12)61816-9

Dickey, A. S., Suminski, A., Amit, Y., and Hatsopoulos, N. G. (2009). Single-unit stability using chronically implanted multielectrode arrays. *J. Neurophysiol.* 102, 1331–1339. doi: 10.1152/jn.90920.2008

Geddes, L. A., and Roeder, R. (2003). Criteria for the selection of materials for implanted electrodes. *Ann. Biomed. Eng.* 31, 879–890. doi: 10.1114/1.1581292

Giaume, C., Koulakoff, A., Roux, L., Holcman, D., and Rouach, N. (2010). Astroglial networks: a step further in neuroglial and gliovascular interactions. *Nat. Rev. Neurosci.* 11, 87–99. doi: 10.1038/nrn2757

Gilletti, A., and Muthuswamy, J. (2006). Brain micromotion around implants in the rodent somatosensory cortex. *J. Neural Eng.* 3, 189–195. doi: 10.1088/1741-2560/3/3/001

Gould, H. J. III. (1986). Body surface maps in the somatosensory cortex of rabbit. *J. Comp. Neurol.* 243, 207–233. doi: 10.1002/cne.902430206

Gourine, A. V., Kasymov, V., Marina, N., Tang, F., Figueiredo, M. F., Lane, S., et al. (2010). Astrocytes control breathing through pH-dependent release of ATP. *Science* 329, 571–575. doi: 10.1126/science.1190721

Gray, C. M., Maldonado, P. E., Wilson, M., and McNaughton, B. (1995). Tetrodes markedly improve the reliability and yield of multiple single-unit isolation from multi-unit recordings in cat striate cortex. *J. Neurosci. Methods* 63, 43–54. doi: 10.1016/0165-0270(95)00085-2

Harris, J. P., Hess, A. E., Rowan, S. J., Weder, C., Zorman, C. A., Tyler, D. J., et al. (2011). In vivo deployment of mechanically adaptive nanocomposites for intracortical microelectrodes. *J. Neural Eng.* 8, 046010. doi: 10.1088/1741-2560/8/4/046010

Harris, K. D., Henze, D. A., Csicsvari, J., Hirase, H., and Buzsáki, G. (2000). Accuracy of tetrode spike separation as determined by simultaneous intracellular and extracellular measurements. *J. Neurophysiol.* 84, 401–414.

Hassler, C., Guy, J., Nietzschmann, M., Staiger, J. F., and Stieglitz, T. (2011). Chronic intracortical implantation of saccharose-coated flexible shaft electrodes into the cortex of rats. *Conf. Proc. IEEE Eng. Med. Biol. Soc.* 2011, 644–647. doi: 10.1109/IEMBS.2011.6090143

Hochberg, L. R., Bacher, D., Jarosiewicz, B., Masse, N. Y., Simeral, J. D., Vogel, J., et al. (2012). Reach and grasp by people with tetraplegia using a neurally controlled robotic arm. *Nature* 485, 372–375. doi: 10.1038/nature11076

Hochberg, L. R., Serruya, M. D., Friehs, G. M., Mukand, J. A., Saleh, M., Caplan, A. H., et al. (2006). Neuronal ensemble control of prosthetic devices by a human with tetraplegia. *Nature* 442, 164–171. doi: 10.1038/nature04970

Hubel, D. H. (1959). Single unit activity in striate cortex of unrestrained cats. *J. Physiol. (Lond.)* 147, 226–238.

Hwang, E. J., and Andersen, R. A. (2013). The utility of multichannel local field potentials for brain-machine interfaces. *J. Neural Eng.* 10, 046005. doi: 10.1088/1741-2560/10/4/046005

Jackson, A., and Fetz, E. E. (2007). Compact movable microwire array for long-term chronic unit recording in cerebral cortex of primates. *J. Neurophysiol.* 98, 3109–3118. doi: 10.1152/jn.00569.2007

Kennedy, P. R. (1989). The cone electrode: a long-term electrode that records from neurites grown onto its recording surface. *J. Neurosci. Methods* 29, 181–193. doi: 10.1016/0165-0270(89)90142-8

Kennedy, P. R., Mirra, S. S., and Bakay, R. A. E. (1992). The cone electrode: ultrastructural studies following long-term recording in rat and monkey cortex. *Neurosci. Lett.* 142, 89–94. doi: 10.1016/0304-3940(92)90627-J

Kim, B. J., Kuo, J. T. W., Hara, S. A., Lee, C. D., Yu, L., Gutierrez, C. A., et al. (2013). 3D Parylene sheath neural probe for chronic recordings. *J. Neural Eng.* 10, 045002. doi: 10.1088/1741-2560/10/4/045002

Kipke, D. R., Vetter, R. J., Williams, J. C., and Hetke, J. F. (2003). Silicon-substrate intracortical microelectrode arrays for long-term recording of neuronal spike activity in cerebral cortex. *IEEE Trans. Neural. Syst. Rehabil. Eng.* 11, 151–155. doi: 10.1109/TNSRE.2003.814443

Kohler, P., Linsmeier, C. E., Thelin, J., Bengtsson, M., Jorntell, H., Garwicz, M., et al. (2009). Flexible multi electrode brain-machine interface for recording in the cerebellum. *Conf. Proc. IEEE Eng. Med. Biol. Soc.* 2009, 536–538. doi: 10.1109/IEMBS.2009.5333498

Kozai, T. D. Y., and Kipke, D. R. (2009). Insertion shuttle with carboxyl terminated self-assembled monolayer coatings for implanting flexible polymer neural probes in the brain. *J. Neurosci. Methods* 184, 199–205. doi: 10.1016/j.jneumeth.2009.08.002

Kozai, T. D. Y., Marzullo, T. C., Hooi, F., Langhals, N. B., Majewska, A. K., Brown, E. B., et al. (2010). Reduction of neurovascular damage resulting from microelectrode insertion into the cerebral cortex using in vivo two-photon mapping. *J. Neural Eng.* 7, 046011. doi: 10.1088/1741-2560/7/4/046011

Kuo, J. T. W., Kim, B. J., Hara, S. A., Lee, C. D., Gutierrez, C. A., Hoang, T. Q., et al. (2013). Novel flexible Parylene neural probe with 3D sheath structure for enhancing tissue integration. *Lab Chip* 13, 554–561. doi: 10.1039/c2lc40935f

LaPlaca, M. C., Cullen, D. K., McLoughlin, J. J., and Cargill, R. S. II. (2005). High rate shear strain of three-dimensional neural cell cultures: a new in vitro traumatic brain injury model. *J. Biomech.* 38, 1093–1105. doi: 10.1016/j.jbiomech.2004.05.032

Lempka, S. F., Johnson, M. D., Barnett, D. W., Moffitt, M. A., Otto, K. J., Kipke, D. R., et al. (2006). Optimization of microelectrode design for cortical recording based on thermal noise considerations. *Conf. Proc. IEEE Eng. Med. Biol. Soc.* 1, 3361–3364. doi: 10.1109/IEMBS.2006.259432

Lind, G., Linsmeier, C. E., Thelin, J., and Schouenborg, J. (2010). Gelatine-embedded electrodes – a novel biocompatible vehicle allowing implantation of highly flexible microelectrodes. *J. Neural Eng.* 7, 046005. doi: 10.1088/1741-2560/7/4/046005

Ludwig, K. A., Langhals, N. B., Joseph, M. D., Richardson-Burns, S. M., Hendricks, J. L., and Kipke, D. R. (2011). Poly(3,4-ethylenedioxythiophene) (PEDOT) polymer coatings facilitate smaller neural recording electrodes. *J. Neural Eng.* 8, 014001. doi: 10.1088/1741-2560/8/1/014001

Ludwig, K. A., Uram, J. D., Yang, J., Martin, D. C., and Kipke, D. R. (2006). Chronic neural recordings using silicon microelectrode arrays electrochemically deposited with a poly(3,4-ethylenedioxythiophene) (PEDOT) film. *J. Neural Eng.* 3, 59–70. doi: 10.1088/1741-2560/3/1/007

Marblestone, A. H., Zamft, B. M., Maguire, Y. G., Shapiro, M. G., Cybulski, T. R., Glaser, J. I., et al. (2013). Physical principles for scalable neural recording. *Front. Comput. Neurosci.* 7:137. doi: 10.3389/fncom.2013.00137

Metzen, R. P. V., and Stieglitz, T. (2012). The influence of annealing on the electrical stability of parylene C structures. *Biomed. Tech. (Berl.)* doi: 10.1515/bmt-2012-4272 [Epub ahead of print].

Miller, K., Chinzei, K., Orssengo, G., and Bednarz, P. (2000). Mechanical properties of brain tissue in vivo: experiment and computer simulation. *J. Biomech.* 33, 1369–1376. doi: 10.1016/S0021-9290(00)00120-2

Nicolelis, M. A. (2001). Actions from thoughts. *Nature* 409, 403–407. doi: 10.1038/35053191

Nicolelis, M. A., Dimitrov, D., Carmena, J. M., Crist, R., Lehew, G., Kralik, J. D., et al. (2003). Chronic, multisite, multielectrode recordings in macaque monkeys. *Proc. Natl. Acad. Sci. U.S.A.* 100, 11041–11046. doi: 10.1073/pnas.1934665100

Pang, C., Cham, J., Nenadic, Z., Musallam, S., Tai, Y. C., Burdick, J., et al. (2005). A new multi-site probe array with monolithically integrated parylene flexible cable for neural prostheses. *Conf. Proc. IEEE Eng. Med. Biol. Soc.* 7, 7114–7117.

Patrick, E., Orazem, M. E., Sanchez, J. C., and Nishida, T. (2011). Corrosion of tungsten microelectrodes used in neural recording applications. *J. Neurosci. Methods* 198, 158–171. doi: 10.1016/j.jneumeth.2011.03.012

Perge, J. A., Homer, M. L., Malik, W. Q., Cash, S., Eskandar, E., Friehs, G., et al. (2013). Intra-day signal instabilities affect decoding performance in an intracortical neural interface system. *J. Neural Eng.* 10, 036004. doi: 10.1088/1741-2560/10/3/036004

Polikov, V. S., Tresco, P. A., and Reichert, W. M. (2005). Response of brain tissue to chronically implanted neural electrodes. *J. Neurosci. Methods* 148, 1–18. doi: 10.1016/j.jneumeth.2005.08.015

Potter, K. A., Buck, A. C., Self, W. K., and Capadona, J. R. (2012). Stab injury and device implantation within the brain results in inversely multiphasic neuroinflammatory and neurodegenerative responses. *J. Neural Eng.* 9, 046020. doi: 10.1088/1741-2560/9/4/046020

Prasad, A., Xue, Q.-S., Sankar, V., Nishida, T., Shaw, G., Streit, W. J., et al. (2012). Comprehensive characterization and failure modes of tungsten microwire arrays in chronic neural implants. *J. Neural Eng.* 9, 056015. doi: 10.1088/1741-2560/9/5/056015

Rousche, P. J., and Normann, R. A. (1998). Chronic recording capability of the Utah intracortical electrode array in cat sensory cortex. *J. Neurosci. Methods* 82, 1–15. doi: 10.1016/S0165-0270(98)00031-4

Sasaki, T., Beppu, K., Tanaka, K. F., Fukazawa, Y., Shigemoto, R., and Matsui, K. (2012). Application of an optogenetic byway for perturbing neuronal activity via glial photostimulation. *Proc. Natl. Acad. Sci. U.S.A.* 109, 20720–20725. doi: 10.1073/pnas.1213458109

Schwartz, A. B. (2004). Cortical neural prosthetics. *Annu. Rev. Neurosci.* 27, 487–507. doi: 10.1146/annurev.neuro.27.070203.144233

Seymour, J. P., and Kipke, D. R. (2006). Fabrication of polymer neural probes with sub-cellular features for reduced tissue encapsulation. *Conf. Proc. IEEE Eng. Med. Biol. Soc.* 1, 4606–4609. doi: 10.1109/IEMBS.2006.260528

Seymour, J. P., Langhals, N. B., Anderson, D. J., and Kipke, D. R. (2011). Novel multi-sided, microelectrode arrays for implantable neural applications. *Biomed. Microdevices* 13, 441–451. doi: 10.1007/s10544-011-9512-z

Simeral, J. D., Kim, S. P., Black, M. J., Donoghue, J. P., and Hochberg, L. R. (2011). Neural control of cursor trajectory and click by a human with tetraplegia 1000 days after implant of an intracortical microelectrode array. *J. Neural Eng.* 8, 025027. doi: 10.1088/1741-2560/8/2/025027

Subbaroyan, J., Martin, D. C., and Kipke, D. R. (2005). A finite-element model of the mechanical effects of implantable microelectrodes in the cerebral cortex. *J. Neural Eng.* 2, 103–113. doi: 10.1088/1741-2560/2/4/006

Suner, S., Fellows, M. R., Vargas-Irwin, C., Nakata, G. K., and Donoghue, J. P. (2005). Reliability of signals from a chronically implanted, silicon-based electrode array in non-human primate primary motor cortex. *IEEE Trans. Neural. Syst. Rehabil. Eng.* 13, 524–541. doi: 10.1109/TNSRE.2005.857687

Suyatin, D. B., Wallman, L., Thelin, J., Prinz, C. N., Jörntell, H., Samuelson, L., et al. (2013). Nanowire-based electrode for acute in vivo neural recordings in the brain. *PLoS ONE* 8:e56673. doi: 10.1371/journal.pone.0056673

Swadlow, H. A. (1989). Efferent neurons and suspected interneurons in S-1 vibrissa cortex of the awake rabbit: receptive fields and axonal properties. *J. Neurophysiol.* 62, 288–308.

Swadlow, H. A. (1990). Efferent neurons and suspected interneurons in S-1 forelimb representation of the awake rabbit: receptive fields and axonal properties. *J. Neurophysiol.* 63, 1477–1498.

Swadlow, H. A. (1994). Efferent neurons and suspected interneurons in motor cortex of the awake rabbit: axonal properties, sensory receptive fields, and subthreshold synaptic inputs. *J. Neurophysiol.* 71, 437–453.

Swadlow, H. A., and Hicks, T. P. (1996). Somatosensory cortical efferent neurons of the awake rabbit: latencies to activation via supra – and subthreshold receptive fields. *J. Neurophysiol.* 75, 1753–1759.

Takeuchi, S., Yoshida, Y., Ziegler, D., Mabuchi, K., and Suzuki, T. (2004). Parylene flexible neural probe with micro fluidic channel. *Lab Chip* 5, 519–523. doi: 10.1039/b417497f

Taylor, D. M., Tillery, S. I. H., and Schwartz, A. B. (2002). Direct cortical control of 3D neuroprosthetic devices. *Science* 296, 1829–1832. doi: 10.1126/science.1070291

Thelin, J., Jörntell, H., Psouni, E., Garwicz, M., Schouenborg, J., Danielsen, N., et al. (2011). Implant size and fixation mode strongly influence tissue reactions in the CNS. *PLoS ONE* 6:e16267. doi: 10.1371/journal.pone.0016267

Tseng, W.-T., Yen, C.-T., and Tsai, M.-L. (2011). A bundled microwire array for long-term chronic single-unit recording in deep brain regions of behaving rats. *J. Neurosci. Methods* 201, 368–376. doi: 10.1016/j.jneumeth.2011.08.028

Vetter, R. J., Williams, J. C., Hetke, J. F., Nunamaker, E. A., and Kipke, D. R. (2004). Chronic neural recording using silicon-substrate microelectrode arrays implanted in cerebral cortex. *IEEE Trans. Biomed. Eng.* 51, 896–904. doi: 10.1109/TBME.2004.826680

Ward, M. P., Rajdev, P., Ellison, C., and Irazoqui, P. P. (2009). Toward a comparison of microelectrodes for acute and chronic recordings. *Brain Res.* 1282, 183–200. doi: 10.1016/j.brainres.2009.05.052

Winslow, B. D., and Tresco, P. A. (2010). Quantitative analysis of the tissue response to chronically implanted microwire electrodes in rat cortex. *Biomaterials* 31, 1558–1567. doi: 10.1016/j.biomaterials.2009.11.049

Winslow, B. D., Christensen, M. B., Yang, W.-K., Solzbacher, F., and Tresco, P. A. (2010). A comparison of the tissue response to chronically implanted Parylene-C-coated and uncoated planar silicon microelectrode arrays in rat cortex. *Biomaterials* 31, 9163–9172. doi: 10.1016/j.biomaterials.2010.05.050

Witteveen, J. A., Suyatin, D. B., Gällentoft, L., Schouenborg, J., Danielsen, N., and Prinz, C. N. (2010). Gelatin/glycerol coating to preserve mechanically compliant nanowire electrodes from damage during brain implantation. *J. Vacuum Sci. Technol. B* 28, C6K13–C6K16. doi: 10.1116/1.3498764

Wu, F., Im, M., and Yoon, E. (2011). "A flexible fish-bone-shaped neural probe strengthened by biodegradable silk coating for enhanced biocompatibility," in *Proceedings of 16th International Solid-State Sensors, Actuators and Microsystems Conference (TRANSDUCERS)*, Beijing, 966–969.

Yoshida Kozai, T. D., Langhals, N. B., Patel, P. R., Deng, X., Zhang, H., Smith, K. L., et al. (2012). Ultrasmall implantable composite microelectrodes with bioactive surfaces for chronic neural interfaces. *Nat. Mater.* 11, 1065–1073. doi: 10.1038/nmat3468

Zimmermann, J. B., Seki, K., and Jackson, A. (2011). Reanimating the arm and hand with intraspinal microstimulation. *J. Neural Eng.* 8, 054001. doi: 10.1088/1741-2560/8/5/054001

Conflict of Interest Statement: The authors declare that the research was conducted in the absence of any commercial or financial relationships that could be construed as a potential conflict of interest.

Received: 26 December 2013; accepted: 07 April 2014; published online: 29 April 2014.
Citation: Sohal HS, Jackson A, Jackson R, Clowry GJ, Vassilevski K, O'Neill A and Baker SN (2014) The sinusoidal probe: a new approach to improve electrode longevity. Front. Neuroeng. ***7****:10. doi: 10.3389/fneng.2014.00010*
This article was submitted to the journal Frontiers in Neuroengineering.

frontiers in
NEUROENGINEERING

ORIGINAL RESEARCH ARTICLE
published: 21 August 2014
doi: 10.3389/fneng.2014.00034

In vivo monitoring of glial scar proliferation on chronically implanted neural electrodes by fiber optical coherence tomography

Yijing Xie*[1], *Nadja Martini*[1], *Christina Hassler*[2], *Robert D. Kirch*[1], *Thomas Stieglitz*[2], *Andreas Seifert*[3] *and Ulrich G. Hofmann*[1]

[1] *Neuroelectronic Systems, Department of General Neurosurgery, University Medical Center Freiburg, Freiburg, Germany*
[2] *Laboratory for Biomedical Microtechnology, Department of Microsystems Engineering(IMTEK), University of Freiburg, Freiburg, Germany*
[3] *Gisela and Erwin Sick Chair of Micro-optics, Department of Microsystems Engineering(IMTEK), University of Freiburg, Freiburg, Germany*

Edited by:
Jürgen Krüger, Bernstein Center for Computational Neuroscience, Germany

Reviewed by:
Luca Berdondini, Italian Institute of Technology, Italy
Pascal Darbon, Université de Strasbourg, France

***Correspondence:**
Ulrich G. Hofmann, Neuroelectronic Systems, Department of General Neurosurgery, University Medical Center Freiburg, Engesser Strasse 4, Freiburg D-79108, Germany
e-mail: ulrich.hofmann@klinikum.uni-freiburg.de

In neural prosthetics and stereotactic neurosurgery, intracortical electrodes are often utilized for delivering therapeutic electrical pulses, and recording neural electrophysiological signals. Unfortunately, neuroinflammation impairs the neuron-electrode-interface by developing a compact glial encapsulation around the implants in long term. At present, analyzing this immune reaction is only feasible with post-mortem histology; currently no means for specific *in vivo* monitoring exist and most applicable imaging modalities can not provide information in deep brain regions. Optical coherence tomography (OCT) is a well established imaging modality for *in vivo* studies, providing cellular resolution and up to 1.2 mm imaging depth in brain tissue. A fiber based spectral domain OCT was shown to be capable of minimally invasive brain imaging. In the present study, we propose to use a fiber based spectral domain OCT to monitor the progression of the tissue's immune response through scar encapsulation progress in a rat animal model. A fine fiber catheter was implanted in rat brain together with a flexible polyimide microelectrode in sight both of which acts as a foreign body and induces the brain tissue immune reaction. OCT signals were collected from animals up to 12 weeks after implantation and thus gliotic scarring *in vivo* monitored for that time. Preliminary data showed a significant enhancement of the OCT backscattering signal during the first 3 weeks after implantation, and increased attenuation factor of the sampled tissue due to the glial scar formation.

Keywords: chronic implants, flexible microelectrodes, foreign body reaction, optical coherence tomography, fiber catheter

1. INTRODUCTION

Intracortical electrodes are often employed in neuroprosthetic applications or in clinical stereotactic surgery, to deliver therapeutic electrical pulses and collect neuronal electrophysiological signals (Tronnier and Fogel, 2000; Stieglitz et al., 2009; Raspopovic et al., 2014). A reliable and dependable electrode-tissue-interface is crucial in this concept since a neuroprosthetic device is supposed to serve functionally over long period in subject's brain. Unfortunately, the lifetime of a such device is always compromised due to electrode corrosion or so called glial scarring around the indwelling electrode (Edell et al., 1992; Schmidt et al., 1993; Turner et al., 1999; Leach et al., 2010).

When an electrode is implanted into the brain, during the acute phase of the immune reaction, microphages settle in on the area and resident microglia cells of the immune system become activated and start proliferating. Then astrocytes are activated to scavenge the leftover large intruders. Unfortunately, any type of the artificial implant is resistant to this bio degradation, which induces a so called frustrated phagocytosis and leads in consequence to a dense glial scar attempting to isolate the implant from the delicate brain tissue (Turner et al., 1999; Biran et al., 2005; Polikov et al., 2005; Winslow et al., 2010; Potter et al., 2012). This isolation performed by glial sheathing not only changes the electrical coupling to the surrounding parenchyma, but may even cause neuronal loss by neurotoxic factors released from glial cells (Block et al., 2007). This leads to a deterioration and loss of electrophysiological signal over time. Electrical characterization of electrode-tissue state over time is attempted by temporally resolved impedance spectroscopy or signal-to-noise ratio analysis (Ludwig et al., 2006; Mcconnell et al., 2009). Immunohistochemical analysis is performed to characterize astrocytes and microglial cells progression over time. However, this requires tissue to be removed for postmortem examination disqualifying for long term *in vivo* process monitoring of the same animal (Szarowski et al., 2003). Lately, Kozai et al. (2012) reported using two-photon microscopy to reveal immediate microglial reaction to electrode insertion *in vivo*. However, this technique is limited to imaging only a shallow part

(∼200 μm) of the brain and only in short term (up to 7 h post implantation).

Alternatively, clinically approved Optical Coherence Tomography, displaying the intrinsic optical scattering properties of the tissue, might be used instead (Huang et al., 1991; Hee et al., 1996; Bonin et al., 2010). OCT features a spatial resolution in cellular range of 5–10 μm, up to 1.2 mm imaging depth in brain tissue, and up to 40,000 axial scans (A-scan) per second (Drexler et al., 2001; Rodriguez-Padilla et al., 2007). When integrated with ultra-small single mode fiber catheter, it is competent to visualize deep brain structures with minimum trauma (Tearney et al., 1997; Böhringer et al., 2006; Xie et al., 2013).

In the present study, we propose to use a fiber based spectral domain OCT to monitor the progression of the tissue's immune response through scar encapsulation progress in a rat animal model. We developed an integrated OCT detection probe consisting of an implantable ferrule based fiber catheter and a fiber patch cable. The fiber catheter was implanted in rat brain together with a flexible polyimide microelectrode array in sight, according to the procedure described in Richter et al. (2013), both intended to induce the brain tissue immune reaction. The OCT backscattering intensity of the brain tissue around the fiber increased during the first 3 weeks. The tissue optical attenuation coefficient altered after implantation and reached a maximum at the week 6 implying that a compact dense tissue sheath has developed around the fiber tip. Further more, the 10 μm thick flexible probe which located up to 2.7 mm away from the fiber catheter tip is still visible in the OCT image and A-scan plot.

2. MATERIALS AND METHODS

2.1. OPTICAL COHERENCE TOMOGRAPHY IMAGING SYSTEM

The imaging modality we used to monitor and assess the foreign body reaction is fiber based spectral domain optical coherence tomography (SDOCT) (Fercher et al., 1995). In this imaging modality, the incident light is transmitted into tissue through an implantable fiber catheter and the backscattered light from the illuminated tissue is also collected by the fiber catheter. The incident light and the backscattered light produce an interference pattern encoding the intrinsic optical properties of the sampled tissue. The interference pattern is detected at a spectrometer to construct A-scan (depth-scan) signals providing the backscattered light intensity as a function of depth.

The imaging system employed composes a commercially available fiber-based OCT module ("Callisto," Thorlabs GmbH, Lübeck, Germany) utilizing a superluminescent diode (SLD) with center wavelength at 840 nm as the light source and a single mode fiber based sampling probe providing the feasibility of minimum-invasive imaging (see **Figure 1**). When equipped with a single mode fiber based detecting catheter, the whole system features an axial resolution of 14 μm and transversal resolution of 20 μm in air. The system's look-ahead capability is 3.5 mm from the tip of the fiber catheter to the tissue, enabling us to evaluate the development of the tissue reaction to the indwelling fiber catheter and to the flexible microelectrode underneath. It has been demonstrated that the fiber based OCT system is competent for imaging brain anatomical structures *in vivo* (Xie et al., 2013).

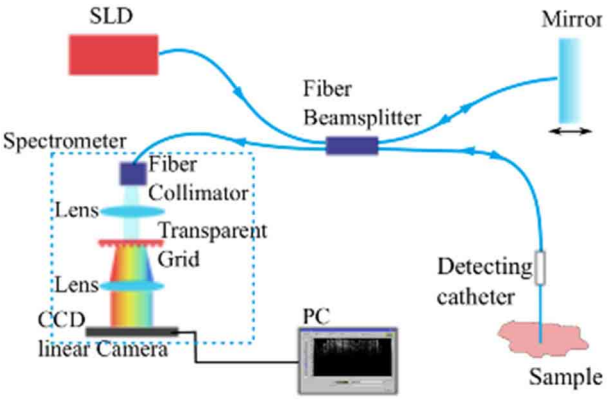

FIGURE 1 | A schematic diagram of the Spectral Domain Optical Coherence Tomography imaging system.

2.2. OPTICAL FIBER DETECTION CATHETER

The aim of this study is to use a chronically implanted OCT fiber cannula to monitor and to assess brain tissue's foreign body reaction to it and to the also chronically implanted flexible microelectrode. The fiber cannula chosen consists of a ceramic FC ferrule (CF126-10, Thorlabs) with 2.5 mm outer diameter and 10.5 mm total length, and a 8 mm long single mode fiber (⌀125 μm, SMF800-5.6-125, Thorlabs) in order to reach deep brain structures (see **Figure 2B** bottom for geometry).

2.3. POLYIMIDE BASED FLEXIBLE MICROELECTRODE

The flexible polyimide microelectrode, which also provokes immune response and which was implanted into the rat brain, is designed and fabricated in-house. The probe shank is 15 mm long, 10 μm thick and 365 μm wide, with a smooth surface. The substrate material of the photolithographically structured probe is a medical grade polyimide type PI2611 (U-Varnish S, UBE, Newyork), with a bulk YoungÕs modulus of around 10 GPa over 20 months in 37°C PBS (Rubehn and Stieglitz, 2010) (**Figure 2B** left). It is exemplifying a "device under test" based on findings (Sohal et al., 2014) that indwelling flexible substrates provoke a less pronounced gliosis compared with rigid micro electrodes presumably due to compliance-matching with brain tissue.

2.4. ANIMAL SURGERY AND DEVICE IMPLANTATION

All animal experiments conducted in this study were performed with approval from the locally responsible Animal Welfare Committe with the Regierungspräsidium Freiburg in accordance with the guidelines of the European Union Directive 2010/63/UE. The animal model chosen consists of adult female Sprague Dawley rats (Charles River, Germany), weighing 280–320 g. The rats were initially anesthetized by administering intraperitoneally a mixture of 100 mg/kg ketamine and 5 mg/kg xylazine. Rats were placed on a the heating pad of a circulating water bath set to 40°C to maintain a body temperature of 35°C. The rat was then fixed into the stereotactic frame with a pair of ear pins and a bite bar. A 15 mm long scalp incision was cut along the midline, the skin was pulled aside to expose the skull surface structure. Bregma was identified and served as coordinate 0.0 mm. A burr hole (0.9 mm

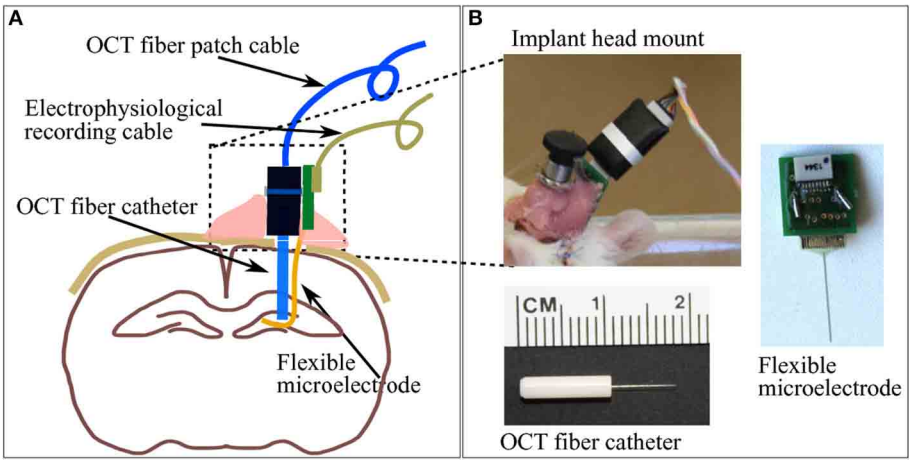

FIGURE 2 | (A) A brief sketch of the implantations including a pair of indwelling probe: the OCT fiber catheter and the flexible polyimide microelectrode. **(B)** The picture on top-left shows the cemented fiber optics connector and PCB for electrophysiology recording taken on the second week after implantation surgery. Pictures on bottom-left and right demonstrate the geometry of the OCT fiber catheter and the flexible microelectrode connected to a PCB, respectively.

in diameter) in the skull at 4.0 mm posterior 2.0 mm lateral from Bregma was drilled. Prior to probe insertion, a small incision was cut on the dura and pia mater underneath the burr hole with a 27 G needle to avoid brain dimpling upon probe penetration.

The flexible microelectrode was inserted in the brain tissue with the OCT fiber catheter, following the protocol prosposed by Richter et al. (2013). The flexible microelectrode was placed on the moist skull surface, with the shank precisely adjusted to overlay the burr hole at the position of 4 mm from the shank distal end. The OCT fiber catheter was firmly clamped to the micro drive equipped stereotaxic frame and positioned on top of the burr hole. The microelectrode shank was placed between the exposed skull and the OCT fiber precisely aligned above the hole (**Figure 3A**). Slowly driving the stereotactic z arm to insert the fiber catheter, the flexible microelectrode was pushed into the brain by the fiber catheter (**Figures 3B,C**). We stopped the insertion when the fiber catheter was at 6 mm under the brain surface (thalamic nucleus area) (**Figure 3D**). In order to avoid electrode displacement while applying dental cement, a small drop of Super Glue (Loctite 4061, Henkel Loctite GmbH) was applied to adhere the rest of the electrode shank to the skull. A small amount of bone wax was plastered to close the skull burr hole. We sealed and tethered the connector part of the fiber catheter and the microelectrode with adequate dental cement (**Figure 2A**). The skin incision was sutured to close and wiped with betaisodona (7.5%, B. Braun Melsungen) to prevent skin infection. Carprofen (4 mg/kg) was then administered subcutaneously for pain management each day for 5 days after surgery. The animals were housed with daily inspection.

2.5. POST SURGERY MEASUREMENT AND OCT SIGNAL ANALYSIS

The OCT signal was collected at week 1, 2, 3, 6, and 12 after the implantation surgery in freely moving rats. During each measurement, the implanted OCT fiber catheter was connected to the OCT sampling cable through FC/FC mating sleeve. Since the FC ferrule features a flat endface, the presence of air at the junction point induces significant signal loss due to the refractive index mismatching between air and fiber material. To achieve the maximum light transmission between the fiber catheter and the sampling cable, we applied a thin layer ($\sim$100 μm thick) of index matching gel (G608N3, Thorlabs) at the junction part. Signal acquisition was performed for about 5 min in each measurement section for analysis.

The OCT signal is presented in gray scale images each of which consists of 1000 A-scan signals aligned in x-axis (see **Figure 4** left panels). Depth-scan profile is plotted by taking an average of 1000 A-scans (see **Figure 4** right panels). For quantification of OCT signals, we calculated the light attenuation factor of the sampled tissue by analysing A-scan signals. The light attenuation factor was defined as the ratio of detected light intensity decline in depth (mm). It is proportional but not equal to the tissue attenuation coefficient which is one of the essential tissue optical properties reflecting the tissue composition and density. A change in attenuation factor implies alterations in tissue properties, such as cell density, cell orientation, predominate cell type and hence backscatter ability. Attenuation factor is calculated as the slope value of the linear fit for the log intensity of the linear portion depth in an A-scan plot (see the red lines on plots in **Figure 4**).

2.6. HISTOLOGY AND IMMUNOSTAINING

Rats were terminated by administering Ketamine and Xylazine mixture intraperitonealy. The brains were removed immediately after decapitation, fixed in 4% paraformaldehyde (PFA) in PBS for 4 days, and then incubated in 30% sucrose in PBS for at least 2 days. During the brain removal procedure, the flexible microelectrode and the OCT fiber probe were carefully cut from their skull-tethered part and were PFA fixed within the brain. Prior to sectioning, the OCT fiber probe was explanted from the brain while the flexible microelectrode was kept *in situ* in the brain. Brains were then embedded in Tissue-Tek O.C.T. (Sakura Finetek,

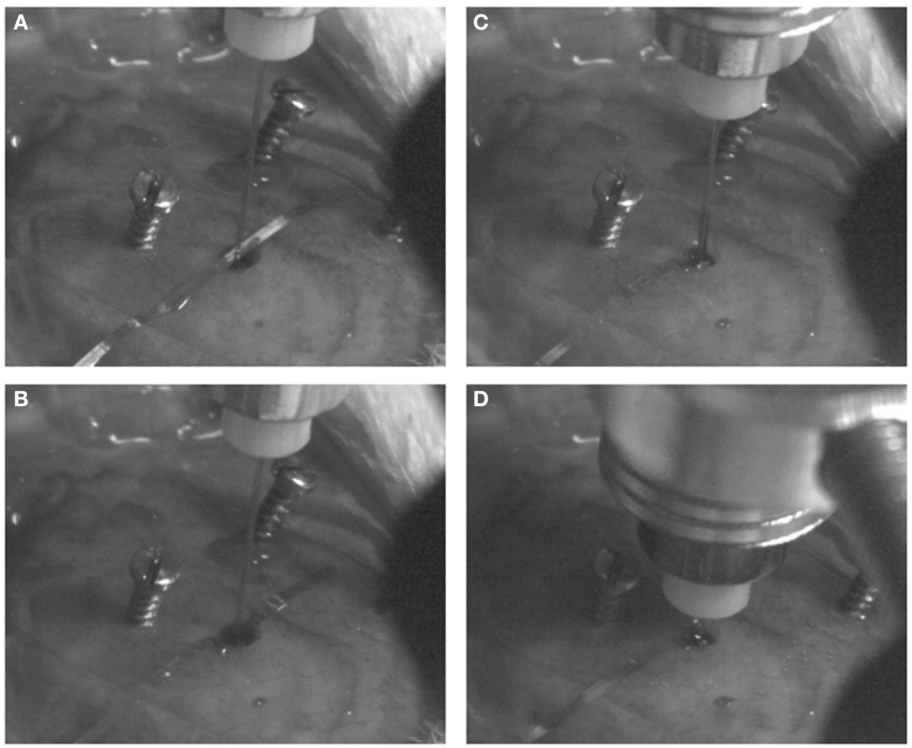

FIGURE 3 | Probe implantation procedures. The flexible microelectrode and fiber catheter are precisely aligned above the burr hole **(A)**. The fiber catheter is slowly and cautiously driven down to push the shank of the flexible mciroelectrode into the brain **(B,C)** until the desired depth is reached **(D)**.

Germany) at −20°C. 20 μm thick transversal or coronal slices were obtained with a cryostat-microtome at −20°C.

Brain slices were double-immunostained for GFAP (glial fibrillary acidic protein) to detect astrocytes and Iba1 (ionized calcium-binding adapter molecule (1) to identify microglia/macrophages. Brain slices were incubated in 10% goat serum to block non-specific binding, then incubated in GFAP antibody (1:1000 dilution, rabbit IgG, Millipore) and Iba1 antibody (1:500 dilution, Goat IgG, Abcam) for 3 h. After 3 rinses in PBS (5 min each), fluorescence-labeled secondary antibodies AlexaFluro 488 anti-rabbit and AlexaFluro 647 anti-goat were applied for 1 h. Both secondary antibodies (Molecular Probes) were used in 1: 1000 dilution. After 3 rinses in PBS (5 min each), brain slices were mounted onto the microscopic slides with Dapi-Fluoromount-G (Southern Biotech) and then covered with a coverslip. Slice images were collected with Jenoptik camera mounted on a Zeiss microscope (Zeiss Imager a1), using the identical exposure time for each immunolabel at each magnification.

3. RESULTS

3.1. OCT SIGNALS FROM THE TISSUE AROUND THE INDWELLING FIBER CATHETER

During 6 weeks after the implantation, the intensity of the OCT signal increased from 60 to 70 dB (**Figures 4A–C**). From week 6 to week 12, the OCT signal intensity didn't demonstrate noticeable change (**Figures 4C,D**). Some sparsely distributed microscopic structures could be identified close to the fiber catheter 1 week post operation, having the shape of as several horizontal stripe patterns and appear in the A-scan signal as multiple peaks (**Figure 4A**). At week 6, a 200 μm thick layer of tissue with high backscattering signal had developed around the fiber catheter (**Figure 4C**). This high reflecting tissue layer developed into a prominent feature in the OCT image at week 12, with a smooth A-scan plot profile (**Figure 4D**). At week 6 and 12, the OCT signal attenuated faster featuring a steep declining slope in the A-scan plot while the backscattering intensity from the tissue surrounding the fiber probe stayed steady at 70 dB (see **Figures 4C,D**). To further characterize the OCT signal, the attenuation factor of 4 animals on each measurement were calculated and presented in **Figure 5**. In general, the attenuation factor evidently raised during the first 3 weeks after the implantation, implying that a compact dense tissue layer was developing during this period. Then the attenuation factor stabilized at 6 weeks and 12 weeks post implantation.

3.2. OCT SIGNALS OF THE INDWELLING FLEXIBLE MICROELECTRODE

At week 1 post implantation, the signal from the flexible probe was evidently visible in the A-scan signal located at 2.3 mm underneath the OCT fiber catheter tip. The maximum backscattering intensity of the OCT signal at week 1 post implantation (p.i.) is about 59 dB, while the backscattering intensity from the flexible electrode is approximately 35 dB presenting a a clearly visible peak (**Figure 6A**). Since before it reached the flexible probe the incident

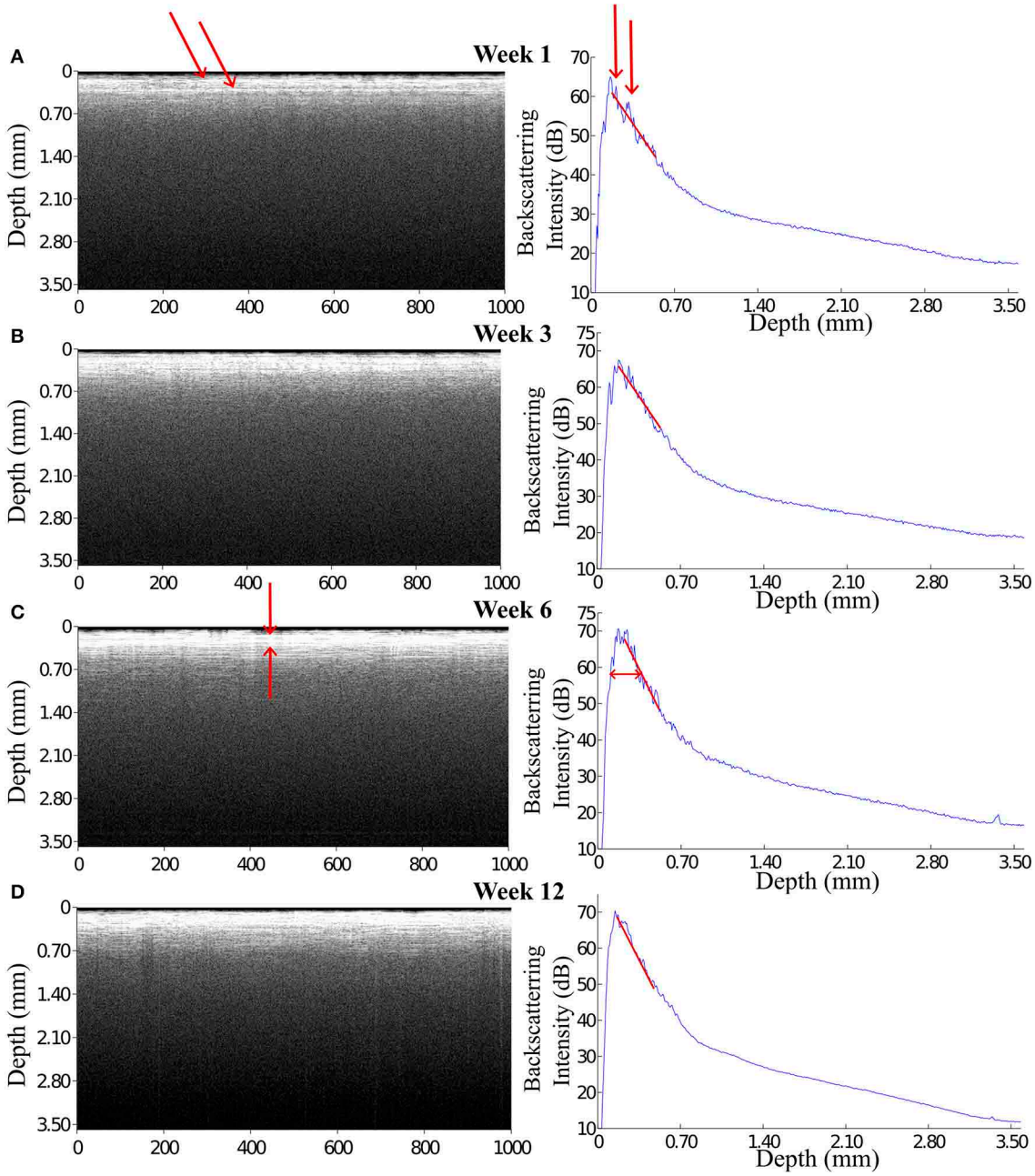

FIGURE 4 | OCT images and the corresponding A-scan profiles acquired at week 1, 3, 6, and 12 after implantation. The intensity of the backscattered light increased during the first 3 weeks post implantation **(A,B)**, while at week 6 and 12 the OCT signal attenuated faster featuring a steep declining slope in the A-scan plot **(C,D)**. Arrows in panel **(A)** indicate the anatomic micro structures viewed by the OCT. Arrows in panel **(C)** indicate a 200 μm thick layer is expressed in the OCT signal.

light was presumably scattered and attenuated by the ongoing scar formation around the glass fiber catheter, the backscattered signal from the flexible electrode dwindled in the following weeks (**Figures 6B,C**). Although the incident light attenuated predominantly in the tissue around the fiber presumably the scar sheath, the flexible electrode was still visible in the OCT scan demonstrating as a noticeable peak in the A-scan plot.

Although the signal of the flexible electrode was expected to diminish due to the strong light scattering in the compact glial sheath around the rigid fiber catheter, we observed in one case that the signal of the flexible electrode reappeared at 6 weeks p.i. (**Figure 7**). This very flexible probe was not visible after the first week, presumably as a result of the incorrect alignment of the flexible electrode and the fiber catheter upon implantation (**Figure 7A**). At week 2 p.i. in addition to the two-layer structure formation at the depth position of around 0.60 mm in the OCT image, a small peak was observed in the A-scan plot at the depth position of 2.70 mm (**Figure 7B**). At week 6 p.i. a pronounced

signal at the depth position of 2.70 mm was detected and visible both in the OCT image and the A-scan plot (**Figure 7C**). We assume, that the high intensity signal that reappeared at the image depth of 2.70 mm at 6 weeks p.i. is originating from the flexible electrode. Since this polyimide-based electrode features much lower elastic modulus compared to the conventional metal microelectrode with similar dimensions, the flexible electrode is supposedly able to float with the brain tissue (Jensen et al., 2007). Therefore, during the 6 weeks the flexible electrode's position in the brain might alter and move back to the detection area of the OCT fiber catheter eliciting the high intensity peak in OCT signal.

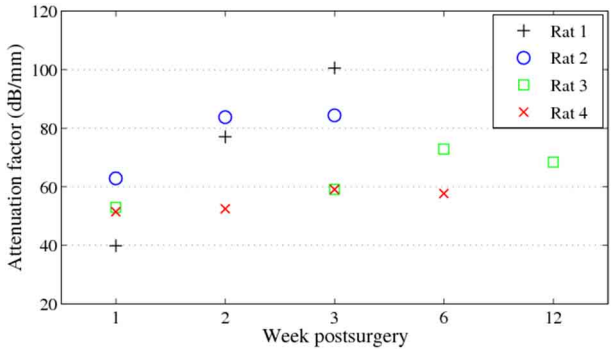

FIGURE 5 | Attenuation factors of the brain tissue around the fiber catheter at week 1, 2, 3, 6, and 12.

3.3. IMMUNOREACTIVITY OF GFAP POSITIVE CELLS AND IBA-1 POSITIVE CELLS AROUND THE INSERTION TRAJECTORY

The reactivity of GFAP-positive cells are widely used to characterize astrocytes star-shaped cell body (Schiffer et al., 1993; Faulkner et al., 2004; Sofroniew, 2005). At week 1, GFAP-positive cells are loosely distributed in an area up to 500 μm from the insertion cavity. A thin layer of the aligned GFAP-positive cells was observed surrounding the insertion channel. At week 3, GFAP-positive cells proliferated and spread to further areas up to 700 μm from the insertion edge with enhanced fluorescence intensity. At week 6, the fluorescence of GFAP-positive cells in the far area appeared reduced. Instead, a layer GFAP-positive cells

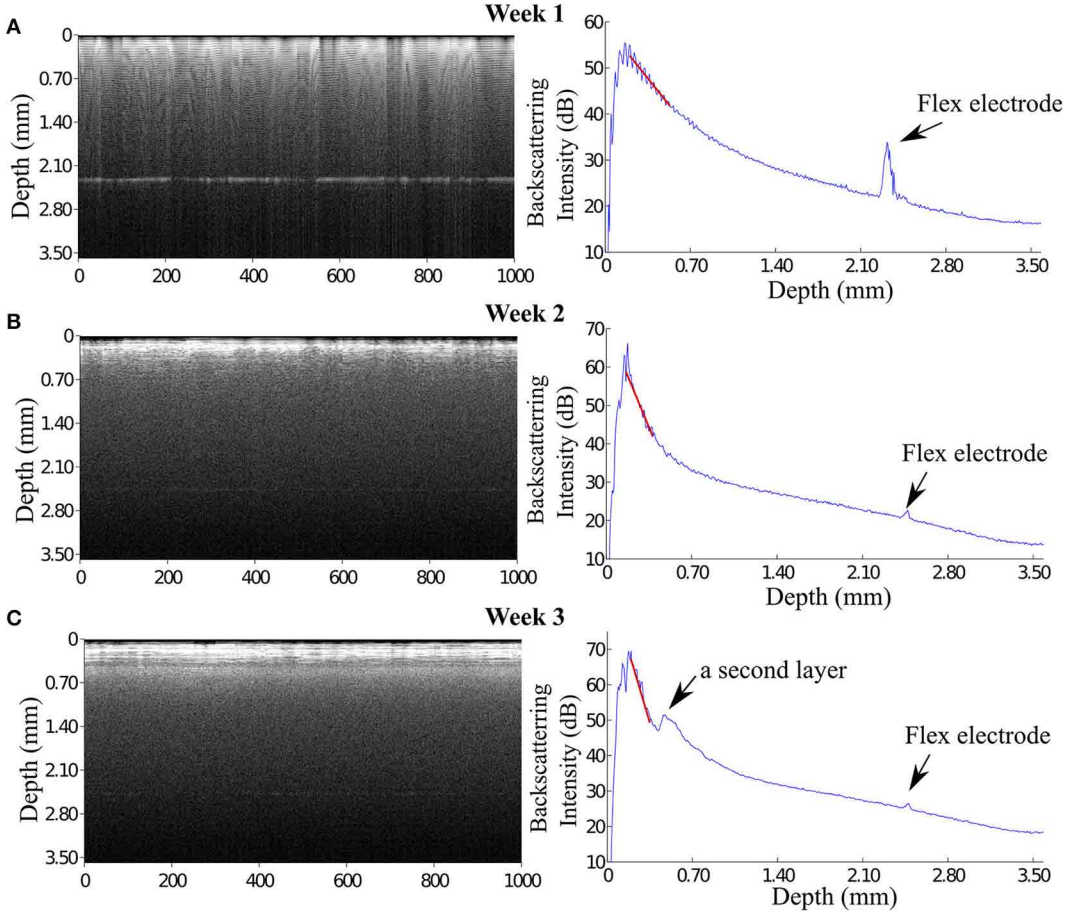

FIGURE 6 | OCT images reveal that the signal of flexible microelectrode underneath the fiber catheter declined. (A) At 1 week, the flexible electrode can be seen distinctly in the OCT image with a approximately 12 dB peak height in the A-scan plot. **(B)** In contrast to the enhanced OCT signal of the brain tissue, the signal of the flexible electrode severely declined. **(C)** Interestingly, at 3 weeks p.i. the OCT image illustrates 2 distinguishable tissue layers. The backscattering intensity of the flexible electrode remains noticeable.

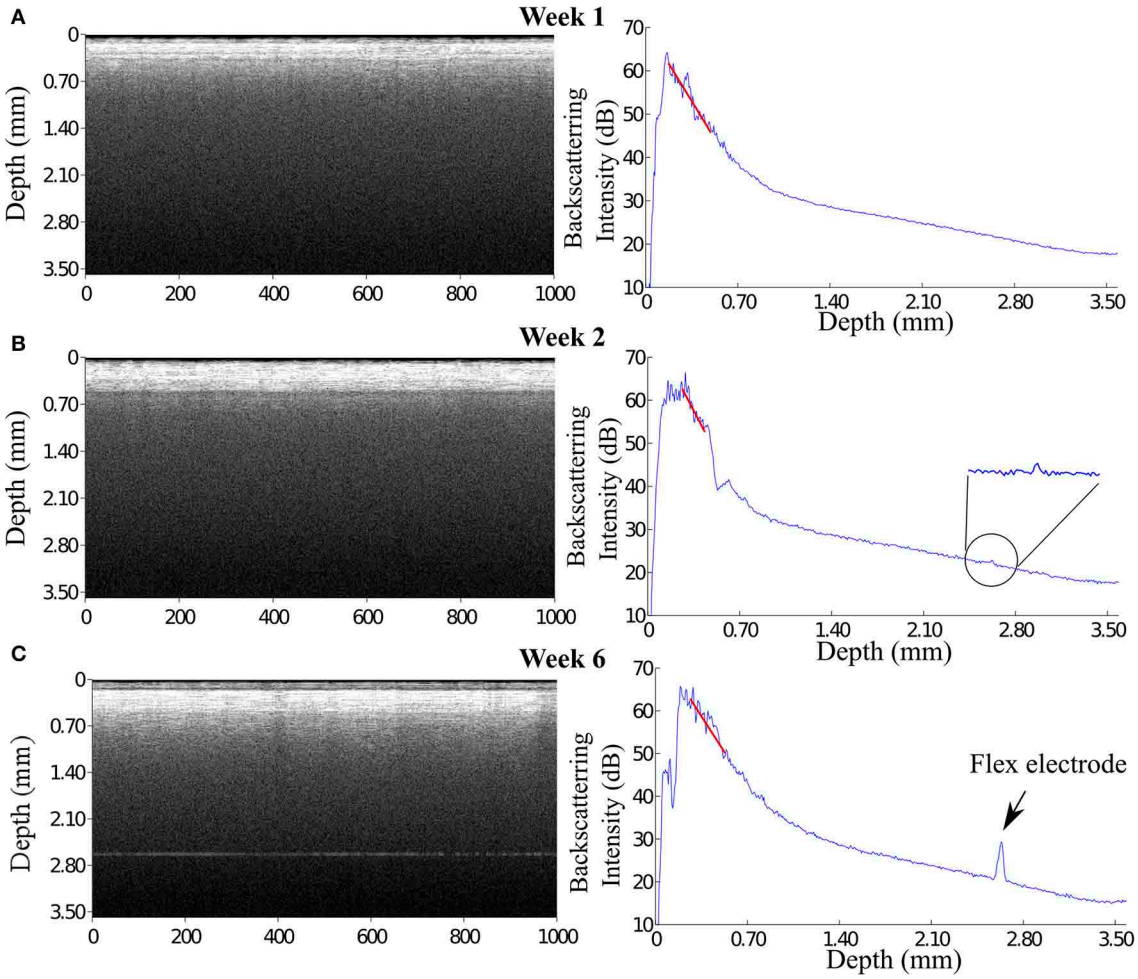

FIGURE 7 | (A) At 1 week, the flexible electrode can not be seen in the OCT image probably because of a misalignment between the flexible electrode and the fiber catheter. **(B)** At 2 weeks, a small but noticeable peak appears in the A-scan plot at the depth position of 2.70 mm. **(C)** At 6 weeks, a pronounced signal is revealed both in the OCT image and in the A-scan plot, presumably, from the flexible electrode.

with high fluorescence intensity encapsulated the insertion site (**Figure 8**).

We assessed the inflammatory process during the experiment by analyzing the expression of the ionized calcium binding adaptor molecule (Iba-1), a marker for both resting and reactive microglia and macrophages (Ito et al., 1998). At 1, 3, 6 weeks, the Iba-1 expression was only found in the close area of the insertion site not in the extended surrounding area (**Figure 8**). The apparent distribution of fluorescence intensity and the number of the Iba-1 positive cells didn't demonstrate any significant changes over time.

4. DISCUSSION

The goal of this study is to introduce a new method to monitor and assess the scarring process around a chronically implanted glass fiber catheter and a synchronously implanted flexible polyimide-based microelectrode by using an OCT imaging system (catheter type, $\varnothing 125\,\mu$m). OCT signals were acquired weekly for 12 weeks after implantation even though no technical obstacles prohibit continuous monitoring. The results corroborate that SDOCT with an *in situ* implanted fiber catheter is capable of visualizing the modification in optical properties of the surrounding tissue over time. During the first 3 weeks after implantation, the intensity of the backscattered light, hence the OCT signal of the surrounding tissue increases monotonically. The intensity levels off at 6 weeks after implantation. The increased backscattering intensity from the surrounding tissue is most likely caused by the increased accumulation of astrocytes around the glass fiber itself, which is referred in literature as glial encapsulation (Leach et al., 2010). The analyzed tissue optical property "attenuation factor" demonstrates that a compact dense tissue sheath has been developing during the 6 weeks after implantation. Since we've obtained the attenuation factor of control brain tissue from a previous study, we are able to compare the current result to naive control tissue (**Figure 9**). Besides, it is promising that within the proposed novel monitoring modality (1) the 10 μm thick flexible probe is still visible up to 2.7 mm away from the fiber tip, (2) alteration in tissue anatomical structure is noticeable in OCT A-scans, such as the two-layered structure that developed from week 3 on in (**Figure 6**).

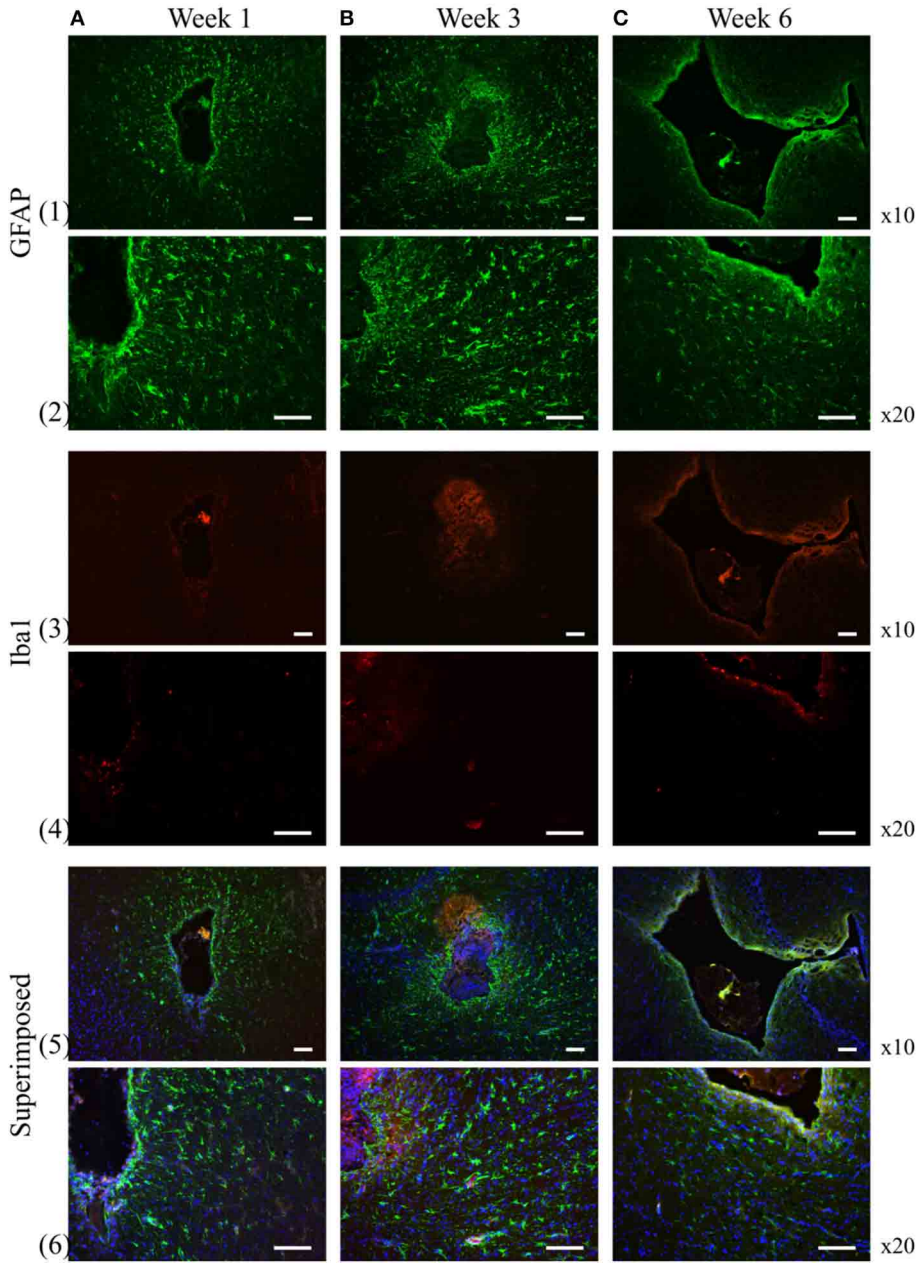

FIGURE 8 | GFAP and Iba-1 reactivity to the chronically implanted fiber catheter and flexible electrode assembly at week 1, 3, and 6, respectively. At week 1 and 3 the GFAP positive cells spread to larger area around the insertion trajectory **(1A,B, 2A,B)**, while at week 6 the GFAP positive cells become less pronounced in the extended surrounding area, instead they construct a compact layer next to the electrode and fiber **(1C, 2C)**. Iba-1 positive cells are much smaller numbers than the GFAP positive cells at all time points **(3A–C, 4A–C)**. No obvious proliferation of the Iba-1 positive cells are observed over time. Row 5 and 6 are the superimposed pictures of GFAP (green), Iba-1 (red) and DAPI (blue) staining. Scale bar = 100 μm.

Since the OCT fiber cannula itself is recognized as a foreign body by the brain tissue, the incident light is scattered and attenuated already at the compact astrocyte sheath around the fiber tip, resulting in a deteriorated detection of the flexible probe, but at the same time providing positive control of immune response. This shortcoming could be overcome by using a probe assembly which consists of a waveguide (for OCT acquisition) that is integrated to a flexible polyimide probe (for electrophysiology acquisition) to gain "inside-out" views of the developing gliosis while maintaining the probe's flexibility.

Still, it must be noted, that the flexible probe remained visible even at distances greater than 1 mm without revealing a change in tissue optical properties. It is a matter for ongoing investigations, whether the flexible probe was indeed not covered by a detectable glial sheath as independent immunocytochemistry results suggest (unpublished data) or whether an existing sheath

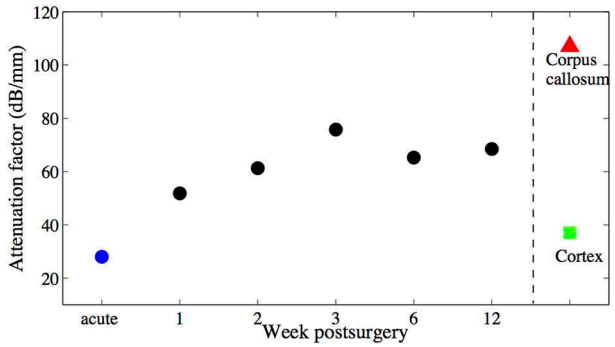

FIGURE 9 | Averaged attenuation factors of the brain tissue around the fiber catheter at week 1, 2, 3, 6, and 12 are marked with black ●, attenuation factor obtained from acute experiment is marked with blue ●. Attenuation factors of other brain tissue types obtained also in acute experiments (Xie et al., 2013) are marked with △ and □ respectively. No error bars are shown, due to the littel number of animals used.

did not sufficiently backscatter for detection. In any ways, to the best of our knowledge, the presented method appears to be the first optical attempt to monitor brain's immune response on deep implants without prior markers *in vivo*.

ACKNOWLEDGMENT

This work was supported by BrainLinks-BrainTools Cluster of Excellence funded by the German Research Foundation (DFG, grant number EXC 1086).

REFERENCES

Biran, R., Martin, D. C., and Tresco, P. A. (2005). Neuronal cell loss accompanies the brain tissue response to chronically implanted silicon microelectrode arrays. *Exp. Neurol.* 195, 115–126. doi: 10.1016/j.expneurol.2005.04.020

Block, M. L., Zecca, L., and Hong, J.-S. (2007). Microglia-mediated neurotoxicity: uncovering the molecular mechanisms. *Nat. Rev. Neurosci.* 8, 57–69. doi: 10.1038/nrn2038

Böhringer, H., Boller, D., Leppert, J., Knopp, U., Lankenau, E., Reusche, E., et al. (2006). Time-domain and spectral-domain optical coherence tomography in the analysis of brain tumor tissue. *Lasers Surg. Med.* 38, 588–597. doi: 10.1002/lsm.20353

Bonin, T., Franke, G., Hagen-Eggert, M., Koch, P., and Hüttmann, G. (2010). *In vivo* fourier-domain full-field oct of the human retina with 1.5 million a-lines/s. *Opt. Lett.* 35, 3432–3434. doi: 10.1364/OL.35.003432

Drexler, W., Morgner, U., Ghanta, R. K., Kartner, F. X., Schuman, J. S., and Fujimoto, J. G. (2001). Ultrahigh-resolution ophthalmic optical coherence tomography. *Nat. Med.* 7, 502–507. doi: 10.1038/86589

Edell, D., Toi, V., McNeil, V., and Clark, L. (1992). Factors influencing the biocompatibility of insertable silicon microshafts in cerebral cortex. *Biomed. Eng. IEEE Trans.* 39, 635–643. doi: 10.1109/10.141202

Faulkner, J. R., Herrmann, J. E., Woo, M. J., Tansey, K. E., Doan, N. B., and Sofroniew, M. V. (2004). Reactive astrocytes protect tissue and preserve function after spinal cord injury. *J. Neurosci.* 24, 2143–2155. doi: 10.1523/JNEUROSCI.3547-03.2004

Fercher, A., Hitzenberger, C., Kamp, G., and El-Zaiat, S. (1995). Measurement of intraocular distances by backscattering spectral interferometry. *Opt. Commun.* 117, 43–48. doi: 10.1016/0030-4018(95)00119-S

Hee, M. R., Baumal, C. R., Puliafito, C. A., Duker, J. S., Reichel, E., Wilkins, J. R., et al. (1996). Optical coherence tomography of age-related macular degeneration and choroidal neovascularization. *Ophthalmology* 103, 1260–1270. doi: 10.1016/S0161-6420(96)30512-5

Huang, D., Swanson, E., Lin, C., Schuman, J., Stinson, W., Chang, W., et al. (1991). Optical coherence tomography. *Science* 254, 1178–1181. doi: 10.1126/science.1957169

Ito, D., Imai, Y., Ohsawa, K., Nakajima, K., Fukuuchi, Y., and Kohsaka, S. (1998). Microglia-specific localisation of a novel calcium binding protein, Iba1. *Brain Res. Mol. Brain Res.* 57, 1–9. doi: 10.1016/S0169-328X(98)00040-0

Jensen, W., Yoshida, K., and Hofmann, U. (2007). "*In vivo* implant mechanics of single-shaft microelectrodes in peripheral nervous tissue," in *Neural Engineering, 2007. CNE '07. 3rd International IEEE/EMBS Conference on* (Hawaii).

Kozai, T. D. Y., Vazquez, A. L., Weaver, C. L., Kim, S.-G., and Cui, X. T. (2012). *In vivo* two-photon microscopy reveals immediate microglial reaction to implantation of microelectrode through extension of processes. *J. Neural Eng.* 9:066001. doi: 10.1088/1741-2560/9/6/066001

Leach, J. B., Achyuta, A. K. H., and Murthy, S. K. (2010). Bridging the divide between neuroprosthetic design, tissue engineering and neurobiology. *Front. Neuroeng.* 2:18. doi: 10.3389/neuro.16.018.2009

Ludwig, K. A., Uram, J. D., Yang, J., Martin, D. C., and Kipke, D. R. (2006). Chronic neural recordings using silicon microelectrode arrays electrochemically deposited with a poly(3,4-ethylenedioxythiophene) (PEDOT) film. *J. Neural Eng.* 3, 59–70. doi: 10.1088/1741-2560/3/1/007

Mcconnell, G. C., Butera, R. J., and Bellamkonda, R. V. (2009). Bioimpedance modeling to monitor astrocytic response to chronically. *J. Neural Eng.* 6:055005. doi: 10.1088/1741-2560/6/5/055005

Polikov, V. S., Tresco, P. A., and Reichert, W. M. (2005). Response of brain tissue to chronically implanted neural electrodes. *J. Neurosci. Methods* 148, 1–18. doi: 10.1016/j.jneumeth.2005.08.015

Potter, K. A., Buck, A. C., Self, W. K., and Capadona, J. R. (2012). Stab injury and device implantation within the brain results in inversely multiphasic neuroinflammatory and neurodegenerative responses. *J. Neural Eng.* 9:046020. doi: 10.1088/1741-2560/9/4/046020

Raspopovic, S., Capogrosso, M., Petrini, F. M., Bonizzato, M., Rigosa, J., Di Pino, G., et al. (2014). Restoring natural sensory feedback in real-time bidirectional hand prostheses. *Sci. Trans. Med.* 6, 222ra19. doi: 10.1126/scitranslmed.3006820

Richter, A., Xie, Y., Schumacher, A., Loeffler, S., Kirch, R., Al-Hasani, J., et al. (2013). A simple implantation method for flexible, multisite microelectrodes into rat brains. *Front. Neuroeng.* 6:6. doi: 10.3389/fneng.2013.00006

Rodriguez-Padilla, J. A., Hedges, T. R. III, Monson, B., Srinivasan, V., Wojtkowski, M., Reichel, E., et al. (2007). High-speed ultra–high-resolution optical coherence tomography findings in hydroxychloroquine retinopathy. *Arch. Ophthalmol.* 125, 775–780. doi: 10.1001/archopht.125.6.775

Rubehn, B., and Stieglitz, T. (2010). *In vitro* evaluation of the long-term stability of polyimide as a material for neural implants. *Biomaterials* 31, 3449–3458. doi: 10.1016/j.biomaterials.2010.01.053

Schiffer, D., Giordana, M. T., Cavalla, P., Vigliani, M. C., and Attanasio, A. (1993). Immunohistochemistry of glial reaction after injury in the rat: double stainings and markers of cell proliferation. *Int. J. Dev. Neurosci.* 11, 269–280. doi: 10.1016/0736-5748(93)90085-R

Schmidt, S., Horch, K., and Normann, R. (1993). Biocompatibility of silicon-based electrode arrays implanted in feline cortical tissue. *J. Biomed. Mater. Res.* 27, 1393–1399. doi: 10.1002/jbm.820271106

Sofroniew, M. V. (2005). Reactive astrocytes in neural repair and protection. *Neuroscientist* 11, 400–407. doi: 10.1177/1073858405278321

Sohal, H. S., Jackson, A., Jackson, R., Clowry, G. J., Vaisilevskiy, K., O'Neill, A., et al. (2014). The sinusoidal probe: a new approach to improve electrode longevity. *Front. Neuroeng.* 7:10. doi: 10.3389/fneng.2014.00010

Stieglitz, T., Rubehn, B., Henle, C., Kisban, S., Herwik, S., Ruther, P., et al. (2009). "Brain–computer interfaces: an overview of the hardware to record neural signals from the cortex," in *Neurotherapy: Progress in Restorative Neuroscience and Neurology, Vol. 175 of Progress in Brain Research*, eds E. M. H. Joost Verhaagen and D. F. Swaab (Oxford, UK: Elsevier), 297–315.

Szarowski, D. H., Andersen, M. D., Retterer, S., Spence, A. J., Isaacson, M., Craighead, H. G., et al. (2003). Brain responses to micro-machined silicon devices. *Brain Res.* 983, 23–35. doi: 10.1016/S0006-8993(03)03023-3

Tearney, G. J., Brezinski, M. E., Bouma, B. E., Boppart, S. A., Pitris, C., Southern, J. F., et al. (1997). *In vivo* endoscopic optical biopsy with optical coherence tomography. *Science* 276, 2037–2039. doi: 10.1126/science.276.5321.2037

Tronnier, V. M., and Fogel, W. (2000). Pallidal stimulation for generalized dystonia. *J. Neurosurg.* 92, 453–456. doi: 10.3171/jns.2000.92.3.0453

Turner, J., Shain, W., Szarowski, D., Andersen, M., Martins, S., Isaacson, M., et al. (1999). Cerebral astrocyte response to micromachined silicon implants. *Exp. Neurol.* 156, 33–49. doi: 10.1006/exnr.1998.6983

Winslow, B. D., Christensen, M. B., Yang, W.-K., Solzbacher, F., and Tresco, P. A. (2010). A comparison of the tissue response to chronically implanted Parylene-C-coated and uncoated planar silicon microelectrode arrays in rat cortex. *Biomaterials* 31, 9163–9172. doi: 10.1016/j.biomaterials.2010.05.050

Xie, Y., Bonin, T., Löffler, S., Hüttmann, G., Tronnier, V., and Hofmann, U. G. (2013). Coronal *in vivo* forward-imaging of rat brain morphology with an ultra-small optical coherence tomography fiber probe. *Phys. Med. Biol.* 58, 555–568. doi: 10.1088/0031-9155/58/3/555

Conflict of Interest Statement: The authors declare that the research was conducted in the absence of any commercial or financial relationships that could be construed as a potential conflict of interest.

Received: 30 April 2014; accepted: 05 August 2014; published online: 21 August 2014.
*Citation: Xie Y, Martini N, Hassler C, Kirch RD, Stieglitz T, Seifert A and Hofmann UG (2014) In vivo monitoring of glial scar proliferation on chronically implanted neural electrodes by fiber optical coherence tomography. Front. Neuroeng. **7**:34. doi: 10.3389/fneng.2014.00034*
This article was submitted to the journal Frontiers in Neuroengineering.

frontiers in
NEUROENGINEERING

ORIGINAL RESEARCH ARTICLE
published: 08 July 2014
doi: 10.3389/fneng.2014.00023

Tracking single units in chronic, large scale, neural recordings for brain machine interface applications

Ahmed Eleryan[1], Mukta Vaidya[2], Joshua Southerland[3], Islam S. Badreldin[1], Karthikeyan Balasubramanian[2], Andrew H. Fagg[3], Nicholas Hatsopoulos[2] and Karim Oweiss[1,4,5]*

[1] *Department of Electrical and Computer Engineering, Michigan State University, East Lansing, MI, USA*
[2] *Department of Organismal Biology and Anatomy, Committee of Computational Neuroscience, University of Chicago, Chicago, IL, USA*
[3] *Department of Computer Science and Bioengineering, University of Oklahoma, Norman, OK, USA*
[4] *Neuroscience Program, Michigan State University, East Lansing, MI, USA*
[5] *Cognitive Science Program, Michigan State University, East Lansing, MI, USA*

Edited by:
Ulrich G. Hofmann, Albert-Ludwigs-University Freiburg, Germany

Reviewed by:
John M. Beggs, Indiana University, USA
Samuel George Ewing, Dresden University of Technology, Germany

***Correspondence:**
Karim Oweiss, Neural Systems Engineering Laboratory, Electrical and Computer Engineering Department, Michigan State University, 428 S. Shaw lane, East Lansing, MI 48824, USA
e-mail: kowiess@msu.edu

In the study of population coding in neurobiological systems, tracking unit identity may be critical to assess possible changes in the coding properties of neuronal constituents over prolonged periods of time. Ensuring unit stability is even more critical for reliable neural decoding of motor variables in intra-cortically controlled brain-machine interfaces (BMIs). Variability in intrinsic spike patterns, tuning characteristics, and single-unit identity over chronic use is a major challenge to maintaining this stability, requiring frequent daily calibration of neural decoders in BMI sessions by an experienced human operator. Here, we report on a unit-stability tracking algorithm that efficiently and autonomously identifies putative single-units that are stable across many sessions using a relatively short duration recording interval at the start of each session. The algorithm first builds a database of features extracted from units' average spike waveforms and firing patterns across many days of recording. It then uses these features to decide whether spike occurrences on the same channel on one day belong to the same unit recorded on another day or not. We assessed the overall performance of the algorithm for different choices of features and classifiers trained using human expert judgment, and quantified it as a function of accuracy and execution time. Overall, we found a trade-off between accuracy and execution time with increasing data volumes from chronically implanted rhesus macaques, with an average of 12 s processing time per channel at ∼90% classification accuracy. Furthermore, 77% of the resulting putative single-units matched those tracked by human experts. These results demonstrate that over the span of a few months of recordings, automated unit tracking can be performed with high accuracy and used to streamline the calibration phase during BMI sessions. Our findings may be useful to the study of population coding during learning, and to improve the reliability of BMI systems and accelerate their deployment in clinical applications.

Keywords: single-units, stability, BMI, waveforms distance, ISIH distance

1. INTRODUCTION

Invasive Brain Machine Interfaces (BMIs) for neuro-motor prosthetics rely on neural signals recorded using chronically implanted microelectrodes to actuate external devices (Serruya et al., 2002; Kim et al., 2008; Velliste et al., 2008; Suminski et al., 2010; Hochberg et al., 2012). In this setting, signal and information stability play a crucial role in maintaining a clinically viable BMI that subjects can use routinely in their home environment. Recent evidence suggest that within-day fluctuations in action potential amplitude and inter-spike intervals recorded with microelectrode arrays implanted in humans could result in a directional "bias" in the decoded neural activity used to actuate an artificial device; and this results in suboptimal performance (Perge et al., 2013). Other studies have shown that when subjects are repeatedly exposed to a neural decoder presumably driven by the same population across days, they build a stable map of cortical responses that "fit" that particular decoder (Ganguly and Carmena, 2009, 2010; Koyama et al., 2010). As such, a fixed decoder model paired with stable neural inputs may permit the consolidation of the motor memory of that particular decoder during BMI practice. Stability of neural recordings with penetrating microelectrodes, however, is hard to maintain due to biotic and abiotic factors beyond the experimenter's control (Karumbaiah et al., 2013). As such, state of the art BMIs lack reliability and require human operators to frequently identify units and to train new decoders on a daily basis- a process that can be viewed as *interference* to motor-memory consolidation, which diminishes the ability to retain motor skills and reduces BMI robustness.

The standard approach to mitigate this instability is to rely on a human operator to ascertain that units intermittently recorded on previous days remain the same on the current day *before* the start of a BMI session. When changes do occur, the operator has to select new populations and perhaps train a new decoder by collecting a few minutes of neural data while subjects are asked to imagine or attempt limb movements, or observe these movements from previous training sessions (Hochberg et al., 2012; Homer et al., 2013). A fast, automatic, and efficient approach to assess stability of these putative single-units at the start of every session would be highly desirable to streamline the calibration phase without much intervention from the human operator and without imposing additional cognitive load on the subject. It could also be beneficial in basic neuroscience investigations of learning and memory formation at the population level (Buzsáki, 2004).

In this study, we propose a fast and accurate algorithm to assess unit stability across days with minimal human expert intervention. We tested the performance of this algorithm on data collected using fixed silicon microelectrode arrays chronically implanted in primary motor cortex (M1) of Rhesus Macaques (*Macaca mulatta*) over many months. The performance was benchmarked against that of human experts who manually labeled the data to provide practical ground truth.

2. MATERIALS AND METHODS

2.1. ALGORITHM OVERVIEW

An overview of the algorithm steps is shown in **Figure 1**. The algorithm first builds a database of profiles of putative single-units recorded across a multi-day interval set by the user. Each putative single-unit profile (hereafter referred to as a profile for simplicity) consists of a collection of spike occurrences from this putative single-unit on each day. Such collection contains user-defined information extracted from the single-unit activity, such as average waveform, spike timestamps, inter-spike interval histogram (ISIH), firing rate, etc.

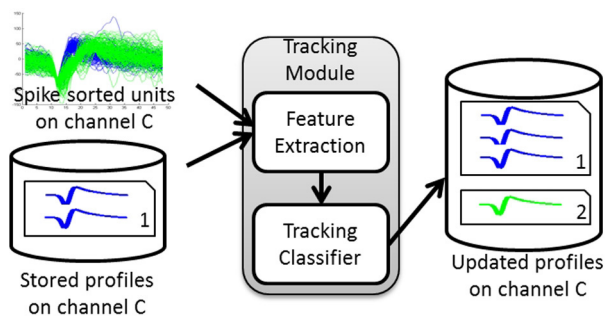

FIGURE 1 | Tracking Algorithm overview. The tracking module takes as input the spike-sorted single unit discharge patterns and the stored profiles for a given channel and calculates the dissimilarity between these units' features and the stored profiles. It then assigns each unit to either an existing profile or a new profile based on the dissimilarity computed. The output is the updated set of profiles for that channel.

The tracking module has two main blocks: (1) feature extraction and (2) tracking classifier. The inputs to the tracking module are the spike-sorted waveforms recorded on any given channel. The module extracts features from these inputs, retrieves the stored single-unit profiles for each channel, and finds the pairwise dissimilarities between the input features and those in the stored profiles. The dissimilarity vectors are then passed to the tracking classifier that makes decisions on whether to add an input unit to an existing profile (match) or to create a new profile (non-match). The output of the tracking module is then a set of updated profiles for each recording channel.

2.2. SINGLE-UNIT WAVEFORM CHARACTERISTICS

We selected four features to extract from each average spike waveform in a unit's profile. We also selected four dissimilarity measures to quantify the difference between features from two average spike waveforms, $\overline{W}_x$ and $\overline{W}_y$, recorded from putative single-units "x" and "y" on the same channel on different days. The average waveform for unit x, $\overline{W}_x$, is calculated as:

$$\overline{W}_x = \left[\sum_{i=1}^{l} \frac{W_x^i(1)}{l} \cdots \sum_{i=1}^{l} \frac{W_x^i(m)}{l} \right], \quad (1)$$

where l is the number of sample waveforms assigned to a single unit x during spike sorting, and m is the number of samples in the waveform.

Table 1 lists the chosen measures and the waveform features that each of these measures relies upon to compute the dissimilarity.

Pearson correlation coefficient (PC) (Nikolić et al., 2012) was used to compare the shape similarity of the waveforms. The **normalized peak-to-peak height difference** (PH) was used to quantify the difference in the amplitude of the two waveforms and to normalize it to the amplitude of one of them as:

$$PH\left(\overline{W}_x, \overline{W}_y\right) = \left| \frac{\left(\max\left(\overline{W}_y\right) - \min\left(\overline{W}_y\right)\right) - \left(\max\left(\overline{W}_x\right) - \min\left(\overline{W}_x\right)\right)}{\left(\max\left(\overline{W}_y\right) - \min\left(\overline{W}_y\right)\right)} \right|, \quad (2)$$

where max and min are the waveform maximum and minimum values, respectively. Therefore, a difference between the peak-to-peak values of two high-amplitude units would result in a smaller PH value than if the same difference was calculated between two low-amplitude units. This is desirable in order to reflect that a

Table 1 | Waveform-derived dissimilarity measures.

Dissimilarity measure	Feature
Correlation coefficient	Waveform shape
Normalized peak-to-peak height difference	Amplitude
Normalized peak-to-peak time difference	Transition time between minimum and maximum peaks
Peak matching	Peaks shape

large difference between two low amplitude units indicates higher variability than the case of two high amplitude units. The **normalized peak-to-peak time difference** (PT) was used to find the difference in the transition time between the minimum and maximum peaks of the waveform and was defined as:

$$PT\left(\overline{\mathrm{W}}_x, \overline{\mathrm{W}}_y\right) = \left| \frac{\left(\underset{i}{\mathrm{argmax}}\left(\overline{\mathrm{W}}_y(i)\right) - \underset{i}{\mathrm{argmin}}\left(\overline{\mathrm{W}}_y(i)\right)\right) - \left(\underset{i}{\mathrm{argmax}}\left(\overline{\mathrm{W}}_x(i)\right) - \underset{i}{\mathrm{argmin}}\left(\overline{\mathrm{W}}_x(i)\right)\right)}{\left(\underset{i}{\mathrm{argmax}}\left(\overline{\mathrm{W}}_y(i)\right) - \underset{i}{\mathrm{argmin}}\left(\overline{\mathrm{W}}_y(i)\right)\right)} \right|, \tag{3}$$

where $\underset{i}{\mathrm{argmax}}$ and $\underset{i}{\mathrm{argmin}}$ are operators that retrieve the sample number i (i.e., time index) corresponding to the waveform maximum and minimum, respectively.

Combined with PH, we are essentially comparing the slopes of the lines joining the minimum and maximum peaks of the two waveforms. The **Peak Matching** (PM) is a measure developed by Strelkov (2008) that heuristically computes the distance between the shapes of the peaks of two signals. The algorithm finds the peaks in both signals and assigns weights to each peak. It then finds pairwise closeness factors (i.e., similarity measures) between these peaks and finally calculates the total distance as the sum of peak weights multiplied by the computed closeness factors. Details of the calculation of each entity can be found in Strelkov (2008). The symmetrized similarity between the two signals is calculated as the geometric mean of the asymmetric similarities.

2.3. SINGLE-UNIT FIRING CHARACTERISTICS

Assuming negligible change in unit recruitment properties, differences in firing patterns can be used as a metric to aid in unit stability assessment (Liu et al., 1999; Chen and Fetz, 2005). These differences can be quantified by computing the dissimilarity between normalized ISIHs H_x and H_y (i.e., empirical probability distributions of inter-spike intervals). We chose four such dissimilarity measures to assess multiple aspects of the difference between two probability distributions. **Table 2** lists the chosen measures and the criterion that each of them uses to compute the dissimilarity. The merit of each dissimilarity measure is explained below.

It should be noted that while the Kullback-Leibler Divergence (KLD) (Kullback and Leibler, 1951; Johnson and Sinanovic, 2001) calculates the total divergence between two distributions, the Kolmogorov-Smirnov Statistic (KS) (Gürel and Mehring, 2012) approximates that divergence by including the maximum difference at any point in the cumulative distributions. Both the KLD and the KS provide different perspectives when comparing two distributions. The former measure overlooks individual points and is only concerned with the total divergence across all the points, while the latter measure does not. The Bhattacharyya Distance (BD) (Bhattacharyya, 1943) quantifies the amount of overlap between the two distributions to decide how similar they are, while the Earth Mover's Distance (EMD) (Rubner et al., 1998) computes the minimum cost of converting one distribution to the other.

2.4. THE TRACKING CLASSIFIER

Given a vector of dissimilarities between the features extracted from two single units recorded on the same channel on two different days, the tracking classifier makes the binary decision of whether these two single-units represent different instances of the same single unit or not. Training a classifier requires supervision and for this purpose two sets were defined:

- **True positives** (**TP**) are vectors of dissimilarities between pairs of instances recorded from the same neuron across a number of days. They were obtained by manual tracking

Table 2 | ISIH-derived dissimilarity measures.

Dissimilarity measure	Calculation	Dissimilarity criterion
Symmetrized KL-divergence	$D(\mathrm{H}_x \| \mathrm{H}_y) = \sum_{i=1}^{I} \ln\left(\frac{\mathrm{H}_x[i]}{\mathrm{H}_y[i]}\right)\mathrm{H}_x[i]$ $D(\mathrm{H}_x, \mathrm{H}_y) = \frac{D(\mathrm{H}_x \| \mathrm{H}_y) + D(\mathrm{H}_y \| \mathrm{H}_x)}{2}$	Total information divergence
Bhattacharyya distance	$BD(\mathrm{H}_x, \mathrm{H}_y) = -\ln \sum_{i=1}^{I} \sqrt{\mathrm{H}_x[i]\mathrm{H}_y[i]}$	Amount of overlap
KS-statistic	$\mathrm{F}[i] = \sum_{k=1}^{i} \mathrm{H}[k]$ $KS(\mathrm{H}_x, \mathrm{H}_y) = \max_{i=1\ldots I} \left\|\mathrm{F}_x[i] - \mathrm{F}_y[i]\right\|$	Maximum divergence
Earth mover's distance	$EMD_0 = 0$ $EMD_{i+1} = (\mathrm{H}_x[i] + EMD_i) - \mathrm{H}_y[i]$ $EMD(\mathrm{H}_x, \mathrm{H}_y) = \sum_{i=1}^{I} \left\|EMD_i\right\|$	Cost of turning one distribution to the other

performed by two experts on the recorded data on those days.

- **True negatives (TN)** are vectors of dissimilarities between pairs of instances recorded from different neurons. They were obtained using different units recorded on the same channel on a given day. Units recorded simultaneously on the same channel on a given day are different units.

For the waveform-based classifier, true positives and true negatives were computed by comparing the average waveforms. **Figure 2** illustrates this process. The same process was applied for training classifiers that used other single-unit characteristics (e.g., ISIHs).

The input to a classifier was a vector, x, of the dissimilarities between the features extracted from two units recorded on the same channel but on different days. The length, n, of the dissimilarities vector is the number of dissimilarity measures used in the comparison. The classifiers' decision is binary, either to assign x to class 0 (c_0), which corresponds to non-matching units, or to class 1 (c_1), which corresponds to matching units. Several types of classifiers were compared in this study. The following section provides a brief summary of the classifiers used.

2.4.1. Support Vector Machine (SVM) classifier

The SVM classifier is a binary classifier that finds a high-dimensional decision plane. This plane is inferred so as to maximize the distance between the plane and the training data points of each class. The SVM model takes the form (Bishop, 2006)

$$\mathrm{y(x)} = \mathrm{w}^{\mathrm{T}}\phi(\mathrm{x}) + \mathrm{b}, \tag{4}$$

where, w defines the decision plane, x is the input dissimilarity vector, ϕ(x) is a projection of the input onto the feature space (basis function), and b is an offset term to account for any bias in the training data.

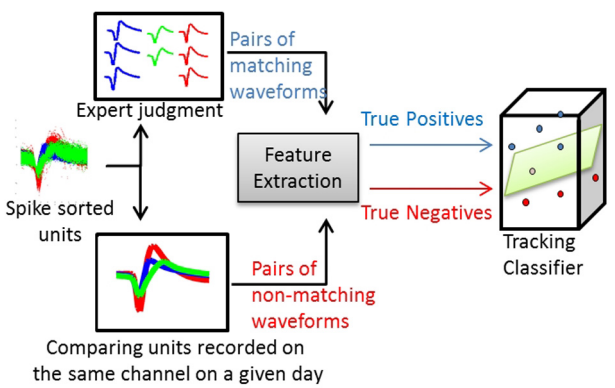

FIGURE 2 | Process of training a waveform-based classifier. Using spike-sorted units recorded across several days, human experts track the units manually and produce pairs of matching average waveforms (true positives). Using the same set of units, pairs of non-matching average waveforms are generated by comparing spike-sorted units recorded simultaneously on the same channel on a given day.

Although the SVM model in Equation (4) is linear, non-linearity can be added to the model by the use of a non-linear basis function (known as kernels) such a Gaussian radial basis function (Bishop, 2006).

2.4.2. Relevance Vector Machine (RVM) classifier

The RVM calculates the classification probability rather than the classification decision as in the case of the SVM. The model then becomes of the form (Bishop, 2006)

$$\mathrm{y(x)} = \sigma\left(\mathrm{w}^{\mathrm{T}}\phi(\mathrm{x}) + \mathrm{b}\right), \tag{5}$$

where $\sigma(.)$ is the sigmoid function.

2.4.3. Maximum A Posteriori classification (MAP)

The MAP is a probabilistic classifier and is used to estimate how likely a new point belongs to a distribution based on empirical data.

Given the dissimilarity vector between two units, $x = [x_1, \ldots, x_n]^T$, the MAP classification rule takes the form (Bishop, 2006):

$$p(x_1, \ldots, x_n|c_1)P(c_1) \underset{c_0}{\overset{c_1}{\gtrless}} p(x_1, \ldots, x_n|c_0)P(c_0), \tag{6}$$

where $p(x_1, \ldots, x_n|c_0)$ and $p(x_1, \ldots, x_n|c_1)$ are the likelihood probabilities that x belongs to c_0 and c_1, respectively, and $P(c_0)$ and $P(c_1)$ are the prior probabilities of c_0 and c_1, respectively.

The likelihood and prior probability distributions are computed from the training data, where the true positives are instances of c_1 and the true negatives are instances of c_0.

2.4.4. Naive Bayesian classification (NB)

The NB is a simple and effective probabilistic classifier that, unlike the MAP, assumes independence between features (Domingos and Pazzani, 1997). Therefore, instead of using a joint conditional probability distribution as in the case of MAP, the NB uses multiple individual conditional probability distributions to infer its decision. For a dissimilarity vector between two units, x, the NB decision is (Manning et al., 2008):

$$\prod_{i=1}^{n} p(x_i|c_1) \underset{c_0}{\overset{c_1}{\gtrless}} \prod_{i=1}^{n} p(x_i|c_0), \tag{7}$$

where $p(x_i|c_0)$ and $p(x_i|c_1)$ are the conditional probability distributions that the i^{th} feature of x belongs to c_0 and c_1, respectively.

As in the MAP, the conditional probability distributions are constructed using training data, where the true positives are instances of c_1 and the true negatives are instances of c_0.

2.5. TRACKING ALGORITHM

The average waveforms were smoothed using a low-pass filter with Gaussian kernel to reduce the high frequency components that result from the short recording duration. Each unit profile stores instances of the corresponding single unit recorded across days. On a given day, units on an arbitrary channel c are spike

sorted and passed to the feature extraction module. Pairwise dissimilarity vectors are computed between the stored profiles on channel c and the input spike sorted units. A dissimilarity vector is the concatenation of the dissimilarity measures computed over an input unit and a stored profile instance.

A dissimilarity matrix is built using the pairwise dissimilarity vectors between the stored profiles and the spike sorted units. The dissimilarity matrix is then input to the tracking classifier to build a membership matrix, where each cell indicates whether a single unit from an input is another instance of a stored profile. **Figure 3** illustrates the structure of a waveform-based classifier.

Denote the set of profiles stored on channel c as P_c, the set of spike sorted input units on channel c as U_c, the dissimilarity between the ith profile and the jth unit as $Dis(P_{c,i}, U_{c,j})$, and the membership of the jth unit to the ith profile as $Mem(P_{c,i}, U_{c,j})$.

Assume there are m stored profiles on c, and n spike sorted units on day x. The dissimilarity matrix is formed as:

$$DisMat_c(P, U) = \begin{bmatrix} Dis(P_{c,1}, U_{c,1}) & \dots & Dis(P_{c,1}, U_{c,n}) \\ \vdots & \ddots & \vdots \\ Dis(P_{c,m}, U_{c,1}) & \dots & Dis(P_{c,m}, U_{c,n}) \end{bmatrix}$$

And the membership matrix is:

$$MemMat_c(P, U) = \begin{bmatrix} Mem(P_{c,1}, U_{c,1}) & \dots & Mem(P_{c,1}, U_{c,n}) \\ \vdots & \ddots & \vdots \\ Mem(P_{c,m}, U_{c,1}) & \dots & Mem(P_{c,m}, U_{c,n}) \end{bmatrix}$$

Finally, the relationship between the dissimilarity and membership matrices can be modeled as:

$$DisMat_c(P, U) \Rightarrow \text{TrackingClassifier} \Rightarrow MemMat_c(P, U) \quad (8)$$

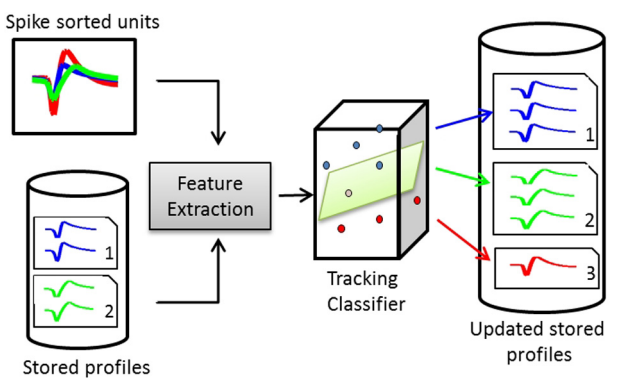

FIGURE 3 | Structure of a waveform-based classifier. On day x, the spike-sorted units of channel c are compared to the stored profiles on the same channel. Pairwise dissimilarity vectors are calculated from features extracted from pairs of waveforms. The tracking classifier makes the decision on whether to add the units to existing profiles or create new profiles for them.

Units are added as instances of the profiles to which they belong. If a new unit is identified, a new profile is initialized and the unit instance is added to it. A profile is composed of all the recorded instances of the single unit it represents. When an input unit is compared to a profile to make the decision as to whether the unit is another instance of the profile, the tracking classifier decides which profile instance (i.e., from which day) to use in such comparison. We developed two techniques—the "**First Matching Dissimilarity (FMD)**" and the "**Maximum Matching Dissimilarity (MMD)**" that use a "stability window" of 7 days based on results in Dickey et al. (2009).

1. **First Matching Dissimilarity (FMD)**: In this technique, the most recent seven instances in a profile during the stability window are used in the comparison, from newest to oldest. Once the tracking classifier indicates that a profile instance and the unit are recorded from the same single unit (a match), the comparison stops and this instance is used for dissimilarity vector calculations.
2. **Maximum Matching Dissimilarity (MMD)**: In this technique, the comparison is performed based on all the profile instances that occurred within the stability window. The dissimilarity vector resulting from this comparison is the dissimilarity between the unit and the profile instance *closest* to it in terms of the distance to the decision boundary.

The intuition behind the two techniques is to tolerate units that undergo some minor instability for a short period of time, for example due to noise from the electronic circuitry used in recording on a given day, and then return to their stable state. We also defined two classes of profiles: *active* and *inactive*. Active profiles are those profiles whose single units have been recorded on any day within the stability window. Inactive profiles, on the other hand, are those profiles whose units did not appear in the recording on all days during the stability window, in which case we consider them "*dropped units*" and are not included in future comparisons.

Training each classifier results in a membership matrix, where each cell in this matrix indicates whether an input unit on a given day should be added to a stored profile. In some cases, the classifier might indicate that the input unit can be added to more than one profile, for example because of misclassifications in the spike sorting algorithm. A putative single-unit, however, can only be added to one profile. Therefore, we developed a back-tracking algorithm to find the best assignment of input single units to existing profiles. Back-tracking is a standard general algorithm for finding all the possible solutions to a problem and then selecting one that most satisfies a set of user-defined objectives (Cormen et al., 2001). In our case, the objectives were as follows:

- **Primary objective**: Maximize the number of assigned units to already existing stored profiles.
- **Secondary objective**: Maximize the total sum of distances to the decision boundary of the assigned units, since the larger the distance to the boundary, the more certain the decision of the tracking classifier is.

Algorithm 1 | Tracking algorithm.

Input: Signal recorded on all channels, database of stored single unit profiles
Output: Updated database of stored single unit profiles
for each channel c **do**
Spike sort the signal recorded on c
Input the spike sorted units to the tracking module
Compute distance vectors between each of the input units and the stored profiles associated with c
Using the distance vectors computed, build a membership matrix between the input units and the stored profiles on c using the tracking classifier
Using back-tracking, generate all possible assignments of the input units to existing profiles
Select the assignment that maximizes the number of assigned units to existing profiles
Create new profiles for unassigned units
end for

This way, the back-tracking algorithm finds the membership matrix $MemMat_c^*(P, U)$ that meets both the primary and secondary objectives while assigning every input unit to one and only one database profile. This means that if two unit assignment solutions have the same number of units assigned to existing profiles, the one with a larger sum of distances to the decision boundary is selected. The relationship between the different data matrices can be modeled as:

$$DisMat_c(P, U) \Rightarrow \text{TrackingClassifier} \Rightarrow MemMat_c(P, U) \Rightarrow \text{Backtracking} \Rightarrow MemMat_c^*(P, U) \quad (9)$$

The tracking algorithm is summarized in Algorithm 1

2.6. DATA ACQUISITION AND BEHAVIORAL TASK

Recordings were obtained using a 96-microelectrode silicon array (Blackrock Microsystems, Inc., Salt Lake City, UT) chronically implanted in the primary motor cortex (M1) of a rhesus macaque (Macaca mulatta). The first recording used in this study was made three months after the implant. The surgical and behavioral procedures of this study were approved by the University of Chicago Institutional Animal Care and Use Committee and conform to the principles outlined in the Guide for the Care and Use of Laboratory Animals. Spike sorting was done using the Cerebus® Online Sorter (Blackrock microsystems, UT) and the sorting templates were updated on a daily basis by a human operator.

The subject performed a brain-controlled reach-to-grasp task. Details of the behavioral task can be found in Balasubramanian et al. (2013). Fifteen datasets, spanning a period of 26 days, were used in training (seven datasets) and testing (eight datasets) the tracking algorithm. We used only the first 15 min of each dataset, which is equivalent to the period of updating the spike sorting templates while the subject is not engaged in any behavioral task. For execution time measurements, we used an Intel-i7 quad-core processor (3.40 GHz) and 16 GB of RAM.

2.7. TRACKING ALGORITHM EVALUATION

The performance of the tracking algorithm was assessed based on two metrics:

1. **Classification Accuracy**: The percentage of correct classification made on a day-to-day basis compared to manual tracking. A correct classification happens when a unit on day x is matched with the correct putative single-unit profile on day $x - 1$.
2. **Percentage of Correct Profiles**: The percentage of profiles that were correctly tracked across all days of the testing datasets compared to manual tracking. A correct profile is a profile that has exactly the same single-unit instances as in the corresponding manually tracked profile across all days.

Classifier implementations were provided by the **newfolder library** (Torrione et al., 2011). We used a radial basis function as the kernel for the SVM and RVM classifiers where the Gaussian kernel sigma was set to the square root of the number of features. The slack variable of the SVM classifer was defaulted to 1. We compared the performance of the classifiers using four different sets of features:

- **Set 1**: 4 waveform-based features (PC, PH, PT, PM) and 4 ISIH-based features (KLD, BD, KS, EMD).
- **Set 2**: 3 waveform-based features (PH, PT, PM) and 3 ISIH-based features (KLD, BD, KS).
- **Set 3**: 3 ISIH-based features (KLD, BD, KS).
- **Set 4**: 3 waveform-based features (PH, PT, PM).

Performing validation was challenging because the calendar-day order of the datasets had to be maintained. This is because changes in the characteristics of a single unit might be small over two successive datasets (calendar-days) but much larger across datasets with longer time separation. We distributed the fifteen datasets (see section 2.6) into six validation datasets. Each validation dataset was divided into five training datasets and five testing datasets. The first validation dataset contained datasets 1–10, the second validation datasets contained datasets 2–11, and so on.

3. RESULTS

3.1. TRAINING FEATURES

Figures 4, **5** show the distributions of the waveform- and ISIH-based dissimilarity measures applied to the TP and TN training datasets. We found a variable degree of separability between the distributions provided by each of the features selected. For example, while the peak matching distance provided the best separability between matching and non-matching waveforms, the other three waveform-based dissimilarity measures did not provide sufficient separation between classes, except in regions where it was very clear that there is a significant difference in the amplitude or time between peaks. The inclusion of the other features, however, was necessary to account for cases when two waveforms had very similar peak shapes, but significantly different amplitude- or time-between-peaks, which occurred frequently in our data (see **Figure 6**).

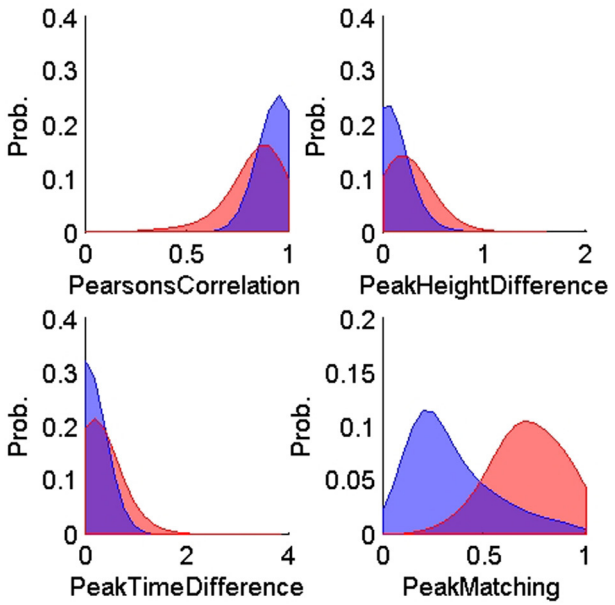

FIGURE 4 | Probability distributions of the training true positives ($n = 900$, blue) and true negatives ($n = 600$, red) for each of the four waveform-based dissimilarity measures: Pearson correlation's, peak-to-peak height difference, peak-to-peak time difference, and peak matching. The training data was obtained using human expert judgment. The peak matching provided the best separability between matching and non-matching waveforms.

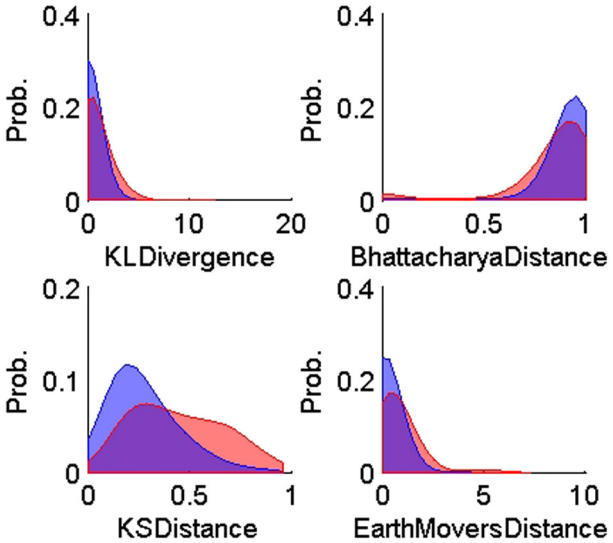

FIGURE 5 | Probability distributions of the training TP ($n = 900$, blue) and TN ($n = 600$, red) for each of the four ISIH-based dissimilarity measures: KL-divergence, Bhattacharya distance, KS-distance, and Earth Mover's distance. The training data was obtained using human expert judgment. All ISIH-based dissimilarity measures did not provide enough separation between matching and non-matching ISIH.

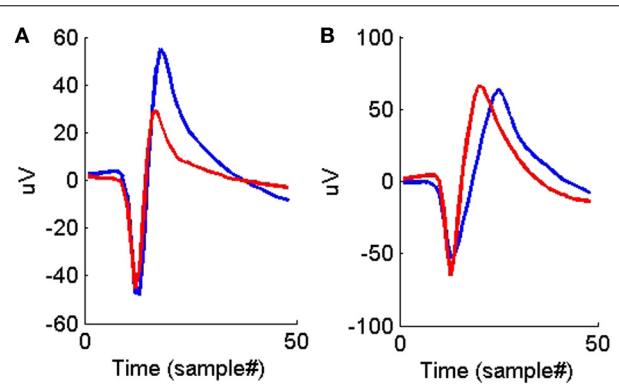

FIGURE 6 | (A) An example of two average waveforms that have very similar peak shapes but different peak-to-peak heights. **(B)** An example of two average waveforms that have very similar peak shapes but different peak-to-peak times.

On the other hand, all the ISIH-based dissimilarity measures did not provide the same degree of separation between classes that was provided by the peak matching. However, their inclusion as features was necessary to account for cases where the waveform shapes of two unit instances had subtle variability but their firing properties remain similar (see **Figure 7**).

3.2. CLASSIFIERS EVALUATION

Figure 8 compares the tracking algorithm performance for the testing datasets using the four feature sets and using the two techniques proposed: FMD and MMD. A Two-way ANOVA test revealed effects by both the type of classifier used ($p < 0.01$) and the feature set used ($p < 0.01$). It is noticeable from **Figure 8** that both the NB and MAP classifiers perform substantially worse than both the RVM and SVM classifiers. We performed another Two-way ANOVA test using **only** RVM and SVM data and it revealed an effect by the feature set used ($p < 0.01$) with no effect caused by the classifier used ($p < 0.7$). It is also noticeable from **Figure 8** that feature sets 1,2, and 4 provide better tracking than feature set 3. Finally, we performed a Three-way ANOVA test to determine which tracking strategy achieves a higher performance (FMD or MMD). The test showed that both strategies performed very similarly ($p < 0.95$). Execution times were similar for different classifiers. Feature set 1 had the largest execution time, which is expected because of the larger number of features used.

We then compared the receiver operating characteristics (ROC) of the four classifiers by computing the area under the curve (AUC) when using each of the four feature sets. A Two-way ANOVA test showed that there was no effect by the type of classifier used ($p < 0.03$). Note that although there was a significant difference in the performance of the classifiers, they had similar ROC curves. The reason behind this is that the ROC curve measures only a classifier's performance in deciding whether two single-units are a possible match, while the calculation of the accuracy of the tracking algorithm measures also the performance of the additional back-tracking step post-processing. **Figure 9** shows the ROC curves of the four classifiers using the four feature sets when trained on all seven training datasets. We also assessed the ROC for an RVM classifier trained by randomly shuffling the

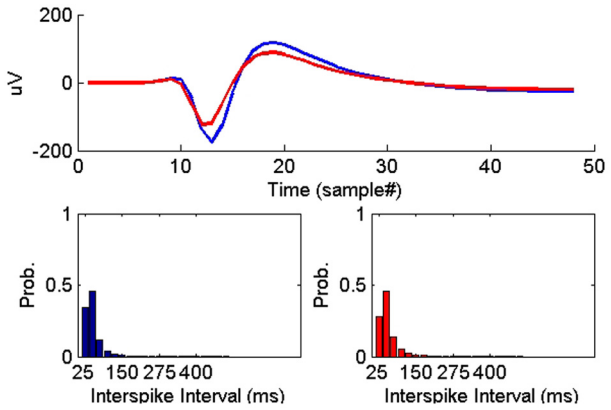

FIGURE 7 | Example of two instances of a single-unit on two successive days where the average waveform experienced subtle change while the ISIHs remained similar.

labels of the training datasets and repeating the process 100 times to establish chance level.

We then examined the tracking algorithm performance when tested on additional datasets. **Tables 3**, **4** list the performance of the tracking algorithm using different classifiers in terms of percentage correct classification and percentage of correct profiles tracked when trained and tested using all 15 datasets described in section 2.6 (i.e., without partitioning). Similarly, the RVM and SVM classifiers performed much better than the NB and MAP classifiers. The RVM classifier was our choice for subsequent analysis due to its advantages of combining the SVM features with probabilistic classification. **Figure 10** illustrates two single-unit profiles that were successfully tracked by the RVM classifier.

We also found that the MMD approach had higher average execution time per channel than the FMD due to the additional number of comparisons the algorithm has to perform to find the closest matching unit within the "stability window." On the other hand, **Tables 3**, **4** indicated that the MMD approach had slightly higher classification accuracy than the FMD because it was designed to find the closest match to the new unit. The MMD approach was therefore the choice for the remainder of the analysis.

We then investigated the trade-off between algorithm speed and accuracy (as listed in **Tables 3–5**). Feature set 1 achieved the highest performance but at the expense of longer execution time on average. On the other hand, feature set 4 had a shorter execution time than feature set 1 but at the expense of lower accuracy (second highest accuracy among the four feature sets). However, the benefit of using feature set 4 is greater than that of using feature set 1, since the drop in accuracy is negligible (1% drop) compared to the large increase in average execution time per channel (17% increase). Therefore, we used feature set 4 for further analysis.

Figure 11 shows that the average execution time per channel increases as more datasets are included on subsequent days of recording until it reaches a plateau. This is expected because generally new units are unlikely to appear as time increases post implant, and thus the number of active profiles remains steady after the initial period has passed. Furthermore, the larger variation in the average execution time per channel in early recording sessions can be attributed to the lower number of comparisons made, which is in turn caused by the small number of instances in each profile and the small number of profiles created. Profiles inactive for a long time (>seven datasets) were dropped and were not included in the tracking.

4. DISCUSSION

Stability of neuronal signals has been traditionally assessed by visual inspection of the similarity between units' waveforms to average waveforms from datasets collected across multiple days of recording (Rousche and Normann, 1998; Nicolelis et al., 2003; Carmena et al., 2005; Linderman et al., 2006; Chestek et al., 2007; Ganguly and Carmena, 2009). Few studies, however, have attempted to develop automated, quantitative solutions to the unit-stability tracking problem. Jackson and Fetz (2007) devised an approach to track units using the peak of the normalized cross-correlation between average spike waveforms. They reported that 80% of the stable units had correlation values of >0.95 across days. Suner et al. (2005) compared the signals recorded on the same channel across days by comparing the centers of clusters in the principal components space and used a Kolmogorov-Smirnov statistic between inter-spike intervals histograms of the formed clusters to ascertain their stability.

Tolias et al. (2007) determined the null distribution of pairwise distances between pairs of average waveforms by comparing signals before and after adjusting the depth of movable tetrodes. This distribution was then used to train a classifier that tracks the stability of single-units. The method, however, is inapplicable in the case of a fixed electrode array.

Dickey et al. (2009) trained a classifier on features extracted from both the unit's average waveform and ISIH. The authors argued that using both the average waveforms and ISIHs resulted in improved accuracy. However, they noted that the use of the ISIH as a stability criterion may not apply when learning is taking place. Furthermore, their method of comparing ISIHs is computationally prohibitive, which makes it unfavorable for BMI applications where the assessment of the single-unit stability from short-duration neural recordings is ultimately desired.

Fraser and Schwartz (2012) used features extracted from functional relations between units, such as pairwise cross correlograms, to track units across days. This method, however, requires the subject to be engaged in a behavioral task and may be susceptible to plasticity-mediated changes in functional connectivity between units as learning progresses.

In this study, we presented an algorithm for automated tracking of multiple single units across many days that addresses most of the aforementioned problems. In particular, it is applicable to recordings from high-channel count microelectrode arrays. Notably, the algorithm requires short-duration neural recordings (15 min) without the need for the subject to be engaged in any behavioral task. The algorithm is not computationally intensive and, therefore, applicable in real time BMI applications.

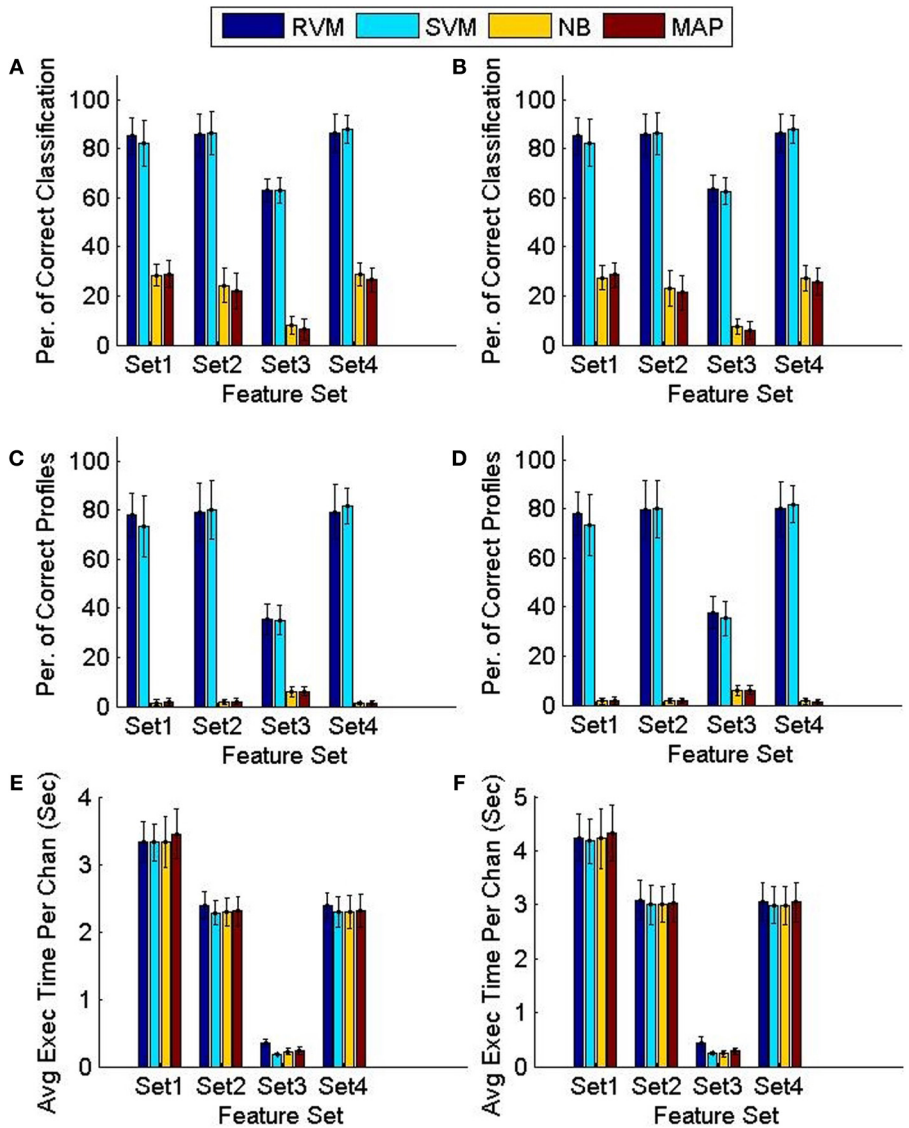

FIGURE 8 | Comparison of the classifiers' performance using the FMD and MMD methods. Four different sets of features were used and the 6 validation datasets were used (each had 5 training datasets and 5 testing datasets). Error bars indicate the standard deviation ($n = 6$). Panels **(A,C,E)** show the performance of the FMD, while Panels **(B,D,F)** show the performance of the MMD. Using a Two-way ANOVA test, the RVM and SVM were found to perform significantly better than the NB and MAP ($p < 0.01$) and that feature set 3 is worse than all other feature sets ($p < 0.01$).

We compared the tracking algorithm accuracy when four classifiers were used: RVM, SVM, MAP, and NB. Both RVM and SVM were superior to MAP and NB and there were no statistically significant differences between their results. We recommend the use of RVM since it combines the advantages of SVM with the notion of a probabilistic classifier and in our experience it constantly provided good tracking results.

We also compared model performance across four different cases of input feature sets based on waveform features and firing characteristics. We also proposed a technique to boost the performance of the tracking algorithm by comparing newly recorded single-units to multiple instances of a putative single-unit from its stored profile across days and selecting the closest instance to the new unit. When the algorithm was tested on eight datasets (corresponding to 16 consecutive calendar-days), this strategy resulted in a classification accuracy of ∼91% when using all the features (feature set 1), and ∼90% when using only ∼37% of the features (feature set 4). Additionally, 82 and 77% of the profiles tracked by the algorithm matched the experts' manual tracking using feature set 1 and feature set 4, respectively. The average execution time was short and converged to ∼12 s per channel after ∼45 data sets (with feature set 1 in use), though can be further reduced to ∼8 s per channel at a slightly lower accuracy (with feature set 4 in use). Thus, as more recordings accumulate across days, the process gets less demanding and can be executed more rapidly. The poorest performance was obtained when we used the ISIH-based

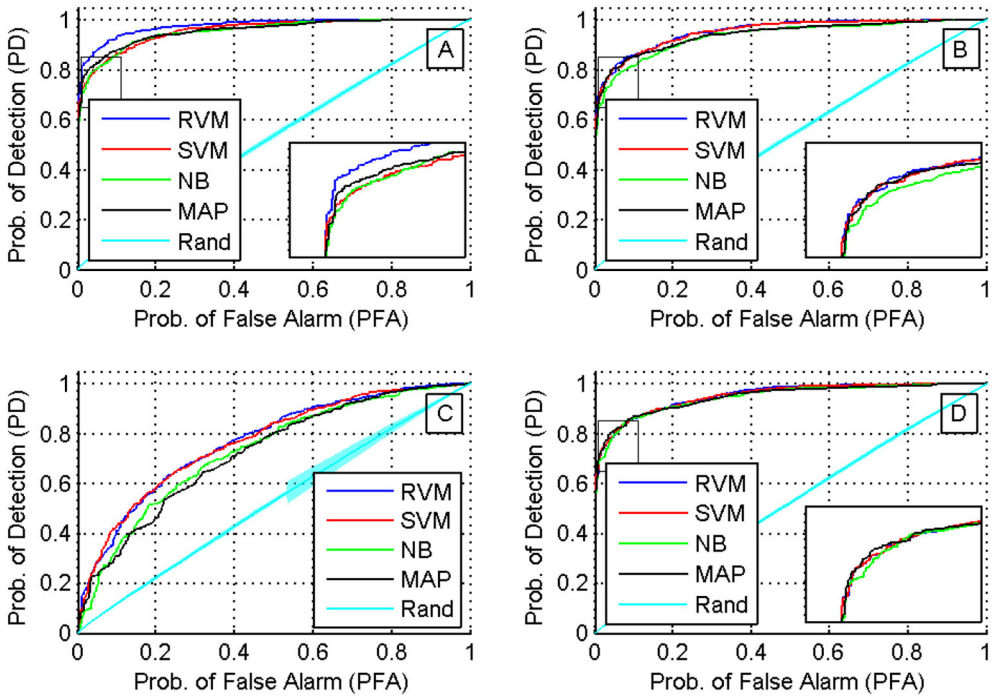

FIGURE 9 | ROC curves for different classifiers using different feature sets (sets 1 through 4 are shown in subfigures (A–D), respectively). A Two-way ANOVA test on the AUC showed that there was no effect by the type of classifier used ($p < 0.03$).

Table 3 | Comparison between the classifiers' performance using the Classification Accuracy when FMD and MMD were used.

Set/class	RVM		SVM		NB		MAP	
Strategy	**FMD**	**MMD**	**FMD**	**MMD**	**FMD**	**MMD**	**FMD**	**MMD**
Set 1	90.51	91.67	87.44	88.05	51.26	50.98	50.85	52.28
Set 2	89.14	89.89	88.05	88.32	48.94	49.01	48.12	47.50
Set 3	61.16	62.11	61.92	67.84	22.45	22.45	16.65	16.99
Set 4	89.62	90.30	89.41	89.55	51.67	49.07	52.76	52.15

All of the 7 training datasets and 8 testing datasets were used to evaluate the classifiers over a longer duration of time. The results show that the performance didn't deteriorate significantly. MMD performed better than FMD in almost all the cases but with no statistical significance.

Table 4 | Comparison between the classifiers' performance using the Percentage of Correct Profiles when FMD and MMD were used.

Set/class	RVM		SVM		NB		MAP	
Strategy	**FMD**	**MMD**	**FMD**	**MMD**	**FMD**	**MMD**	**FMD**	**MMD**
Set 1	78.34	82.67	73.62	74.80	2.75	3.14	1.96	2.36
Set 2	74.01	75.98	72.83	74.80	3.14	3.14	3.54	2.75
Set 3	20.47	26.37	15.74	29.92	5.90	5.11	5.51	5.90
Set 4	75.98	77.16	77.16	75.19	1.96	1.57	2.36	1.57

All of the 7 training datasets and 8 testing datasets were used to evaluate the classifiers over a longer duration of time. The results show that the performance did not deteriorate significantly. MMD performed better than FMD in almost all the cases but with no statistical significance.

features only. The results show that adding the ISIH-based features can help improve the performance but cannot successfully track single units on their own. This can be explained by the fact that subjects were not over-trained on the Brain-control task, and thus single units' firing characteristics were largely variable during the learning phase (Hikosaka et al., 2002). Given the speed-accuracy tradeoff, we suggest using feature set 4 which includes a subset of waveform-based dissimilarity measures: normalized

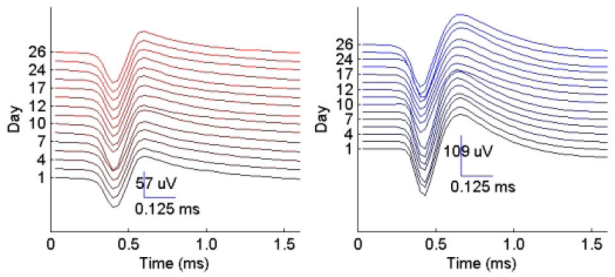

FIGURE 10 | Example of two single-unit profiles tracked by the RVM classifier across 15 datasets spanning a period of 26 days.

Table 5 | Average execution time per channel when the RVM was used to track 15 datasets.

Feature set	1	2	3	4
Time (s)	5.24	4.03	0.62	4.48

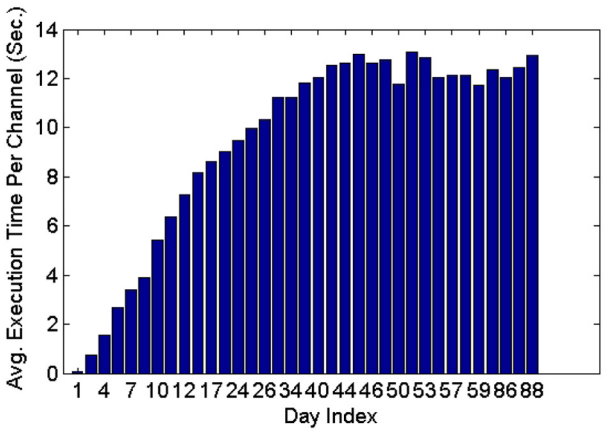

FIGURE 11 | Average execution time per channel when feature set 4, the RVM classifier and the MMD method were used. The classifier was applied on 35 datasets spanning 88 days.

peak-to-peak height difference, normalized peak-to-peak time difference, and peak matching. In addition, using feature set 4 minimizes the adverse effect that variable ISIHs may have on performance.

Our algorithm is based on one generic classifier that is used for all channels. However, different channels may have different characteristics. For example, units may vary on one (or more) channel more than others. A human expert can capture the extent of variability of a specific channel across days, while an automated method cannot because some training samples might be outliers. One possible improvement in such case is to perform a two-level classification paradigm. In this paradigm, a custom classifier for each channel is trained using features extracted from this channel's units only.

It is noteworthy that the single-unit stability tracking problem can be postulated as a Graph Matching or a Graph Cut problem (Cormen et al., 2001). In particular, a node in the graph would represent each single-unit occurrence on a given day, and the edges between nodes would represent the dissimilarity measure between the single-units appearing on two different days. A graph matching procedure that matches single-units across two different days is equivalent to Maximum Bipartite Graph Matching (Cormen et al., 2001). Generalizing the tracking problem to more than two recordings requires solving a Graph Partition problem which generally falls in the category of NP-hard problems (Bichot and Siarry, 2013). The algorithm provided in this paper is a fast approximate solution to the single-unit tracking problem.

We note that our algorithm performance was based on spike data sorted online using the spike sorter tool in the Cerebus® software (Blackrock microsystems, UT). Online spike sorters that use the "hoops" method for labeling spikes based on time and amplitude features of the waveforms perform poorer than offline spike sorting algorithms that use more sophisticated feature extraction and clustering techniques, since spike-amplitude instability is known to cause spike detection and sorting errors for such methods (Perge et al., 2013). As such, it is expected that more sophisticated online spike detection (Oweiss, 2010) and sorting techniques (Aghagolzadeh and Oweiss, 2009), particularly those that permit efficient tracking using simple methods (Aghagolzadeh et al., 2013) would result in an overall performance gain compared to the traditional methods implemented in commercially available systems.

The proposed technique may also improve the clinical viability of BMI systems in a patient's home settings. If single units can be autonomously, accurately and rapidly tracked across days without much supervision from a caregiver, this would ease its use, and would facilitate maintaining a fixed mapping between the neural input space and the decoded output, which may likely increase the utility of the BMIs over the long term.

Finally, the application of the technique may extend well beyond ensuring that a stable BMI is maintained over days. In particular, studies of learning that aim to elucidate neural mechanisms of plasticity at the cellular and population levels *in vivo* can significantly benefit from the proposed approach. These studies, however, are in their infancy, primarily due to the inability to validate unit identity in intermittent extracellular recording sessions across multiple days. As such, it is often assumed that units recorded on a given day are not the same as the ones recorded on other days, which "artificially inflates" the unit sample size. With technological advances that lead to ever increasing number of electrodes, the approach provides a novel framework to streamline the process over consecutive days that can help assess learning-induced plasticity in local and distributed neural circuits.

In conclusion, we proposed a technique that could substantially alleviate the burden on the caregiver as well as the patient in a clinical BMI setting. By automating the tracking of multiple single-units across many days of recordings from high-channel-count microelectrode arrays, we're essentially maximizing the likelihood of maintaining a fixed mapping between the neural input space and the decoded output, which in turn may accelerate

BMI learning and reduce the cognitive load on the patient side. This may improve the clinical viability and rapid adoption of BMI systems in home settings by end users.

ACKNOWLEDGMENT

This work was supported by NIH-NINDS grant# NS062031 and DARPA grant# N66 001-12-1-4023.

REFERENCES

Aghagolzadeh, M., Mohebi, A., and Oweiss, K. (2013). Sorting and tracking neuronal spikes via simple thresholding. *Neural Syst. Rehabil. Eng. IEEE Trans.* doi: 10.1109/TNSRE.2013.2289918. [Epub ahead of print].

Aghagolzadeh, M., and Oweiss, K. (2009). Compressed and distributed sensing of neuronal activity for real time spike train decoding. *Neural Syst. Rehabil. Eng. IEEE Trans.* 17, 116–127. doi: 10.1109/TNSRE.2009.2012711

Balasubramanian, K., Southerland, J., Vaidya, M., Qian, K., Eleryan, A., Fagg, A. H., et al. (2013). "Operant conditioning of a multiple degree-of-freedom brain-machine interface in a primate model of amputation," in *Engineering in Medicine and Biology Society (EMBC), 2013 35th Annual International Conference of the IEEE* (New York, NY), 303–306. doi: 10.1109/EMBC.2013.6609497

Bhattacharyya, A. (1943). On a measure of divergence between two statistical populations defined by their probability distributions. *Bull. Calcutta Math. Soc.* 35, 4.

Bichot, C.-E., and Siarry, P. (2013). *Graph Partitioning*. New York, NY: John Wiley & Sons.

Bishop, C. M. (2006). *Pattern Recognition and Machine Learning*, Vol. 1. New York, NY: Springer.

Buzsáki, G. (2004). Large-scale recording of neuronal ensembles. *Nat. Neurosci.* 7, 446–451. doi: 10.1038/nn1233

Carmena, J. M., Lebedev, M. A., Henriquez, C. S., and Nicolelis, M. A. (2005). Stable ensemble performance with single-neuron variability during reaching movements in primates. *J. Neurosci.* 25, 10712–10716. doi: 10.1523/JNEUROSCI.2772-05.2005

Chen, D., and Fetz, E. E. (2005). Characteristic membrane potential trajectories in primate sensorimotor cortex neurons recorded *in vivo*. *J. Neurophysiol.* 94, 2713–2725. doi: 10.1152/jn.00024.2005

Chestek, C. A., Batista, A. P., Santhanam, G., Byron, M. Y., Afshar, A., Cunningham, J. P., et al. (2007). Single-neuron stability during repeated reaching in macaque premotor cortex. *J. Neurosci.* 27, 10742–10750. doi: 10.1523/JNEUROSCI.0959-07.2007

Cormen, T. H., Leiserson, C. E., Rivest, R. L., and Stein C. (2001). *Introduction to Algorithms*, Vol. 2, Cambridge: MIT press.

Dickey, A. S., Suminski, A., Amit, Y., and Hatsopoulos, N. G. (2009). Single-unit stability using chronically implanted multielectrode arrays. *J. Neurophysiol.* 102, 1331. doi: 10.1152/jn.90920.2008

Domingos, P., and Pazzani, M. (1997). On the optimality of the simple bayesian classifier under zero-one loss. *Mach. Learn.* 29, 103–130. doi: 10.1023/A:1007413511361

Fraser, G. W., and Schwartz, A. B. (2012). Recording from the same neurons chronically in motor cortex. *J. Neurophysiol.* 107, 1970. doi: 10.1152/jn.01012.2010

Ganguly, K., and Carmena, J. M. (2009). Emergence of a stable cortical map for neuroprosthetic control. *PLoS Biol.* 7:e1000153. doi: 10.1371/journal.pbio.1000153

Ganguly, K., and Carmena, J. M. (2010). Neural correlates of skill acquisition with a cortical brain–machine interface. *J. Mot. Behav.* 42, 355–360. doi: 10.1080/00222895.2010.526457

Gürel, T., and Mehring, C. (2012). Unsupervised adaptation of brain-machine interface decoders. *Front. Neurosci.* 6:164. doi: 10.3389/fnins.2012.00164

Hikosaka, O., Nakamura, K., Sakai, K., and Nakahara, H. (2002). Central mechanisms of motor skill learning. *Curr. Opin. Neurobiol.* 12, 217–222. doi: 10.1016/S0959-4388(02)00307-0

Hochberg, L. R., Bacher, D., Jarosiewicz, B., Masse, N. Y., Simeral, J. D., Vogel, J., et al. (2012). Reach and grasp by people with tetraplegia using a neurally controlled robotic arm. *Nature* 485, 372–375. doi: 10.1038/nature11076

Homer, M. L., Nurmikko, A. V., Donoghue, J. P., and Hochberg, L. R. (2013). Sensors and decoding for intracortical brain computer interfaces. *Ann. Rev. Biomed. Eng.* 15, 383–405. doi: 10.1146/annurev-bioeng-071910-124640

Jackson, A., and Fetz, E. E. (2007). Compact movable microwire array for long-term chronic unit recording in cerebral cortex of primates. *J. Neurophysiol.* 98, 3109. doi: 10.1152/jn.00569.2007

Johnson, D., and Sinanovic, S. (2001). *Symmetrizing The Kullback-Leibler Distance*. Technical Report, Rice University.

Karumbaiah, L., Saxena, T., Carlson, D., Patil, K., Patkar, R., Gaupp, E. A., et al. (2013). Relationship between intracortical electrode design and chronic recording function. *Biomaterials* 34, 8061–8074. doi: 10.1016/j.biomaterials.2013.07.016

Kim, S.-P., Simeral, J. D., Hochberg, L. R., Donoghue, J. P., and Black, M. J. (2008). Neural control of computer cursor velocity by decoding motor cortical spiking activity in humans with tetraplegia. *J. Neural Eng.* 5, 455. doi: 10.1088/1741-2560/5/4/010

Koyama, S., Chase, S. M., Whitford, A. S., Velliste, M., Schwartz, A. B., and Kass, R. E. (2010). Comparison of brain–computer interface decoding algorithms in open-loop and closed-loop control. *J. Comput. Neurosci.* 29, 73–87. doi: 10.1007/s10827-009-0196-9

Kullback, S., and Leibler, R. A. (1951). On information and sufficiency. *Ann. Math. Stat.* 22, 79–86.

Linderman, M. D., Gilja, V., Santhanam, G., Afshar, A., Ryu, S., Meng, T. H., et al. (2006). "Neural recording stability of chronic electrode arrays in freely behaving primates," in *Engineering in Medicine and Biology Society, 2006. EMBS'06. 28th Annual International Conference of the IEEE* (New York, NY), 4387–4391.

Liu, X., McCreery, D. B., Carter, R. R., Bullara, L. A., Yuen, T. G., and Agnew, W. F. (1999). Stability of the interface between neural tissue and chronically implanted intracortical microelectrodes. *Rehabil. Eng. IEEE Trans.* 7, 315–326. doi: 10.1109/86.788468

Manning, C. D., Raghavan, P., and Schütze, H. (2008). *Introduction to Information Retrieval*, Vol. 1, Cambridge: Cambridge university press. doi: 10.1017/CBO9780511809071

Nicolelis, M. A., Dimitrov, D., Carmena, J. M., Crist, R., Lehew, G., Kralik, J. D., et al. (2003). Chronic, multisite, multielectrode recordings in macaque monkeys. *Proc. Natl. Acad. Sci. U.S.A.* 100, 11041–11046. doi: 10.1073/pnas.1934665100

Nikolić, D., Mureşan, R. C., Feng, W., and Singer, W. (2012). Scaled correlation analysis: a better way to compute a cross-correlogram. *Eur. J. Neurosci.* 35, 742–762. doi: 10.1111/j.1460-9568.2011.07987.x

Oweiss, K. G. (2010). *Statistical Signal Processing for Neuroscience and Neurotechnology*. Academic Press.

Perge, J. A., Homer, M. L., Malik, W. Q., Cash, S., Eskandar, E., Friehs, G., et al. (2013). Intra-day signal instabilities affect decoding performance in an intracortical neural interface system. *J. Neural Eng.* 10, 036004. doi: 10.1088/1741-2560/10/3/036004

Rousche, P. J., and Normann, R. A. (1998). Chronic recording capability of the utah intracortical electrode array in cat sensory cortex. *J. Neurosci. Methods* 82, 1–15. doi: 10.1016/S0165-0270(98)00031-4

Rubner, Y., Tomasi, C., and Guibas, L. J. (1998). "A metric for distributions with applications to image databases," in *Computer Vision, 1998. Sixth International Conference on* (New York, NY), 59–66.

Serruya, M. D., Hatsopoulos, N. G., Paninski, L., Fellows, M. R., and Donoghue, J. P. (2002). Brain-machine interface: instant neural control of a movement signal. *Nature* 416, 141–142. doi: 10.1038/416141a

Strelkov, V. (2008). A new similarity measure for histogram comparison and its application in time series analysis. *Patt. Recogn. Lett.* 29, 1768–1774. doi: 10.1016/j.patrec.2008.05.002

Suminski, A. J., Tkach, D. C., Fagg, A. H., and Hatsopoulos, N. G. (2010). Incorporating feedback from multiple sensory modalities enhances brain–machine interface control. *J. Neurosci.* 30, 16777–16787. doi: 10.1523/JNEUROSCI.3967-10.2010

Suner, S., Fellows, M. R., Vargas-Irwin, C., Nakata, G. K., and Donoghue, J. P. (2005). Reliability of signals from a chronically implanted, silicon-based electrode array in non-human primate primary motor cortex. *Neural Syst. Rehabil. Eng. IEEE Trans.* 13, 524–541. doi: 10.1109/TNSRE.2005.857687

Tolias, A. S., Ecker, A. S., Siapas, A. G., Hoenselaar, A., Keliris, G. A., and Logothetis, N. K. (2007). Recording chronically from the same neurons in awake, behaving primates. *J. Neurophysiol.* 98, 3780–3790. doi: 10.1152/jn.00260.2007

Torrione, P., Keene, S., and Morton, K. (2011). *PRT: The Pattern Recognition Toolbox for MATLAB*. Available online at: http://newfolderconsulting.com/prt.

Velliste, M., Perel, S., Spalding, M. C., Whitford, A. S., and Schwartz, A. B. (2008). Cortical control of a prosthetic arm for self-feeding. *Nature* 453, 1098–1101. doi: 10.1038/nature06996

Conflict of Interest Statement: The authors declare that the research was conducted in the absence of any commercial or financial relationships that could be construed as a potential conflict of interest.

Received: 11 March 2014; accepted: 17 June 2014; published online: 08 July 2014.
Citation: Eleryan A, Vaidya M, Southerland J, Badreldin IS, Balasubramanian K, Fagg AH, Hatsopoulos N and Oweiss K (2014) Tracking single units in chronic, large scale, neural recordings for brain machine interface applications. Front. Neuroeng. ***7****:23. doi: 10.3389/fneng.2014.00023*
This article was submitted to the journal Frontiers in Neuroengineering.

suggested by Löffler et al. (2012). Another field of needed improvement is the electrical connection of the probe to the periphery in response to wound closure procedures and probe specifications. However, for our histological study tethering by super glue (Loctite) proved sufficient. We were thus able to demonstrate with a simple method the repeatable implantation of these flexible electrodes to deep brain areas of rats.

ACKNOWLEDGMENTS

We acknowledge the partial funding by the Graduate School for Computing in Medicine and Life Sciences [DFG GSC 235/1]. This study was additionally supported by the German Research Ministry project "BiCIRTS"-13N9190, grants of the European Union (European Fund for regional development (EFRE)) and by the Business Development and Technology Transfer Corporation of Schleswig-Holstein (WTSH).

SUPPLEMENTARY MATERIAL

The Supplementary Material for this article can be found online at: http://figshare.com/articles/Implant_of_flexible_probes_Supplemental/703574

REFERENCES

Andrei, A., Tutunjyan, N., Verbinnen, G., VanPut, S., Krylychkina, O., Eberle, W., et al. (2012). Fabrication and successful *in-vivo* implantation of a flexible neural implant with a hybrid polyimide-silicon design Int. *Conf. Proc. IEEE Eng. Med. Biol. Soc.* 2012, 3890–3893. doi: 10.1109/EMBC.2012.6346817

Biran, R., Martin, D. C., and Tresco, P. A. (2007). The brain tissue response to implanted silicon microelectrode arrays is increased when the device is tethered to the skull. *J. Biomed. Mater. Res. A* 82, 169–178. doi: 10.1002/jbm.a.31138

Campbell, P. K., Jones, K. E., Huber, R. J., Horch, K. W., and Normann, R. A. (1991). A silicon based three dimensional neural interface: manufacturing processes for an intracortical electrode array. *IEEE Trans. Biomed. Eng.* 38, 758–768. doi: 10.1109/10.83588

Chen, Z. J., Gillies, G. T., Broaddus, W. C., Prabhu, S. S., Fillmore, H., Mitchell, R. M., et al. (2004). A realistic brain tissue phantom for intraparenchymal infusion studies. *J. Neurosurg.* 101, 314–322. doi: 10.3171/jns.2004.101.2.0314

Hassler, C., Boretius, T., and Stieglitz, T. (2011). Polymers for neural implants. *J. Polym. Sci. B Polym. Phys.* 49, 18–33. doi: 10.1002/polb.22169

Hiller, A., Loeffler, S., Haupt, C., Litza, M., Hofmann, U., and Moser, A. (2007). Electrical high frequency stimulation induces GABA outflow in freely moving rats. *J. Neurosci. Methods* 159, 286–290. doi: 10.1016/j.jneumeth.2006.07.023

Kim, B. J., Kuo, J. T. W., Hara, S. A., Lee, C. D., Yu, L., Gutierrez, C. A., et al. (2013). 3D Parylene sheath neural probe for chronic recordings. *J. Neural Eng.* 10:045002. doi: 10.1088/1741-2560/10/4/045002

Kozai, T. D. Y., and Kipke, D. R. (2009). Insertion shuttle with carboxyl terminated self-assembled monolayer coatings for implanting flexible polymer neural probes in the brain. *J. Neurosci. Methods* 184, 199–205. doi: 10.1016/j.jneumeth.2009.08.002

Leach, J. B., Achyuta, A. K., and Murthy, S. K. (2010). Bridging the divide between neuroprosthetic design, tissue engineering and neurobiology. *Front. Neuroeng.* 2:18. doi: 10.3389/neuro.16.018.2009

Lee, S. E., Jun, S. B., Lee, H. J., Kim, J., Lee, S. W., Im, C., et al. (2012). A flexible depth probe using liquid crystal polymer *IEEE Trans. Biomed. Eng.* 59, 2085–2094. doi: 10.1109/TBME.2012.2196274

Löffler, S., Xie, Y., Detemple, P., Moser, A., and Hofmann, U. G. (2012). An implantation technique for polyimide based flexible array probes facilitating neuronavigation and chronic implantation. *Biomed. Tech.* 57(Suppl. 1), 860–863.

Martens, H. C. F., Toader, E., Decre, M. M. J., Anderson, D. J., Vetter, R., Kipke, D. R., et al. (2010). Spatial steering of deep brain stimulation volumes using a novel lead design. *Clin. Neurophysiol.* 122, 558–566. doi: 10.1016/j.clinph.2010.07.026

McConnell, G. C., Rees, H. D., Levey, A. I., Gutekunst, C. A., Gross, R. E., and Bellamkonda, R. V. (2009). Implanted neural electrodes cause chronic, local inflammation that is correlated with local neurodegeneration. *J. Neural Eng.* 6:056003. doi: 10.1088/1741-2560/6/5/056003

Mercanzini, A., Colin, P., Bensadoun, J. C., Bertsch, A., and Renaud, P. (2009). *In vivo* electrical impedance spectroscopy of tissue reaction to microelectrode arrays. *IEEE Trans. Biomed. Eng.* 56, 1909–1918. doi: 10.1109/TBME.2009.2018457

Pizzolato, G., and Mandat, T. (2012). Deep brain stimulation for movement disorders. *Front. Integr. Neurosci.* 6:2. doi: 10.3389/fnint.2012.00002

Pohl, B. M., Jungmann, J. O., Christ, O., and Hofmann, U. G. (2012). Automated drill-stop by SVM classified audible signals. *Conf. Proc. IEEE Eng. Med. Biol. Soc.* 2012, 956–959. doi: 10.1109/EMBC.2012.6346091

Pohl, B. M., Schumacher A., and Hofmann, U. G. (2011). "Towards an automated, minimal invasive, precision craniotomy on small animals," in *5th Int'l Conf on Neural Eng. Cancun, IEEE EMBS 2011*, 302–305. doi: 10.1109/NER.2011.5910547

Polikov, V. S., Tresco, P. A., and Reichert, W. M. (2005). Response of brain tissue to chronically implanted neural electrodes. *J. Neurosci. Methods* 148, 1–18. doi: 10.1016/j.jneumeth.2005.08.015

Rousche, P. J., and Normann, R. A. (1992). A method for pneumatically inserting an array of penetrating electrodes into cortical tissue. *Ann. Biomed. Eng.* 20, 413–422. doi: 10.1007/BF02368133

Rousche, P. J., Pellinen, D. S., Pivin, D. P. Jr., Williams, J. C., Vetter, R. J., and Kipke, D. R. (2001). Flexible polyimide-based intracortical electrode arrays with bioactive capability. *IEEE Trans. Biomed. Eng.* 48, 361–371. doi: 10.1109/10.914800

Rubehn, B., and Stieglitz, T. (2010). *In vitro* evaluation of the long-term stability of polyimide as a material for neural implants. *Biomaterials* 31, 3449–3458. doi: 10.1016/j.biomaterials.2010.01.053

Schjetnan, A. G., and Luczak, A. (2011). Recording large-scale neuronal ensembles with silicon probes in the anesthetized rat. *J. Vis. Exp.* 56:e3282. doi: 10.3791/3282

Schlapfer, T. E., and Bewernick, B. H. (2009). Deep brain stimulation for psychiatric disorders–state of the art. *Adv. Tech. Stand. Neurosurg.* 34, 37–57. doi: 10.1007/978-3-211-78741-0_2

Stieglitz, T., and Meyer, J. U. (1999). Implantable microsystems. Polyimide-based neuroprostheses for interfacing nerves. *Med. Device Technol.* 10, 28–30.

Szarowski, D. H., Andersen, M. D., Retterer, S., Spence, A. J., and Isaacson, M. (2003). Brain responses to micro-machined silicon devices. *Brain Res.* 983, 23–35. doi: 10.1016/S0006-8993(03)03023-3

Takeuchi, S., Yoshida, Y., Ziegler, D., Mabuchi, K., and Suzuki, T. (2005). Parylene flexible neural probes integrated with microfluidic channels. *Lab. Chip.* 5, 519–523. doi: 10.1039/b417497f

Turner, J. N., Shain, W., Szarowski, D. H., Andersen, M., Martins, S., Isaacson, M. et al. (1999). Cerebral astrocyte response to micromachined silicon implants. *Exp. Neurol.* 156, 33–49. doi: 10.1006/exnr.1998.6983

Williams, D. F. (2008). On the mechanisms of biocompatibility. *Biomaterials* 29, 2941–2953. doi: 10.1016/j.biomaterials.2008.04.023

Conflict of Interest Statement: The authors declare that the research was conducted in the absence of any commercial or financial relationships that could be construed as a potential conflict of interest.

Received: 13 May 2013; paper pending published: 02 June 2013; accepted: 02 July 2013; published online: 24 July 2013. Citation: Richter A, Xie Y, Schumacher A, Loeffler S, Kirch RD, Al-Hasani J, Rapoport DH, Kruse C, Moser A, Tronnier V, Danner S and Hofmann UG (2013) A simple implantation method for flexible, multisite microelectrodes into rat brains. Front. Neuroeng. ***6****:6. doi: 10.3389/fneng.2013.00006*